Fu-Bao Yang
Ji-Ping Huang

Diffusionics

Diffusion Process Controlled by Diffusion Metamaterials

OPEN ACCESS

Springer

Diffusionics

Fu-Bao Yang · Ji-Ping Huang

Diffusionics

Diffusion Process Controlled by Diffusion Metamaterials

Springer

Fu-Bao Yang
Department of Physics
Fudan University
Shanghai, China

Ji-Ping Huang
Department of Physics
Fudan University
Shanghai, China

ISBN 978-981-97-0486-6 ISBN 978-981-97-0487-3 (eBook)
https://doi.org/10.1007/978-981-97-0487-3

This Springer imprint is published by the registered company Springer Nature Singapore Pte Ltd.
The registered company address is: 152 Beach Road, #21-01/04 Gateway East, Singapore 189721, Singapore

Paper in this product is recyclable.

Preface

The concept of thermal cloak was first proposed in 2008 [1, 2]. At that time, scholars developed the steady-state transformation thermotics theory by referring to the transformation optics theory and proposed a new concept of thermal cloak inspired by the concept of optical or electromagnetic [1–3]. The so-called thermal cloak refers to a shell layer wrapped around an object that allows heat flow to bypass the object and propagate forward without interfering with the temperature and heat flow fields in the background.

The concept of thermal cloak was proposed after the concept of acoustic cloak, which was also derived from the concept of optical cloak. Therefore, the birth of the thermal cloak is merely a small extension of the optical cloak to the field of thermal science. However, it is surprising that the thermal cloak has enormous value, which involves two aspects: practical value and academic value. I will describe them separately below.

Regarding the practical value of the thermal cloak, it can be used for infrared thermal protection of underground shelters. Its working mechanism is "guidance," which is entirely distinct from existing protection or camouflage mechanisms that primarily rely on "blocking." So far, due to its groundbreaking military value, the thermal cloak structure has begun to receive special attention and application. In addition, it also has other civilian applications, such as thermal management of printed circuit boards or electronic devices [4].

The academic value of thermal cloak is significant as it has significantly promoted the extension of related scientific concepts. As shown in Fig. 1, diffusion metamaterials originated from thermal cloak. So far, diffusion metamaterials have become an important branch of metamaterials. Its governing equation is the diffusion equation, which can be used to handle pure diffusion and generalized diffusion, such as conduction-convection coupling systems, etc. The emergence of diffusion metamaterials has significantly enriched the research of metamaterial science and engineering because previous research on metamaterials was almost entirely based on wave systems, whose governing equations were wave equations, such as Maxwell's equations, acoustic wave equations, elastic wave equations, etc.

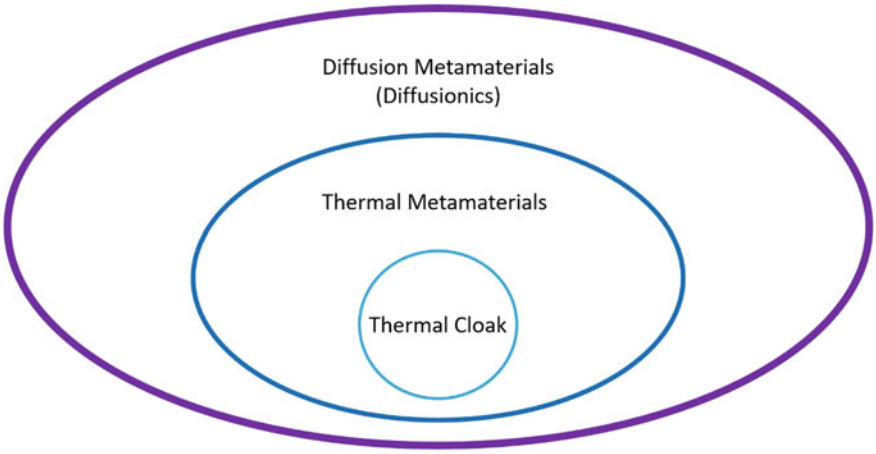

Fig. 1 Extension of the Thermal Cloak Concept: First, from thermal cloak to thermal metamaterials [5]; second, from thermal metamaterials to diffusion metamaterials [6, 7]. Here, diffusion metamaterials are described using transformation theory and extended theories (diffusionics), and they have already served as a newly developed branch of metamaterials; see Section I.B of Ref. [7]

Here, it is important to note that wave and diffusion are two different ways of energy transfer, which are controlled by wave equations and diffusion equations, respectively. In terms of physical mechanisms, they are completely different. This may also be a direct reason why research on diffusion in the field of metamaterials is later than research on waves. For example, before 2008, almost no one realized that the transformation optics theory could also be used to handle heat conduction equations. Indeed, as people have realized today, transformation theory is not omnipotent and cannot handle all equations, such as Navier-Stokes equation. Finally, it's worth adding that there are many classification methods for metamaterials. The method based on governing equations introduced above is just one of them. Additionally, there are methods based on dimension classification, programmability classification, and so on.

In addition, it is necessary to explain that metamaterials (or metadevices, i.e., devices based on metamaterials) are a class of artificial structural materials whose properties are determined by the geometric structure of the component materials, rather than by the intrinsic physical properties of the component materials. The most critical aspect is that they must have a characteristic length, and the size of the structural unit must be much smaller than or less than this characteristic length. At this point, effective medium theory can be used to understand the properties or functions of metamaterials. For example, for thermal metamaterials that control heat conduction, this characteristic length is the (time-dependent yet frequency-independent) thermal diffusion length [8]; for electromagnetic metamaterials that manipulate electromagnetic waves, this characteristic length is the (time-independent yet frequency-dependent) wavelength of the incident electromagnetic wave. In other words, if there is no corresponding characteristic length, effective medium

theory cannot be used to explain or predict their properties or functions. Such materials cannot belong to "metamaterials" [9, 10], such as photonic crystals and other artificial materials.

This book was co-authored by Dr. Fu-Bao Yang and myself. Dr. Yang graduated from my group as a Ph.D. student in June 2023. Currently, he is finalizing some of his work during his doctoral period in my group and preparing for his upcoming postdoctoral position.

All the chapters in this book were independently written by current or former members of my group, and these contents are an integral part of the emerging discipline of diffusionics composed of transformation theory and extended theories. Here, diffusionics represents the fundamental theory for diffusion metamaterials, and also begins to extend beyond the scope of diffusion metamaterials.

Last, we acknowledge the financial support provided by the National Natural Science Foundation of China under Grants No. 12035004 and No. 12320101004, the Science and Technology Commission of Shanghai Municipality under Grant No. 20JC1414700, and the Innovation Program of Shanghai Municipal Education Commission under Grant No. 2023ZKZD06.

Notes: This preface was written by referring to Ref. [11].

Shanghai, China Ji-Ping Huang
October 2023

References

1. Fan, C.Z., Gao, Y., Huang, J.P.: Shaped graded materials with an apparent negative thermal conductivity. Appl. Phys. Lett. **92**, 251907 (2008)
2. Chen, T.Y., Weng, C.N., Chen, J.S.: Cloak for curvilinearly anisotropic media in conduction. Appl. Phys. Lett. **93**, 114103 (2008)
3. Yeung, W.S., Yang, R.J.: Introduction to Thermal Cloaking: Theory and Analysis in Conduction and Convection. Springer, Singapore (2022)
4. Kim, J.C., Ren, Z., Yuksel, A., Dede, E.M., Bandaru, P.R., Oh, D., Lee, J.: Recent advances in thermal metamaterials and their future applications for electronics packaging. J. Electron. Packag. **143**, 010801 (2021)
5. Maldovan, M.: Sound and heat revolutions in phononics. Nature **503**, 209–217 (2013)
6. Zhang, Z.R., Xu, L.J., Qu, T., Lei, M., Lin, Z.K., Ouyang, X.P., Jiang, J.-H., Huang, J.P.: Diffusion metamaterials. Nat. Rev. Phys. **5**, 218–235 (2023)
7. Yang, F.B., Zhang, Z.R., Xu, L.J., Liu, Z.F., Jin, P., Zhuang, P.F., Lei, M., Liu, J.R., Jiang, J.-H., Ouyang, X.P., Marchesoni, F., Huang, J.P.: Controlling mass and energy diffusion with metamaterials. Rev. Mod. Phys. **96**, 015002 (2024)
8. Wegener, M.: Metamaterials beyond optics. Science **342**, 939–940 (2013)
9. Xu, L.J., Huang, J.P.: Transformation Thermotics and Extended Theories: Inside and Outside Metamaterials. Springer, Singapore (2023)
10. Huang, J.P.: Theoretical Thermotics: Transformation Thermotics and Extended Theories for Thermal Metamaterials. Springer, Singapore (2020)
11. Statistical Physics and Complex Systems Research Group: Thermal cloak: small concept, big applications. Physics **52**, 605–611 (2023). (In Chinese)

Contents

Part VI Metamaterials for Plasma Diffusion

Chapter 1
Diffusionics: Basic Theory and Theoretical Framework

Pengfei Zhuang

1.1 Opening Remarks

The development of physics has robustly characterized the microscopic and macroscopic mechanisms of diffusion systems. The first law of thermodynamics asserts the conservation of energy, while Fourier's law articulates the connection between temperature gradients and heat flux. These laws are traditionally oriented towards describing thermal phenomena in natural contexts and do not inherently provide for the deliberate manipulation of artificial systems. By synthesizing the first law of thermodynamics with Fourier's law, one can derive the governing equation for the temperature field, which is determined by its inherent structure and boundary conditions. On the one hand, boundary conditions typically stem from the ambient environment and are challenging to alter. On the other hand, the form of the heat conduction equation is intimately linked with variables such as density, specific heat capacity, and thermal conductivity. The task of actively modulating the temperature field, therefore, hinges on the strategic design of these parameters. Similar principles apply to other diffusion systems like the electric potential field in charge diffusion systems [1–3] and the concentration field in particle diffusion systems [4, 5], where field equations can be controlled exerted tailoring pertinent parameters. This encapsulates the core concept of diffusionics [6], which aims to steer diffusion fields through the deliberate adjustment of these parameters.

Altering the distributions of physical fields via modification of material properties is a familiar concept, yet deducing the spatial arrangement of such material parameters from a specified physical field configuration is a mathematically intricate inverse problem. Typically addressed through numerical methods, these problems demand considerable computational resources. A breakthrough came in 2006 when Pendry et al. [7] put forth a transformation theory that enables precise construc-

P. Zhuang (✉)
Department of Physics, Key Laboratory of Micro and Nano Photonic Structures (MOE), and State Key Laboratory of Surface Physics, Fudan University, Shanghai 200438, China
e-mail: 22110190096@m.fudan.edu.cn

F.-B. Yang and J.-P. Huang, *Diffusionics*,
https://doi.org/10.1007/978-981-97-0487-3_1

tion of material parameters to match desired field distributions. Drawing inspiration from Einstein's general relativity, they formulated a mapping that transform a virtual space into real Cartesian space, thereby computing the necessary distribution of dielectric constants and magnetic permeability for the material. This transformation theory has been expanded to encompass various physical fields such as acoustics [8], thermotics [9–14], particle dynamics [15], and plasma physics [16]. The theory has provided a roadmap for material parameter manipulation to control diffusion fields at will. The resulting parameters, including diffusion coefficients, however, are often anisotropic, inhomogeneous, and sometimes singular, depending on the nature of the coordinate transformation. Recent advances have employed linear transformations [17] and pseudo-conformal transformations [18] to eliminate the inhomogeneity and anisotropy of the material parameters, significantly simplifying the challenge of experimental realization.

Despite these advancements, identifying natural materials that satisfy the stipulations of transformation theory remains a formidable challenge. The solution has been the development of metamaterials [19–21], engineered structures composed of multiple densely packed segments that collectively behave as an effective medium [22]. The design of metamaterials is anchored in the effective medium theory, with the Maxwell-Garnett formula, Bruggeman formula, and series-parallel formula serving as its foundational theoretical apparatus. Beyond the realm of metamaterial design, effective medium theory also facilitates the calculation of nonlinear effective thermal conductivities in random [23] and periodic particle systems [24], alongside the observation of enhanced effective nonlinear coefficients. The idea of scattering cancellation is also implicit in effective medium theory. For example, a metamaterial, through the spatial arrangement of several natural materials, placed in a background with the same effective thermal conductivity. This means that the scattering of these materials on the background field cancels each other out, yielding the distribution of the background field undisturbed. Recently, scattering cancellation theory [25–28] has emerged as an alternative to transformation theory, guiding the fabrication of thermal metamaterials with desired characteristics. Moreover, introducing effective convection through rotating disks [29–31] and direct heat source contact [32, 33] can also perturb the background temperature field, offering adjustable solutions adaptable to complex environments.

The vigorous expansion of topological physics [34, 35] in the last two decades has seen a multitude of topological phases of matter both theoretically conjectured and experimentally verified. Given that diffusion systems are inherently non-Hermitian, their governing equations can be likened to the Schrödinger equation, making the exploration of non-Hermitian physics and its topological characteristics [36] within macroscopic diffusion systems a tantalizing prospect. Analogies with the Schrödinger equation reveal that its potential energy term corresponds to the diffusion term of the diffusion equation, allowing the Bloch series expansion method to be aptly applied to spatiotemporally modulated diffusion systems [37].

This chapter explores diffusion systems, establishing the foundational theories and frameworks for manipulating diffusion fields. Section 1.2 sets out the theoretical underpinnings of transformation theory, exemplified through the heat conduction equation, proceeds with the implementation of various mappings, and then broadens the scope of transformation theory to encompass additional diffusion fields. Section 1.3 delves into the core equations of effective medium theory that are essential for actualizing the parameters dictated by transformation theory. Section 1.4 delineates the scattering cancellation theory, which bifurcates into passive and active strategies. The passive approach operates without the need for external energy inputs, distinguishing it from the active strategy which necessitates such inputs. Section 1.5 commences with an exposition on the fundamental approach to examining diffusion topological phenomena. This is achieved by discretizing the diffusion equation to draw parallels with the Schrödinger equation, subsequently facilitating the computation of energy bands and topological invariants. Following this, the section introduces the Bloch series expansion method, a valuable tool for addressing systems characterized by periodically modulated material parameters. The chapter concludes with Sect. 1.6, which synthesizes the content discussed throughout and offers insights into the prospective advancements in the field of diffusionics.

1.2 Transformation Theory

1.2.1 Foundation Framework

It is widely recognized that the unique determination of a physical field hinges on its governing equations coupled with boundary conditions. For illustrative purposes, let us consider the transient heat conduction process. The predominant equation governing this process is presented as: [2]

$$\rho c \frac{\partial T}{\partial t} - \nabla \cdot (\kappa \nabla T) = Q, \tag{1.1}$$

where ρ represents the mass density, c the heat capacity, κ the thermal conductivity, and Q the heat power density. This equation has different forms in different coordinate systems, and we're going to expand it in any coordinates $\{x_u\}$ (u can take 1, 2, and 3), consisting of a set of contravariant basis $\{\mathbf{g}^u\}$. In general, the thermal conductivity is a tensor κ^{uv}, rendering the conductive term of the Eq. (1.1) as follows:

$$
\begin{aligned}
\nabla \cdot (\kappa \nabla T) &= \mathbf{g}_k \cdot \frac{\partial}{\partial x_k}\left(\kappa^{uv}\mathbf{g}^u \otimes \mathbf{g}^v \cdot \mathbf{g}_l \frac{\partial T}{\partial x_l}\right) \\
&= \mathbf{g}_k \cdot \frac{\partial}{\partial x_k}\left(\kappa^{uv}\frac{\partial T}{\partial x_v}\mathbf{g}^u\right) \\
&= \mathbf{g}_k \cdot \mathbf{g}^u \frac{\partial}{\partial x_k}\left(\kappa^{uv}\frac{\partial T}{\partial x_v}\right) + \mathbf{g}_k \cdot \frac{\partial \mathbf{g}^u}{\partial x_k}\left(\kappa^{uv}\frac{\partial T}{\partial x_v}\right) \\
&= \frac{\partial}{\partial x_u}\left(\kappa^{uv}\frac{\partial T}{\partial x_v}\right) + \Gamma^k_{ku}\left(\kappa^{uv}\frac{\partial T}{\partial x_v}\right) \\
&= \frac{\partial}{\partial x_u}\left(\kappa^{uv}\frac{\partial T}{\partial x_v}\right) + \frac{1}{\sqrt{g}}\left(\frac{\partial \sqrt{g}}{\partial x_u}\right)\left(\kappa^{uv}\frac{\partial T}{\partial x_v}\right) \\
&= \frac{1}{\sqrt{g}}\partial_u\left(\sqrt{g}\kappa^{uv}\partial_v T\right).
\end{aligned}
\tag{1.2}
$$

Here, g represents the determinant of the metric g_{ij} and the Christoffel symbol is defined as $\Gamma^k_{ku} = \mathbf{g}_k \cdot \partial \mathbf{g}^u / \partial x_k$. So far, we have derived the general form of heat conduction equation in any coordinates,

$$
\rho c \partial_t T - \frac{1}{\sqrt{g}}\partial_u\left(\sqrt{g}\kappa^{uv}\partial_v T\right) = Q, \tag{1.3}
$$

Consideration is then given to a rectangular region with isotropic thermal conductivity κ within the Cartesian coordinate framework $\{x_{u'}\}$. The left and right boundaries are maintained at constant high and low temperatures, respectively, while the remaining boundaries are insulated. Illustrated in Fig. 1.1a are the uniform temperature gradients and isotherms within the domain. To fulfill particular requirements, such as those of a thermal guide capable of conducting heat flow uniformly, a coordinate transformation is performed:

$$
\begin{aligned}
x_{1^*} &= x_{1'}\cos x_{2'}, \\
x_{2^*} &= x_{1'}\sin x_{2'}, \\
x_{3^*} &= x_{3'},
\end{aligned}
\tag{1.4}
$$

Figure 1.1b depicts the transformed domain, showcasing isotherms (red line) and streamlines (yellow line) which run parallel and perpendicular to the radial direction, respectively. The transformation from Fig. 1.1a, b involves only a coordinate change, allowing the constitutive parameters in curvilinear coordinates to be expressed as:

$$
\begin{aligned}
\kappa^{u^*v^*} &= J^{u^*}{}_{u'}\kappa^{u'v'}J^{v^*}{}_{v'}, \\
J^{j^*}{}_{j'} &= \partial x_{j^*} / \partial x_{j'}.
\end{aligned}
\tag{1.5}
$$

By substituting Eq. (1.5) into Eq. (1.3), the component form of the heat conduction equation in the curvilinear coordinate system $\{x_{u^*}\}$ is obtained and expressed as:

$$\rho c \partial_t T - \frac{1}{\sqrt{g^*}} \partial_{u^*} \left(\sqrt{g^*} \kappa^{u^* v^*} \partial_{v^*} T \right) = Q, \tag{1.6}$$

where $g_{i^* j^*} = \frac{\partial x_{i'}}{\partial x_{i^*}} g_{i' j'} \frac{\partial x^{j'}}{\partial x^{j^*}} = (J J^{\tau})^{-1}$, thus resulting in $\sqrt{g^*} = \det^{-1}(J)$. Thus, Eq. (1.6) reduces to

$$\frac{\rho c \partial_t T}{\det J} - \partial_{u^*} \left(\frac{J^{u^}{}_{u'} \kappa^{u' v'} J^{v^*}{}_{v'}}{\det J} \partial_{v^*} T \right) = \frac{Q}{\det J}. \tag{1.7}$$

It is pertinent to note that these two coordinates describe the same temperature distribution ($T(x_{1'}, x_{2'}, x_{3'}) = T(x_{1^*}, x_{2^*}, x_{3^*})$), despite the isotherm shape appearing distinct in the curvilinear coordinates compared to Cartesian coordinates. In other words, while the shape plotted in the curvilinear coordinates is virtual, an equivalent temperature distribution is attainable in the physical space. This equivalence is founded upon the domain equation and boundary conditions that govern the temperature field distribution. To materialize such a concept, one need to consider a curved tube replicating the shape illustrated in Fig. 1.1b within the Cartesian coordinate system $\{x_{\tilde{u}}\}$. Setting constant temperatures at both ends of this tube, with the remaining two walls maintained as adiabatic, keeping the same boundary conditions. Moreover, to align with the form of Eq. (1.7), there is a necessity to choose appropriate parameters that yield an analogous heat conduction equation within the Cartesian coordinate system, expressed as:

$$\tilde{\rho} \tilde{c} \partial_t \tilde{T} - \partial_u \left(\tilde{\kappa}^{\tilde{u}\tilde{v}} \partial_v \tilde{T} \right) = \tilde{Q} \tag{1.8}$$

Comparing Eqs. (1.7) and (1.8), one derives the transformation relations for the constitutive parameters as $\tilde{\kappa}^{\tilde{u}\tilde{v}} = J^{u^}{}_{u'} \kappa^{u' v'} J^{v^*}{}_{v'} / \det(J)$, $\tilde{\rho}\tilde{c} = \rho c / \det(J)$, and $\tilde{Q} = Q / \det(J)$. These can be succinctly represented in matrix form as prescribed in [2]:

$$\begin{cases} \tilde{\boldsymbol{\kappa}} = \dfrac{\boldsymbol{J} \boldsymbol{\kappa} \boldsymbol{J}^{\tau}}{\det(A)}, \\ \tilde{\rho}\tilde{c} = \dfrac{\rho c}{\det(J)}, \\ \tilde{Q} = \dfrac{Q}{\det J}. \end{cases} \tag{1.9}$$

This set of relationships ensures the preservation of the heat conduction equation's form post-coordinate transformation and affirms that the temperature profile in the virtual coordinate system $T(x_{1^*}, x_{2^*}, x_{3^*})$ can be manifested in the newly established Cartesian system $\tilde{T}(x_{\tilde{1}}, x_{\tilde{2}}, x_{\tilde{3}})$.

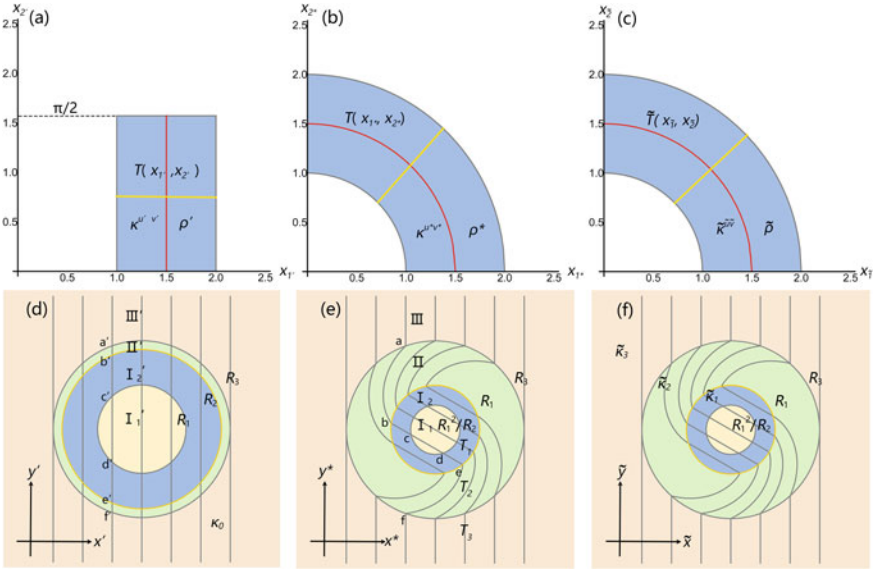

Fig. 1.1 Schematic diagram of the coordinate transformation process in cylinder structure. **a**, **d**, **c**, **f** Cartesian coordinates. **b**, **e** Curvilinear coordinates. The red (yellow) lines denote isotherms (stream). From **a**, **d** to **b**, **e**: only coordinate transformation. From **a**, **d** to **c**, **f**: only constitutive parameters' transformation. The isotherm shape in **c**, **f** is the same as that in **b**, **e**, indicating that the effect of parameters' transformation is equivalent to coordinate transformation. (from Ref. [2], licensed under CC-BY 4.0)

1.2.2 Mapping Application

1.2.2.1 General Mapping

The manipulation of heat flux typically revolves around two key aspects: density and direction. Thermal concentrators, for example, are designed to enhance the heat flux density within a specified region, while thermal rotators are engineered to alter the direction of heat flow. This study integrates both functions within a singular device. As depicted in Fig. 1.1d, the Cartesian coordinate space is partitioned into four regions, each with uniform thermal conductivity κ: Region I'_1 for $r' < R_1$; Region I'_2 for $R_1 < r' < R_2$; Region II' for $R_2 < r' < R_3$; and Region III' for $r' > R_3$. Subsequently, specific coordinate transformations are applied to these regions as follows:

$$\begin{cases} r^* = \dfrac{R_1}{R_2} r', \\ \theta^* = \theta' + \theta_0, \end{cases} \quad (0 < r' < R_2) \tag{1.10}$$

$$\begin{cases} r^* = \dfrac{(R_3 - R_1)r' + (R_1 - R_2)R_3}{R_3 - R_2}, \\ \theta^* = \theta' + \dfrac{r - R_3}{R_2 - R_3}\theta_0, \end{cases} \quad (R_2 < r' < R_3) \tag{1.11}$$

$$\begin{cases} r^* = r', \\ \theta^* = \theta'. \end{cases} \quad (r' > R_3) \tag{1.12}$$

Here, R_2 spans from 0 to R_3, resulting in three distinct devices: a rotating imperfect (or perfect) cloak for $R_2 < R_1$ ($R_2 = 0$); a rotator for $R_2 = R_1$; and a rotating concentrator for $R_1 < R_2 < R_3$. Such transformations enable the compression and rotation of the temperature distribution in Regions I_1' and I_2' without perturbing the physical fields within the background (Region III′). As shown in Fig. 1.1e, the isotherm labeled $a' - b' - c' - d' - e' - f'$ transitions into the curvilinear shape $a - b - c - d - e - f$ following the coordinate transformation. The Jacobian transformation matrix corresponding to Eqs. (1.10)–(1.12) is computed by

$$\mathbf{J} = \begin{pmatrix} \partial r^*/\partial r' & \partial r^*/(r'\partial\theta') \\ r^*\partial\theta^*/\partial r' & r^*\partial\theta^*/(r'\partial\theta') \end{pmatrix}. \tag{1.13}$$

By inserting Eq. (1.13) into Eq. (1.9), the spatial distribution of the material parameters can be ascertained (Fig. 1.1f),

$$\begin{cases} \tilde{\kappa}_1 = \tilde{\kappa}_3 = \kappa \\ \tilde{\kappa}_2 = M\kappa \end{cases}, \begin{cases} \tilde{\rho}_1\tilde{c}_1 = \rho c R_2^2/R_1^2 \\ \tilde{\rho}_2\tilde{c}_2 = (R_3 - R_2)^2\tilde{r}/\left[(R_3 - R_2)((R_3 - R_2)\tilde{r} + (R_2 - R_1)R_3)\right] \\ \tilde{\rho}_3\tilde{c}_3 = \rho c \end{cases}. \tag{1.14}$$

The transformation matrix is presented as follow:

$$M = \begin{bmatrix} m_{\tilde{r}\tilde{r}} & m_{\tilde{r}\tilde{\theta}} \\ m_{\tilde{\theta}\tilde{r}} & m_{\tilde{\theta}\tilde{\theta}} \end{bmatrix}, \tag{1.15}$$

where

$$\begin{aligned} m_{\tilde{r}\tilde{r}} &= 1 + \frac{(R_1 - R_2)R_3}{(R_2 - R_3)\tilde{r}}, \\ m_{\tilde{r}\tilde{\theta}} &= m_{\tilde{\theta}\tilde{r}} = \frac{[R_3\tilde{r} + R_2(R_3 - \tilde{r}) - R_1R_3]\theta_0}{(R_2 - R_3)(R_3 - R_1)}, \\ m_{\tilde{\theta}\tilde{\theta}} &= \frac{(R_3 - R_2)\tilde{r}}{R_3\tilde{r} + R_2(R_3 - \tilde{r}) - R_1R_3} + \frac{[R_3\tilde{r} + R_2(R_3 - \tilde{r}) - R_1R_3]\theta_0^2\tilde{r}}{(R_1 - R_3)^2(R_3 - R_2)}. \end{aligned} \tag{1.16}$$

1.2.2.2 Linear Mapping

This robust theoretical framework offers a roadmap for the precise manipulation of thermal fields. The trade-off, however, lies in the need for materials with anisotropic, inhomogeneous, and potentially singular thermal conductivities, a requirement that stems from the non-conformal and heterogeneous nature of the coordinate transformation employed. Addressing this challenge, Xu et al. [38] introduced an innovative approach to construct polygonal thermal harvesting devices—concentrators with homogeneous and nonsingular parameters—using a linear mapping function. The method for fabricating these polygonal concentrators is illustrated in Fig. 1 of Ref. [38]. To avoid disturbances in the background temperature distribution, one edge of the outer polygon is transformed to be congruent with the background. The transformation for the inner polygon involves a two-step process: firstly, rotation, and secondly, compression. In the initial step, the inner polygon is rotated around the central point $O(0, 0)$ relative to the outer polygon by an angle π/N, where N is the number of polygon sides ($N \geq 3$). In the subsequent step, the rotated inner polygon is compressed into a smaller physical space, and the intermediate area is expanded to recapture the heat flux. The intermediate region is partitioned into two distinct types of triangular elements by connecting the vertices of both polygons in an alternating sequence. Triangular elements sharing two vertices with the outer polygon are classified as type I, whereas those with only one vertex on the outer polygon are classified as type II. To illustrate this transformation succinctly, consider the regions $A_0B_0A_{in}$ to $A_0B_0A_0''$ and $A_0A_{in}E_{in}$ to $A_0A_0''E_0''$ as exemplars. Through these two transformation steps, the coordinates of the vertices for both the inner and outer polygons can be expressed accordingly:

$$\begin{array}{l} A_{\mathrm{n}}\left(r_2\sin\frac{(2\mathrm{n}-1)\pi}{N}, r_2\cos\frac{(2\mathrm{n}-1)\pi}{N}\right);\ B_{\mathrm{n}}\left(r_2\sin\frac{(2\mathrm{n}+1)\pi}{N}, r_2\cos\frac{(2\mathrm{n}+1)\pi}{N}\right); \\ A'_{\mathrm{n}}\left(r_1\sin\frac{2\mathrm{n}\pi}{N}, r_1\cos\frac{2\mathrm{n}\pi}{N}\right); \qquad\qquad A''_{\mathrm{n}}\left(r_0\sin\frac{2\mathrm{n}\pi}{N}, r_0\cos\frac{2\mathrm{n}\pi}{N}\right); \\ E'_{\mathrm{n}}\left(r_1\sin\frac{2(\mathrm{n}-1)\pi}{N}, r_1\cos\frac{2(\mathrm{n}-1)\pi}{N}\right);\ E''_{\mathrm{n}}\left(r_0\sin\frac{2(\mathrm{n}-1)\pi}{N}, r_0\cos\frac{2(\mathrm{n}-1)\pi}{N}\right), \end{array} \tag{1.17}$$

with n denoting the sequential number of each adjacent element of the same type, respecting their geometric attributes. Given the linear correlation between the original and transformed elements, the intended harvesting region can be achieved by mapping two corresponding contiguous curves. Therefore, the transformation process for Type I is described as:

$$\begin{array}{c} \begin{pmatrix} x''_{A_{\mathrm{n}}} \\ x''_{B_{\mathrm{n}}} \\ x''_{A''_{\mathrm{n}}} \end{pmatrix} = \begin{pmatrix} x'_{A_{\mathrm{n}}} & y'_{A_{\mathrm{n}}B_{\mathrm{n}}}\left(x'_{A_{\mathrm{n}}}\right) & 1 \\ x'_{B_{\mathrm{n}}} & y'_{B_{\mathrm{n}}A'_{\mathrm{n}}}\left(x'_{B_{\mathrm{n}}}\right) & 1 \\ x'_{A''_{\mathrm{n}}} & y'_{A'_{\mathrm{n}}A_{\mathrm{n}}}\left(x'_{A'_{\mathrm{n}}}\right) & 1 \end{pmatrix} \cdot \begin{pmatrix} a_{\mathrm{I,n}} \\ b_{\mathrm{I,n}} \\ c_{\mathrm{I,n}} \end{pmatrix}, \\ \begin{pmatrix} y''_{A_{\mathrm{n}}B_{\mathrm{n}}}\left(x''_{A_{\mathrm{n}}}\right) \\ y''_{B_{\mathrm{n}}A''_{\mathrm{n}}}\left(x''_{B_{\mathrm{n}}}\right) \\ y''_{A_{\mathrm{n}}A_{\mathrm{n}}}\left(x''_{A''_{\mathrm{n}}}\right) \end{pmatrix} = \begin{pmatrix} x'_{A_{\mathrm{n}}} & y'_{A_{\mathrm{n}}B_{\mathrm{n}}}\left(x'_{A_{\mathrm{n}}}\right) & 1 \\ x'_{B_{\mathrm{n}}} & y'_{B_{\mathrm{n}}A'_{\mathrm{n}}}\left(x'_{B_{\mathrm{n}}}\right) & 1 \\ x'_{A''_{\mathrm{n}}} & y'_{A'_{\mathrm{n}}A_{\mathrm{n}}}\left(x'_{A'_{\mathrm{n}}}\right) & 1 \end{pmatrix} \cdot \begin{pmatrix} d_{\mathrm{I,n}} \\ e_{\mathrm{I,n}} \\ f_{\mathrm{I,n}} \end{pmatrix}. \end{array} \tag{1.18}$$

Utilizing Eq. (1.18), the Jacobian matrix pertinent to the polygonal coordinate transformation is derived as:

$$J = \frac{\partial(x'', y'', z'')}{\partial(x', y', z')} = \begin{pmatrix} a_{I,n} & b_{I,n} & 0 \\ d_{I,n} & e_{I,n} & 0 \\ 0 & 0 & 1 \end{pmatrix} \tag{1.19}$$

Taking Eqs. (1.9) and (1.19) together, the conductivity components of Type I can be written as follows:

$$\begin{aligned} \kappa''_{xx} &= \frac{\left(a_{I,\mathrm{n}}^2 + b_{I,\mathrm{n}}^2\right)}{\det(J)}\kappa \\ \kappa''_{xy} &= \kappa''_{yx} = \frac{\left(a_{I,\mathrm{n}} d_{I,\mathrm{n}} + b_{I,\mathrm{n}} e_{I,\mathrm{n}}\right)}{\det(J)}\kappa \\ \kappa''_{yy} &= \frac{\left(d_{I,\mathrm{n}}^2 + e_{I,\mathrm{n}}^2\right)}{\det(J)}\kappa \\ \kappa''_{zz} &= \frac{\kappa}{\det(J)} \end{aligned} \tag{1.20}$$

The thermal conductivity for Type II can be calculated in the same way. These constant conductivity tensors can be obtained by alternating the arrangement of two layered isotropic thermal materials. Utilizing effective medium theory, the thermal conductivity components aligned with the principal axes in both parallel and perpendicular orientations were determined and an arbitrarily shaped polygonal thermal concentrator were realized [38]. Notably, the thermal field external to the heat harvesting region remains unperturbed, while a substantial amplification of the temperature gradient is observed within the harvesting zone. Moreover, additional research efforts [17, 39, 40] have employed a similar methodology for the creation of polygonal thermal cloaks, optical illusions, and acoustic rotators utilizing exclusively homogeneous materials.

1.2.2.3 Pseudo-conformal Mapping

The anisotropy of constitute parameters derived from transformation theory poses a significant challenge for experimental fabrication. This challenge was addressed in 2006 that Leonhardt et al. [41] proposed conformal optical mapping and deduced the isotropic refractive index transformation relation. An optical cloak requiring only isotropic materials was realized by using Zhuokousky mapping. Despite its utility, this method has yet to find application in diffusion systems, where the apparent diffusive nature and the unavoidable interface mismatch hinder its development. In a groundbreaking approach, Dai et al. [18] introduced the concept of diffusion pseudo-conformal mapping, as seen in [Fig. 1.2]. This concept reconciles the disparities between diffusion and wave propagation, achieving seamless interface matching. Starting with classical Zhukovsky mapping $z_1 = z + 1/z$ and its inverse, where $z_1 =$

$x_1 + iy_1$ and $z = x + iy$ represent the auxiliary and physical complex planes, they ensured that the Cauchy-Riemann conditions were satisfied:

$$\begin{aligned} \frac{\partial x}{\partial x_1} &= \frac{\partial y}{\partial y_1}, \\ \frac{\partial x}{\partial y_1} &= \frac{\partial y}{\partial x_1}. \end{aligned} \tag{1.21}$$

Substituting Zhukowski mapping and Eq. (1.21) into Eq. (1.9), the inherent parameter of thermal cloak is derived,

$$\begin{aligned} \kappa &= \kappa_1, \\ \rho c &= \frac{(\rho c)_1}{(\partial x/\partial x_1)^2 + (\partial x/\partial y_1)^2}. \end{aligned} \tag{1.22}$$

This mapping compressed an half-ellipse $\mathbf{E}^+ = \left\{z_1 : 0 \leqslant x_1^2/a^2 + y_1^2/b^2 \leqslant 1,\ y_1 \geqslant 0\right\}$ (Fig. 1.2b) into a half ring $\mathbf{A}^+ = \{z : R_1 \leqslant |z| \leqslant R_2,\ y \geqslant 0$ (Fig. 1.2c), where $R_1 =$ 1 m, $a = (R_2^2 + R_1^2)/R_2$, and $b = (R_2^2 - R_1^2)/R_2$. Obviously, the outer boundary is not matched before and after this mapping unless the outer boundary is large enough $R_2 \gg R_1$. To address this issue, a further transformation is introduced:

$$\begin{aligned} x_1 &= ax_0/R_2, \\ y_1 &= by_0/R_2. \end{aligned} \tag{1.23}$$

This mapping transform the ellipse into a circular $\mathbf{D}^+ = \{z_0 : 0 \leqslant z_0 \leqslant R_2,\ y_1 \geqslant 0\}$, whose outer boundary is the same as $\mathbf{D}^+$. Taking Eqs. (1.9) and (1.23) together, another set of constitutive parameter transformations is derived,

$$\begin{aligned} \kappa_1 &= \kappa_0 \begin{pmatrix} a/b & 0 \\ 0 & b/a \end{pmatrix} \\ (\rho c)_1 &= \frac{(\rho c)_0}{ab/R_2^2} \end{aligned} \tag{1.24}$$

When a temperature gradient is applied along the x_0-axis, only the thermal conductivity in the x_1-axis is relevant. Combing Eq. (1.22) with Eq. (1.24), the conductivity for a bilayer cloak in the x-direction is thus given by:

$$\kappa = \frac{R_2^2 + R_1^2}{R_2^2 - R_1^2}\kappa_0. \tag{1.25}$$

Conversely, when the gradient is along the y_0-axis, the conductivity for a zero index cloak in the y-direction is:

$$\kappa = \frac{R_2^2 - R_1^2}{R_2^2 + R_1^2}\kappa_0. \tag{1.26}$$

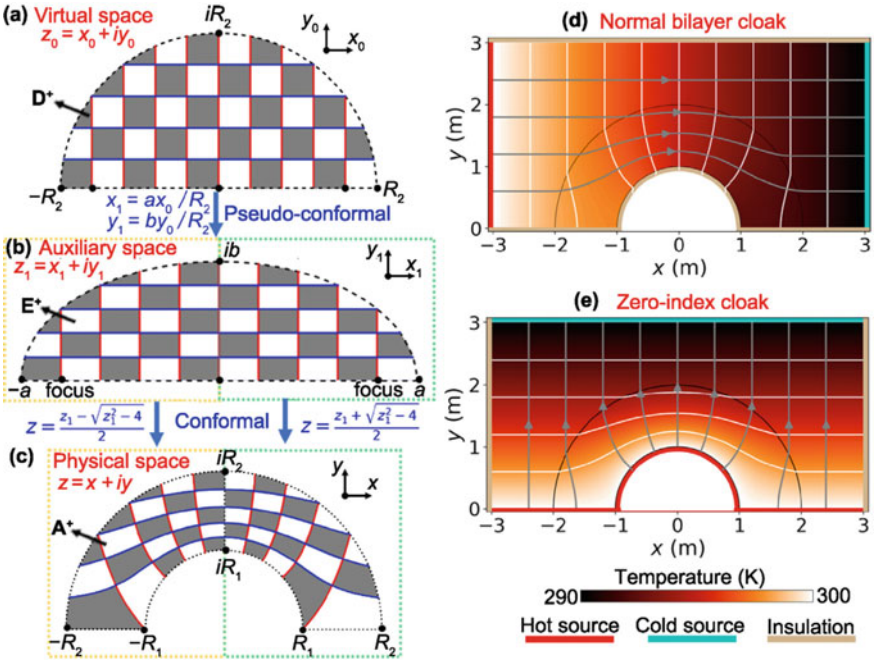

Fig. 1.2 Carpet cloaks. **a**–**c** show the geometric transformation to construct such a cloak. **a**, **b**, and **c** are the virtual space, auxiliary space and the physical space, respectively. **d** is the computed temperature profile of a normal bilayer cloak with an insulating inner layer. **e** is the computed temperature profile of a zero-index cloak with an constant-temperature inner layer (realized by an external source). Parameters: $R_2 = 2R_1 = 2$ m, $a = 2.5$ m, and $b = 1.5$ m. (from Ref. [18], licensed under CC-BY 4.0)

The numerical simulations depicted in Fig. 1.2d and e validate the effectiveness of both cloaking strategies. Additionally, an orthogonal relationship between the isotherms and the streamline patterns is observed.

1.2.3 Extension to Other Diffusion Fields

1.2.3.1 Concentration Field

The heat conduction equation serves as an exemplar for demonstrating the invariance of physical laws under coordinate transformations. This invariance is equally significant when considering mass transport in systems critical for biochemical reactions, drug delivery, and particle separation. From a physics standpoint, the essence of mass transport is encapsulated by the convection-diffusion equation:

$$\frac{\partial c}{\partial t} - \nabla \cdot (\overleftrightarrow{D}\, c - \vec{v}c) = 0. \tag{1.27}$$

In this equation, c, t, $\overleftrightarrow{D}$, and $\vec{v}$ are representative of concentration, time, tensorial diffusivity, and advection velocity, respectively. According to the traditional transformation theory, the component forms of the diffusion-convection equations before $\{x_i\}$ and after $\{x_{i'}\}$ the transformation are derived,

$$\begin{aligned} \partial_t c &= \partial_i \left(D^{ij} \partial_j c - v_i c \right), \\ \sqrt{g}\partial_t c &= \partial_{i'} \left(\frac{\partial x_i'}{\partial x_i} \sqrt{g} D^{ij} \frac{\partial x_j'}{\partial x_j} \partial_{j'} c - \frac{\partial x_i'}{\partial x_i} \sqrt{g} v_i c \right), \end{aligned} \tag{1.28}$$

with the terms $\partial x_i'/\partial x_i$ and $\partial x_j'/\partial x_j$ representing components of the Jacobian transformation matrix J. Equation (1.28) shows that the time-dependent term is preceded by an extra metric caused by a spatial transformation, which in turn cannot be absorbed by the physical quantity of the medium material. As a consequence, the transient convective-diffusion equation does not satisfy the condition for an invariant transformation form, revealing a discrepancy with traditional transformation theory, particularly for transient processes. Nevertheless, if the determinant of J is 1, the theory retains its rigor. To address the limitations of transformation theory concerning transient convective-diffusion, an approximate method is suggested, as demonstrated by Zhang et al. [42]. By multiplying the determinant of J to both sides of the relevant equation and thus negating the additional metric, the following parameter transformation relationship is derived:

$$\begin{aligned} \tilde{D} &= J D J^{\tau}, \\ \tilde{v} &= J v, \end{aligned} \tag{1.29}$$

where $\tilde{D}$ and $\tilde{v}$ are parameters in new Cartesian coordinates $\{x_{\tilde{u}}\}$. The accuracy of this approximation is contingent upon the Jacobian matrix, which in turn depends on the specific nature of the spatial transformation. The magnitude of error introduced by this method is thus related to the system's physical parameters and the concrete form of spatial transformation. To minimize this error, the optimization theory stipulates that both the diffusion rate and flow rate should be relatively low.

1.2.3.2 Thermoelectric Coupling Field

A steady-state thermoelectric transport process adheres to the governing equations as cited in the literature [2, 43]:

$$\begin{cases} 0 = \nabla \cdot (\boldsymbol{\sigma} \nabla \mu + \boldsymbol{\sigma} \boldsymbol{S} \nabla \mathrm{T}), \\ 0 = \nabla \cdot \left[\boldsymbol{\kappa} \nabla \mathrm{T} + T \boldsymbol{S}^{\tau} \boldsymbol{\sigma} \boldsymbol{S} \nabla T + T \boldsymbol{S}^{\tau} \boldsymbol{\sigma} \nabla \mu \right] + \nabla \mu \cdot [\boldsymbol{\sigma} \nabla \mu + \boldsymbol{\sigma} \boldsymbol{S} \nabla T]. \end{cases} \tag{1.30}$$

Here, T and μ denote the spatially dependent temperature and electrical potential, respectively. The electrical conductivity $\boldsymbol{\sigma}$, thermal conductivity $\boldsymbol{\kappa}$, and Seebeck coefficient $\boldsymbol{S}$ (with $\boldsymbol{S}^{\boldsymbol{\tau}}$ as its transpose) are second-order tensors. These equations are subsequently expressed in component form within an arbitrary coordinate system $\{x_1, x_2, x_3\}$, denoted as:

$$\begin{cases} 0 = \dfrac{1}{\sqrt{g}}\partial_u\left[\sqrt{g}\left(\sigma^{uv}\partial_v\mu + \sigma^{um}g_{mk}S^{kn}g_{nl}g^{lv}\partial_v T\right)\right], \\ 0 = \dfrac{1}{\sqrt{g}}\partial_u\left[\sqrt{g}\left(\kappa^{uv} + T(S^{\tau})^{um}g_{mk}\sigma^{kn}g_{nl}S^{lv} + T(S^{\tau})^{um}g_{mk}\sigma^{kv}\right)\partial_v T\right] \\ \quad + (\partial_u\mu)\left(\sigma^{uv}\partial_v\mu + \sigma^{um}g_{mk}S^{kv}\partial_v T\right), \end{cases} \tag{1.31}$$

where indices u, l, v, k, m, n assume the values 1, 2, 3, and g represents the determinant of the metric tensor g_{ij}. Assuming the transformation from the Cartesian coordinate system $\{x_{1'}, x_{2'}, x_{3'}\}$ to this arbitrary system, one can invoke the coordinate transformation relation,

$$\begin{cases} \kappa^{uv} = A^{u}{}_{u'}\kappa^{u'v'}A^{v}{}_{v'}, \\ \sigma^{uv} = A^{u}{}_{u'}\sigma^{u'v'}A^{v}{}_{v'}, \\ S^{uv} = A^{u}{}_{u'}S^{u'v'}A^{v}{}_{v'}, \\ g^{uv} = A^{u}{}_{u'}\delta^{u'v'}A^{v}{}_{v'}, \\ g_{uv} = A^{u'}{}_{u}\delta_{u'v'}A^{v'}{}_{v} \\ \sqrt{g} = \det^{-1}(A) \end{cases} \tag{1.32}$$

to rewrite Eq. (1.31) as:

$$\begin{cases} 0 = \partial_u\left[\dfrac{1}{\det(A)}\left(A^{u}{}_{u'}\sigma^{u'v'}A^{v}{}_{v'}\partial_v\mu + A^{u}{}_{u'}\sigma^{u'k'}S^{k'v'}A^{v}{}_{v'}\partial_v T\right)\right], \\ 0 = \partial_u\left[\dfrac{A^{u}{}_{u'}}{\det(A)}\left(\kappa^{u'v'} + T(S^{\tau})^{u'k'}\sigma^{k'l'}S^{l'v'} + T(S^{\tau})^{u'k'}\sigma^{k'v'}\right)A^{v}{}_{v'}\partial_v T\right] \\ \quad + \dfrac{1}{\det(A)}(\partial_u\mu)\left(A^{u}{}_{u'}\sigma^{u'v'}A^{v}{}_{v'}\partial_v\mu + A^{u}{}_{u'}\sigma^{u'k'}S^{k'v'}A^{v}{}_{v'}\partial_v T\right). \end{cases} \tag{1.33}$$

In the context, $\partial x_i'/\partial x_i$ and $\partial x_j'/\partial x_j$ are components of the Jacobian-transformation matrix A, and $\delta_{u'v'}$ and $\delta^{u'v'}$ is equal to 1 (0) only if $u' = v'$ (otherwise). Furthermore, the component form of thermoelectric equations in Cartesian coordinates are expressed as:

$$\begin{cases} 0 = \partial_{\tilde{u}} \left(\tilde{\sigma}^{\tilde{u}\tilde{v}} \partial_{\tilde{v}} \tilde{\mu} + \tilde{\sigma}^{\tilde{u}\tilde{k}} \tilde{S}^{\tilde{k}\tilde{v}} \partial_{\tilde{v}} \tilde{T} \right), \\ 0 = \partial_{\tilde{u}} \left[\left(\tilde{\kappa}^{\tilde{u}\tilde{v}} + \tilde{T} (\tilde{S}^{\tau})^{\tilde{u}\tilde{k}} \tilde{\sigma}^{\tilde{k}\tilde{l}} \tilde{S}^{\tilde{l}\tilde{v}} + \tilde{T} (\tilde{S}^{\tau})^{\tilde{u}\tilde{k}} \tilde{\sigma}^{\tilde{k}\tilde{v}} \right) \partial_{\tilde{v}} \tilde{T} \right] \\ \quad + (\partial_{\tilde{u}} \tilde{\mu}) \left[\tilde{\sigma}^{\tilde{u}\tilde{v}} \partial_{\tilde{v}} \tilde{\mu} + \tilde{\sigma}^{\tilde{u}\tilde{k}} \tilde{S}^{\tilde{k}\tilde{v}} \partial_{\tilde{v}} \tilde{T} \right], \end{cases} \tag{1.34}$$

By comparing Eq. (1.33) with Eq. (1.34), the transformation relations of constitutive parameters in a new Cartesian coordinate $\{x_{\tilde{u}}\}$ can be ascertained, denoted as:

$$\begin{cases} \tilde{\boldsymbol{\kappa}} = \dfrac{A \boldsymbol{\kappa}' A^{\tau}}{\det(A)}, \\ \tilde{\boldsymbol{\sigma}} = \dfrac{A \boldsymbol{\sigma}' A^{\tau}}{\det(A)}, \\ \tilde{\boldsymbol{S}} = A^{-\tau} \boldsymbol{S}' A^{\tau}, \end{cases} \tag{1.35}$$

The discussions above establish the invariance of the diffusion-convection and thermoelectric coupling equations under coordinate transformation. Equations (1.29) and (1.35) provide the foundational guidance for designing an array of diffusion metamaterials.

1.3 Effective Medium Theory

Linear mapping and conformal mapping can mitigate the singularity of parameters, yet their direct application using natural materials is impractical; thus, the necessity for an effective medium theory arises. This theory enables the realization of complex parameters through the spatial arrangement of two isotropic materials, most commonly in a layered alternating structure.

1.3.1 Classical Effective Medium Approximation Theories

1.3.1.1 Maxwell–Garnett Theory

Consider a two-component composite (refer to Fig. 1.3a), wherein numerous particles characterized by thermal conductivity κ_p and area fraction f_p for the 2D scenario (or volume fraction for 3D) are randomly dispersed within a matrix with thermal conductivity κ_m. An external temperature gradient ∇T_0 is applied along the x_i-axis. Here, the subscripts p and m signify the particle and matrix, respectively. By invoking Fourier's law, the thermal conductivity of the composite is calculated as:

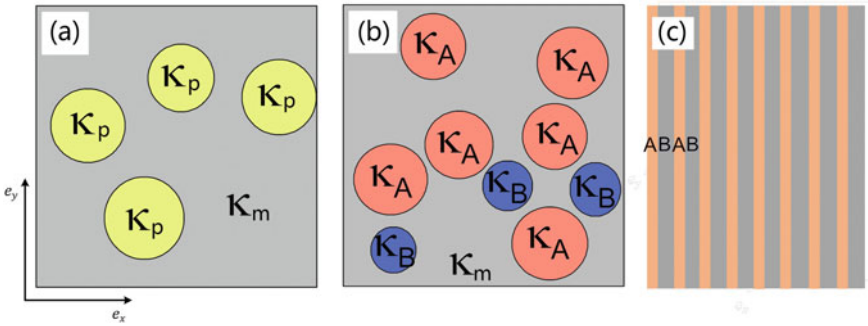

Fig. 1.3 **a** Schematic diagram illustrating a randomly distributed mixture of particles κ_p within a matrix κ_m. **b** Schematic representation of particles A and B dispersed within the matrix material. **c** Schematic of the layered structure showing an alternating, interleaved configuration of layers A and B. Adapted from Ref. [44]

$$\kappa_{ei} = -\frac{\langle J \rangle}{\langle \nabla T \rangle} = \frac{f_p \langle J_p \rangle + (1 - f_p) \langle J_m \rangle}{f_p \langle \nabla T_p \rangle + (1 - f_p) \langle \nabla T_m \rangle}, \tag{1.36}$$

where $\langle J \rangle$ and $\langle \nabla T \rangle$ denote the average heat flux and temperature gradient across the resultant composite particle structure. The average heat flux within the particle and matrix phases is represented as:

$$\begin{aligned} \langle J_p \rangle &= -\kappa_p \langle \nabla T_p \rangle, \\ \langle J_m \rangle &= -\kappa_m \langle \nabla T_m \rangle. \end{aligned} \tag{1.37}$$

Resolution of a fundamental equation in thermal dynamics yields [45]

$$\langle \nabla T_p \rangle = \varepsilon_{pi} \langle \nabla T_m \rangle = \frac{\kappa_m}{\kappa_p L_{pi} + \kappa_m \left(1 - L_{pi}\right)} \langle \nabla T_m \rangle, \tag{1.38}$$

where L_{pi} denotes the shape factor along x_i-axis, quantifying the flattening of an ellipse. In a two-dimensional setting, this is expressed as $L_{p1} = r_{p2} / \left(r_{p1} + r_{p2}\right)$ and $L_{p2} = r_{p1} / \left(r_{p1} + r_{p2}\right)$, with r_{pi} as the half-axis length of elliptical particles corresponding to x_i-direction. The deviation of the shape factor from 0.5 correlates with the degree of ellipse flattening. In three dimensions, the shape factors are defined through:

$$L_{pi} = \frac{g\left(\rho_p\right)}{2} \int_{\rho_p}^{\infty} \frac{d\rho}{\left(\rho + r_{pi}^2\right) g\left(\rho\right)}, \tag{1.39}$$

with definitions of $g\left(\rho_p\right) = \prod_i r_{pi}$. Substituting Eqs. (1.37) and (1.38) into Eq. (1.36), the expression for the Maxwell–Garnett theory is obtained

$$\kappa_{ei} = \frac{f_p \varepsilon_{pi} \kappa_p + (1 - f_p)\kappa_m}{f_p \varepsilon_{pi} + (1 - f_p)}. \tag{1.40}$$

For circular and spherical particles, the shape factors are 1/2 and 1/3, respectively. Consequently, the effective thermal conductivities for mixtures containing these particles are:

$$\begin{aligned} \kappa_e^{circle} &= \kappa_m \frac{\kappa_p(1 + 2f_p) + 2\kappa_m(1 - f_p)}{\kappa_p(1 - f_p) + \kappa_m(2 + f_p)}, \\ \kappa_e^{sphere} &= \kappa_m \frac{\kappa_p(1 + 1f_p) + \kappa_m(1 - f_p)}{\kappa_p(1 - f_p) + \kappa_m(1 + f_p)}. \end{aligned} \tag{1.41}$$

Since the weight $f_p \varepsilon_{pi}$ of the particles is different from that of the matrix $1 - f_p$, Eq. (1.40) is suitable for calculating the effective thermal conductivity of asymmetric structures.

1.3.1.2 Bruggeman Theory

The Bruggeman theory provides an approach for evaluating the effective thermal conductivity of symmetric composite structures. Consider a medium with particles A and B, possessing thermal conductivities κ_A and κ_B, and occupying area fractions f_A and f_B, respectively. These particles are randomly distributed within a parent medium with thermal conductivity κ_m, subject to an external temperature gradient ∇T_0 aligned along the x-axis as depicted in (Fig. 1.3b). The average heat flux and temperature gradient in this system adhere to the following relations:

$$\begin{aligned} \langle J_A \rangle &= -\kappa_A \langle \nabla T_A \rangle, \\ \langle J_m \rangle &= -\kappa_m \langle \nabla T_m \rangle, \\ \langle \nabla T_A \rangle &= \varepsilon_A \langle \nabla T_m \rangle = \frac{\kappa_m}{\kappa_A L_A + \kappa_m (1 - L_A)} \langle \nabla T_m \rangle, \\ \langle \nabla T_B \rangle &= \varepsilon_B \langle \nabla T_m \rangle = \frac{\kappa_m}{\kappa_B L_B + \kappa_m (1 - L_B)} \langle \nabla T_m \rangle, \end{aligned} \tag{1.42}$$

where L_A and L_B denote the shape factors for particles A and B, respectively. Based on Eqs. (1.36) and (1.42), the thermal conductivity for the composite can be expressed as:

$$\kappa_e = \frac{f_A \varepsilon_A \kappa_A + f_B \varepsilon_B \kappa_B + (1 - f_A - f_B)\kappa_m}{f_A \varepsilon_A + f_B \varepsilon_B + (1 - f_A - f_B)} \tag{1.43}$$

When considering particles A and B as a single entity, Eq. (1.43) simplifies to:

$$\kappa_e = \frac{f_{AB} \varepsilon_{AB} \kappa_{AB} + (1 - f_{AB})\kappa_m}{f_{AB} \varepsilon_{AB} + (1 - f_{AB})}, \tag{1.44}$$

where $f_{AB} = f_A + f_B$ represents the combined area fraction, and κ_{AB} is the effective conductivity of the two particle types. Combining Eqs. (1.43) and (1.44), the following relation is obtained:

$$f_A \varepsilon_A (\kappa_m - \kappa_A) + f_b \varepsilon_B (\kappa_m - \kappa_B) = f_{AB} \varepsilon_{AB} (\kappa_m - \kappa_{AB}) \tag{1.45}$$

To characterize the interaction between particles, it is posited that $\kappa_e = \kappa_m$, which means that the effects of particles A and B on the matrix cancel each other out. This leads to the derivation of Bruggeman's equation:

$$f_A \varepsilon_A (\kappa_m - \kappa_A) + f_b \varepsilon_B (\kappa_m - \kappa_B) = 0 \tag{1.46}$$

As Eq. (1.46) suggests, the contributions of both particle types to the overall thermal properties are balanced. Furthermore, extending Bruggeman's theory to accommodate multi-component composites is straightforward, just utilizing the same methodology delineated herein.

1.3.1.3 Series and Parallel Formulas of Thermal Conductivity

The analysis of anisotropic effects in composite materials often employs a layered structure model. As illustrated in Fig. 1.3c, materials A and B are adjoined to form a stratified configuration, with thermal conductivities κ_A and κ_B, respectively. Within this model, heat transfer along the x-direction is conceptualized as a serial coupling of A and B. In contrast, the y-direction heat transfer is analogous to a parallel coupling of the two materials. Initially, constant temperature boundary conditions T_L and T_R are imposed on the system's left and right interfaces, respectively, while the remaining boundaries are insulated. Fourier's law is then employed to define the x-direction thermal conductivity as follows:

$$\kappa_{xx} = -\frac{\langle J_x \rangle}{\langle \nabla T_x \rangle} = \frac{f_A \kappa_A \langle \nabla T_{Ax} \rangle + f_B \kappa_B \langle \nabla T_{Bx} \rangle}{f_A \langle \nabla T_{Ax} \rangle + f_B \langle \nabla T_{Bx} \rangle}, \tag{1.47}$$

where f_A and f_B are the area fraction of materials A and B. According to the normal direction boundary condition, $\kappa_A \langle \nabla T_A \rangle = \kappa_B \langle \nabla T_B \rangle$, and Eq. (1.47) we obtain the series thermal conductivity,

$$\kappa_{xx} = \frac{1}{f_A/\kappa_A + f_B/\kappa_B}. \tag{1.48}$$

Subsequently, constant temperature conditions T_t and T_b are applied to the top and bottom surfaces of the structure, with adiabatic conditions on the lateral edges. Fourier's law facilitates the parallel formulas of thermal conductivity:

$$\kappa_{yy} = -\frac{\langle J_y \rangle}{\langle \nabla T_y \rangle} = \frac{f_A \kappa_A \langle \nabla T_y \rangle + f_B \kappa_B \langle \nabla T_y \rangle}{f_A \langle \nabla T_y \rangle + f_B \langle \nabla T_y \rangle} = f_A \kappa_A + f_B \kappa_B, \tag{1.49}$$

1.3.2 Model Application

1.3.2.1 Nonlinear Enhancement in Random Particle Composites

In the context of two-dimensional composites with circular inclusions, the effective thermal conductivity can be characterized using the Maxwell-Garnett (M&G) formula and Bruggeman's formula as delineated by the following relations:

$$\begin{aligned} &\frac{\kappa_e - \kappa_h}{\kappa_e + \kappa_h} = f_i \frac{\kappa_i - \kappa_h}{\kappa_i + \kappa_h}, \\ &f_i \frac{\kappa_e - \kappa_i}{\kappa_e + \kappa_i} + f_h \frac{\kappa_e - \kappa_h}{\kappa_e + \kappa_h} = 0 \end{aligned}, \tag{1.50}$$

where f_i and f_h are area fractions of embedded particles or matrix material, and κ_i and κ_h denote corresponding thermal conductivity. For composite materials comprising nonlinear or temperature-dependent heat conduction constituents, Dai et al. [44] propose the following temperature dependence for their thermal conductivities:

$$\kappa_j = \kappa_{j0} + \chi_j (T + T_{\mathrm{rt}})^{\alpha}, (j = i, h) \tag{1.51}$$

where κ_{j0} is the temperature-independent linear part of the κ_j of the total thermal conductivity, χ_j is the nonlinear coefficient, T_{rt} is some reference temperature, and α is the power of the temperature-dependent dependence of the nonlinear thermal conductivity, which can be formally taken by any real number. In mathematical form, we can substitute Eq. (1.51) into Eq. (1.50) to obtain the temperature-dependent equivalent thermal conductivity $\kappa_e(\kappa_i(T), \kappa_h(T), f_i)$. In scenarios where material nonlinearity is weak, the study focuses on two distinct cases: (I) The embedded particles are weakly nonlinear materials, whose thermal conductivity is denoted by $\kappa_i = \kappa_{i0} + \chi_i (T + T_{\mathrm{rt}})^{\alpha}$, and the host is a linear material with a thermal conductivity denoted by $\kappa_h = \kappa_{h0}$; (II) The embedded particles are linear materials and their thermal conductivity is expressed as $\kappa_i = \kappa_{i0}$; the host material is a nonlinear material and its thermal conductivity is expressed as $\kappa_h = \kappa_{h0} + \chi_h (T + T_{\mathrm{rt}})^{\alpha}$. The effective thermal conductivity κ_e can hence be approximated by:

$$\begin{aligned} \kappa_e &= \kappa_{e0} + \chi_e (T + T_{rt})^{\alpha} + O((T + T_{rt})^{2\alpha}) \\ &= \kappa_{e0} + c_j \chi_j (T + T_{rt})^{\alpha} + O((T + T_{rt})^{2\alpha}). \end{aligned} \tag{1.52}$$

Herein, the coefficient ratio $c_j = \chi_e / \chi_j$ signifies the relative increase (or decrease) in nonlinearity of the system's heat conduction. For convenience, subsequent formulations assume $\alpha = 1$ and disregard the reference temperature T_{rt} to demonstrate that

these parameters do not influence the theoretical calculation of the effective nonlinear coefficient or the proportionality factor for nonlinear enhancement via the effective medium theory. Under this framework, the nonlinear modulation coefficient c for both asymmetric and symmetric cases of I and II can be computed as:

$$\begin{aligned}
c_{\mathrm{I}}^{\mathrm{M\&G}} &= \frac{4f_i}{(1+\kappa_{i0}/\kappa_{h0}+f_i-f_i\kappa_{i0}/\kappa_{h0})^2} \\
c_{\mathrm{II}}^{\mathrm{M\&G}} &= \frac{(1-f_i^2)\left[1+(\kappa_{i0}/\kappa_{h0})^2\right]+2(1-f_i)^2\kappa_{i0}/\kappa_{h0}}{(1+\kappa_{i0}/\kappa_{h0}+f_i-f_i\kappa_{i0}/\kappa_{h0})^2} \\
C_{\mathrm{I}}^{\mathrm{Bruggeman}} &= \frac{1}{2}\Big[\frac{(2f_i-1)\,(2f_i-2f_i\kappa_{h0}/\kappa_{i0}-1+\kappa_{h0}\kappa_{i0})+2\kappa_{h0}/\kappa_{i0}}{\sqrt{(2f_i-2f_i\kappa_{h0}/\kappa_{i0}-1+\kappa_{h0}/\kappa_{i0})^2+4\kappa_{h0}/\kappa_{i0}}}+2f_i-1\Big], \\
c_{\mathrm{II}}^{\mathrm{Bruggeman}} &= \frac{1}{2}\Big[\frac{(2f_i-1)\,(2f_i-2f_i\kappa_{i0}/\kappa_{h0}-1+\kappa_{i0}/\kappa_{h0})+2\kappa_{i0}/\kappa_{h0}}{\sqrt{(2f_i-2f_i\kappa_{i0}/\kappa_{h0}-1+\kappa_{i0}/\kappa_{h0})^2+4\kappa_{i0}/\kappa_{h0}}}-2f_i+1\Big]
\end{aligned} \tag{1.53}$$

The interest lies in instances where $c > 1$, indicating an amplified equivalent nonlinear coefficient for the composite. It is easy to see that Eq. (1.53) is only related to f_i and $\kappa_{i.}/\kappa_{h0}$. In Fig. 1.4, the proportional coefficient c changes with f_i for the ratios of κ_{i0}/κ_{h0} of the above four expressions.

According to Fig. 1.4, for the M&G model, a prerequisite for nonlinear enhancement is the embedding of linear particles within a nonlinear matrix, provided the ratio κ_{i0}/κ_{h0} exceeds unity, and the particle area fraction remains relatively low. It is critical to note that this constitutes a necessary condition. Analysis of additional data curves for various κ_{i0}/κ_{h0} ratios suggests a threshold value for nonlinear enhancement in the vicinity of 2.5. Conversely, Bruggeman's theory also forecasts the possibility of nonlinear enhancement, contingent upon the linear component of the nonlinear material's thermal conductivity being less than that of the linear material and a sufficiently large area fraction of the nonlinear constituent.

1.3.2.2 Nonlinear Enhancement in Periodic Particle Composites

In addition to their disordered counterparts, periodic composite structures play a pivotal role in the architecture of artificial crystals and have various applications in linear heat conduction, such as in thermal transparency devices [46], Janus thermal illusions [47], and phantom thermal diodes. Previous studies have indicated that effective medium theory correlates well with the linear thermal conductivity in composites of a periodic structure when the area fraction of the embedded particles is small. However, notable discrepancies arise as this fraction increases. Dai et al. [24] have employed the Rayleigh method, a first-principles approach, to calculate the equivalent thermal conductivity of periodic nonlinear thermal conductivity composites.

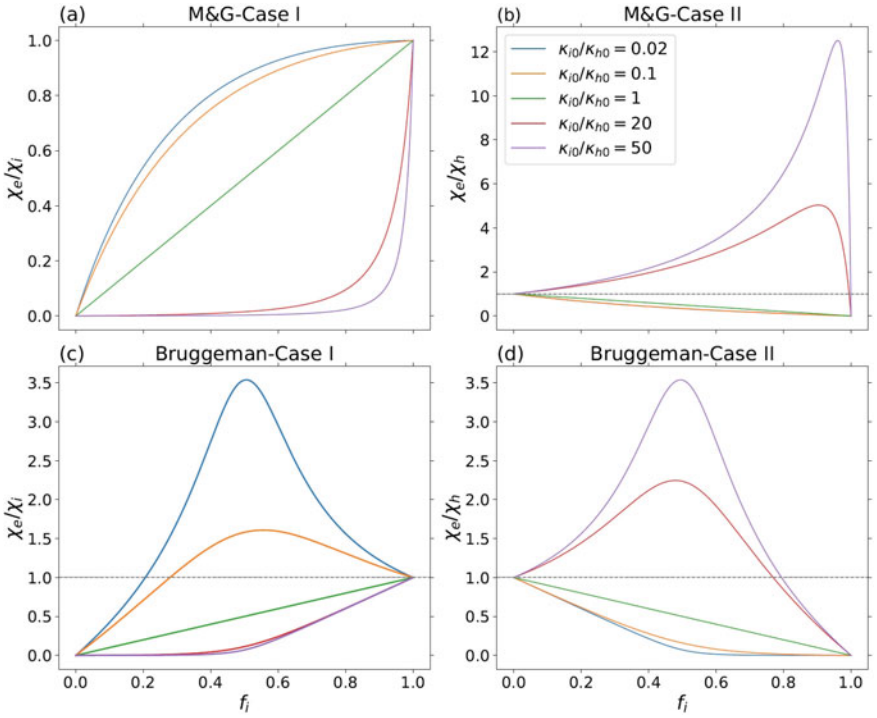

Fig. 1.4 The enhancement of the equivalent nonlinear coefficient is calculated according to the theory of effective medium. **a** M&G-Case I. **b** M&G-Case II. **c** Bruggeman-Case I. **d** Bruggeman-Case II. Adapted from Ref. [44]

They extend the analysis to two-dimensional composites with circular particles embedded in a matrix in a quadrangular lattice pattern. Corresponding to the examination of disordered structures, the two configurations depicted in Fig. 1.5 are considered: configuration I involves nonlinear particles embedded in a linear host material as shown in Fig. 1.5a, whereas configuration II involves linear particles in a nonlinear host material as illustrated in Fig. 1.5b. The derived expression for the linear effective thermal conductivity,

$$\kappa_e = \kappa_h \frac{(-\beta_1 + \beta_1 f_i + f_i^4)\kappa_h^2 - 2(\beta_1 + f_i^4)\kappa_h\kappa_i + (-\beta_1 - \beta_1 f_i + f_i^4)\kappa_i^2}{(-\beta_1 - \beta_1 f_i + f_i^4)\kappa_h^2 - 2(\beta_1 + f_i^4)\kappa_h\kappa_i + (-\beta_1 + \beta_1 f_i + f_i^4)\kappa_i^2}, \tag{1.54}$$

where $\beta_1 = 3.31248$. This result is consistent with the calculation of the linear equivalent conductivity [48], confirming that a constant temperature differential does not influence the outcome of the equivalent thermal conductivity in the linear case. By integrating Eq. (1.51) into Eq. (1.54) and utilizing Taylor series expansion, the nonlinear modulation coefficient c is determined as:

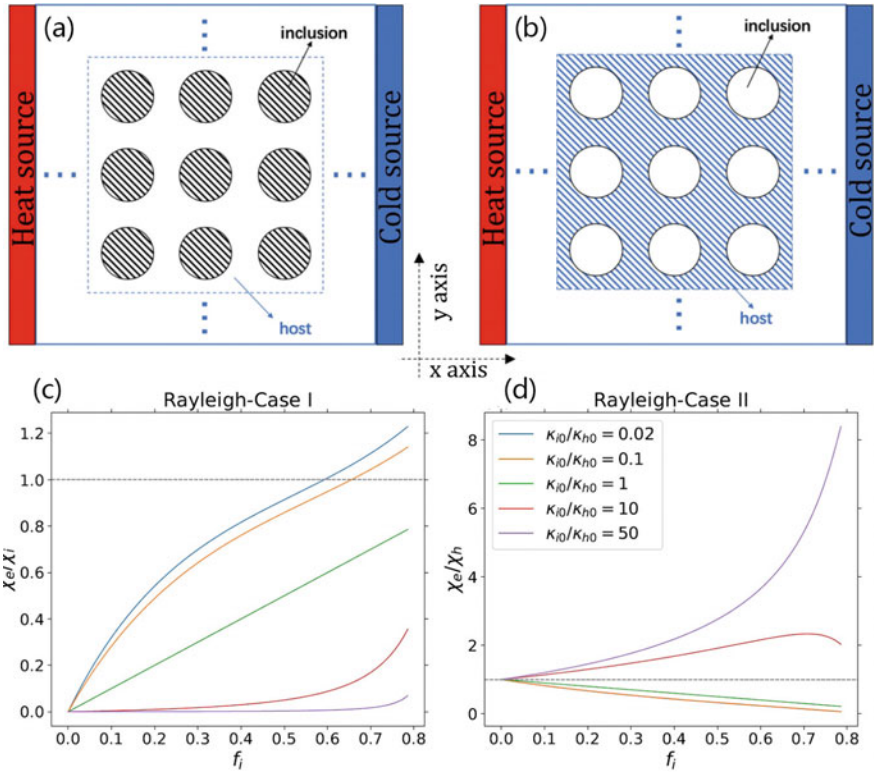

Fig. 1.5 Schematic diagram illustrating two classes of periodic composites: **a** nonlinear inclusions are periodically embedded in a linear (temperature-independent) host; **b** linear inclusions are periodically embedded in a nonlinear host. The nonlinear modulation coefficients of Cases **c** I and **d** II predicted by Rayleigh method. Adapted from Ref. [24]

$$
\begin{aligned}
c_{\mathrm{I}}^{\mathrm{Rayleigh}} &= \frac{4\beta_1 f_i \kappa_{h0}^2 \left[\beta_1(\kappa_{h0}+\kappa_{i0})^2 + f_i^4(\kappa_{h0}-\kappa_{i0})^2\right]}{\left[\beta_1(\kappa_{h0}+\kappa_{i0})(f_i\kappa_{h0}-f_i\kappa_{i0}+\kappa_{h0}+\kappa_{i0}) - f_i^4(\kappa_{h0}-\kappa_{i0})^2\right]^2} \\
c_{\mathrm{II}}^{\mathrm{Rayleigh}} &= \frac{-\beta_1^2(f_i-1)(\kappa_{h0}+\kappa_{i0})^2\left[(f_i+1)\kappa_{h0}^2 - 2(f_i-1)\kappa_{h0}\kappa_{i0} + (f_i+1)\kappa_{i0}^2\right]}{\left[\beta_1(\kappa_{h0}+\kappa_{i0})(f_i\kappa_{h0}-f_i\kappa_{i0}+\kappa_{h0}+\kappa_{i0}) - f_i^4(\kappa_{h0}-\kappa_{i0})^2\right]^2} \\
&\quad + \frac{-2\beta_1 f_i^4(\kappa_{h0}-\kappa_{i0})^2\left[2(f_i+1)\kappa_{h0}\kappa_{i0} + \kappa_{h0}^2 + \kappa_{i0}^2\right] + f_i^8(\kappa_{h0}-\kappa_{i0})^4}{\left[\beta_1(\kappa_{h0}+\kappa_{i0})(f_i\kappa_{h0}-f_i\kappa_{i0}+\kappa_{h0}+\kappa_{i0}) - f_i^4(\kappa_{h0}-\kappa_{i0})^2\right]^2}
\end{aligned}
\tag{1.55}
$$

To elucidate the conditions under which nonlinear enhancement occurs, Fig. 1.5c and d plot the variation of $c = \chi_e/\chi_j$ ($j = i$ or h) against f_i for values of $\kappa_{i0}/\kappa_{h0} = 0.02$, 0.1, 1, 10, and 50. In both configurations corresponding to Fig. 1.5c and d, it is observed that $c > 1$. However, it is imperative to recognize that these conditions are merely sufficient. In the context of nonlinear particles embedded within a linear host

material, a critical threshold for the enhanced ratio κ_{i0}/κ_{h0} is approximately 1/3.5, constrained by a maximum f_i value of $\pi/4$. Conversely, when linear particles are embedded within a nonlinear host, the critical ratio κ_{i0}/κ_{h0} is about 2.5.

1.4 Scattering Cancellation Theory

The strictness of the transformation thermotics ensures its powerful ability to manipulate the thermal field, but the parameters predicted by the theory are often non-uniform and anisotropic, which brings great challenges to the practical preparation. The linear/conformal mapping and effective medium theory previously discussed provide theoretical frameworks for designing the parameters in the production of transformation optics devices. In pursuit of alternative methodologies, some scholars have applied scattering cancellation theory to directly resolve the governing equations and determine the distribution of the physical field. This approach utilizes isotropic homogeneous media to replace the complex components of the original structure, thereby replicating the external field distribution. It is acknowledged that obstacles or external heat sources (besides the uniform gradient field) disrupt the background temperature field. Depending on the need for external stimuli, thermal metamaterials are typically categorized into passive or active designs.

1.4.1 Passive Scheme: No External Energy Input

1.4.1.1 Circular Shape

Xu et al. [49, 50] examined a core-shell configuration with inner and outer radii denoted by r_c and r_s in (Fig. 1.6a), respectively. The thermal conductivities of the core and shell are $\boldsymbol{\kappa}_c$ and $\boldsymbol{\kappa}_s$, respectively, and both are anisotropic,

$$\left[\boldsymbol{\kappa}_c^{ij}\right] = \begin{pmatrix} \kappa_{crr} & 0 \\ 0 & \kappa_{c\theta\theta} \end{pmatrix}, \left[\boldsymbol{\kappa}_s^{ij}\right] = \begin{pmatrix} \kappa_{srr} & 0 \\ 0 & \kappa_{s\theta\theta} \end{pmatrix}. \tag{1.56}$$

The metric of polar coordinates is

$$\left[g_{ij}\right] = \begin{pmatrix} 1 & 0 \\ 0 & r^2 \end{pmatrix}. \tag{1.57}$$

By incorporating Eqs. (1.56) and (1.57) into Eq. (1.3) and neglecting both the time-dependent term and the internal heat source term, the heat conduction equation in polar coordinates is given by:

$$\frac{1}{r}\frac{\partial}{\partial r}\left(r\kappa_{rr}\frac{\partial T}{\partial r}\right)+\frac{1}{r}\frac{\partial}{\partial \theta}\left(\kappa_{\theta\theta}\frac{\partial T}{r\partial \theta}\right)=0. \tag{1.58}$$

The general solution for Eq. (1.58) is expressed as:

$$\begin{aligned} T = A_0 + B_0 \ln r + \sum_{i=1}^{\infty} r^{u_i^+} \left(A_i \cos(i\theta) + C_i \sin(i\theta)\right) \\ + \sum_{i=1}^{\infty} r^{u_i^-} \left(B_i \cos(i\theta) + D_i \sin(i\theta)\right) \end{aligned}, \tag{1.59}$$

where $u_i^{\pm} = \pm i\sqrt{\kappa_{\theta\theta}/\kappa_{\mathrm{rr}}}$. Due to the symmetry inherent in the core-shell structure, Eq. (1.59) can be simplified as follows:

$$T = A_0 + \left(A_1 r^{u_1^+} + B_1 r^{u_1^-}\right)\cos\theta, \tag{1.60}$$

where A_0 is a constant set to zero for convenience, A_1 and B_1 are two constants to be determined, and $u^{\pm}$ are respectively $\pm\sqrt{\kappa_{\theta\theta}/\kappa_{rr}}$ in 2D and $-1/2 \pm \sqrt{1/4 + 2\kappa_{\theta\theta}/\kappa_{rr}}$ in 3D. Then, the temperature distributions in the core (T_c), shell (T_s), and matrix (T_m) are represented as follows:

$$T_c = A_c r^{u_c^+}\cos\theta, \tag{1.61a}$$

$$T_s = \left(A_s r^{u_s^+} + B_s r^{u_s^-}\right)\cos\theta, \tag{1.61b}$$

$$T_m = \left(A_m r + B_m r^{u_m^-}\right)\cos\theta, \tag{1.61c}$$

where A_c, A_s, B_s, and B_m are four constants determined by boundary conditions, and A_m is the applied temperature gradient. In 2D, $u_c^+ = \sqrt{\kappa_{c\theta\theta}/\kappa_{crr}}$, $u_s^{\pm} = \pm\sqrt{\kappa_{s\theta\theta}/\kappa_{srr}}$, and $u_m^- = -1$; in 3D, $u_c^+ = -1/2 + \sqrt{1/4 + 2\kappa_{c\theta\theta}/\kappa_{crr}}$, $u_s^{\pm} = -1/2 \pm \sqrt{1/4 + 2\kappa_{s\theta\theta}/\kappa_{srr}}$, and $u_m^- = -2$.

The boundary conditions necessitate the continuity of temperature and normal heat flux, expressed as follows:

$$T_c\,(r = r_c) = T_s\,(r = r_c)\,, \tag{1.62a}$$

$$T_m\,(r = r_s) = T_s\,(r = r_s)\,, \tag{1.62b}$$

$$-\kappa_{crr}\frac{\partial T_c}{\partial r}\,(r = r_c) = -\kappa_{srr}\frac{\partial T_s}{\partial r}\,(r = r_c)\,, \tag{1.62c}$$

$$-\kappa_m\frac{\partial T_m}{\partial r}\,(r = r_s) = -\kappa_{srr}\frac{\partial T_s}{\partial r}\,(r = r_s)\,, \tag{1.62d}$$

where κ_m is the thermal conductivity of the matrix. Substituting Eq. (1.61) into Eq. (1.62) yields

$$A_c r_c^{u_c^+} = A_s r_c^{u_s^+} + B_s r_c^{u_s^-}, \tag{1.63a}$$

$$A_m r_s + B_m r_s^{u_m^-} = A_s r_s^{u_s^+} + B_s r_s^{u_s^-}, \tag{1.63b}$$

$$-\kappa_{crr} u_c^+ A_c r_c^{u_c^+ - 1} = -\kappa_{srr} \left(u_s^+ A_s r_c^{u_s^+ - 1} + u_s^- B_s r_c^{u_s^- - 1} \right), \tag{1.63c}$$

$$-\kappa_m \left(A_m + u_m^- B_m r_s^{u_m^- - 1} \right) = -\kappa_{srr} \left(u_s^+ A_s r_s^{u_s^+ - 1} + u_s^- B_s r_s^{u_s^- - 1} \right). \tag{1.63d}$$

Solving these equations enables the analytical determination of coefficients A_c, A_s, B_s, and B_m. The condition of scattering cancellation is met when the influence of the core-shell structure is nullified, denoted by $B_m = 0$. Applying this condition, one can deduce the necessary thermal conductivity:

$$\begin{aligned} \kappa_e &= \kappa_m \\ &= \kappa_{srr} \frac{u_s^+ \left(u_c^+ \kappa_{crr} - u_s^- \kappa_{srr} \right) - u_s^- \left(u_c^+ \kappa_{crr} - u_s^+ \kappa_{srr} \right) (r_c/r_s)^{u_s^+ - u_s^-}}{u_c^+ \kappa_{crr} - u_s^- \kappa_{srr} - \left(u_c^+ \kappa_{crr} - u_s^+ \kappa_{srr} \right) (r_c/r_s)^{u_s^+ - u_s^-}}, \end{aligned} \tag{1.64}$$

where κ_e signifies the effective thermal conductivity of the core-shell configuration. This computational approach extends beyond a single-shell model. For configurations with n shells, the effective thermal conductivity can be derived using $2n + 2$ boundary conditions analogous to Eq. (1.62), where $n + 1$ equations describe the temperature continuity, and the other $n + 1$ equations indicate the normal heat flux continuity. An alternative methodology involves a recursive, shell-by-shell calculation of the effective thermal conductivity. For example, Eq. (1.64) can be employed to compute the effective thermal conductivity of the core combined with the first shell, κ_{e1}. Thereafter, the core and the first shell are treated as a new core with thermal conductivity κ_{e1}. Subsequently, Eq. (1.64) can be applied again to calculate the effective thermal conductivity of this new core in conjunction with the second shell, κ_{e2}, and the process is repeated for all n shells. Notably, Li et al. [51] have crafted components characterized by diverse diffusion rates employing scattering cancellation theory. The insertion of these varied components enables switching between cloaking and concentrating functions in the concentration field. This innovative design boasts adaptability and reconfigurability, rendering it applicable across a broad spectrum of uses without necessitating a comprehensive redesign of the existing system.

1.4.1.2 Elliptical Shape

In the study of geometrically anisotropic confocal core-shell structures [52, 53], we assume isotropic thermal conductivities for the core, κ_c, and the shell, κ_s, as depicted in Fig. 1.6b. Anisotropy in the shell results in the loss of a degree of design freedom compared to isotropic materials, often necessitating an additional shell layer for compensation. Without loss of generality, let us first discuss the calculation method of the single shell, which can be naturally generalized to the double shell or multiple shell. Within a Cartesian coordinate system denoted by x_i, a two-dimensional scenario

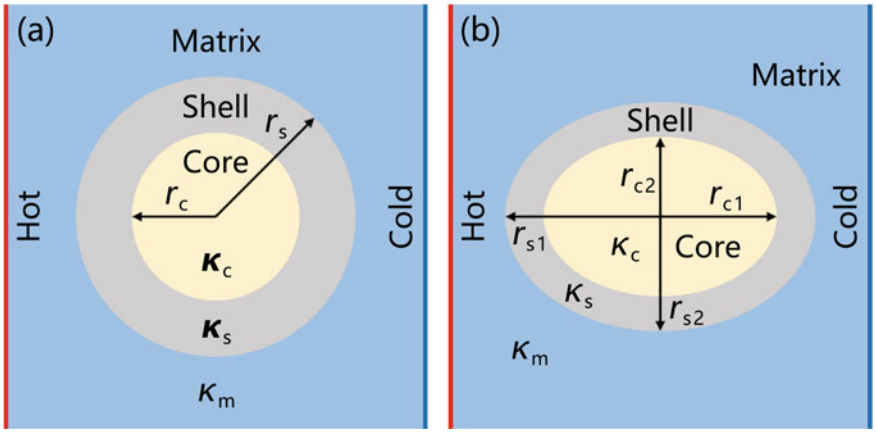

Fig. 1.6 Schematic diagram of two representative schemes. **a** Isotropic geometry with anisotropic thermal conductivity; **b** Anisotropic geometry with isotropic thermal conductivity. (from Ref. [50])

permits i to assume the values of 1 and 2, while a three-dimensional scenario allows i to be 1, 2, and 3. The semi-axes of the core and shell in the x_i direction are represented by r_{ci} and r_{si}, respectively. The transformation from Cartesian coordinates x_i to elliptic or ellipsoidal coordinates ρ_j is governed by the relation:

$$\sum_i \frac{x_i^2}{\rho_j + r_{ci}^2} = 1, \tag{1.65}$$

where j takes on values of 1, 2, and 3 for three-dimensional spaces and 1 and 2 for two-dimensional spaces. The coordinate ρ_1, which is greater than $-r_{ci}^2$, functions similarly to the radial coordinate in spherical systems. For instance, the shell's inner and outer boundaries correspond to $\rho_1 = \rho_c$ (which equals zero) and $\rho_1 = \rho_s$, respectively. In the presence of a uniform thermal field along the x_i axis, thermal conduction equation can be expressed in the elliptical (or ellipsoidal) coordinate system as [45]

$$\frac{\partial}{\partial \rho_1}\left[g\left(\rho_1\right)\frac{\partial T}{\partial \rho_1}\right] + \frac{g\left(\rho_1\right)}{\rho_1 + r_{ci}^2}\frac{\partial T}{\partial \rho_1} = 0, \tag{1.66}$$

with a definition of $g\left(\rho_1\right) = \prod_i \left(\rho_1 + r_{ci}^2\right)^{1/2}$. For three dimensions, $4\pi g\left(\rho_1 = 0\right)/3 = 4\pi r_{c1}r_{c2}r_{c3}/3$ (or $4\pi g\left(\rho_1 = \rho_s\right)/3 = 4\pi r_{s1}r_{s2}r_{s3}/3$) represents the volume of the core (or the core plus the shell). For two dimensions, $\pi g\left(\rho_1 = 0\right) = \pi r_{c1}r_{c2}$ (or $\pi g\left(\rho_1 = \rho_s\right) = \pi r_{s1}r_{s2}$) denotes the area of the core (or the core plus the shell). The temperature distributions within the core (T_{ci}), the shell (T_{si}), and the matrix (T_{mi}) along the x_i axis are formulated as:

$$\begin{cases} T_{ci} = A_{ci} x_i, \\ T_{si} = \left[A_{si} + B_{si} \phi_i\left(\rho_1\right)\right] x_i, \\ T_{mi} = \left[A_{mi} + B_{mi} \phi_i\left(\rho_1\right)\right] x_i, \end{cases} \tag{1.67}$$

with a definition of $\phi_i\left(\rho_1\right) = \int_{\rho_c}^{\rho_1} \left[\left(\rho_1 + r_{ci}^2\right) g\left(\rho_1\right)\right]^{-1} d\rho_1$. The constants A_{ci}, A_{si}, B_{si}, and B_{mi} are ascertainable through the continuity conditions of temperature and normal heat flux. Since the temperature distribution in the background should be undistorted, we take $B_{mi} = 0$ and leads to the following expression for the effective thermal conductivity κ_e:

$$\kappa_e = \kappa_m = \frac{L_{ci}\kappa_c + \left(1 - L_{ci}\right)\kappa_s + \left(1 - L_{si}\right)\left(\kappa_c - \kappa_s\right) f}{L_{ci}\kappa_c + \left(1 - L_{ci}\right)\kappa_s - L_{si}\left(\kappa_c - \kappa_s\right) f}\kappa_s, \tag{1.68}$$

Here, $f = g\left(\rho_c\right)/g\left(\rho_s\right) = \prod_i r_{ci}/r_{si}$ and L_{wi} is the shape factor of the ellipse along x_i-direction, which can refer to the definition of Eq. (1.39). This method can be easily extended to calculate the effective thermal conductivity of a core-shell structure with n shells, as we did for the geometrically isotropic case.

1.4.1.3 Irregular Shape

The challenge of solving the steady-state heat conduction equation for boundaries with irregular geometries is significant, as it complicates the analytical approach. Traditional scattering cancellation theories often struggle to maintain an undisturbed background thermal field in such cases. Addressing this, Xu et al. [54] introduced a concept referred to as a thermal supercavity, as illustrated in Fig. 1.7. This design adheres to the thermal uniqueness theorem, which suggests that matching the boundary conditions of the shell with those of the surrounding environment will preserve the undisturbed nature of the background temperature field. The assumption is made that the thermal gradient in the background, ∇T_0, is oriented along the x-direction, and the thermal conductivity of the shell in the y-direction is taken to be infinitely large. Contrasting with a conventional circular cloak (see Fig. 1.7a), the shell in this scheme (see Fig. 1.7b) ensures that the temperature gradient component along the y-direction is negligible. Furthermore, the cavity's interior is filled with air and objects, implying an equivalent thermal conductivity close to zero. By considering the conservation of heat flux across the shell and background interface, the following relationship is established,

$$\begin{aligned} -\kappa_{xx}[g(x) - f(x)]|(\text{Gradient } T_s)_x| &= -\kappa_b g(x)|\nabla T_0|, \\ |(\text{Gradient } T_s)_x| &= |\nabla T_0|, \end{aligned} \tag{1.69}$$

where Gradient T_s denotes the horizontal temperature gradient within the shell, and κ_b represents the thermal conductivity of the background. The functions $f(x)$ and

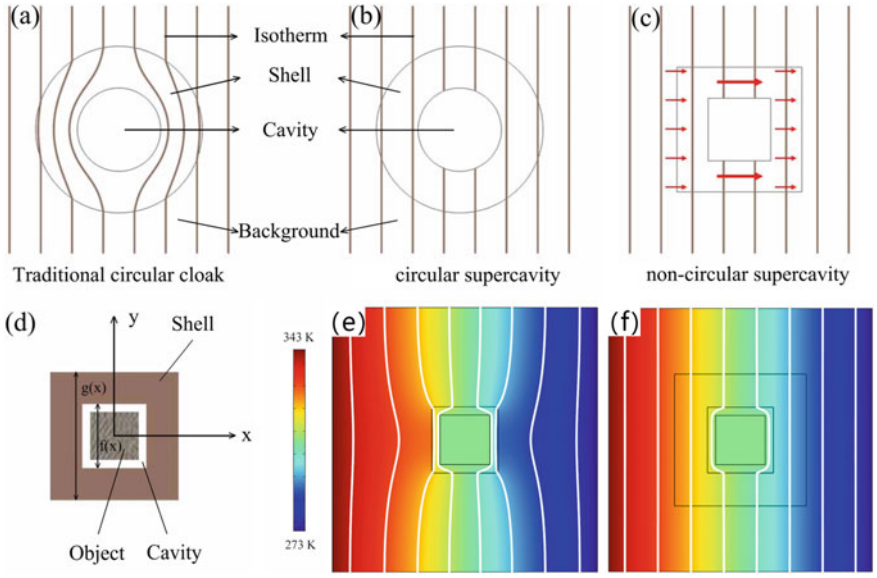

Fig. 1.7 Schematic diagram of **a** the traditional circular cloak and **b** circular supercavity. **c** shows an example of square supercavity, whose details are indicated in **d**. Brown lines and red arrows represent isotherms and heat flux, respectively. Temperature distribution **e** without cavity and with **f** cavity. (from Ref. [54])

$g(x)$ describe the lengths of the cavity and shell at the position x, respectively, as depicted in Fig. 1.7c and d. Consequently, the thermal conductivity of the shell, comprising an anisotropic material, is derived as:

$$\kappa_s = \begin{pmatrix} \frac{g(x)\kappa_b}{g(x)-f(x)} & 0 \\ 0 & \infty \end{pmatrix} \tag{1.70}$$

Equation (1.70) facilitates the design of a shell with tailored properties, ensuring its invisibility within the thermal landscape, as presented in Fig. 1.7e and f. Subsequently, Wang et al. [55] expanded upon this approach within the conduction-radiation domain, developing thermal cloaks and sensors for irregular-shaped objects.

1.4.2 Active Scheme: External Energy Input

The above discussion has centered on passive heat transfer mechanisms. However, in many practical applications, the introduction of external energy inputs can unlock additional functionalities. This discussion will delve into two types of external energy

inputs: one achieved through the rotation of a rotor to induce heat flow, and the other by means of direct contact with an external heat source.

1.4.2.1 Introduce Thermal Convection by Rotating Particle

Xu et al. [29] investigate a scenario involving a rotating particle characterized by an angular velocity Ω, radius R, and thermal conductivity κ_p, situated within a finite matrix with thermal conductivity κ_m. This setup is visualized in Fig. 1.8. For a steady-state and passive system, the governing equation is given by

$$v\nabla T - D\nabla^2 T = 0, \tag{1.71}$$

where $D = \kappa/\rho c$ is thermal diffusivity and $v = \Omega r$ is linear velocity. Utilizing the metric of polar coordinate (Eq. (1.57)), Eq. (1.71) can be rewritten as:

$$\Omega\frac{\partial T}{\partial \theta} - D\left(\frac{\partial^2 T}{\partial r^2} + \frac{1}{r}\frac{\partial T}{\partial r} + \frac{1}{r^2}\frac{\partial^2 T}{\partial \theta^2}\right) = 0. \tag{1.72}$$

The temperature profile T_p in the particle has the form of

$$T_{\mathfrak{p}} = F(r)G(\theta), \tag{1.73}$$

where $F(r)$ and $G(\theta)$ correspond to the radial and angular distribution functions, respectively. On substituting Eq. (1.73), the resulting equation is:

$$\frac{1}{F}(r^2F'' + rF') = \frac{1}{G}\left(\frac{\Omega r^2}{D}G' - G''\right). \tag{1.74}$$

Considering that G varies periodically with θ and transitions smoothly in this system, the assumption that $G = \exp(i\theta)$, with i being the imaginary unit, is made. This leads to a tractable solution of Eq. (1.74), wherein F satisfies:

$$r^2F'' + rF' - \left(\frac{\Omega r^2}{D}i + 1\right)F = 0. \tag{1.75}$$

By performing Variable substitution $r = \sqrt{D/\Omega}x$, Eq. (1.75) reduces to

$$x^2f'' + xf' - (x^2i + 1)f = 0, \tag{1.76}$$

where the solution is a combination of the first-order Kelvin functions:

$$f(x) = \mathrm{ber}(x) + i\,\mathrm{bei}(x) \tag{1.77}$$

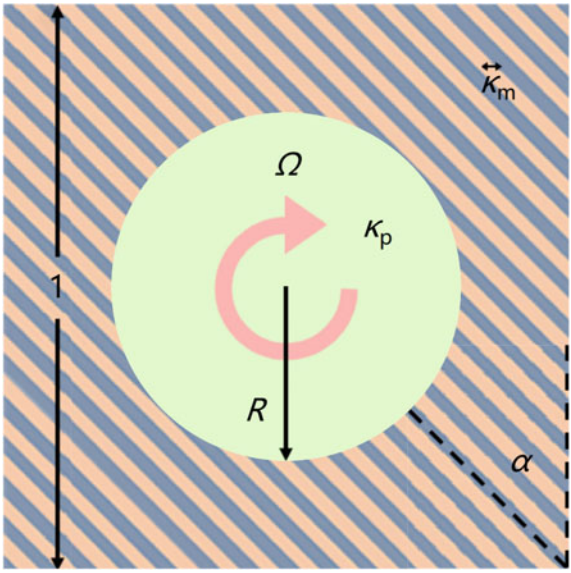

Fig. 1.8 The schematic diagram of rotating particle embed in a finite matrix. Adapted from Ref. [29]

In scenarios where the velocity is significantly high, and consequently, x is large, the following expression is derived:

$$\begin{aligned} T_{\mathrm{p}}(r,\theta) &= M\big(x(r)\big)\cos\big(\theta-\phi\big(x(r)\big)\big)\,, \\ \frac{\partial T_{\mathrm{p}}(r,\theta)}{\partial r} &= \sqrt{\frac{\Omega}{D}}M\big(x(r)\big)\cos\Big(\theta-\phi\big(x(r)\big)+\frac{\pi}{4}\Big), \end{aligned} \tag{1.78}$$

where $M(x)$ signifies the amplitude of $f(x)$, and $\phi(x)$ encapsulates the influence of rotation.

The replacement of a rotating particle with a stationary one with an effective thermal conductivity κ_p leads to the heat conduction equation without rotation given by

$$\kappa\left(\frac{\partial^2 T}{\partial r^2}+\frac{1}{r}\frac{\partial T}{\partial r}+\frac{1}{r^2}\frac{\partial^2 T}{\partial\theta^2}\right)=0. \tag{1.79}$$

The general solution to this equation is expressed as:

$$T = T_0+\left(Ar+\frac{B}{r}\right)\cos\theta, \tag{1.80}$$

where T_0 represents a reference temperature, here set to zero for simplicity, and A and B are constants. The temperature distributions in the matrix (T_m) and in the particle (T_p^*) are described by

$$\begin{aligned} T_{\mathrm{m}} &= \left(A_{\mathrm{m}} r + \frac{B_{\mathrm{m}}}{r}\right)\cos\theta, \\ T_{\mathrm{p}}^{*} &= A_{\mathrm{p}}^{*} r\cos\theta, \end{aligned} \tag{1.81}$$

where B_m and A_p^* are two constants determined by the boundary conditions, and A_m is the applied temperature gradient. The continuity of temperatures and heat fluxes at the boundary is characterized by

$$\begin{aligned} T_{\mathrm{m}}(r=R) &= T_{\mathrm{p}}^{*}(r=R) \\ -\kappa_{\mathrm{m}}\frac{\partial T_{\mathrm{m}}}{\partial r}(r=R) &= -\kappa_{\mathrm{p}}^{*}\frac{\partial T_{\mathrm{p}}^{*}}{\partial r}(r=R), \end{aligned} \tag{1.82}$$

Substituting Eq. (1.81) into Eq. (1.82), the relationship is derived as follow:

$$\begin{aligned} A_{\mathrm{p}}^{*} &= \frac{2\kappa_{\mathrm{m}}}{\kappa_{\mathrm{m}}+\kappa_{\mathrm{p}}^{*}}A_{\mathrm{m}}, \\ B_{\mathrm{m}} &= \frac{(\kappa_{\mathrm{m}}-\kappa_{\mathrm{p}}^{*})R^{2}}{\kappa_{\mathrm{m}}+\kappa_{\mathrm{n}}^{*}}A_{\mathrm{m}}. \end{aligned} \tag{1.83}$$

It is worth mentioning that T_p^* generally differs from T_p, yet their difference can be minimized by a specific condition. They define the difference as

$$\int_{0}^{2\pi}\left(T_{\mathrm{p}}(r=R)-T_{\mathrm{p}}^{*}(r=R)\right)^{2}d\theta \tag{1.84}$$

According to the minimum entropy production principle, the condition $\phi(x(R)) = \pi/4$ should be satisfied to attain the minimum value of this integral, resulting in

$$M(x(R))\cos\left(\phi(x(R))\right) = \frac{2\kappa_{\mathrm{m}}}{\kappa_{\mathrm{m}}+\kappa_{\mathrm{p}}^{*}}A_{\mathrm{m}}R. \tag{1.85}$$

Reconsidering the rotating particle, and the boundary conditions are

$$\begin{aligned} T_{\mathrm{m}}(r=R) &= T_{\mathrm{p}}(r=R), \\ -\kappa_{\mathrm{m}}\frac{\partial T_{\mathrm{m}}}{\partial r}(r=R) &= -\kappa_{\mathrm{p}}\frac{\partial T_{\mathrm{p}}}{\partial r}(r=R). \end{aligned} \tag{1.86}$$

Substituting Eqs. (1.78) and (1.81) into Eq. (1.86), one can derive

$$-\kappa_{\mathrm{m}}\left(A_{\mathrm{m}}-\frac{B_{\mathrm{m}}}{R^{2}}\right)\cos\theta = -\kappa_{\mathrm{p}}\sqrt{\frac{\Omega}{D}}M\big(x(R)\big)\cos\left(\theta-\phi\big(x(R)\big)+\frac{\pi}{4}\right). \tag{1.87}$$

The substitution of Eqs. (1.83) and (1.85) into Eq. (1.87) yields

$$-\kappa_{\mathrm{m}}\left(A_{\mathrm{m}}-\frac{\kappa_{\mathrm{m}}-\kappa_{\mathrm{p}}^{*}}{\kappa_{\mathrm{m}}+\kappa_{\mathrm{p}}^{*}}A_{\mathrm{m}}\right)=-\kappa_{\mathrm{p}}\sqrt{\frac{\Omega}{D}}\frac{2\kappa_{\mathrm{m}}}{\kappa_{\mathrm{m}}+\kappa_{\mathrm{p}}^{*}}A_{\mathrm{m}}R\frac{1}{\cos\left(\phi\left(x(R)\right)\right)}, \tag{1.88}$$

which can be simplified to:

$$\kappa_{\mathrm{p}}^{*}=\kappa_{\mathrm{p}}\sqrt{\frac{2\Omega R^{2}}{D}} \tag{1.89}$$

Building on Eq. (1.89), Xu et al. [30] realized an analog thermal material whose effective conductivity can be in-situ tuned from near-zero to near-infinity. Moreover, Li et al. [31] introduced a rotating ring to realized effective infinite thermal conductivity, demonstrating a thermal zero-index cloak theoretically and experimentally. Compared with traditional thermal cloaks, this metadevice can operate in a background of high thermal conductivity, and the sheltered object maintains a high sensitivity to external temperature changes.

1.4.2.2 Introduce Energy by Contacting External Heat Sources

A thermal dipole can be analogized to an electric dipole, comprising both a heat source and a cold source. As a result of this thermal dipole, the generated thermal fields can assume a comparable shape. Xu et al. [32] introduced the concept of a thermal metamaterial that is assisted by thermal dipoles, as depicted in Fig. 1.9.

Consider a circular particle with thermal conductivity κ_p and radius r_p embedded in a matrix with thermal conductivity κ_m, as illustrated in Fig. 1.9. When a uniform thermal field G_0 is applied, the temperature distribution within the matrix is disrupted due to the disparity in thermal conductivities between the particle and the matrix. Drawing on the two-dimensional temperature general solution provided by Eq. (1.60), the temperature distributions for the particle T_{pe} and the matrix T_{me} can be expressed as follows:

$$\begin{aligned} T_{pe} &= A_1 r\cos\theta + T_r, \\ T_{me} &= -G_0 r\cos\theta + A_2 r^{-1}\cos\theta + T_r, \end{aligned} \tag{1.90}$$

where G_0 denotes the thermal gradient at infinity and T_r represents the reference temperature. Constants A_1 and A_2 are ascertainable via the boundary conditions:

$$\begin{aligned} T_{pe}\left(r=r_p\right) &= T_{me}\left(r=r_p\right), \\ \kappa_p\frac{\partial T_{pe}}{\partial r}\left(r=r_p\right) &= \kappa_m\frac{\partial T_{me}}{\partial r}\left(r=r_p\right). \end{aligned} \tag{1.91}$$

From these conditions, one can solve for A_2, hence depicting the temperature distribution of the matrix as presented in (Fig. 1.9a and b):

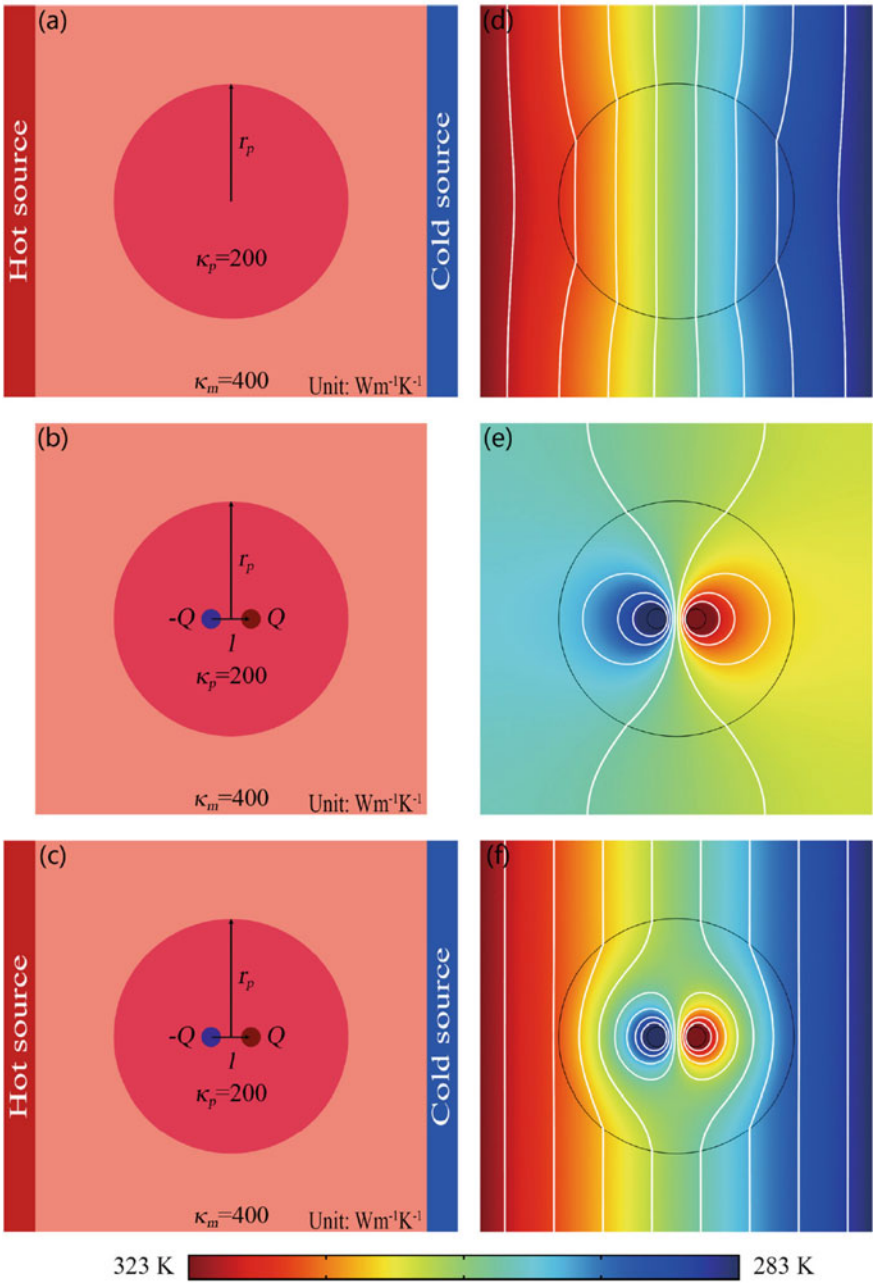

Fig. 1.9 Finite-element simulations in the presence of **a**, **d** an external uniform thermal field, **b**, **e** a thermal dipole, and **c**, **f** an external uniform thermal field and a thermal dipole together. (from Ref. [32])

$$T_{me} = -G_0 r\cos\theta - \frac{\kappa_m - \kappa_p}{\kappa_m + \kappa_p} r_p^2 G_0 r^{-1}\cos\theta + T_r. \tag{1.92}$$

On the other hand, the temperature distribution induced by a thermal dipole can be characterized as:

$$\begin{aligned} T_{pd} &= \frac{M}{2\pi\kappa_p} r^{-1}\cos\theta + B_1 r\cos\theta + T_r \\ T_{md} &= B_2 r^{-1}\cos\theta + T_r. \end{aligned} \tag{1.93}$$

with the corresponding boundary conditions:

$$\begin{aligned} T_{pd}\left(r = r_p\right) &= T_{md}\left(r = r_p\right), \\ \kappa_p \frac{\partial T_{pd}}{\partial r}\left(r = r_p\right) &= \kappa_m \frac{\partial T_{md}}{\partial r}\left(r = r_p\right). \end{aligned} \tag{1.94}$$

Therefore, B_2 is determined and the temperature distribution for the matrix is acquired as shown in (Fig. 1.9c and d),

$$T_{md} = \frac{M}{\pi\left(\kappa_m + \kappa_p\right)} r^{-1}\cos\theta + T_r, \tag{1.95}$$

where $M = Ql$ is the dipole moment. According to the superposition principle, the total temperature distribution T_s (Fig. 1.9e and f) in the matrix is

$$T_s = -G_0 r\cos\theta - \left(\frac{\kappa_m - \kappa_p}{\kappa_m + \kappa_p} r_p^2 G_0 - \frac{M}{\pi\left(\kappa_m + \kappa_p\right)}\right) r^{-1}\cos\theta + T_r \tag{1.96}$$

To maintain a uniform thermal field in the matrix, the second term to the right of Eq. (1.96) must be nullified, which leads to determining the appropriate thermal dipole moment:

$$M = \left(\kappa_m - \kappa_p\right) A G_0, \tag{1.97}$$

where $A = \pi r_p^2$ denotes the area of the particle. After applying Eq. (1.97), the distortion could be reduced to ensure a uniform temperature gradient. These discoveries are poised to facilitate advancements in thermal management applications, including infrared signature minimization, thermal protection, and infrared camouflage. Moreover, various scholars have employed linear heat sources with either a constant temperature [33] or constant gradient [56] to neutralize external fields. The findings have potential applications in other Laplace fields, including direct current [1] and fluid dynamics [57].

1.5 Special Theories

1.5.1 Topology-Related Theory: Geometric Phases and Edge State

Topology, initially a geometrical concept, has extended its reach to elucidate electron transport phenomena in condensed matter physics due to its formal similarity with the Schrödinger equation [58]. Over the last two decades, topological physics has experienced a surge in growth, leading to the theoretical prediction and experimental discovery of numerous topological matter phases. The wave equation's resemblance to the Schrödinger equation has also stimulated research interests in various wave systems, encompassing electromagnetic waves [59] and acoustic waves [60].

1.5.1.1 Geometrical Phase

Phase, a pivotal concept in physics, has significantly influenced topology studies. While the geometric phase has been investigated within micro heat transfer domains, discerning the geometric phase at the macroscopic scale has been challenging due to the divergent mechanisms—phonon-based micro heat transfer versus the macroscopic Fourier law. Research efforts have thus been channeled towards exploring the wave-like nature of temperature fields, aiming to unveil the geometric phase of macroscopic heat transfer by encircling anomalies in parameter space.

In pursuit of understanding the thermal geometric phase, Xu et al. [61] scrutinized anomalies within heat transfer systems. They considered a configuration involving two rings moving at equal velocities but in opposite directions, $(+u, -u)$, flanking a stationary ring with inner and outer radii r_1 and r_2, respectively, as illustrated in Fig. 1.10b. This figure demonstrates the 3D model projection along the yz plane, where the internal surface length is $l = 2\pi r_1$ and the width of the moving ring (intermediate layer) is denoted by w (w_i). Temperatures for the upper ring, lower ring, and intermediate layer are represented by T_1, T_2, and T_i correspondingly. The macroscopic heat conduction-convection process adheres to an energy conservation equation detailed as:

$$\begin{aligned}
\frac{\partial T_1}{\partial t} &= D_1\left(\frac{\partial^2 T_1}{\partial x^2}+\frac{\partial^2 T_1}{\partial z^2}\right)-u\frac{\partial T_1}{\partial x}(w_\mathrm{i}/2 \le z \le w_\mathrm{i}/2+w),\\
\frac{\partial T_\mathrm{i}}{\partial t} &= D_\mathrm{i}\left(\frac{\partial^2 T_\mathrm{i}}{\partial x^2}+\frac{\partial^2 T_\mathrm{i}}{\partial z^2}\right)(-w_\mathrm{i}/2 < z < w_\mathrm{i}/2),\\
\frac{\partial T_2}{\partial t} &= D_2\left(\frac{\partial^2 T_2}{\partial x^2}+\frac{\partial^2 T_2}{\partial z^2}\right)+u\frac{\partial T_2}{\partial x}(-w_\mathrm{i}/2-w \le z \le -w_\mathrm{i}/2),
\end{aligned} \tag{1.98}$$

where D_1 $(= D + d)$, D_2 $(= D - d)$, and D_i signify the thermal diffusivities of the upper ring, lower ring, and middle layer, respectively. The quasi-one-dimensional

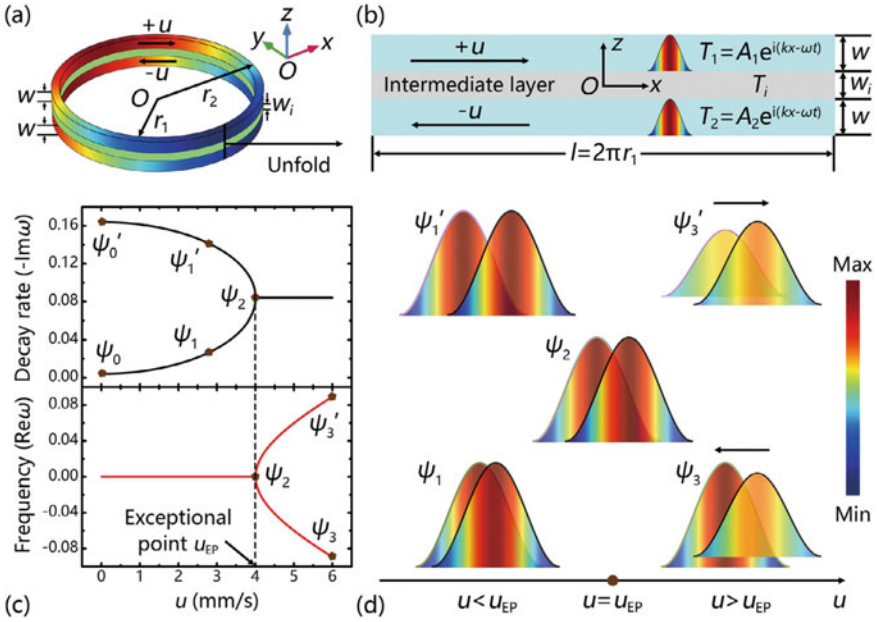

Fig. 1.10 Basic heat transfer properties of macroscopic heat conduction-convective systems. **a** Three-dimensional ring model. **b** Simplified two-dimensional models. **c** Decay rate -Im (w) and frequency Re (w) as a function of velocity u. **d** Illustration of five representative eigenstates of the system. The phase shift for Ψ_1 (or Ψ_1') is depicted as $\pi/4$ (or $3\pi/4$), while Ψ_2, Ψ_3, and Ψ_3' exhibit a phase difference of $\pi/2$. The temperature profiles on the left and right for each eigenstate correspond to the thermal distributions in the lower and upper sections of the rings, respectively. Adapted from Ref. [61]

model presupposes $l \gg w$, allowing for the assumption that temperature variations along the z axis are negligible. With heat exchange occurring between the two moving rings through the intermediate layer, the energy conservation equation can be reformulated as:

$$\begin{aligned}
\frac{\partial T_1}{\partial t} &= D_1 \frac{\partial^2 T_1}{\partial x^2} - u\frac{\partial T_1}{\partial x} + h\,(T_2 - T_1) \quad w_\mathrm{i}/2 \le z \le w_\mathrm{i}/2 + w, \\
\frac{\partial T_2}{\partial t} &= D_2 \frac{\partial^2 T_2}{\partial x^2} + u\frac{\partial T_2}{\partial x} + h\,(T_1 - T_2) \quad -w_\mathrm{i}/2 - w \le z \le -w_\mathrm{i}/2,
\end{aligned} \tag{1.99}$$

Incorporating the wave-like properties of temperature fields introduces phase characteristics, which can be mathematically represented as:

$$\begin{aligned}
T_1 &= A_1 \mathrm{e}^{\mathrm{i}(\beta x - \omega t)} + T_\mathrm{r}, \\
T_2 &= A_2 \mathrm{e}^{\mathrm{i}(\beta x - \omega t)} + T_\mathrm{r},
\end{aligned} \tag{1.100}$$

Where A_1 and A_2 denote the amplitudes of the temperature field in the upper and lower rings, respectively. β is the wave number, ω is the frequency, and T_r is the reference temperature, which can be regarded as 0. By substituting the Eq. (1.100) into the Eq. (1.99) and discussing the special case of $d = 0$, i.e. $D_1 = D_2 = D$, the following relationship is derived:

$$\boldsymbol{H}|\boldsymbol{\psi}\rangle = \omega|\boldsymbol{\psi}\rangle. \tag{1.101}$$

In the context, $|\boldsymbol{\psi}\rangle = [A_1, A_2]^\dagger$ represents the eigenstate with $\dagger$ indicating transposed conjugation. The Hamiltonian $\boldsymbol{H}$ and the corresponding eigenvalues are expressed as:

$$\begin{aligned} \boldsymbol{H} &= \begin{bmatrix} -\mathrm{i}\left(\beta^2 D + h\right) + \beta u & \mathrm{i}h \\ \mathrm{i}h & -\mathrm{i}\left(\beta^2 D + h\right) - \beta u \end{bmatrix}, \\ \omega_\pm &= -\mathrm{i}\left(\beta^2 D + h \pm \sqrt{h^2 - \beta^2 u^2}\right) \end{aligned} \tag{1.102}$$

where $D = \kappa_1/(\rho C) = \kappa_2/(\rho C)$. As the parameter u increases from zero to infinity, the system transitions between two distinct states. The exceptional point, denoted as $u_\mathrm{EP} = h/\beta$, marks the boundary between these states. For values of u less than u_EP, the frequency $\omega_\pm$ is purely imaginary, as illustrated in Fig. 1.10c. This corresponds to a scenario where the temperature fields of the two moving rings exhibit a static phase difference, merely decaying over time without any propagation, as depicted in ψ_1 and ψ_1' within Fig. 1.10d. Upon reaching the velocity $u = u_\mathrm{EP}$, the disparity between ω_+ and ω_- vanishes, as shown in Fig. 1.10c. At this point, the eigenstates share a phase difference of $\pi/2$ and continue to decay without propagation, as shown in ψ_2 and ψ_2' in Fig. 1.10d. As u surpasses u_EP, the real parts of the frequencies $\omega_\pm$ emerge and become significant, as indicated in Fig. 1.10c. Consequently, the eigenstates maintain a $\pi/2$ phase difference, exhibiting both decay and propagation. The direction of motion is governed by the ring which manifests a greater amplitude in its temperature field, as demonstrated in ψ_3 and ψ_3' in Fig. 1.10d.

Subsequently, simulations are conducted to examine the thermal geometric phase,

$$\varphi_\pm = \mathrm{i}\int \frac{\langle \overline{\boldsymbol{\psi}}_\pm(u)|\mathrm{d}\boldsymbol{\psi}_\pm((u))\rangle}{\langle \overline{\boldsymbol{\psi}}_\pm(u)\left|\boldsymbol{\psi}_\pm(u)\right\rangle}, \tag{1.103}$$

which aligns with analogous findings in quantum systems. The simulations encompass a cyclic path of velocity depending on time, described by the Hamiltonian $\boldsymbol{H}(u(t))$. Five distinct loop paths are investigated, as depicted in Fig. 1.11a. The initial condition sets the velocity at $u = 0$ mm/s and the state at the eigenstate 0, corresponding to the eigenvalue ω_-. In this regime, since the velocity is below the exceptional point, the eigenvalue is purely imaginary, signifying the absence of an accumulated phase difference. The evolutionary trajectories for both routes ultimately revert to their initial states, as demonstrated in Fig. 1.11b through Fig. 1.11f. Additionally, Xu et al. [62] explored the geometric phases in particle diffusion systems.

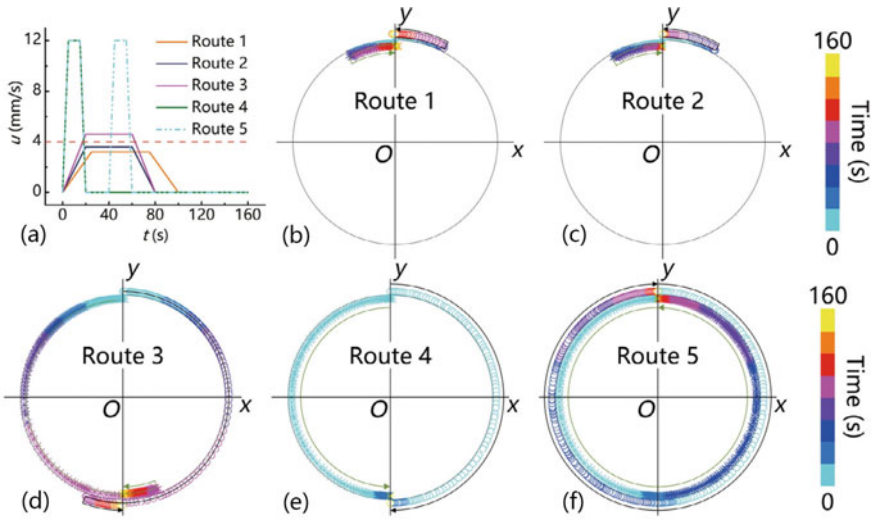

Fig. 1.11 Thermal geometry phase simulation results. **a** Five different evolutionary routes. **b**, **c**, **d**, **e** and **f** respectively show the Max (T_1) and Max (T_2) trajectories corresponding to the five evolutionary routes. Adapted from Ref. [61]

1.5.1.2 Topological Edge State

The preceding analysis demonstrates that a macroscopic thermal system, undergoing convection and conduction, can exhibit geometric phase, characteristic of a non-Hermitian system. Recently, other pivotal concepts such as topological invariance and bulk-edge correspondence have been investigated through the discretization of diffusion processes. Yoshidae et al. [36] integrated Fick's law with the continuity equation to derive the one-dimensional diffusion equation for a continuous scalar field, given by

$$\partial_t \phi\,(t, x) = D\partial_x^2 \phi\,(t, x)\,, \tag{1.104}$$

where $\partial_{t(x)}$ represents the derivative with respect to time t (spatial coordinate x).

The diffusion Eq. (1.104) was then discretized, establishing an analogy between diffusion phenomena and a tightly bound model in quantum systems. As depicted in Fig. 1.12a, consider a system composed of two sites where the discrete field values ϕ_0 and ϕ_1 are defined. By applying Fick's law, the flux from site 0 to 1 is expressed as $J_{0\to 1} = -D(\phi_0 - \phi_1)$, assuming a unit-length distance between the sites. Consequently, the temporal evolution of the vector $\vec{\phi} = (\phi_0, \phi_1)^T$ is governed by:

$$\partial_t \vec{\phi}(t) = -D \begin{pmatrix} 1 & -1 \\ -1 & 1 \end{pmatrix} \vec{\phi}(t). \tag{1.105}$$

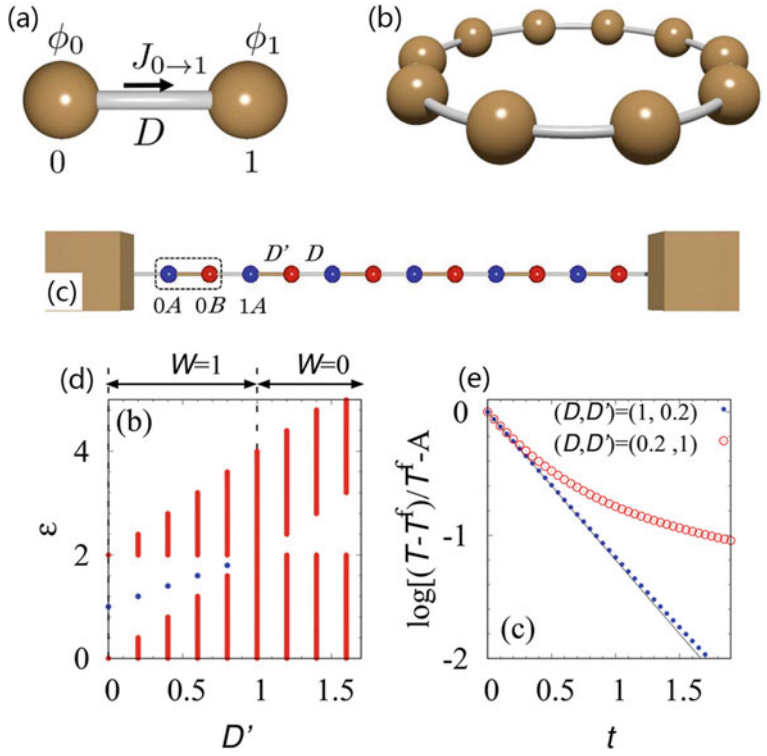

Fig. 1.12 **a** System composed of two sites coupled with the diffusion coefficient D. **b** One-dimensional chain under the periodic boundary condition for $L_x = 10$. **c** Sketch of the model under the fixed boundary condition for $L_x = 6$. **d** Spectrum of $\tilde{H}_{\text{SSH}}$ for $D = 1$ and $L_x = 240$. **e** The time-evolution of in the case for $(D, D') = (1, 0.2)$ $[(D, D') = (0.2, 1)]$, where the system is topologically nontrivial (trivial). The function $-(D + D')t$ is plotted with a black line. (from Ref. [36], licensed under CC-BY 4.0)

Extending this framework to a one-dimensional chain with L_x sites, as illustrated in Fig. 1.12b, the time evolution of the vector $\vec{\phi} = (\phi_0, \phi_1, \ldots, \phi_{L_x-1})^T$ is similarly described as:

$$\partial_t \vec{\phi}(t) = -\hat{H}\vec{\phi}(t),$$
$$\hat{H} = D \begin{pmatrix} 2 & -1 & 0 & \cdots & -1 \\ -1 & 2 & -1 & \cdots & 0 \\ 0 & -1 & 2 & \cdots & 0 \\ \vdots & \vdots & \vdots & \ddots & \vdots \\ -1 & 0 & 0 & \cdots & 2 \end{pmatrix}. \tag{1.106}$$

The discrete diffusion equation reveals that the dynamics of classical diffusion can be encapsulated within a tightly bound model, suggesting that diffusion systems could

serve as a novel platform for topological investigations beyond the realm of quantum systems.

The study progresses by analyzing a one-dimensional system with dimeric compounds (Fig. 1.12c) that corresponds to the Su-Schrieffer-Heeger (SSH) model of quantum systems. Following the procedure used to derive Eq. (1.106), the equation satisfied by $\vec{T} = (T_{0A}, T_{0B}, T_{1A}, \cdots, T_{L_X-1B})^{\mathrm{T}}$ is obtained,

$$\begin{aligned} &\partial_t \vec{T}(t) = -\hat{H}\vec{\phi}(t), \\ &\hat{H}_{\mathrm{SSH}} = \begin{pmatrix} D+D' & -D & 0 & \cdots & -D' \\ -D & D+D' & -D' & \cdots & 0 \\ 0 & -D' & D+D' & \cdots & 0 \\ \vdots & \vdots & \vdots & \ddots & \vdots \\ -D' & 0 & 0 & \cdots & D+D' \end{pmatrix}. \end{aligned} \tag{1.107}$$

It can be found that $\hat{H}_{\mathrm{SSH}}$ is similar to the one-dimensional SSH model in the quantum system, only the onsite energy is shifted. Therefore, the topological nature of the one-dimensional SSH model is preserved. Focusing on the bulk properties under periodic boundary conditions applied to the structure in Fig. 1.12c, the Hamiltonian matrix $\hat{H}_{\mathrm{SSH}}$ in momentum space is represented by:

$$\hat{h}_{\mathrm{SSH}}(k) = \begin{pmatrix} D+D' & -D'-De^{ik} \\ -D'-De^{-ik} & D+D' \end{pmatrix}, \tag{1.108}$$

where k is the Bloch vector. $\hat{h}_{\mathrm{SSH}}(k)$ represents the gap and maintains chiral symmetry, potentially harboring topologically non-trivial features indicated by the winding number:

$$W = -\int_{-\pi}^{\pi} \frac{dk_x}{4\pi i} \mathrm{tr}[\sigma_3 \hat{h}'^{-1}_{\mathrm{SSH}}(k_x)\partial_{k_x}\hat{h}'_{\mathrm{SSH}}(k_x)]. \tag{1.109}$$

This winding number quantifies the encirclements made by a non-diagonal element of $\hat{h}_{\mathrm{SSH}}(k)$ around the origin in the complex plane and is hence an integer. Figure 1.12d illustrates the spectrum of $\hat{H}_{\mathrm{SSH}}$ under fixed boundary conditions, indicating the presence of localized edge states (or absence thereof) corresponding to the winding number $W = 1$ ($W = 0$), with each state represented by a blue dot for different values of D'. In Fig. 1.12e, the temporal evolution of the temperature at the edge $(ix, \alpha) = (0, A)$ is plotted. Here, the temperature T_{0A} exhibits exponential decay for $t \leq 2\tau$, with a half-life $\tau = 1/(D + D') = 0.83$ influenced by the edge state when $(D, D') = (1, 0.2)$. This deviates from the standard exponential decay near $t = 0.5$ and results in a shorter half-life compared to when $(D, D') = (0.2, 1)$.

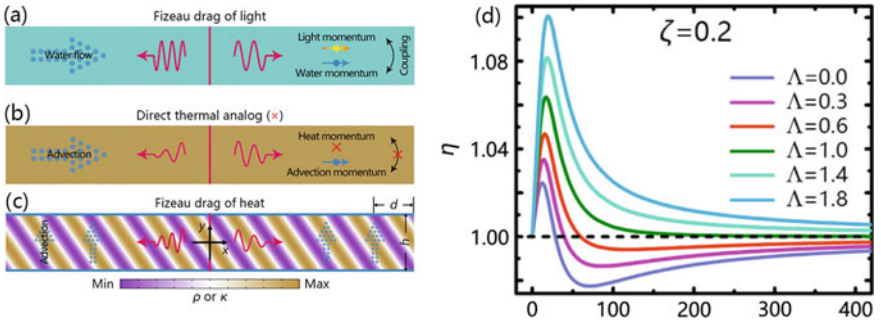

Fig. 1.13 **a** Fizeau drag of light. **b** Failure of direct thermal simulation due to lack of macroscopic heat momentum. **c** Diffusion Fizeau drag in spatiotemporal thermal metamaterials, based on thermal Willis coupling. **d** Numerical results of the speed ratio of $\eta = |v_f/v_b|$ as a function of $2\pi\Gamma = \phi\epsilon u_y d/D_0$, with constant $\Lambda = \Delta_\rho \cos\theta/\Delta_\kappa$. Adapted from Ref. [37]

1.5.2 The Bloch Series Expansion Method

The heat conduction equation has been previously compared to the Schrödinger equation, with the conduction term of the former analogous to the potential energy term of the latter. According to Bloch's theorem, the periodic potential field and wave function can be expanded into a series of periodically modulated plane waves. Analogously, in the context of heat conduction, this corresponds to the periodic modulation of thermal conductivity, resulting in temperature fluctuations [64, 65]. The Bloch series expansion method is adept at addressing such problems.

A significant instance of this analogy is observed in the context of diffusion Fizeau drag within spatiotemporal thermal metamaterials. The Fizeau drag phenomenon, originally discovered by Fizeau in 1851, describes the differential speeds of light traveling with and against a current of water, as illustrated in Fig. 1.13a. This behavior has been comprehensively explained by relativistic kinematics and observed in various moving media or spatiotemporal media, attributable to the nonlinear motion of Dirac electrons. In simpler terms, while photons interact with momentum in a water flow and polarons in an electric current, heat does not carry momentum. Therefore, even when advection is introduced, the temperature field propagates at the same speed in both directions (Fig. 1.13b), although the amplitude [63] of the temperature field in the opposite direction may vary.

To achieve diffused Fizeau drag, Xu et al. [37] engineered a spatiotemporal thermal superlattice to study the diffusion of Fizeau drag in heat conduction, as depicted in (Fig. 1.13c). They introduced periodic inhomogeneity into a porous medium as described by:

$$\begin{aligned} \rho(\xi) &= \rho_0 \left(1 + \Delta_\rho \cos(G\xi + \theta)\right), \\ \kappa(\xi) &= \kappa_0 \left(1 + \Delta_\kappa \cos(G\xi)\right), \end{aligned} \tag{1.110}$$

where Δ_ρ and Δ_κ represent the modulation amplitudes of density and thermal conductivity, respectively; $G = 2\pi/d$ is the wave number for modulation; d is the modulation wavelength along the horizontal axis; $\xi = x + \zeta y$ denotes the generalized coordinate; $\zeta = d/h$ is the ratio with h as the vertical height; and θ is the phase difference in modulation. To eliminate any asymmetry in the amplitude of the temperature field caused by horizontal advection, the consideration is directed towards normal advection u_y, which typically does not lead to asymmetry along the horizontal axis. The heat transfer equation governing the inhomogeneous medium is then articulated as:

$$\rho(\xi)\frac{\partial T}{\partial t} + \nabla \cdot (\phi \rho_a \boldsymbol{u} T - \kappa(\xi)\nabla T) = 0. \tag{1.111}$$

Consider the upward advection velocity denoted as u_y, Eq. (1.112) is expanded to:

$$\rho(\xi)\frac{\partial T}{\partial t} + \phi\rho_\alpha u_y \frac{\partial T}{\partial y} + \frac{\partial}{\partial x}\left(-\kappa(\xi)\frac{\partial T}{\partial x}\right) + \frac{\partial}{\partial y}\left(-\kappa(\xi)\frac{\partial T}{\partial y}\right) = 0. \tag{1.112}$$

According to Bloch's theorem, they introduce a wavelike temperature field with spatial modulation,

$$T(\xi) = F(\xi)\,\mathrm{e}^{\mathrm{i}(\beta x - \omega t)} = \left(\sum_s F_s \mathrm{e}^{\mathrm{i}sG\xi}\right)\mathrm{e}^{\mathrm{i}(\beta x - \omega t)}, \tag{1.113}$$

where $s = 0, \pm 1, \pm 2, \ldots, \pm\infty$ and $F_0 = 1$. Subsequent expression of the partial derivatives of temperature in relation to time and space yields:

$$\begin{aligned}
\frac{\partial T}{\partial t} &= -\mathrm{i}\omega\left(\sum_s F_s \mathrm{e}^{\mathrm{i}sG\xi}\right)\mathrm{e}^{\mathrm{i}(\beta x - \omega t)}, \\
\frac{\partial T}{\partial x} &= \mathrm{i}\left(\sum_S (\beta + sG) F_s \mathrm{e}^{\mathrm{i}sG\xi}\right)\mathrm{e}^{\mathrm{i}(\beta x - \omega t)}, \\
\frac{\partial T}{\partial y} &= \mathrm{i}\left(\sum_S sG\zeta F_S \mathrm{e}^{\mathrm{i}sG\xi}\right)\mathrm{e}^{\mathrm{i}(\beta x - \omega t)}.
\end{aligned} \tag{1.114}$$

Using Fourier expansions, Eq. (1.110) can be written as:

$$\begin{aligned}
\rho(\xi) &= \sum_{r=0,\pm1} \rho_r \mathrm{e}^{\mathrm{i}rG\xi}, \\
\kappa(\xi) &= \sum_{r=0,\pm1} \kappa_r \mathrm{e}^{\mathrm{i}rG\xi},
\end{aligned} \tag{1.115}$$

where $\rho_{\pm1} = e^{\pm\mathrm{i}\theta}\rho_0\Delta_\rho/2$ and $\kappa_{\pm1} = \kappa_0\Delta_\kappa/2$ are defined. By substituting Eqs. (1.114) and (1.115) into Eq. (1.112), the component form of the governing equation is represented as:

$$-\mathrm{i}\omega\left(\sum_{r=0,\pm1}\rho_r F_{s-r}\right)+\mathrm{i}\phi\rho_a u_y s G\zeta F_s$$
$$+(\beta+sG)\sum_{r=0,\pm1}\kappa_r(\beta+(s-r)G)F_{s-r}+\mathrm{s}G\zeta\sum_{r=0,\pm1}\kappa_r(s-r)G\zeta F_{s-r}=0. \tag{1.116}$$

To derive the numerical results, the series is truncated for $s = 0, \pm1, \ldots, \pm10$, positing that $F_{|s|>10} = 0$. This results in twenty-one equations that facilitate the resolution of the unknown quantities for β and $F_{|s|\leq10}$. With β determined, the propagation speed of the wavelike temperature fields is computed as $v = \omega/\mathrm{Re}[\beta]$. Furthermore, the speed ratio $\eta = |v_f/v_b| = |\mathrm{Re}[\beta_b]/\mathrm{Re}\left[\beta_f\right]|$ is derived.

The terms v_f and v_b correspond to the forward and backward propagation speeds of the temperature field. The magnitude of the diffused Fizeau drag, denoted by η, is predominantly dependent on three non-dimensional parameters: $2\pi\Gamma = \phi\epsilon u_y d/D_0$, $\Lambda = \Delta\rho\cos\theta/\delta\kappa$, and $\zeta = d/h$. The influence of Λ on the diffused Fizeau drag, for a fixed ζ of 0.2, is explored. It is found that both $2\pi\Gamma = 0$ and $2\pi\Gamma \to \infty$ yield $\eta = 1$, signifying the necessity of vertical advection for modulation, but a larger Λ does not always correspond to enhanced performance. Figure 1.13a delineates two categories of curves: Type I consistently maintains an η above 1, as demonstrated by the top three curves; Type II displays an initial η above 1 that subsequently diminishes below this threshold, as depicted by the bottom three curves. A critical juncture at $\Lambda = 1$ marks the transition between Type I and II, as illustrated by the third curve from the top. These two types of curves highlights the flexible control achievable over the diffused Fizeau drag. The Bloch series expansion method introduced earlier can be applied to other wave-like systems, such as chemical waves [66].

1.6 Conclusion and Outlook

Over the past decade, since the advent of transformation optics, the domain has evolved to encompass diffusion systems, extending from static passive configurations to dynamic active ones, from pure heat conduction to the intertwined dynamics of heat conduction-convection and thermoelectric phenomena, and from linear to nonlinear realms. Moreover, the ascent of transformation theory has catalyzed the refinement of other theoretical approaches relevant to diffusion processes, such as effective media theories, scattering cancellation techniques, non-Hermitian topologies, and series expansions. While these theoretical methods were exhaustively explored prior to the inception of transformation theory, the emerging trend of deploying composite methods to actively steer diffusion fields is unprecedented.

Within the foundational theoretical scaffolding of diffusion studies, a plethora of new functionalities have been actualized, and numerous novel phenomena have been unveiled. Nonetheless, several pivotal challenges and questions persist unaddressed. A primary concern is that certain some governing equations do not satisfy transformation invariance before and after coordinate transformations; that is, transformable

parameters remain elusive, as deliberated in Sect. 1.2.3.1. Therefore, it is meaningful to Enhance the universality of transformation thermotics to accommodate more intricate and varied diffusion fields. The second challenge involves refining a more comprehensive effective medium theory within thermotics to simplify the complexity inherent in parameterization. Although theoretical advancements in effective thermal conductivity have been considerable, computational strategies, such as machine learning [67] and topological optimization, are increasingly recognized for their superiority in devising complex structures. The third challenge is that the scattering cancellation approach is constrained to diffusion fields with simplistic boundaries and falters with more complicated configurations. The recent introduction of the transformation field method [68] promises to circumvent the intricacies associated with solving complex boundary problems. The final challenge lies in elucidating the topological characteristics within the diffusion process. Despite the proliferation of scholarly articles, translating these insights into practical applications necessitates further in-depth investigation.

References

1. Yang, T., Bai, X., Gao, D., Wu, L., Li, B., Thong, J.T., Qiu, C.W.: Invisible sensors: simultaneous sensing and camouflaging in multiphysical fields. Adv. Mater. **27**, 7752–7758 (2015)
2. Zhuang, P.F., Huang, J.P.: Multiple control of thermoelectric dual-function metamaterials. Int. J. Mech. Sys. Dyna. **3**, 127–135 (2023)
3. Huang, J.P., Karttunen, M., Yu, K.W., Dong, L.: Dielectrophoresis of charged colloidal suspensions. Phys. Rev. E **67**, 021403 (2003)
4. Li, Y., Liu, C., Bai, Y., Qiao, L., Zhou, J.: Ultrathin hydrogen diffusion cloak. Adv. Theory Simul. **1**, 1700004 (2018)
5. Gao, Y., Jian, Y.C., Zhang, L.F., Huang, J.P.: Magnetophoresis of nonmagnetic particles in ferrofluids. J. Phys. Chem. C **111**, 10785–10791 (2007)
6. Yang, F.B., Zhang, Z.R., Xu, L.J., Liu, Z.F., Jin, P., Zhuang, P.F., Lei, M., Liu, J.R., Jiang, J.-H., Ouyang, X.P., Marchesoni, F., Huang, J.P.: Controlling mass and energy diffusion with metamaterials. Rev. Mod. Phys. **96**, 015002 (2024)
7. Pendry, J.B., Schurig, D., Smith, D.R.: Controlling electromagnetic fields. Science **312**, 1780–1782 (2006)
8. Cummer, S.A., Popa, B.I., Schurig, D., Smith, D.R., Pendry, J.B., Rahm, M., Starr, A.: Scattering theory derivation of a 3D acoustic cloaking shell. Phys. Rev. Lett. **100**, 024301 (2008)
9. Yang, S., Wang, J., Dai, G.L., Yang, F.B., Huang, J.P.: Controlling macroscopic heat transfer with thermal metamaterials: theory, experiment and application. Phys. Rep. **908**, 1–65 (2021)
10. Fan, C.Z., Gao, Y., Huang, J.P.: Shaped graded materials with an apparent negative thermal conductivity. Appl. Phys. Lett. **92**, 251907 (2008)
11. Dai, G.L., Huang, J.P.: A transient regime for transforming thermal convection: cloaking, concentrating and rotating creeping flow and heat flux. J. Appl. Phys. **124**, 235103 (2018)
12. Xu, L.J., Yang, S., Dai, G.L., Huang, J.P.: Transformation omnithermotics: simultaneous manipulation of three basic modes of heat transfer. ES Energy Environ. **7**, 65–70 (2020)

13. Xu, L.J., Huang, J.P.: Active thermal wave cloak. Chin. Phys. Lett. **37**, 120501 (2020)
14. Xu, L.J., Dai, G.L., Huang, J.P.: Transformation multithermotics: controlling radiation and conduction simultaneously. Phys. Rev. Appl. **13**, 024063 (2020)
15. Guenneau, S., Puvirajesinghe, T.M.: Fick's second law transformed: one path to cloaking in mass diffusion. J. R. Soc. Interface **10**, 20130106 (2013)
16. Zhang, Z.R., Huang, J.P.: Transformation plasma physics. Chin. Phys. Lett. **39**, 075201 (2022)
17. Mei, J.S., Wu, Q., Zhang, K., He, X.J., Wang, Y.: Homogeneous illusion device exhibiting transformed and shifted scattering effect. Optics Commun. **368**, 113–118 (2016)
18. Dai, G.L., Yang, F.B., Xu, L.J., Huang, J.P.: Diffusive pseudo-conformal mapping: anisotropy-free transformation thermal media with perfect interface matching. Chaos, Solitons & Fractals. **174**, 113849 (2023)
19. Zhang, Z.R., Xu, L.J., Qu, T., Lei, M., Lin, Z.K., Ouyang, X.P., Jiang, J.H., Huang, J.P.: Diffusion metamaterials. Nat. Rev. Phys. **5**, 218–235 (2023)
20. Wang, J., Dai, G.L., Huang, J.P.: Thermal metamaterial: fundamental, application, and outlook. iScience **23**, 101637 (2020)
21. Shen, X.Y., Jiang C.R., Li, Y., Huang, J.P.: Thermal metamaterial for convergent transfer of conductive heat with high efficiency. Appl. Phys. Lett. **109**, 201906
22. Dong, L., Huang, J.P., Yu, K.W., Gu, G.Q.: Dielectric response of graded spherical particles of anisotropic materials. J. Appl. Phys. **95**, 621–624 (2004)
23. Tian, B.Y., Wang, J., Dai, G.L., Ouyang, X.P., Huang, J.P.: Thermal metadevices with geometrically anisotropic heterogeneous composites. Int. J. Heat Mass Transf. **174**, 121312 (2021)
24. Dai, G.L., Huang, J.P.: Nonlinear thermal conductivity of periodic composites. Int. J. Heat Mass Transf. **147**, 118917 (2020)
25. Han, T., Bai, X., Gao, D., Thong, J.T., Li, B., Qiu, C.W.: Experimental demonstration of a bilayer thermal cloak. Phys. Rev. Lett. **112**, 054302 (2014)
26. Yang, S., Xu, L.J., Wang, R.Z., Huang, J.P.: Full control of heat transfer in single-particle structural materials. Appl. Phys. Lett. **111**, 121908 (2017)
27. Xu, L.J., Yang, S., Huang, J.P.: Thermal theory for heterogeneously architected structure: fundamentals and application. Phys. Rev. E **98**, 052128 (2018)
28. Jin, P., Xu, L.J., Jiang, T., Zhang, L., Huang, J.P.: Making thermal sensors accurate and invisible with an anisotropic monolayer scheme. Int. J. Heat Mass Transf. **163**, 120437 (2020)
29. Xu, L.J., Liu, J,R., Xu, G.Q., Huang, J.P., Qiu, C.W.: Giant, magnet-free, and room-temperature Hall-like heat transfer. Proc. Natl. Acad. Sci. U.S.A. **120**, e2305755120 (2023)
30. Xu, G., Dong, K., Li, Y., Li, H., Liu, K., Li, L., W, J., Qiu, C.W.: Tunable analog thermal material. Nat. Commun. **11**, 6028 (2020)
31. Li, Y., Zhu, K.J., Peng, Y.G., Li, W., Yang, T., Xu, H.X., Chen, H., Zhu, X.F., Fan, S.H., Qiu, C.W.: Thermal meta-device in analogue of zero-index photonics. Nat. Mater. **18**, 48–54 (2019)
32. Xu, L.J., Yang, S., Huang, J.P.: Dipole-assisted thermotics: experimental demonstration of dipole-driven thermal invisibility. Phys. Rev. E **100**, 062108 (2019)
33. Xu, L.J., Yang, S., Huang, J.P.: Effectively infinite thermal conductivity and zero-index thermal cloak. Europhys. Lett. **131**, 24002 (2020)
34. Kane, C.L., Mele, E.J.: Quantum spin Hall effect in graphene. Phys. Rev. Lett. **95**, 226801 (2005)
35. Sato, M., Ando, Y.: Topological superconductors: a review. Rep. Prog. Phys. **80**, 076501 (2017)
36. Yoshida, T., Hatsugai, Y.: Bulk-edge correspondence of classical diffusion phenomena. Sci. Rep. **11**, 888 (2021)
37. Xu, L.J., Xu, G.Q., Huang, J.P., Qiu, C.W.: Diffusive Fizeau drag in spatiotemporal thermal metamaterials. Phys. Rev. Lett. **128**, 145901 (2022)
38. Xu, G.Q., Zhang, H.C., Jin, Y.: Achieving arbitrarily polygonal thermal harvesting devices with homogeneous parameters through linear mapping function. Energy Conv. Manag. **165**, 253–262 (2018)
39. Liu, Y., Guo, W., Han, T.: Arbitrarily polygonal transient thermal cloaks with natural bulk materials in bilayer configurations. Int. J. Heat Mass Transf. **115**, 1–5 (2017)

40. Wang, H., Zhang, L., Shah, S., Zhu, R.R., Zheng, B.: Homogeneous material based acoustic concentrators and rotators with linear coordinate transformation. Sci. Rep. **11**, 11531 (2021)
41. Leonhardt, U.: Optical conformal mapping. Science **312**, 1777–1780 (2006)
42. Zhang, Z.R., Xu, L.J., Huang, J.P.: Controlling chemical waves by transforming transient mass transfer. Adv. Theory Simul. **5**, 2100375 (2022)
43. Lei, M., Wang, J., Dai, G.L., Tan, P., Huang, J.P.: Temperature-dependent transformation multiphysics and ambient-adaptive multiphysical metamaterials. Europhys. Lett. **135**, 54003 (2021)
44. Dai, G.L., Shang, J., Wang, R.Z., Huang, J.P.: Nonlinear thermotics: nonlinearity enhancement and harmonic generation in thermal metasurfaces. Eur. Phys. J. B **91**, 59 (2018)
45. Milton, G.M.: The theory of composites. Cambridge University Press (2002)
46. Xu, L.J., Yang, S., Huang, J.P.: Thermal transparency induced by periodic interparticle interaction. Phys. Rev. Appl. **11**, 034056 (2019)
47. Xu, L.J., Jiang, C.R., Shang, J., Wang R.Z., Huang, J.P: Periodic composites: quasi-uniform heat conduction, Janus thermal illusion, and illusion thermal diodes. Eur. Phys. J. B **90**, 221 (2017)
48. Gu, G., Yu, K.W., Hui, P.M.: First-principles approach to conductivity of a nonlinear composite. Phys. Rev. B **58**, 3057 (1998)
49. Xu, L.J., Huang, J.P., Jiang, T., Zhang, L., Huang, J.P.: Thermally invisible sensors. Europhys. Lett. **132**, 14002 (2020)
50. Xu, L.J., Yang, S., Huang, J.P.: Passive metashells with adaptive thermal conductivities: chameleonlike behavior and its origin. Phys. Rev. Appl. **11**, 054071 (2019)
51. Li, Y., Yu, C. Y., Liu, C. B., Xu, Z. J., Su, Y, J., Qiao, L. J., Zhou, J., Bai, Y.: Mass diffusion metamaterials with "plug and switch" modules for Ion cloaking, concentrating, and selection: design and experiments. Adv. Sci. **9**, 2201032 (2022)
52. Xu, L.J., Huang, J.P.: Metamaterials for manipulating thermal radiation: transparency, cloak, and expander. Phys. Rev. Appl. **12**, 044048 (2019)
53. Zhuang, P.F., Xu, L.J., Tan, P., Ouyang, X.P., Huang, J.P.: Breaking efficiency limit of thermal concentrators by conductivity couplings. Sci. China Phys. Mech. Astron. **65**, 117007 (2022)
54. Xu, L.J., Wang, R.Z., Huang, J.P.: Camouflage thermotics: a cavity without disturbing heat signatures outside. J. Appl. Phys. **123**, 245111 (2018)
55. Wang, C.Q., Xu, L.J., Jiang, T., Zhang, L., Huang, J.P.: Multithermally invisible cloaks and sensors with complex shapes. Europhys. Lett. **133**, 20009 (2021)
56. Nguyen, D.M., Xu, H., Zhang, Y., Zhang, B.: Active thermal cloak. Appl. Phys. Lett. **107**, 121901 (2015)
57. Dai, G., Wang, J.: Transformation hydrodynamic metamaterials: rigorous arguments on form invariance and structural design with spatial variance. Phys. Rev. E **107**, 055108 (2023)
58. Qi, X.L., Zhang, S.C.: Topological insulators and superconductors. Rev. Mod. Phys. **83**, 1057 (2011)
59. Wang, Z., Chong, Y., Joannopoulos, J.D., Soljacic, M.: Observation of unidirectional backscattering-immune topological electromagnetic states. Nature **461**, 772–775 (2009)
60. Ma, G., Xiao, M., Chan, C.T.: Topological phases in acoustic and mechanical systems. Nat. Rev. Phys. **1**, 281–294 (2019)
61. Xu, L.J., Wang, J., Dai, G.L., Yang, S., Yang, F.B., Wang, G., Huang, J.P.: Geometric phase, effective conductivity enhancement, and invisibility cloak in thermal convection-conduction. Int. J. Heat Mass Transf. **165**, 120659 (2021)
62. Xu, L.J., Dai, G.L., Wang, G., Huang, J.P.: Geometric phase and bilayer cloak in macroscopic particle-diffusion systems. Phys. Rev. E **102**, 032140 (2020)
63. Xu, L.J., Huang, J.P., Ouyang, X.P.: Tunable thermal wave nonreciprocity by spatiotemporal modulation. Phys. Rev. E **103**, 032128 (2021)
64. Ye, C., Huang, J.P.: Non-classical oscillator model for persistent fluctuations in stock markets. Phys. A **387**, 1255–1263 (2008)
65. Liu, L., Wei, J.R., Zhang, H.S., Xin, J.H., Huang, J.P.: A statistical physics view of pitch fluctuations in the classical music from Bach to Chopin: evidence for scaling. PLoS ONE **8**, e58710 (2013)

66. Avanzini, F., Falasco, G., Esposito, M.: Thermodynamics of chemical waves. J. Chem. Phys. **151**, 234103 (2019)
67. Liu, B., Xu, L.J., Huang, J.P.: Thermal transparency with periodic particle distribution: a machine learning approach. J. Appl. Phys. **129**, 065101 (2021)
68. Zou, W.N., He, Q.C., Zheng, Q.S.: Thermal inclusions inside a bounded medium. Proc. R. Soc. A-Math. Phys. Eng. Sci. **469**, 20130221 (2013)

Chapter 2
Diffusion Metamaterials: Basic Simulation Methods

Peng Jin

2.1 Opening Remarks

The emergence of diffusion metamaterials [1–16] marks a transformative era in materials science, with theoretical advancements [17–19] in heat and mass transfer being actualized into dynamic, practical innovations [20–22]. This chapter navigates through the intricate terrain of simulation methodologies that are pivotal to this evolution, especially when contending with complex geometries. It dissects the role of finite-element simulations in visualizing physical field distributions, the strategic use of particle swarm optimization for crafting optimal designs [23, 24], the ingenuity behind topology optimization [25, 26] for emulating inhomogeneous and anisotropic properties, and the profound impact of machine learning algorithms [27] in refining design parameters and enhancing material functionality. Together, these simulation strategies, supported by intelligent algorithms and finite element analysis, are not merely reshaping metamaterials; they are setting the stage for a future where the versatility and ingenuity of these materials [28–30] could fundamentally alter the domain of thermal management and metamaterial engineering [31–36].

2.2 Finite-Element Simulation

Finite-element simulation [37] stands as a cornerstone in the design and analysis of diffusion metamaterials, providing a robust computational framework to predict and visualize the behavior of complex systems. At its core, this technique subdivides a large problem into smaller, simpler parts that are easier to understand, analyze, and solve—these are known as finite elements. What sets finite-element simulation

P. Jin (✉)
Department of Physics, Key Laboratory of Micro and Nano Photonic Structures (MOE), and State Key Laboratory of Surface Physics, Fudan University, Shanghai 200438, China
e-mail: 19110190022@fudan.edu.cn

F.-B. Yang and J.-P. Huang, *Diffusionics*,
https://doi.org/10.1007/978-981-97-0487-3_2

apart is its adaptability and exactitude. It initiates with the crafting of a geometric mesh that echoes the actual structure of the material or system under study. This mesh comprises elements, each endowed with attributes that mirror the actual properties of the material, encompassing thermal conductivity, density, and specific heat capacity. The simulation then invokes the fundamental laws of physics, like the principles of energy and momentum conservation, expressed through differential equations. These equations are methodically spread across the mesh, effectively turning a continuous space into a solvable numerical puzzle of algebraic equations. This pivotal step permits the computation of critical field variables—temperature, pressure, stress—at specific junctures, thereby shedding light on the material's behavior in diverse scenarios. Finite-element simulations shine particularly when applied to materials with unconventional geometries and boundary conditions—scenarios where analytical solutions are elusive. They provide granular analysis of variations and distributions within the metamaterial, thereby aiding the fine-tuning of thermal attributes and forecasting performance under real-world pressures. When enhanced by advanced algorithms, finite element analysis transcends mere prediction; it becomes an oracle that guides the iterative journey of design, leading to the conception of metamaterials with bespoke diffusion traits. This approach is a catalyst in the evolution of metamaterials, clearing a path for groundbreaking advancements in thermal regulation, wave control, and more. As our exploration deepens into the science of diffusion metamaterials, the role of finite element simulation becomes ever more crucial. It acts as a bridge from the theoretical to the tangible, helping to craft materials that rise to meet the multifaceted challenges of today's technological landscape.

2.3 Particle Swarm Optimization

Particle swarm optimization is a computational method inspired by the social behaviors observed in flocks of birds or schools of fish. This technique, conceptualized by Kennedy, a social psychologist, and Eberhart, an electrical engineer, treats the search for solutions as a process of collective intelligence, much like a swarm's natural movement toward the most promising paths [38]. The particle swarm optimization journey begins with assigning a flock of candidate solutions throughout the available solution space, with each 'bird' representing a possible answer to the problem at hand, evaluated by a designated fitness function that measures the quality of the solution. The method then involves calculating the fitness for each candidate's current location and pinpointing the best solutions found by any individual and the collective swarm up to that point. As the optimization unfolds, the swarm's individuals adjust their trajectories based on the best solutions identified, leveraging the wisdom of the group to navigate towards the optimal outcome. This iterative process of evaluation and adjustment continues until a candidate solution satisfies a predetermined threshold for success, signaling the end of the search. Particle swarm optimization proves particularly adept as an inverse design tool for complex problems that defy traditional analytical approaches. It has recently been harnessed for the

reverse engineering of diffusion metamaterials, allowing for the deduction of geometric or material parameters based on specific desired properties [24]. This makes particle swarm optimization a powerful ally in the development of metamaterials, where the target performance dictates the design parameters.

2.4 Topology Optimization

Topology optimization has emerged as a versatile algorithm for crafting thermal metamaterials, enabling the fine-tuning of natural material distributions to achieve exceptional thermal performances. This method, pioneered by Svanberg [39], has catalyzed the development of metadevices that leverage the optimized arrangement of their components to enhance their thermal properties. The power of topology optimization shines in its ability to fabricate transformation-theory based metamaterials, which traditionally grapple with the need for materials exhibiting inhomogeneous and anisotropic parameters—qualities rarely found in nature. Researchers have embraced this challenge by innovating a concept of topological functional cells, a strategy that permits the crafting of materials with the required complex properties [26]. Their methodology unfolds in a three-step process: First, they compute the desired thermal conductivity distribution across the metamaterial domain, guided by transformation theory. Next, they apply topology optimization to each functional cell to sculpt the desired thermal conductivity tensor. Finally, these optimized cells are assembled to form a metamaterial endowed with tailored inhomogeneous and anisotropic conductivities. The optimization of a single topological functional cell adheres to the following formulation:

$$
\begin{aligned}
&\min C = \frac{1}{|V|}\sum_{e=1}^{N}\rho_e,\\
&s.t.: \mathbf{K}(\rho_e)\mathbf{T} = \mathbf{Q},\\
&G = f((\kappa_{lm}^{\text{Output}} - \kappa_{lm}^{\text{Input}})^2) = 0,\\
&0 \le \rho_e \le 1,\ e = 1,\ 2...N,\\
&\kappa_{lm}^{\text{Input}} = \begin{pmatrix} \kappa_{11}^{\text{Input}} & \kappa_{12}^{\text{Input}} \\ \kappa_{21}^{\text{Input}} & \kappa_{22}^{\text{Input}} \end{pmatrix} (l, m = 1, 2),\\
&\kappa_{lm}^{\text{Output}} = \begin{pmatrix} \kappa_{11}^{\text{Output}} & \kappa_{12}^{\text{Output}} \\ \kappa_{21}^{\text{Output}} & \kappa_{22}^{\text{Output}} \end{pmatrix} (l, m = 1, 2).
\end{aligned}
\tag{2.1}
$$

In this formula, ρ_e signifies a variable dictating the material makeup, which ranges from $\rho_e = 0$ (material 1) to $\rho_e = 1$ (material 2). N represents the amount of ρ_e, and $|V|$ encapsulates the volume of the whole topological functional cell. $\mathbf{K}(\rho_e)$, $\mathbf{T}$, and $\mathbf{Q}$ are globally heat conduction, temperature, and heat load matrices, respectively. $\kappa_{lm}^{\text{Input}}$

and $\kappa_{lm}^{\text{Output}}$ represent target and optimized thermal conductivity tensors, respectively. f is a function to evaluate the discrepancy between $\kappa_{lm}^{\text{Output}}$ and $\kappa_{lm}^{\text{Input}}$. The distribution of ρ_e is refined via the classical method of moving asymptotes, ensuring a precise and efficient optimization process.

2.5 Machine Learning

Intelligent materials that incorporate artificial intelligence algorithms into their design have garnered significant attention in diverse fields like optics, nanotechnology, and acoustics. Yet, in the realm of diffusion physics, the paucity of controllable degrees of freedom presents a formidable challenge to applying these innovative technologies to diffusion metamaterials. Thermal metamaterials provide a pertinent case in point. Current advancements have primarily been confined to inverse design strategies concerning geometrical or material parameters. For instance, researchers have adeptly utilized machine learning algorithms to optimize a four-layer thermal cloak [40]. They trained an artificial neural network to process the thermal conductivities k_1, k_2, k_3, and k_4 of four isotropic materials (four middle layers) and output two objective functions that assess the cloak's efficacy. One function gauges the temperature uniformity within the cloaked area,

$$\Delta T = |T_{x=r_1} - T_{x=-r_1}|, \tag{2.2}$$

while the other measures the thermal neutrality against the ambient background,

$$M_V = \frac{\int_\Omega |T(x, y, z) - T_r(x, y, z)| d\Omega}{\int_\Omega d\Omega}, \tag{2.3}$$

where Ω represents the domain $r > r_5$, and T_r is the temperature distribution of a uniform medium. After processing 10,000 design samples, the neural network achieved an inverse mapping between the output metrics $\{\Delta T, M_V\}$ and the input thermal conductivities. This mapping facilitated the calculation of optimal material conductivities for superior cloaking, resulting in a device engineered from copper and poly-dimethylsiloxane based on effective medium theory, which upheld a uniform temperature in the cloaked region without disturbing the surrounding thermal field. However, this machine-learning-assisted thermal cloak is inherently static, lacking the ability to adapt dynamically to changing conditions. In a leap forward, further integration of artificial intelligence and advanced hardware led to the conception of a new class of thermal metamaterial. This design is distinguished by its parameters that autonomously adjust to environmental changes [27]. A micro infrared camera monitors the temperature of a bilayer structure, and a computing system equipped with a trained artificial neural network dynamically modulates the core region's thermal conductivity by altering the spinning angular velocity via a stepper motor.

The network's architecture, connecting input and output through four hidden layers, is defined as follows:

$$\begin{cases} \boldsymbol{H}^{(i+1)} = \mathrm{ReLU}\left(\boldsymbol{W}^{(i)}\boldsymbol{T}^{(i)} + \boldsymbol{b}^{(i+1)}\right), \ i = 0 \\ \boldsymbol{H}^{(i+1)} = \mathrm{ReLU}\left(\boldsymbol{W}^{(i)}\boldsymbol{H}^{(i)} + \boldsymbol{b}^{(i+1)}\right), \ 0 < i < 4 \\ \omega_1 = \mathrm{ReLU}\left(\boldsymbol{W}^{(i)}\boldsymbol{H}^{(i)} + \boldsymbol{b}^{(i+1)}\right), \ i = 4 \end{cases} \tag{2.4}$$

where $\boldsymbol{H}^{(i)}$ represent the activations of the current layer, ReLU (a) = max (0, a) is the rectified linear unit function, $\boldsymbol{W}^{(i)}$ and $\boldsymbol{b}^{(i)}$ are the weights and biases for neurons in the i-th layer. This sophisticated setup connects ambient temperature changes to thermal functionality, creating a responsive device that epitomizes the next wave in intelligent material design: self-adaptive metamaterials, which are poised to redefine the landscape of material science.

2.6 Outlook

Contemporary computational techniques, such as finite-element simulations, offer a direct method to model the physical field distributions of metamaterials under specified environmental conditions [41]. For problems lacking analytical solutions, particle swarm optimization can be utilized to find the optimal configurations. Notably, thermal sensors can achieve superior performance using conventional bulk materials by fine-tuning their dimensions [23, 24]. Topology optimization [25, 26] is instrumental in manipulating the placement of natural materials to simulate inhomogeneous and anisotropic thermal conductivities, enabling metamaterials to maintain high efficiency across various shapes. Machine learning algorithms have the potential to act as inverse design solvers, deducing the necessary geometric structures and material parameters based on desired physical attributes. Furthermore, machine learning can significantly enhance the adaptability and functionality of traditional static metamaterials. A recent landmark study introduced a deep learning-assisted active metamaterial [27] that functions as a configurable nonlinear thermal material. Such nonlinear materials pave the way for unidirectional heat transfer [42, 43], offering fresh perspectives for creating asymmetric thermal couplings used for the classical Su-Schrieffer-Heeger model. Consequently, these innovative active metamaterials may serve as platforms for exploring novel mechanisms in topological thermal transport and the development of advanced thermal metadevices.

References

1. Yang, F.B., Zhang, Z.R., Xu, L.J., Liu, Z.F., Jin, P., Zhuang, P.F., Lei, M., Liu, J.R., Jiang, J.-H., Ouyang, X.P., Marchesoni, F., Huang, J.P.: Controlling mass and energy diffusion with metamaterials. Rev. Mod. Phys. **96**, 015002 (2024)
2. Zhang, Z.R., Xu, L.J., Qu, T., Lei, M., Lin, Z.K., Ouyang, X.P., Jiang, J.-H., Huang, J.P.: Diffusion metamaterials. Nat. Rev. Phys. **5**, 218–235 (2023)
3. Yang, S., Wang, J., Dai, G.L., Yang, F.B., Huang, J.P.: Controlling macroscopic heat transfer with thermal metamaterials: theory, experiment and application. Phys. Rep. **908**, 1–65 (2021)
4. Xu, L.J., Huang, J.P.: Active thermal wave cloak. Chin. Phys. Lett. **37**, 120501 (2020)
5. Xu, L.J., Xu, G.Q., Huang, J.P., Qiu, C.-W.: Diffusive Fizeau Drag in Spatiotemporal Thermal Metamaterials. Phys. Rev. Lett. **128**, 145901 (2022)
6. Shen, X.Y., Jiang, C.R., Li, Y., Huang, J.P.: Thermal metamaterial for convergent transfer of conductive heat with high efficiency. Appl. Phys. Lett. **109**, 201906 (2016)
7. Xu, L.J., Yang, S., Dai, G.L., Huang, J.P.: Transformation omnithermotics: simultaneous manipulation of three basic modes of heat transfer. ES Energy Environ. **7**, 65–70 (2020)
8. Xu, L.J., Wang, J., Dai, G.L., Yang, S., Yang, F.B., Wang, G., Huang, J.P.: Geometric phase, effective conductivity enhancement, and invisibility cloak in thermal convection-conduction. Int. J. Heat Mass Transf. **165**, 120659 (2021)
9. Xu, L.J., Yang, S., Huang, J.P.: Thermal theory for heterogeneously architected structure: fundamentals and application. Phys. Rev. E **98**, 052128 (2018)
10. Dong, L., Huang, J.P., Yu, K.W., Gu, G.Q.: Dielectric response of graded spherical particles of anisotropic materials. J. Appl. Phys. **95**, 621–624 (2004)
11. Gao, Y., Jian, Y.C., Zhang, L.F., Huang, J.P.: Magnetophoresis of nonmagnetic particles in ferrofluids. J. Phys. Chem. C **111**, 10785–10791 (2007)
12. Dai, G.L., Huang, J.P.: A transient regime for transforming thermal convection: Cloaking, concentrating, and rotating creeping flow and heat flux. J. Appl. Phys. **124**, 235103 (2018)
13. Yang, S., Xu, L.J., Wang, R.Z., Huang, J.P.: Full control of heat transfer in single-particle structural materials. Appl. Phys. Lett. **111**, 121908 (2017)
14. Xu, L.J., Yang, S., Huang, J.P.: Thermal transparency induced by periodic interparticle interaction. Phys. Rev. Appl. **11**, 034056 (2019)
15. Xu, L.J., Dai, G.L., Huang, J.P.: Transformation multithermotics: controlling radiation and conduction simultaneously. Phys. Rev. Appl. **13**, 024063 (2020)
16. Wang, J., Dai, G.L., Huang, J.P.: Thermal metamaterial: fundamental, application, and outlook. iScience **23**, 101637 (2020)
17. Fan, C.Z., Gao, Y., Huang, J.P.: Shaped graded materials with an apparent negative thermal conductivity. Appl. Phys. Lett. **92**, 251907 (2008)
18. Dai, G.L., Shang, J., Huang, J.P.: Theory of transformation thermal convection for creeping flow in porous media: cloaking, concentrating, and camouflage. Phys. Rev. E **97**, 022129 (2018)
19. Jin, P., Liu, J.R., Xu, L.J., Wang, J., Ouyang, X.P., Jiang, J.-H., Huang, J.P.: Tunable liquid-solid hybrid thermal metamaterials with a topology transition. Proc. Natl. Acad. Sci. U.S.A. **120**, e2217068120 (2023)
20. Ye, C., Huang, J.P.: Non-classical oscillator model for persistent fluctuations in stock markets. Phys. A **387**, 1255–1263 (2008)
21. Liu, L., Wei, J.R., Zhang, H.S., Xin, J.H., Huang, J.P.: A statistical physics view of pitch fluctuations in the classical music from Bach to Chopin: evidence for scaling. PLoS ONE **8**, e58710 (2013)
22. Huang, J.P., Karttunen, M., Yu, K.W., Dong, L.: Dielectrophoresis of charged colloidal suspensions. Phys. Rev. E **67**, 021403 (2003)
23. Jin, P., Xu, L.J., Jiang, T., Zhang, L., Huang, J.P.: Making thermal sensors accurate and invisible with an anisotropic monolayer scheme. Int. J. Heat Mass Transf. **163**, 120437 (2020)
24. Jin, P., Yang, S., Xu, L.J., Dai, G.L., Huang, J.P., Ouyang, X.P.: Particle swarm optimization for realizing bilayer thermal sensors with bulk isotropic materials. Int. J. Heat Mass Transfer **172**, 121177 (2021)

25. Fujii, G., Akimoto, Y.: Optimizing the structural topology of bifunctional invisible cloak manipulating heat flux and direct current. Appl. Phys. Lett. **115**, 174101 (2019)
26. Sha, W., Xiao, M., Zhang, J.H., Ren, X.C., Zhu, Z., Zhang, Y., Xu, G.Q., Li, H.G., Liu, X.L., Chen, X., Gao, L., Qiu, C.W., Hu, R.: Robustly printable freeform thermal metamaterials. Nat. Commun. **12**, 7228 (2021)
27. Jin, P., Xu, L., Xu, G., Li, J., Qiu, C.-W., Huang, J.P.: Deep learning-assisted active metamaterials with heat-enhanced thermal transport. Adv. Mater. **36**, 2305791 (2024)
28. Li, Y., Zhu, K.J., Peng, Y.G., Li, W., Yang, T., Xu, H.X., Chen, H., Zhu, X.F., Fan, S., Qiu, C.W.: Thermal meta-device in analogue of zero-index photonics. Nat. Mater. **18**, 48–54 (2019)
29. Xu, G., Dong, K., Li, Y., Li, H., Liu, K., Li, L., Wu, J., Qiu, C.W.: Tunable analog thermal material. Nat. Commun. **11**, 6028 (2020)
30. Li, J., Li, Y., Cao, P.C., Yang, T., Zhu, X.F., Wang, W., Qiu, C.W.: A continuously tunable solid-like convective thermal metadevice on the reciprocal line. Adv. Mater. **32**, 2003823 (2020)
31. Zhang, C.X., Li, T.J., Jin, P., Yuan, Y., Ouyang, X.P., Marchesoni, F., Huang, J.P.: Extracting stellar emissivity via a machine learning analysis of MSX and LAMOST catalog data. Phys. Rev. D. **106**, 123035 (2022)
32. Wang, C.M., Jin, P., Yang, F.B., Xu, L.J., Huang, J.P.: Click metamaterials: Fast acquisition of thermal conductivity and functionality diversities (2023). Preprint at https://doi.org/10.48550/arXiv.2308.16057
33. Jin, P., Liu, J.R., Yang, F.B., Marchesoni, F., Jiang, J.-H., Huang, J.P.: In-situ simulation of thermal reality. Research **6**, 0222 (2023)
34. Xu, L.J, Liu, J.R., Jin, P., Xu, G.Q., Li, J.X., Ouyang, X.P., Li, Y., Qiu, C.-W., Huang, J.P.: Black-hole-inspired thermal trapping with graded heat-conduction metadevices. Nat. Sci. Rev. **10**, nwac159 (2023)
35. Yang, F.B., Jin, P., Lei, M., Dai, G.L., Wang, J., Huang, J.P.: Space-time thermal binary coding by spatiotemporally modulated metashell. Phys. Rev. Appl. **19**, 054096 (2023)
36. Zhou, X.C., Xu, X., Huang, J.P.: Adaptive multi-temperature control for transport and storage containers enabled by phase change materials. Nat. Commun. **14**, 5449 (2023)
37. Logan, D.L.: A First Course in the Finite Element Method. Cengage Learning, Stamford (2012)
38. Kennedy, J., Eberhart, R.C.: Particle swarm optimization. In: Proceedings of the IEEE International Conference on Neural Networks, vol. 4, pp. 1942–1948 (1995)
39. Svanberg, K.: The method of moving asymptotes–a new method for structural optimization. Int. J. Numer. Meth. Eng. **24**, 359–373 (1987)
40. Ji, Q.X., Qi, Y.C., Liu, C.W., Meng, S.H., Liang, J., Kadic, M., Fang, G.D.: Design of thermal cloaks with isotropic materials based on machine learning. Int. J. Heat Mass Tran. **189**, 122716 (2022)
41. Tan, Y., Chen, Y., Liu, X., Tang, Y., Lao, Z., Wei, G.: Dissecting how ALS-associated D290V mutation enhances pathogenic aggregation of hnRNPA2286-291 peptides: dynamics and conformational ensembles. Int. J. Biol. Macromol. **241**, 124659–124669 (2023)
42. Li, Y., Shen, X.Y., Wu, Z.H., Huang, J.Y., Chen, Y.X., Ni, Y.S., Huang, J.P.: Temperature-dependent transformation thermotics: from switchable thermal cloaks to macroscopic thermal diodes. Phys. Rev. Lett. **115**, 195503 (2015)
43. Shen, X.Y., Li, Y., Jiang, C.R., Huang, J.P.: Temperature trapping: energy-free maintenance of constant temperatures as ambient temperature gradients change. Phys. Rev. Lett. **117**, 055501 (2016)

Chapter 3
Diffusion Metamaterials: Basic Experimental Methods

Jinrong Liu

3.1 Opening Remarks

The intersection of theoretical modeling and experimental techniques has been pivotal in the advancement of metamaterials, enabling the realization of artificial properties with remarkable precision and versatility. Rooted in a variety of theoretical frameworks [1–6], experimental techniques under the effective medium theory range from the utilization of composites for inhomogeneous properties [7], to the employment of layered structures for pronounced anisotropic properties [8], and the application of rotating structures for tunability [9]. Further extending into the realm of adaptive or active responses, metamaterials incorporate intricate control mechanisms such as motors [10] and convection processes [11], showcasing their potential for dynamic and responsive applications. This chapter aims to elucidate the experimental realizations of these theoretical concepts, emphasizing how their practical implementation aligns with and enriches the theoretical predictions, thereby laying the groundwork for innovative applications in various scientific domains (Table 3.1).

3.2 Passive Artificial Metamaterials Like Composites and Layered Structures

Both the Maxwell-Garnett and Bruggeman theories serve as core components of the effective medium theory (EMT) when dealing with composites. Given that we can perforate a single structure with varying shapes of holes, densities, and distributions [7, 12, 13], these theories are frequently used to model artificial isotropic yet inho-

J. Liu (✉)
Department of Physics, Key Laboratory of Micro and Nano Photonic Structures (MOE), and State Key Laboratory of Surface Physics, Fudan University, Shanghai 200438, China
e-mail: 20110190007@fudan.edu.cn

F.-B. Yang and J.-P. Huang, *Diffusionics*,
https://doi.org/10.1007/978-981-97-0487-3_3

Table 3.1 Common experimental methods employed in metamaterials for passive, adaptive and active regulation and their corresponding applications. Some of applications may work well in heat transfer, electromagnetic, Darcy fluid, particle diffusion, etc

Type	Method	Main experimental methods	Applications
Passive	EMT of composites	Embedded particles or air hole array	Inhomogeneous properties with one material [14], bilayer cloak and sensor [39]
	EMT of layered structures	Alternating layers of different materials with interfacial resistance	Highly anisotropic properties [8], diverse functions including cloak, concentrator, rotator and sensor [12, 40]
Adaptive		Nearly 0 and ∞ materials to be transformation-invariant	Chameleonlike rotator and concentrator with adaptive responses [20], out of plane cloak [21]
	Temperature-related function	Shape-memory alloy, temperature-related resonance frequency or radiation emissivity, nonlinear thermal radiation	Temperature-dependent thermal diodes [22], energy-free temperature maintenance [24], adaptive optical cloak [23], ultra sensitivity infrared image [25]
Active	EMT of rotation	Motor-controlled rotating unit, array or intelligent structure	Hall-like heat transfer [10], tunable thermal conductivity to infinity [27], Deep learning thermal enhancement [11]
	Spatiotemporal theory	Temporal mechanical deformation cycle	Thermal and thermalelectric encoding [32]
	Sources with external gain or loss	Thermoelectric elements with active heating/cooling	Active thermal cloak, real-time self-adaptive thermal metasurface [35]
		Pairs of cylinders with different temperature or pressure	Tunable diodes to overcome different background distortion [36]
	Topological Hamiltonian in convection	Channel pairs with opposite convection velocity as gain or loss	Anti–parity-time symmetry and symmetry broken in diffusive systems [37], dynamical EP encircling [41]

mogeneous parameters using only one material and a single fabrication step. The Maxwell-Garnett theory applies particularly in scenarios where unconnected particles are uniformly embedded in an isotropic matrix, in which the deviation become larger when particle fraction is higher. In contrast, the Bruggeman theory is pertinent in systems where it's impossible to distinguish between the overlapping particles and the matrix, allowing for a varied particle fraction ranging from 0 to 1. At some cases the embedded particle can be elliptical and ordered-oriented to achieve anisotropy, as confirmed by a thermal conduction experiment [14]. These models facilitate the design of materials with specific electromagnetic, thermal or diffusion parameters [15], essential for various practical applications.

Layered structures represent another critical aspect of effective medium theory. The first experimental demonstration of thermal metamaterials used layered structures to realize anisotropic material parameters [8]. The layered structures are later extended to diverse functions [12, 16, 17]. As an example, we use the isotropic materials B and C to construct an alternate layered structure A. The effective parameters in the perpendicular, $A_\perp$, and parallel direction, $A_\parallel$, are different, i.e., $A_\perp = 1/(f_B/A_B + f_C/A_C)$ and $A_\parallel = f_B A_B + f_C A_C$. f_B and $f_C = 1 - f_B$ are their area/volume fractions. Here, interfacial resistance may slightly affect these parameters and reduce the effective anisotropy [18, 19], but this effect can be easily compensated by fine-tuning the fractions f_B and f_C. Later the extremely anisotropic metamaterials is developed [20], with almost infinite thermal conductivity in one direction and zero in perpendicular directions. One can choose air as material C in layered structures to achieve such extreme anisotropy with only one natural material. And the designed metamaterials adaptively respond to environment change because of the transformation-invariance [21].

3.3 Adaptive Metamaterials with External Field-Dependent Response

Different with extremely anisotropic metamaterials, materials boasting adaptive capabilities are crucial for real-time responsiveness to environment changes in the domain of dynamic thermal or diffusion management. These include materials sensitive to external fields, such as shape-memory alloys [22] and certain ferroelectric substances [23], together with substances with nonlinear thermal radiation characteristics [2], which are the cornerstones of the engineering of adaptive thermal metamaterials.

Shape-memory alloy serves a prime example in temperature-dependent materials. This alloy undergoes a reversible phase transformation in response to changes in ambient temperature, which allows it to 'remember' and revert to touched or untouched state upon heating cycle. Autonomous huge adjust of thermal conductivity can perform different functions in different backgrounds, such as temperature-dependent thermal diodes [22] or structures that maintain temperature without energy

input [24]. This is of particular value in precision instruments where equilibrium must be maintained despite fluctuations, and in passive thermal management systems where active control is not feasible. On the other hand, ferroelectric materials such as Strontium Titanate (SrTiO3) cuboids illustrate the capacity of temperature-dependent materials to adaptively modify frequency bands [23], thereby enabling frequency-agile invisibility according to transformation optics. This adaptability eliminates the necessity for complex redesigns across varying frequency regions.

As for nonlinear thermal radiation, the $\varepsilon\sigma T^4$ nature leads to nonlinear temperature-related emissivity ε [23] or combines radiative T^4 with conductive $(\nabla T)^1$ for adaptive tuning [2]. Nanoscale Pt and Ag electrodeposition can exhibit a sharp emissivity transition at a specific temperature [25], enhancing infrared imaging around particular temperatures and increasing the sensitivity. Such materials adjust their radiation profiles, allowing for modulation that aligns with the surrounding thermal environment. Another kind of material, taking cues from omnithermal metamaterials [3], leverages the interplay of conduction, convection, and radiation to adaptively switch its thermal properties. With precise engineering, these materials demonstrate a dual behavior that they exhibit thermal transparency at normal temperatures through conduction, and switch to thermal cloaking at higher temperatures by prioritizing radiation.

In summary, the development of external field-dependent diffusion metamaterials signals a transformative leap in adaptive control strategies, offering a major advancement over traditional systems and heralding a new era of intelligent management systems.

3.4 Active Controllable Metamaterials

Active materials usually undergo real-time changes in their properties or behavior under artificial control, enabling a single structure to actively adapt to multiple application scenarios beyond fixed adaptive parameters. The adaptive materials typically respond passively to environmental changes. While the active materials not only adjust to suit various functional requirements but also possess additional capabilities, such as hall-like thermal chirality, spatiotemporal encircle, self-repair or environmental responsiveness and dynamical EP encircling with geometric phase.

The introduction of rotating structures [9, 26, 27] facilitates room-temperature, Hall-like heat transfer without magnetic influence [10]. This structure composed of a stationary solid framework interspersed with rotating particles, breaks the conventional Onsager reciprocal relations, resulting in a marked increase in thermal chirality, and pushing the boundaries of effective thermal conductivity to levels unachievable through the thermal Hall effect alone. When the rotating structure equipped with intelligent environment sensing, the thermal transport will react automatically with deep learning [28]. These breakthroughs light the way for novel explorations in topological and non-Hermitian thermal transport and propose innovative pathways for efficient heat utilization that deviate from phonon-dominated models.

Drawing upon temporal mechanical deformation cycles, active materials informed by spatiotemporal theory have been developed [29–31]. Structures can be engineered as composite systems [32–34], featuring concentric rings differentiated by their thermal conductivities. Designed for periodic structural modulation over time, they manipulate heat flow in a controlled manner. The metamaterials employ an advanced actuation mechanism that rotates the ring layers, creating an effectively time-variant structure. This adaptability allows the materials to oscillate between thermal states, ranging from insulating to conducting [34], echoing the dynamic control seen in electromagnetic metamaterials over wave propagation. The precision of these rotations facilitates the replication of sophisticated thermal phenomena such as thermal cloaking and concentration, granting the power to dictate thermal visibility. In addition to modulating thermal pathways, these materials can apply to thermoelectric encoding sequences [32], marking an evolution in adaptive material systems that are not only responsive to environmental changes but also exhibit intelligent, autonomous behavior.

The integration of rotation structures and mechanical cycles necessitates precise design parameters for both the structure and its background. To bolster robustness, advanced designs of active materials now incorporate mechanisms for energy gain and loss. For example, the integration of thermoelectric generators into active materials considerably broadens their applicability [35]. This union of materials with programmed control systems gives rise to real-time, self-adaptive metasurfaces capable of active temperature regulation. Such platforms function through the autonomous evaluation of thermoelectric heat sources and the real-time modulation of driven voltage, and maintain predefined thermal patterns irrespective of external environmental influences. Another strategic innovation within external gain and loss is the implementation of copper cylinders to delineate isothermal boundaries [36]. These cylinders serve as thermal dipoles, a concept extendable to quadrupoles and higher-order moments. By employing a core-shell structure with these dipoles, one can achieve simultaneous invisibility in thermal and electrical domains using commonplace materials and straightforward architectures. The exploration of dipole effects and the derivation of requirements for the shell and dipole, even in anisotropic materials, align with finite-element simulations. Such theoretical and practical alignments not only streamline thermal and electrical management but may also extend benefits to other physical domains, like electrostatics and magnetostatics. This multifaceted approach to material design underscores a trend towards integration and intellectualization in metamaterials, aiming to elevate the efficiency of physical field manipulation.

To obtain a topological Hamiltonian in thermal system, the convection pairs are considered to obtain relevant gain and loss [37], and ρc in thermal system can mimic diffusive nonreciprocal SSH model [38]. The thermal dynamics thus reveal a previously underemphasized topological propagation with channel pairs with opposite convection velocity. Varying advective configurations lead to moving around the parameter space, creating the dynamic encircling of EP and realizing the geometric phase. The exponential gradient of ρc corresponds to the nonreciprocal coupling coefficient between the nearest units, indicating the bulk and edge states in

a thermal system. These approaches illuminates distinct phase transitions, offering pathways for robust thermal processes and nonchiral thermal diffusion, previously uncharted territories in conventional thermal materials. These advancements herald fresh prospects for topological thermal sciences.

3.5 Conclusions and Outlook

This chapter traces the evolution of metamaterials, with a particular focus on how experimental methods have enabled the progression from passive to adaptive, and ultimately to active metamaterials. Passive metamaterials, foundational to this field, mostly utilize effective medium theory with composites and layered structures, achieving control over properties like inhomogeneity and anisotropy. Despite their foundational role, the static nature of these materials lead to the exploration of more dynamic systems. Adaptive metamaterials emerge next, featuring materials with external field-dependent functions, showcasing adaptability to environmental changes through intricate experimental methods. However, their dependence on external stimuli for adaptation underscore the necessity for more autonomous systems. Addressing this, active metamaterials represent the current pinnacle of this evolution. Incorporating advanced experimental techniques such as motor-controlled units and thermoelectric elements, and applying principles like topological Hamiltonian in convection, these materials demonstrate a high degree of control and functionality, capable of dynamically responding to changes and user inputs. This chapter highlights the critical role of experimental methodologies in transforming the theoretical potential of metamaterials into reality, especially in the development of active systems that autonomously respond to environmental and operational conditions. The future of metamaterials points towards integrating sophisticated technologies such as artificial intelligence and machine learning, pushing the experimental capabilities to new frontiers.

References

1. Dai, G.L., Huang, J.P.: A transient regime for transforming thermal convection: cloaking, concentrating and rotating creeping flow and heat flux. J. Appl. Phys. **124**, 235103 (2018)
2. Xu, L.J., Dai, G.L., Huang, J.P.: Transformation multithermotics: controlling radiation and conduction simultaneously. Phys. Rev. Appl. **13**, 024063 (2020)
3. Xu, L.J., Yang, S., Dai, G.L., Huang, J.P.: Transformation omnithermotics: simultaneous manipulation of three basic modes of heat transfer. ES Energy Environ. **7**, 65–70 (2020)
4. Guenneau, S., Puvirajesinghe, T.M.: Fick's second law transformed: one path to cloaking in mass diffusion. J. R. Soc. Interface **10**, 20130106 (2013)
5. Guenneau, S., Petiteau, D., Zerrad, M., Amra, C., Puvirajesinghe, T.: Transformed Fourier and Fick equations for the control of heat and mass diffusion. AIP Adv. **5**, 053404 (2015)
6. Restrepo-Florez, J.M., Maldovan, M.: Mass separation by metamaterials. Sci. Rep. **6**, 21971 (2016)

7. Xu, L.J., Yang, S., Huang, J.P.: Thermal transparency induced by periodic interparticle interaction. Phys. Rev. Appl. **11**, 034056 (2019)
8. Narayana, S., Sato, Y.: Heat flux manipulation with engineered thermal materials. Phys. Rev. Lett. **108**, 214303 (2012)
9. Li, Y., Zhu, K.-J., Peng, Y.-G., Li, W., Yang, T., Xu, H.-X., Chen, H., Zhu, X.-F., Fan, S., Qiu, C.-W.: Thermal meta-device in analogue of zero-index photonics. Nat. Mater. **18**, 48–54 (2019)
10. Xu, L.J., Liu, J.R., Xu, G.Q., Huang, J.P., Qiu, C.-W.: Giant, magnet-free, and room-temperature Hall-like heat transfer. Proc. Natl. Acad. Sci. U.S.A. **120**, e2305755120 (2023)
11. Jin, P., Liu, J., Xu, L.J., Wang, J., Ouyang, X., Jiang, J.-H., Huang, J.P.: Tunable liquid-solid hybrid thermal metamaterials with a topology transition. Proc. Natl. Acad. Sci. U.S.A. **120**, e2217068120 (2023)
12. Yang, S., Xu, L.J., Wang, R.Z., Huang, J.P.: Full control of heat transfer in single-particle structural materials. Appl. Phys. Lett. **111**, 121908 (2017)
13. Zhou, X.C., Lin, W.Y., Yang, F.B., Zhou, X.D., Shen, J., Huang, J.P.: Effective medium theory with hybrid impacts of phase symmetry and asymmetry for analyzing phase transition behavior. Eur. Phys. Lett. **141**, 16001 (2023)
14. Tian, B., Wang, J., Dai, G., Ouyang, X., Huang, J.P.: Thermal metadevices with geometrically anisotropic heterogeneous composites. Int. J. Heat Mass Transf. **174**, 121312 (2021)
15. Li, Y., Yu, C., Liu, C., Xu, Z., Su, Y., Qiao, L., Zhou, J., Bai, Y.: Mass diffusion metamaterials with "plug and switch" modules for ion cloaking, concentrating, and selection: design and experiments. Adv. Sci. **9**, 2201032 (2022)
16. Schittny, R., Kadic, M., Guenneau, S., Wegener, M.: Experiments on transformation thermodynamics: molding the flow of heat. Phys. Rev. Lett. **110**, 195901 (2013)
17. Xu, L.J., Yang, S., Huang, J.P.: Thermal theory for heterogeneously architected structure: fundamentals and application. Phys. Rev. E **98**, 052128 (2018)
18. Li, J., Gao, Y., Huang, J.: A bifunctional cloak using transformation media. J. Appl. Phys. **108**, 074504 (2010)
19. Zheng, X., Li, B.: Effect of interfacial thermal resistance in a thermal cloak. Phys. Rev. Appl. **13**, 024071 (2020)
20. Yang, F.B., Tian, B.Y., Xu, L.J., Huang, J.P.: Experimental demonstration of thermal chameleonlike rotators with transformation-invariant metamaterials. Phys. Rev. Appl. **14**, 054024 (2020)
21. Peng, Y.-G., Li, Y., Cao, P.-C., Zhu, X.-F., Qiu, C.-W.: 3D printed meta-helmet for wide-angle thermal camouflages. Adv. Funct. Mater. **30**, 2002061 (2020)
22. Shen, X.Y., Li, Y., Jiang, C.R., Huang, J.P.: Temperature trapping: energy-free maintenance of constant temperatures as ambient temperature gradients change. Phys. Rev. Lett. **117**, 055501 (2016)
23. Peng, R., Xiao, Z., Zhao, Q., Zhang, F., Meng, Y., Li, B., Soukoulis, C.M.: Temperature-controlled chameleonlike cloak. Phys. Rev. X **7**(1), 011033 (2017)
24. Li, Y., Shen, X.Y., Wu, Z.H., Huang, J.Y., Chen, Y.X., Ni, Y.S., Huang, J.P.: Temperature-dependent transformation thermotics: from switchable thermal cloaks to macroscopic thermal diodes. Phys. Rev. Lett. **115**, 195503 (2015)
25. Li, M., Liu, D., Cheng, H., Peng, L., Zu, M.: Manipulating metals for adaptive thermal camouflage. Sci. Adv. **6**(22), eaba3494 (2020)
26. Li, J., Li, Y., Cao, P.-C., Yang, T., Zhu, X.-F., Wang, W., Qiu, C.-W.: A continuously tunable solid-like convective thermal metadevice on the reciprocal line. Adv. Mater. **32**, 2003823 (2020)
27. Li, J., Li, Y., Wang, W., Li, L., Qiu, C.-W.: Effective medium theory for thermal scattering off rotating structures. Opt. Express **28**, 25894–25907 (2020)
28. Jin, P., Xu, L.J., Xu, G.Q., Li, J.X., Qiu, C.-W., Huang, J.P.: Deep learning-assisted active metamaterials with heat-enhanced thermal transport. Adv. Mater. **36**, 2305791 (2024)
29. Xu, L.J., Xu, G.Q., Huang, J.P., Qiu, C.-W.: Diffusive Fizeau drag in spatiotemporal thermal metamaterials. Phys. Rev. Lett. **128**, 145901 (2022)
30. Li, J., Li, Y., Cao, P.-C., Qi, M., Zheng, X., Peng, Y.-G., Li, B., Zhu, X.-F., Alù, A., Chen, H., Qiu, C.-W.: Reciprocity of thermal diffusion in time-modulated systems. Nat. Commun. **13**, 167 (2022)

31. Xu, L.J., Huang, J.P., Ouyang, X.P.: Tunable thermal wave nonreciprocity by spatiotemporal modulation. Phys. Rev. E **103**, 032128 (2021)
32. Lei, M., Xu, L.J., Huang, J.P.: Spatiotemporal multiphysics metamaterials with continuously adjustable functions. Mat. Today. Phys. **34**, 101057 (2023)
33. Lei, M., Jiang, C., Yang, F., Wang, J., Huang, J.P.: Programmable all-thermal encoding with metamaterials. Int. J. Heat Mass Transf. **207**, 124033 (2023)
34. Yang, F., Jin, P., Lei, M., Dai, G., Wang, J., Huang, J.P.: Space-time thermal binary coding by a spatiotemporally modulated metashell. Phys. Rev. Appl. **19**, 054096 (2023)
35. Guo, J., Xu, G., Tian, D., Qu, Z., Qiu, C.-W.: A real-time self-adaptive thermal metasurface. Adv. Mater. **34**, 2201093 (2022)
36. Xu, L., Yang, S., Huang, J.: Dipole-assisted thermotics: experimental demonstration of dipole-driven thermal invisibility. Phys. Rev. E **100**, 062108 (2019)
37. Li, Y., Peng, Y.-G., Han, L., Miri, M.-A., Li, W., Xiao, M., Zhu, X.-F., Zhao, J., Alù, A., Fan, S., Qiu, C.-W.: Anti-parity-time symmetry in diffusive systems. Science **364**, 170–173 (2019)
38. Hu, H., Han, S., Yang, Y., Liu, D., Xue, H., Liu, G.-G., Cheng, Z., Wang, Q.J., Zhang, S., Zhang, B., Luo, Y.: Observation of topological edge states in thermal diffusion. Adv. Mater. **34**, 2202257 (2022)
39. Wang, R.Z., Xu, L.J., Ji, Q., Huang, J.P.: A thermal theory for unifying and designing transparency, concentrating and cloaking. J. Appl. Phys. **123**, 115117 (2018)
40. Xu, L.J., Jiang, C.R., Huang, J.P.: Heat-source transformation thermotics: from boundary-independent conduction to all-directional replication. Eur. Phys. J. B **91**, 166 (2018)
41. Xu, G., Li, Y., Li, W., Fan, S., Qiu, C.-W.: Configurable phase transitions in topological thermal material. Phys. Rev. Lett. **127**, 105901 (2021)

Part I
Metamaterials for Thermal Diffusion: Thermal Conduction

Chapter 4
Transformation Thermotics and Effective Medium Theory for Thermal Conduction

Zhixin Li, Zeren Zhang, Liujun Xu, and Min Lei

4.1 Opening Remarks

Transformation thermotics stems from the form-invariance of the governing heat transfer equations under specific coordinate transformations. This approach facilitates the engineering of material thermal properties, particularly thermal conductivity, enabling advanced manipulation of heat flux in distinct modalities, such as thermal cloaking, concentration, and rotation [1–3]. In contemporary literature, descriptions of transformation thermotics are prevalent. In this chapter, we will begin by delving into the underlying motivations behind the transformation theory and subsequently provide an introduction to its foundational concepts. Consider light propagating across a uniform plane, where its trajectory is linear. To compel the light to follow a curved path, one might intuitively think of deforming the plane. Subsequently, it might be anticipated that the light's trajectory would adjust in tandem with this deformation. We have been told in general relativity that the change of energy-momentum tensor can bend the space so we can have a more general guess here that if one wants to manipulate some physical fields as if the space is changed, he/she can change some important properties of the space or the material on it, for example, the thermal conductivity tensor.

Z. Li (✉) · Z. Zhang · M. Lei
Department of Physics, Key Laboratory of Micro and Nano Photonic Structures (MOE), and State Key Laboratory of Surface Physics, Fudan University, Shanghai 200438, China
e-mail: 22210190026@m.fudan.edu.cn

L. Xu
Graduate School of China Academy of Engineering Physics, Beijing 100193, China

F.-B. Yang and J.-P. Huang, *Diffusionics*,
https://doi.org/10.1007/978-981-97-0487-3_4

4.2 Transformation Thermotics for Thermal Conduction

4.2.1 Basic Theory

In 2007, it was shown that transformation theory and metamaterials can be used in the zero-frequency limit of electromagnetic waves, for example for electrostatic and magnetostatic fields [4, 5]. Subsequently, the cloaking of electrostatic fields [6], magnetostatic fields [7] and direct current fields [8, 9] were theoretically predicted and experimentally demonstrated. Research interests then turned to heat conduction, which is described by the Laplace equation at the steady state, similar to electrostatics.

Thermal cloaking inspired by transformation optics was then discussed [10, 11], opening a pathway towards transformation thermotics and its extended theories. Before 2012, transformed thermal media were mainly applied to steady-state heat transfer, which limited the applications of transformation thermotics. Transformation thermotics was then extended from the steady state to the transient state by considering the time-dependent term in the conduction equation [12]. Based on this generalized theory, thermal cloaking and concentrating suitable for transient heat transport were designed. In general, heat conduction with a heat source is described by

$$\rho C \frac{\partial T}{\partial t} + \nabla \cdot (-\kappa \nabla T) = S \tag{4.1}$$

where t is time, ρ, C, T and κ are the density, heat capacity, temperature and thermal conductivity of the system, respectively, and S is the power density generated by the external heat source. Under a 2D coordinate transformation from (x, y) to (x', y'), this equation becomes

$$\rho' C' \frac{\partial T}{\partial t} + \nabla' \cdot \left(-\kappa' \nabla' T\right) = S' \tag{4.2}$$

where $\rho' C' = \frac{\rho C}{\det J}$, $\kappa' = \frac{J \kappa J^T}{\det J} T$, and $S' = \frac{S}{\det J}$, where J is the Jacobian transformation matrix. Therefore, Eq. 4.1 is form-invariant.

Transformation thermotics faces various challenges: for example, materials with singular and anisotropic thermal conductivities are needed, which do not often exist naturally. Thus, a method that can experimentally achieve transformed parameters is urgently required. Thermal metamaterials, the thermal counterpart of electromagnetic metamaterials, make transformation theory applicable in practice.

As a type of macroscopic composite, the properties of thermal metamaterials can be predicted using effective medium theory. The Maxwell–Garnett theory and the Bruggeman formula are two basic theoretical tools. An early experiment on thermal metamaterials was performed using an ABAB layered structure to achieve anisotropic thermal conductivity. This study experimentally demonstrated that the structure was capable of cloaking a steady heat flux. Subsequent experiments on thermal metamaterials extended this approach to transient cases [13].

4.2.2 Application

Many proposals and designs targeting various applications have emerged to enrich and develop transformation thermotics. Intelligent and multifunctional thermal metamaterials have been proposed to explore new applications. Advanced methods using effective medium theories and numerical algorithms guided by the theory of transformation thermotics have achieved unprecedented phenomena and applications, such as intelligent thermal metamaterials that adapt their responses and functions to the environment. Additionally, smart thermal devices, such as chameleon-like concentrators [14] and rotators [15], have been investigated. Based on transformation-invariant thermal metamaterials with highly anisotropic thermal conductivities, these chameleon-like devices work even when the properties of the surroundings change. Thermal-null media have also been presented [16]: these devices have highly anisotropic thermal conductivities that are homogeneous and independent of the geometry of the device. In other words, the conductivity does not have to be recalculated when the shape changes. The principle of extreme anisotropy is similar to that of chameleon-like devices. Nevertheless, these devices still face challenges because materials with extreme anisotropy do not exist naturally. Fortunately, artificial materials such as multilayer graphene or van der Waals thin films may provide alternatives [17].

Thermal metamaterials with multiple functions are also desirable. Such metamaterials are achieved by transforming multiple physical fields and the relevant material parameters. Simultaneously managing heat and electric currents is one of the key topics [18]. In 2010, a cloak for electric and heat currents was proposed [19], showing that it could be possible to construct bifunctional devices based on transformation theory. A bifunctional cloak was experimentally demonstrated in 2014 [20]. Coupled thermoelectric transport, where heat and electric currents influence each other, was also considered [21], leading to the development of a thermoelectric cloak that shields both electric and thermal fields. Other multifunctional devices such as thermo-hydrodynamic cloaks [22] and thermoelastic cloaks [23] have also been proposed.

The scattering cancellation method, which was initially used for cloaking electromagnetic fields, has also been widely applied to the design of thermal metamaterials [24]. Here, for brevity, thermal invisibility and illusion are collectively treated as thermal camouflage. In 2014 one study demonstrated a 2D bilayer thermal cloak made of bulk isotropic materials that was designed by calculating the thermal conductivity of each layer by directly solving the heat-conduction equation [25]. Based on this bilayer structure, a camouflage device was reported that can transform the thermal scattering signature of a hidden object into another fake signature [26]. Although this device worked well for steady-state cases, the performance under transient conditions was unsatisfactory because the scattering cancellation method only considers the steady state. Later, an improved scattering cancellation method, which is suitable for transient cases, was proposed [27]. Therefore, the scattering cancellation method can solve the problem of extreme parameters Anisotropic core-shell structure introduced by transformation theory and aid the design of new thermal metamaterials.

The other primary application of thermal metamaterials is heat management in fields ranging from electronics to biology. For example, with the rapid development of nanoelectronics, conventional thermal management approaches, such as through-silicon-via optimization and thermal pipes, face many challenges that could be addressed by thermal metamaterials [28, 29]. Unlike conventional methods, thermal metamaterials can dissipate heat at will and avoid thermal crosstalk and local hot spots. Additionally, thermal memory and computing could be implemented by defining binary states of heat flux using preset alternating sequences of concentrating and cloaking states [30]. Thermal encoding has been proposed as a possible scheme for encoding optical or electronic information [31]. Personal thermal management is another exciting application. For example, a Janus layered textile was developed that works as a heating or cooling device [32]. The textile could increase (or decrease) the temperature of a skin simulator under sunlight.

Numerical optimization algorithms can also help the design and fabrication of thermal metamaterials [33]. In 2014, topology optimization was used to design thermal-composite structures for heat flux manipulation, including shielding, focusing and rotating the heat flux [34]. The anisotropic thermal composite consists of elliptical inclusions embedded in the surrounding matrix. To simplify the structures, a covariance matrix adaption evolution strategy, a powerful stochastic method, was used to tackle nonlinear optimization problems and design a thermal cloak composed of natural materials [35]. Constructing such a thermal cloak involves two steps. First, the background temperature distribution must be preset without the obstacle present. Second, the undisturbed temperature field must be reproduced using a thermal cloak designed by topology optimization. Printable freeform thermal metamaterials have been proposed by directly creating functional cells [36]. The thermal conductivity tensor is calculated according to transformation thermotics and realized using local microstructures composed of die steel and polydimethylsiloxane [37]. This approach solves challenges such as the limited shape adaptability of thermal metadevices and the need for prior knowledge of the background temperatures. Numerical methods have now become advanced and powerful for designing feasible thermal metamaterials with various applications such as invisible sensors [38, 39], not to mention the emerging machine-learning techniques [40].

4.3 Effective Medium Theory for Thermal Conduction

The generalized transformation thermal theory can effectively improve the thermal control ability, but the parameters predicted by the theory are often non-uniform and anisotropic, which brings great challenges to the actual preparation. One solution is to use thermal effective medium theory to approximate these complex parameters, most commonly layered alternating structures, where transformation theory remains at the heart of the design. Another solution is to start from scratch and start research directly from the thermal effective medium theory, the most representative of which

is the double-layer thermal invisibility cloak, at this time the effective medium theory has become the core of the research [41].

For this reason, thermal effective medium theory has been widely proposed and developed for designing smart thermal metamaterials. Linear theory, nonlinear theory and theory with heat source were proposed. Among them, the linear theory is heat conduction in which thermal conductivity is independent of temperature. The nonlinear theory is that thermal conductivity depends on temperature for heat conduction. Containing source theory is a theory that considers external energy input in the heat transfer process, such as thermal dipole structure, apparent negative thermal conductivity and thermal zero refractive index. The introduction of nonlinearity and external heat source makes the device responsive to external field, which is helpful for the design of smart thermal metamaterials [42].

4.3.1 Linearization Theory and Structure

In the realm of heat conduction studies, passive linear heat conduction stands paramount. This model, devoid of heat sources and characterized by materials whose thermal conductivity remains invariant with temperature fluctuations, serves as the foundational bedrock. Within this research framework, structures such as the core-shell configuration, periodic architectures, and their multifarious amalgamations take precedence [43].

4.3.1.1 Core-Shell Structure

Predominantly employed in the design of thermal metamaterials, the core-shell structure emerges as an archetype, exemplified by its use in thermal cloaking. Delving deeper into the equivalent thermal conductivity of this core-shell paradigm could potentially unveil novel functionalities. With this objective, we first lay down a comprehensive theoretical framework, accommodating both material and geometric anisotropies. Subsequent to this, we conceptualized a chameleon-esque shell and a thermal stealth detector.

Material Anisotropy Consider a core-shell structure with inner and outer radii r_c and r_s respectively, the thermal conductivities of the core and shell are κ_c and κ_s respectively and both are anisotropic, as shown in Fig. 4.1a. The thermal conductivities of the core and shell can be written in cylindrical coordinates as $\kappa_c = diag[\kappa_{crr}, \kappa_{c\theta\theta}]$ and $\kappa_s = diag[\kappa_{srr}, \kappa_{s\theta\theta}]$, respectively. The heat conduction equation can be expanded in the cylindrical coordinate system (r, θ) as

$$\frac{1}{r}\frac{\partial}{\partial r}\left(r\kappa_{\mathrm{rr}}\frac{\partial T}{\partial r}\right)+\frac{1}{r}\frac{\partial}{\partial \theta}\left(\kappa_{\theta\theta}\frac{\partial T}{r\partial \theta}\right)=0 \tag{4.3}$$

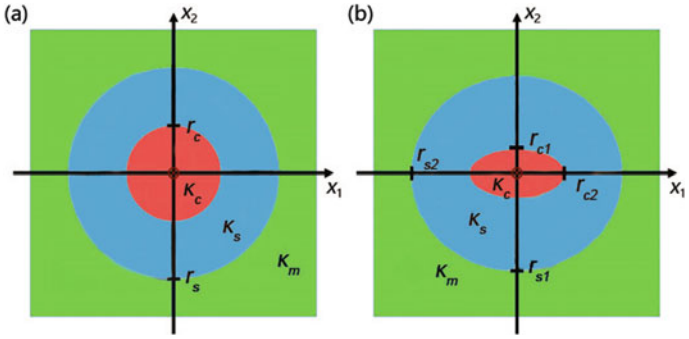

Fig. 4.1 **a** Anisotropic core-shell structure of materials. **b** Geometrically anisotropic core-shell structure

where κ_{rr} and $\kappa_{\theta\theta}$ are the radial and tangential thermal conductivity of a certain region, respectively. So the core temperature T_c, the shell temperature T_s and the matrix temperature T_m can be written as

$$T_{\mathrm{c}} = A_{\mathrm{s}} r^{u_{\mathrm{c}}^{+}} \cos\theta \tag{4.4}$$

$$T_{\mathrm{s}} = \left(A_{\mathrm{s}} r^{u_{\mathrm{s}}^{+}} + B_{\mathrm{s}} r^{u_{\mathrm{s}}^{-}}\right) \cos\theta \tag{4.5}$$

$$T_{\mathrm{s}} = \left(A_{\mathrm{m}} r + B_{\mathrm{m}} r^{-1}\right) \cos\theta \tag{4.6}$$

when the equivalent thermal conductivity of the core-shell structure is consistent with the thermal conductivity of the matrix, the temperature distribution of the matrix will not be disturbed, so solving $B_{\mathrm{m}} = 0$ can further write the equivalent thermal conductivity κ_e of the core-shell structure as

$$\kappa_{\mathrm{e}} = \kappa_{\mathrm{m}} = \kappa_{\mathrm{srr}} \frac{u_{\mathrm{s}}^{+}\left(u_{\mathrm{c}}^{+}\kappa_{\mathrm{crr}} - u_{\mathrm{s}}^{-}\kappa_{\mathrm{srr}}\right) - u_{\mathrm{s}}^{-}\left(u_{\mathrm{c}}^{+}\kappa_{\mathrm{crr}} - u_{\mathrm{s}}^{+}\kappa_{\mathrm{srr}}\right)\left(r_{\mathrm{c}}/r_{\mathrm{s}}\right)^{u_{\mathrm{s}}^{+}-u_{\mathrm{s}}^{-}}}{u_{\mathrm{c}}^{+}\kappa_{\mathrm{crr}} - u_{\mathrm{s}}^{-}\kappa_{\mathrm{srr}} - \left(u_{\mathrm{c}}^{+}\kappa_{\mathrm{crr}} - u_{\mathrm{s}}^{+}\kappa_{\mathrm{srr}}\right)\left(r_{\mathrm{c}}/r_{\mathrm{s}}\right)^{u_{\mathrm{s}}^{+}-u_{\mathrm{s}}^{-}}} \tag{4.7}$$

We can also get the expression for the inner temperature coefficient

$$\frac{A_{\mathrm{c}}}{A_{\mathrm{m}}} = \frac{\left(u_{\mathrm{s}}^{+} - u_{\mathrm{s}}^{-}\right)\kappa_{\mathrm{srr}}\left(r_{\mathrm{c}}/r_{\mathrm{s}}\right)^{u_{\mathrm{s}}^{+}-1} r_{\mathrm{c}}^{1-u_{\mathrm{c}}^{+}}}{u_{\mathrm{c}}^{+}\kappa_{\mathrm{crr}} - u_{\mathrm{s}}^{-}\kappa_{\mathrm{srr}} - \left(u_{\mathrm{c}}^{+}\kappa_{\mathrm{crr}} - u_{\mathrm{s}}^{+}\kappa_{\mathrm{srr}}\right)\left(r_{\mathrm{c}}/r_{\mathrm{s}}\right)^{u_{\mathrm{s}}^{+}-u_{\mathrm{s}}^{-}}} \tag{4.8}$$

Obviously, $A_c/A_m \approx 0$, $A_c/A_m = 1$, and $A_c/A_m > 1$ correspond to the characteristics of thermal cloaks, thermal cloaking detectors, and thermal concentrators, respectively. For 3D conclusions, the form of the equivalent thermal conductivity (or temperature coefficient) is exactly the same.

Geometrically Anisotropy For the geometrically anisotropic confocal core-shell structure, assuming that the thermal conductivities of the core and the shell are κ_c and κ_s respectively and both are isotropic, as shown in Fig. 4.1b. Assume that the semi-axis lengths of the core and shell along the xi direction are r_{ci} and r_{si}, respectively. The conversion between Cartesian coordinates x_i and ellipsoidal or ellipsoidal coordinates ρ_j can be written as

$$\sum_i \frac{x_i^2}{\rho_j + r_{\mathrm{ci}}^2} = 1 \tag{4.9}$$

so the heat conduction equation can be written as [47]

$$\frac{\partial}{\partial \rho_1}\left(g\left(\rho_1\right)\frac{\partial T}{\partial \rho_1}\right) + \frac{g\left(\rho_1\right)}{\rho_1 + r_{\mathrm{ci}}^2}\frac{\partial T}{\partial \rho_1} = 0 \tag{4.10}$$

here we introduce the shape factor

$$L_{\mathrm{c1}} = \frac{r_{\mathrm{c2}}}{r_{\mathrm{c1}} + r_{\mathrm{c2}}} \tag{4.11}$$

$$L_{\mathrm{c2}} = \frac{r_{\mathrm{c1}}}{r_{\mathrm{c1}} + r_{\mathrm{c2}}} \tag{4.12}$$

$$L_{\mathrm{s1}} = \frac{r_{\mathrm{s2}}}{r_{\mathrm{c1}} + r_{\mathrm{s2}}} \tag{4.13}$$

$$L_{\mathrm{s2}} = \frac{r_{\mathrm{s1}}}{r_{\mathrm{c1}} + r_{\mathrm{s2}}} \tag{4.14}$$

We can get the equivalent thermal conductivity of the core-shell structure

$$\kappa_{\mathrm{e}} = \kappa_{\mathrm{m}} = \kappa_{\mathrm{s}}\frac{L_{\mathrm{ci}}\kappa_{\mathrm{c}} + \left(1 - L_{\mathrm{ci}}\right)\kappa_{\mathrm{s}} + \left(1 - L_{\mathrm{si}}\right)\left(\kappa_{\mathrm{c}} - \kappa_{\mathrm{s}}\right) f}{L_{\mathrm{ci}}\kappa_{\mathrm{c}} + \left(1 - L_{\mathrm{ci}}\right)\kappa_{\mathrm{s}} - L_{\mathrm{si}}\left(\kappa_{\mathrm{c}} - \kappa_{\mathrm{s}}\right) f} \tag{4.15}$$

where f represents the volume ratio.

Sturctures Leveraging the core-shell architecture, myriad functionalities such as thermal stealth, thermal aggregation, and thermal rotation have been forecasted by the transformation thermotics. To underscore the intrinsic merits of the thermal effective medium theory, we elucidate the conception of two salient functionalities, as anticipated by the non-transformation thermal theory rooted in the core-shell framework: namely, the chameleon-esque shell and the thermal stealth detector.

Drawing from the core-shell structural paradigm, functionalities like thermal stealth, thermal aggregation, and thermal rotation are envisioned. To accentuate the inherent strengths of the thermal effective medium theory, we illuminate functionalities anticipated by two distinct non-transformation thermotics frameworks, specifi-

cally the chameleon-esque shell and the thermal stealth detector, both rooted in the core-shell schema [45].

Chameleon-like Shell The so-called chameleon-like shell means that the thermal conductivity of the shell changes with the thermal conductivity of the core, just as the color of a chameleon changes with the color of the environment. Since this is an adaptive change without human intervention, the chameleon-like shell can also be called an intelligent thermal metamaterial. Mathematically, the chameleon-like shell can be defined as the equivalent thermal conductivity κ_e of the core-shell structure is always equal to the thermal conductivity κ_c of the core (isotropic)

$$\kappa_{\mathrm{e}} \equiv \kappa_{\mathrm{c}} \tag{4.16}$$

as Eq. (4.7) shows, when

$$\kappa_{s\theta\theta} \to 0 \tag{4.17}$$

$$\kappa_{\mathrm{srr}} \gg \kappa_{\mathrm{c}} \tag{4.18}$$

Equation (4.7) can be simplified to $\kappa_e = \kappa_c$, thus satisfying the requirement of a chameleon-like shell. But this conclusion does not hold in the three-dimensional case.

Conclusively, the capabilities of the chameleon-like shell have been empirically validated, with the apparatus depicted in Fig. 4.2a. To underscore the shell's adaptability across diverse environments, a duo of copper samples, crafted via laser cutting,

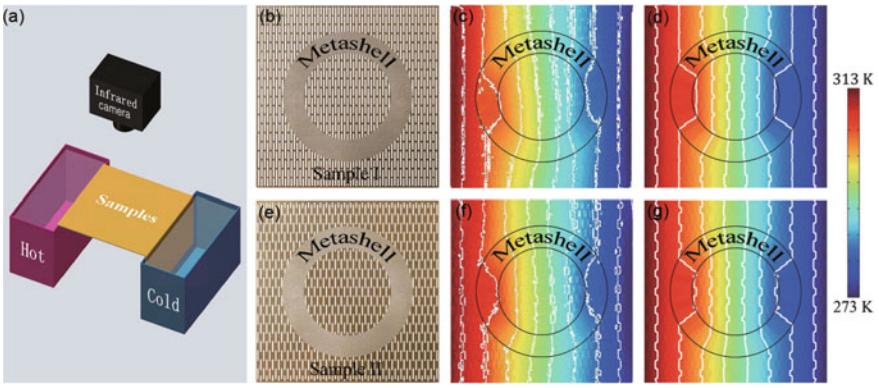

Fig. 4.2 Experimental results of chameleon-like shells. **a** Schematic diagram of the experimental setup. **b** and **e** Two pictures of experimental samples. **c** and **d** show the experimental and simulated results for sample (**b**), respectively. **f** and **g** show the experimental and simulated results for sample (**e**), respectively. The equivalent thermal conductivity of the environment along the horizontal direction is 20 and 60 W m^{-1} K^{-1}. The equivalent thermal conductivity of the chameleon-like shell is diag [264.68, 0.08] W m^{-1} K^{-1}. The thermal conductivities of copper and air are 400 and 0.026 W m^{-1} K^{-1}, respectively. (from Ref. [14])

were readied. Although these samples differ in their environmental thermal conductivity, their shell thermal conductivity remains invariably consistent, as illustrated in Fig. 4.2b and e. While approximate parameters have been employed, their influence on outcomes remains marginal. Respective experimental outcomes are portrayed in Fig. 4.2c and f. Given the undistorted temperature distribution of the substrate, it can be inferred that the chameleonoid shell's thermal conductivity is attuned to the ambient thermal conductivity. To negate the potential distortions from thermal convection and radiation, simulations were conducted for both specimens, as represented in Fig. 4.2d and g, thereby affirming the chameleon-like shell's functionality [46].

The salient feature of the chameleon-like shell lies in its inherent ability to modulate its thermal conductivity, synchronizing it with the ambient environment, all without prior knowledge of the latter's thermal attributes. Building on this unique adaptability, we've synergized it with the thermal rotation function, culminating in the creation of a chameleon-esque thermal spinner [15]. Moreover, the pronounced anisotropic thermal conductivity inherent to the chameleon-like shell remains invariant to transformations [48]. Owing to its autonomous adaptive capabilities, the chameleon-like shell stands as an intelligent thermal metamaterial, poised to significantly influence domains such as camouflage and welding.

Thermal Stealth Detector Measuring temperature typically necessitates embedding a detector within a matrix. However, a discrepancy in thermal conductivity between the detector and the matrix can perturb the innate temperature distribution, rendering the detector discernible to infrared cameras. To mitigate this thermal disturbance, researchers have encased the detector within an isotropic shell, aiming for its thermal stealth [51]. Notwithstanding, this does not ensure that the detector's temperature distribution mirrors the original, introducing potential measurement inaccuracies. To address this conundrum, transitioning from an isotropic to an anisotropic shell is proposed. Through the solutions presented by either Eq. (4.8) or Eq. (4.8), by ensuring $A_c/A_m = 1$, one can achieve a harmonious balance between thermal stealth and precise temperature measurement [38].

Furthermore, comparable functionality can be realized employing isotropic materials. Given that isotropy offers one fewer degree of design liberty compared to anisotropy, the introduction of an additional shell becomes requisite, culminating in a double-shell configuration. When juxtaposed with its single-shell counterpart, the double-shell structured thermal stealth detectors offer not only precision in temperature measurement but also aptness for scenarios with geometric anisotropy [39]. While our discourse thus far has centered on regular geometries, we have expanded our design horizons to encompass diverse shapes of thermal stealth detectors, harnessing the prowess of particle swarm optimization, thereby amplifying the application spectrum [49].

4.3.1.2 Periodic Structure

Apart from the single core-shell configuration, the multi-body periodic arrangement also serves as a prevalent model. However, the utilization of this model for crafting thermal metamaterials remains relatively uncommon [50]. From a physical perspective, the core-shell structure exhibits asymmetry due to the contrasting attributes of its core and shell components. Conversely, the periodic structure embodies symmetry as the states of its constituent particles are uniform. In the forthcoming section, we will delve into elucidating the interplay between particles and their impact on the matrix. This exploration will pave the way for devising multi-body thermotransparent functions.

Maxwell-Garnett and Bruggeman Theories Within the matrix, a square lattice arrangement features red spherical particles labeled as A (demonstrating material anisotropy), and blue oval particles marked as B (exhibiting geometric anisotropy), as depicted in Fig. 4.3. Given the geometric anisotropy of particle B, the composite's effective thermal conductivity also displays anisotropic behavior. For the sake of simplicity, we will primarily focus on evaluating the effective thermal conductivity in the horizontal direction. Upon applying a uniform thermal gradient G_0 horizontally (where the thermal gradient represents a negative temperature gradient), the resultant equivalent thermal conductivity κ_e can be derived through the principles of Fourier's law.

$$\kappa_{\mathrm{e}} = \frac{\langle J \rangle}{\langle G \rangle} \tag{4.19}$$

where J and G are the heat flow and thermal field in the composite, respectively. Assuming that the local heat fluxes in particle A, particle B and matrix are J_a, J_b and J_m, and the corresponding local heat fields are G_a, G_b and G_m, Eq. (4.19) can be rewritten as

$$\kappa_{\mathrm{e}} = \frac{f_{\mathrm{a}} \langle J_{\mathrm{a}} \rangle + f_{\mathrm{b}} \langle J_{\mathrm{b}} \rangle + f_{\mathrm{m}} \langle J_{\mathrm{m}} \rangle}{f_{\mathrm{a}} \langle G_{\mathrm{a}} \rangle + f_{\mathrm{b}} \langle G_{\mathrm{b}} \rangle + f_{\mathrm{m}} \langle G_{\mathrm{m}} \rangle} \tag{4.20}$$

where f_a, f_b and $f_m = 1 - f_a - f_b$ are the proportions of particle A, particle B and matrix, respectively. By calculating the average thermal field and heat flow respectively, we can get the effective thermal conductivity of the material.

$$\kappa_{\mathrm{e}} = \frac{f_{\mathrm{a}}\kappa_{\mathrm{a}} \langle G_{\mathrm{a}} \rangle + f_{\mathrm{b}}\kappa_{\mathrm{b}} \langle G_{\mathrm{b}} \rangle + f_{\mathrm{m}}\kappa_{\mathrm{m}} \langle G_{\mathrm{m}} \rangle}{f_{\mathrm{a}} \langle G_{\mathrm{a}} \rangle + f_{\mathrm{b}} \langle G_{\mathrm{b}} \rangle + f_{\mathrm{m}} \langle G_{\mathrm{m}} \rangle} = \frac{f_{\mathrm{a}}\varepsilon_{\mathrm{a}}\kappa_{\mathrm{a}} + f_{\mathrm{b}}\varepsilon_{\mathrm{b}}\kappa_{\mathrm{b}} + f_{\mathrm{m}}\kappa_{\mathrm{m}}}{f_{\mathrm{a}}\varepsilon_{\mathrm{a}} + f_{\mathrm{b}}\varepsilon_{\mathrm{b}} + f_{\mathrm{m}}} \tag{4.21}$$

From this we can derive the famous Maxwell-Garnett formula [54].

Furthermore, in order to describe the interaction between particles, we further assume that $\kappa_e = \kappa_m$, which means that the influence of particle A and particle B on the matrix cancels each other out [55]. At this time, the effective thermal conductivity of particles can be calculated to obtain the Bruggeman formula [56].

Sturctures The presented theories offer a pathway to engineer devices featuring multi-body thermal transparency. The concept of thermal transparency involves two

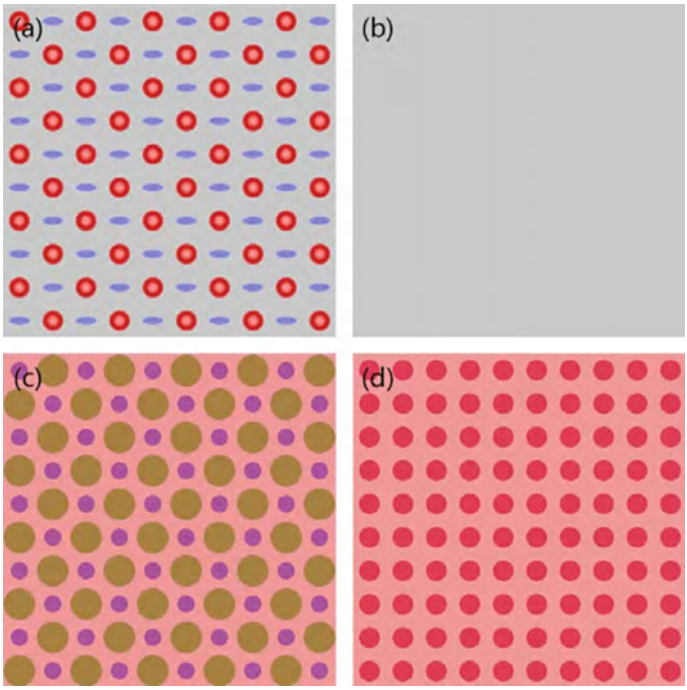

Fig. 4.3 Schematic of a many-body periodic structure. In **a** and **b**, particle interactions nullify their impact on the matrix, giving the impression of absent particles [52]. However, in **c** and **d**, these interactions persist, making one particle effectively represent the other. Adapted from Ref. [53]

distinct strategies [57]. Firstly, for the single core-shell structure, achieving thermal transparency necessitates adjusting the equivalent thermal conductivity to match that of the matrix [57]. This alignment minimizes any external field perturbation introduced by the core-shell structure. Conversely, thermal transparency rooted in periodic structures revolves around orchestrating a mutual nullification of the effects exerted by the two particle types on the matrix. This delicate balance ensures the preservation of an undisturbed thermal field [58, 59].

Throughout the design process, three pivotal parameters—thermal conductivities κ_a, κ_b, and κ_m—stand central. Without sacrificing generality, these parameters are assumed isotropic.

As shown in Fig. 4.4d–f. When there is only particle A in the matrix, the isotherm will repel outward, because the thermal conductivity of particle A is greater than that of the matrix, as shown in Fig. 4.4d. When there is only particle B in the matrix, the isotherm will shrink inward because the thermal conductivity of particle B is smaller than that of the matrix, as shown in Fig. 4.4e. When there are particles A and B in the matrix at the same time, the disturbance of the two on the temperature of the matrix cancels out, as shown in Fig. 4.4f.

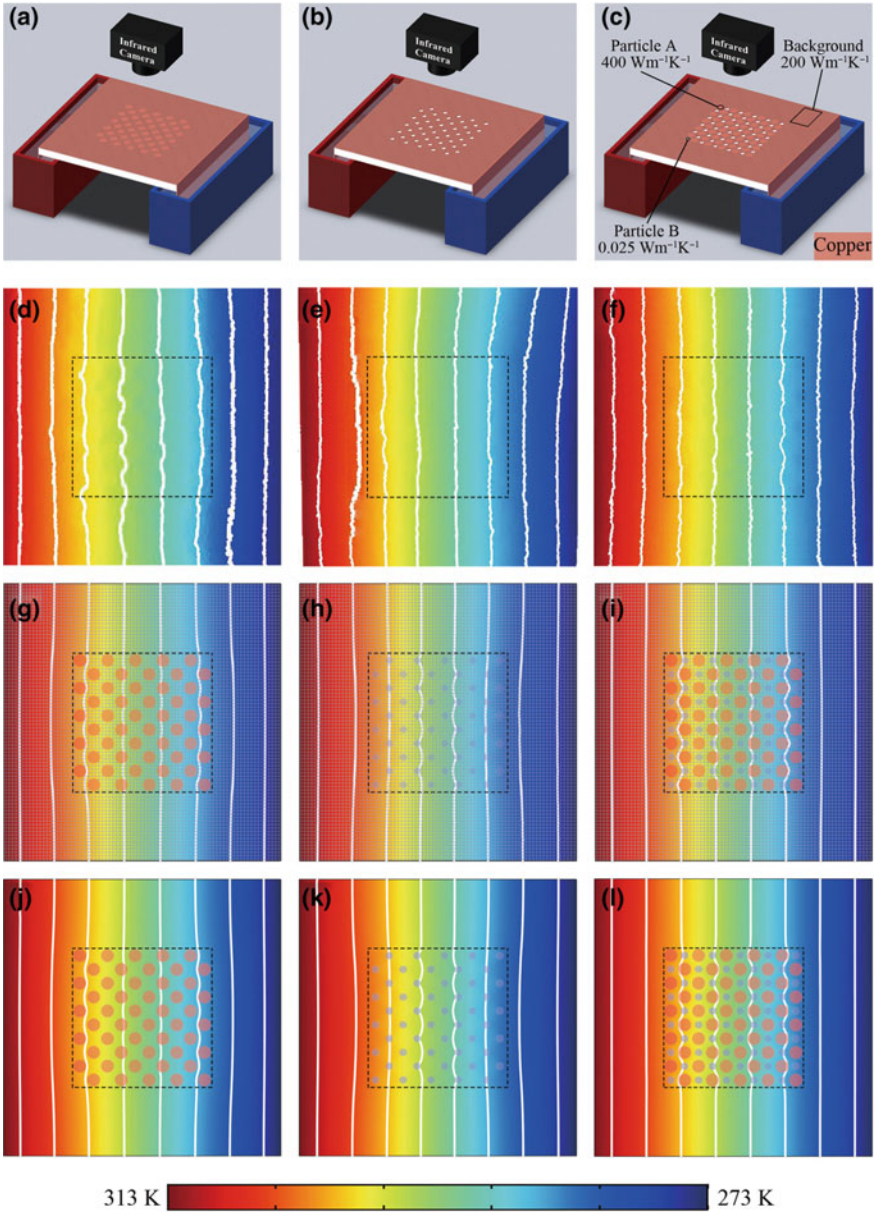

Fig. 4.4 Experimental results of many-body thermal transparency. **a**–**c** Three schematic diagrams. **d**–**f** Experimental results. **g**–**i** Simulation results. **j**–**l** Simulation results where the matrix thermal conductivity is directly set to $\kappa_m = 200\,\mathrm{W\,m^{-1}\,K^{-1}}$. The size of the bulk sample is $20 \times 20\,\mathrm{cm^2}$ and the size of the intermediate composite structure is $10 \times 10\,\mathrm{cm^2}$. The specific parameters of pellet A and pellet B are $d_0 = 1\,\mathrm{cm}$, $f_a = 0.33$, $f_b = 0.11$. Other particles have an area fraction of 0.33 and a spacing of 0.25 cm. The thermal conductivities of copper and air are $400\,\mathrm{W\,m^{-1}\,K^{-1}}$ and $0.026\,\mathrm{W\,m^{-1}\,K^{-1}}$, respectively. In the simulation results, the particles are marked with circles with 50% transparency, but the color of the particles does not represent the temperature. (from Ref. [52])

Xu et al. innovatively harnessed machine learning to achieve multi-body thermal transparency, streamlining the complexities of formula derivation and manual computation [60]. This breakthrough not only mitigates the thermal stress concentrations induced by discrepancies in thermal conductivity within devices, but also extends the concept to encompass multi-body thermal camouflage [53]. This novel extension involves crafting two distinct periodic structures wherein temperature distributions align, while differing in particle types, quantities, and dimensions, as exemplified in Fig. 4.4c and d.

Comparatively, in the realm of multi-body thermal camouflage, the particles within a solitary periodic structure do influence the matrix. These findings present a resilient strategy for effectively managing thermal dynamics within intricate multi-body structures.

4.3.1.3 Composite Structure

While the previously discussed structures are conventional models, practical applications often involve more intricate combinations. This entails a holistic arrangement of core-shell structures, periodic structures, or other variations. For instance, Xu et al. conducted an exploration into a composite structure that melds the core-shell configuration with the Janus structure—where "Janus" invokes the concept of duality from mythology. In this context, the Janus structure signifies a core comprising two entirely dissimilar materials. Accompanying theories are formulated to estimate the composite structure's equivalent thermal conductivity, yielding errors that fall within acceptable limits. This adeptly accounts for complex scenarios in practical use [61].

Basic Theroy As shown in the two-dimensional structure (Fig. 4.5), assuming that the thermal conductivity $\kappa_c(x, y)$ of the core is non-uniform and anisotropic, it can be written as

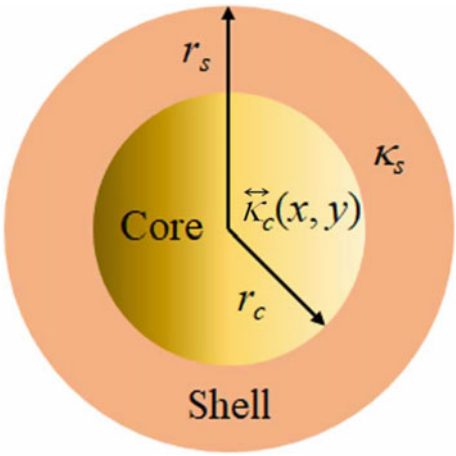

Fig. 4.5 Combination structure diagram. (from Ref. [61])

$$\boldsymbol{\kappa}_{\mathrm{c}}(x, y) = \begin{bmatrix} \kappa_{\mathrm{xx}}(x, y) & 0 \\ 0 & \kappa_{\mathrm{yy}}(x, y) \end{bmatrix} \tag{4.22}$$

Using the thermal conductivity series-parallel analysis method, it can be obtained that the effective thermal conductivity of the core-shell is only related to κ_{xx}, as

$$\kappa_{\mathrm{e}} = \kappa_{\mathrm{s}} \frac{\kappa_{\mathrm{c}} + \kappa_{\mathrm{s}} + (\kappa_{\mathrm{c}} - \kappa_{\mathrm{s}})\, f}{\kappa_{\mathrm{c}} + \kappa_{\mathrm{s}} - (\kappa_{\mathrm{c}} - \kappa_{\mathrm{s}})\, f} \tag{4.23}$$

where κ_s is the thermal conductivity of the shell and $f = r_c/r_s$ is the area fraction. In this way, we can approximate the equivalent thermal conductivity of the combined structure.

Sturctures Above, we tackled the generalized scenario involving non-uniform conditions. In real-world applications, a potent approach involves engineering a Janus kernel to manipulate the distribution of isotherms [61]. To elucidate, envision a kernel split into two distinct materials on its left and right facets, illustrated in Fig. 4.6a. Upon the imposition of an external uniform thermal field, the isotherms amass on the left side of the nucleus, causing the right-side isotherms to disperse, as depicted in Fig. 4.6b. Subsequently, by executing a 90° counterclockwise rotation of the Janus nucleus, uniform isotherm congregation within the nucleus is reinstated, as vividly portrayed in Fig. 4.6c. This ingenious maneuvering empowers precise thermal field control.

4.3.2 Nonlinearization Theory

In our preceding discourse, we delved into the linear scenario characterized by uniform distribution of matrix isotherms. Nonetheless, numerous heat transfer phenomena manifest non-linear tendencies, resulting in disparate matrix isotherm arrangements [62]. This non-linearity predominantly stems from two key scenarios: multi-field coupled heat transport and the temperature-dependent nature of thermal conductivity.

4.3.2.1 Multi-field Coupled Heat Transport

Given the inherent impracticality of exclusively relying on a singular mode of heat conduction within real-world heat transfer processes, it becomes imperative to account for the remaining two fundamental modes: heat convection and radiation. This holistic consideration inevitably introduces nonlinearity into the heat transfer process.

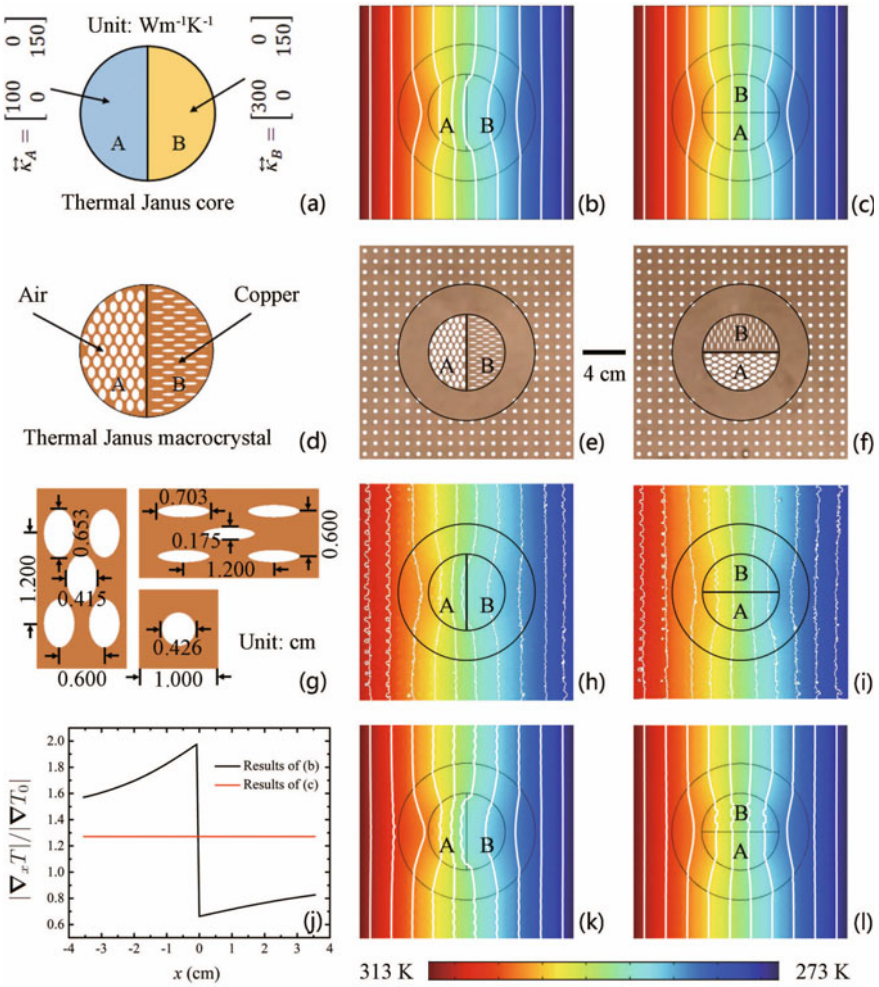

Fig. 4.6 Janus thermal metamaterial experiment results. **a** and **d** Schematic diagram of the structure of the Janus nucleus. **b** Simulation results, the isotherms are clustered on the left of the Janus nucleus and become sparse on the right. **c** Simulation results of the Janus nucleus rotated 90° counterclockwise, the isotherms are uniformly gathered in the nucleus. **e** and **f** Two sample plots. **h** and **i** the corresponding experimental results. **k** and **l** corresponding simulation results. **g** Structural dimensions. **j** Temperature gradient inside the core. The equivalent thermal conductivities of the two materials of the Janus core are $\kappa_a = \text{diag}[100, 150]$ and $\kappa_b = \text{diag}[300, 150]\,\text{W m}^{-1}\text{K}^{-1}$, respectively. The thermal conductivities of copper and air are $400\,\text{W m}^{-1}\text{K}^{-1}$ and $0.026\,\text{W m}^{-1}\text{K}^{-1}$, respectively. (from Ref. [61])

Basic Theory In the heat transfer model for porous media, three fundamental modes are considered: conduction, convection, and radiation. The corresponding energy equation is given by

$$\nabla \cdot \left(-\kappa_{\mathrm{m}} \nabla T - \phi \rho_{\mathrm{f}} C_{\mathrm{f}} T (\eta/\mu) \nabla P - \zeta_{\mathrm{m}} T^3 \nabla T\right) = 0 \tag{4.24}$$

In the porous medium, κ_m represents thermal conductivity and ϕ denotes porosity. For the fluid, ρ_f and C_f are its density and heat capacity, respectively. The medium's permeability is given by η, while μ is the fluid's dynamic viscosity. The radiation coefficient of the porous medium is ζ_m, and T and P correspond to temperature and pressure, respectively.

By employing the generalized potential definition, the given equation can be reformulated into the Laplace equation [63].

$$\nabla \cdot \left(-\kappa_{\mathrm{m}} \left(1 + \omega T f(r) + \nu T^3\right) \nabla T\right) = \nabla \cdot \left(-\kappa_{\mathrm{m}} \nabla \left(T + F(r, T) + \nu T^4/4\right)\right) = \nabla \cdot (-\kappa_{\mathrm{m}} \nabla \Phi) = 0 \tag{4.25}$$

Given that Eq. (4.24) has been converted to a linear Laplace equation, the linear theory can proceed without requiring the specific form of the generalized potential $F(r, T)$.

Sturctures Drawing from the foundational theoretical insights expounded earlier, it becomes evident that a significant share of linear heat transfer phenomena can be extended to encompass intricate multi-field coupling scenarios. On this trajectory, we have conceived a comprehensive multi-field coupled thermal transparency system that seamlessly integrates both heat conduction and radiation mechanisms [65].

The inaugural thermal transparency design involved crafting a tailored shell structure around the object, thereby guaranteeing an unaltered external temperature distribution—a focus predominantly rooted in the heat conduction transfer mode [66]. Elevating this concept to a multi-field coupling paradigm necessitates congruent consideration of not only the thermal conductivity criteria but also the radiation coefficient. This alignment ensures that both heat conduction and radiation, when scrutinized independently, achieve thermal transparency. Consequently, their combined influence collaborates to attain this state.

Simulated outcomes for circular and elliptical thermal transparency configurations are vividly depicted in Fig. 4.7a–f, unmasking undistorted isotherms gracefully pervading the matrix. This sophisticated endeavor substantiates the efficacy of the multi-field coupled approach.

Further simulations involving homogeneous matrices are presented in Fig. 4.7g–i, depicting temperature distributions mirroring those of the reference—a compelling validation of the efficacy inherent in the multi-field coupled thermal transparency [67].

In an additional light, Fig. 4.7j–l elucidate the theoretical temperature distribution derived from the overarching potential ϕ, establishing a coherent match between theoretical projections and simulated data. This alignment convincingly substantiates the validity of the generalized potential definition [68].

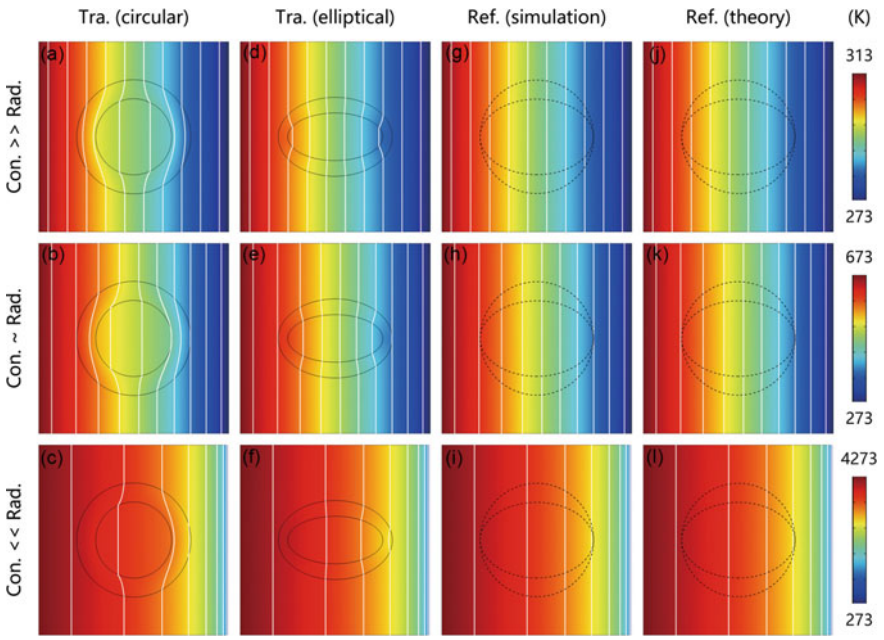

Fig. 4.7 Multi-field coupled thermotransparency simulation results. **a–c** Circular structure with dimensions $r_{c1} = r_{c2} = 2$ cm, $r_{s1} = r_{s2} = 3$ cm, material $\kappa_c = 2\,\mathrm{W\,m^{-1}\,K^{-1}}$, $\beta_c = 50\,\mathrm{m^{-1}}$, $\kappa_s = 0.62\,\mathrm{W\,m^{-1}\,K^{-1}}$, $\beta_s = 161.1\,\mathrm{m^{-1}}$. **d–f** Ellipse structure with dimensions $r_{c1} = 2.5$ cm, $r_{c2} = 1.25$ cm, $r_{s1} = 3$ cm, $r_{s2} = 2.08$ cm, material $\kappa_c = 0.5\,\mathrm{W\,m^{-1}\,K^{-1}}$, $\beta_c = 200\,\mathrm{m^{-1}}$. $\kappa_s = 1.6\,\mathrm{W\,m^{-1}\,K^{-1}}$, $\beta_s = 62\,\mathrm{m^{-1}}$. Simulation and theoretical results for a homogeneous matrix are shown in (**g**)–(**i**) and (**j**)–(**l**), respectively. (from Ref. [64])

In scenarios where heat conduction significantly outweighs radiation, the isotherms exhibit uniformity, illustrated in the initial segment of Fig. 4.7. Conversely, when radiation takes precedence over conduction, the isotherms deviate from uniformity, predominantly shifting to the right. This differential behavior vividly epitomizes the intrinsic nonlinearity, as aptly illustrated in the latter segment of Fig. 4.7.

Transcending the confines of multi-field coupled thermal transparency [69], our exploration extends to the intricate realm of a multi-field coupled thermal cloaking detector [63, 70]. This holistic endeavor encompasses scenarios of coupled heat transfer wherein conduction, convection, and radiation seamlessly interplay. Moreover, the thermal domain harmoniously converges with the electric field through the thermoelectric effect [71].

Essentially, the bedrock tenet underlying multi-field coupling can be succinctly encapsulated as follows: the progression from a solitary field to a multifaceted array is an inherent evolution. To materialize a distinct function within a multi-field coupling milieu, it becomes imperative to meticulously ensure its viability within each individual field. This pursuit is fundamentally anchored in upholding the consistent definition of the generalized potential ϕ across diverse regions [72].

4.3.2.2 Temperature-Dependent Thermal Conductivity

Throughout the preceding discourse, we operated under the assumption of temperature-invariant thermal conductivity [73]. However, a multitude of real-world materials, particularly phase change materials, prominently display a discernible temperature dependence in their thermal conductivity [38]. Within the realm of research, it becomes an imperative task to construct a comprehensive theoretical framework that not only acknowledges but adeptly accommodates the ensuing nonlinearity stemming from temperature-dependent thermal conductivity [74].

Basic Theory We consider a temperature-dependent thermal conductivity $\kappa(T)$, which can usually be expanded as

$$\kappa(T) = \sum_{i=1}^{n} u_i T^{v_i} \tag{4.26}$$

Both the complexities arising from multi-field coupled heat transport and the intricacies tied to temperature-dependent thermal conductivity can be effectively linearized through the unifying concept of generalized potentials, contingent upon upholding consistent definitions across diverse regions. Particularly noteworthy is the case of the Rossland diffusion approximation employed for thermal radiation. In this context, radiative heat flow, dictated by the cube of temperature, ushers in a notable degree of nonlinearity. This phenomenon can be ascribed to either the interplay of multi-field coupling or the temperature dependency intrinsic to equivalent thermal conductivity.

Sturctures In juxtaposition to the singular function delineated, Xu et al. pioneered the conception of a functionally switchable thermal metamaterial harnessing the potential of nonlinearity [75]. This innovative proposition was subsequently substantiated through meticulous finite element simulations. Notably, researchers have endeavored to engineer macroscopic thermal bistable or multistable systems by capitalizing on nonlinear effects. Moreover, a segment of the scientific community has meticulously computed the equivalent nonlinear thermal conductivity inherent to periodic structures.

In its essence, the integration of nonlinearity injects a responsiveness within devices, enabling them to aptly react to external fields, encompassing variations in temperature [76]. This pivotal shift lays the groundwork for the creation of multifunctional and intelligent thermal metamaterials, ushering in a realm of promising design possibilities.

4.3.3 Heat Source Theory

The aforementioned discourse pertains to passive heat transfer. However, in numerous practical scenarios, external energy input can enhance thermal regulation flexibility and introduce novel functionalities [77].

4.3.3.1 Thermocouple Dipole Structure

A thermal dipole, analogous to an electric dipole, comprises a hot and a cold source. Given the resemblance between the thermal fields of thermal dipoles and particles, regulation of the thermal field can be facilitated through thermal dipoles.

Thermal dipoles primarily serve to neutralize particle-induced thermal field disturbances, facilitating thermal cloaking. As depicted in Fig. 4.8a and d, the left and right boundaries are maintained at 323K and 283K, respectively, with the top and bottom boundaries being adiabatic. A particle with lower thermal conductivity than its matrix causes isotherm contraction, evident in Fig. 4.8d. Such isotherm distortions can be discerned via infrared detection. Subsequent simulations, shown in Fig. 4.8b and e, detail the temperature distribution influenced by thermal dipoles, with adiabatic conditions set for the system's outer boundaries and a reference temperature, Tr = 303 K, at $\theta = \pm \mathrm{pi}/2$. Merging the configurations from Fig. 4.8a and b results in the structure in Fig. 4.8c. With the intervention of thermal dipoles, the perturbed temperature profile is rectified to its initial state, as illustrated in Fig. 4.8f. Consequently, infrared detection remains oblivious to particle presence, achieving thermal stealth.

Thermal cloaking via thermal dipoles offers two distinct benefits: controllable cloaking switchability and feasibility within matrices of exceptionally high thermal conductivity. Building on this concept, Xu et al. achieved dual-function cloaking for both thermal and electric fields [67], thereby expanding the versatility of thermal metamaterials.

4.3.3.2 Apparent Negative Thermal Conductivity

Given the stipulations of the second law of thermodynamics, negative thermal conductivity is deemed unphysical, implying a spontaneous heat transfer from cooler to warmer regions. Yet, with external energy input, apparent negative thermal conductivity becomes attainable, paving the way for innovative thermal phenomena [79].

In both two-dimensional and three-dimensional contexts, the equivalent thermal conductivity expression incorporates a tangent function [80]. This suggests that with variations in the core-shell structure's size, the equivalent thermal conductivity undergoes periodic shifts.

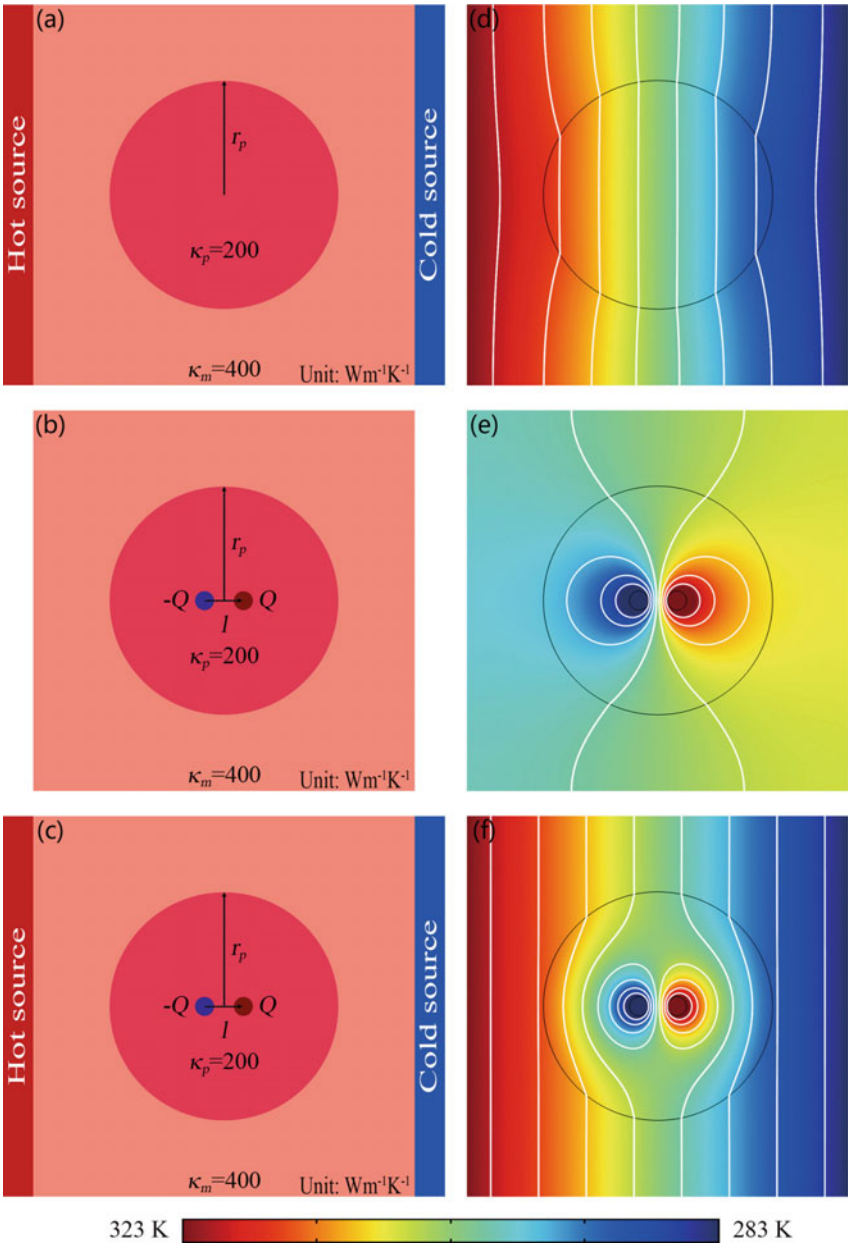

Fig. 4.8 Simulation results of thermal stealth based on thermal dipole structure. **a** and **d** apply a uniform external field alone. **b** and **e** thermodipoles placed individually. **c** and **f** Simultaneous application of a uniform external field and placement of a thermal dipole. The simulated dimensions are 20×20 cm^2, $r_p = 6$ cm, $l = 2$ cm. It can be obtained that the corresponding thermal dipole moment is 452.4 W m, and the power is $Q = 22620$ W. The particle and matrix thermal conductivity are 200 and 400 W m^{-1} K^{-1}. The thermal dipole cold and heat source has a radius of 0.5 cm. Temperatures above 323 K are displayed as 323 K and temperatures below 283 K are displayed as 283 K. (from Ref. [78])

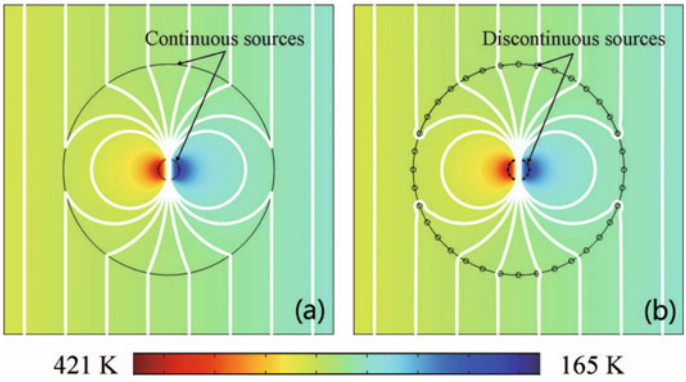

Fig. 4.9 A method for achieving apparent negative thermal conductivity. **a** A continuous heat source is added on the shell boundary. **b** A discrete heat source is added on the shell boundary. The thermal conductivity of the shell is $\kappa_s = 1\,\mathrm{W\,m^{-1}K^{-1}}$. The temperature distribution of the continuous heat source is $T = -81.9x/r_c^2; s + 293\,\mathrm{K}$, where $r_c = 0.64\,\mathrm{cm}$, $r_s = 6.4\,\mathrm{cm}$. There are 12 heat sources with a radius of 0.05 cm on the inner boundary, and 36 heat sources with a radius of 0.15 cm on the outer boundary. The temperature of each discrete heat source is consistent with the temperature in (**a**). (from Ref. [80])

Leveraging this finding, researchers devised a transformative structure. With a core-shell design, even a minuscule core proportion can extend its properties throughout the shell, optimizing the utilization of pivotal materials.

While nature doesn't offer negative thermal conductivity, it can be emulated using source-containing active materials. Consider the metaphorical "touch stone into gold" for simulation [79]. We assign the shell a positive thermal conductivity distinct from the core's. To mirror this effect, we introduce either a continuous or discrete heat source at the shell's boundary, as depicted in Fig. 4.9. Pertinent literature has showcased a device achieving a discrete heat source, hinting at the potential realization of apparent negative thermal conductivity [77].

Apparent negative thermal conductivity starkly contrasts with its positive counterpart. This divergence stems from the heat conduction equation's general solution undergoing a discontinuous shift as components of the thermal conductivity tensor cross a critical threshold. This shift mirrors the topological transition in fluctuating systems when a permittivity tensor component transitions from positive to negative. Beyond thermal conductivity, analogous phenomena can be explored in other diffusive systems, leveraging negative magnetic permeability or negative electrical conductivity.

4.3.3.3 Thermal Zero Refractive Index

The concept of a thermal zero refractive index implies infinite thermal conductivity. Current research achieves this through fluid rotation, necessitating external actua-

tion. Researchers have introduced an alternative approach: the constant-temperature boundary condition. This condition showcases an equivalence to infinite thermal conductivity in terms of temperature distribution, though not precisely for heat flow distribution. In thermal cloak design, the focus is predominantly on temperature distribution rather than heat flow. Hence, this method, which equivalently attains infinite thermal conductivity, is viable for crafting thermal invisibility cloaks.

The strength of this approach lies in its simplicity, eliminating the need for intricate temperature management while enabling thermal cloaking in high-conductivity matrices. Furthermore, to flexibly modulate thermal conductivity between zero and infinity, researchers introduced a method involving the rotation of multi-layered structures through external forces, broadening the potential spectrum of equivalent thermal conductivity.

4.4 Conclusion

In summary, this chapter offers a concise examination of heat conduction complexities, focusing on transition heat and effective medium theories. We addressed the foundational Fourier's law and clarified the invariance of its equations under coordinate transformations, introducing a method to manage temperature and heat flux dynamics.

The practicality of thermal transformation was exemplified by the design and realization of a thermal cloak. Theoretically projected parameters often appear inhomogeneous and anisotropic, creating synthesis challenges. A shift towards the thermally effective medium theory offers a solution.

We further provided a structured analysis of the effective medium theory, leading to the development of structures based on linear, nonlinear, and heat source theories. Applications of thermal cloaks, metamaterials, and advancements in numerical and machine learning methods in thermal conduction were explored.

Collectively, this chapter underscores advancements in thermal conduction, emphasizing the potential of transformation thermotics, effective medium theory, and metamaterials. The emergence of thermal cloaking and multi-body thermal transparency, combined with numerical and machine learning potentials, heralds a promising trajectory for thermal conduction research and innovation.

References

1. Wang, J., Dai, G.L., Huang, J.P.: Thermal metamaterial: fundamental, application, and outlook. iScience **23**, 101637 (2020)
2. Xu, L.J., Dai, G.L., Huang, J.P.: Transformation multithermotics: controlling radiation and conduction simultaneously. Phys. Rev. Appl. **13**, 024063 (2020)
3. Xu, L.J., Yang, S., Dai, G.L., Huang, J.P.: Transformation omnithermotics: simultaneous manipulation of three basic modes of heat transfer. ES Energy Environ. **7**, 65–70 (2020)

4. Wood, B., Pendry, J.B.: Metamaterials at zero frequency. J. Phys.: Condens. Matter **19**, 076208 (2007)
5. Gömöry, F., Solovyov, M., Šouc, J., Navau, C., Prat-Camps, J., Sanchez, A.: Experimental realization of a magnetic cloak. Science **335**, 1466–1468 (2012)
6. Zhang, R.-Y., Zhao, Q., Ge, M.-L.: The effect of electrostatic shielding using invisibility cloak. AIP Adv. **1**, 042126 (2011)
7. Narayana, S., Sato, Y.: DC magnetic cloak. Adv. Mater. **24**, 71–74 (2012)
8. Yang, F., Mei, Z.L., Jin, T.Y., Cui, T.J.: DC electric invisibility cloak. Phys. Rev. Lett. **109**, 053902 (2012)
9. Guenneau, S., Amra, C., Veynante, D.: Transformation thermodynamics: cloaking and concentrating heat flux. Opt. Express **20**, 8207–8218 (2012)
10. Fan, C.Z., Gao, Y., Huang, J.P.: Shaped graded materials with an apparent negative thermal conductivity. Appl. Phys. Lett. **92**, 251907 (2008)
11. Zhang, R.-Y., Weng, C.-N., Chen, J.-S.: Cloak for curvilinearly anisotropic media in conduction. Appl. Phys. Lett. **93**, 114103 (2008)
12. Guenneau, S., Amra, C., Veynante, D.: Transformation thermodynamics: cloaking and concentrating heat flux. Opt. Express **20**, 8207-C8218 (2012)
13. Schittny, R., Kadic, M., Guenneau, S., Wegener, M.: Experiments on transformation thermodynamics: molding the flow of heat. Phys. Rev. Lett. **110**, 195901 (2013)
14. Xu, L.J., Yang, S., Huang, J.P.: Passive metashells with adaptive thermal conductivities: chameleonlike behavior and its origin. Phys. Rev. Appl. **11**, 054071 (2019)
15. Yang, F.B., Tian, B.Y., Xu, L.J., Huang, J.P.: Experimental demonstration of thermal chameleonlike rotators with transformation-invariant metamaterials. Phys. Rev. Appl. **14**, 054024 (2020)
16. Barati Sedeh, H., Fakheri, M.H., Abdolali, A., Sun, F., Ma, Y.: Feasible thermodynamics devices enabled by thermal-null medium. Phys. Rev. Appl. **14**, 064034 (2020)
17. Kim, S.E., et al.: Extremely anisotropic van der Waals thermal conductors. Nature **597**, 660–665 (2021)
18. Moccia, M., Castaldi, G., Savo, S., Sato, Y., Galdi, V.: Independent manipulation of heat and electrical current via bifunctional metamaterials. Phys. Rev. X **4**, 021025 (2014)
19. Li, J.Y., Gao, Y., Huang, J.P.: A bifunctional cloak using transformation media. J. Appl. Phys. **108**, 074504 (2010)
20. Ma, Y., Liu, Y., Raza, M., Wang, Y., He, S.: Experimental demonstration of a multiphysics cloak: manipulating heat flux and electric current simultaneously. Phys. Rev. Lett. **113**, 205501 (2014)
21. Stedman, T., Woods, L.M.: Cloaking of thermoelectric transport. Sci. Rep. **7**, 6988 (2017)
22. Yeung, W.-S., Mai, V.-P., Yang, R.-J.: Cloaking: controlling thermal and hydrodynamic fields simultaneously. Phys. Rev. Appl. **13**, 064030 (2020)
23. Tian, Y.-Z., Wang, Y.-F., Huang, G.-Y., Laude, V., Wang, Y.-S.: Dual-function thermoelastic cloak based on coordinate transformation theory. Int. J. Heat Mass Transf. **195**, 123128 (2022)
24. Xu, H., Shi, X., Gao, F., Sun, H., Zhang, B.: Ultrathin three-dimensional thermal cloak. Phys. Rev. Lett. **112**, 054301 (2014)
25. Han, T., et al.: Experimental demonstration of a bilayer thermal cloak. Phys. Rev. Lett. **112**, 054302 (2014)
26. Han, T.C., Bai, X., Thong, J.T., Li. B., Qiu, C.W.: Full control and manipulation of heat signatures: cloaking, camouflage and thermal metamaterials. Adv. Mater. **26**, 1731–1734 (2014)
27. Farhat, M., et al.: Thermal invisibility based on scattering cancellation and mantle cloaking. Sci. Rep. **5**, 9876 (2015)
28. Kim, J.C., et al.: Recent advances in thermal metamaterials and their future applications for electronics packaging. J. Electron. Packag. **143**, 010801 (2021)
29. Dede, E.M., Zhou, F., Schmalenberg, P., Nomura, T.: Thermal metamaterials for heat flow control in electronics. J. Electron. Packag. **140**, 010801 (2018)
30. Loke, D., Skelton, J.M., Chong, T.C., Elliott, S.R.: Design of a nanoscale, CMOS-integrable, thermal-guiding structure for Boolean-logic and neuromorphic computation. ACS Appl. Mater. Interfaces **8**, 34530–34536 (2016)

31. Hu, R., et al.: Binary thermal encoding by energy shielding and harvesting units. Phys. Rev. Appl. **10**, 054032 (2018)
32. Luo, H., et al.: Outdoor personal thermal management with simultaneous electricity generation. Nano Lett. **21**, 3879–3886 (2021)
33. Xu, L.J., Xu, G.Q., Huang, J.P., Qiu, C.-W.: Diffusive Fizeau drag in spatiotemporal thermal metamaterials. Phys. Rev. Lett. **128**, 145901 (2022)
34. Dede, E.M., Nomura, T., Lee, J.: Thermal-composite design optimization for heat flux shielding, focusing, and reversal. Struct. Multidiscipl. Optim. **49**, 59–68 (2014)
35. Fujii, G., Akimoto, Y., Takahashi, M.: Exploring optimal topology of thermal cloaks by CMA-ES. Appl. Phys. Lett. **112**, 061108 (2018)
36. Sha, W., et al.: Robustly printable freeform thermal metamaterials. Nat. Commun. **12**, 7228 (2021)
37. Shen, X.Y., Jiang, C.R., Li, Y., Huang, J.P.: Thermal metamaterial for convergent transfer of conductive heat with high efficiency. Appl. Phys. Lett. **109**, 201906 (2016)
38. Jin, P., Xu, L.J., Jiang, T., Zhang, L., Huang, J.P.: Making thermal sensors accurate and invisible with an anisotropic monolayer scheme. Int. J. Heat Mass Transf. **163**, 120437 (2020)
39. Jin, P., Yang, S., Xu, L.J., Dai, G.L., Huang, J.P., Ouyang, X.P.: Particle swarm optimization for realizing bilayer thermal sensors with bulk isotropic materials. Int. J. Heat Mass Transf. **172**, 121177 (2021)
40. Ma, W., Cheng, F., Liu, Y.: Deep-learning-enabled on-demand design of chiral metamaterials. ACS Nano **12**, 6326–6334 (2018)
41. Huang, J.P.: Theoretical Thermotics: Transformation Thermotics and Extended Theories for Thermal Metamaterials. Springer, Singapore (2020)
42. Xu, L.J., Wang, J., Dai, G.L., Yang, S., Yang, F.B., Wang, G., Huang, J.P.: Geometric phase, effective conductivity enhancement, and invisibility cloak in thermal convection-conduction. Int. J. Heat Mass Transf. **165**, 120659 (2021)
43. Huang, J.P., Karttunen, M., Yu, K.W., Dong, L.: Dielectrophoresis of charged colloidal suspensions. Phys. Rev. E **67**, 021403 (2003)
44. Xu, L.J., Huang, J.P., Jiang, T., Zhang, L., Huang, J.P.: Thermally invisible sensors. Europhys. Lett. **132**, 14002 (2020)
45. Dong, L., Huang, J.P., Yu, K.W., Gu, G.Q.: Dielectric response of graded spherical particles of anisotropic materials. J. Appl. Phys. **95**, 621–624 (2004)
46. Gao, Y., Jian, Y.C., Zhang, L.F., Huang, J.P.: Magnetophoresis of nonmagnetic particles in ferrofluids. J. Phys. Chem. C **111**, 10785–10791 (2007)
47. Milton, G.W.: The Theory of Composites. Cambridge University Press, Cambridge (2002)
48. Chen, H.C., Sun, F., Wang, B., Liu, Y.C., Chen, Z.H., Yang, Y.B.: Thermal camouflages based on 3D thermal-null medium. Int. J. Therm. Sci. **176**, 107506 (2022)
49. Yang, S., Xu, L.J., Wang, R.Z., Huang, J.P.: Full control of heat transfer in single-particle structural materials. Appl. Phys. Lett. **111**, 121908 (2017)
50. Dai, G.L., Huang, J.P.: A transient regime for transforming thermal convection: Cloaking, concentrating and rotating creeping flow and heat flux. J. Appl. Phys. **124**, 235103 (2018)
51. Yang, T., et al.: Invisible sensors: simultaneous sensing and camouflaging in multiphysical fields. Adv. Mater. **27**, 7752–7758 (2015)
52. Xu, L.J., Yang, S., Huang, J.P.: Thermal transparency induced by periodic interparticle interaction. Phys. Rev. Appl. **11**, 034056 (2019)
53. Xu, L.J., Yang, S., Huang, J.P.: Thermal illusion with the concept of equivalent thermal dipole. Eur. Phys. J. B **92**, 264 (2019)
54. Maxwell-Garnett, J.C.: Colours in metal glasses and in metallic films. Philos. Trans. R. Soc. Lond. **203**, 385–420 (1904)
55. Li, X.H., Yang, G., An, K.N., Huang, J.P.: Human behavioral regularity, fractional Brownian motion, and exotic phase transition. Phys. Lett. A **380**, 2912–2919 (2016)
56. Bruggeman, D.A.G.: Calculation of various physics constants in heterogeneous substances: dielectricity constants and conductivity of mixed bodies from isotropic substances. Ann. Phys. **24**, 636–664 (1935)

57. He, X., Wu, L.Z.: Thermal transparency with the concept of neutral inclusion. Phys. Rev. E **88**, 033201 (2013)
58. Liu, L., Wei, J.R., Zhang, H.S., Xin, J.H., Huang, J.P.: A statistical physics view of pitch fluctuations in the classical music from Bach to Chopin: evidence for scaling. PLoS ONE **8**, e58710 (2013)
59. Ye, C., Huang, J.P.: Non-classical oscillator model for persistent fluctuations in stock markets. Phys. A **387**, 1255–1263 (2008)
60. Liu, B., Xu, L.J., Huang, J.P.: Reinforcement learning approach to thermal transparency with particles in periodic lattices. J. Appl. Phys. **130**, 045103 (2021)
61. Xu, L.J., Yang, S., Huang, J.P.: Thermal theory for heterogeneously architected structure: fundamentals and application. Phys. Rev. E **98**, 052128 (2018)
62. Dai, G.L.: Designing nonlinear thermal devices and metamaterials under the Fourier law: a route to nonlinear thermotics. Front. Phys. **16**, 53301 (2021)
63. Yang, S., Xu, L.J., Dai, G.L., Huang, J.P.: Omnithermal metamaterials switchable between transparency and cloaking. J. Appl. Phys. **128**, 095102 (2020)
64. Xu, L.J., Huang, J.P.: Metamaterials for manipulating thermal radiation: transparency, cloak, and expander. Phys. Rev. Appl. **12**, 044048 (2019)
65. Xu, L.J., Huang, J.P.: Active thermal wave cloak. Chin. Phys. Lett. **37**, 120501 (2020)
66. Wang, R.Z., Xu, L.J., Huang, J.P.: Thermal imitators with single directional invisibility. J. Appl. Phys. **122**, 215107 (2017)
67. Xu, L.J., Zhao, X.T., Zhang, Y.P., Huang, J.P.: Tailoring dipole effects for achieving thermal and electrical invisibility simultaneously. Eur. Phys. J. B **93**, 101 (2020)
68. Meng, X.W., Huang, J.P.: Control water molecules across carbon-based nanochannels. Chin. Phys. B **27**, 013101 (2018)
69. Wang, C.Q., Xu, L.J., Jiang, T., Zhang, L., Huang, J.P.: Multithermally invisible cloaks and sensors with complex shapes. Europhys. Lett. **133**, 20009 (2021)
70. Xu, L.J., Huang, J.P.: Chameleonlike metashells in microfluidics: a passive approach to adaptive responses. Sci. China-Phys. Mech. Astron. **63**, 228711 (2020)
71. Shi, W., Stedman, T., Woods, L.M.: Thermoelectric transport control with metamaterial composites. J. Appl. Phys. **128**, 025104 (2020)
72. Fan, C.Z., Wang, G., Huang, J.P.: Magneto-controllable photonic crystals based on colloidal ferrofluids. J. Appl. Phys. **103**, 094107 (2008)
73. Zhang, Z.R., Huang, J.P.: Transformation plasma physics. Chin. Phys. Lett. **39**, 075201 (2022)
74. Xu, L.J., Huang, J.P.: Negative thermal transport in conduction and advection. Chin. Phys. Lett. (Express Lett.) **37**, 080502 (2020)
75. Su, C., Xu, L.J., Huang, J.P.: Nonlinear thermal conductivities of core-shell metamaterials: rigorous theory and intelligent application. EPL **130**, 34001 (2020)
76. Kang, S., Cha, J., Seo, K., Kim, S., Cha, Y., Lee, H., Park, J., Choi, W.: Temperatureresponsive thermal metamaterials enabled by modular design of thermally tunable unit cells. Int. J. Heat Mass Transf. **130**, 469–482 (2019)
77. Nguyen, D.M., Xu, H.Y., Zhang, Y.M., Zhang, B.L.: Active thermal cloak. Appl. Phys. Lett. **107**, 121901 (2015)
78. Xu, L.J., Yang, S., Huang, J.P.: Dipole-assisted thermotics: experimental demonstration of dipole-driven thermal invisibility. Phys. Rev. E **100**, 062108 (2019)
79. Shen, X.Y., Huang, J.P.: Thermally hiding an object inside a cloak with feeling. Int. J. Heat Mass Transf. **78**, 1–6 (2014)
80. Xu, L.J., Yang, S., Huang, J.P.: Designing the effective thermal conductivity of materials of core-shell structure: theory and simulation. Phys. Rev. E **99**, 022107 (2019)

Chapter 5
Unveiling the Thermal Cloak: A Journey from Theoretical Foundations to Cutting-Edge Applications

Yuhong Zhou and Zeren Zhang

5.1 Opening Remarks

The concept of invisibility, historically shrouded in tales and legend, found its scientific grounding with the publication of two seminal papers in 2006 [1, 2]. At the heart of this scientific renaissance was Professor Pendry's pioneering use of the coordinate transformation theory. This theoretical leap sparked an explosion of research in metamaterials, diversifying into myriad sectors such as optics [3], acoustics [4], thermodynamics [5], and mass transport [6]. Particularly in thermodynamics, the revolutionary idea of thermal invisibility surfaced in 2008, trailblazed by Fan and colleagues [7]. Their work underscored that the heat conduction equation also retains transformation invariance. This insight extended the applicability of the coordinate transformation theory to heat transfer, marking the dawn of thermal metamaterials.

In traditional terms, thermal cloak, when related to heat conduction, can be characterized as such: an object, endowed with distinctive thermal characteristics, influences the background's temperature distribution due to its varied thermal conductivities. The quintessential role of a thermal invisibility apparatus is to counteract this influence, ensuring that the ambient temperature persists unaltered, as if the intervening entity were absent. The overarching aim is to shield the presence of the intruding object from an observer who relies solely on the temperature gradient, thereby realizing thermal invisibility. Broadly, the assessment of thermal invisibility pivots on two foundational tenets: firstly, the ambient temperature remains undisturbed by the intrusive object; and secondly, the object's temperature stands autonomously from the surrounding temperature landscape.

Y. Zhou (✉) · Z. Zhang
Department of Physics, Key Laboratory of Micro and Nano Photonic Structures (MOE), and State Key Laboratory of Surface Physics, Fudan University, Shanghai 200438, China
e-mail: 20210190004@fudan.edu.cn

F.-B. Yang and J.-P. Huang, *Diffusionics*,
https://doi.org/10.1007/978-981-97-0487-3_5

The advent of thermal metamaterials [8–12] has laid a theoretical groundwork for crafting thermal invisibility devices. As previously highlighted, the transformation theory [13–16] served as an initial blueprint for devising thermal cloaks. Nevertheless, intrinsic attributes of this theory lead to material anisotropy and inhomogeneity, posing hurdles for practical implementation. In response to this challenge, scholars integrated the scattering cancellation theory [17, 18] into heat conduction, yielding a thermal cloak design that leans on bulk materials alone. Furthermore, to circumvent the constraints of standardized shapes in invisibility apparatus conceptualized via analytical approaches, the scientific community has embraced topology optimization [19–21]. This inclusion paves the way for a richer variety of invisibility device designs.

In addressing engineering challenges, various factors come into play. For instance, the enclosed design of thermal cloaks based on the discussed theories can lead to difficulties in manufacturing. To counteract this, the "carpet cloak" concept emerged [22–25], tailored to conceal objects on insulating surfaces. Moreover, the implications of interface thermal resistance (ITR) [26, 27] in tangible settings are critical. This resistance is prevalent not only between the thermal invisibility device and its surroundings but also notably inside the device, particularly in layered configurations. To navigate this, the notion of an ITR-free cloak was introduced [28], bypassing ITR challenges. In recent developments, the concept of thermal domes [29] has been proposed for engineering applications, addressing the challenge that traditional thermal cloaks do not have the capability to protect objects with self-generated heat. The field has also witnessed the deployment of sophisticated methods to boost the versatility and intelligence of thermal invisibility. This encompasses leveraging adjustable thermal convection to achieve optimal thermal conductivity [30, 31] and integrating machine learning for smarter operations [32, 33]. In essence, the evolution of thermal invisibility has shifted from two-dimensional designs to three-dimensional constructs, and from complex, hard-to-fabricate materials to more accessible and simpler alternatives, positioning it aptly for real-world integration.

This chapter delves into thermal invisibility technology from both theoretical methods and advanced techniques perspectives. Section 5.2 discusses coordinate transformation techniques, scattering cancellation, and topology optimization. In Sect. 5.3, we introduce three typical devices in the development history of thermal invisibility: carpet cloaks, ITR-free thermal cloaks, and thermal domes. These technologies have played a significant role in bringing thermal invisibility into practical applications. Lastly, we explore potential applications in this field and provide an outlook on its future developments.

5.2 Foundations of Theory: The Pillars of Thermal Invisibility

5.2.1 Transformation Theory: The Key to Controlling Heat Flow

Designing thermal metamaterials using transformation theory is essentially an inverse problem, much like optical transformation theory. The heat conduction equation informs us about how heat flows under a specific thermal conductivity coefficient κ. However, with transformation theory, we obtain a specific thermal conductivity coefficient based on a predetermined heat flow direction. For this process to work, there is a prerequisite: the heat conduction equation must remain unchanged under coordinate transformations so that solving the inverse problem can proceed smoothly. In general, the application of this theory involves the following steps:

Step 1: Checking if heat conduction's governing equations remain consistent under coordinate transformations.

Step 2: Crafting transformations to steer the heat flow's desired direction in the transformed virtual space.

Step 3: Applying the transformation matrix to the thermal conductivity, substituting thermal conductivity's anisotropy for spatial non-uniformity, hence reproducing the same heat flow direction in the actual and virtual spaces.

This process is depicted in Fig. 5.1. Researchers have already demonstrated that the heat conduction equation remains invariance under coordinate transformations, whether in steady state or transient conditions [7, 34, 35]. Generally, the transient heat conduction is described by the Fourier equation:

$$\rho C \frac{\partial T}{\partial t} - \nabla \cdot (\kappa \cdot \nabla T) = 0, \tag{5.1}$$

where t is time, ρ, C, T and κ are the density, heat capacity, temperature and thermal conductivity. Post-coordinate transformation, this equation evolves into:

$$\rho' C' \frac{\partial T}{\partial t} - \nabla' \cdot (\kappa' \cdot \nabla' T) = 0. \tag{5.2}$$

$\rho' C' = \rho C / \det J$, $\kappa' = J \kappa J^{\mathrm{T}} / \det J$, [38]. J is the Jacobian transformation matrix. Therefore, achieving the desired functionalities can be accomplished by manipulating either the thermal conductivity κ or the ρC. For example, when designing a spherical thermal cloak, one can utilize the following transformation: $r = R_1 + (R_2 - R_1) r'/R_2$. In this case, a point in the original space is stretched into a circular region with a radius of R_1. Within this region, heat flow will not penetrate, and its interior won't affect the external background, thereby achieving the invisibility effect. Finally, we need to apply the transformation matrix to the material coefficients within the shell region ($R_1 < r < R_2$) to replace the spatial non-uniformity: $\kappa_{rr}/\kappa_0 = \kappa_0/\kappa_{\theta\theta} =$

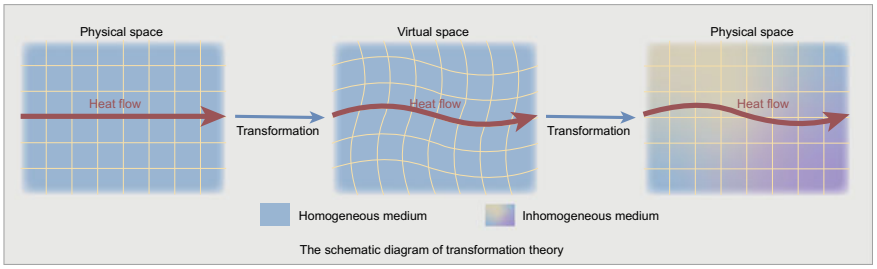

Fig. 5.1 Transformation theory schematic

$(r - R_1)/r$, $\kappa_{r\theta} = \kappa_{\theta r} = 0$ and $\rho c_p = \rho_0 c_{p0}[R_2/(R_2 - R_1)]^2(r - R_1)/r$ [35]. κ_0, ρ_0, c_{p0} are the thermal conductivity, density and specific heat capacity of the background, respectively.

Fan et al. were at the forefront of utilizing this approach to design thermal cloaks [7]. Chen et al. subsequently broadened the scope of transformation thermotics to accommodate anisotropic backgrounds, moving beyond merely isotropic ones, signifying preliminary advancements in thermal invisibility [34]. However, the central challenge lies in achieving anisotropic thermal conductivity in practical applications.

Employing the effective medium theory, Narayana and his team, in 2012, showcased an experimental model of thermal invisibility using a stratified material composition [36]. This technique entailed alternating between two isotropic substances with distinct thermal conductivities to realize anisotropic thermal conductivity.

Guenneau et al. explored the realm of transient thermal invisibility, unveiling the transformation principles associated with density and heat capacity during such operations [35]. Schittny et al. engineered a microstructured thermal cloak that redirects heat flow around an encased object within a metal plate, providing transient thermal shielding [37]. Their contributions cemented the foundational principles of the transformation theory for heat conduction, furthering the development of thermal metamaterials.

The subsequent research further enriched the field. For instance, Li and his team introduced nonlinear elements into the fundamental equations, allowing the thermal conductivity to vary with temperature [39, 40]. This innovation established the foundation for adaptive thermal invisibility solutions and deepened our understanding of nonlinear thermal phenomena and intelligent thermal cloaks.

5.2.2 Scattering Cancellation: A Streamlined Approach for Implementation

Thermal cloaks, developed using transformation theory, typically require materials characterized by anisotropic, inhomogeneous, and singular thermal conductivi-

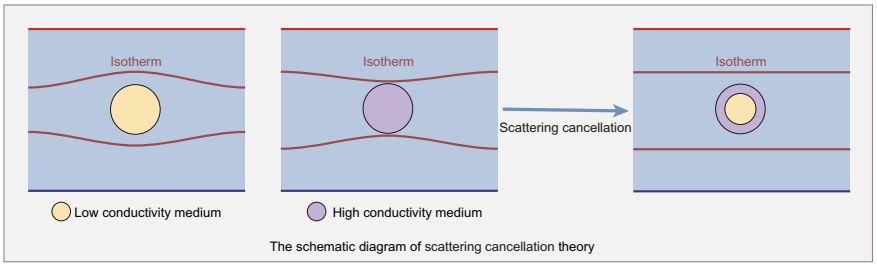

Fig. 5.2 A schematic diagram of the scattering cancellation theory

ties, complicating their production. A significant breakthrough occurred when two research teams [17, 18], inspired by prior studies on scattering cancellation methods for static magnetic field shielding [41], incorporated this idea into heat conduction. Consequently, they crafted bilayer thermal cloaks using common materials.

The core principle of scattering cancellation warrants elucidation. Scattering phenomena are prevalent across many domains, particularly in electromagnetics and acoustics. In these contexts, waves change direction when meeting varied media or obstacles. Regarding heat conduction, materials with distinct thermal conductivities from their environment can cause deviations in heat flow. Observing through isotherm lines, one can discern these perturbations: isotherms are drawn towards areas with higher thermal conductivity and repelled by those with lower. As illustrated in Fig. 5.2, strategic placement of these materials facilitates a state of thermal invisibility, mimicking an environment undisturbed by thermal fluctuations.

To craft a thermal cloak using the scattering cancellation approach, one must:

Step 1: Establish the governing equation for heat conduction.

Step 2: Derive the general solution for temperature distribution.

Step 3: Identify the coefficients of this solution, based on boundary conditions, ensuring the external thermal field remains unaffected. This also helps deduce cloak parameters like its shape and thermal conductivities.

Using a 3D bilayer cloak as an illustration, in the absence of heat sources, the heat conduction equation transforms into Laplace's equation:

$$\nabla(-\kappa \nabla T) = 0. \tag{5.3}$$

The temperature within various regions can be generalized as:

$$T_i = \sum_{m=1}^{\infty} [\mathrm{A}_m^i r^m + \mathrm{B}_m^i r^{-m-1}] P_m(\cos\theta), \tag{5.4}$$

where A_m^i and B_m^i (i=1, 2, 3, 4) are constants to be determined by the boundary conditions and T_i denotes the temperature in different regions. The boundary conditions primarily encompass four aspects: Finite temperature at r→0, uniform external

temperature field, temperature equality at interfaces between different regions and equal heat flux at interfaces. From the established boundary conditions, the design blueprint for a bilayer cloak is inferred: its inner layer functions as an adiabatic barrier. The relationship between the outer layer's thermal conductivity and that of the backdrop is described by [18]:

$$\kappa_s = \frac{2R_2^3 + R_1^3}{2(R_2^3 - R_1^3)}\kappa_b. \tag{5.5}$$

κ_s represents the thermal conductivity of the outer layer of the thermal cloak, κ_b represents the thermal conductivity of the background, and R_1 and R_2 represent the inner and outer radii of the outer layer.

In thermal cloaking, the 2D bilayer cloak is a notable milestone. Han and his team spearheaded its theoretical and empirical validation [18]. The thermal cloak they designed is cylindrical, with the direction of heat flow following a radial path. This means that when viewed in cross-section, it appears as a circular cloak within a two-dimensional thermal field. The entire cloak is made from bulk materials, greatly simplifying the manufacturing process. Both simulation and experimental results have demonstrated its exceptional thermal invisibility performance.

Shifting to a three-dimensional perspective, Xu's team was the inaugural group to experimentally verify a 3D bilayer cloak [17]. Adopting an innovative approach, they used a compression technique to produce half of the cloak. These halves were then merged to complete a full 3D bilayer cloak.

A shared feature between the 2D and 3D bilayer cloaks is their architecture: both utilize an adiabatic inner layer paired with a high thermal conductive outer layer, facilitating scattering cancellation. There's merit in designating the inner layer as adiabatic: it offers the cloak adaptability for various objectives. Certainly, we can also opt for a combination of an outer layer made of low thermal conductivity material and an inner layer made of high thermal conductivity material. Likewise, to make this cloak applicable to any target, the ideal scenario would require the thermal conductivity of the inner material to be infinitely high. A cloak designed with this approach is termed a "zero-index cloak", which was proposed and realized by Li and his colleagues [42]. To approximate an infinitely high thermal conductivity, they ingeniously incorporated thermal convection as an equivalent.

It's worth noting that although the scattering cancellation theory avoids the use of singular materials, it still has limitations. Firstly, cloaks designed based on it are only suitable for steady-state situations, and their performance is not optimal in transient scenarios. Secondly, only some specific shapes of thermal cloaks can obtain exact analytical solutions from this method; designing cloaks of more complex shapes is extremely challenging.

5.2.3 *Topology Optimization: Crafting Thermal Cloaks for Every Shape*

Up to now, the design of thermal cloaks has mainly relied on materials with anisotropic thermal conductivity or specially shaped thermal cloaks made from natural materials. With the advancement of computational technology and the increasing power of computers, numerical optimization has emerged as an innovative method for designing thermal stealth devices. In 2014, Dede and his colleagues utilized numerical optimization techniques to develop composite structures that can manipulate heat flux to achieve functionalities like shielding, concentrating, and rotating [19]. These anisotropic thermal composite materials consist of elliptical inclusions that are uniformly integrated into the primary matrix.

Advancing this methodology, Fujii and his group employed the Covariance Matrix Adaptation Evolution Strategy (CMA-ES)–a sophisticated optimization algorithm–to refine the material design structure [20]. Their primary objective was to produce thermal cloaks using naturally existing materials. The typical steps of this optimization method include:

Step 1: Obtain a reference temperature distribution, which represents the undisturbed temperature field.

Step 2: Formulate an objective function that measures the discrepancy between the reference and optimized temperature fields. This function is crucial as it gauges the effectiveness of the thermal cloak.

Step 3: Apply advanced optimization techniques, like CMA-ES, to enhance the material structure. The primary aim is to ensure the optimized temperature profile closely matches the reference.

Step 4: Continue optimization until the required accuracy in the objective function is attained.

Using this optimization procedure, the thermal cloak's structure can be perfected, enabling it to achieve thermal invisibility using natural materials. This approach offers a pathway to develop versatile thermal cloak designs, eliminating the need for complex material structures. Researchers can customize thermal cloaks to various shapes based on precision requirements, utilizing common materials such as aluminum and iron. This approach significantly enhances the diversity of thermal cloaks available.

As previously mentioned, the optimization approach heavily depends on the prior knowledge of the background temperature field. Achieving the desired accuracy might not always be possible for all cloak shapes. Addressing this challenge, Sha and his colleagues proposed an innovative method that uses topology optimization to directly design foundational functional units [21]. These units are then assembled to achieve thermal invisibility. Their detailed process includes: First, determining the necessary thermal conductivity tensor for the cloak based on transformation theory. Next, they segment the entire area into foundational units and use topology optimization to shape topological functional cells (TFCs). These TFCs have distinct microstructures specific to each unit. Finally, these units are combined to realize ther-

mal invisibility. Remarkably, the TFCs combine two different materials: Die steel (H13) and polydimethylsiloxane. This groundbreaking strategy offers unparalleled flexibility, facilitating the creation of thermal solutions previously deemed challenging. This pioneering approach sets the stage for a new chapter in the adaptive fabrication of thermal cloaking devices.

Furthermore, many recent studies are merging deep learning with topology optimization [33], paving the way for a more sophisticated application of the optimization technique in thermal invisibility technology.

5.3 From Blueprint to Reality: Advancements in Thermal Cloaking Technology

5.3.1 The Revolutionary Thermal Carpet Cloak: Concealment on Surfaces

The concept of the "carpet cloak" originated from the study of optical invisibility cloaks [43]. In terms of heat conduction, a carpet cloak is a device designed to conceal objects placed on an insulating surface. It emerged as a solution to the challenges faced in crafting traditional thermal cloaks and to enhance their applicability in specific scenarios. The foundational principles of designing carpet cloaks are derived from the methodologies we discussed in the previous section, which we will further elaborate on in the following sections.

Transformation theory laid the groundwork for one of the initial iterations of the thermal carpet cloak [23, 25]. The cloak's distinct shape derives from a transformation applied to the y-coordinate, described by the equation [23]:

$$y' = \frac{c-a}{c}y + \frac{b - x\mathrm{sgn}(x)}{b}a, \tag{5.6}$$

where a, b, and c denote geometric parameters. It's important to highlight that devices tailored for thermal invisibility via the outlined methods exhibit strong directionality. As demonstrated in Ref. [23], they are more effective in a vertical temperature gradient than a horizontal one.

Drawing inspiration from the bilayer thermal cloak, the bilayer thermal carpet cloak emerged. Analyzing the heat flow within a bilayer thermal cloak uncovers a remarkable symmetry. For example, when a temperature gradient aligns with the major axis of the elliptical bilayer cloak, the heat flow symmetrically aligns as well. Modifying the major axis to an adiabatic state does not hinder the heat flow direction. Building on this observation, Han and his team developed a carpet cloak based on the principle of scattering cancellation [24]. This model features a bilayer composition: an inner adiabatic layer complemented by an outer layer possessing high thermal conductivity. Set atop an adiabatic foundation, it ensures perfect invisibility against a

horizontal temperature gradient. Made entirely from natural materials, this invention accentuates the practicality of carpet cloaks.

Topology optimization further facilitates the crafting of carpet cloaks using natural materials. In a similar vein, Fujii and his team employed the covariance matrix adaptation evolution strategy to refine carpet cloak designs [44]. These cloaks showcase outstanding performance under diverse heat flow angles.

Of course, some entirely new methods have also been employed in the design of carpet cloaks, such as the law of thermal refraction [22]. The law of thermal refraction states that heat flow will propagate in the direction of the least thermal resistance. Based on this, one can directly control the direction of heat flow to achieve the purpose of invisibility.

5.3.2 ITR-Free Thermal Cloak: Overcoming Interface Thermal Resistance

In practical applications, heat flow can be influenced by the interface thermal resistance (ITR) between different materials. Unfortunately, most existing thermal cloaks require the use of two or more materials to manufacture [26]. For example, using scattering cancellation methods or topology optimization typically necessitates at least two materials–one with high thermal conductivity and one with low thermal conductivity. Similarly, cloaks designed based on coordinate transformation theory often require multiple layers of materials, exacerbating the interface thermal resistance effect. Consequently, thermal cloaking devices designed under ideal conditions (neglecting interface thermal resistance) may face functionality issues when applied in real-world scenarios.

At the macro level, ITR primarily arises from incomplete contact between material surfaces and their intervening voids. This resistance is intrinsically tied to the involved materials' mechanical and thermophysical attributes. Furthermore, factors like contact surface shape, interfacial pressure, temperature, and the intervening medium can modulate ITR. In scenarios where ultra-precision isn't paramount, various techniques, such as stress application during installation, inter-material gap filling using thermally conductive grease, precision enhancement in manufacturing, and surface roughness reduction, can mitigate ITR.

For applications that require high precision or when the above methods are not effective, it becomes necessary to consider the impact of interface thermal resistance during the design of thermal invisibility devices. Zheng and Li carefully examined the boundary conditions that need to be satisfied for temperature and heat flux at different interfaces when interface ITR is present [26]. In the presence of ITR, temperature continuity is disrupted while heat flux continuity is maintained, as expressed by the following equations:

$$\begin{aligned} T_{i+1}|_{\partial\Omega} &= T_i|_{\partial\Omega} + R_{i,i+1}\mathbf{n}\cdot(\kappa_i\nabla T_i)|_{\partial\Omega}, \\ \mathbf{n}\cdot(\kappa_i\nabla T_i)|_{\partial\Omega} &= \mathbf{n}\cdot(\kappa_{i+1}\nabla T_{i+1})|_{\partial\Omega}, \end{aligned} \tag{5.7}$$

where $R_{i,i+1}$ is the ITR between the ith region and the $(i+1)$th region. After considering the above boundary conditions, modifications can be made to the design formula for the thermal cloak. For example, the modification of a bilayer cloak designed using the scattering cancellation method can be expressed in the following form:

$$\frac{\kappa_1}{\kappa_2} = \frac{b^2 + a^2}{(b^2 - a^2)(1 - R_i\kappa_2/b)}, \tag{5.8}$$

where a is the inner radius and b is the outer radius of the outer shell. κ_1 is the thermal conductivity of the outer shell, and κ_2 is the thermal conductivity of the background region. R_i denotes the ITR which includes thermal contact resistance and thermal boundary resistance. The introduction of $\mathrm{Q} = 1 - R_i\kappa_2/b$ is used to represent the impact of ITR on the thermal cloak. When $\mathrm{Q} = 1$, the above equation transforms into the design formula for the ideal case.

However, even when ITR has been considered in the design, determining its specific impact can still be challenging. To address this, Han and colleagues proposed a method to circumvent ITR [28]. Their design inspiration draws from the concept of equivalent thermal conductivity, which is achieved by varying the cross section of heat conduction. In simple terms, for two-dimensional heat conduction, we can achieve an equivalent high thermal conductivity by adding a third dimension, namely increasing the thickness h. According to the law of energy conservation, we can derive the following relationship to achieve the equivalence of a material with thermal conductivity κ_2 to a material with thermal conductivity κ_1:

$$\frac{\kappa_1}{\kappa_2} = \frac{t + h}{t} = 1 + \frac{h}{t}, \tag{5.9}$$

where t represents the thickness of the background material, h represents the added interface thickness. In this process, the same material is used throughout, thereby eliminating the presence of interfacial thermal resistance. Consequently, a method for achieving any thermal conductivity without ITR is obtained. When applied to a bilayer thermal cloak, this approach results in a thermal invisibility device without interfacial thermal resistance.

5.3.3 The Thermal Dome: A New Horizon in Thermal Shielding

Despite the innovative designs of various thermal cloaks with some undergoing successful experimental validation, their foundational design principle hinders widespread engineering application. This principle, involving the complete encase-

ment of the target object with an insulating material followed by heat flow redirection around it, inevitably leads to a fully enclosed hidden area. This aspect presents significant manufacturing, installation, and reusability challenges, especially in three-dimensional structures. Further, these cloaks are unsuitable for providing thermal invisibility to objects with heat sources, an overlooked common reality in prior research. Additionally, these cloaks' custom design for specific environments renders them ineffective when environmental conditions or background thermal conductivity changes. Therefore, traditional thermal invisibility devices still have a long way to go before they can be engineered.

To address these issues, Zhou et al. proposed a novel thermal invisibility device tailored for engineering applications called the "thermal dome" [29]. This device features an open hidden region, facilitating easy installation and reuse. Importantly, it represents a significant advancement in thermal invisibility technology as it achieves thermal invisibility for objects containing heat sources, marking a major breakthrough in this field. Furthermore, due to the open structure of the thermal dome, concepts involving multiple layers can be applied to make it reconfigurable, similar to LEGO blocks, enabling it to adapt to dynamic environmental changes.

Similar to the bilayer cloak, the thermal dome is also constructed using natural materials only, and its structure is depicted in Fig. 5.3. The semi-axis of the core (dome) is specified as l_{ci} (l_{di}) along the x_i axis, where $i = 1, 2, 3$ represents the three dimensions. After solving the heat conduction equation under special boundary conditions, we obtain the design requirement for the thermal dome:

$$\kappa_b = \frac{L_{ci}\kappa_c + (1 - L_{ci})\,\kappa_d + (1 - L_{di})\,(\kappa_c - \kappa_d)\,f}{L_{ci}\kappa_c + (1 - L_{ci})\,\kappa_d - L_{di}\,(\kappa_c - \kappa_d)\,f}\kappa_d, \tag{5.10}$$

where $f = g\,(\rho_c)\,/g\,(\rho_d) = \prod_i l_{ci}/l_{di}$ denotes the volume fraction, L_{ci} and L_{di} are the shape factors. κ_b denotes the thermal conductivity of the background, κ_d denotes the thermal conductivity of the thermal dome.

The method described above can be easily extended to accommodate a core-shell structure with n layers. Computational software can be used to determine the parameters of the thermal domes in each layer. Another rapid method for design-

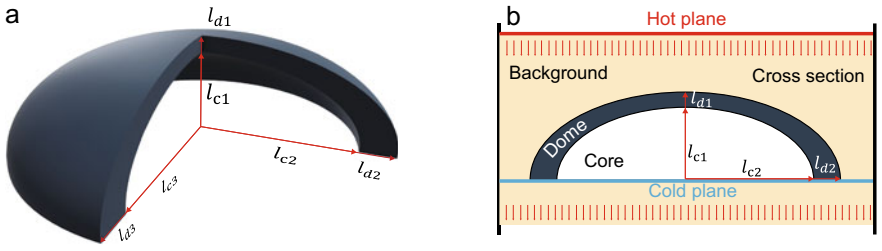

Fig. 5.3 **a** Presents a schematic representation of the thermal dome, while **b** exhibits its cross-sectional view. (from Ref. [29], licensed under CC-BY 4.0)

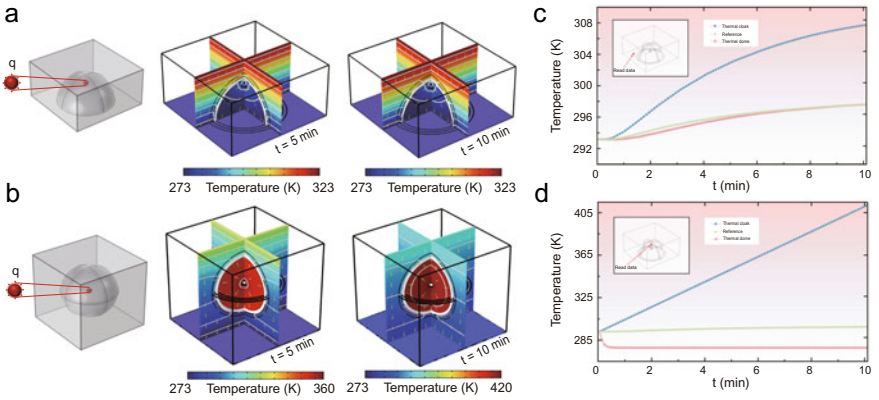

Fig. 5.4 **a** and **b** Compare the performance of the thermal dome and thermal cloak with a heat source in the hidden area at 5 and 10 min respectively. The heat source in the thermal dome and thermal cloak emitting heat outward at a rate of 500 kW per square meter. In **c** and **d**, we quantitatively show the variation of temperature at different positions with time. (from Ref. [29], licensed under CC-BY 4.0)

ing multi-layer thermal domes is to use effective medium theory, where the design process can be done layer by layer in an iterative manner.

As mentioned earlier, a prominent feature of the thermal dome is its ability to achieve thermal invisibility for objects containing heat sources. As shown in Fig. 5.4a and c, the open design of the thermal dome allows it to directly contact the cold source, enabling the heat flux generated by internal heat sources to be absorbed through the bottom. In contrast, traditional thermal cloaks lose their functionality when there are internal heat sources, and the temperature inside their enclosed space continues to rise, leading to catastrophic consequences as shown in Fig. 5.4b and d.

5.4 Conclusion and Outlook

In this chapter, we present three mainstream theories for the design of thermal cloaks. Subsequently, by introducing three specific thermal invisible devices, we illustrate the primary challenges and solutions encountered when adapting the traditional thermal cloak to practical engineering applications. It's noteworthy that some novel theories, such as topological phenomena [45–47] and conformal mapping theory [51], have emerged and are being employed in the design and understanding of thermal cloaks, injecting new vitality into the field of thermal invisibility. Furthermore, the content of statistical physics can also be utilized to manufacture the required materials [48–50].

It should be noted that the research on thermal invisibility holds significant practical importance. Firstly, it offers a novel method for precise control of heat flow, which is crucial for thermal management. This can be used to regulate the distribution

of heat flow in chips to protect vital components, or combined with solar panels to enhance power generation efficiency. Secondly, the concept of "thermal invisibility" itself plays a significant role, especially in the defense sector, where it can shield crucial targets from being detected by infrared cameras.

Lastly, as previously mentioned, the advancement of thermal invisibility has been in tandem with the development of thermal metamaterials [52, 53]. Theories utilized for designing thermal cloaks, such as transformation theory or scattering cancellation theory, among others, have also been employed to design other functional devices. These include thermal concentrators [54, 55], thermal sensors [56–58], thermal transparency [59], thermal chameleonlike devices [60, 61] and thermal illusions [62, 63], greatly enriching the content of thermal metamaterials. Similar theories can even be extended to economics and music research [64, 65]. It is hoped that this chapter on thermal invisibility technology will serve as a stepping stone, offering a fresh perspective on the development of thermal metamaterials.

References

1. Pendry, J.B., Schurig, D., Smith, D.R.: Controlling electromagnetic fields. Science **312**, 1780 (2006)
2. Leonhardt, U.: Optical conformal mapping. Science **312**, 1777 (2006)
3. Kadic, M., Milton, G.W., van Hecke, M., Wegener, M.: 3D metamaterials. Nat. Rev. Phys. **1**, 198–210 (2019)
4. Cummer, S.A., Christensen, J., Alu, A.: Controlling sound with acoustic metamaterials. Nat. Rev. Mater. **1**, 16001 (2016)
5. Yang, S., Wang, J., Dai, G.L., Yang, F.B., Huang, J.P.: Controlling macroscopic heat transfer with thermal metamaterials: theory, experiment and application. Phys. Rep. **908**, 1–65 (2021)
6. Zhang, Z.R., Xu, L.J., Qu, T., Lei, M., Lin, Z.K., Ouyang, X.P., Jiang, J.-H., Huang, J.P.: Diffusion metamaterials. Nat. Rev. Phys. **5**, 218–235 (2023)
7. Fan, C.Z., Gao, Y., Huang, J.P.: Shaped graded materials with an apparent negative thermal conductivity. Appl. Phys. Lett. **92**, 251907 (2008)
8. Shen, X.Y., Jiang, C.R., Li, Y., Huang, J.P.: Thermal metamaterial for convergent transfer of conductive heat with high efficiency. Appl. Phys. Lett. **109**, 201906 (2016)
9. Yang, S., Xu, L.J., Wang, R.Z., Huang, J.P.: Full control of heat transfer in single-particle structural materials. Appl. Phys. Lett. **111**, 121908 (2017)
10. Xu, L.J., Yang, S., Huang, J.P.: Thermal theory for heterogeneously architected structure: fundamentals and application. Phys. Rev. E **98**, 052128 (2018)
11. Wang, J., Dai, G.L., Huang, J.P.: Thermal metamaterial: fundamental, application, and outlook. iScience **23**, 101637 (2020)
12. Xu, L.J., Xu, G.Q., Huang, J.P., Qiu, C.-W.: Diffusive Fizeau drag in spatiotemporal thermal metamaterials. Phys. Rev. Lett. **128**, 145901 (2022)
13. Xu, L.J., Huang, J.P.: Transformation Thermotics and Extended Theories: Inside and Outside Metamaterials. Springer, Berlin (2023)
14. Xu, L.J., Dai, G.L., Huang, J.P.: Transformation multithermotics: controlling radiation and conduction simultaneously. Phys. Rev. Appl. **13**, 024063 (2020)
15. Dai, G.L., Huang, J.P.: A transient regime for transforming thermal convection: cloaking, concentrating and rotating creeping flow and heat flux. J. Appl. Phys. **124**, 235103 (2018)
16. Xu, L.J., Yang, S., Dai, G.L., Huang, J.P.: Transformation omnithermotics: simultaneous manipulation of three basic modes of heat transfer. ES Energy Environ. **7**, 65–70 (2020)

17. Xu, H., Shi, X., Gao, F., Sun, H., Zhang, B.L.: Experimental demonstration of an ultrathin three-dimensional thermal cloak. Phys. Rev. Lett. **112**, 054301 (2014)
18. Han, T.C., Bai, X., Gao, D., Thong, J.T.L., Li, B.W., Qiu, C.-W.: Experimental demonstration of a bilayer thermal cloak. Phys. Rev. Lett. **112**, 054302 (2014)
19. Dede, E.M., Nomura, T., Lee, J.: Thermal-composite design optimization for heat flux shielding, focusing, and reversal. Struct. Multidiscip. Optim. **49**, 59–68 (2014)
20. Fujii, G., Akimoto, Y., Takahashi, M.: Exploring optimal topology of thermal cloaks by CMA-ES. Appl. Phys. Lett. **112**, 061108 (2018)
21. Sha, W., Xiao, M., Zhang, J.H., Ren, X.C., Zhu, Z., Zhang, Y., Xu, G.Q., Li, H.G., Liu, X.L., Chen, X., Gao, L., Qiu, C.W., Hu, R.: Robustly printable freeform thermal metamaterials. Nat. Commun. **12**, 7228 (2021)
22. Hu, R., Xie, B., Hu, J., Chen, Q., Luo, X.: Carpet thermal cloak realization based on the refraction law of heat flux. EPL **111**, 54003 (2015)
23. Yang, T., Wu, Q., Xu, W., Liu, D., Huang, L., Chen, F.: A thermal ground cloak. Phys. Lett. A **380**, 965–969 (2016)
24. Qin, J., Luo, W., Yang, P., Wang, B., Deng, T., Han, T.C.: Experimental demonstration of irregular thermal carpet cloaks with natural bulk material. Int. J. Heat Mass Transf. **141**, 487–490 (2019)
25. Peng, Y.G., Li, Y., Cao, P.C., Zhu, X.F., Qiu, C.W.: 3D printed meta-helmet for wide-angle thermal camouflages. Adv. Funct. Mater. **30**, 2002061 (2020)
26. Zheng, X., Li, B.: Effect of interfacial thermal resistance in a thermal cloak. Phys. Rev. Appl. **13**, 024071 (2020)
27. Chen, T., Lin, J.H.: Exact thermal invisibility for spherical cloaks with imperfect interfaces. AIP Adv. **12**, 075214 (2022)
28. Han, T.C., Nangong, J., Li, Y.: ITR-free thermal cloak. Int. J. Heat Mass Transf. **203**, 123779 (2023)
29. Zhou, Y.H., Yang, F.B., Xu, L.J., Zhuang, P.F., Wang, D., Ouyang, X.P., Li, Y., Huang, J.P.: Reconfigurable three-dimensional thermal dome (2023). arXiv: 2309.04745
30. Li, J.X., Li, Y., Cao, P.C., Yang, T.Z., Zhu, X.F., Wang, W.Y., Qiu, C.W.: A continuously tunable solid-like convective thermal metadevice on the reciprocal line. Adv. Mater. **32**, 2003823 (2020)
31. Xu, G.Q., Dong, K.C., Li, Y., Li, H.G., Liu, K.P., Li, L.Q., Wu, J.Q., Qiu, C.W.: Tunable analog thermal material. Nat. Commun. **11**, 6028 (2020)
32. Yang, S., Xu, L.J., Huang, J.P.: Intelligence thermotics: correlated self-fixing behavior of thermal metamaterials. Europhys. Lett. **126**, 54001 (2019)
33. Wang, Y., Sha, W., Xiao, M., Qiu, C.W., Gao, L.: Deep-learning-enabled intelligent design of thermal metamaterials. Adv. Mater. **35**, 2302387 (2023)
34. Chen, T., Weng, C.-N., Chen, J.-S.: Cloak for curvilinearly anisotropic media in conduction. Appl. Phys. Lett. **93**, 114103 (2008)
35. Guenneau, S., Amra, C., Veynante, D.: Transformation thermodynamics: cloaking and concentrating heat flux. Opt. Express **20**, 8207–8218 (2012)
36. Narayana, S., Sato, Y.: Heat flux manipulation with engineered thermal materials. Phys. Rev. Lett. **108**, 214303 (2012)
37. Schittny, R., Kadic, M., Guenneau, S., Wegener, M.: Experiments on transformation thermodynamics: molding the flow of heat. Phys. Rev. Lett. **110**, 195901 (2013)
38. Huang, J.P.: Theoretical Thermotics: Transformation Thermotics and Extended Theories for Thermal Metamaterials. Springer, Singapore (2020)
39. Li, Y., Shen, X.Y., Wu, Z.H., Huang, J.Y., Chen, Y.X., Ni, Y.S., Huang, J.P.: Temperature-dependent transformation thermotics: from switchable thermal cloaks to macroscopic thermal diodes. Phys. Rev. Lett. **115**, 195503 (2015)
40. Shen, X.Y., Li, Y., Jiang, C.R., Huang, J.P.: Temperature trapping: energy-free maintenance of constant temperatures as ambient temperature gradients change. Phys. Rev. Lett. **117**, 055501 (2016)
41. Goemoery, F., Solovyov, M., Souc, J., Navau, C., Prat-Camps, J., Sanchez, A.: Experimental realization of a magnetic cloak. Science **335**, 1466–1468 (2012)

42. Li, Y., Zhu, K.J., Peng, Y.G., Li, W., Yang, T.Z., Xu, H.X., Chen, H., Zhu, X.F., Fan, S.H., Qiu, C.W.: Thermal meta-device in analogue of zero-index photonics. Nat. Mater. **18**, 48 (2019)
43. Li, J., Pendry, J.B.: Hiding under the carpet: a new strategy for cloaking. Phys. Rev. Lett. **101**, 203901 (2008)
44. Fujii, G., Akimoto, Y.: Topology-optimized thermal carpet cloak expressed by an immersed-boundary level-set method via a covariance matrix adaptation evolution strategy. Int. J. Heat Mass Transf. **137**, 1312–1322 (2019)
45. Li, Y., Qi, M.H., Li, J.X., Cao, P.-C., Wang, D., Zhu, X.-F., Qiu, C.-W., Chen, H.S.: Heat transfer control using a thermal analogue of coherent perfect absorption. Nat. Commun. **13**, 2683 (2022)
46. Qi, M.H., Wang, D., Cao, P.-C., Zhu, X.-F., Qiu, C.-W., Chen, H.S., Li, Y.: Geometric phase and localized heat diffusion. Adv. Mater. **34**, 2202241 (2022)
47. Hu, H., Han, S., Yang, Y.H., Liu, D.J., Xue, H.R., Liu, G.-G., Cheng, Z.Y., Wang, Q.J., Zhang, S., Zhang, B.L., Luo, Y.: Observation of topological edge states in thermal diffusion. Adv. Mater. **34**, 2202257 (2022)
48. Gao, Y., Jian, Y.C., Zhang, L.F., Huang, J.P.: Magnetophoresis of nonmagnetic particles in ferrofluids. J. Phys. Chem. C **111**, 10785 (2007)
49. Dong, L., Huang, J.P., Yu, K.W., Gu, G.Q.: Dielectric response of graded spherical particles of anisotropic materials. J. Appl. Phys. **95**, 621–624 (2004)
50. Huang, J.P., Karttunen, M., Yu, K.W., Dong, L.: Dielectrophoresis of charged colloidal suspensions. Phys. Rev. E **67**, 021403 (2003)
51. Dai, G.L., Yang, F.B., Xu, L.J., Huang, J.P.: Diffusive pseudo-conformal mapping: anisotropy-free transformation thermal media with perfect interface matching. Chaos, Solitons Fractals **174**, 113849 (2023)
52. Xu, L.J., Wang, J., Dai, G.L., Yang, S., Yang, F.B., Wang, G., Huang, J.P.: Geometric phase, effective conductivity enhancement, and invisibility cloak in thermal convection-conduction. Int. J. Heat Mass Transf. **165**, 120659 (2021)
53. Xu, L.J., Huang, J.P.: Active thermal wave cloak. Chin. Phys. Lett. **37**, 120501 (2020)
54. Shen, X.Y., Li, Y., Jiang, C.R., Ni, Y.S., Huang, J.P.: Thermal cloak-concentrator. Appl. Phys. Lett. **109**, 031907 (2016)
55. Zhuang, P.F., Xu, L.J., Tan, P., Ouyang, X.P., Huang, J.P.: Breaking efficiency limit of thermal concentrators by conductivity couplings. Sci. China Phys. Mech. Astron. **65**, 117007 (2022)
56. Xu, L.J., Huang, J.P., Jiang, T., Zhang, L., Huang, J.P.: Thermally invisible sensors. Europhys. Lett. **132**, 14002 (2020)
57. Jin, P., Xu, L.J., Jiang, T., Zhang, L., Huang, J.P.: Making thermal sensors accurate and invisible with an anisotropic monolayer scheme. Int. J. Heat Mass Transf. **163**, 120437 (2020)
58. Jin, P., Yang, S., Xu, L.J., Dai, G.L., Huang, J.P., Ouyang, X.P.: Particle swarm optimization for realizing bilayer thermal sensors with bulk isotropic materials. Int. J. Heat Mass Transfer **172**, 121177 (2021)
59. Xu, L.J., Yang, S., Huang, J.P.: Thermal transparency induced by periodic interparticle interaction. Phys. Rev. Appl. **11**, 034056 (2019)
60. Xu, L.J., Yang, S., Huang, J.P.: Passive metashells with adaptive thermal conductivities: chameleonlike behavior and its origin. Phys. Rev. Appl. **11**, 054071 (2019)
61. Zhang, Z.R., Yang, F.B., Huang, J.P.: Intelligent chameleonlike metashells for mass diffusion. Phys. Rev. Appl. **19**, 024009 (2023)
62. Zhu, N.Q., Shen, X.Y., Huang, J.P.: Converting the patterns of local heat flux via thermal illusion device. AIP Adv. **5**, 053401 (2015)
63. Yang, F.B., Xu, L.J., Huang, J.P.: Thermal illusion of porous media with convection-diffusion process: transparency, concentrating, and cloaking. ES Energy Environ. **6**, 45–50 (2019)
64. Ye, C., Huang, J.P.: Non-classical oscillator model for persistent fluctuations in stock markets. Phys. A **387**, 1255–1263 (2008)
65. Liu, L., Wei, J.R., Zhang, H.S., Xin, J.H., Huang, J.P.: A statistical physics view of pitch fluctuations in the classical music from Bach to Chopin: evidence for scaling. PLoS ONE **8**, e58710 (2013)

Chapter 6
Spatial and Temporal Modulation of Thermoelectric Metamaterials

Min Lei, Liujun Xu, and Fubao Yang

6.1 Opening Remarks

Whether in daily life or science and technology, the scenarios people face are always complex [1, 2]. The manipulation of intricate physical fields within complex scenarios plays a pivotal role across a broad spectrum of applications, spanning power generation [3], radiative cooling [4], biomedical engineering [5], and energy management [6]. Metamaterials [7–9] emerge as a formidable platform for orchestrating diverse physical domains encompassing optics [10], plasma physics [11], acoustics [12, 13], thermotics [14–22], electrics [23, 24], and fluidics [25, 26]. Exciting functions like cloaking, sensing, and concentrating allow for the physical field intensity in the working region to be far smaller, equal, or larger than in the background [27–30]. As the demand for multifaceted applications escalates, the evolution of metamaterial design transcends the confines of single-field manipulation. Multiphysics metamaterials emerge as a beacon of promise, heralding the potential to govern multiple physical domains in concert. This transformative trajectory gives rise to the simultaneous governance of electromagnetic and acoustic fields [31, 32], conductive and convective or radiative domains [33–36], and the nuanced interplay of thermal and electric realms [37–42]. The intertwining of thermal and electrical transport, often intertwined, spawns a quintessential multi-physics paradigm. The employment of transformation theory to craft thermoelectric metamaterials provides a potent avenue to realize spatial modulation within the thermal and electric landscapes. Expanded theories, including effective medium and scattering cancellation theories, furnish blueprints for the tangible realization of functional thermal

M. Lei (✉) · F. Yang
Department of Physics, Key Laboratory of Micro and Nano Photonic Structures (MOE), and State Key Laboratory of Surface Physics, Fudan University, Shanghai 200438, China
e-mail: 22110190026@m.fudan.edu.cn

L. Xu
Graduate School of China Academy of Engineering Physics, Beijing 100193, China

F.-B. Yang and J.-P. Huang, *Diffusionics*,
https://doi.org/10.1007/978-981-97-0487-3_6

and electric domains. However, extant multiphysics metamaterials are not without their limitations. Traditional methodologies proffer fixed functionalities owing to unyielding structures and materials. The quest for continuous controllability is met with tribulation, as it necessitates concurrent and on-demand adjustments to multiphysical parameters. Thus, the pursuit of multifunctionality within each physical domain, not to mention its seamless toggling, remains an imposing challenge within the realm of multiphysics metamaterials.

Recently, metamaterial designs incorporating the temporal dimension have garnered considerable attention due to their promising degree of freedom [43, 44]. This augmentation with spatiotemporal modulation not only begets unforeseen nonreciprocal phenomena [45–50] and captivating topological transport [51–53] from a fundamental physics perspective but also finds pragmatic application in adaptive thermal camouflage [54] and real-time digital coding [55, 56]. However, the current scope of spatiotemporal strategies is predominantly constrained to single physical fields, and extending their purview to multiphysics domains presents a formidable conundrum, entailing intricate coordination of parameters across diverse physical realms, all while adhering to the constraints of materials and structures.

In this chapter, we introduce the field of spatially regulated thermoelectric metamaterials based on transformation thermoelectricity and provide a summary of the existing functionalities. Furthermore, we unravel the conceptual framework of spatiotemporal multiphysics metamaterials, which represents an innovative approach enabling simultaneous manipulation of thermal and electric fields [57]. To incorporate the temporal dimension, we employ a rotatable checkerboard structure that facilitates continuous tuning of its geometric configuration over time. This characteristic grants us flexible control over thermal and electric conductivities, thus enabling the realization of various functions in both fields. Our spatiotemporal multiphysics metamaterials offer the flexibility to switch between three or five function combinations, depending on the number of constituent materials used. These findings unlock novel possibilities for flexible and intelligent control of multiphysics fields, presenting opportunities for advanced applications.

6.2 Space-Regulated Thermoelectric Metamaterials

Thermoelectric devices are pivotal in both industrial applications and daily life, necessitating the control of thermal and electric fields within a single unit. Within the thermoelectric field, the thermal and electric fields can either operate independently (decoupled) or in conjunction (coupled). In a decoupled scenario, a device demonstrating temperature and voltage differences manages its thermal and electric fields independently, with each field unaffected by the other. On the other hand, in a coupled setup, the thermal and electric fields influence each other, rendering their separate control unfeasible. Thus, when considering the thermoelectric effect, the coupling term becomes indispensable, adding a layer of complexity to the analysis of thermoelectric metamaterials.

6.2.1 Decoupled Transformation Thermoelectrics

First, we consider the transformation theory within decoupled thermoelectric fields. In such fields, the steady-state heat conduction equation without a heat source parallels the electrical conduction equation without a power supply in form, both of which can be expressed as

$$\nabla \cdot (\kappa \nabla T) = 0, \quad \nabla \cdot (\sigma \nabla \mu) = 0, \tag{6.1}$$

where κ and σ are thermal conductivity tensor and electrical conductivity tensor, T and μ are temperature and potential. Li et al. proved that the Eq. (6.1) satisfies formal invariance under coordinate transformation, and the transformation rule is [37]

$$\kappa' = \frac{\mathsf{A}\kappa_0\mathsf{A}^{tr}}{\det \mathsf{A}}, \quad \sigma' = \frac{\mathsf{A}\sigma_0\mathsf{A}^{tr}}{\det \mathsf{A}}, \tag{6.2}$$

where κ' and σ' are transformed thermal conductivity and electric conductivity, κ_0 and σ_0 are thermal conductivity and electric conductivity of the background, A is the Jacobian transformation matrix. The physical parameters of real space can be obtained by substituting coordinate transformation into the Jacobi matrix.

6.2.2 Coupled Transformation Thermoelectrics

In coupled thermoelectric fields, a mutual conversion between electricity and heat exists. The Peltier effect refers to the generation of a heat flow due to a potential difference. As charge carriers flow from higher to lower energy levels, surplus heat is discharged into the material. Conversely, when charge carriers move inversely, heat is absorbed, leading to the material's cooling. The Seebeck effect, on the other hand, describes the current induced by a temperature gradient. Here, charge carriers move from the hot to the cold end, accumulating at the latter. This buildup results in an electric potential difference, subsequently inducing an electric current in the reverse direction. The Seebeck coefficient captures the strength of this interaction, coupling the thermal and electric fields. When a temperature and voltage difference coexist, coupled heat and current emerge alongside their independent movements. In the linear regime, the coupling between the electric, $\boldsymbol{J}_E$, and the heat current density, $\boldsymbol{J}_Q$, is expressed as

$$\begin{aligned} \boldsymbol{J}_E &= -\sigma \nabla \mu - \sigma S \nabla T, \\ \boldsymbol{J}_Q &= -\kappa \nabla T + T S^{\dagger} \boldsymbol{J}_E, \end{aligned} \tag{6.3}$$

where κ and σ are thermal and electrical conductivity tensors, respectively. T is temperature, μ is the electric potential, S is the Seebeck coefficient tensor, and $S^{\dagger}$ is its transpose. When considering the steady state with local equilibrium and the absence

of external heat and power sources, the governing equation for the thermoelectric effect can be expressed as follows

$$\begin{aligned} \nabla \cdot \boldsymbol{J}_E &= 0, \\ \nabla \cdot \boldsymbol{J}_Q &= -\nabla\mu \cdot \boldsymbol{J}_E. \end{aligned} \tag{6.4}$$

These two equation express the local conservation in the steady state of charge and energy, respectively. The thermoelectric coupling transport produces a heat source term, $-\nabla\mu \cdot \boldsymbol{J}_E$, corresponding to the Joule effect. In view of Onsager reciprocal relations, electric and thermal conductivity matrices should be symmetric, $\sigma = \sigma^\dagger$ and $\kappa = \kappa^\dagger$. Substituting Eq. (6.3) into Eq. (6.4), the complete governing equation for the thermoelectric effect can be formulated as

$$\nabla \cdot (\sigma\nabla\mu + \sigma S\nabla T) = 0 \tag{6.5}$$

and

$$-\nabla \cdot \left(\kappa\nabla T + TS^\dagger\sigma S\nabla T + TS^\dagger\sigma\nabla\mu\right) = \nabla\mu \cdot (\sigma\nabla\mu + \sigma S\nabla T)\,. \tag{6.6}$$

Next, it needs to be proved that the governing equations (6.5) and (6.6) remain invariant under any coordinate transformation. In a curvilinear coordinate system characterized by contravariant bases $\boldsymbol{g}^i, \boldsymbol{g}^j, \boldsymbol{g}^k$, covariant bases $\boldsymbol{g}_i, \boldsymbol{g}_j, \boldsymbol{g}_k$, and their respective contravariant components (x^i, y^j, z^k), the heat and electrical conduction terms on the left side of Eq. (6.5) can be reformulated as

$$\nabla \cdot (\sigma\nabla\mu + \sigma S\nabla T) = \frac{1}{\sqrt{g}}(\partial_i\sqrt{g}\sigma^{ij}\partial_j\mu + \partial_i\sqrt{g}\sigma^{ij}S^k_j\partial_k T), \tag{6.7}$$

where g is the determinant of the matrix with components $g_{ij} = \boldsymbol{g}_i \cdot \boldsymbol{g}_j$. Hence, the component form of Eq. (6.5) can be expressed as

$$\partial_i(\sqrt{g}\sigma^{ij}\partial_j\mu) + \partial_i(\sqrt{g}\sigma^{ij}S^k_j\partial_k T) = 0. \tag{6.8}$$

According to Eq. (6.8), the form invariance of Eq. (6.5) is verified. Following the above deduction, the component form of Eq. (6.6) can be written. The right-hand term of Eq. (6.6) can be written as

$$\nabla\mu \cdot (\sigma\nabla\mu + \sigma S\nabla T) = (\partial_i\mu)(\sigma^{ij}\partial_j\mu + \sigma^{ij}S^k_j\partial_k T). \tag{6.9}$$

Then the component form of each term on the left side of the Eq. (6.6) is written as

$$\begin{aligned} -\nabla \cdot (\kappa\nabla T) &= -\partial_j[\sqrt{g}\kappa^{jk}\partial_k T]/\sqrt{g}; \\ -\nabla \cdot \left(TS^\dagger\sigma S\nabla T\right) &= -\partial_j[\sqrt{g}T(S^{\mathrm{tr}})^j_i\sigma^{ij}S^k_j\partial_k T]/\sqrt{g}; \\ -\nabla \cdot \left(TS^\dagger\sigma\nabla\mu\right) &= -\partial_j[\sqrt{g}T(S^{\mathrm{tr}})^j_i\sigma^{ij}\partial_j\mu]/\sqrt{g}, \end{aligned} \tag{6.10}$$

where $(S^{\mathrm{tr}})_i^j$ is the transpose of S_i^j. Substituting Eqs. (6.9) and (6.10) into Eq. (6.6), the result can be written as

$$\begin{aligned}\partial_j[\sqrt{g}(\kappa^{jk}\partial_k T + T(S^{\mathrm{tr}})_i^j \sigma^{ij} S_j^k \partial_k T + T(S^{\mathrm{tr}})_i^j \sigma^{ij}\partial_j \mu)] \\ = -\sqrt{g}(\partial_i \mu)(\sigma^{ij}\partial_j \mu + \sigma^{ij} S_j^k \partial_k T).\end{aligned} \tag{6.11}$$

Similarly, Eq. (6.11) maintains its form across various coordinates, akin to Eq. (6.8). With this, the form invariance of the coupled thermoelectric governing equations under coordinate transformations has confirmed in Eqs. (6.8) and (6.11). The sole distinction across different coordinate systems is the coefficient g. As a result, transformation theory can be applied to the coupled thermoelectric field to regulate the linearly coupled heat charge flow.

To obtain transformation rules for material properties, the approach shifts from coordinate transformation to geometric mapping. Consider a bijection $f : r \mapsto r'$ in the three-dimensional Euclidean space that smoothly maps the pre-transformed space to the transformed space. Owing to the diffeomorphism between the pre-transformed space (virtual space) with curvilinear coordinates $\{x^i, x^j, x^k\}$ and the transformed space (physical space) with Cartesian coordinates $\{x', y', z'\}$, the temperature and electrochemical potential in Eqs. (6.5) and (6.6) are replaced by $T'(r') = T'(x', y', z')$ and $\mu'(r') = \mu'(x', y', z')$ if $T'(r') = T(f^{-1}(r'))$ and $\mu'(r') = \mu(f^{-1}(r'))$. They still satisfy

$$\nabla' \cdot (\sigma' \nabla' \mu' + \sigma' S' \nabla' T') = 0, \tag{6.12}$$

and

$$\begin{aligned}-\nabla' \cdot (\kappa' \nabla' T' + T'(S')^{\mathrm{tr}} \sigma' S' \nabla' T' + T'(S')^{\mathrm{tr}} \sigma' \nabla' \mu') \\ = \nabla' \mu' \cdot (\sigma' \nabla' \mu' + \sigma' S' \nabla' T').\end{aligned} \tag{6.13}$$

Comparing Eqs. (6.8) and (6.12), (6.11) and (6.13), the transformed thermal conductivity κ', electrical conductivity σ', and Seebeck coefficient S' in the coupled thermoelectric field can be written as

$$\begin{aligned}\kappa'(r') &= \frac{\mathsf{A}\kappa\mathsf{A}^{\mathrm{tr}}}{\det \mathsf{A}} \\ \sigma'(r') &= \frac{\mathsf{A}\sigma\mathsf{A}^{\mathrm{tr}}}{\det \mathsf{A}} \\ S'(r') &= \mathsf{A}^{-\mathrm{tr}} S \mathsf{A}^{\mathrm{tr}}.\end{aligned} \tag{6.14}$$

By designing the coordinate transformation and substituting it into the Jacobian matrix to obtain the transformed rules, the spatial function adjustment of the thermal field and electric field can be realized.

6.2.3 Temperature-Dependent Transformation Thermoelectrics

Nonlinear materials open new avenues in material design and functional deployment. Introducing nonlinearity in thermal metamaterial designs expands the scope for modifying thermal field functions. Transitioning from linear to nonlinear transformation theories across diverse physical fields enhances flexibility and adaptability in complex real-world scenarios. In the nonlinear approach, one can either consider transformations that are temperature-dependent or independent, juxtaposed with temperature-dependent background parameters. In the realm of the thermoelectric effect, characterized by the Seebeck coefficient, the structure of the governing equation aligns with Eq. (6.3). It considers the temperature-dependent thermal conductivity $\kappa(T)$, electrical conductivity $\sigma(T)$, and Seebeck coefficient $S(T)$. Notably, even with temperature changes, these equations maintain their structural integrity during coordinate changes, giving rise to the concept of temperature-dependent transformation thermoelectricity [58]. As per this theory, the transformation rules manifest as

$$\begin{aligned} \kappa'(T') &= \frac{\mathsf{A}\kappa(T)\mathsf{A}^{\mathrm{tr}}}{\det \mathsf{A}} \\ \sigma'(T') &= \frac{\mathsf{A}\sigma(T)\mathsf{A}^{\mathrm{tr}}}{\det \mathsf{A}} \\ S'(T') &= \mathsf{A}^{-\mathrm{tr}} S(T)\mathsf{A}^{\mathrm{tr}}. \end{aligned} \tag{6.15}$$

where $\kappa(T)$, $\sigma(T)$, $S(T)$ are the pre-transformation parameters that are the temperature-dependent background parameters. The transformed parameters $\kappa'(T')$, $\sigma'(T')$, $S'(T')$ are related to temperature and the transformed coordinates. The temperature-dependent transformation theory also applies to the decoupling thermoelectric field, corresponding to the coupled thermoelectric field at $S(T) = 0$.

In essence, both decoupled and coupled thermoelectric fields maintain their structural integrity in coordinate transformations, irrespective of the temperature sensitivity of the background parameters. This means transformation theories, both temperature-dependent and independent, apply seamlessly to these fields. Thermal and electric fields can be designed to achieve specific tasks by using coordinate transformations. For example, cloak transformations can be embedded into Eqs. (6.2), (6.14), and (6.15) to manifest thermal and electric cloaking, granting dual-field control in diverse settings. Transformation theory thus paves the way for a multitude of functionalities, such as sensors, concentrators, rotators, and camouflages.

6.2.4 Functional Realization of Thermal and Electric Fields

In practical applications, the search for anisotropic thermoelectric materials required by transformation theory poses a challenge. Therefore, in the realm of thermoelectric metamaterials, the effective medium theory and scattering cancellation theory

are commonly employed. To begin with, let's discuss the functionality of decoupled thermoelectric fields. An experimental realization of a thermal and electric concentrator was achieved by employing the effective medium theory [41]. In this proposed configuration, the concentrator shell comprises wedges made of two different materials, arranged alternately to form an annulus. Similarly, different functions can be attained for electric and thermal fields. Simultaneous thermal concentration and electric cloaking were accomplished by embedding a mixture of various shapes and materials within the host medium [39]. Additionally, an invisible sensor capable of sensing and cloaking thermal and electric fields simultaneously was proposed and realized [40]. Rich composite materials bring new life to functional designs. Controlling colloidal particles in soft matter enables the control of the properties of electric and magnetic fields [59–61]. Similarly, composite thermal cloak shells can be realized by distributing non-spherical nanoparticles of different shapes and volume fractions along the radius of the cloak [37]. The effective electric and thermal conductivity, calculated using the effective medium theory, was found to satisfy the cloaking requirements derived from transformation theory [37]. Furthermore, thermal and electric cloaks were experimentally realized in a bilayer structure designed based on scattering cancellation theory [38].

Transformation theory also provides insights into achieving fundamental functions such as cloaking, concentration, and rotation in coupled thermoelectric fields [58, 62]. To address the challenge of preparing coupled thermoelectric metamaterials with parameters required by transformation theory, a bilayer structure based on the generalized scattering-cancellation method has been developed, effectively reducing the difficulty [63]. Practical applications in coupled thermoelectric fields have been proposed, leveraging the temperature-dependent transformation theory [58]. Firstly, a switchable thermoelectric device has been introduced, capable of adapting to ambient temperature by switching between cloak and concentrator modes. Secondly, an improved thermoelectric cloak has been devised to maintain a nearly constant internal temperature. In coupled thermoelectric fields, independent control of thermal and electric fields is challenging due to coupling terms, limiting the flexible control of functions. However, this challenge can be overcome through a general computational scheme that designs composite materials based on the principles of simple circuit theory, enabling enhanced or suppressed current and thermal current in the desired direction [64].

6.3 Spatiotemporal Thermoelectric Metamaterials

6.3.1 Spatiotemporal Efficient Medium Theory

For enhanced functionality in thermoelectric metamaterials, it's imperative to explore strategies beyond just the temperature-dependent transformation theory. A notable approach focuses on tweaking the geometric configurations of the metamaterials. Yet,

managing multiple physical fields in tandem is complex, primarily due to the intricacies of adjusting various parameters simultaneously. To address this, spatiotemporal multiphysics metamaterials are introduced. This approach extends the available degrees of freedom, facilitating more precise functional adjustments [57]. The ambition is to craft a singular device, versatile in housing numerous functions for both thermal and electric fields, whilst permitting ongoing function switching. A typical combination in metamaterial functionality is the simultaneous realization of thermal cloaking and electric concentration. This dual capability is achievable through spatiotemporal multiphysics metamaterials designed as rotatable checkerboards. As illustrated in Fig. 6.1a, b, these checkerboard configurations incorporate either two or four isotropic materials. These materials play a pivotal role in dictating the potential function combinations for thermal and electric fields. By systematically rotating the even-numbered layers of the checkerboard, one can achieve dynamic functional adaptability. The inherent geometry of the structure defines the specific functions exhibited during this rotation. By expertly controlling the spatial arrangement and rotation time of the checkerboard components, one can finely tune both thermal and electric fields.

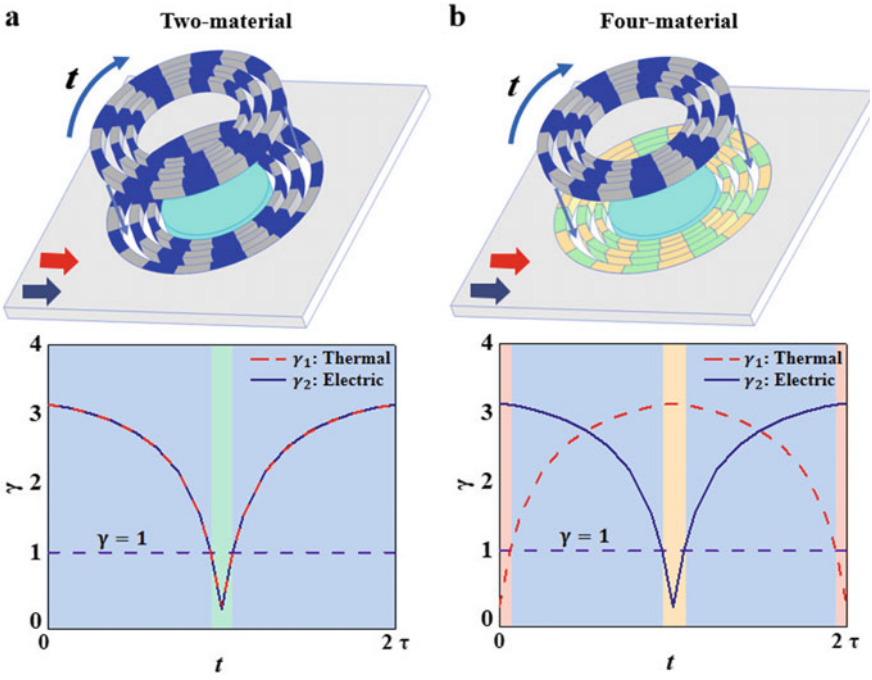

Fig. 6.1 Multifunctional devices for decoupled thermoelectric fields. Concept of spatiotemporal multiphysics metamaterials. The two-material-based and four-material-based checkerboard structures are shown in **a** and **b**, respectively. By rotating the even-numbered layers at a constant angular speed, the heat and electric currents in the central region can be altered, allowing for continuous and seamless function adjustment. (from Ref. [57], licensed under CC-BY 4.0)

The checkerboard's effective thermal and electric conductivities determines the thermal and electric currents in the central sector. Building upon the Keller theorem [65] and the effective medium theory [66], the checkerboard's effective thermal and electrical conductivities in polar coordinates are given by

$$\kappa_r \kappa_\theta = \kappa_1 \kappa_2, \quad \sigma_r \sigma_\theta = \sigma_1 \sigma_2, \tag{6.16}$$

where κ_r (σ_r) and κ_θ (σ_θ) represent the effective radial and tangential thermal (electric) conductivities. κ_1 (σ_1) and κ_2 (σ_2) denote the thermal (electric) conductivities of the two materials constituting the checkerboard. It's to note that $\kappa_1\kappa_2 = \kappa_r\kappa_\theta = \kappa_b^2$ ($\sigma_1\sigma_2 = \sigma_r\sigma_\theta = \sigma_b^2$), meaning the effective product of the radial and tangential thermal (electrical) conductivities equals the square of the background thermal (electrical) conductivity. This ensures that the background heat (electric) flow remains undisturbed. The ratio κ_r/κ_θ (σ_r/σ_θ) dictates the heat (electric) flow distribution within the central region.

If $\kappa_r/\kappa_\theta < 1$ ($\sigma_r/\sigma_\theta < 1$), heat (electric) flow diverts around the central zone, leading to thermal (electric) cloaking. A ratio of zero produces an ideal cloaking effect. For $\kappa_r/\kappa_\theta = 1$ ($\sigma_r\sigma_\theta = 1$), the heat (electric) flow remains consistent within the center, resulting in thermal (electric) sensing. When $\kappa_r/\kappa_\theta > 1$ ($\sigma_r/\sigma_\theta > 1$), heat (electric) flow accumulates in the central region, achieving thermal (electric) concentration. Thus, forecasting the spatiotemporal function primarily hinges on determining the effective radial and tangential thermal (electric) conductivities of the checkerboard design.

A checkerboard structure can be composed of either two or four distinct materials. Figure 6.2a depicts an exemplary configuration utilizing two isotropic materials, each characterized by constant thermal (κ) and electrical (σ) conductivities. In this structure, even-numbered layers rotate clockwise while the odd-numbered layers remain stationary. The fixed boundary is highlighted by a red dashed line in Fig. 6.2a, with the evolving boundary indicated by a rotating brown dashed line. The term $\Delta\theta$ represents the central angle for a single phase unit, and τ denotes the duration needed for the even-numbered layers to complete a rotation of $\Delta\theta$. The angular displacement, represented by $\theta(t)$, follows the equation $\theta(t) = \Delta\theta t/\tau$, where t indicates the time elapsed. After a rotation spanning 2τ, the checkerboard returns to its initial position. Owing to this periodic behavior, the analysis focuses on one rotational cycle. By modulating the angle $\theta(t)$, the sector associated with the central angle $\Delta\theta$ can be segmented into areas displaying both uniform and alternating phases.

Within the rotatable checkerboard design, electric and thermal conductivities can be modulated independently, facilitating separate control of electric and thermal flows. This is evident from Fig. 6.2c. Due to the analogous variations in thermal and electric conductivities in the two-material checkerboard setup, theoretical analysis predominantly centers on thermal conductivity. The subsequent analysis for effective electric conductivity is achieved by substituting κ_1 and κ_2 with σ_1 and σ_2.

The homogeneous phase is characterized by units made of the same materials, with thermal and electrical conductivities designated as either (κ_1, σ_1) or (κ_2, σ_2). Conversely, the staggered phase integrates two interleaved isotropic material units.

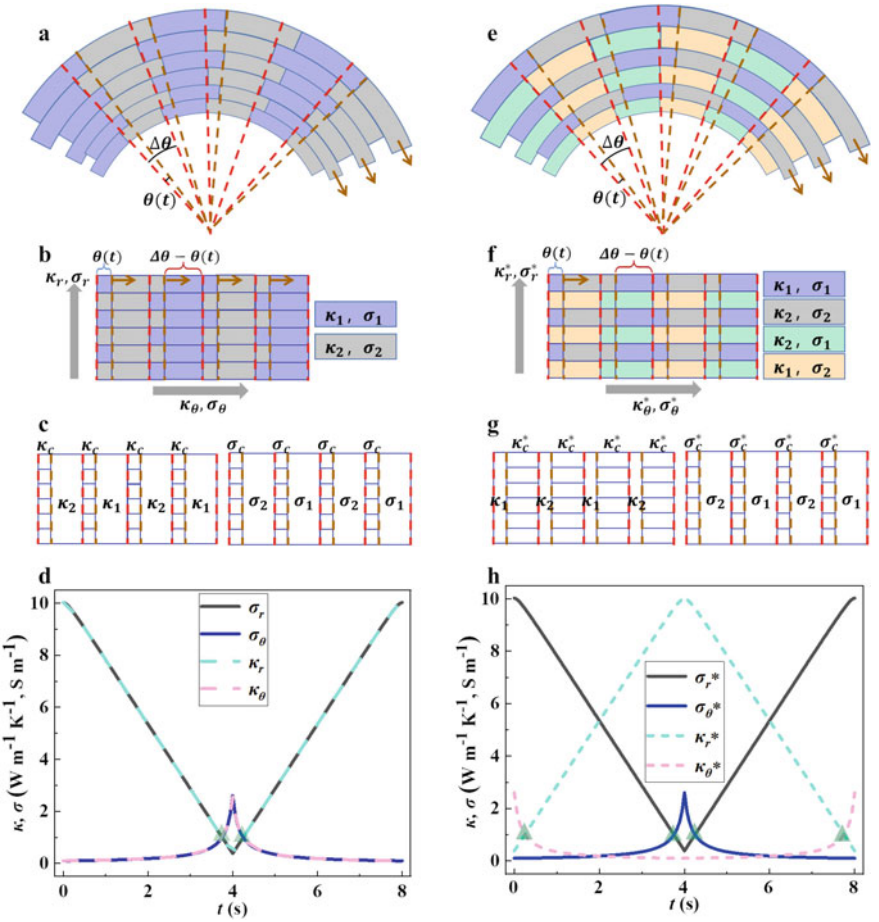

Fig. 6.2 Schematic diagram of partial structure of space-time thermoelectric metamaterial. **a** A checkerboard structure composed of two materials. Brown arrows depict the rotation direction of even layers. **b** An expanded version of the structure from **a**, showcasing a multilayered configuration. **c** Individual presentation of thermal and electric conductivities. **d** Theoretical analyses correlating to the structure described in **a**. **e**–**h** Structures analogous to **a**–**d**, with the key difference being that the checkerboard design incorporates four materials. Functions underscored by green triangles denote sensing. (from Ref. [57], licensed under CC-BY 4.0)

Over the duration 2τ, the central angle corresponding to the staggered phases is defined as

$$\theta_s(t) = \begin{cases} \frac{\Delta\theta}{\tau}t, & 0 < t < \tau \\ 2\Delta\theta - \frac{\Delta\theta}{\tau}t. & \tau < t < 2\tau \end{cases} \tag{6.17}$$

In the timeframe $0 < t < \tau$, the angle $\theta_s(t)$ expands, whereas in $\tau < t < 2\tau$, it contracts. This results in the checkerboard configuration reverting to its original

state at 2τ, devoid of any staggered phase. The effective thermal conductivity of these staggered phases is determined by both the material and geometric attributes of their building blocks [67]. The staggered phases' geometric parameter evolves with time and is articulated as $\eta(t) = \ln(r_{i+1}/r_i)/\theta_s(t)$, where r_i signifies the radius of the ith layer. And the shape parameter $\eta = \ln(r_{i+1}/r_i)/\Delta\theta$ is dictated by the geometric attributes of the checkerboard structure and is time-independent. In polar coordinates, the effective thermal conductivity κ_c of the staggered phases can be divided into radial thermal conductivity κ_{cr} and tangential thermal conductivity $\kappa_{c\theta}$, respectively,

$$\kappa_{cr} = \begin{cases} \dfrac{\sqrt{\kappa_1\kappa_2}}{(1-\frac{2\sqrt{\kappa_1\kappa_2}}{\kappa_1+\kappa_2})(\frac{t}{\eta\tau}-1)+1}, & 0 \le t \le \eta\tau \\ \sqrt{\kappa_1\kappa_2}\left[(1-\frac{2\sqrt{\kappa_1\kappa_2}}{\kappa_1+\kappa_2})(\frac{\eta\tau}{t}-1)+1\right], & \eta\tau \le t \le \tau \\ \sqrt{\kappa_1\kappa_2}\left[(1-\frac{2\sqrt{\kappa_1\kappa_2}}{\kappa_1+\kappa_2})(\frac{\eta\tau}{2\tau-t}-1)+1\right], & \tau \le t \le (2-\eta)\tau \\ \dfrac{\sqrt{\kappa_1\kappa_2}}{(1-\frac{2\sqrt{\kappa_1\kappa_2}}{\kappa_1+\kappa_2})(\frac{2\tau-t}{\eta\tau}-1)+1}, & (2-\eta)\tau \le t \le 2\tau \end{cases}$$

$$\kappa_{c\theta} = \begin{cases} \sqrt{\kappa_1\kappa_2}\left[(1-\frac{2\sqrt{\kappa_1\kappa_2}}{\kappa_1+\kappa_2})(\frac{t}{\eta\tau}-1)+1\right], & 0 \le t \le \eta\tau \\ \dfrac{\sqrt{\kappa_1\kappa_2}}{(1-\frac{2\sqrt{\kappa_1\kappa_2}}{\kappa_1+\kappa_2})(\frac{\eta\tau}{t}-1)+1}, & \eta\tau \le t \le \tau \\ \dfrac{\sqrt{\kappa_1\kappa_2}}{(1-\frac{2\sqrt{\kappa_1\kappa_2}}{\kappa_1+\kappa_2})(\frac{\eta\tau}{2\tau-t}-1)+1}, & \tau \le t \le (2-\eta)\tau \\ \sqrt{\kappa_1\kappa_2}\left[(1-\frac{2\sqrt{\kappa_1\kappa_2}}{\kappa_1+\kappa_2})(\frac{2\tau-t}{\eta\tau}-1)+1\right]. & (2-\eta)\tau \le t \le 2\tau \end{cases} \tag{6.18}$$

Throughout the entire 2τ duration, the effective radial and tangential thermal conductivities of the staggered phase are defined by segmentation functions, displaying a temporal variation. The effective thermal conductivity of the interleaved phase is closely tied to the checkerboard unit's shape parameter, η, with outcomes from Eq. (6.18) applying for $\eta \le 1$. For instances where $\eta > 1$, the contradictory time range in the piecewise function of Eq. (6.18) can be omitted. It's noteworthy that the staggered phase's thermal conductivity, represented as κ_c, shows distinct values in the radial versus tangential directions.

The transformation of the fan-shaped configuration in Fig. 6.2a into a multi-layer arrangement as depicted in Fig. 6.2b involves the incorporation of staggered and homogeneous phases. The lateral thermal conductivity of this multi-layer structure corresponds to the tangential thermal conductivity of the initial fan-shaped design,

while the longitudinal thermal conductivity aligns with the radial thermal conductivity of the original structure. Employing a stepwise application of the effective medium theory enables an approximation of the multi-layer structure, thus yielding the effective radial and tangential thermal conductivities for the rotatable checkerboard arrangement.

A strategic approach combines staggered and homogeneous phases to form a core unit. As a result, two distinct combined units, labeled as unit A and unit B, are defined: the former pairs κ_c with κ_1, and the latter associates κ_c with κ_2. Leveraging the effective medium theory, the radial and tangential effective thermal conductivity for these units can be derived as

$$\begin{aligned} \kappa_{Ar} &= \tfrac{\theta_s(t)}{\Delta\theta}\kappa_{cr} + \tfrac{\Delta\theta-\theta_s(t)}{\Delta\theta}\kappa_2,\ \kappa_{Br} = \tfrac{\theta_s(t)}{\Delta\theta}\kappa_{cr} + \tfrac{\Delta\theta-\theta_s(t)}{\Delta\theta}\kappa_1. \\ \tfrac{1}{\kappa_{A\theta}} &= \tfrac{\theta_s(t)}{\Delta\theta}\tfrac{1}{\kappa_{c\theta}} + \tfrac{\Delta\theta-\theta_s(t)}{\Delta\theta}\tfrac{1}{\kappa_2},\ \tfrac{1}{\kappa_{B\theta}} = \tfrac{\theta_s(t)}{\Delta\theta}\tfrac{1}{\kappa_{c\theta}} + \tfrac{\Delta\theta-\theta_s(t)}{\Delta\theta}\tfrac{1}{\kappa_1}. \end{aligned} \tag{6.19}$$

where $\theta_s(t)/\Delta\theta$ represents the staggered phase's proportion within a unit, while $(\Delta\theta - \theta_s(t))/\Delta\theta$ is indicative of the homogeneous phase. With this understanding, the entire structure can be visualized as a multi-layered arrangement with alternating units. By applying the effective medium theory

$$\kappa_r = \frac{\kappa_{Ar} + \kappa_{Br}}{2},\ \frac{1}{\kappa_\theta} = \frac{1}{2\kappa_{A\theta}} + \frac{1}{2\kappa_{B\theta}}. \tag{6.20}$$

Both units A and B in the checkerboard layout share equivalent central angles. By solving Eqs.(6.18)–(6.20), the radial and tangential effective thermal conductivities for a rotatable checkerboard structure with two isotropic materials can be expressed as

$$\kappa_r = \begin{cases} \dfrac{t}{\tau}\dfrac{\sqrt{\kappa_1\kappa_2}}{(1-\frac{2\sqrt{\kappa_1\kappa_2}}{\kappa_1+\kappa_2})(\frac{t}{\eta\tau}-1)+1} + (\frac{1}{2}-\frac{t}{2\tau})(\kappa_1+\kappa_2), & 0 \le t \le \eta\tau \\ \dfrac{t}{\tau}\sqrt{\kappa_1\kappa_2}\left[(1-\dfrac{2\sqrt{\kappa_1\kappa_2}}{\kappa_1+\kappa_2})(\eta\dfrac{\tau}{t}-1)+1\right] + (\frac{1}{2}-\frac{t}{2\tau})(\kappa_1+\kappa_2), & \eta\tau \le t \le \tau \\ (2-\dfrac{t}{\tau})\sqrt{\kappa_1\kappa_2}\left[(1-\dfrac{2\sqrt{\kappa_1\kappa_2}}{\kappa_1+\kappa_2})(\dfrac{\eta\tau}{2\tau-t}-1)+1\right] + (\dfrac{t}{2\tau}-\dfrac{1}{2})(\kappa_1+\kappa_2), & \tau \le t \le (2-\eta)\tau \\ (2-\dfrac{t}{\tau})\dfrac{\sqrt{\kappa_1\kappa_2}}{(1-\frac{2\sqrt{\kappa_1\kappa_2}}{\kappa_1+\kappa_2})(\frac{2\tau-t}{\eta\tau}-1)+1} + (\dfrac{t}{2\tau}-\dfrac{1}{2})(\kappa_1+\kappa_2), & (2-\eta)\tau \le t \le 2\tau \end{cases}$$

$$\kappa_\theta = \begin{cases} \dfrac{\kappa_1\kappa_2}{\frac{t}{\tau}\frac{\sqrt{\kappa_1\kappa_2}}{(1-\frac{2\sqrt{\kappa_1\kappa_2}}{\kappa_1+\kappa_2})(\frac{t}{\eta\tau}-1)+1} + (\frac{1}{2}-\frac{t}{2\tau})(\kappa_1+\kappa_2)}, & 0 \le t \le \eta\tau \\ \dfrac{\kappa_1\kappa_2}{\sqrt{\kappa_1\kappa_2}\frac{t}{\tau}\left[(1-\frac{2\sqrt{\kappa_1\kappa_2}}{\kappa_1+\kappa_2})(\frac{\eta\tau}{t}-1)+1\right] + (\frac{1}{2}-\frac{t}{2\tau})(\kappa_1+\kappa_2)}, & \eta\tau \le t \le \tau \\ \dfrac{\kappa_1\kappa_2}{(2-\frac{t}{\tau})\sqrt{\kappa_1\kappa_2}\left[(1-\frac{2\sqrt{\kappa_1\kappa_2}}{\kappa_1+\kappa_2})(\frac{\eta\tau}{2\tau-t}-1)+1\right] + (\frac{t}{2\tau}-\frac{1}{2})(\kappa_1+\kappa_2)}, & \tau \le t \le (2-\eta)\tau \\ \dfrac{\kappa_1\kappa_2}{(2-\frac{t}{\tau})\frac{\sqrt{\kappa_1\kappa_2}}{(1-\frac{2\sqrt{\kappa_1\kappa_2}}{\kappa_1+\kappa_2})(\frac{2\tau-t}{\eta\tau}-1)+1} + (\frac{t}{2\tau}-\frac{1}{2})(\kappa_1+\kappa_2)}. & (2-\eta)\tau \le t \le 2\tau \end{cases}$$

(6.21)

Replacing κ_1 and κ_2 with σ_1 and σ_2 can obtain the radial and tangential effective conductivities of the rotatable checkerboard structure composed of two isotropic materials.

Figure 6.2d describes the time variation of the effective thermal conductivity and electrical conductivity of the rotatable checkerboard structure within a single period 2τ, where $\tau = 4$ s. This checkerboard design consists of two materials characterized by parameters ($\kappa_1 = 20\ \mathrm{Wm^{-1}K^{-1}}, \sigma_1 = 20\ \mathrm{Sm^{-1}}$) and ($\kappa_2 = 0.05\ \mathrm{Wm^{-1}K^{-1}}$, $\sigma_2 = 0.05\ \mathrm{Sm^{-1}}$). Furthermore, the background and central regions exhibit thermal and electric conductivities of $\kappa_b = 1\ \mathrm{Wm^{-1}K^{-1}}$ and $\sigma_b = 1\ \mathrm{Sm^{-1}}$, respectively. The outcomes displayed in Fig. 6.2d are computed utilizing Eq. (6.21). In the figure, the thermal and electric conductivities are represented by dashed and solid lines, respectively. The convergence of these two lines signifies the fulfillment of the same equation for both thermal and electric conductivities. Distinct points in time, specifically $t = 3.75$ s and $t = 4.25$ s, showcase the equivalence of the effective radial and tangential thermal (electric) conductivities, thereby elucidating the system's thermal (electric) sensing capability. In the time intervals $0\ \mathrm{s} < t < 3.75$ s and $4.25\ \mathrm{s} < t < 8$ s, the radial thermal (electric) conductivity surpasses its tangential counterpart, establishing the scenario $\kappa_r/\kappa_\theta > 1$ ($\sigma_r/\sigma_\theta > 1$) and illustrating the thermal (electric) concentrating function. Conversely, during $3.75\ \mathrm{s} < t < 4.25$ s, the radial thermal (electric) conductivity dips below its tangential equivalent, manifesting as $\kappa_r/\kappa_\theta < 1$ ($\sigma_r/\sigma_\theta < 1$) and effectively demonstrating the thermal (electric) cloaking function. The alignment between thermal and electric fields within these two-material-based checkerboard structures yields congruent functions that remain adjustable over time. This adaptability results in the creation of spatiotemporal multiphysics metamaterials comprised of just two materials, achieving three distinctive functional combinations simultaneously.

The thermal and electric functions can be toggled based on distinct rules. As depicted in Fig. 6.2e, a checkerboard pattern comprises four isotropic materials characterized by parameters (κ_1, σ_1), (κ_1, σ_2), (κ_2, σ_1), and (κ_2, σ_2). It's noteworthy that the electric conductivities for checkerboard configurations, whether assembled from two or four isotropic materials (as shown in Fig. 6.2c, g), exhibit the same variations. This observation leads to the conclusions $\sigma_r^* = \sigma_r$ and $\sigma_\theta^* = \sigma_\theta$. A notable difference emerges concerning the thermal conductivity when comparing the four-material-based checkerboard to its two-material analog. As the even-numbered layers rotate by an angle $\theta(t)$, the central angle defining the staggered region is represented as $\theta_s^*(t)$. The shape parameters for the staggered area in the four-material checkerboard are redefined as

$$\theta_s^*(t) = \begin{cases} \Delta\theta - \frac{\Delta\theta}{\tau}t, & 0 < t < \tau \\ \frac{\Delta\theta}{\tau}t - \Delta\theta. & \tau < t < 2\tau \end{cases} \tag{6.22}$$

In the calculation of the checkerboard structure of two materials, replacing $\theta_s(t)$ with $\theta_s^*(t)$, the effective thermal conductivity of the checkerboard structure of four materials can be obtained.

Figure 6.2h visually illustrates the temporal progression of effective thermal and electric conductivities within the four-material-based checkerboard structure. This

configuration incorporates materials with attributes denoted as (κ_1, σ_1), (κ_1, σ_2), (κ_2, σ_1), and (κ_2, σ_2). Their respective values are $\kappa_1 = 20\,\mathrm{Wm^{-1}K^{-1}}$, $\sigma_1 = 20\,\mathrm{Sm^{-1}}$, $\kappa_2 = 0.05\ \mathrm{Wm^{-1}K^{-1}}$, and $\sigma_2 = 0.05\ \mathrm{Sm^{-1}}$. The theoretical results presented in Fig. 6.2h, analytical assessments indicate that the four-material-based checkerboard structure supports five unique functional combinations. These functions include: Thermal sensing with electric concentrating at $t = 0.25$ s and $t = 7.75$ s. Thermal concentrating paired with electric sensing at $t = 3.75$ s and $t = 4.25$ s. Thermal cloaking with electric concentrating before 0.25 s and after 7.75 s. Thermal concentrating combined with electric cloaking between 3.75 s and 4.25 s. At all other instances, thermal and electric concentrating coexist. In summary, spatiotemporal multiphysics metamaterials comprising four materials have the versatility to manifest these five distinct functional combinations.

6.3.2 *Multi-functional Regulation of Thermal and Electric Field*

The dynamics of thermal and electric fields within a rotatable checkerboard structure can be precisely forecasted using the spatiotemporal effective medium theory. For experimental corroboration of the functionalities inherent to spatiotemporal multiphysics metamaterials, finite element simulations are conducted. The initial focus is on a rotatable checkerboard setup made of two isotropic materials. This structure takes the form of a hollow cylinder, segmented into 15 sub-layers. Each of these is further partitioned into 24 fan-shaped unit cells, which alternate between the two materials. A distinguishing feature is that the even-numbered layers of this configuration rotate clockwise as time progresses, as illustrated in Fig. 6.2a. To determine the radius r_i of each layer, the equation $\ln(r_{i+1}/r_i) = \eta\Delta\theta$ is employed, where $\eta = 1/\sqrt{10}$, the innermost layer has a diameter of $r_1 = 4$ cm, and the central angle per unit is given by $\Delta\theta = 2\Pi/24$. This checkerboard construct is set within a square boundary with 45 cm sides, and thermal impedance between units is neglected. Temperature and potential gradients applied at the boundaries generate heat and electric currents throughout. The left boundary holds a temperature and potential of 373 K and 10 mV, respectively, while the right boundary remains at 273 K and 0 mV. Importantly, the overall thermal and electric conductivities of this spatiotemporal metamaterial coincide with theoretical anticipations. With a rotation duration of $2\tau = 8$ s, the system undergoes two full rotations. The outcomes of these simulations corroborate the theoretical projections, confirming the functional viability of spatiotemporal multiphysics metamaterials.

The introduced theory offers a predictive framework for the behaviors of thermal and electric fields at any specific time. Using just two materials, spatiotemporal multiphysics metamaterials can manifest three unique functional combinations, as highlighted in Fig. 6.3. For demonstration, three time snapshots–corresponding to different functional combinations within the checkerboard structure–were chosen for

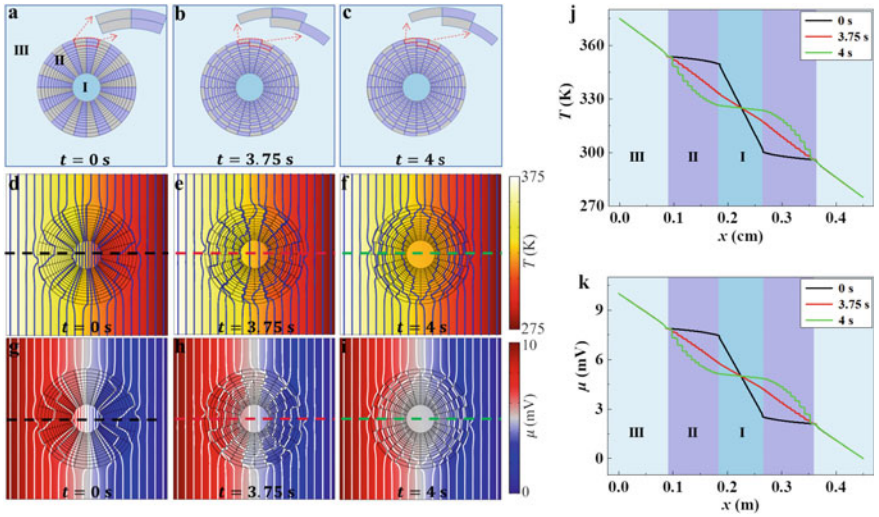

Fig. 6.3 Illustrative diagrams and simulation outcomes showcasing a checkerboard structure grounded in two distinct materials. In panels **a**–**c**, the structures at time instances $t = 0$ s, $t = 3.75$ s, and $t = 4$ s. Here, I, II, and III denote the central, checkerboard, and background regions, respectively. Correspondingly, panels **d**–**f** exhibit simulated thermal field results, with blue lines tracing isotherms. Furthermore, panels **g**–**i** present simulation findings of the electric field, with white lines indicating equipotential lines. Notably, panels **j** and **k** capture data from the simulation outcomes' horizontal centerline in **d**–**f** and **g**–**i**. Particularly, in region III, the three temperature (or potential) lines converge, as depicted. (from Ref. [57], licensed under CC-BY 4.0)

simulation: $t = 0$ s, $t = 3.75$ s, and $t = 4$ s. In the schematic presented in Fig. 6.2d, these instances represent concentration, sensing, and cloaking functions, respectively.

Regardless of the time point, the background's isotherms and equipotential lines remain consistent, indicating that the background heat and electric currents are undisturbed. At the initial time mark, the even-numbered layers are static, resulting in a checkerboard pattern made of alternating, uniform fan-shaped segments. Simulation outcomes manifest the phenomena of thermal and electric concentration, where the heat and electric currents focus on the central region without perturbing the background. As seen in Fig. 6.3j, k, the central area displays heightened temperature and electric potential gradients relative to the background, confirming the concentration effects of both thermal and electric fields.

Transitioning to $t = 3.75$ s, the temperature and potential gradients in the central region replicate those of the background, showcasing thermal and electric sensing functionalities. When $t = 4$ s, the entire checkerboard structure assumes a composition of alternating materials. The simulation outcomes depict the absence of isotherms and equipotential lines within the central region. Temperature and potential gradients in this zone approach zero, confirming the achievement of thermal and electric cloaking. Refer to Fig. 6.3j, k. It's noteworthy that the isotherms and equipotential lines in region II of the spatiotemporal metamaterial at $t = 4$ s exhibit more

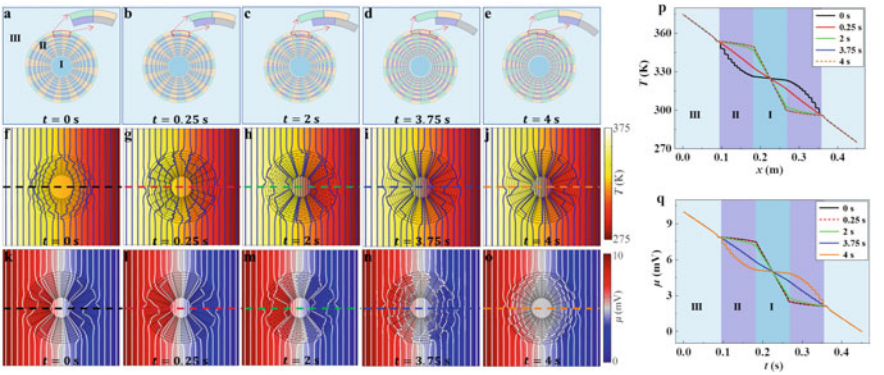

Fig. 6.4 Schematic diagrams and simulation results of a four-material-based checkerboard structure. Panels **a**–**e** showcase the structures at time points $t = 0$ s, $t = 0.25$ s, $t = 2$ s, $t = 3.75$ s, and $t = 4$ s. Panels **f**–**j** exhibit simulated thermal field results, while panels **k**–**o** present simulation outcomes of the electric field. Panels **p** and **q** present data derived from the simulation outcomes' horizontal centerline in **f**–**j** and **k**–**o**. Notably, within region III, the five temperature (or potential) lines converge, as illustrated. (from Ref. [57], licensed under CC-BY 4.0)

irregularities compared to those at $t = 3.75$ s. This phenomenon can be attributed to the absence of a uniform region in the alternating structure at $t = 4$ s. Continuous time adaptation of thermal and electrical functions is achieved by using a rotatable checkerboard structure. Consequently, the simulation verifies the reliability of the theoretical framework, effectively showcasing that spatiotemporal multiphysics metamaterials composed of just two materials have the capacity to achieve three diverse functional combinations.

Thermal and electric fields can exhibit varying functionalities. Introducing a unique checkerboard design with four isotropic materials, parameters are aligned with those depicted in Fig. 6.2h. The simulation outcomes at key moments–0 s, 0.25 s, 2 s, 3.75 s, and 4 s–are showcased in Fig. 6.4. The left boundary conditions for temperature and potential are fixed at 373 K and 10 mV, respectively, while the right boundary maintains 273 K and 0 mV. Significantly, the background remains consistently unperturbed in terms of heat and electric flow.

At the outset, $t = 0$ s, the heat flow avoids the central region, while electric currents converge, embodying thermal cloaking alongside electric concentration. Conversely, at $t = 4$ s, electric currents bypass the core as the heat flow concentrates, signifying electric cloaking with thermal concentration. The time frame of $t = 0.25$ s demonstrates thermal sensing paired with electric concentration, and $t = 3.75$ s showcases thermal concentration coupled with electric sensing. Crucially, the simulated results resonate with theoretical expectations. By $t = 2$ s, the even-numbered layers have rotated by half of the unit's central angle, as illustrated in Fig. 6.2h. As a result, radial thermal (and electric) conductivity surpasses its tangential counterpart. Both heat and electric currents center on the core region, representing concurrent thermal and electric concentration. As supported by Fig. 6.2h, the phase from 0.25 s to

3.75 s exemplifies concurrent thermal and electric concentration. This demonstrates that spatiotemporal multiphysics metamaterials built from four distinct materials can achieve five functional combinations.

6.4 Conclusions and Outlook

In this chapter, we have introduced an innovative approach to designing spatially modulated thermoelectric metamaterials, grounded in the principles of transformation theory. We have explored various transformation rules encompassing coupled thermoelectric fields, decoupled thermoelectric fields, and nonlinear thermoelectric fields. Through the strategic application of spatial transformations, we have successfully achieved the fusion of thermal and electric fields into a single unified function.

To amplify the functionality and versatility of these metamaterials, we have put forth the concept of a spatiotemporal multiphysics metamaterial employing a rotatable checkerboard structure. This structure unlocks the capability for simultaneous modulation of thermal and electric fields. By introducing a temporal dimension, specifically encapsulated in the rotation time, we enable a continuous and dynamic control over effective thermal and electric conductivities. This temporal manipulation facilitates seamless transitions between diverse functions of thermal and electric fields, fostering enhanced adaptability and performance.

The spatiotemporal checkerboard structure, whether composed of two or four materials, not only offers three or five distinct function combinations, respectively, but also showcases remarkable potential for advanced applications. As we look forward, the integration of these principles with emerging technologies and materials could open up new avenues for efficient energy management, multifunctional devices, and transformative solutions across multiple industries. The interplay between spatial and temporal dimensions within metamaterials presents a promising frontier for researchers and engineers alike, guiding us towards groundbreaking innovations in the realm of functional materials and device design.

References

1. Ye, C., Huang, J.P.: Non-classical oscillator model for persistent fluctuations in stock markets. Phys. A **387**, 1255 (2008)
2. Liu, L., Wei, J.R., Zhang, H.S., Xin, J.H., Huang, J.P.: A statistical physics view of pitch fluctuations in the classical music from Bach to Chopin: evidence for Scaling. PLoS ONE **8**, e58710 (2013)
3. Gao, M.Y., Wang, P., Jiang, L.L., Wang, B.W., Yao, Y., Liu, S., Chu, D.W., Cheng, W.L., Lu, Y.R.: Power generation for wearable systems. Energy Environ. Sci. **14**, 2114–2157 (2021)
4. Fan, S.H., Li, W.: Photonics and thermodynamics concepts in radiative cooling. Nat. Photon. **16**, 182–190 (2022)
5. Wang, C.Y., Vangelatos, Z., Grigoropoulos, C.P., Ma, Z.: Micro-engineered architected metamaterials for cell and tissue engineering. Mater. Today Adv. **13**, 100206 (2022)

6. Ma, Z., Zhao, D., She, C., Yang, Y., Yang, R.: Personal thermal management techniques for thermal comfort and building energy saving. Mater. Today Phys. **20**, 100465 (2021)
7. Xu, L., Chen, H.Y.: Transformation metamaterials. Adv. Mater. **33**, 2005489 (2021)
8. Martinez, F., Maldovan, M.: Metamaterials: optical, acoustic, elastic, heat, mass, electric, magnetic, and hydrodynamic cloaking. Mater. Today Phys. **27**, 100819 (2022)
9. Xu, L.J., Yang, S., Huang, J.P.: Thermal theory for heterogeneously architected structure: fundamentals and application. Phys. Rev. E **98**, 052128 (2018)
10. Shi, Y.Z., Song, Q.H., Toftul, I., Zhu, T.T., Yu, Y.F., Zhu, W.M., Tsai, D.P., Kivshar, Y., Liu, A.Q.: Optical manipulation with metamaterial structures. Appl. Phys. Rev. **9**, 031303 (2022)
11. Zhang, Z.R., Huang, J.P.: Transformation plasma physics. Chin. Phys. Lett. **39**, 075201 (2022)
12. Xue, H.R., Yang, Y.H., Zhang, B.L.: Topological acoustics. Nat. Rev. Mater. **7**, 974–990 (2022)
13. Huang, J.P.: Negative refraction of phononic crystals. College Phys. **32**, 44–51 (2013)
14. Yang, S., Wang, J., Dai, G.L., Yang, F.B., Huang, J.P.: Controlling macroscopic heat transfer with thermal metamaterials: Theory, experiment and application. Phys. Rep. **908**, 1–65 (2021)
15. Shen, X.Y., Huang, J.P.: Transformation thermotics: Thermal metamaterials and their applications. Acta Physica Sinica. **65**, 178103 (2016)
16. Zhang, Z.R., Xu, L.J., Qu, T., Lei, M., Lin, Z.K., Ouyang, X.P., Jiang, J.-H., Huang, J.P.: Diffusion metamaterials. Nat. Rev. Phys. **5**, 218–235 (2023)
17. Wang, J., Dai, G.L., Huang, J.P.: Thermal metamaterial: Fundamental, application, and outlook. iScience **23**, 101637 (2020)
18. Shen, X.Y., Jiang, C.R., Li, Y., Huang, J.P.: Thermal metamaterial for convergent transfer of conductive heat with high efficiency. Appl. Phys. Lett. **109**, 201906 (2016)
19. Xu, L.J., Huang, J.P.: Active thermal wave cloak. Chin. Phys. Lett. **37**, 120501 (2020)
20. Jin, P., Liu, J.R., Xu, L.J., Wang, J., Ouyang, X.P., Jiang, J.-H., Huang, J.P.: Tunable liquid-solid hybrid thermal metamaterials with a topology transition. Proc. Natl. Acad. Sci. U.S.A. **120**, e2217068120 (2023)
21. Jin, P., Liu, J.R., Yang, F.B., Marchesoni, F., Jiang, J.-H., Huang, J.P.: In-situ simulation of thermal reality. Research **6**, 0222 (2023)
22. Yang, S., Xu, L.J., Wang, R.Z., Huang, J.P.: Full control of heat transfer in single-particle structural materials. Appl. Phys. Lett. **111**, 121908 (2017)
23. Fan, C.Z., Gao, Y.H., Gao, Y., Huang, J.P.: Apparently negative electric polarization in shaped graded dielectric metamaterials. Commun. Theor. Phys. **53**, 913–919 (2010)
24. Gao, Y., Wang, W.H., Huang, J.P.: Transformation electrics: Cloaking and rotating electric current. Commun. Theor. Phys. **61**, 517–520 (2014)
25. Park, J., Youn, J.R., Song, Y.S.: Hydrodynamic metamaterial cloak for drag-free flow. Phys. Rev. Lett. **123**, 074502 (2019)
26. Chen, M.Y., Shen, X.Y., Chen, Z., Lo, J.H.Y., Liu, Y., Xu, X.L., Wu, Y.L., Xu, L.: Realizing the multifunctional metamaterial for fluid flow in a porous medium. Proc. Natl. Acad. Sci. U.S.A. **119**, e2207630119 (2022)
27. Lei, M., Jiang, C.R., Yang, F.B., Wang, J., Huang, J.P.: Programmable all-thermal encoding with metamaterials. Int. J. Heat Mass Transfer. **207**, 124033 (2023)
28. Jin, P., Xu, L.J., Jiang, T., Zhang, L., Huang, J.P.: Making thermal sensors accurate and invisible with an anisotropic monolayer scheme. Int. J. Heat Mass Transf. **163**, 120437 (2020)
29. Xu, L.J., Yang, S., Huang, J.P.: Thermal transparency induced by periodic interparticle interaction. Phys. Rev. Appl. **11**, 034056 (2019)
30. Dai, G.L., Huang, J.P.: A transient regime for transforming thermal convection: Cloaking, concentrating and rotating creeping flow and heat flux. J. Appl. Phys. **124**, 235103 (2018)
31. Zhang, C., Cao, W.K., Yang, J., Ke, J.C., Chen, M.Z., Wu, L.T., Cheng, Q., Cui, T.J.: Multiphysical digital coding metamaterials for independent control of broadband electromagnetic and acoustic waves with a large variety of functions. ACS Appl. Mater. Interfaces. **11**, 17050–17055 (2019)
32. Zhou, Y., Chen, J., Chen, R., Chen, W.J., Fan, Z., Ma, Y.G.: Ultrathin electromagnetic-acoustic amphibious stealth coats. Adv. Opt. Mater. **8**, 2000200 (2020)

33. Li, Y., Zhu, K.J., Peng, Y.G., Li, W., Yang, T.Z., Xu, H.X., Chen, H., Zhu, X.F., Fan, S.H., Qiu, C.W.: Thermal meta-device in analogue of zero-index photonics. Nat. Mater. **18**, 48–54 (2019)
34. Xu, L.J., Dai, G.L., Huang, J.P.: Transformation multithermotics: Controlling radiation and conduction simultaneously. Phys. Rev. Appl. **13**, 024063 (2020)
35. Xu, L.J., Yang, S., Dai, G.L., Huang, J.P.: Transformation omnithermotics: Simultaneous manipulation of three basic modes of heat transfer. ES Energy Environ. **7**, 65–70 (2020)
36. Xu, L.J., Wang, J., Dai, G.L., Yang, S., Yang, F.B., Wang, G., Huang, J.P.: Geometric phase, effective conductivity enhancement, and invisibility cloak in thermal convection-conduction. Int. J. Heat Mass Transf. **165**, 120659 (2021)
37. Li, J.Y., Gao, Y., Huang, J.P.: A bifunctional cloak using transformation media. J. Appl. Phys. **108**, 074504 (2010)
38. Ma, Y.G., Liu, Y.C., Raza, M., Wang, Y.D., He, S.L.: Experimental demonstration of a multiphysics cloak: manipulating heat flux and electric current simultaneously. Phys. Rev. Lett. **113**, 205501 (2014)
39. Moccia, M., Castaldi, G., Savo, S., Sato, Y., Galdi, V.: Independent manipulation of heat and electrical current via bifunctional metamaterials. Phys. Rev. X **4**, 021025 (2014)
40. Yang, T.Z., Bai, X., Gao, D.L., Wu, L.Z., Li, B.W., Thong, J.T.L., Qiu, C.W.: Invisible sensors: simultaneous sensing and camouflaging in multiphysical fields. Adv. Mater. **27**, 7752–7758 (2015)
41. Lan, C.W., Li, B., Zhou, J.: Simultaneously concentrated electric and thermal fields using fan-shaped structure. Opt. Express **23**, 24475–24483 (2015)
42. Stedman, T., Woods, L.M.: Cloaking of thermoelectric transport. Sci. Rep. **7**, 6988 (2017)
43. Yin, S.X., Galiffi, E., Alù, A.: Floquet metamaterials. eLight **2**, 8 (2022)
44. Galiffi, E., Tirole, R., Yin, S.X., Li, H.N., Vezzoli, S., Huidobro, P.A., Silveirinha, M.G., Sapienza, R., Alù, A., Pendry, J.B.: Photonics of time-varying media. Adv. Photonics **4**, 014002 (2022)
45. Zhang, L., Chen, X.Q., Shao, R.W., Dai, J.Y., Cheng, Q., Castaldi, G., Galdi, V., Cui, T.J.: Breaking reciprocity with space-time-coding digital metasurfaces. Adv. Mater. **31**, 1904069 (2019)
46. Taravati, S., Eleftheriades, G.V.: Microwave space-time-modulated metasurfaces. ACS Photon. **9**, 305–318 (2022)
47. Chen, Z.X., Peng, Y.G., Li, H.X., Liu, J.J., Ding, Y.J., Liang, B., Zhu, X.F., Lu, Y.Q., Cheng, J.C., Alù, A.: Efficient nonreciprocal mode transitions in spatiotemporally modulated acoustic metamaterials. Sci. Adv. **7**, eabj1198 (2021)
48. Jia, Y.R., Liu, Y.M., Hu, B.L., Xiong, W., Bai, Y.C., Cheng, Y., Wu, D., Liu, X.J., Christensen, J.: Orbital angular momentum multiplexing in space-time thermoacoustic metasurfaces. Adv. Mater. **34**, 2202026 (2022)
49. Xu, L.J., Xu, G.Q., Huang, J.P., Qiu, C.-W.: Diffusive Fizeau Drag in spatiotemporal thermal metamaterials. Phys. Rev. Lett. **128**, 145901 (2022)
50. Xu, L.J., Xu, G.Q., Li, J.X., Li, Y., Huang, J.P., Qiu, C.-W.: Thermal Willis coupling in spatiotemporal diffusive metamaterials. Phys. Rev. Lett. **129**, 155901 (2022)
51. Wu, H.T., Gao, X.X., Liu, S., Ma, Q., Zhang, H.C., Wan, X., Cui, T.J.: Robust Spin-momentum coupling induced by parity-time symmetric spatiotemporal metasurface. Adv. Opt. Mater. **9**, 210132 (2021)
52. Zhu, W.W., Xue, H.R., Gong, J.B., Chong, Y.D., Zhang, B.L.: Time-periodic corner states from Floquet higher-order topology. Nat. Commun. **13**, 11 (2022)
53. Xu, G.Q., Yang, Y.H., Zhou, X., Chen, H.S., Alù, A., Qiu, C.W.: Diffusive topological transport in spatiotemporal thermal lattices. Nat. Phys. **18**, 450–456 (2022)
54. Coppens, Z.J., Valentine, J.G.: Spatial and temporal modulation of thermal emission. Adv. Mater. **29**, 1701275 (2017)
55. Zhang, L., Chen, X.Q., Liu, S., Zhang, Q., Zhao, J., Dai, J.Y., Bai, G.D., Wan, X., Cheng, Q., Castaldi, G., Galdi, V., Cui, T.J.: Space-time-coding digital metasurfaces. Nat. Commun. **9**, 4334 (2018)

56. Li, L.L., Ruan, H.X., Liu, C., Li, Y., Shuang, Y., Alù, A., Qiu, C.W., Cui, T.J.: Machine-learning reprogrammable metasurface imager. Nat. Commun. **10**, 1082 (2019)
57. Lei, M., Xu, L.J., Huang, J.P.: Spatiotemporal multiphysics metamaterials with continuously adjustable functions. Mat. Today. Phys. **34**, 101057 (2023)
58. Lei, M., Wang, J., Dai, G.L., Tan, P., Huang, J.P.: Temperature-dependent transformation multiphysics and ambient-adaptive multiphysical metamaterials. EPL **135**, 54003 (2021)
59. Gao, Y., Jian, Y.C., Zhang, L.F., Huang, J.P.: Magnetophoresis of nonmagnetic particles in ferrofluids. J. Phys. Chem. C **111**, 10785 (2007)
60. Dong, L., Huang, J.P., Yu, K.W., Gu, G.Q.: Dielectric response of graded spherical particles of anisotropic materials. J. Appl. Phys. **95**, 621–624 (2004)
61. Huang, J.P., Karttunen, M., Yu, K.W., Dong, L.: Dielectrophoresis of charged colloidal suspensions. Phys. Rev. E **67**, 021403 (2003)
62. Shi, W.C., Stedman, T., Woods, L.M: Transformation optics for thermoelectric flow. J. Phys.: Energy **1**, 025002 (2019)
63. Qu, T., Wang, J., Huang, J.P.: Manipulating thermoelectric fields with bilayer schemes beyond Laplacian metamaterials. EPL **135**, 54004 (2021)
64. Shi, W.C., Stedman, T., Woods, L.M: Thermoelectric transport control with metamaterial composites. J. Appl. Phys. **128**, 025104 (2020)
65. Keller, J.B.: A theorem on the conductivity of a composite medium. Physics **5**, 548 (1964)
66. Narayana, S., Sato, Y.: Heat Flux Manipulation with engineered thermal materials. Phys. Rev. Lett. **108**, 214303 (2012)
67. Li, J.X., Li, Y., Li, T., Li, T.L., Wang, W.Y., Li, L.Q., Qiu, C.W.: Doublet thermal metadevice. Phys. Rev. Appl. **11**, 044021 (2019)

Part II
Metamaterials for Thermal Diffusion: Thermal Conduction and Convection

Chapter 7
Convective Heat Transfer in Porous Materials

Peng Jin, Gaole Dai, and Fubao Yang

7.1 Opening Remarks

Over the past decade, the emergence of thermal metamaterials [1–11] and transformation thermotics [12, 13] has greatly broadened the horizons of heat manipulation [14–27]. This expansion has proven invaluable in a variety of applications from thermal cloaking and camouflage [14, 28, 29] to heat management in microchips [30, 31], energy conservation in everyday life [32–34], statistical physics [35–37], and thermoregulation in biological cells [14]. Yet, much of the progress in this field has been concentrated on conductive thermal metamaterials [12, 38, 39]. These materials primarily rely on diffusive or effective heat conduction, which is constrained by Onsager's reciprocity. Such reliance places constraints on the versatility of heat manipulation. Additionally, traditional thermal metamaterials lack the flexibility to adjust their functions based on given temperature conditions [38, 39], depriving them of the adaptive control often required.

Thermal convection [13, 33, 40–45], with its distinct nature, plays a crucial role as a mechanism for thermal transport. Historically, its role was often overshadowed in the realms of thermal metamaterials and transformation thermotics. Only recently has the theory of transformation thermotics expanded its scope to include thermal convection [33, 40, 41, 44], necessitating the creation of a novel theoretical framework. Yet, merging thermal convection in liquids with thermal conduction in solids to create hybrid thermal metamaterials presents a significant challenge. This is because these distinct paths of heat transport must align and collaborate harmoniously to generate stable heat and liquid flows that fulfill the requirements of the underlying

P. Jin (✉) · F. Yang
Department of Physics, Key Laboratory of Micro and Nano Photonic Structures (MOE), and State Key Laboratory of Surface Physics, Fudan University, Shanghai 200438, China
e-mail: 19110190022@fudan.edu.cn

G. Dai
School of Sciences, Nantong University, Nantong 226019, China

F.-B. Yang and J.-P. Huang, *Diffusionics*,
https://doi.org/10.1007/978-981-97-0487-3_7

thermotic transformation. Designing such hybrid materials proves more intricate than traditional all-solid thermal metamaterials. While there have been efforts to integrate thermal convection to achieve remarkable thermal conductivity levels (exemplifying synthetic Onsager reciprocity) [46–48], there is a pressing need to develop thermal metamaterials that can simultaneously control both conductive and convective heat flows beyond the bounds of Onsager reciprocity.

In this chapter, we present the latest advancements in heat transfer of porous materials. We commence by elaborating on the foundational principles of transformation thermotics, addressing both steady-state and transient-state challenges of convective heat transfer in porous mediums [33, 40, 41]. This potent theory paves the way for the conceptual design of innovative thermal devices, including illusion and camouflage mechanisms [42, 43]. Further, we clarify the emergence of experimental platforms for the realization of continuous switch between thermal cloak and thermal concentration [13], which reveals the significant tunability of the hybrid thermal metamaterial. Finally, we envision that such porous mediums could serve as the ideal physical platform for achieving robust thermal-protected transport with topological features.

7.2 Steady-State Transformation Thermo-Hydrodynamics

When addressing heat transfer in fluids, we begin by adjusting the heat conduction equation for incompressible flow, excluding heat sources and disregarding the viscous dissipation term [49], as

$$\rho C_p \nabla \cdot (\vec{v} T) = \nabla \cdot (\eta \nabla T), \tag{7.1}$$

where ρ, C_p, η, and $\vec{v}$ are respectively the density, specific heat at constant pressure, thermal conductivity, and the velocity of the fluid. As is known, $\rho C_p \nabla \cdot (\vec{v} T)$ is the term due to advection. Equation (7.1) represents the convection-diffusion equation. For the sake of clarity, we assume a laminar, Newtonian flow and consider the density to be unaffected by temperature variations.

For the coordinate transformation $\{x_i\} \to \{y_j\}$ and the associated Jacobian matrix $\mathbf{J} = \frac{\partial(y_1, y_2, y_3)}{\partial(x_1, x_2, x_3)}$, we can write [50]

$$\rho C_p \sum_j \frac{\partial}{\partial y_i} \left(\frac{1}{\det \mathbf{J}} \sum_i J_{ij}^{\intercal} v_i T \right) = \sum_{ijkl} \frac{\partial}{\partial y_k} \left(\frac{1}{\det \mathbf{J}} J_{ki} \eta_{ij} J_{jl}^{\intercal} \frac{\partial T}{\partial y_l} \right). \tag{7.2}$$

Let $\vec{v}' = \frac{\mathbf{J}\vec{v}}{\det \mathbf{J}}$ and $\eta' = \frac{\mathbf{J}\eta\mathbf{J}^{\intercal}}{\det \mathbf{J}}$, and we achieve

$$\rho C_p \left[\nabla' \cdot (\vec{v}' T) \right] = \nabla' \cdot (\eta' \nabla' T). \tag{7.3}$$

Equations (7.1) and (7.3) have the consistent form, and thermal convection are included in transformation thermotics.

Following this, we conceptualize and determine the velocity distribution $\vec{v}'(\vec{r}, t)$ and the anisotropic thermal conductivity η' of the liquid medium. Typically, to fully characterize the state of fluids, we require knowledge of the velocity $\vec{v}$ and two additional thermodynamic quantities, such as ρ and pressure p. These parameters are ascertained using Eq. (7.1) in conjunction with the Navier-Stokes equations and the continuity equation [49]

$$(\vec{v} \cdot \nabla)\vec{v} = -\frac{1}{\rho}\nabla p + \frac{\beta}{\rho}\nabla \cdot \nabla \vec{v}, \tag{7.4}$$

$$\nabla \cdot \vec{v} = 0. \tag{7.5}$$

Here, β denotes the dynamic viscosity. For clarity, we take $\vec{v}(\vec{r}, t) = \vec{v}(\vec{r})$ and $\rho(\vec{r}, t) \equiv \rho$. However, Eq. (7.5) retains its form under coordinate transformation whereas Eq. (7.4) typically does not. But we can overlook nonlinear term $(\vec{v} \cdot \nabla)\vec{v}$ when Reynolds number Re is small (akin to the elastic equation in [51]). Experimentally, inducing anisotropy in η' for fluids poses challenges, even though this has been effectively achieved for heat conduction in solids. Encouragingly, recent progress in velocity control, as highlighted in [52], spurs us to simultaneously explore heat transfer and velocity management in porous media.

In fully-filled porous media, we give equations for steady flow as [53, 54]

$$\rho_f C_{p,f}(\vec{v} \cdot \nabla T) = \nabla \cdot (\eta_m \nabla T), \tag{7.6}$$

$$\nabla p + \frac{\beta}{k}\vec{v} = 0, \tag{7.7}$$

$$\nabla \cdot \vec{v} = 0, \tag{7.8}$$

where k denotes the permeability and η_m is the effective thermal conductivity of the porous media. Meanwhile, ρ_f and $C_{p,f}$ are the density and specific heat at constant pressure of fluid material, respectively. By taking the volume average of solid and liquid components [54], the effective conductivity η_m is given by

$$\eta_m = (1 - \phi)\eta_s + \phi\eta_f. \tag{7.9}$$

where ϕ represents the porosity and η_f and η_s are the thermal conductivity of fluid and solid material of porous media, respectively. In Eq. (7.6), the local thermal equilibrium of fluids and solid materials is assumed, indicating that they possess the same temperature at the contact point. Meanwhile, we assume $\nabla \cdot (\vec{v}T) = \vec{v} \cdot \nabla T$, given by Eq. (7.8). Equation (7.7) denotes the Darcy's law, in case of small-enough Re and k. From $\lambda = -\frac{k}{\beta}$ and $\vec{v}' = \mathbf{J}\vec{v}/(\det \mathbf{J})$, we easily rewrite Eq. (7.7) under transformation $\{x_i\} \to \{y_j\}$,

$$v'_j = \sum_i J_{ji} v_i / (\det \mathbf{J}) = \sum_{ik} J_{ji} \lambda_{ki} \frac{\partial p}{\partial x_k} / (\det \mathbf{J}) = \sum_{ikl} J_{lk} \lambda_{ki} J^{\intercal}_{ij} \frac{\partial p}{\partial y_l} / (\det \mathbf{J}), \tag{7.10}$$

which indicates the relationships: $\vec{v}' = \lambda' \nabla' p$ and $\lambda' = \frac{\mathbf{J}\lambda\mathbf{J}^{\intercal}}{\det \mathbf{J}}$.

All the Eqs. (7.6)–(7.8) keep invariant form under any coordinate transformation, and we can obtain the wanted temperature and velocity distribution without tuning properties of fluid materials. That is to say, we only need to transform the permeability

$$k' = \frac{\mathbf{J} k \mathbf{J}^{\intercal}}{\det \mathbf{J}}, \tag{7.11}$$

and the thermal conductivity

$$\begin{cases} \eta'_m = \dfrac{\mathbf{J}\eta_m \mathbf{J}^{\intercal}}{\det \mathbf{J}}, \\ \eta'_f = \eta_f, \\ \eta'_s = \dfrac{\eta'_m - \phi \eta_f}{1 - \phi}. \end{cases} \tag{7.12}$$

Using different spatial transformations, we can manipulate the heat flow as we wish.

7.3 Transient-State Transformation Thermo-Hydrodynamics

In this section, we extend the transformation theory to encompass transient thermal convection in porous media. The Darcy's law can be generalized as follows [41, 55–57]:

$$\tau \frac{\partial \vec{v}}{\partial t} + \vec{v} = -\frac{\beta}{\eta} \nabla p. \tag{7.13}$$

Here, τ denotes the characteristic time measuring the velocity varying. Additionally, β signifies the permeability of porous medium, while η stands for the dynamic viscosity. In many scenarios, the relaxation process within porous media is rapid, resulting in the term $\tau \frac{\partial \vec{v}}{\partial t}$ being quite negligible [57]. Consequently, we can omit this term and continue to operate within the steady Darcy framework. Furthermore, the continuity equation can be modified as [49]

$$\frac{\partial (\phi \rho_f)}{\partial t} + \nabla \cdot (\rho_f \vec{v}) = 0, \tag{7.14}$$

where ρ_f denotes the density of the fluid medium and ϕ stands for the porosity. Then, the heat transfer of incompressible flow in fully-filled porous media is given by [53, 54]

$$\frac{\partial(\rho C)_m T}{\partial t} + \nabla \cdot (\rho_f C_f \vec{v} T) = \nabla \cdot (\kappa_m \nabla T), \tag{7.15}$$

where T is temperature, and ρ_s is the density of solid in porous media, respectively. Here, C_f and C_s are the specific heat of the fluid and solid porous materials, respectively. The effective product of density and specific heat of the whole porous material, governed by the average-volume method [54],

$$(\rho C)_m = (1-\phi)(\rho_s C_s) + \phi(\rho_f C_f). \tag{7.16}$$

Similarly, the effective thermal conductivity κ_m are also the summation of κ_f (for fluids) and κ_s (for solids),

$$\kappa_m = (1-\phi)\kappa_s + \phi\kappa_f. \tag{7.17}$$

Note that the Eq. (7.15) is the unsteady convection-diffusion equation whose form-invariance under coordinate transformations are proved [50, 58]. Additionally, the substitution of Eq. (7.14) into Eq. (7.15) leads

$$(\rho C)_m \frac{\partial T}{\partial t} + \rho_f C_f (\vec{v} \cdot \nabla T) = \nabla \cdot (\kappa_m \nabla T). \tag{7.18}$$

Like the steady-state scenarios, we can see all governing equitations satisfy the transformation theory. [33]. For both these steady and unsteady situations, the transformation matrix for an isotropic virtual space is as follows: $\frac{\mathbf{J}\mathbf{J}^\intercal}{\det \mathbf{J}}$, where $\mathbf{J}$ signifies the Jacobian matrix mapping from the transformed coordinate to its original counterpart. It's also essential to adjust the permeability and heat conductivity as $\beta' = \dfrac{\mathbf{J}\beta\mathbf{J}^\intercal}{\det \mathbf{J}}$ and $\kappa'_m = \dfrac{\mathbf{J}\kappa_m\mathbf{J}^\intercal}{\det \mathbf{J}}$. Distinctively, for the unsteady scenarios, it becomes necessary to modify both the porosity and the product of density and specific heat. The transformation is

$$\begin{cases} \phi' = \dfrac{\phi}{\det \mathbf{J}} \\ (\rho_f C_f)' = \rho_f C_f \\ (\rho_s C_s)' = \dfrac{1-\phi}{\det \mathbf{J} - \phi} \rho_s C_s \end{cases} \tag{7.19}$$

Using this approach, we maintain the properties of fluid unchanged, focusing solely on crafting the required solid metamaterial. It's noteworthy that ρ_f is not a constant anymore if we further consider its correlation with temperature variations over time and space. For clarity, we make the assumption that

$$\rho = \rho_0[1 - \gamma(T - T_0)], \tag{7.20}$$

where $\gamma = (\frac{\partial \rho}{\partial T})_p / \rho$ represents the density expansion ratio at a constant pressure. Without loss of generality, we give the $\gamma > 0$. Therefore, we consider the transformed

equations:

$$\begin{cases} \vec{v}' = -\dfrac{\beta'}{\eta}\nabla p \\ \dfrac{\partial(\phi'\rho_f)}{\partial t} + \nabla\cdot(\rho_f\vec{v}') = 0 \\ (\rho C)'_m\dfrac{\partial T}{\partial t} + \rho_f C_f(\vec{v}'\cdot\nabla T) = \nabla\cdot(\kappa'_m\nabla T) \end{cases}, \tag{7.21}$$

where the transformed velocity $\vec{v}'$ is $\mathbf{J}\vec{v}/\det\mathbf{J}$ [33, 50, 58] and $(\rho C)'_m = (1-\phi')(\rho_s C_s)' + \phi'(\rho_f C_f)$.

7.4 Potential Applications

Actually, metamaterials designed by transformation thermotics typically exhibit characteristics that are anisotropic, inhomogeneous, and at times even singular. These traits present significant fabrication challenges. For addressing these complexities in hybrid thermal systems, researchers turn to effective medium theories and multi-layered composite structures to achieve the desired outcomes. Regrettably, a fitting theory for managing such hybrid thermal systems has not been developed yet. As a result, there is a pressing need to devise a theory that streamlines the intricate parameters introduced by transformation thermotics.

To address this challenge, we draw inspiration from the concept of neutral inclusion within porous materials. By tailoring two pivotal parameters–thermal conductivity and permeability–we are able to achieve three distinct types of thermal illusions: transparency, concentration, and cloaking. To elaborate, thermal transparency involves creating a core-shell structure to preserve the temperature, velocity, and heat flux distributions of the background undisturbed. Notably, this approach obviates the need for anisotropy, inhomogeneity, and singularity. Similarly, to attain thermal concentration or cloaking, we fashion an anisotropic shell, eliminating the necessity for inhomogeneous and singular parameters. As these three functions–transparency, concentration, and cloaking–maintain the background's temperature, velocity, and heat flux distributions undisturbed, we conveniently term them collectively as thermal illusion.

We assume a steady-state thermal convection-diffusion process in porous materials with incompressible fluids and neglect the viscous dissipation term. Therefore, the governing equation is expressed as

$$\rho_f C_{p,f}(\vec{v}\cdot\nabla T) = \nabla\cdot(\overleftrightarrow{\kappa}\cdot\nabla T), \tag{7.22}$$

where ρ_f, $C_{p,f}$, and $\vec{v}$ are the density, heat capacity, and the velocity of the fluid at constant pressure, respectively, and T denotes the temperature when the porous material reach equilibrium. Moreover, $\overleftrightarrow{\kappa}$, representing the average thermal conductivity tensor of the solid and the fluid material, is defined as $\overleftrightarrow{\kappa} = (1-\phi)\overleftrightarrow{\kappa}_s + \phi\overleftrightarrow{\kappa}_f$,

where ϕ stands for the porosity of the media. $\overleftrightarrow{\kappa}_s$ and $\overleftrightarrow{\kappa}_f$ are the thermal conductivity tensors of the solid and the fluid material, respectively. In cases where the fluid exhibits laminar flow at a minimal velocity, the velocity $\vec{v}$ is described by Darcy's law,

$$\vec{v} = -\left(\overleftrightarrow{\sigma}/\eta\right) \cdot \nabla p, \tag{7.23}$$

where $\overleftrightarrow{\sigma}$ and η is the permeability tensor and dynamic viscosity, respectively. p stands for pressure. In such case, both Re (Reynolds number) and $\overleftrightarrow{\sigma}$ are small enough. The conductive flux $\vec{j}$ is governed by Fourier's law,

$$\vec{j} = -\overleftrightarrow{\kappa} \cdot \nabla T. \tag{7.24}$$

For clarity, we consider the steady state

$$\nabla \cdot \vec{v} = 0, \tag{7.25}$$
$$\nabla \cdot \vec{j} = 0. \tag{7.26}$$

We also consider one type of fluid with constant dynamic viscosity η. Then, Eqs. (7.25) and (7.26) are expressed as

$$\nabla \cdot (-\overleftrightarrow{\sigma} \cdot \nabla p) = 0, \tag{7.27}$$
$$\nabla \cdot (-\overleftrightarrow{\kappa} \cdot \nabla T) = 0. \tag{7.28}$$

Finally, Eqs. (7.27) and (7.28) share a comparable mathematical structure. Therefore, the effective medium theory is capable of addressing both thermal conductivity and permeability. Using τ, we can harmonize the representation of κ and σ.

We aspire to eliminate the need for anisotropic, inhomogeneous, and singular parameters. To this end, we turn to the concept of neutral inclusion. This idea provides a methodology to determine the effective thermal conductivity of a core-shell configuration. Subsequently, it becomes essential to compute the effective permeability for the same structure. As depicted in Fig. 7.1, we designate the core to be isotropic with parameter τ_1, the metashell to be anisotropic with parameter $\overleftrightarrow{\tau}_2 = \mathrm{diag}(\tau_{rr}, \tau_{\theta\theta})$ (the shell becomes isotropic when $\tau_{rr} = \tau_{\theta\theta}$), and the background to be isotropic with parameter τ_3. Consequently, the core-shell structure's effective parameter τ_e can be deduced as follows:

$$\tau_e = c\tau_{rr} \frac{\tau_1 + c\tau_{rr} + (\tau_1 - c\tau_{rr}) f^c}{\tau_1 + c\tau_{rr} - (\tau_1 - c\tau_{rr}) f^c}, \tag{7.29}$$

where $c = \sqrt{\tau_{\theta\theta}/\tau_{rr}}$ denotes the anisotropy of the shell, and $f = (r_1/r_2)^2$ represents the core fraction. To maintain the heat flux and velocity distributions in the background (region III) as though the core-shell structure is absent at the center, we define $\tau_e = \tau_3$.

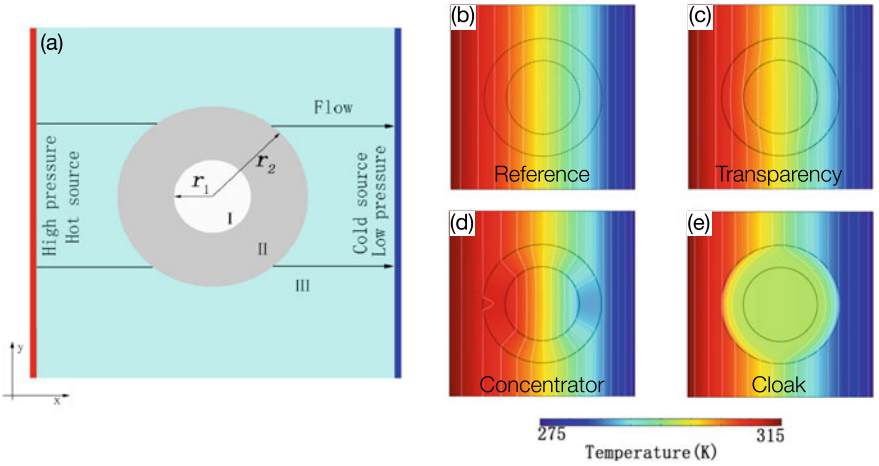

Fig. 7.1 Thermal illusion in porous materials. The scale of the system is 10^{-5} m. **a** Schematic. The background velocity is along the x direction, as described by the black flow lines. Region I ($r < r_1$) is composed of isotropic porous media, region II ($r_1 < r < r_2$) is composed of isotropic media for thermal transparency, and anisotropic media for thermal concentrator or cloak, and region III ($r > r_2$) is composed of isotropic background porous media. For thermal illusion in porous media, the black lines in region III with the core-shell structure should be undistorted. **b** Temperature profile of a pure background (reference). **c** Temperature profile of a thermal transparency. **d** Temperature profile of a thermal concentrator. **e** Temperature profile of a thermal cloak. White lines are the isotherms. (from Ref. [42])

Next, we perform finite-element simulations to validate the theory. As shown in schematic of Fig. 7.1, we take the pressure source as $\Delta p = 400$ Pa and the heat source $\Delta T = 40$ K. The liquid in porous material is set as water with $\rho_f = 10^3$ kg/m^3, $C_{p,f} = 4.2 \times 10^3$ J·kg^{-1}K^{-1}, the dynamic viscosity $\eta = 10^{-3}$ Pa·s, and $\kappa_f = 0.6$ Wm^{-1}K^{-1}. The porosity is $\phi = 0.9$. The size parameters are $r_1 = 2 \times 10^{-5}$ m and $r_2 = 3.2 \times 10^{-5}$ m. The average thermal conductivity tensors are set to be $\kappa_1 = 6$ Wm^{-1}K^{-1}, $\overleftrightarrow{\kappa}_2 = \text{diag}(4, 4)$ Wm^{-1}K^{-1}, and $\kappa_3 = \kappa_e$ given by Eq. (7.29). The thermal conductivity tensor of the solid are calculated as $\overleftrightarrow{\kappa}_s = (\overleftrightarrow{\kappa} - \phi\kappa_f)/(1 - \phi)$. The permeability tensors are set to be $\sigma_1 = 5 \times 10^{-12}$ m^2, $\overleftrightarrow{\sigma}_2 = \text{diag}(2, 2) \times 10^{-12}$ m^2 (the magnitude 10^{-12} is common in nature), and $\sigma_3 = \sigma_e$ given by Eq. (7.29). In all these cases, we calculate Reynolds numbers $\text{Re} = r_2\rho_f v/\eta < 1$ (the maximum value is 0.64) and $\sigma \ll r_2^2$, ensuring the applicability of Darcy's law. The simulation results are shown in Fig. 7.1. Figure 7.1b displays a simulation of a pure background without the core-shell structure, serving as a reference. Based on the above core-shell parameters, we then produce a thermal transparency pattern; see Fig. 7.1c. For realizing a thermal cloak (or concentrator) pattern, we set $\tau_{rr} \ll \tau_{\theta\theta}$ (or $\tau_{rr} > \tau_{\theta\theta}$). Temperature profiles are shown in Fig. 7.1d, e. Finally, different thermal patterns are created including thermal transparency, thermal cloak and thermal concentrator.

The performance of thermal illusion are not affected as long as the permeability and thermal conductivity satisfy Eq. (7.29).

7.5 Experiment of Steady-State Transformation Thermo-Hydrodynamics

In crafting the hybrid thermal metamaterial, we employ fine-designed porous structures, enabling both thermal convection and conduction to coexist within the same space, as illustrated in Fig. 7.2a. This design process is bifurcated into two stages. Initially, by sculpting the basic unit, we engineer a porous substance that allows localized, independent modulation of both thermal conduction and convection attributes. Subsequently, leveraging the advanced principles of transformation thermotics, we shape the spatial characteristics of these thermal properties to realize the intended functionalities of the thermal metadevice.

The local manipulation of both conductive and convective thermal properties is achieved through the design of basic units. We have two types of units. The type-I unit comprises a cuboid featuring a hemispherical region filled with water (see lower-right inset of Fig. 7.2a). In contrast, the type-II unit is a cuboid possessing cylindrical five air holes. The effective thermal conductivity of each unit is given by $\boldsymbol{\kappa} = (1 - \phi_l - \phi_a)\,\boldsymbol{\kappa}_\mathrm{s} + \phi_l \boldsymbol{\kappa}_\mathrm{l} + \phi_a \boldsymbol{\kappa}_\mathrm{a}$ where $\boldsymbol{\kappa}_\mathrm{s}$, $\boldsymbol{\kappa}_\mathrm{l}$, and $\boldsymbol{\kappa}_\mathrm{a}$ are the thermal conductivity of the solid, liquid, and air, respectively. ϕ_l and ϕ_a represent the filling fraction of the liquid and air region, respectively. Within each unit, the thermal conductivity can be adjusted based on the selected solid material and the filling fractions ϕ_l and ϕ_a. Concurrently, the permeability $\boldsymbol{\sigma}$ can be modulated based on the geometry of the liquid or air region. For instance, in the type-II units air holes are employed to deflect the liquid flow. The orientation of such units can be strategically adjusted to modify the permeability $\boldsymbol{\sigma}$.

We craft a metashell design wherein the thermal conductivity $\boldsymbol{\kappa}'$ distribution is tailored for thermal cloaking, guided by our choice of the transformation $\boldsymbol{\Xi}$. This transformation correlates to a virtual space with a hole at the center. The hole in the virtual space is exactly the origin of the thermal cloaking effect: The heat flows cannot touch any object in the hole in the virtual space, while in real space, an object in the core region remains unaffected by the heat flows. Conversely, the liquid permeability distribution $\boldsymbol{\sigma}'$ arises from the transformation of the thermal convection $\boldsymbol{\Lambda}$, crafted for thermal concentration. This transformation maps to a virtual space with no hole. From the geometric point of view, the virtual space with a hole is topologically distinct from the virtual spaces with no hole. Consequently, with increasing hydraulic pressure difference $\Delta P = P_\mathrm{h} - P_\mathrm{l}$ (P_h and P_l are the hydraulic pressure at the hot and cold sides of the metadevice, respectively), thermal convection becomes dominant and the device function switches from thermal cloaking to thermal concentration. Meanwhile, the virtual space undergoes topology switch (see Fig. 7.2c). In particular, the nontrivial topology within the virtual space for thermal cloaking indicates

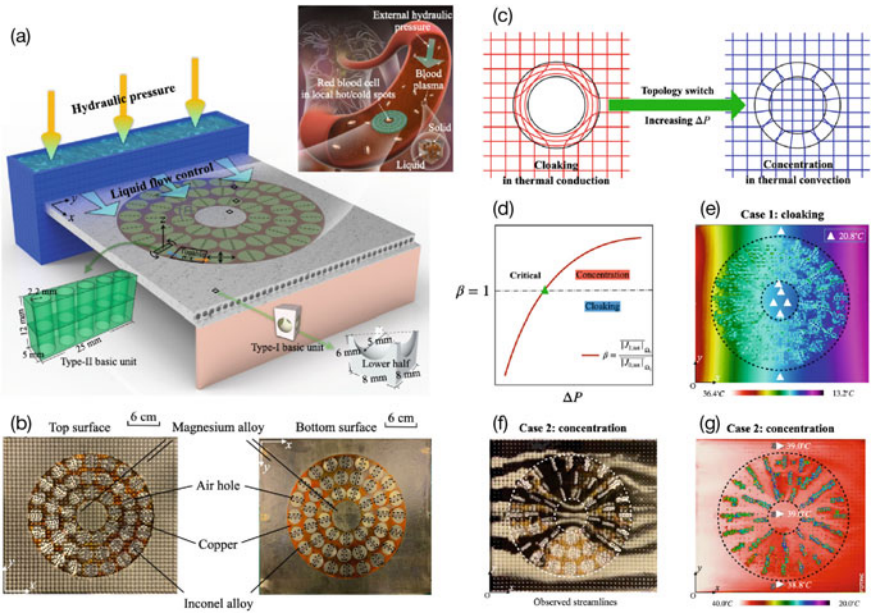

Fig. 7.2 Liquid-solid hybrid thermal metamaterial. **a** Illustration of the metadevice based on the liquid-solid hybrid thermal metamaterial. **b** Photos of the top and the bottom of the sample. Scale bar is 6 cm. **c** The switch between thermal cloaking and thermal concentration corresponds to a topological switch in virtual space. **d** The heat flux amplification factor β can be tuned continuously by the external hydraulic pressure. Meanwhile, the function of the metadevice is switched. **e** Measured temperature profile of the thermal metadevice at $\Delta P = 0$. White triangles denote the positions with the temperature of 20.8 °C. **f** Observed streamlines of the thermal metadevice at $\Delta P \neq 0$. **g** Measured temperature profile of the thermal metadevice at $\Delta P \neq 0$. Horizontal white triangles denote the positions with the temperature (from up to down) of 39.0 °C, 39.0 °C, and 38.8 °C, respectively. (from Ref. [13])

that there are some properties robust to external conditions. These properties are the heat current in the core region. In the thermal cloaking regime, such a heat current is irrelevant with external temperature distributions. In contrast, for thermal concentration, the heat current in the core region is highly sensitive to external temperature regions. The switch between these two functions reflect the topology change in the virtual space. To provide a quantitative assessment of our metadevice's function, we introduce the heat flux amplification factor β. This is determined by the averaged amplitude of the total heat flux in the core region (Ω_1) over the same quantity when the system is changed to the background (henceforth denoted as "the reference").

We proceed to showcase the transition between thermal cloaking and thermal concentration through regulated hydrodynamics. Under boundary condition I, where $\Delta P = 0$, we evaluate the temperature profile within the metadevice. As depicted in Fig. 7.2e, the temperature distribution captured by the infrared camera displays a perfect pattern of thermal cloaking. Notably, the core region has a consistent tem-

perature distribution around 20.8 °C. This suggests no conductive heat flow in the core region. Additionally, the temperature profile in the background region remains mostly undisturbed. Therefore, it can be interpreted as $\beta < 1$, signifying that the metadevice is operating in the cloaking mode.

Under boundary condition II, we target for the realization of the thermal concentration. We ensure that thermal convection takes precedence in these scenarios. We experimentally showcase the performance of thermal concentration, examining it through the lens of fluid dynamics and temperature profiling. To visualize the fluid flow, we perforate six holes beneath a colorant container, a concoction of alkanes and toner. Once the system stabilizes into a nonequilibrium steady-state, the colorant is methodically dripped from the metadevice's left boundary through these holes, ensuring simultaneous and equidistant distribution. Figure 7.2f showcases the six streamlines. The central four streamlines converge into the core area, and all the streamlines outside the region Ω_2 are only marginally distorted. This pattern underscores that the core zone experiences a more substantial flow (or a heightened fluid velocity) compared to the backdrop. It is worth noting that within the Ω_2 region, colorant distribution differs between the upper and lower sections. This discrepancy arises from the asymmetrical layout of the type-II basic units, further compounded by the unequal positioning of the six holes in relation to these sections. Yet, the fluid flow's concentration remains distinctly visible in Fig. 7.2g. Subsequently, we gauge the temperature profile in the metadevice under identical conditions. The measured temperature profile (see Fig. 7.2g) exhibits several features. First, the overall temperature of the metadevice is higher than in the cloaking case. Moreover, the temperature gradient is pushed to the right side of the metadevice. There are visible correlations between the temperature profile and liquid flow profile, indicating that the thermal transport is now dominated by the convective heat flow carried by the water. The convective heat flow in the core region is larger than that in the background region because of $v_{\Omega_1} > v_{\Omega_3}$ with $T_{\Omega_1} \approx T_{\Omega_3}$ (see the white triangles in Fig. 7.2g). In this phase, $\beta > 1$. Consequently, the metadevice is transitioned into thermal concentration by increasing the external hydraulic pressure.

7.6 Discussion and Conclusion

In conclusion, we delve into the transformation thermo-hydrodynamics theory and the corresponding experimental methodologies that probe heat transfer in porous materials. These specially engineered porous materials exhibit remarkable adaptability in heat management, all while ensuring the temperature field in the backdrop remains undisturbed—a feat beyond the capabilities of traditional thermal metamaterials. Characterized by their unique liquid-solid amalgamation, these hybrid thermal metamaterials hold immense promise for a plethora of applications. These include thermal illusions and camouflage, enhanced cooling and heat regulation in electronic gadgets, sustainable infrastructure, and sophisticated heat modulation in intelligent materials and machinery. Delving deeper into these hybrid metamaterials might just

unveil groundbreaking insights into the intricacies of complex systems, including nonlinear systems, soft matter systems, and statistical physics.

Let's delve into the topological transition inherent to the hybrid metamaterial. From a physics standpoint, the transformation theory serves as a conduit, bridging geometric transformations with their parametric counterparts. As a result, the topological attributes of a geometric transformation find their mirrored representation in material parameters. This allows us to explore topology via (effective) thermal conductivity. For instance, when considering a core-shell structure designed for thermal cloaking, its effective thermal conductivity can be perceived as a topological invariant—it remains unaltered by the thermal conductivity of the core. This implies that a geometric transformation with a distinct topological nature can lead to singular (either zero or infinite) thermal conductivity, effectively segmenting a region from its surroundings. Hence, transformation thermotics becomes instrumental in drawing connections between geometric and parametric topologies. Broadly speaking, situations with zero or infinite thermal conductivity bear topological significance. This is analogous to the unique nature of zero-index metamaterials: they facilitate seamless transport without reflections in real space and correspond to materials showcasing Dirac dispersions in wave-vector space.

In wrapping up, we foresee a transformative application of our metadevice in managing localized temperature variations within biological cells or tissues [59], all while ensuring the broader environment of the human body remains unperturbed. The extracellular fluid within organisms, a composite of liquid and solid-like elements (as illustrated in Fig. 7.2a), can be conceptualized as a porous medium. By designing porous metamaterials tailored to a specific scale, we can effectively model this environment. In a consistent external setting, discerning the direction of localized heat flow is feasible. Given our structure's axisymmetric design, as guided by the transformation theory, there's no external deviation. This implies that our model can be oriented along the direction of this localized heat flow. The adiabatic boundaries positioned at the top and bottom mirror open boundaries since there's a null heat flow vertically. This makes our model an apt representation of real conditions. By manipulating external hydraulic pressures, our uniquely designed metamaterials can regulate localized temperature variations in living cells or tissues. These hot/cold spots typically correspond to temporary temperature deviations. Harnessing hydraulic pressure control, these deviations can be mitigated swiftly. For such localized temperature variances, elevating fluid velocity and heat flow can expedite the shift towards a more stable temperature environment. Moreover, within a biological context, this supplemental flux aids in balancing chemical concentrations, such as ATPs and CO_2, further bolstering the restoration of biological functions. Furthermore, embedding these micro-scale metamaterials within the human body for therapeutic purposes is a tangible possibility. Our design's capability to operate without disrupting the background thermal or fluidic environment is of paramount significance, especially given its implications for human health.

References

1. Xu, L.J., Huang, J.P.: Active thermal wave cloak. Chin. Phys. Lett. **37**, 120501 (2020)
2. Dai, G.L., Huang, J.P.: Nonlinear thermal conductivity of periodic composites. Int. J. Heat Mass Transf. **147**, 118917 (2020)
3. Yang, F.B., Zhang, Z.R., Xu, L.J., Liu, Z.F., Jin, P., Zhuang, P.F., Lei, M., Liu, J.R., Jiang, J.-H., Ouyang, X.P., Marchesoni, F., Huang, J.P.: Controlling mass and energy diffusion with metamaterials. Rev. Mod. Phys. in press (2023). Preprint at http://arxiv.org/abs/2309.04711
4. Wang, C.M., Jin, P., Yang, F.B., Xu, L.J., Huang, J.P.: Click metamaterials: Fast acquisition of thermal conductivity and functionality diversities. Preprint at https://doi.org/10.48550/arXiv.2308.16057 (2023)
5. Jin, P., Liu, J.R., Yang, F.B., Marchesoni, F., Jiang, J.-H., Huang, J.P.: In-situ simulation of thermal reality. Research **6**, 0222 (2023)
6. Jin, P., Xu, L., Xu, G., Li, J., Qiu, C.-W., Huang, J.P.: Deep learning-assisted active metamaterials with heat-enhanced thermal transport. Adv. Mater. **36**, 2305791 (2024)
7. Zhou, X.C., Xu, X., Huang, J.P.: Adaptive multi-temperature control for transport and storage containers enabled by phase change materials. Nat. Commun. **14**, 5449 (2023)
8. Huang, J.P.: Theoretical Thermotics: Transformation Thermotics and Extended Theories for Thermal Metamaterials. Springer, Singapore (2020)
9. Jin, P., Xu, L.J., Jiang, T., Zhang, L., Huang, J.P.: Making thermal sensors accurate and invisible with an anisotropic monolayer scheme. Int. J. Heat Mass Transf. **163**, 120437 (2020)
10. Yang, S., Wang, J., Dai, G.L., Yang, F.B., Huang, J.P.: Controlling macroscopic heat transfer with thermal metamaterials: theory, experiment and application. Phys. Rep. **908**, 1–65 (2021)
11. Jin, P., Yang, S., Xu, L.J., Dai, G.L., Huang, J.P., Ouyang, X.P.: Particle swarm optimization for realizing bilayer thermal sensors with bulk isotropic materials. Int. J. Heat Mass Transf. **172**, 121177 (2021)
12. Fan, C.Z., Gao, Y., Huang, J.P.: Shaped graded materials with an apparent negative thermal conductivity. Appl. Phys. Lett. **92**, 251907 (2008)
13. Jin, P., Liu, J.R., Xu, L.J., Wang, J., Ouyang, X.P., Jiang, J.-H., Huang, J.P.: Tunable liquid-solid hybrid thermal metamaterials with a topology transition. Proc. Natl. Acad. Sci. U.S.A. **120**, e2217068120 (2023)
14. Zhang, Z.R., Xu, L.J., Qu, T., Lei, M., Lin, Z.K., Ouyang, X.P., Jiang, J.-H., Huang, J.P.: Diffusion metamaterials. Nat. Rev. Phys. **5**, 218–235 (2023)
15. Xu, L.J., Liu, J,R., Xu, G.Q., Huang, J.P., Qiu, C.-W.: Giant, magnet-free, and room-temperature Hall-like heat transfer. Proc. Natl. Acad. Sci. U.S.A. **120**, e2305755120 (2023)
16. Dai, G.L., Yang, F.B., Xu, L.J., Huang, J.P.: Diffusive pseudo-conformal mapping: Anisotropy-free transformation thermal media with perfect interface matching. Chaos, Solitons & Fractals. **174**, 113849 (2023)
17. Xu, L.J., Xu, G.Q., Huang, J.P., Qiu, C.-W.: Diffusive Fizeau Drag in spatiotemporal thermal metamaterials. Phys. Rev. Lett. **128**, 145901 (2022)
18. Shen, X.Y., Jiang, C.R., Li, Y., Huang, J.P.: Thermal metamaterial for convergent transfer of conductive heat with high efficiency. Appl. Phys. Lett. **109**, 201906 (2016)
19. Xu, L.J., Yang, S., Dai, G.L., Huang, J.P.: Transformation omnithermotics: simultaneous manipulation of three basic modes of heat transfer. ES Energy Environ. **7**, 65–70 (2020)
20. Xu, L.J., Wang, J., Dai, G.L., Yang, S., Yang, F.B., Wang, G., Huang, J.P.: Geometric phase, effective conductivity enhancement, and invisibility cloak in thermal convection-conduction. Int. J. Heat Mass Transf. **165**, 120659 (2021)
21. Xu, L.J., Yang, S., Huang, J.P.: Thermal theory for heterogeneously architected structure: fundamentals and application. Phys. Rev. E **98**, 052128 (2018)
22. Dong, L., Huang, J.P., Yu, K.W., Gu, G.Q.: Dielectric response of graded spherical particles of anisotropic materials. J. Appl. Phys. **95**, 621–624 (2004)
23. Gao, Y., Jian, Y.C., Zhang, L.F., Huang, J.P.: Magnetophoresis of nonmagnetic particles in ferrofluids. J. Phys. Chem. C **111**, 10785–10791 (2007)

24. Yang, S., Xu, L.J., Wang, R.Z., Huang, J.P.: Full control of heat transfer in single-particle structural materials. Appl. Phys. Lett. **111**, 121908 (2017)
25. Xu, L.J., Yang, S., Huang, J.P.: Thermal transparency induced by periodic interparticle interaction. Phys. Rev. Appl. **11**, 034056 (2019)
26. Xu, L.J., Dai, G.L., Huang, J.P.: Transformation multithermotics: controlling radiation and conduction simultaneously. Phys. Rev. Appl. **13**, 024063 (2020)
27. Wang, J., Dai, G.L., Huang, J.P.: Thermal metamaterial: fundamental, application, and outlook. iScience **23**, 101637 (2020)
28. Xu, L.J, Liu, J.R., Jin, P., Xu, G.Q., Li, J.X., Ouyang, X.P., Li, Y., Qiu, C.-W., Huang, J.P.: Black-hole-inspired thermal trapping with graded heat-conduction meta devices. Nat. Sci. Rev. **10**, nwac159 (2023)
29. Yang, F.B., Jin, P., Lei, M., Dai, G.L., Wang, J., Huang, J.P.: Space-time thermal binary coding by spatiotemporally modulated metashell. Phys. Rev. Appl. **19**, 054096 (2023)
30. Yao, N.Z., Wang, H., Wang, B., Wang, X.S., Huang, J.P.: Convective thermal cloaks with homogeneous and isotropic parameters and drag-free characteristics for viscous potential flows. iScience. **25**, 105461 (2022)
31. Lei, M., Jiang, C.R., Yang, F.B., Wang, J., Huang, J.P.: Programmable all-thermal encoding with metamaterials. Int. J. Heat Mass Transf. **207**, 124033 (2023)
32. Dai, G.L., Shang, J., Wang, R.Z., Huang, J.P.: Nonlinear thermotics: nonlinearity enhancement and harmonic generation in thermal metasurfaces. Eur. Phys. J. B **91**, 59 (2018)
33. Dai, G.L., Shang, J., Huang, J.P.: Theory of transformation thermal convection for creeping flow in porous media: cloaking, concentrating, and camouflage. Phys. Rev. E **97**, 022129 (2018)
34. Zhang, C.X., Li, T.J., Jin, P., Yuan, Y., Ouyang, X.P., Marchesoni, F., Huang, J.P.: Extracting stellar emissivity via a machine learning analysis of MSX and LAMOST catalog data. Phys. Rev. D. **106**, 123035 (2022)
35. Ye, C., Huang, J.P.: Non-classical oscillator model for persistent fluctuations in stock markets. Phys. A **387**, 1255–1263 (2008)
36. Liu, L., Wei, J.R., Zhang, H.S., Xin, J.H., Huang, J.P.: A statistical physics view of pitch fluctuations in the classical music from Bach to Chopin: evidence for Scaling. PLoS ONE **8**, e58710 (2013)
37. Huang, J.P., Karttunen, M., Yu, K.W., Dong, L.: Dielectrophoresis of charged colloidal suspensions. Phys. Rev. E **67**, 021403 (2003)
38. Li, Y., Shen, X.Y., Wu, Z.H., Huang, J.Y., Chen, Y.X., Ni, Y.S., Huang, J.P.: Temperature-dependent transformation thermotics: from switchable thermal cloaks to macroscopic thermal diodes. Phys. Rev. Lett. **115**, 195503 (2015)
39. Shen, X.Y., Li, Y., Jiang, C.R., Huang, J.P.: Temperature trapping: energy-free maintenance of constant temperatures as ambient temperature gradients change. Phys. Rev. Lett. **117**, 055501 (2016)
40. Dai, G.L., Wang, J.: Transformation hydrodynamic metamaterials: rigorous arguments on form invariance and structural design with spatial variance. Phys. Rev. E **107**, 055108 (2023)
41. Dai, G.L., Huang, J.P.: A transient regime for transforming thermal convection: cloaking, concentrating and rotating creeping flow and heat flux. J. Appl. Phys. **124**, 235103 (2018)
42. Yang, F.B., Xu, L.J., Huang, J.P.: Thermal illusion of porous media with convection-diffusion process: transparency, concentrating, and cloaking. ES Energy Environ. **6**, 45–50 (2019)
43. Xu, L.J., Huang, J.P.: Chameleonlike metashells in microfluidics: a passive approach to adaptive responses. Sci. China-Phys. Mech. Astron. **63**, 228711 (2020)
44. Xu, L.J., Huang, J.P.: Controlling thermal waves with transformation complex thermotics. Int. J. Heat Mass Transf. **159**, 120133 (2020)
45. Dai, G.L., Zhou, Y.H., Wang, J., Yang, F.B., Qu, T., Huang, J.P.: Convective cloak in hele-shaw cells with bilayer structures: hiding objects from heat and fluid motion simultaneously. Phys. Rev. Appl. **17**, 044006 (2022)
46. Li, Y., Zhu, K.J., Peng, Y.G., Li, W., Yang, T., Xu, H.X., Chen, H., Zhu, X.F., Fan, S., Qiu, C.W.: Thermal meta-device in analogue of zero-index photonics. Nat. Mater. **18**, 48–54 (2019)

47. Xu, G., Dong, K., Li, Y., Li, H., Liu, K., Li, L., Wu, J., Qiu, C.W.: Tunable analog thermal material. Nat. Commun. **11**, 6028 (2020)
48. Li, J., Li, Y., Cao, P.C., Yang, T., Zhu, X.F., Wang, W., Qiu, C.W.: A continuously tunable solid-like convective thermal metadevice on the reciprocal line. Adv. Mater. **32**, 2003823 (2020)
49. Landau, L.D., Lifshitz, E.M.: Fluid Mechanics. Pergamon, United Kingdom (1987)
50. Guenneau, S., Puvirajesinghe, T.M.: Fick's second law transformed: one path to cloaking in mass diffusion. J. Roy. Soc. Interface. **10**, 20130106 (2013)
51. Milton, G.W., Briane, M., Willis, J.R.: On cloaking for elasticity and physical equations with a transformation invariant form. New J. Phys. **8**, 248 (2006)
52. Urzhumov, Y.A., Smith, D.R.: Fluid flow control with transformation media. Phys. Rev. Lett. **107**, 074501 (2011)
53. Bear, J.: Dynamics of Fluids in Porous Media. American Elsevier, New York (1972)
54. Bear, J., Corapcioglu, M.Y.: Fundamentals of Transport Phenomena in Porous Media. Springer, Netherlands (1984)
55. Burcharth, H.F., Andersen, O.H.: On the one-dimensional steady and unsteady porous flow equations. Coast Eng. **24**, 233 (1995)
56. Zhu, T., Waluga, C., Wohlmuth, B., Manhar, M.: A study of the time constant in unsteady porous media flow using direct numerical simulation. Transp. Porous Media **104**, 161 (2014)
57. Zhu, T., Manhar, M.: Oscillatory Darcy flow in porous media. Transp. Porous Media **111**, 521 (2016)
58. Guenneau, S., Petiteau, D., Zerrad, M., Amra, C., Puvirajesinghe, T.: Transformed Fourier and Fick equations for the control of heat and mass diffusion. AIP Adv. **5**, 053404 (2015)
59. Tan, Y., Chen, Y., Liu, X., Tang, Y., Lao, Z., Wei, G.: Dissecting how ALS-associated D290V mutation enhances pathogenic aggregation of hnRNPA2286-291 peptides: Dynamics and conformational ensembles. Int. J. Biol. Macromol. **241**, 124659–124669 (2023)

Chapter 8
Non-Hermitian Physics and Topological Phenomena in Convective Thermal Metamaterials

Zhoufei Liu

8.1 Opening Remarks

The effective non-Hermitian Hamiltonian provides a simple and intuitive method to understand the dynamics of open systems [1, 2]. In recent decades, the study of non-Hermitian physics has been a frontier and attracted many researchers from condensed matter physics, optics, quantum information, etc. Among this field, parity-time (PT) symmetry is one of the most important symmetries because the system will exhibit a real spectrum [3, 4]. When the eigenstate of PT-symmetric Hamiltonian preserves (violates) PT symmetry, the system is in the PT unbroken (broken) phase. The critical point between these two phases is called the exceptional point (EP). Besides, many interesting phenomena without the Hermitian counterpart are proposed in non-Hermitian physics, such as non-Hermitian skin effect [5–8] and non-Hermitian topological classification [9, 10].

The quantum Hall effect discovered in the 1980s is the first proposed topological phase beyond the conventional Landau paradigm [11, 12]. In the last twenty years, it witnessed the flourishing of topological physics, and plenty of topological phases of matter have been theoretically predicted and experimentally discovered [13, 14]. Apart from condensed matter physics, topology has been incorporated into classical wave systems, giving rise to many new fields. One most typical and significant example is topological photonics [15, 16]. The basic principle for topological photonics is the mapping between Maxwell's equations in electrodynamics and Schrödinger equation in quantum mechanics. Other examples, such as topological acoustics [17, 18] and topological mechanics [19], have also been good platforms for realizing topological states.

Thermal metamaterials have become the focus of growing interest in physics, materials science, and thermophysics [20–26]. Based on transformation thermotics,

Z. Liu (✉)
Department of Physics, Key Laboratory of Micro and Nano Photonic Structures (MOE), and State Key Laboratory of Surface Physics, Fudan University, Shanghai 200438, China
e-mail: zfliu20@fudan.edu.cn

F.-B. Yang and J.-P. Huang, *Diffusionics*,
https://doi.org/10.1007/978-981-97-0487-3_8

thermal cloaking was first proposed in 2008 [27]. After that, more thermal functions with different artificial structures became possible, such as thermal illusion [28, 29] and thermal transparency [30, 31]. However, the above works are all constrained to purely thermal conduction. Thermal convection, as another fundamental mechanism of heat transfer, is usually dominant in moving media such as fluids. After considering it, hybrid thermal diffusion systems can revive many interesting phenomena in dissipative diffusion beyond pure conduction [32, 33]. Nonreciprocal heat transfer can be easily implemented with the help of convection due to its directional nature, such as spatiotemporal modulation [34–38] and angular momentum bias [39, 40]. Transformation thermotics has been extended to thermal radiation [41–43]. Besides, the concept of thermal metamaterials has also been generalized to other diffusion processes, such as particle diffusion [44, 45] and plasma transport [46, 47].

Recently, diffusion system has become a brand new platform to realize the topological phase and non-Hermitian physics. For heat conduction, there are two paradigms for implementing these phases. The first paradigm is spatially discretizing the diffusion equation [48]. Though with some imperfections in theory [49], the proposal has been experimentally confirmed to observe the edge state of one-dimensional (1D) Su-Schrieffer-Heeger model [50]. As a natural generalization, this proposal can be extended to higher-dimensional systems, such as higher-order topological insulators [51–53]. The other paradigm is constructing the coupled ring chain structure. The structure consists of several rings vertically coupled in one direction to form a chain through interlayers. It has been proposed that the non-Hermitian skin effect [54, 55] and the quasicrystal [56] can be realized within this structure. Besides, the thermal analogue of coherent perfect absorption may support the establishment of non-Hermitian diffusive scattering theory [57].

However, when convection is introduced as a new degree of freedom into heat transfer, increasingly non-Hermitian phenomena and topological physics can be realized in thermal diffusion beyond purely conduction. In this chapter, we will present some important works in this area, organized as follows. In Section II, we will discuss the work about the realization of EP in diffusion systems. In addition, we will present how to implement high-order EPs and dynamically enclose EPs in thermal diffusion. In Section III, we will discuss two works about the extensions of EP in convective thermal metamaterials, i.e., chiral thermal behaviour in the vicinity of EP and Weyl exceptional ring. In Section IV, we will introduce the topological physics in convection-conduction systems. Two topological phases, a 1D topological insulator and a 2D quadrupole insulator, have been realized with the help of thermal convection. A concluding discussion is presented in Section V, accompanying a reasonable outlook that may come true in the near future.

8.2 Non-Hermitian Physics in Convective Thermal Metamaterials: The Implementation of EP

The research on non-Hermitian convective thermal metamaterials starts from the implementation of anti-parity-time (APT) symmetry and EP in diffusion systems [58]. This work lays the foundation of non-Hermitian convective thermal metamaterials because of the importance of EP in non-Hermitian physics. In the wave systems, realizing the PT symmetry is very intuitive by introducing balanced gain and loss. However, it is not easy to realize the PT-related phenomenon in diffusion systems that are intrinsically dissipative (anti-Hermitian). This problem can be solved by introducing the forward and backward wave-like field, i.e., heat convection, which acts as a Hermitian component. After the introduction of thermal convection, the diffusive system will become APT symmetric and its effective Hamiltonian anti-commutes with the PT operator.

The basic structure for realizing the APT symmetry and EP in thermotics is two coupled rings with equal but opposite rotating velocities. The governing heat transfer equations for this double ring model can be written as

$$\frac{\partial T_1}{\partial t} = D\frac{\partial^2 T_1}{\partial x^2} - v\frac{\partial T_1}{\partial x} + h(T_2 - T_1) \tag{8.1}$$

$$\frac{\partial T_2}{\partial t} = D\frac{\partial^2 T_2}{\partial x^2} + v\frac{\partial T_2}{\partial x} + h(T_1 - T_2) \tag{8.2}$$

where D is the diffusivity of rings, h is the heat exchange rate between two rings, and v is the rotating velocity of rings. Using the plane-wave solution, the effective APT symmetric Hamiltonian is obtained as:

$$\hat{H} = \begin{pmatrix} -i(k^2 D + h) + kv & ih \\ ih & -i(k^2 D + h) - kv \end{pmatrix} \tag{8.3}$$

where k is the wave number. The corresponding eigenvalues of the effective Hamiltonian are

$$\omega_{\pm} = -i\left[(k^2 D + h) \pm \sqrt{h^2 - k^2 v^2}\right] \tag{8.4}$$

Then the EP emerges when $h^2 = k^2 v_{\mathrm{EP}}^2$. The fundamental mode $k = 1/R$ is chosen because only the slowest decaying mode can be observed. The theoretical decay rates and eigenfrequencies of the effective Hamiltonian are shown in Figs. 2A and 2B in Ref. [58], which are in accordance with the simulation results. The two branches of decay rates coalesce at the EP, and the nonzero eigenfrequency appears as the v increases. In the APT unbroken phase, the temperature profile of ring 1 remains motionless, and the maximum temperature point is fixed after evolving a certain time [see Figs. 4D and 4E in Ref. [58]]. However, the temperature profile keeps moving because of nonzero eigenfrequency in the APT broken phase [see Fig. 4F in

Ref. [58]]. The key point behind these thermal behaviours is the competition between thermal convection and coupled thermal conduction.

Further increasing the number of rings, high-order EP can be achieved in convection-diffusion systems, which is robust against perturbations and phase oscillations [59]. The model is the quadruple ring structure with opposite but equal velocities between adjacent channels. Similar with the derivation in Ref. [58], the effective Hamiltonian is a four by four matrix:

$$\hat{H} = \begin{pmatrix} -i(k^2 D + h) - kv & ih & 0 & 0 \\ ih & -i(k^2 D + h) - ih + kv & ih & 0 \\ 0 & ih & -i(k^2 D + h) - ih - kv & ih \\ 0 & 0 & ih & -i(k^2 D + h) + kv \end{pmatrix} \tag{8.5}$$

After diagonalizing the Hamiltonian, a third-order EP can be obtained at the critical velocity when APT phase transition occurs. In the APT symmetric phase, the temperature profile remains stationary with a phase-locked difference despite the velocity perturbation. While in the APT broken phase, the temperature field starts to dynamically evolve with phase oscillations regardless of the initial conditions.

In order to reveal the nontrivial topology of EPs in non-Hermitian physics, a sufficiently large parameter space is essential for dynamical EP encircling. However, the fixed and positive conductivity and structural parameters prevent the encircling from occurring in thermal diffusion. To address this problem, a recent work has created an orthogonal convection space to provide enough degrees of freedom [60]. The first step is to mimic two pairs of orthogonal oscillations as a complex parameter space. In order to easily implement such periodic convection, it is necessary to devise a multiple ring system consisting of two orthogonal pairs of counter-convective rings. One pair is rotating in $r - \theta$ space, and the other pair is translating along the z direction. Substituting the wave-like solution into the heat transfer equation, the effective Hamiltonian can be written as

$$\hat{H} = i \begin{pmatrix} -\left(\frac{\kappa}{\rho c} k_{r\theta}^2 + 2m\right) - k_{\text{eff}} v_{\text{eff}} \left[\cos(n) + i \sin(n)\right] & 2m \\ 2m & -\left(\frac{\kappa}{\rho c} k_{r\theta}^2 + 2m\right) + k_{\text{eff}} v_{\text{eff}} \left[\cos(n) + i \sin(n)\right] \end{pmatrix} \tag{8.6}$$

where κ, ρ, and c are the thermal conductivity, mass density, and heat capacity of rings. m is the heat exchange rate, which is fixed and positive. For clarity, the orthogonal convection space is denoted as $[k_{\text{eff}} v_{\text{eff}} \cos(n), k_{\text{eff}} v_{\text{eff}} \sin(n)]$, where $k_{\text{eff}} v_{\text{eff}} = \sqrt{(k_{r\theta} v_{r\theta})^2 + (k_z v_z)^2}$ and $n = \arctan(k_{r\theta} v_{r\theta} / k_z v_z)$. $v_{r\theta}$ and v_z are the rotating and translating velocities of rings. The effective wave numbers are $k_{r\theta} = 1/r$ in $r - \theta$ plane and $k_z = 1/d$ along the z direction, where r is the radius of ring and d is the thickness of the medium layer.

The topological properties of the EP are determined by the geometric phase generated by a dynamically encircling trajectory. It is related to two quantized topological

invariants: the eigenstate winding number ω [61] and the eigenvalue vorticity ν [62]. When the evolutionary trajectory of convections encircles two EPs, both topological invariants are integer numbers, revealing a non-Hermitian thermal topology. The temperature profile of the surface of the central medium exhibits a dynamic-equilibrium distribution without much deviation, and so does the location of the maximum temperature point. In this case, the initial state undergoes a full Riemann sheet during the adiabatic evolution and returns to itself at the end of one period. By comparison, when the trajectory encloses only one EP, both topological invariants are half-integer. The temperature profile and the location of maximum temperature show a step-like π-phase transition after one period. The eigenstate will exchange to another state with a π-phase winding after one period and return to its initial position after two periods. Furthermore, both topological invariants are zero when the EPs are not enclosed in the locus. Then the system becomes a conventional thermal metamaterial. For large advection modulations, the maximum temperature locations continuously change with the convection. While for small convection, the maximum temperature locations keep unchanged. In this way, the dynamical encircling of the EP in thermal diffusion is realized and the configurable topological phase transition of thermal systems is observed for the first time.

Meanwhile, a separate work shows the geometric phase induced by heat convection in diffusion systems [63]. Based on the double ring model, the temperature field will accumulate an extra π phase when the cyclic evolution of time-varying rotating velocity contains the EP.

8.3 Non-Hermitian Physics in Convective Thermal Metamaterials: The Extension of EP

In this section, we will introduce two extended researches based on the previous works about EP in thermal diffusion, namely the chiral behaviour in the vicinity of EP [64] and the Weyl exceptional ring [65].

The chiral behaviour at the EP has been proposed to achieve asymmetric wave propagation and unidirectional invisibility in carefully designed whispering-gallery-mode resonators [66–68]. However, the chirality has not been demonstrated in thermal diffusion so far. The reason is that the moving temperature field only follows the dominating advection introduced into the system [58, 60, 65, 74]. A recent work has shown the chiral heat transport after imposing the thermal perturbation [64]. The asymmetric thermal profile can be observed regardless of the directions and magnitudes of advections. Two thin plates are employed on the central fluid to impose the counter-advection at its upper and lower boundaries. The heating and cooling sources are directly imposed as perturbations on the boundary of the circular fluid region. These sources are retained after observing the steady-state thermal distribution, and advection is subsequently activated. After substituting the initial perturbed temperature field into the heat transfer equation, the effective Hamiltonian for the global system can be written as:

$$\hat{H} = i \begin{pmatrix} -\left(\frac{k^2\kappa_0}{\rho_0 c_0} + \frac{h}{\rho_0 c_0 b}\right) - ik|v_{\text{up}}| & \frac{k^2\kappa_0}{\rho_0 c_0} + \frac{h}{\rho_0 c_0 b} \\ -\frac{k^2\kappa_0}{\rho_0 c_0} + \frac{h}{\rho_0 c_0 b} & -\left(\frac{k^2\kappa_0}{\rho_0 c_0} + \frac{h}{\rho_0 c_0 b}\right) + ik|v_{\text{low}}| \end{pmatrix} \tag{8.7}$$

where k, h, and b denote the effective wave number, the convective heat transfer coefficient, and the thickness of the spinning plate. v_{up} and v_{low} are the rotating velocities of the upper and lower plates. An EP can be found in the spectrum of this Hamiltonian.

Then the temperature field of the central fluid is explored in different regions. In the vicinity of EP in region A (APT broken phase), the thermal field at the fluid interface moves towards the CW direction, though the rotating velocity at CW is smaller than the one at CCW. These positive phase deflections are caused by the velocity difference of the imposed advection. However, when the advection is extremely large, that is, away from the EP in region A, the temperature field becomes homogeneous without any chiral behaviour. When in region B (APT symmetric phase), the temperature field is unbiased with nonchiral heat transport. Moreover, the chirality vanishes at the EP due to purely imaginary eigenvalues and zero phase deflections in the eigenstates. Chiral thermal transport refers to an effectively anisotropic thermal conductivity, whereas the nonchiral one can be treated as isotropic. Based on these facts, the combination of nonchiral and chiral heat transports within one fluid may attribute to a twisted thermal profile. Thus, the chiral temperature field exhibits a large power in the free manipulation of the heat current.

Weyl point is a band degeneracy point whose dispersion satisfies the Weyl equation in high-energy physics [69, 70]. It can be regarded as a magnetic monopole in 3D momentum space and possesses a quantized Chern number. Moreover, due to the fermion doubling theorem, the Weyl points must pair with opposite topological charges. When the non-Hermitian term is introduced into Weyl Hamiltonian, the Weyl point will evolve into the Weyl exceptional ring composed of EPs [71]. The Weyl exceptional ring has been implemented in topological photonics [72] and topological acoustics [73].

A recent work demonstrates the realization of Weyl exceptional ring in diffusion systems [65]. Inspired by helical waveguides with helicoidal properties in optics [72], a central strip is surrounded by four counter-convection components in orthogonal spaces [see the schematic diagram in Fig. 1B in Ref. [65]]. To realize the periodic wave-like field, the initial temperature profile on the combined structure is imposed periodically and alternatively by the heating and cooling sources [see the experimental setup in Fig. 2B in Ref. [65]]. Substituting the periodic wave-like solution into a heat transfer process, the diffusive Weyl exceptional ring Hamiltonian is:

$$\hat{H} = \begin{pmatrix} -i\left[\frac{\kappa}{\rho c}(k_{\text{hor}}^2 + ik_{\text{ver}}^2) + m_{\text{hor}} + im_{\text{ver}}\right] + k_{\text{hor}} v_{\text{hor}} & i(m_{\text{hor}} + im_{\text{ver}} + k_{\text{ver}} v_{\text{ver}}) \\ i(m_{\text{hor}} + im_{\text{ver}} - k_{\text{ver}} v_{\text{ver}}) & -i\left[\frac{\kappa}{\rho c}(k_{\text{hor}}^2 + ik_{\text{ver}}^2) + m_{\text{hor}} + im_{\text{ver}}\right] - k_{\text{hor}} v_{\text{hor}} \end{pmatrix} \tag{8.8}$$

where κ, ρ, and c are the central strip's thermal conductivity, mass density, and heat capacity. v_{hor} and v_{ver} are the velocities of horizontal and vertical strips. The effective wave numbers can be indicated as $k_{\text{hor}} = k_{\text{ver}} = 1/L$ where L is the length of the central strip in one period. m_{hor} and m_{ver} denote the heat exchange rate in the horizontal and vertical plane. Because of the large vertical thickness of the central strip and material parameters of vertical strips, m_{ver} is proportional to the square root of v_{ver}. So a 3D synthetic parameter space (m_{ver}, $k_{\text{ver}} v_{\text{ver}}$, $k_{\text{hor}} v_{\text{hor}}$) can be generated, and it provides enough degrees of freedom to encircle the Weyl exceptional ring. When m_{ver} keeps unchanged, a Weyl exceptional ring can be found in the spectrum as shown in Figs. 1C and 1D in Ref. [65].

Next the thermal behaviour of Weyl exceptional ring is investigated. If the integration surface encircles the whole Weyl exceptional ring, the temperature profile and the location of the maximum temperature point remain stationary [see Fig. 2C in Ref. [65]], which is a signature of nontrivial topology. Besides, the Fermi arc state still exists but is suppressed in the Weyl exceptional ring system [71]. To observe the Fermi arc in diffusion systems, an additional subsystem should be inserted into the initial system, and it contributes to an opposite topological charge with an opposite integral direction [see the schematic diagram in Fig. 3B in Ref. [65]]. The evolution of maximum temperature positions for the inserted system also remains stationary with robustness [see Fig. 3E in Ref. [65]], and so does one for the original system.

8.4 Topological Phenomena in Convective Thermal Metamaterials

A problem that limits the development of thermal topology is that only the temperature field of the slowest decaying branch can be observed in purely diffusive systems. But the introduction of thermal convection can evade this disadvantage. Essentially, thermal convection is a wave-like field that induces a wave topology rather than a diffusive one. Based on this fact, many interesting and important topological states can be realized in diffusion systems. In this section, we will introduce two works about topological physics in convective thermal metamaterials, i.e., 1D topological insulator [74] and 2D quadrupole topological insulator [75].

The topological edge state can be probed by tracing the temperature evolution in pure conduction systems [48, 50]. However, the temperature field for the edge states decays rapidly and is not clearly observed, which is unfavorable for localized thermal management. With the help of convection modulation, a recent work states that the edge state for a 1D system has been observed with a robust temperature profile [74]. A planar fluid surface is considered in the virtual space (x_p, y_p, z) [see in Fig. 1a in Ref. [74]]. The periodic heat convections along the x_p direction are imposed on the corresponding regions marked by different colours. One lattice with four units along the z direction has been generated. Furthermore, the two ends for one unit along the x_p direction should be connected to form a ring in the transformed space (x, y, z) for

practical implementation [see the ring structure in Fig. 1c in Ref. [74]]. Substituting the wave-like solution into the heat transfer process, the Bloch Hamiltonian for this coupled ring chain structure can be written as

$$\hat{H} = i \begin{pmatrix} ikv_{\mathrm{i}} & m & 0 & me^{ik_t 4a} \\ m & -ikv_{\mathrm{ii}} & m & 0 \\ 0 & m & -ikv_{\mathrm{i}} & m \\ me^{-ik_t 4a} & 0 & m & ikv_{\mathrm{ii}} \end{pmatrix} - i \left(\frac{\kappa}{\rho c} k^2 + m \right) I_{4\times 4} \tag{8.9}$$

where κ, ρ, and c are the thermal conductivity, mass density, and heat capacity of rings. $m = \kappa/\rho cbd$ is the heat exchange rate between two adjacent rings. b and d are the thickness of the ring and interlayer. v_{i} and v_{ii} are the modulation velocities and a is the length of one unit. k denotes the fundamental wave number of ring and k_t indicates the effective Bloch wave number. I is the identity matrix. The topological properties of this system are nontrivial with a pair of edge states under this convective arrangement.

Coming to the temperature profile, the locations of maximum temperature points at the specific moments are presented in Fig. 2c in Ref. [74] for this arrangement. In this case, the thermal profile is robust and stationary, with some slight deviations with respect to the initial position at the two boundaries of the system, which is a signature of topological edge states. Besides, one domain wall composed of five nontrivial (20 units) and five trivial (20 units) lattices can be configured to implement an interface state. The temperature field shows a robust and stationary profile in the nontrivial lattice while it shows large deviations to the initial state and becomes homogenized finally in the trivial lattice. This exotic thermal profile shows great potential for manipulating the thermal field.

Higher-order topological insulator, which is beyond the conventional bulk-boundary correspondence, arouses much attention from the community of condensed matter physics [76–79]. Generally speaking, a d-dimensional nth-order topological insulator exhibits $(d-n)$-dimensional gapless boundary state ($n > 1$). Except in condensed matter physics, the higher-order topological insulator has also been realized in the classical wave systems [80–83]. There are two classes of higher-order topological insulators in the physics community, those without multipole moments, denoted by the 2D Su-Schrieffer-Heeger model, and those with multipole moments, denoted by the Benalcazar-Bernevig-Hughes model. Though there are some works which have realized the higher-order topological insulator without multipole moment in thermal diffusion [51–53], the quadrupole topological phase has not been implemented due to the absent bulk quadrupole moment and undefined negative couplings in heat transfer. A recent work has addressed these problems and realized the non-Hermitian quadrupole topological insulator in diffusion systems [75].

A convective thermal lattice with multiple discrete sites is shown in Fig. 1a in Ref. [75]. Each site represents a finite volume heat transfer process and the grid lines between neighboring sites correspond to their thermal couplings. Then the tunable advections $\Omega_{I/II}$ are adopted on each site to form a unit-structure consisting of four neighboring sites. The neighboring sites are coupled via the heat exchanges

induced by intracells and intercells. β is denoted as the ratio between the intercell and intracell thermal coupling strengths. Two types of tilted connections (over-coupling and under-coupling) are designed to mimic the coexisting positive and negative nearest-neighbor couplings with opposite isotherms.

With this structure, Hermitian advection and non-Hermitian couplings provide two modulations that enable a quadrupole topological phase. For the Hermitian advections, the Ω_{II} is adjusted while the Ω_I is kept unchanged. Besides, β is set to be one to ensure the heat exchange areas of the intracell and intercell components are the same. When modulating the Ω_{II} at $\Omega_{II} = -1.385\Omega_I$, the robust in-gap corner states can be found in the theoretical real band. In order to experimentally observe these corner states, a thermal system consisting of 12×12 sites is fabricated. All of the sites are hollowed out to allow water to pass. The measured temperature profile at the corner state is shown in Fig. 2d in Ref. [75], with a relatively high field intensities at four corners. Then the non-Hermitian thermal couplings are modulated as shown in Fig. 3a in Ref. [75]. With the same advections on all sites and intercell coupling channels, the intracell coupling channels are enlarged by inserting internal fins to modulate the β. At $\beta = 0.5$, the 0D corner states exist in the imaginary spectrum. The experimental temperature field distribution for the corner state is shown in Fig. 4d in Ref. [75]. The higher-order topological state can be observed both in the real-valued (modulated by advections) and imaginary-valued (modulated by thermal couplings) bands, which breaks the restriction that only real-valued band can exhibit corner states in classical wave systems.

Besides, a separate work exhibits the implementation of a Chern insulator with the chiral edge state in diffusion systems [84]. The basic unit is a hexagonal structure with thermal convection. Based on this structure, a honeycomb lattice can be designed to mimic the Haldane model [85]. A steady temperature field will propagate unidirectionally along the boundary of the system without backscattering.

8.5 Conclusion and Outlook

As a conclusion, we discuss some works on non-Hermitian physics and topological phenomena in convection-conduction systems. From the point of view of non-Hermitian physics, we first discuss the realization of EP in thermal diffusion, followed by the high-order EP and the dynamically encirclement of EP. As two extensions of the EP, we introduce chiral heat transport around the EP and diffusive Weyl exceptional ring. From topological physics, 1D thermal topological insulators and 2D thermal quadrupole topological insulators have been introduced as two examples of diffusive topological phases.

The promising future of topological and non-Hermitian convective thermal metamaterials can be anticipated [86]. Until now, only a small fraction of exotic phases of matter have been realized in diffusive systems. The realization of a wide variety of topological states is a prevailing trend in this field. From the non-equilibrium dynamics, except for non-Hermitian physics, Floquet thermal metamaterials can be devised

by spatiotemporal modulating the materials–parameters [87]. From the higher-dimensional systems, many peculiar configurations, such as fractal systems [88], moiré lattices [89], and disclinations [90], can be engineered in the thermal lattices. Potential applications in topological convective thermal materials are also to be expected. Topological edge states may be useful for localized heat management and robust heat transport. In brief, topological and non-Hermitian convective thermal metamaterials are highly interdisciplinary and of great scientific and technological values.

References

1. Ashida, Y., Gong, Z.P., Ueda, M.: Non-Hermitian physics. Adv. Phys. **69**, 249 (2020)
2. Bergholtz, E.J., Budich, J.C., Kunst, F.K.: Exceptional topology of non-Hermitian systems. Rev. Mod. Phys. **93**, 015005 (2021)
3. Bender, C.M.: Making sense of non-Hermitian Hamiltonians. Rep. Prog. Phys. **70**, 947 (2007)
4. Bender, C.M., Boettcher, S.: Real spectra in non-Hermitian Hamiltonians having PT symmetry. Phys. Rev. Lett. **80**, 5243 (1998)
5. Borgnia, D.S., Kruchkov, A.J., Slager, R.-J.: Non-Hermitian boundary modes and topology. Phys. Rev. Lett. **124**, 056802 (2020)
6. Yao, S.Y., Wang, Z.: Edge states and topological invariants of non-Hermitian systems. Phys. Rev. Lett. **121**, 086803 (2018)
7. Okuma, N., Kawabata, K., Shiozaki, K., Sato, M.: Topological origin of non-Hermitian skin effects. Phys. Rev. Lett. **124**, 086801 (2020)
8. Zhang, K., Yang, Z.S., Fang, C.: Correspondence between winding numbers and skin modes in non-Hermitian systems. Phys. Rev. Lett. **125**, 126402 (2020)
9. Gong, Z.P., Ashida, Y., Kawabata, K., Takasan, K., Higashikawa, S., Ueda, M.: Topological phases of non-Hermitian systems. Phys. Rev. X **8**, 031079 (2018)
10. Kawabata, K., Shiozaki, K., Ueda, M., Sato, M.: Symmetry and topology in non-Hermitian physics. Phys. Rev. X **9**, 041015 (2019)
11. Klitzing, K.v., Dorda, G., Pepper, M.: New method for high-accuracy determination of the fine-structure constant based on quantized Hall resistance. Phys. Rev. Lett. **45**, 494 (1980)
12. Klitzing, K.v.: Developments in the quantum Hall effect. Philos. Trans. R. Soc. London, Ser. A **363**, 2203 (2005)
13. Hasan, M.Z., Kane, C.L.: Colloquium: Topological insulators. Rev. Mod. Phys. **82**, 3045 (2010)
14. Qi, X.-L., Zhang, S.-C.: Topological insulators and superconductors. Rev. Mod. Phys. **83**, 1057 (2011)
15. Lu, L., Joannopoulos, J.D., Soljačić, M.: Topological photonics. Nat. Photon. **8**, 821 (2014)
16. Ozawa, T., Price, H.M., Amo, A., Goldman, N., Hafezi, M., Lu, L., Rechtsman, M.C., Schuster, D., Simon, J., Zilberberg, O., Carusotto, I.: Topological photonics. Rev. Mod. Phys. **91**, 015006 (2019)
17. Yang, Z.J., Gao, F., Shi, X.H., Lin, X., Gao, Z., Chong, Y.D., Zhang, B.L.: Topological acoustics. Phys. Rev. Lett. **114**, 114301 (2015)
18. Xue, H.R., Yang, Y.H., Zhang, B.L.: Topological acoustics. Nat. Rev. Mater. **7**, 974 (2022)
19. Huber, S.D.: Topological mechanics. Nat. Phys. **12**, 621 (2016)
20. Huang, J.-P.: Theoretical Thermotics: Transformation Thermotics and Extended Theories for Thermal Metamaterials. Springer, Singapore (2020)
21. Xu, L.-J., Huang, J.-P.: Transformation Thermotics and Extended Theories: Inside and outside Metamaterials. Springer, Singapore (2023)
22. Yang, S., Wang, J., Dai, G.L., Yang, F.B., Huang, J.P.: Controlling macroscopic heat transfer with thermal metamaterials: theory, experiment and application. Phys. Rep. **908**, 1–65 (2021)

23. Zhang, Z.R., Xu, L.J., Qu, T., Lei, M., Lin, Z.-K., Ouyang, X.P., Jiang, J.-H., Huang, J.P.: Diffusion metamaterials. Nat. Rev. Phys. **5**, 218 (2023)
24. Yang, F.B., Zhang, Z.R., Xu, L.J., Liu, Z.F., Jin, P., Zhuang, P.F., Lei, M., Liu, J.R., Jiang, J.-H., Ouyang, X.P., Marchesoni, F., Huang, J.P.: Controlling mass and energy diffusion with metamaterials. Rev. Mod. Phys. **96**, 015002 (2024)
25. Li, Y., Li, W., Han, T.C., Zheng, X., Li, J.X., Li, B.W., Fan, S.H., Qiu, C.-W.: Transforming heat transfer with thermal metamaterials and devices. Nat. Rev. Mater. **6**, 488–507 (2021)
26. Ju, R., Xu, G.Q., Xu, L.J., Qi, M.H., Wang, D., Cao, P.-C., Xi, R., Shou, Y.F., Chen, H.S., Qiu, C.-W., Li, Y.: Convective thermal metamaterials: Exploring high-efficiency, directional, and wave-like heat transfer. Adv. Mater. **35**, 2209123 (2022)
27. Fan, C.Z., Gao, Y., Huang, J.P.: Shaped graded materials with an apparent negative thermal conductivity. Appl. Phys. Lett. **92**, 251907 (2008)
28. Han, T.C., Bai, X., Thong, J.T.L., Li, B.W., Qiu, C.W.: Full control and manipulation of heat signatures: cloaking, camouflage and thermal metamaterials. Adv. Mater. **26**, 1731 (2014)
29. Hu, R., Zhou, S.L., Li, Y., Lei, D.Y., Luo, X.B., Qiu, C.-W.: Illusion thermotics. Adv. Mater. **30**, 1707237 (2018)
30. Xu, L.J., Yang, S., Huang, J.P.: Thermal transparency induced by periodic interparticle interaction. Phys. Rev. Appl. **11**, 034056 (2019)
31. Wang, R.Z., Xu, L.J., Ji, Q., Huang, J.P.: A thermal theory for unifying and designing transparency, concentrating and cloaking. J. Appl. Phys. **123**, 115117 (2018)
32. Dai, G.L., Shang, J., Huang, J.P.: Theory of transformation thermal convection for creeping flow in porous media: cloaking, concentrating, and camouflage. Phys. Rev. E **97**, 022129 (2018)
33. Dai, G.L., Huang, J.P.: A transient regime for transforming thermal convection: cloaking, concentrating, and rotating creeping flow and heat flux. J. Appl. Phys. **124**, 235103 (2018)
34. Xu, L.J., Xu, G.Q., Huang, J.P., Qiu, C.-W.: Diffusive Fizeau drag in spatiotemporal thermal metamaterials. Phys. Rev. Lett. **128**, 145901 (2022)
35. Xu, L.J., Xu, G.Q., Li, J.X., Li, Y., Huang, J.P., Qiu, C.-W.: Thermal willis coupling in spatiotemporal diffusive metamaterials. Phys. Rev. Lett. **129**, 155901 (2022)
36. Torrent, D., Poncelet, O., Batsale, J.-C.: Nonreciprocal thermal material by spatiotemporal modulation. Phys. Rev. Lett. **120**, 125501 (2018)
37. Camacho, M., Edwards, B., Engheta, N.: Achieving asymmetry and trapping in diffusion with spatiotemporal metamaterials. Nat. Commun. **11**, 3733 (2020)
38. Li, J.X., Li, Y., Cao, P.-C., Qi, M.H., Zheng, X., Peng, Y.-G., Li, B.W., Zhu, X.-F., Alù, A., Chen, H.S., Qiu, C.-W.: Reciprocity of thermal diffusion in time-modulated systems. Nat. Commun. **13**, 167 (2022)
39. Li, Y., Li, J.X., Qi, M.H., Qiu, C.-W., Chen, H.S.: Diffusive nonreciprocity and thermal diode. Phys. Rev. B **103**, 014307 (2021)
40. Xu, L.J., Huang, J.P., Ouyang, X.P.: Nonreciprocity and isolation induced by an angular momentum bias in convection-diffusion systems. Appl. Phys. Lett. **118**, 221902 (2021)
41. Xu, L.J., Dai, G.L., Huang, J.P.: Transformation multithermotics: Controlling radiation and conduction simultaneously. Phys. Rev. Appl. **13**, 024063 (2020)
42. Yang, S., Xu, L.J., Dai, G.L., Huang, J.P.: Omnithermal metamaterials switchable between transparency and cloaking. J. Appl. Phys. **128**, 095102 (2020)
43. Xu, L.J., Huang, J.P.: Metamaterials for manipulating thermal radiation: Transparency, cloak, and expander. Phys. Rev. Appl. **12**, 044048 (2019)
44. Xu, L.J., Dai, G.L., Wang, G., Huang, J.P.: Geometric phase and bilayer cloak in macroscopic particle-diffusion systems. Phys. Rev. E **102**, 032140 (2020)
45. Zhang, Z.R., Yang, F.B., Huang, J.P.: Intelligent chameleonlike metashells for mass diffusion. Phys. Rev. Appl. **19**, 024009 (2023)
46. Zhang, Z.R., Huang, J.P.: Transformation plasma physics. Chin. Phys. Lett. **39**, 075201 (2022)
47. Liu, Z.F., Huang, J.P.: Topological plasma transport from a diffusion view. Chin. Phys. Lett. **40**, 110305 (2023)
48. Yoshida, T., Hatsugai, Y.: Bulk-edge correspondence of classical diffusion phenomena. Sci. Rep. **11**, 888 (2021)

49. Qi, M.H., Wang, D., Cao, P.-C., Zhu, X.-F., Qiu, C.-W., Chen, H.S., Li, Y.: Geometric phase and localized heat diffusion. Adv. Mater. **34**, 2202241 (2022)
50. Hu, H., Han, S., Yang, Y.H., Liu, D.J., Xue, H.R., Liu, G.-G., Cheng, Z.Y., Wang, Q.J., Zhang, S., Zhang, B.L., Luo, Y.: Observation of topological edge states in thermal diffusion. Adv. Mater. **34**, 2202257 (2022)
51. Liu, Z.F., Xu, L.J., Huang, J.P.: Higher-dimensional topological insulators in pure diffusion systems (2022). arXiv:2206.09837
52. Qi, M.H., Wang, Y.X., Cao, P.-C., Zhu, X.-F., Gao, F., Chen, H.S., Li, Y.: Observation of multiple topological corner states in thermal diffusion (2023). arXiv:2304.12641
53. Wu, H.T., Hu, H., Wang, X.X., Xu, Z.X., Zhang, B.L., Wang, Q.J., Zheng, Y.J., Zhang, J.J., Cui, T.J., Luo, Y.: Higher-order topological states in thermal diffusion. Adv. Mater. **35**, 202210825 (2023)
54. Cao, P.-C., Li, Y., Peng, Y.-G., Qi, M.H., Huang, W.-X., Li, P.-Q., Zhu, X.-F.: Diffusive skin effect and topological heat funneling. Commun. Phys. **4**, 230–237 (2021)
55. Cao, P.-C., Peng, Y.-G., Li, Y., Zhu, X.-F.: Phase-locking diffusive skin effect. Chin. Phys. Lett. **39**, 057801 (2022)
56. Liu, Z.F., Huang, J.P.: Non-Hermitian diffusive quasicrystal (2022). arXiv:2208.06765
57. Li, Y., Qi, M.H., Li, J.X., Cao, P.-C., Wang, D., Zhu, X.-F., Qiu, C.-W., Chen, H.S.: Heat transfer control using a thermal analogue of coherent perfect absorption. Nat. Commun. **13**, 2683 (2022)
58. Li, Y., Peng, Y.G., Han, L., Miri, M.A., Li, W., Xiao, M., Zhu, X.F., Zhao, J.L., Alu, A., Fan, S.H., Qiu, C.W.: Anti-parity-time symmetry in diffusive systems. Science **364**, 170 (2019)
59. Cao, P.C., Li, Y., Peng, Y.G., Qiu, C.W., Zhu, X.F.: High-order exceptional points in diffusive systems: robust APT symmetry against perturbation and phase oscillation at APT symmetry breaking. ES Energy Environ. **7**, 48 (2020)
60. Xu, G.Q., Li, Y., Li, W., Fan, S.H., Qiu, C.-W.: Configurable phase transitions in a topological thermal material. Phys. Rev. Lett. **127**, 105901 (2021)
61. Leykam, D., Bliokh, K.Y., Huang, C.L., Chong, Y., Nori, F.: Edge modes, degeneracies, and topological numbers in non-Hermitian systems. Phys. Rev. Lett. **118**, 040401 (2017)
62. Shen, H.T., Zhen, B., Fu, L.: Topological band theory for non-Hermitian Hamiltonians. Phys. Rev. Lett. **120**, 146402 (2018)
63. Xu, L.J., Wang, J., Dai, G.L., Yang, S., Yang, F.B., Wang, G., Huang, J.P.: Geometric phase, effective conductivity enhancement, and invisibility cloak in thermal convection-conduction. Int. J. Heat Mass Transf. **165**, 120659 (2021)
64. Xu, G.Q., Zhou, X., Li, Y., Cao, Q.T., Chen, W.J., Xiao, Y.F., Yang, L., Qiu, C.-W.: Non-Hermitian chiral heat transport. Phys. Rev. Lett. **130**, 266303 (2023)
65. Xu, G.Q., Li, W., Zhou, X., Li, H.G., Li, Y., Fan, S.H., Zhang, S., Christodoulides, D.N., Qiu, C.-W.: Observation of Weyl exceptional rings in thermal diffusion. Proc. Natl. Acad. Sci. U.S.A. **119**, e2110018119 (2022)
66. Wang, C.Q., Jiang, X.F., Zhao, G.M., Zhang, M.Z., Hsu, C.W., Peng, B., Stone, A.D., Jiang, L., Yang, L.: Electromagnetically induced transparency at a chiral exceptional point. Nat. Phys. **16**, 334 (2020)
67. Peng, B., Özdemir S.K., Liertzer, M., Chen, W.J., Kramer, J., Yilmaz, H., Wiersig, J., Rotter, S., Yang, L.: Chiral modes and directional lasing at exceptional points. Proc. Natl. Acad. Sci. U.S.A. **113**, 6845 (2016)
68. Peng, B., Özdemir S.K., Lei, F.C., Monifi, F., Gianfreda, M., Long, G.L., Fan, S.H., Nori, F., Bender, C.M., Yang, L.: Parity-time-symmetric whispering-gallery microcavities. Nat. Phys. **10**, 394 (2014)
69. Wan, X.G., Turner, A.M., Vishwanath, A., Savrasov, S.Y.: Topological semimetal and Fermi-arc surface states in the electronic structure of pyrochlore iridates. Phys. Rev. B **83**, 205101 (2011)
70. Armitage, N.P., Mele, E.J., Vishwanath, A.: Weyl and Dirac semimetals in three-dimensional solids. Rev. Mod. Phys. **90**, 015001 (2018)

71. Xu, Y., Wang, S.-T., Duan, L.-M.: Weyl exceptional rings in a three-dimensional dissipative cold atomic gas. Phys. Rev. Lett. **118**, 045701 (2017)
72. Cerjan, A., Huang, S., Chen, K.P., Chong, Y.D., Rechtsman, M.C.: Experimental realization of a Weyl exceptional ring. Nat. Photon. **13**, 623 (2019)
73. Liu, J.J., Li, Z.-W., Chen, Z.-G., Tang, W.Y., Chen, A., Liang, B., Ma, G.C., Cheng, J.-C.: Experimental realization of Weyl exceptional rings in a synthetic three-dimensional non-Hermitian phononic crystal. Phys. Rev. Lett. **129**, 084301 (2022)
74. Xu, G.Q., Yang, Y.H., Zhou, X., Chen, H.S., Alù, A., Qiu, C.-W.: Diffusive topological transport in spatiotemporal thermal lattices. Nat. Phys. **18**, 450 (2022)
75. Xu, G.Q., Zhou, X., Yang, S.H., Wu, J., Qiu, C.-W.: Observation of bulk quadrupole in topological heat transport. Nat. Commun. **14**, 3252 (2023)
76. Benalcazar, W.A., Bernevig, B.A., Hughes, T.L.: Quantized electric multipole insulators. Science **357**, 61 (2017)
77. Benalcazar, W.A., Bernevig, B.A., Hughes, T.L.: Electric multipole moments, topological multipole moment pumping, and chiral hinge states in crystalline insulators. Phys. Rev. B **96**, 245115 (2017)
78. Schindler, F., Cook, A.M., Vergniory, M.G., Wang, Z.J., Parkin, S.S.P., Bernevig, B.A., Neupert, T.: Higher-order topological insulators. Sci. Adv. **4**, eaat0346 (2018)
79. Benalcazar, W.A., Li, T.H., Hughes, T.L.: Quantization of fractional corner charge in C_n-symmetric higher-order topological crystalline insulators. Phys. Rev. B **99**, 245151 (2019)
80. Xie, B.Y., Wang, H.-X., Zhang, X.J., Zhan, P., Jiang, J.-H., Lu, M.H., Chen, Y.F.: Higher-order band topology. Nat. Rev. Phys. **3**, 520 (2021)
81. Imhof, S., Berger, C., Bayer, F., Brehm, J., Molenkamp, L., Kiessling, T., Schindler, F., Lee, C.H., Greiter, M., Neupert, T., Thomale, R.: Topolectrical-circuit realization of topological corner modes. Nat. Phys. **14**, 925 (2018)
82. He, L., Addison, Z., Mele, E.J., Zhen, B.: Quadrupole topological photonic crystals. Nat. Commun. **11**, 3119 (2020)
83. Qi, Y.J., Qiu, C.Y., Xiao, M., He, H.L., Ke, M.Z., Liu, Z.Y.: Acoustic realization of quadrupole topological insulators. Phys. Rev. Lett. **124**, 206601 (2020)
84. Xu, L.J., Huang, J.P.: Robust one-way edge state in convection-diffusion systems. EPL **134**, 60001 (2021)
85. Haldane, F.D.M.: Model for a quantum Hall effect without Landau levels: Condensed-matter realization of the "parity anomaly". Phys. Rev. Lett. **61**, 2015 (1988)
86. Liu, Z.F., Jin, P., Lei, M., Wang, C.M., Jiang, J.-H., Huang, J.P.: Topological diffusionics: controlling particle and energy diffusion withtopological principles. to be submitted
87. Yin, S.X., Galiffi, E., Alù, A.: Floquet metamaterials. eLight **2**, 8 (2022)
88. Biesenthal, T., Maczewsky, L.J., Yang, Z.J., Kremer, M., Segev, M., Szameit, A., Heinrich, M.: Fractal photonic topological insulators. Science **376**, 1114 (2022)
89. Wang, P., Zheng, Y.L., Chen, X.F., Huang, C.M., Kartashov, Y.V., Torner, L., Konotop, V.V., Ye, F.W.: Localization and delocalization of light in photonic moiré lattices. Nature **577**, 42 (2020)
90. Liu, Y., Leung, S.W., Li, F.-F., Lin, Z.-K., Tao, X.F., Poo, Y., Jiang, J.-H.: Bulk-disclination correspondence in topological crystalline insulators. Nature **589**, 381 (2021)

Chapter 9
Beyond Traditional Thermal Convection: Spatiotemporal Modulation in Metamaterials

Yuqian Zhao, Liujun Xu, and Fubao Yang

9.1 Opening Remarks

Given the pressing global energy crisis, the importance of efficient thermal management has come to the forefront. In recent times, advancements in the field of convective heat metamaterials have introduced innovative design possibilities for controlling heat transfer. These metamaterials have created macroscopic thermal meta-devices like heat concentrators, thermal rotators, and thermal illusions by manipulating thermal conductivity distribution. Additionally, they have facilitated the exploration of microscopic devices for thermal information processing, leveraging phonon transport and scattering theories. Examples include thermal storage units, thermal logic gates, and thermal diodes. However, many of these metamaterials operate under static conditions, making them susceptible to external disturbances and restricting their broader applications. To overcome this, the spatiotemporal modulation technique has emerged as a promising solution. By dynamically adjusting these microstructures over time and space, it significantly boosts the development of managing heat transfer.

In the domain of thermal transport, thermal convection has always been a focal point. This chapter delves into the origins and implications of thermal convection. At its core, thermal convection is triggered by the movement of liquids or solids, instigated by temperature differentials or external forces. As these substances heat up, their molecular activity increases, causing density fluctuations. This movement of molecules, carrying thermal energy, results in thermal convection. Liu-Jun Xu and Ji-Ping Huang's book [1] offers a comprehensive insight into this phenomenon,

Y. Zhao (✉) · F. Yang
Department of Physics, Key Laboratory of Micro and Nano Photonic Structures (MOE), and State Key Laboratory of Surface Physics, Fudan University, Shanghai 200438, China
e-mail: zyq18834286856@163.com

L. Xu
Graduate School of China Academy of Engineering Physics, Beijing 100193, China

F.-B. Yang and J.-P. Huang, *Diffusionics*,
https://doi.org/10.1007/978-981-97-0487-3_9

discussing ways to manipulate thermal waves and achieve Hele-Shaw convective cloaking. Their work emphasizes the central role of thermal convection in heat transfer. Other related research areas, like thermal diodes and solar cells, have also gained traction. Spatiotemporal modulation is believed to mimic traditional thermal convection effects, a notion inspired by modulation research in acoustics and optics. This approach not only provides a novel perspective on non-reciprocity but also broadens the scope of material parameter space. Furthermore, it sets the stage for discovering unique functionalities and physical phenomena [2–6]. Thus, we believe that spatiotemporal modulation, by inducing equivalent thermal convection, addresses current challenges and sets the direction for future metamaterial research.

Since the inception of spatiotemporal modulation, its applications have spanned wave systems, photonics [7–10], acoustics [11–14] and more, see Fig. 9.1. It's instrumental in realizing non-reciprocity, leading to asymmetric propagation. Beyond electrical systems, its use in elastic wave systems has broken mechanical reciprocity, enabling unidirectional propagation. In photonics, it offers multi-dimensional control, emphasizing time as an added dimension. This modulation technique, combined with the observed drag effects in various physical fields, signifies the essence of non-reciprocity in diffusion-related periodic transmission, heralding a new era in applications like alternating current (AC) and fluctuating temperatures.

In this chapter, we initially introduce the mechanisms and developments of spatiotemporal modulation. Subsequently, we delve into the non-reciprocal phenomena induced by thermal spatiotemporal modulation. In conclusion, we summarize the advancements and future prospects in this domain. We aspire for this chapter to elucidate that spatiotemporal modulation, as equivalent thermal convection, offers us an opportunity to explore physical phenomena from a novel perspective.

9.2 Mechanism and Development of Spatiotemporal Modulation

In the realm of thermal metamaterials [17–27], spatiotemporal modulation typically involves the periodic or aperiodic adjustment of a material's thermal conductivity or heat capacity in both time and space. Such modulation can be achieved through the external application of electric fields, magnetic fields, mechanical stresses, or other methods. The primary objective of this modulation is to control heat flux without altering the intrinsic structure of the material.

The mechanisms to achieve this equivalent thermal convection through spatiotemporal modulation are as follows: Through spatiotemporal modulation, external signals such as voltage, light, or acoustic waves can be applied to specific parts of a material, altering its thermal properties. If oriented in a distinct direction, such modulation can emulate the flow effect within the material. Moreover, it can introduce a localized phase delay; when this delay varies across space, it effectively simulates an equivalent convective velocity. Furthermore, when metamaterials engage with exter-

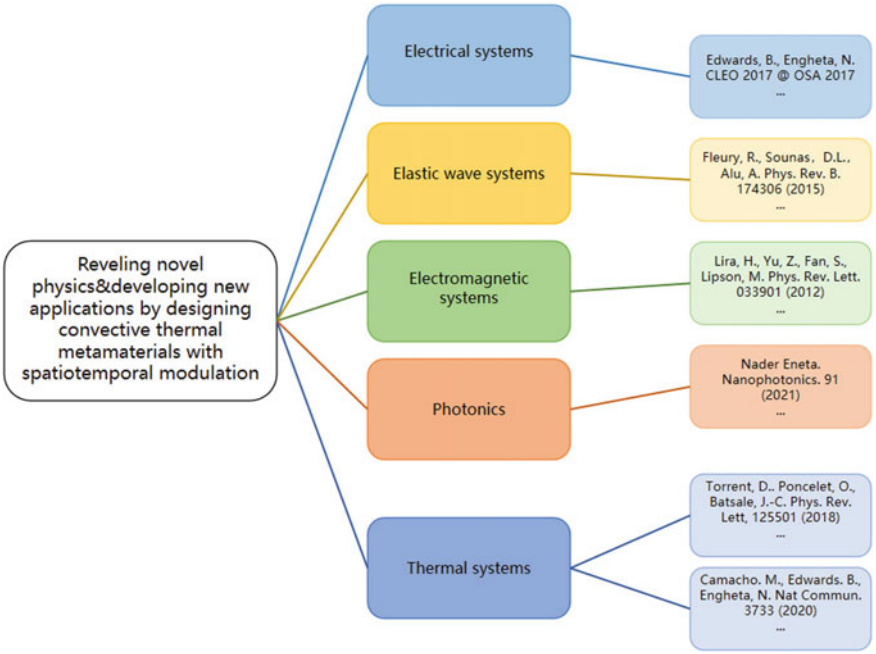

Fig. 9.1 A large number of novel physics and applications have arisen from convective thermal metamaterials with spatiotemporal modulation [15]. Ever since the introduction of spatiotemporal modulation [16], it has found applications in electrical systems, elastic wave systems, electromagnetic systems, photonics, and thermal systems

nal heat sources, spatiotemporal modulation possesses the capability to transform the nature of this interaction, thus mirroring convective effects.

Given that such equivalent convection can influence the direction and speed of heat flux propagation, it offers tremendous potential for the design and realization of innovative and tunable thermal metamaterials. This not only opens up new possibilities in areas like thermal management, heat storage, and heat conversion but also paves the way for novel methods of controlling and manipulating heat flux.

Having established the foundational concepts and mechanisms of spatiotemporal modulation, let us now delve into its practical applications and implications across various domains. Since the introduction of the concept of spatiotemporal modulation, it has been intensively studied not only in wave systems but also in diffusive systems [15, 28]. One direct application of spatiotemporal modulation is to realize non-reciprocity, i.e., asymmetric propagation in opposite directions. For instance, once the dielectric constant is modulated, electromagnetic waves will propagate non-reciprocally in two interconnected waveguides [29]. Subsequent research has theoretically demonstrated how time-varying material parameters (capacitance and conductivity) produce effective media with asymmetric diffusive properties, applied in thermodynamics and electrostatics.

Beyond electrical systems, spatiotemporal modulation has also been employed in elastic wave systems. In 2015, the propagation of longitudinal and transverse waves in beams with spatially and temporally varying elastic properties was reported [11]. The spatiotemporal modulation of elastic properties broke mechanical reciprocity and led to unidirectional propagation. Using an analytical approach, the authors characterized the structure's non-reciprocal behavior by analyzing symmetry-breaking in the dispersion spectrum, leading to the formation of directional band gaps and shifts in the first Brillouin zone boundaries. This method connected the position and width of the directional band gaps with modulation parameters. In addition, the research identified the critical modulation speed to maximize non-reciprocal effects. Spatiotemporal modulation has paved new paths for unidirectional propagation in elastic wave systems [11].

Beyond applications in elastic wave systems, spatiotemporal modulation holds broad potential in various domains. In photonics, for instance, it facilitates multi-dimensional control. Recently, researchers have delved deeply into the high degrees of freedom and multi-dimensionality of metamaterials. In this context, time is emphasized as an additional dimension, granting more opportunities to modulate light-matter interactions. Moreover, these studies have also explored applications in photonics.

Beyond the aforementioned applications, spatiotemporal modulation also intersects with specific phenomena in various fields of physics, notably non-reciprocity. As a typical feature of non-reciprocal transmission, drag effects of some physical fields, such as the Fizeau drag of light [30–34], plasmon excitations, and thermal waves, have been observed. This means that waves propagate at different speeds along or against the direction of media movement or modulation. Recent studies have reported another drag effect on diffusion waves, exploring non-reciprocal mode transitions under periodic excitation, akin to tunable thermal rectification caused by conductivity modulation. By modulating conductivity, a significant rectification effect on the diffusion wave field was observed, and irreversible transmission of heat flux was observed. The successful realization of a spatiotemporal diffusion wave metamaterial signifies the fundamental meaning of non-reciprocity in diffusion-related periodic transmission and the industrial benefits in applications like alternating current (AC), fluctuating temperatures, varying particle concentrations, etc.

9.3 Spatiotemporal Thermal Modulation

9.3.1 Tunable Thermal Wave Nonreciprocity by Spatiotemporal Modulation

Regarding thermal spatiotemporal modulation, pioneering studies on non-reciprocal thermal materials [35] have shown that if thermal conductivity and mass density undergo spatiotemporal modulation, advection terms appear in the quasi-steady con-

duction equations, thus realizing non-reciprocity. A similar approach is viable for electric diffusion systems, starting from Fick's diffusion equation in one-dimensional settings and experimentally achieving the first asymmetric control and capture effects in electrically diffusive metamaterials [36]. From the standpoint that all diffusion-based phenomena tend toward equilibrium as dictated by the second law of thermodynamics, this seems unproblematic. However, constrained by mass conservation, matter, as a thermal energy carrier, cannot be created or destroyed without a cost. Recent findings suggest that "with temporal and spatial modulation of density, a mass movement is inevitable even without a net directional mass flow" Therefore, realizing non-reciprocity in time-modulated density and thermal conductivity is challenging, as effects from the "motion" of parameters and the unavoidable mass flow counteract each other [37]. Clearly thermal spatiotemporal modulation presents new opportunities for creating thermal materials with unconventional properties.

While various wave types have been investigated to achieve non-reciprocity based on spatiotemporal modulation, most studies focus only on heat transfer scenarios with constant boundary temperatures. There remains a gap in understanding mechanisms for realizing thermal wave non-reciprocity. Mechanistically, thermal waves can be conceptualized as periodic temperature fluctuations, a unique wave primarily is governed by the diffusion equation (i.e., the Fourier equation), termed diffusion waves [38]. Application-wise, thermal waves are apt for thermal detection and are widely utilized in the aerospace, mechanical, and electrical sectors [39–41]. Some research has explored spatiotemporal modulation to achieve thermal wave non-reciprocity [42]. The physical rationale is that modulating two physical parameters in an open thermal system leads to a virtual advective term, resulting in momentum bias. The phase difference between these two parameters provides a crucial means to control asymmetric heat transfer. Considering a 1D passive thermal conduction process governed by an equation involving thermal conductivity $\sigma\,(x-ut)$ and the product of mass density and heat capacity $\rho\,(x-ut)$.

$$\rho\,(x-ut)\,\frac{\partial T}{\partial t}+\frac{\partial}{\partial x}\left[-\sigma\,(x-ut)\,\frac{\partial T}{\partial x}\right]=0, \tag{9.1}$$

$$\sigma\,(x-ut)=\sigma_A+\sigma_B\cos\left[K\,(x-ut)\right], \tag{9.2a}$$

$$\rho\,(x-ut)=\rho_A+\rho_B\cos\left[K\,(x-ut)+\alpha\right], \tag{9.2b}$$

where σ_A, σ_B, ρ_A, and ρ_B are four constants. $K=2\pi/\gamma$ is wave number, γ is wavelength, u is modulation speed, and α is phase difference. Since $\sigma\,(x-ut)$ and $\rho\,(x-ut)$ are periodic functions, the Bloch theorem is applicable and the temperature solution can be expressed as

$$T=\phi(x-ut)\mathrm{e}^{\mathrm{i}(kx-\omega t)} \tag{9.3}$$

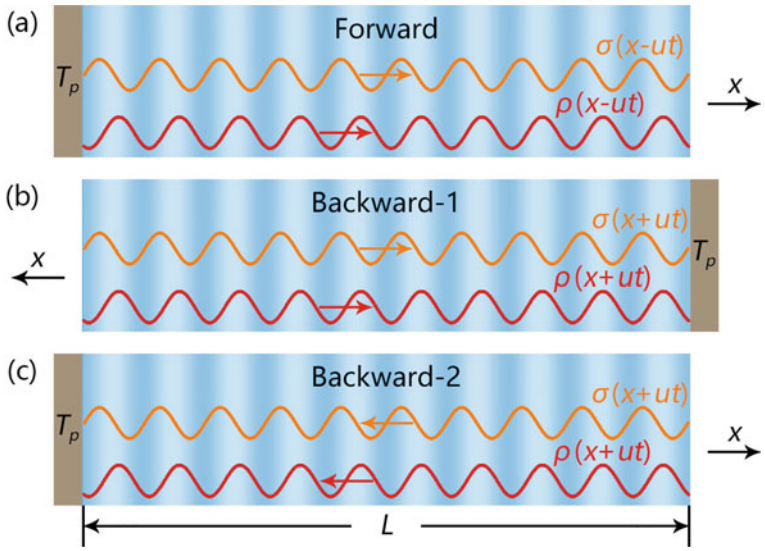

Fig. 9.2 Tunable thermal wave nonreciprocity by spatiotemporal modulation **a** Forward case. **b** Backward-1 case by changing the source position. **c** Backward-2 case by changing the modulation direction. (from Ref. [42])

where k and ω are, respectively, the wave number and circular frequency of a thermal wave. $\phi\,(x-ut)$ is an amplitude modulation function that has the same periodicity as $\sigma\,(x-ut)$ and $\rho\,(x-ut)$. Equation (9.1) can then be homogenized with the approximations of $k \ll K$ and $\omega \ll uK$,

$$\tilde{\rho}\frac{\partial \tilde{T}}{\partial t} + C\frac{\partial \tilde{T}}{\partial x} - \tilde{\sigma}\frac{\partial^2 \tilde{T}}{\partial x^2} - S\frac{\partial^2 \tilde{T}}{\partial x \partial t} = 0 \tag{9.4}$$

Researchers delve into the nonreciprocity brought about by spatiotemporal modulation. Subsequently, the subscripts of f, $b1$, and $b2$ signify the parameters associated with the forward scenario, the backward-1 scenario, and the backward-2 scenario as depicted in Fig. 9.2. The two backward scenarios are congruent only when $\alpha = 0$. Given that $\tilde{\sigma}$ and $\tilde{\rho}$ don't play a role in nonreciprocity, the primary focus is on C and S. For the forward case, we know $C_f = C$ and $S_f = S$. For the backward-1 case, we can derive $C_{b1} = -C$ and $S_{b1} = -S$. Nonreciprocity requires $C_f \neq C_{b1}$ (or $S_f \neq S_{b1}$). Therefore, as long as $C \neq 0$ (or $S \neq 0$), nonreciprocity will occur and a larger C (or S) yields larger nonreciprocity.

9.3.2 *Theory for Diffusive Fizeau Drag: Willis Coupling*

It is well known that porous media theory has been used to adapt to transformation theory, paving the way for the design of novel convective thermal metamaterials. This has sparked new research hotspots in thermal wave detection, thermal sensing, and thermal wave modulation. Recently, a spatiotemporal thermal metamaterial based on porous media heat transfer was designed to demonstrate the diffusion simulation of Fizeau drag, see Fig. 9.3 [43]. Unlike the dragging of photons and polaritons due to momentum interaction, see Fig. 9.3a, b, dragging the macroscopic heat by biased advection is inherently difficult because of the lack of macroscopic heat momentum, see Fig. 9.3c. As a result, the speeds of forward and backward-propagating temperature fields remain the same. However, the temperature field amplitudes differ in opposite directions because of the heat transfer's dissipative nature. Thus, achieving diffusive Fizeau drag remains a formidable challenge. Researchers designed a spatiotemporal thermal metamaterial characterized by space-related inhomogeneity and time-related advection to explore diffusive Fizeau drag in heat transfer, see

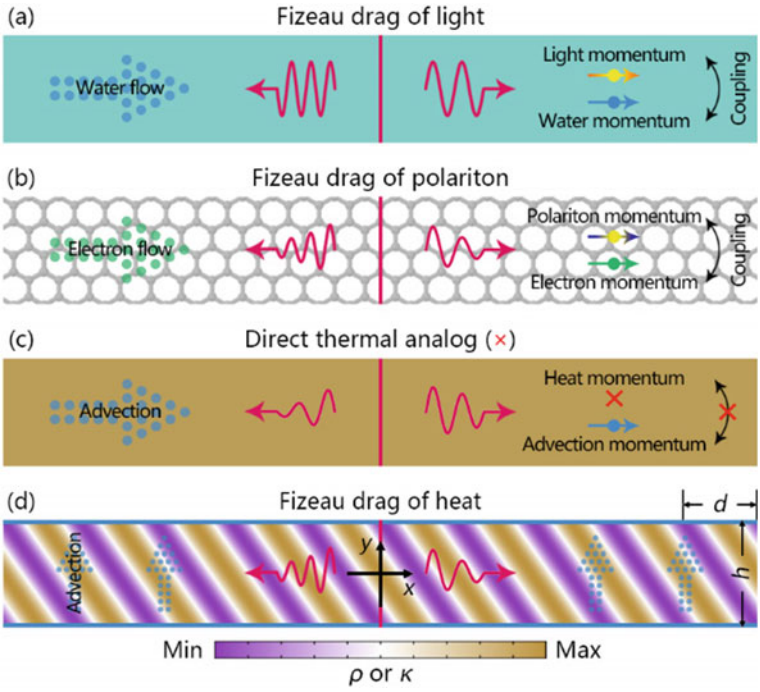

Fig. 9.3 Origin of diffusive Fizeau drag. Fizeau drag of **a** light and **b** polariton by the momentum interaction. **c** Failure of a direct thermal analog due to the lack of macroscopic heat momentum. **d** Fizeau drag of heat in a spatiotemporal thermal metamaterial by thermal Willis coupling. The red arrows contain information on wave number and amplitude, indicating the forward and backward cases with **a**, **b**, **d** different wave numbers, and **c** different amplitudes. (from Ref. [43])

Fig. 9.3d. Given that the spatiotemporal modulation's characteristic length is significantly smaller than the wavelike temperature fields' wavelength, the suggested structure can be considered a metamaterial. Neither periodic inhomogeneity nor vertical advection individually leads to horizontal nonreciprocity. However, their combined effect can induce diffusive Fizeau drag. The fundamental principle is rooted in the coupling between heat flux and the rate of temperature change, akin to the Willis coupling observed in mechanical waves. Hence, this form of nonreciprocity is notably distinct from synthetic-motion-induced nonreciprocity. This phenomenon persists even when the advection direction is perpendicular to the temperature field's propagation. To achieve diffusive Fizeau drag, researchers modify the porous medium using spatially-periodic inhomogeneity defined by equations (9.5).

$$\begin{aligned} \rho(\xi) &= \rho_0 \left(1 + \Delta_\rho \cos(G\xi + \theta)\right), \\ \kappa(\xi) &= \kappa_0 \left(1 + \Delta_\kappa \cos(G\xi)\right) \end{aligned} \tag{9.5}$$

These equations introduce modulation amplitudes, wave number, wavelength, generalized coordinate, and phase difference. For accuracy in heat transfer, we derive the governing equation (9.6).

$$\begin{aligned} \bar{\rho}(\xi)\frac{\partial T}{\partial t} + \phi u_y \frac{\partial T}{\partial y} + \frac{\partial}{\partial x}\left(-D_0 \bar{\kappa}(\xi)\frac{\partial T}{\partial x}\right) \\ + \frac{\partial}{\partial y}\left(-D_0 \bar{\kappa}(\xi)\frac{\partial T}{\partial y}\right) = 0 \end{aligned} \tag{9.6}$$

A wavelike temperature field as described in equation (9.7).

$$T = F(\xi) e^{i(\beta x - \omega t)} = \left(\sum_s F_s e^{isG\xi}\right) e^{i(\beta x - \omega t)} \tag{9.7}$$

Finite-element simulations were conducted with COMSOL Multiphysics. It aimed to uncover the mechanism of diffusive Fizeau drag, finding it shared similarities with Willis metamaterial properties. The heat flux, J, is influenced not just by the temperature gradient but also by the temperature change rate, known as the thermal Willis term. This term can result in nonreciprocal speeds in opposite directions but no amplitude difference. The role of inhomogeneity is vital for thermal Willis coupling, see Fig. 9.4. It vanishes when considering solely the horizontal inhomogeneity [Fig. 9.4a1, a2] or just the vertical inhomogeneity [Figs. 9.4b1, b2]. Researchers then modify the modulations from cosine functions to square wave functions denoted by Π. When the inhomogeneity's periodicity mirrors, a time difference of $\Delta t^* = 0.32$ is discerned [Fig. 9.4c1, c2]. Thus, square wave modulation proves more effective than cosine modulation ($\Delta t^* = 0.14$). Reducing the modulation wavelength by a factor of five is then explored [Fig. 9.4d1]. With $2\pi\Gamma = 8$, a time difference of $\Delta t^* = 0.04$ emerges Fig. 9.4d2, substantially less than the $\Delta t^* = 0.32$ in Fig. 9.4c2. Consequently, more homogeneous parameters result in diminished thermal Willis

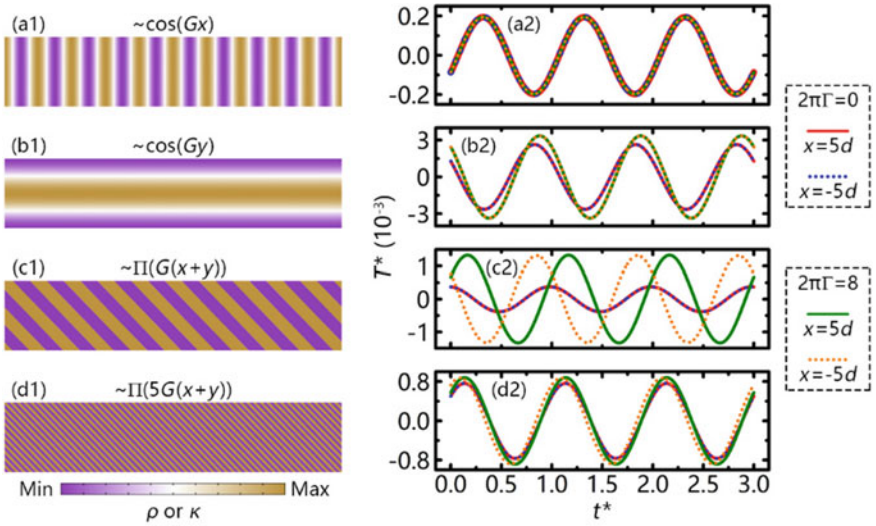

Fig. 9.4 Influences of inhomogeneity on thermal Willis coupling. The left column shows different kinds of inhomogeneity. The right column shows the evolution of T^*. (from Ref. [43])

coupling, aligning with current insights in mechanical waves. When only considering either horizontal or vertical inhomogeneity, the coupling disappears. By changing modulations from cosine to square wave functions, the efficiency increased. However, reducing modulation wavelength weakened thermal Willis coupling, consistent with current mechanical wave understanding.

9.3.3 Application

For practical implementation, the key is achieving spatiotemporal modulations of thermal conductivity (σ) and the product of mass density and heat capacity (ρ). Research indicates that σ can be manipulated using electric and light fields, and ρ can be modulated considering heat capacity and phase changes in response to electric fields.

Engineering thermal radiation necessitates precise control over a material's infrared optical properties, most crucially emissivity. Spatiotemporal modulation can be harnessed for this purpose. Some studies have demonstrated synchronous spatial and temporal control over emissivity using a metamaterial thermal emitter activated by spatially patterned ultraviolet (UV) light. The adoption of an all-optical modulation technique enables complexity associated with pixel-level control to be shifted to the illumination source or an intermediary mask layer. This greatly simplifies the manufacturing of nanophotonic materials and, when paired with projection systems, facilitates large-area emissivity control. Based on recent work, thermally responsive

materials, like azobenzene polymers, undergo reversible transitions in their thermal properties under UV (375 nm) and green light (530 nm) exposure within seconds at room temperature. Generally, these unique material parameters are sensitive to external stimuli, such as electric or magnetic fields. By illuminating such materials in a periodically arranged fashion, one can achieve a stratified medium instead of a uniform one. Envisioned applications include a thermal wave diode with relatively minor frequency-modulated thermal currents. These investigations underscore that spatiotemporal modulation offers a fresh avenue for studying non-reciprocal transmission of thermal waves.

9.4 Conclusion and Outlook

In this chapter, we delve into the role and significance of spatiotemporal modulation in the thermal convection field. Spatiotemporal modulation can produce equivalent thermal convection and is widely used in wave systems, photonics, acoustics, metasurfaces, and diffusion system. As research deepens into non-reciprocity caused by spatiotemporal modulation, typical features of non-reciprocal transmission have been observed in multiple physical scenarios, including the Fizeau drag of light, plasmon excitations, and thermal waves, highlighting the importance of wave propagation at different speeds along or against the media movement or modulation direction. It provides unprecedented opportunities for controlling and manipulating various physical phenomena, especially in the field of thermal convection.

In the realm of spatiotemporal modulation materials research, the horizon is vast and promising. While time-related convection, driven by external forces, is a prevalent phenomenon in convective thermal metamaterials, the temporal modulation of structural parameters stands as a relatively untapped area, warranting primary attention in contemporary research. This modulation can be achieved through two predominant methods: the periodic movement of meticulously designed mechanical units and the employment of materials that undergo parameter changes in response to external stimuli. Furthermore, a pivotal aspect of this research lies in the exploration of the specific forms of the external field and the potential applications of the designed thermal metamaterial, a venture that holds significance for both metamaterial design and the broader domain of material science. However, it's imperative to note that temporal modulation in isolation might not always meet the desired objectives. Hence, the integration of spatial modulation becomes indispensable. Most natural materials exhibit homogeneity and isotropy, but the advent of transformation theory is challenging these conventional paradigms. A particularly intriguing avenue for exploration is the transition from modulating isotropic parameters to an anisotropic tensor value. While this endeavor is intricate, it holds the potential to reveal unprecedented functionalities and physical phenomena, marking a transformative direction for future research in spatiotemporal thermal modulation.

A deeper study of these phenomena reveals that spatiotemporal modulation provides key technology to achieve these characteristics. Not only does it offer opportu-

nities to explore physical phenomena from new angles, but it also reveals unexplored properties in diffusion systems. Typically, materials provided by nature are homogeneous and isotropic, but spatiotemporal modulation opens new possibilities, allowing us to change relevant parameters from a single isotropic scalar value to an anisotropic tensor value over time. This exploration might reveal new functionalities or physical phenomena. Furthermore, the combination of spatiotemporal modulation with other modern technologies, such as machine learning and micro-nano technology, predicts broader application areas and business opportunities. Finally, from creating thermal materials with unconventional properties to realizing non-reciprocal and directed transmission of mass and energy, spatiotemporal modulation provides an innovative platform. Given the academic research and the current trend of carbon neutrality, both thermal metamaterials and spatiotemporal modulation will play an increasingly important role in future scientific research and technological development. We hope that this research can bring practical, innovative solutions for industrial applications, thus promoting rapid development in related fields.

References

1. Xu, L.J., Huang, J.P.: Transformation Thermotics and Extended Theories: Inside and Outside Metamaterials. Springer, Singapore (2023)
2. Huang, J.P., Karttunen, M., Yu, K.W., Dong, L.: Dielectrophoresis of charged colloidal suspensions. Phys. Rev. E **67**, 021403 (2003)
3. Dong, L., Huang, J.P., Yu, K.W., Gu, G.Q.: Dielectric response of graded spherical particles of anisotropic materials. J. Appl. Phys. **95**, 621–624 (2004)
4. Gao, Y., Jian, Y.C., Zhang, L.F., Huang, J.P.: Magnetophoresis of nonmagnetic particles in ferrofluids. J. Phys. Chem. C **111**, 10785–10791 (2007)
5. Ye, C., Huang, J.P.: Non-classical oscillator model for persistent fluctuations in stock markets. Phys. A **387**, 1255–1263 (2008)
6. Liu, L., Wei, J., Zhang, H., Xin, J., Huang, J.: A statistical physics view of pitch fluctuations in the classical music from Bach to Chopin: Evidence for scaling. PLoS ONE **8**, e58710 (2013)
7. Sounas, D.L., Caloz, C., Alù, A.: Giant non-reciprocity at the subwavelength scale using angular momentum-biased metamaterials. Nat. Commun. **4**, 2407 (2013)
8. Sounas, D.L., Alù, A.: Angular-momentum-biased nanorings to realize magnetic-free integrated optical isolation. ACS Photonics **1**, 198 (2014)
9. Sounas, D.L., Alù, A.: Non-reciprocal photonics based on time modulation. Nat. Photonics **11**, 774 (2017)
10. Mock, A., Sounas, D., Alù, A.: Magnet-free circulator based on spatiotemporal modulation of photonic crystal defect cavities. ACS Photonics **6**, 2056 (2019)
11. Fleury, R., Sounas, D.L., Alù, A.: Subwavelength ultrasonic circulator based on spatiotemporal modulation. Phys. Rev. B **91**, 174306 (2015)
12. Shen, C., Li, J.F., Jia, Z.T., Xie, Y.B., Cummer, S.A.: Nonreciprocal acoustic transmission in cascaded resonators via spatiotemporal modulation. Phys. Rev. B **99**, 134306 (2019)
13. Shen, C., Zhu, X.H., Li, J.F., Cummer, S.A.: Nonreciprocal acoustic transmission in space-time modulated coupled resonators. Phys. Rev. B **100**, 054302 (2019)
14. Zhu, X.H., Li, J.F., Shen, C., Peng, X.Y., Song, A.L., Li, L.Q., Cummer, S.A.: Non-reciprocal acoustic transmission via space-time modulated membranes. Appl. Phys. Lett. **116**, 034101 (2020)

15. Zhang, Z., Xu, L., Qu, T., Lei, M., Lin, Z.-K., Ouyang, X., Jiang, J.-H., Huang, J.: Diffusion metamaterials. Nat. Rev. Phys. **5**, 218–235 (2023)
16. Kofané, T.C., Tabi, C.B., Moubissi, A.B., Tchawoua, C.: From African "am-ta" to nonlinear optics [Invited]. J. Opt. Soc. Am. B **37**, A346–A355 (2023)
17. Wang, J., Dai, G.L., Huang, J.P.: Thermal metamaterial: fundamental, application, and outlook. iScience **23**, 101637 (2020)
18. Xu, L.J., Dai, G.L., Huang, J.P.: Transformation multithermotics: controlling radiation and conduction simultaneously. Phys. Rev. Appl. **13**, 024063 (2020)
19. Xu, L.J., Yang, S., Huang, J.P.: Thermal transparency induced by periodic interparticle interaction. Phys. Rev. Appl. **11**, 034056 (2019)
20. Yang, S., Xu, L.J., Wang, R.Z., Huang, J.P.: Full control of heat transfer in single-particle structural materials. Appl. Phys. Lett. **111**, 121908 (2017)
21. Dai, G.L., Huang, J.P.: A transient regime for transforming thermal convection: cloaking, concentrating and rotating creeping flow and heat flux. J. Appl. Phys. **124**, 235103 (2018)
22. Xu, L.J., Yang, S., Huang, J.P.: Thermal theory for heterogeneously architected structure: fundamentals and application. Phys. Rev. E **98**, 052128 (2018)
23. Xu, L.J., Wang, J., Dai, G.L., Yang, S., Yang, F.B., Wang, G., Huang, J.P.: Geometric phase, effective conductivity enhancement, and invisibility cloak in thermal convection-conduction. Int. J. Heat Mass Transf. **165**, 120659 (2021)
24. Xu, L.J., Yang, S., Dai, G.L., Huang, J.P.: Transformation omnithermotics: Simultaneous manipulation of three basic modes of heat transfer. ES Energy Environ. **7**, 65–70 (2020)
25. Shen, X.Y., Jiang, C.R., Li, Y., Huang, J.P.: Thermal metamaterial for convergent transfer of conductive heat with high efficiency. Appl. Phys. Lett. **109**, 201906 (2016)
26. Xu, L.J., Huang, J.P.: Active thermal wave cloak. Chin. Phys. Lett. **37**, 120501 (2020)
27. Jin, P., Xu, L.J., Jiang, T., Zhang, L., Huang, J.P.: Making thermal sensors accurate and invisible with an anisotropic monolayer scheme. Int. J. Heat Mass Transf. **163**, 120437 (2020)
28. Yang, F.B., Zhang, Z.R., Xu, L.J., Liu, Z.F., Jin, P., Zhuang, P.F., Lei, M., Liu, J.R., Jiang, J.-H., Ouyang, X.P., Marchesoni, F., Huang, J.P.: Controlling mass and energy diffusion with metamaterials. Rev. Mod. Phys. **96**, 015002 (2024)
29. Lira, H., Yu, Z., Fan, S., Lipson, M.: Electrically driven nonreciprocity induced by interband photonic transition on a silicon chip. Phys. Rev. Lett. **109**, 033901 (2012)
30. Fresnel, A.: Lettre d'Augustin Fresnel à François Arago sur l'influence du mouvement terrestre dans quelques phénomènes d'optique. Ann. Chem. Phys. **9**, 57 (1818)
31. Fizeau, H.: Sur les hypothèses relatives àl'éther lumineux. C. R. Acad. Sci. **33**, 349 (1851)
32. Kuan, P.-C., Huang, C., Chan, W.S., Kosen, S., Lan, S.-Y.: Large Fizeau's light-dragging effect in a moving electromagnetically induced transparent medium. Nat. Commun. **7**, 13030 (2016)
33. Qin, T., Yang, J.F., Zhang, F.X., Chen, Y., Shen, D.Y., Liu, W., Chen, L., Jiang, X.S., Chen, X.F., Wan, W.J.: Fast- and slow-light-enhanced light drag in a moving microcavity. Commun. Phys. **3**, 118 (2020)
34. Huidobro, P.A., Galiffi, E., Guenneau, S., Craster, R.V., Pendry, J.B.: Fresnel drag in space-time-modulated metamaterials. Proc. Natl. Acad. Sci. U. S. A. **116**, 24943 (2019)
35. Torrent, D., Poncelet, O., Batsale, J.-C.: Nonreciprocal thermal material by spatiotemporal modulation. Phys. Rev. Lett. **120**, 125501 (2018)
36. Camacho, M., Edwards, B., Engheta, N.: Achieving asymmetry and trapping in diffusion with spatiotemporal metamaterials. Nat. Commun. **11**, 3733 (2020)
37. Li, J., Li, Y., Cao, P.-C., Qi, M., Zheng, X., Peng, Y.-G., Li, B., Zhu, X.-F., Alù, A., Chen, H., Qiu, C.-W.: Thermal reciprocity in metamaterials. Nat. Commun. **13**, 167 (2022)
38. Farhat, M., Chen, P.-Y., Bagci, H., Amra, C., Guenneau, S., Alù, A.: Thermal invisibility based on scattering cancellation and mantle cloaking. Sci. Rep. **5**, 9876 (2015)
39. Mulaveesala, R., Tuli, S.: Theory of frequency modulated thermal wave imaging for nondestructive subsurface defect detection. Appl. Phys. Lett. **89**, 191913 (2006)
40. Tuli, S., Chatterjee, K.: Frequency modulated thermal wave imaging. AIP Conf. Proc. **1430**, 523 (2012)

41. Mulaveesala, R., Tuli, S.: Applications of frequency modulated thermal wave imaging for nondestructive characterization. AIP Conf. Proc. **1004**, 15 (2008)
42. Xu, L.J., Huang, J.P., Ouyang, X.P.: Tunable thermal wave nonreciprocity by spatiotemporal modulation. Phys. Rev. E **103**, 032128 (2021)
43. Xu, L.J., Xu, G.Q., Huang, J.P., Qiu, C.-W.: Diffusive Fizeau Drag in Spatiotemporal Thermal Metamaterials. Phys. Rev. Lett. **128**, 145901 (2022)

Chapter 10
Thermal Metamaterials for Temperature Maintenance: From Advances in Heat Conduction to Future Convection Prospects

Xinchen Zhou

10.1 Opening Remarks

Temperature maintenance plays a pivotal role in our daily lives and industrial applications. In building environments, it ensures human comfort, while in battery thermal management, it underpins the performance and safety of the battery. Given the increasing emphasis on energy-saving and emission reduction, achieving efficient temperature maintenance sustainably has never been more paramount [1–3].

As a main part of temperature control, temperature maintenance processes can be categorized into two main types based on their energy requirements: active and passive. Notably, passive temperature maintenance has emerged as a significant player in energy-saving temperature control strategies. Cutting-edge technologies such as phase change temperature control [4, 5], shape memory alloy [6, 7], solar thermal utilization [8, 9], sky radiation cooling [10, 11], and heat pipe systems [12, 13], have showcased exemplary performance in efficiently regulating heat flow between objects and their surroundings. The underlying principle of these technologies hinges on the self-regulation capability of their thermal/structural properties.

In the realm of phase change temperature maintenance, phase change materials (PCMs) are deployed to modulate an object's temperature, leveraging the near-constant temperature maintained during the phase transition process. Consider the realm of cold chain logistics as an illustrative example: the temperature of transported goods is regulated by phase change materials during their phase transition, all contained within thermally insulating packages [14].

Shape memory alloys (SMAs) are another fascinating domain. The structural changes they undergo before and after phase transitions can alter the system's effective thermal properties, enabling temperature regulation. A case in point is explored in Ref. [15]. Here, a thermal regulator based on SMA with an optimal phase change

X. Zhou (✉)
Department of Physics, Key Laboratory of Micro and Nano Photonic Structures (MOE), and State Key Laboratory of Surface Physics, Fudan University, Shanghai 200438, China
e-mail: 20110190014@fudan.edu.cn

F.-B. Yang and J.-P. Huang, *Diffusionics*,
https://doi.org/10.1007/978-981-97-0487-3_10

temperature is utilized to regulate the heat exchange between a battery and its environment. In high-temperature conditions, the thermal regulator constricts, enhancing heat flow, whereas in cooler environments, it expands, reducing heat flow.

Both solar thermal utilization and sky radiation cooling strategies involve modulating the radiation heat transfer rate between objects and their surroundings to control object temperature. An innovative approach to achieving thermal comfort in building environments, presented in Ref. [16], utilizes a liquid-vapor phase transition. When exposed to high outdoor temperatures, the working fluid in the thermal management device assumes a gaseous form, diminishing its transmittance and thereby cooling the indoor environment. Conversely, in colder conditions, the fluid transitions to a liquid state, increasing its transmittance and warming the interior.

Heat pipe technology similarly exploits vapor-liquid phase transitions. Ref. [17] unveils a pioneering application that marries phase change technology with heat pipe systems to recuperate industrial waste heat. This intricate setup comprises two main components: a micro heat pipe array and a phase change energy storage device. The micro heat pipe array is designed to channel heat from the hot end (representing industrial waste heat sources) to the cold end (representing user heating requirements). The phase change energy storage device's role is to harness surplus waste heat. When an abundance of waste heat is present, the material melts, storing this thermal energy. However, in the absence or scarcity of waste heat, the material solidifies, liberating the previously stored thermal energy, which is subsequently transferred to the cold end via the micro heat pipe array. This cycle ensures a stable temperature for the heat-carrying fluid channeled to the user end.

It is clear that the applications mentioned utilize the phase transition properties of materials to achieve temperature regulation by qualitatively adjusting the heat transfer rate between the object and its surroundings. From an energy conservation standpoint, strict temperature maintenance is only achievable when the net heat flow across the temperature control zone (i.e., the object) is zero. Developing more quantitative analytical tools to explore passive temperature maintenance technologies could lead to improved temperature control efficiency.

In recent times, the advent of thermal metamaterials has shown promise in the realm of passive temperature control, given their proficiency in modulating temperature fields [18–24]. This advancement is rooted in the evolution of theoretical thermotics since 2008 [23]. A range of thermal functionalities have been demonstrated, showcasing the vast potential of this innovative tool in temperature regulation [24–30].

For instance, in a display of temperature field manipulation, a thermal metamaterial named the "thermal cloak" was introduced [18–23]. It essentially renders objects invisible within a classical core-shell model [20, 22]. Heat seamlessly flows from the high-temperature boundary to the low-temperature boundary across the shell. As a result, the internal object remains thermally unaffected, while the external temperature distribution remains undisturbed by the object's presence. Following this breakthrough, a slew of functionalities has been introduced, expanding the scope of thermal metamaterials. Notable examples include the thermal expander [31], thermal concentrator [32, 33], thermal rotator [34], thermal sensor [35–37], etc. [38–41].

Examining the triad of fundamental heat transfer modes - heat conduction, heat convection, and heat radiation - it is found that the evolution of thermal metamaterials began with systems focused on heat conduction. This subsequently expanded to include coupled heat convection systems and eventually integrated systems addressing radiant heat [42–47]. The upshot is a comprehensive capability to control heat flow across the entire spectrum of heat transfer processes. This relates to so-called overall heat transfer, omnithermotics, and omnithermal metamaterials [48–50]. Since the thermal parameters of the system were calculated by theory, this might lead to difficulty in finding the materials in nature. To address this obstacle, the effective medium theory was employed for fabricating thermal metamaterials [51–54]. Consequently, contemporary thermal metamaterials, bolstered by robust analytical theories, sophisticated design methodologies, and state-of-the-art experimental apparatuses, exhibit immense potential for real-world applications in passive temperature control.

In the realm of temperature control, the development of temperature maintenance is vital for energy conservation. This chapter showcases three devices rooted in thermal metamaterials designed for conduction heat transfer: an energy-free thermostat utilizing temperature trapping theory with SMA; a groundbreaking negative-energy thermostat that produces electrical energy by merging thermotics with electricity; and a versatile multi-temperature maintenance container, deploying adaptive controls and PCMs to cater to diverse transportation needs. Building upon these innovations, this chapter also hints at the future of temperature maintenance in convection heat transfer scenarios. Overall, the insights offered here, viewed through the lens of thermal metamaterials, illuminate pathways for enhancing temperature maintenance methodologies.

10.2 Developments in Conduction Heat Transfer System

10.2.1 Energy-Free Thermostat

10.2.1.1 Principle and Function

Ref. [55] introduced an energy-free thermostat for a conduction heat transfer system, as depicted in Fig. 10.1. This thermostat comprises three distinct materials: Type A, Type B, and a common material. The common material is designated as the functional region for temperature maintenance. Similar to designs found in other thermal metamaterials, the thermostat features a high-temperature boundary on the right (T_H) and a low-temperature boundary (T_L) on the left. Both the upper and lower boundaries are adiabatic. Impressively, this design aims to ensure that the temperature of the functional region remains stable under varying temperature gradients without any additional energy input.

The aforementioned functionality is achieved using the so-called "temperature trapping theory." This theory originates from the one-dimensional Fourier's law, expressed as:

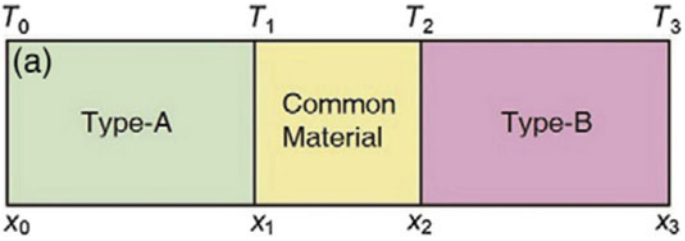

Fig. 10.1 Schematic of an energy-free thermostat. Materials type-A and type-B are designed to regulate the temperature gradient from high to low. The region labeled "common material" is designated for temperature maintenance. (from Ref. [55])

$$q = -\kappa\,(x, T)\,\frac{\mathrm{d}T}{\mathrm{d}x}, \tag{10.1}$$

where q represents the heat flux, κ denotes thermal conductivity, T is the temperature, and x indicates position. To maintain a consistent heat flux from the high-temperature boundary to the low-temperature boundary, represented as $q = C$, $\kappa(x, T)$ needs to be symmetric with $T = T_\mathrm{c}$. Furthermore, to ensure temperature uniformity in the central region, making $T_1 \approx T_2 \approx T_\mathrm{c}$, there ought to be two pronounced temperature gradients in the regions $[x_0, x_1]$ and $[x_2, x_3]$, and a subdued gradient in the region $[x_1, x_2]$. As a result, the researchers determined the thermal conductivities of materials type-A and type-B as:

$$\begin{cases} \kappa_\mathrm{A} = L(T_\mathrm{c} - T) = \delta + \dfrac{\varepsilon e^{T-T_\mathrm{c}}}{1 + e^{T-T_\mathrm{c}}} \\ \kappa_\mathrm{B} = L(T - T_\mathrm{c}) = \delta + \dfrac{\varepsilon}{1 + e^{T-T_\mathrm{c}}} \end{cases}, \tag{10.2}$$

where L is a logistic function dependent on T, δ is a small value, and ε is a substantial value. By employing this strategy, the temperature is consistently maintained within the central region.

Figure 10.2 presents a set of finite element simulations for the thermostat. Observably, with T_L held constant at 273.2 K, and as T_H varies from 323.2 K, 338.2 K, to 353.2 K, the temperature in the central region consistently remains within the range of $293.3 - 293.5$ K. This confirms the successful realization of the described temperature maintenance functionality.

For a comparative analysis, a reference system was established by substituting the type-A and type-B materials with materials having a constant thermal conductivity of 50 W m^{-1} K^{-1}, as shown in Fig. 10.3. In the absence of the specialized designs of κ_A and κ_B, the central region's temperature fails to remain stable under conditions identical to those of the energy-free thermostat, as depicted in Fig. 10.4. Notably, the temperature in the central region escalates in tandem with the rise in the ambient temperature gradient magnitude.

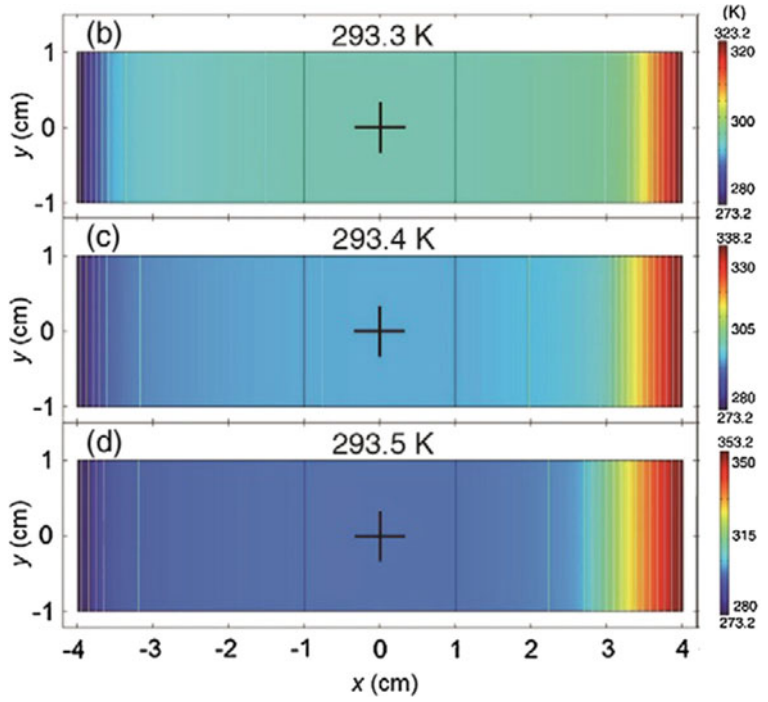

Fig. 10.2 Simulation results for the energy-free thermostat. From the top subgraph to the bottom subgraph, the temperature at the low-temperature boundary stays consistent, while that of the high-temperature boundary incrementally rises. (from Ref. [55])

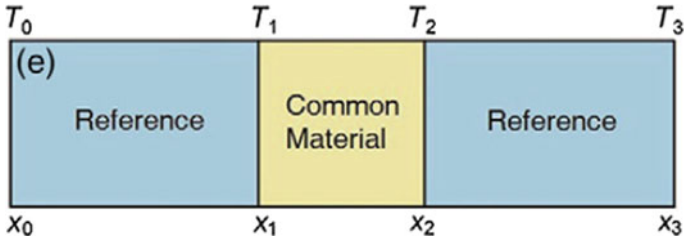

Fig. 10.3 Schematic for a reference system. (from Ref. [55])

While the ideal design of the energy-free thermostats demonstrates notable efficacy, the practical task of identifying suitable materials for type-A and type-B remains a significant challenge. To achieve the desired nonlinear thermal conductivity function, researchers employed a two-component system: a stationary component and a movable one. The movable component was realized using an SMA, while phosphor copper was chosen as the stationary component. This sophisticated structure is illustrated in Fig. 10.5a. When the temperature of the SMA surpasses its phase transition

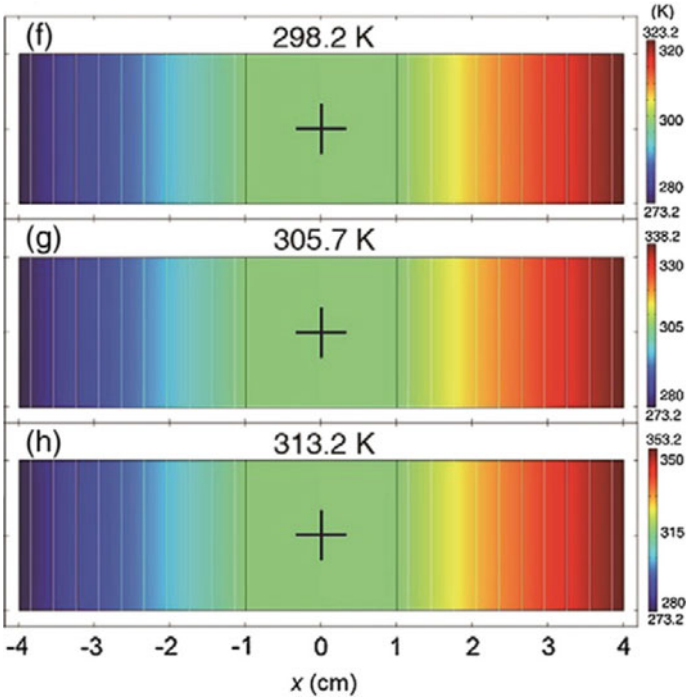

Fig. 10.4 Simulation results for the reference system, serving as a control group for Fig. 10.2. (from Ref. [55])

threshold, it experiences deformation. Capitalizing on this behavior facilitates the embodiment of the previously discussed function.

A juxtaposition between the theoretical projections in Eq. (10.2) and the empirical results of the composite structure, as shown in Fig. 10.5b, confirms that the design captures the targeted nonlinear properties. To validate the performance of the proposed energy-free thermostat, the researchers carried out experiments based on the configuration detailed in Fig. 10.5a, as shown in Fig. 10.6. The stable temperature observed in the central region, even amidst fluctuating external temperature gradients, hints at the feasibility of realizing the energy-free thermostat in real-world settings. Conversely, in scenarios where the SMA was excluded from the thermostat setup, the design's nonlinear thermal conductivity characteristics were compromised. As a result, the temperature in the central zone escalated from 294.4 K to 299.0 K, and subsequently to 304.8 K, in response to an increasing ambient temperature gradient.

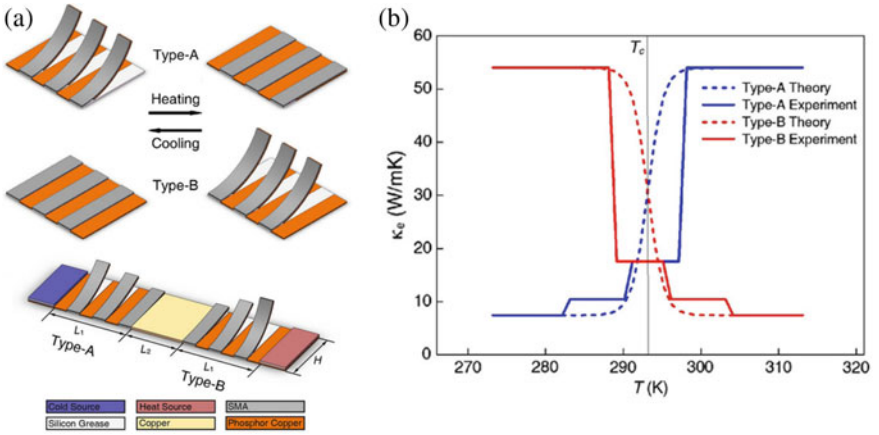

Fig. 10.5 Schematic diagram of materials type-A and type-B. **a** Fabrication of the energy-free thermostat using shape memory alloy. **b** Comparison between theoretical and experimental results on the relationships of thermal conductivity and temperature for materials type-A and type-B. (from Ref. [55])

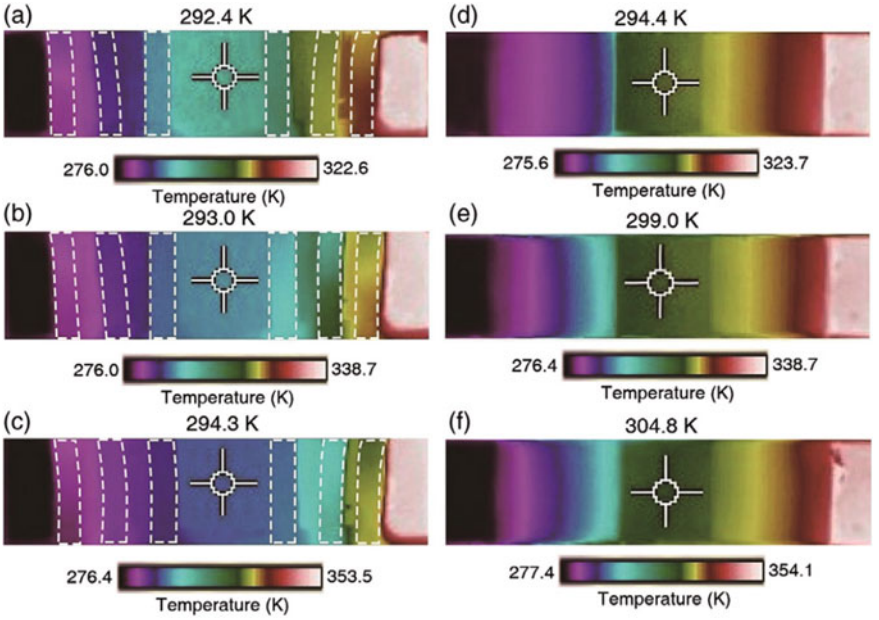

Fig. 10.6 Experimental results showcasing the system's temperature distributions under various ambient temperature gradients. **a–c** Energy-free thermostat. **d–f** Control group. From the top subgraph to the bottom one, the temperature at the low-temperature boundary remains consistent, while the temperature at the high-temperature boundary incrementally rises. (from Ref. [55])

10.2.1.2 Comparison with Existing Technology

The temperature trapping theory, combined with the design of energy-free thermostats, offers a revolutionary approach to efficient temperature maintenance. When juxtaposed with prevailing industrial solutions such as vapor compression refrigeration, thermal insulation, or phase-change temperature control, this strategy emerges as a quantitative, energy-saving alternative. It intricately regulates heat flow, obviating the need for energy input, and thus, perpetually sustains the desired temperature within the central region. This approach is especially promising for environments with fluctuating temperature gradients, be it the lunar surface or the contrasting sunlit and shaded facades of edifices [56].

Furthermore, researchers harnessed this structure to enhance the inherent functionalities of thermal metamaterials, as depicted in Fig. 10.7a. Defining the thermal conductivities of zones I-VI as

$$\begin{cases} \kappa_{\mathrm{I}} = \kappa_0 - \dfrac{(\kappa_0 - \kappa_{\mathrm{i}})}{1 + e^{T - T_{\mathrm{c}}}}, \\ \kappa_{\mathrm{II}} = \kappa_0 - \dfrac{(\kappa_0 - \kappa_{\mathrm{i}}) e^{T - T_{\mathrm{c}}}}{1 + e^{T - T_{\mathrm{c}}}}, \\ \kappa_{\mathrm{III}} = \kappa_0 + \dfrac{(\kappa_{\mathrm{e}} - \kappa_0)}{1 + e^{T - T_{\mathrm{c}}}}, \\ \kappa_{\mathrm{IV}} = \kappa_0 + \dfrac{(\kappa_{\mathrm{e}} - \kappa_0) e^{T - T_{\mathrm{c}}}}{1 + e^{T - T_{\mathrm{c}}}}, \\ \kappa_{\mathrm{V}} \to 0, \\ \kappa_{\mathrm{VI}} = \kappa_0 \dfrac{R_3^2 + R_2^2}{R_3^2 - R_2^2}, \end{cases} \tag{10.3}$$

it is discerned that the classical core-shell structure can now encapsulate the energy-free thermostat's capabilities. Figure 10.7b-d elucidates the temperature maintenance attributes of a thermal cloak, for instance. As traditionally expected of thermal cloaks, the exterior temperature distribution around the shell remains unperturbed [18–22]. This innovative design preserves this characteristic, while simultaneously ensuring that, irrespective of shifting temperature gradients, the central region's temperature remains steadfast, thus augmenting the existing suite of thermal cloak functionalities [18–22].

10.2.2 Negative-Energy Thermostat

10.2.2.1 Principle and Function

Building upon the foundation of the energy-free thermostat, Ref. [57] introduced an innovative concept that harnesses thermoelectric effects to generate electricity, aptly

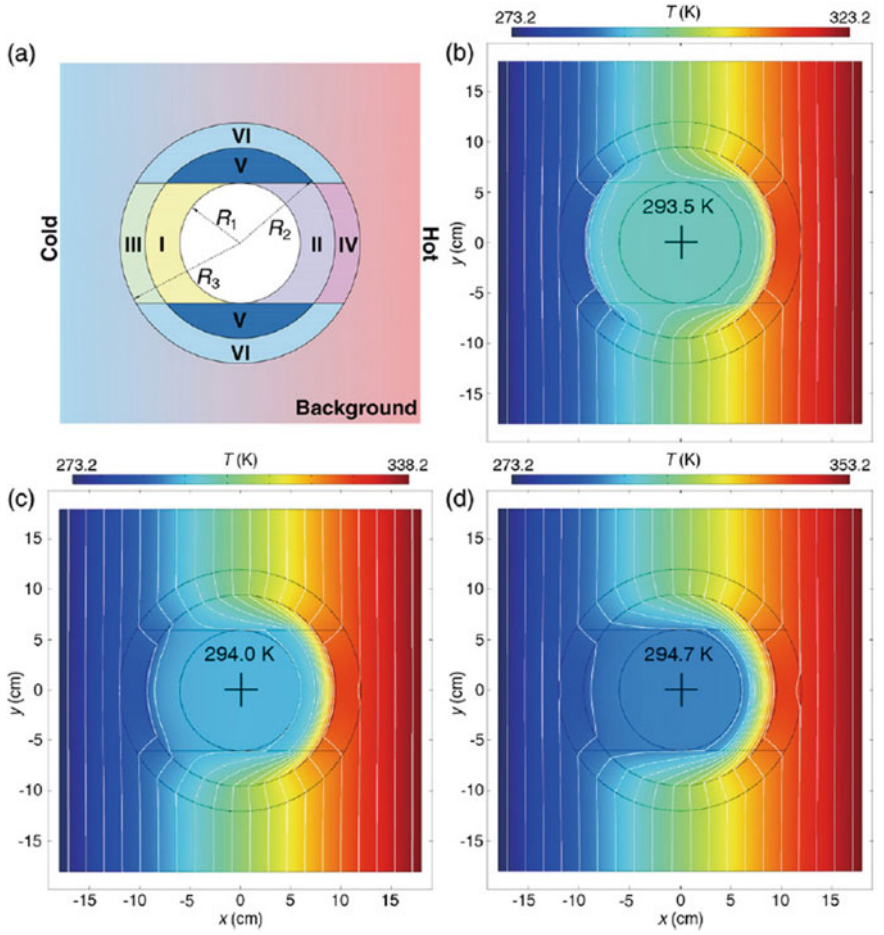

Fig. 10.7 Improved thermal cloak with temperature maintenance capability. **a** Schematic representation. **b–d** Temperature distributions under various ambient temperature gradients. (from Ref. [55])

termed the "negative-energy thermostat." The underlying schematic, when devoid of load, bears resemblance to that of the energy-free thermostat, as depicted in Fig. 10.8. While the temperature regulation mechanism echoes that of the energy-free thermostat, the ensuing discourse primarily elucidates the principles governing electricity control. Given that the bulk of the temperature gradient is confined to zones A and B, the thermoelectromotive force is described as follows:

$$\begin{aligned} \Delta U_{\mathrm{ad}} &= \Delta U_{\mathrm{ab}} + \Delta U_{\mathrm{cd}} \\ &= S(T_2 - T_1) + S(T_4 - T_3) \\ &\approx S(T_4 - T_1), \end{aligned} \tag{10.4}$$

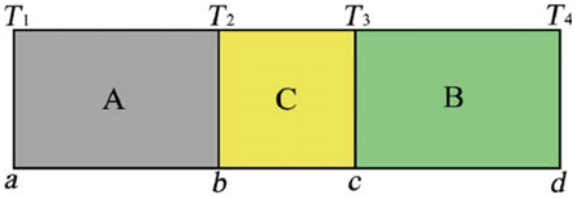

Fig. 10.8 Schematic diagram of the negative-energy thermostat. The boundary conditions are analogous to those in Fig. 10.1. (from Ref. [57])

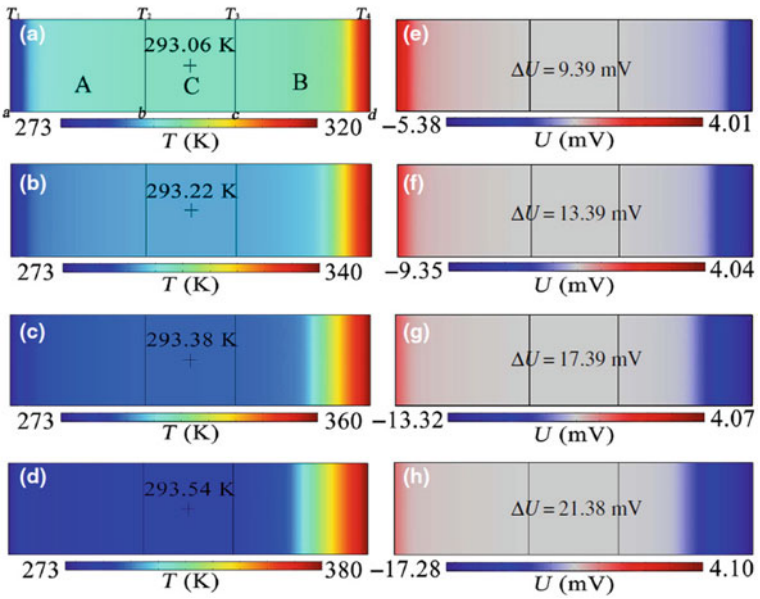

Fig. 10.9 Finite element simulations of the negative-energy thermostat. **a–d** Temperature distributions and **e–h** electric potential distributions under various ambient temperature gradients. (from Ref. [57])

where S is the Seebeck coefficient.

In conjunction with the capabilities of the energy-free thermostat, it can be inferred that the potential for electricity output escalates as the ambient temperature gradient increases, all while the temperature of the central region remains stable.

Figure 10.9 displays the finite element simulations, highlighting both the temperature maintenance performance and the electric potential of the negative-energy thermostat. Observations reveal that as the ambient temperature gradient intensifies, the central region's temperature is consistently maintained within the range of 293.06 – 293.54 K. Simultaneously, ΔU experiences a surge, increasing from 9.39 mV to 21.38 mW. This underscores the promising application potential of the negative-energy thermostat.

In consideration of real-world applications, an external load is incorporated into the device. Given this modification, thermoelectrics come into play, necessitating a revision to the governing equation. The revised formulation was given by:

$$\begin{aligned} q(x) &= -\kappa(T)\frac{\mathrm{d}T}{\mathrm{d}x} + \Pi j(x), \\ j(x) &= -\sigma\frac{\mathrm{d}\mu}{\mathrm{d}x} - \sigma S\frac{\mathrm{d}T}{\mathrm{d}x}, \end{aligned} \tag{10.5}$$

where $j(x)$ denotes the electric current density induced by the Seebeck effect, μ represents the electrochemical potential at a given position, and σ signifies the electrical conductivity. Π is the Peltier coefficients and it is noted that $\Pi = TS$.

Figure 10.10 displays the temperature distribution of the negative-energy thermostat, incorporating the external load, as portrayed in finite element simulations. As observed, an electrical load is connected to the original thermostat using copper. Two scenarios, concerning the thermal and electrical properties of the load, were examined. The first scenario focuses on low values of σ and κ (as shown in Fig. 10.10a–d), while the latter encompasses high σ and high κ values (depicted in Fig. 10.10e–h). The results show that both extreme conditions do not affect the central temperature of the thermostat.

10.2.2.2 Comparison with Existing Technology

Compared to the application of the energy-free thermostat in the thermal cloak, the negative-energy thermostat can be integrated into the thermoelectric cloak, as depicted in Fig. 10.11. The thermal and electrical conductivities for all regions were set as:

$$\begin{cases} \kappa_{\mathrm{I}} = \phi + \psi\dfrac{e^{T-T_{\mathrm{c}}}}{1+e^{T-T_{\mathrm{c}}}} \\ \kappa_{\mathrm{II}} = \phi + \psi\dfrac{1}{1+e^{T-T_{\mathrm{c}}}} \\ \kappa_{\mathrm{III}} \to 0 \\ \kappa_{\mathrm{IV}} = \kappa_0\dfrac{R_3^2+R_2^2}{R_3^2-R_2^2} \end{cases}, \tag{10.6}$$

and

$$\begin{cases} \sigma_{\mathrm{I}} = \mu + \nu\dfrac{e^{T-T_{\mathrm{c}}}}{1+e^{T-T_{\mathrm{c}}}} \\ \sigma_{\mathrm{II}} = \mu + \nu\dfrac{1}{1+e^{T-T_{\mathrm{c}}}} \\ \sigma_{\mathrm{III}} \to 0 \\ \sigma_{\mathrm{IV}} = \sigma_0\dfrac{R_3^2+R_2^2}{R_3^2-R_2^2} \end{cases}, \tag{10.7}$$

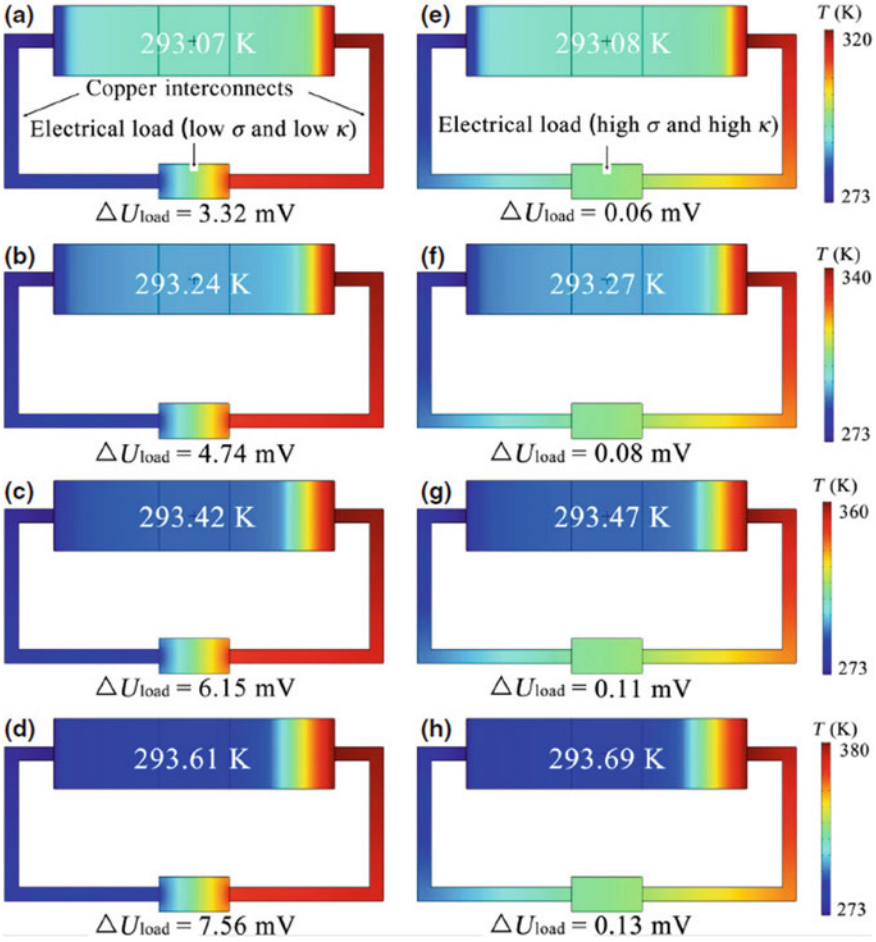

Fig. 10.10 Finite element simulations showcasing the temperature distributions of the negative-energy thermostat with load under varying ambient temperature gradients. **a–d** Cases with low σ and low κ. **e–h** Cases with high σ and high κ. (from Ref. [57])

where ϕ and ψ are parameters with the same units as κ, while μ and ν are parameters with the same units as σ ($\phi \ll \psi$ and $\mu \ll \nu$).

Initially, the thermoelectric cloak demonstrates an adeptness in maintaining the temperature within its central region. As evidenced by the temperature distribution in Fig. 10.12a–d, with the low-temperature boundary anchored at 273 K and the high-temperature boundary ranging from 320 K to 350 K, the temperature within the central region remains remarkably steady, fluctuating between 293.40 K and 295.07 K. Concurrently, the distribution of electrical potential follows a comparable trajectory, as depicted in 10.12e–h. Setting the baseline electrical potential boundary at 0 mV and escalating the high-end electrical potential boundary from 9.4 mV to

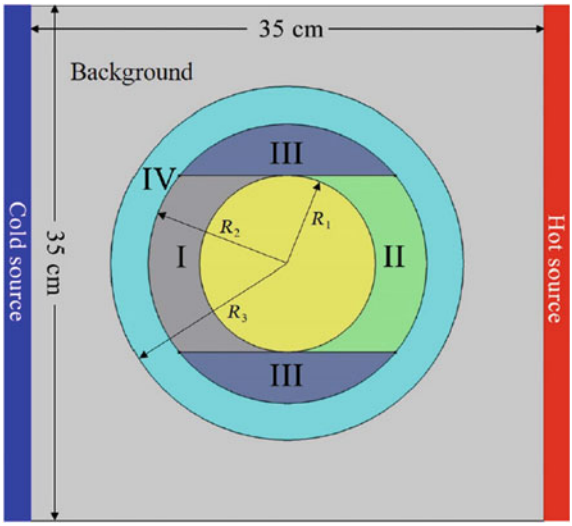

Fig. 10.11 Schematic representation of a thermoelectric thermostat cloak. (from Ref. [57])

15.4 mV, the central region's electrical potential stabilizes within the 4.08–4.42 mV bracket. Intriguingly, this stability persists even in the presence of a current flowing from left to right, ensuring both the temperature and electrical potential remain constant (Fig. 10.12i–l). These findings underscore the enhanced functionalities of this modified thermoelectric cloak. Relative to the temperature-maintenance thermal cloak, it offers the additional advantage of electric potential regulation. Moreover, when set against a traditional thermoelectric cloak [57, 58], this advanced iteration notably curtails the temperature/electric potential deviations within the central region amid escalating ambient temperature/electric potential disparities, as illustrated in Fig. 10.13.

10.2.3 Multi-temperature Maintenance Container

10.2.3.1 Principle and Function

The two previously mentioned types of thermostats employ SMA to regulate heat flow across a temperature control zone, ensuring its temperature remains consistent. Both in everyday scenarios and industrial applications, there is often a need for multi-temperature control. For instance, in indoor settings, different rooms might have specific temperature needs based on their functions. Similarly, for goods transportation, varying goods will have distinct temperature demands to preserve their quality. Ref. [59] examined goods transportation and suggested an efficient multi-temperature control methodology.

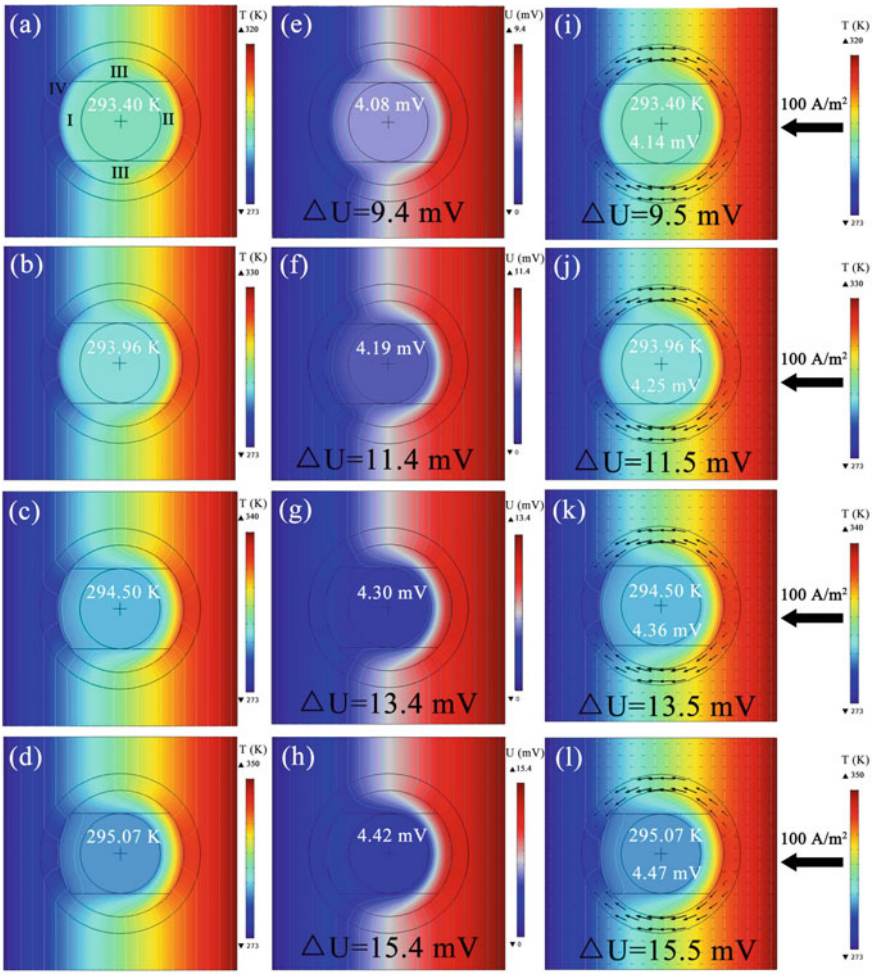

Fig. 10.12 Finite element simulation of the thermoelectric thermostat cloak under various ambient temperature gradients. **a–d** Temperature distributions. **e–h** Thermoelectric potential distributions. **i–l** Temperature distribution featuring characteristic temperature and electric potential in the central region with input electric current. (from Ref. [57])

As depicted in Fig. 10.14a, when transported goods are at different temperatures (each with distinct temperature needs), heat transfer occurs amongst them. To ensure the safety of these goods, an efficient multi-temperature control mechanism is vital. An advanced temperature control method based on PCMs, commonly used in cold chain logistics, could offer guidance in this situation [60–62]. This principle is illustrated in Fig. 10.14b. There are two types of PCMs utilized for temperature control. PCM A, termed the heat storage PCM, has a phase change temperature ($T_{p,a}$) that's higher than the environmental temperature (T_E). In contrast, PCM B, known

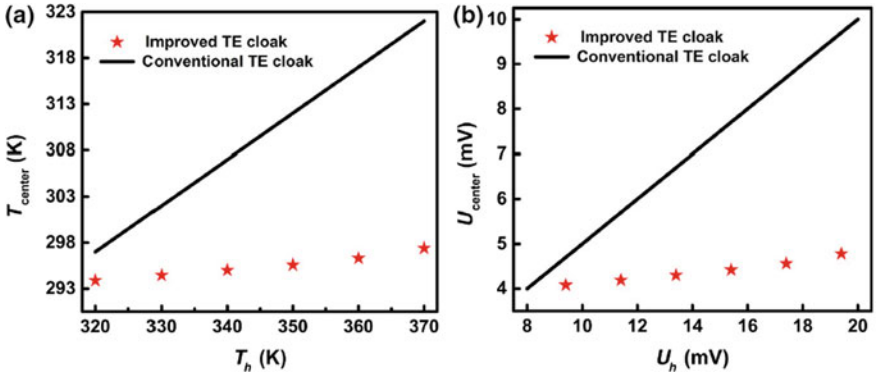

Fig. 10.13 Comparison of the variations in **a** temperatures and **b** potentials for the thermoelectric thermostat cloak and the conventional thermoelectric cloak under varying ambient temperature and electric potential gradients. (from Ref. [57])

as the cold storage PCM, has a phase change temperature ($T_{p,b}$) below T_E. The temperature-time curves can be divided into six stages based on their phase change processes. The segments $[a, b] \cup [c, d]$ signify the sensible heat (or cold) storage process. The segment $[b, c]$ describes the latent heat (or cold) storage process. Meanwhile, $[d, e] \cup [f, g]$ indicates the sensible heat (or cold) release process, and $[e, f]$ represents the latent heat (or cold) release process. This method leverages the substantial latent heat storage capacity of the PCMs, controlling temperature through the release of latent heat (or cold). By packaging goods in PCMs and placing them in thermally insulating containers, the goods' temperature can be maintained over extended periods.

Yet, while utilizing PCMs to achieve multi-temperature control seems promising, the authors highlighted two primary challenges. First, it is crucial that the phase change temperature of the PCMs aligns with the goods' temperature needs, and they must also possess properties like thermal stability, chemical compatibility, cycle longevity, and cost-effectiveness [59–62]. If suitable natural PCMs are not available, the creation of high-performance composite PCMs might be necessary, which might require a huge initial investment. Secondly, employing one PCM per zone and inserting thermal insulation materials does not entirely address the heat transfer issue between zones with varying temperature demands. Since the temperature range for goods transportation often surpasses that of cold chain logistics, the temperature disparity between zones can be significant, potentially requiring more energy to mitigate any multi-temperature control setbacks. Thus, the researchers aimed to devise a strategy to circumvent these challenges.

Their solution drew inspiration from terraced structures found in agricultural production, as portrayed in Fig. 10.14c. Recognizing that substances placed between hot and cold sources exhibit temperature drops, the team proposed creating multiple temperature platforms tailored for goods with diverse temperature requirements. This approach only necessitates the heat (or cold) source's temperature to be higher (or

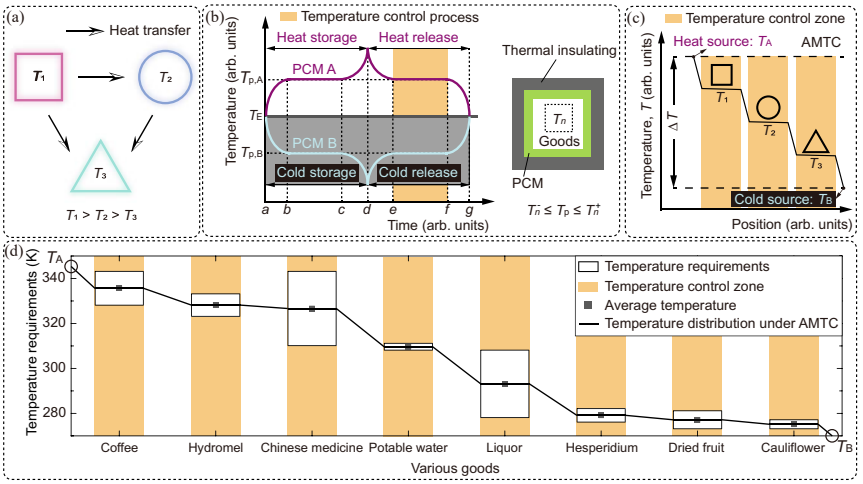

Fig. 10.14 Multi-temperature control. **a** Heat transfer among various goods with different temperature requirements. **b** Principle of phase change temperature control and its utilization in cold chain logistics. **c** Schematic representation of adaptive multi-temperature control (AMTC). **d** Impact of AMTC in meeting multi-temperature requirements for eight goods. (from Ref. [59], licensed under CC-BY 4.0)

lower) than the goods with the most extreme temperature demands. Given the rapid advancements in phase change technology, selecting two high-performing PCMs to act as the primary hot and cold sources is feasible. Moreover, this strategy fully capitalizes on heat transfer between varying objects with diverse temperatures. Every object plays a part in facilitating multi-temperature control. Figure 10.14d displays eight distinct goods, each with its temperature requirement. It demonstrates that using just one pair of hot and cold sources can naturally regulate the temperature of these eight items, underscoring the strategy's effectiveness. This strategy was termed as adaptive multi-temperature control (AMTC).

The researchers developed a conduction heat transfer system, illustrated in Fig. 10.15. The left and right boundaries are set to high and low temperatures (T_A and T_B), while the upper and lower boundaries are adiabatic. The system comprises four types of zones: $L_{\{i,j\}}$, $C_{\{i,j\}}$, $R_{\{i,j\}}$, and R, where i $(= 1, 2, 3, \cdots, m)$ symbolizes rows, and j $(= 1, 2, 3, \cdots, n)$ represents columns. $C_{\{i,j\}}$ designates the temperature control zone for storing goods. For effective multi-temperature control, researchers introduced thermal insulating materials into zone S and then moderated the temperature gradient in $L_{\{i,j\}}$ and $R_{\{i,j\}}$. The temperature in the control zone on column m can be expressed as

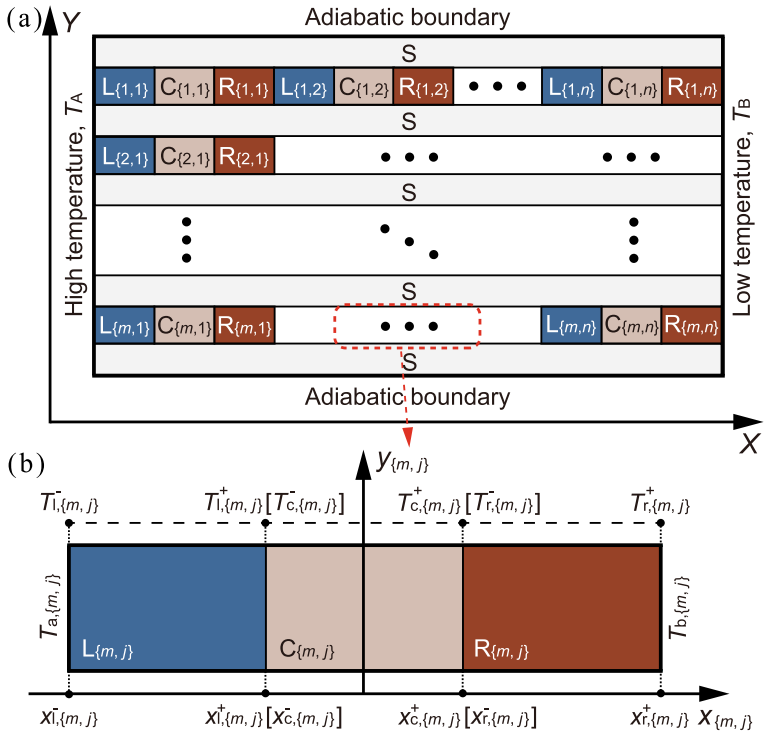

Fig. 10.15 Multi-temperature control system. **a** Global system designed for multi-temperature control. **b** Local system located at the mth row and jth column. (from Ref. [59], licensed under CC-BY 4.0)

$$T_{c,\{m,j\}} = T_A - \frac{T_A - T_B}{\sum_{j^\#=1}^{n}\sum_{\epsilon=l,c,r}\frac{d_{\epsilon,\{m,j^\#\}}}{\kappa_{\epsilon,\{m,j^\#\}}}}\left(-\frac{d_{r,\{m,j\}}}{\kappa_{r,\{m,j\}}}\right.$$
$$\left. - \frac{d_{c,\{m,j\}}/2 - x_{\{m,j\}}}{\kappa_{c,\{m,j\}}} + \sum_{j^*=1}^{j}\sum_{\epsilon=l,c,r}\frac{d_{\epsilon,\{m,j^*\}}}{\kappa_{\epsilon,\{m,j^*\}}}\right). \tag{10.8}$$

In this equation, ϵ denotes zone E, where $\epsilon = l, c, r$ corresponds to $E = L, C, R$, respectively. For $j^\# = \{1, 2, 3 \ldots n\}$ and $j^* = \{1, 2, 3 \cdots j\}$, $\kappa_{\epsilon,\{m,j\}}$ and $d_{\epsilon,\{m,j\}}$ represent the thermal conductivity and the length traversed by heat flow in $E_{\{m,j\}}$, respectively. When $\kappa_{l,\{m,j^\#\}} \ll \kappa_{c,\{m,j\}}$ and $\kappa_{r,\{m,j^\#\}} \ll \kappa_{c,\{m,j\}}$, the temperature distribution in $C_{\{i,j\}}$ is nearly uniform, allowing Eq. (10.8) to be simplified as

$$T_{c,\{m,j\}} \approx T_A - \frac{T_A - T_B}{\sum_{j^\#=1}^{n}\sum_{\epsilon=l,r}\frac{d_{\epsilon,\{m,j^\#\}}}{\kappa_{\epsilon,\{m,j^\#\}}}}\left(-\frac{d_{r,\{m,j\}}}{\kappa_{r,\{m,j\}}} + \sum_{j^*=1}^{j}\sum_{\epsilon=l,r}\frac{d_{\epsilon,\{m,j^*\}}}{\kappa_{\epsilon,\{m,j^*\}}}\right). \tag{10.9}$$

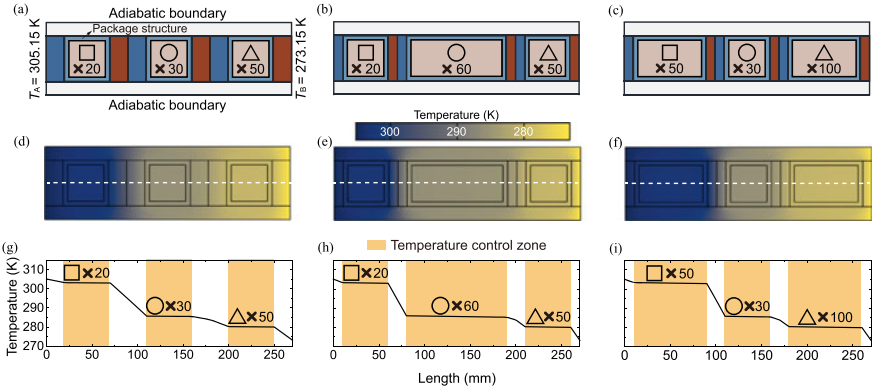

Fig. 10.16 Multi-temperature control capability. **a–c** Various multi-temperature control systems designed for storing distinct goods in different quantities. **d–f** Finite element simulations illustrating the temperature distributions of the multi-temperature control system under steady-state conditions. **g–i** Terraced-shaped temperature profiles along the characteristic lines in **d–f**. (from Ref. [59], licensed under CC-BY 4.0)

This suggests that the temperature in the control zone can be managed by adjusting the thermal or structural parameters of the system, specifically $\kappa_{\epsilon,\{m,j^{\#}\}}$ and $d_{\epsilon,\{m,j^{\#}\}}$.

This concept was validated through finite element simulations, as depicted in Fig. 10.16. Initially, the authors established a scenario wherein three types of goods required transportation, represented by square, circle, and triangle symbols. Their temperature requirements were defined as 303.15 K, 285.65 K, and 280.15 K, respectively. Figure 10.16a-c illustrates the design of the multi-temperature control systems with varying structural parameters to accommodate these goods in different quantities. Adhering to the previously mentioned equation, the system's thermal parameters were computed, and the finite element simulations were executed, as presented in Fig. 10.16d–f. These figures demonstrate that the temperature distributions within the control zones were uniform. Additionally, to further evaluate the temperature control capability of the AMTC method, the authors studied the temperature distribution along the white characteristic lines. The findings, showcased in Fig. 10.16g–i, confirm that the terrace-shaped temperature distribution discussed earlier was effectively achieved, meeting the temperature needs of the goods impeccably.

Using the AMTC approach, the capability for multi-temperature maintenance was evaluated under transient heat transfer conditions, as depicted in Fig. 10.17. Figure 10.17a presents a scenario for transporting a variety of goods with distinct temperature requirements. For generality, the researchers employed normalized temperatures for this investigation. The temperatures of the heat and cold sources were defined as 1.0 and 0.0, respectively, while the initial temperatures of the goods in zones ①, ②, ⋯, ⑨ were designated as 0.9, 0.8, ⋯, 0.1, respectively. The thermal conductivities of the marked zones a, b, ⋯, r were determined using the AMTC method. As illustrated in case 1 of Fig. 10.17b, after a brief initial disturbance to equalize temperature differences, the temperatures of all goods were effectively

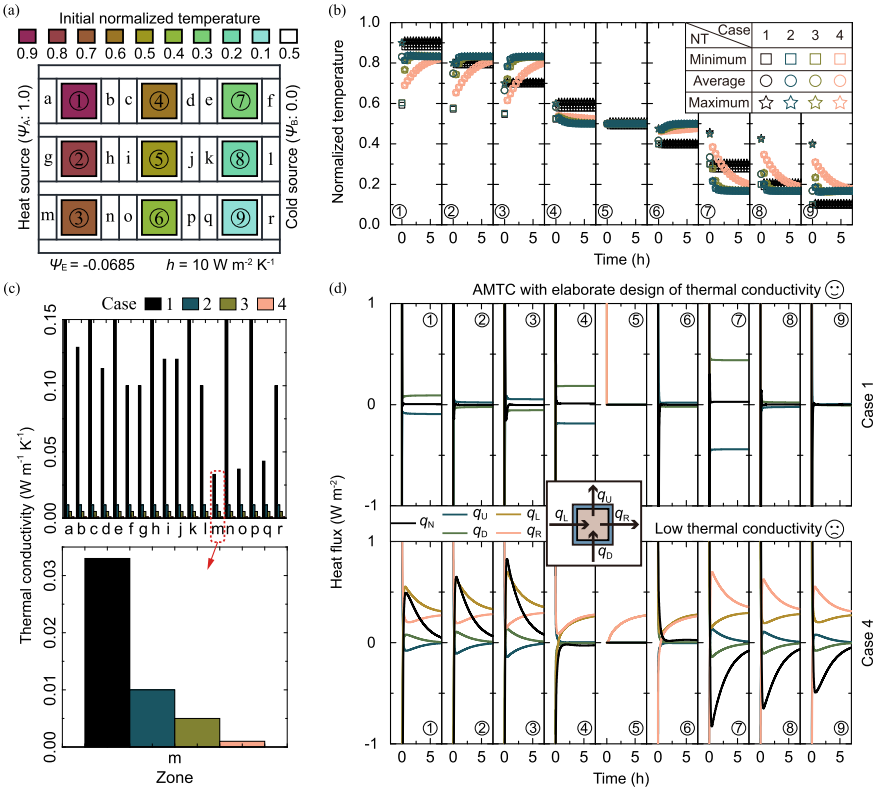

Fig. 10.17 Multi-temperature maintenance. **a** Initial temperature distribution in the multi-temperature control system. **b** Temperature variations of objects within each temperature control zone for cases 1–4. **c** Thermal conductivities of the zones marked in **a**. **d** Heat flux analysis for each temperature control zone during case 1 and case 4. (from Ref. [59], licensed under CC-BY 4.0)

maintained by the multi-temperature control system. For comparison, three scenarios with diminished thermal conductivities were considered: 0.01 W m^{-1} K^{-1} for case 2, 0.005 W m^{-1} K^{-1} for case 3, and 0.001 W m^{-1} K^{-1} for case 4 (Fig. 10.17c). Observations indicate that while decreasing thermal conductivities appears beneficial for enhancing multi-temperature maintenance performance, even when conductivities were minimized to an extremely low value (as in case 4), the desired multi-temperature maintenance characteristics were not achieved, as presented in Fig. 10.17b. To delve deeper, the researchers conducted a heat flux analysis for each temperature control zone, showcased in Fig. 10.17d. Cases 1 and 4 were selected for comparison. The heat flux traversing the temperature control zone from the left, right, top, and bottom were labeled as q_L, q_R, q_U, and q_D, respectively. The net heat flux is expressed as $q_N = q_L - q_R + q_D - q_U$, representing the intensity of heat exchange both inside and outside the temperature control zone. It is evident that in case 1, employing the AMTC strategy, the net heat flux approaches zero after a brief dis-

turbance, which is consistent with the temperature variation behavior of the goods. However, in case 4, regardless of the extent to which thermal conductivities were reduced, the erratic heat flux across each temperature control zone compromised the multi-temperature maintenance performance.

Building on the findings, the authors ventured to design a multi-temperature maintenance container suited for real-world goods transportation. The conceptual design is presented in Fig. 10.18a. This apparatus consists of four primary components: a pair of portable hot and cold sources, a multi-temperature control system, a standard insulation box, and nine compartments tailored to house items at diverse temperatures. The heat source is fashioned from stearic acid (PCM A), which has a phase-change temperature around 340.15 K, whereas the cold source is derived from distilled water (PCM B) with a phase-change temperature close to 273.15 K. Given that the thermal characteristics of the multi-temperature control system are derived from computational methods, it is conceivable that no naturally occurring materials might fulfill these specifications. To address this, the authors employed the effective thermal resistance approach, constructing the system by amalgamating various commercially available materials. For operation, the stearic acid needs to be thoroughly melted to serve as the heat reservoir, and the distilled water must be fully frozen to act as the cold reservoir. Positioned in their designated spots, these elements offer consistent high and low-temperature boundaries, facilitating multi-temperature regulation throughout the transportation process.

The tangible engineering prototype for the multi-temperature maintenance container is displayed in Fig. 10.18b and is conveniently termed the "container with AMTC." To highlight the efficiency of the AMTC, the authors also crafted two control variants. One is a container without the AMTC feature (a conventional thermal insulating container, termed control group 1), while the other employs a container using materials with low thermal conductivity as a substitute for AMTC (designated as a commercial thermal insulating container, or control group 2). Figure 10.18c illustrates a three-dimensional representation of the aforementioned prototypes accompanied by corresponding sectional diagrams. Each distinct color in the temperature control zones denotes the initial temperature of the stored goods. For the sake of generality, water was utilized to emulate the goods, given its prototypical thermophysical properties and ease of initial temperature setup.

The efficacy of multi-temperature maintenance provided by the aforementioned three devices is illustrated by the temperature-time curves of the simulacra, as presented in Fig. 10.19. Figure 10.19a showcases five independent tests, whereas Fig. 10.19b contrasts simulation results with the average values derived from experimental outcomes. When juxtaposing the trajectories of the temperature-time curves from the container without AMTC, with LTCM, and with AMTC, a discernible observation is that the temperature fluctuation rates of the simulacra housed in the container with AMTC are the most subdued. This underscores the beneficial impact of the AMTC method in enhancing multi-temperature maintenance performance. Additionally, a separate evaluation was conducted for the mobile heat and cold sources, depicted in Fig. 10.19c–d. The steady temperature they furnish aligns with the requirements for high-/low- temperature boundaries as illustrated in Fig. 10.15.

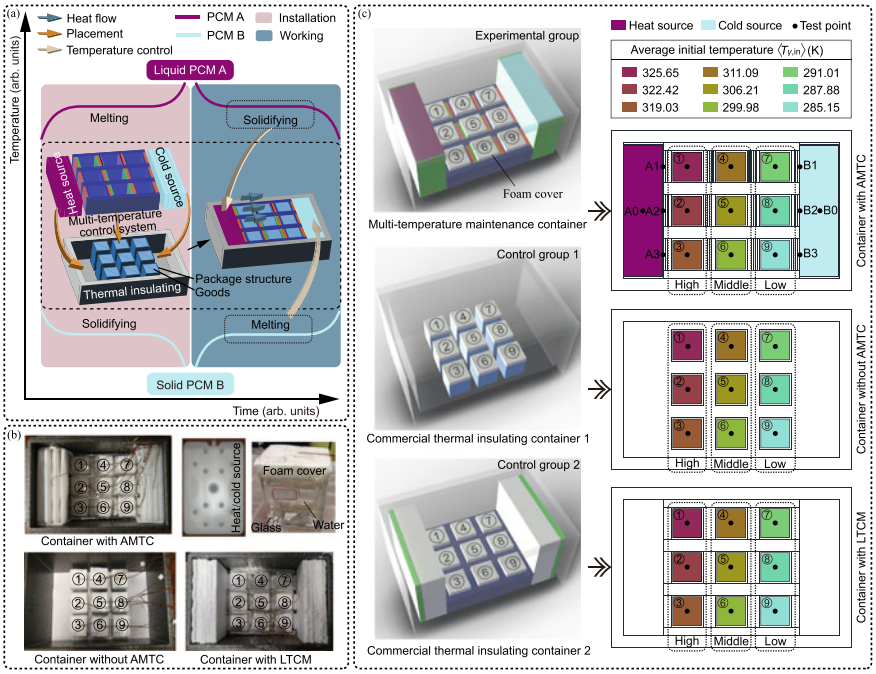

Fig. 10.18 Multi-temperature maintenance container. **a** Schematic illustration of the operation mechanism. **b, c** Experimental setup and schematic representation for the container with AMTC (multi-temperature maintenance container), without AMTC (commercial thermal insulating container 1, and with LTCM (commercial thermal insulating container 2. AMTC stands for adaptive multi-temperature control, while LTCM represents low thermal conductivity materials. (from Ref. [59], licensed under CC-BY 4.0)

Following an in-depth analysis of the multi-temperature maintenance mechanisms, finite element simulations were utilized to visually elucidate temperature gradients within the storage compartments across specific time intervals, as depicted in Fig. 10.20a. The comprehensive heat flux assessment for each designated temperature zone highlighted that in the absence of AMTC, erratic temperature fluxes between simulacra of disparate temperatures impeded the proficient maintenance of multiple temperature zones, especially in regions with pronounced temperature extremes, as evidenced in Fig. 10.20b. Subsequently, a quantitative metric, $\langle \eta_{\gamma,\tau,u} \rangle$, was formulated to gauge the average temperature variation rate of the simulacrum within the container, as showcased in Fig. 10.20c.

Insights revealed that over two hours, the magnitude of temperature deviation, $|\langle \eta_{\gamma,\tau,u} \rangle|$, for simulacra contained in the AMTC-equipped storage ranged narrowly between 0.14% and 2.05%. A comparative scrutiny among containers devoid of AMTC, those outfitted with LTCM, and those incorporating AMTC, accentuated a correlation: amplified temperature fluctuations inversely influenced the efficiency of multi-temperature maintenance, underscoring the pivotal role of AMTC. Delving deeper, in high- and low-temperature regions with extreme temperature vari-

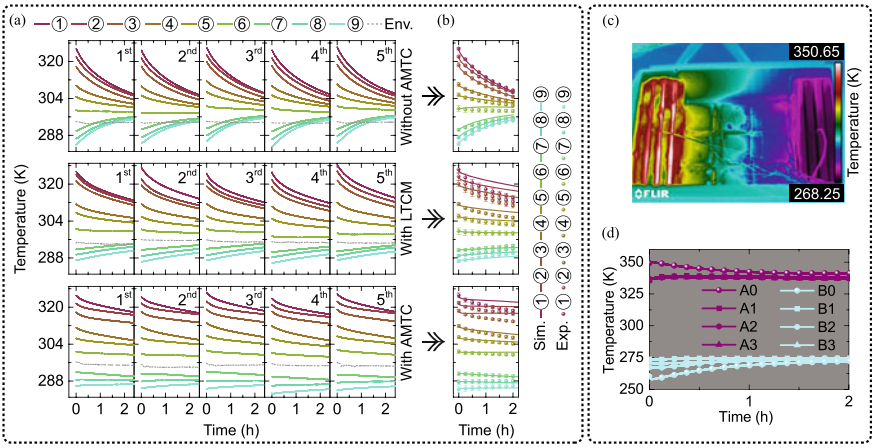

Fig. 10.19 Multi-temperature maintenance performance. **a** Temperature-time curves for the simulacrum in each temperature control zone across five independent tests. **b** Comparison between experimental and simulation results for the temperature-time curves of each simulacrum. **c** Infrared image showing the temperature distribution inside the container after opening the lid. **d** Temperature-time curves for each test point corresponding to the mobile heat and cold sources. (from Ref. [59], licensed under CC-BY 4.0)

ations, the deviation, $\left|\langle \eta_{\gamma,\tau,u} \rangle\right|$, for containers employing AMTC was curtailed by 53.3%–69.2% and 78.0%–94.7% respectively in contrast to their non-AMTC equivalents, and by 34.7%–56.3% and 33.0%–85.9% respectively when contrasted against LTCM-integrated containers, as illuminated in Fig. 10.20d, e. Such pronounced performance enhancement attributed to AMTC underscores its indispensable utility, particularly for the reliable transport of sensitive goods.

10.2.3.2 Comparison with Existing Technology

Integrating the principles of thermal metamaterials' heat flow modulation with phase change mechanisms, the development of multi-temperature maintenance container offers innovative solutions to pivotal societal issues in the realm of dependable goods transportation. While most contemporary temperature regulation strategies prioritize meticulous heat flow control within a singular domain in the above energy-free thermostat and negative-energy thermostat, the presented methodology champions the establishment of multiple zones, each having tunable temperatures. This not only augments its pragmatic aspect but also accentuates its portability and storage-centric attributes.

When benchmarked against prevalent temperature maintenance techniques that employ phase change modalities to engineer multi-temperature insulating chambers for cold chain management, often employing composite PCMs of optimal phase change temperatures, the devised strategy in this study curtails the necessity for extensive heat and cold source deployment. Furthermore, it amplifies the scope of

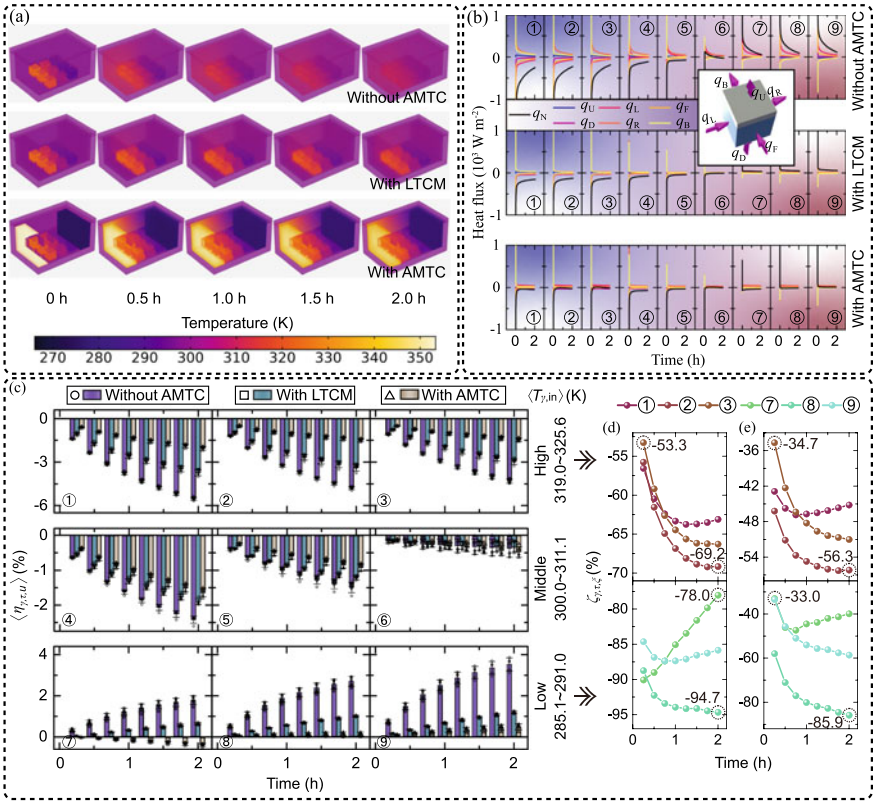

Fig. 10.20 Effect of AMTC on multi-temperature maintenance performance. **a** Temperature distributions inside the container without AMTC, with LTCM, and with AMTC, at specific times. **b** Heat flux analysis for each temperature control zone. **c** Temperature variation rates for the simulacrum in each temperature control zone. **d, e** Changes in temperature variation rates of the simulacrum in the high- (**d**) and low-temperature (**e**) regions. (from Ref. [59], licensed under CC-BY 4.0)

temperature modulation domains. Such an enhancement translates to a streamlined operational protocol and a more economical upfront investment. In essence, this research harmoniously marries core principles of physics with actionable insights from engineering, paving the way for a simplified yet more versatile temperature modulation framework.

10.3 Prospects for Convection Heat Transfer System

The preceding sections presented three specific cases demonstrating temperature maintenance with diverse functionalities within a conduction heat transfer system. Following the developmental trajectory in thermal metamaterials, the logical next step is to explore temperature maintenance in a convection heat transfer system.

Given the ubiquity of convection heat transfer in various scenarios, advancing in this direction will foster broader applications in the field of temperature maintenance.

From the discussed operations, two pivotal factors emerge in the fabrication of actual devices. First is the SMA characterized by variable structural parameters, and the second is the phase transition of liquid-solid PCMs. Both elements, individually or in tandem with thermal metamaterials, are instrumental in achieving meticulous heat flow regulation. The pertinent question then arises: can this precise control be replicated in a convection heat transfer setting?

Citing SMA as a reference, Ref. [6] unveiled a cutting-edge heat exchanger underpinned by SMA. SMA, conceptualized as the linchpin, automatically modulates the convective heat transfer performance. The mechanism driving the SMA employs NiTi as the foundational material. Its capability to oscillate between austenite and martensite phases ensures that the SMA can toggle between active and inactive states. Crafting the heat exchanger, the objective was to leverage the SMA's transformative capacity to alter the flow channel's architecture. In cooler temperatures, the SMA remains dormant, but as temperatures soar, it becomes active. Analyzing the flow dynamics, it is evident that the activated state induces fluid turbulence, bolstering heat transfer.

Conversely, employing PCMs primarily aims to stabilize the temperature within a designated region. Numerous studies have showcased the adeptness of PCMs in modulating temperature amidst convective heat transfer—examples span applications in aircraft, vehicles, and even in systems that store heat energy to subsequently convert it into electricity [63, 64].

While both these technologies exhibit the prowess to qualitatively manage temperature under convection heat transfer, thermal metamaterials bring to the table a quantitative toolkit rooted in analytical theory. Integrating thermal metamaterials into this domain could be a potential move, amplifying the precision and scope of temperature control.

10.4 Conclusion

This chapter delves into three innovative temperature maintenance devices rooted in the advancements of conduction heat transfer, all harnessing the potential of thermal metamaterials: the energy-free thermostat, the negative-energy thermostat, and the multi-temperature maintenance container. The energy-free thermostat stands out with its capability to stabilize the temperature in the central region under fluctuating temperature gradients without necessitating any additional energy. The negative-energy thermostat, on the other hand, can uphold both temperature and electrical potential in the central area of thermoelectric cloak amidst varying temperature and electrical potential gradients, all while producing electrical energy. The third, the multi-temperature maintenance container, offers the versatility of concurrently maintaining different objects, each with unique temperature requirements, a feature especially pertinent for goods transportation applications. The design methodologies

underpinning these devices may well pave the way for future innovations in passive temperature control technology. Moreover, the principles of heat flow regulation, informed by thermal metamaterials, are extended to encompass situations involving convection heat transfer. Building on pioneering passive temperature control techniques from relevant research domains, this chapter concludes the current state of temperature maintenance using thermal metamaterials and discusses its promising future.

In recent research, thermal metamaterials have been extended to chemical systems [65], plasma systems [66], and more, collectively termed as diffusion metamaterials [18, 19]. Drawing inspiration from a variety of systems in physics, chemistry, and engineering, such as phase-transition systems [67], complex systems [68, 69], colloidal systems [70, 71], graded materials [72], and others novel mechanisms/functions, the principle of temperature maintenance could be further refined and made more advantageous for practical applications.

References

1. Gao, Y., Miyata, S., Akashi, Y.: Energy saving and indoor temperature control for an office building using tube-based robust model predictive control. Appl. Energy **341**, 121106 (2023)
2. Zhang, Q., Lv, Y., Wang, Y., Yu, S., Li, C., Ma, R., Chen, Y.: Temperature-dependent dual-mode thermal management device with net zero energy for year-round energy saving. Nat. Commun. **13**, 4874 (2022)
3. Wang, X., Narayan, S.: Thermal radiative switching interface for energy-efficient temperature control. Renew. Energy **197**, 574–582 (2022)
4. Chen, Z., Zhang, X., Ji, J., Lv, Y.: A review of the application of hydrated salt phase change materials in building temperature control. J. Energy Storage **56**, 106157 (2022)
5. Guo, R., Shan, L., Wu, Y., Cai, Y., Huang, R., Ma, H., Tang, K., Liu, K.: Phase-change materials for intelligent temperature regulation. Mater. Today Energy **23**, 100888 (2022)
6. Wang, B., Deng, H., Li, L.A., Li, H.: Design and test of smart heat exchanger based on shape memory alloys. Appl. Therm. Eng. **221**, 119911 (2023)
7. Regany, D., Majos, F., Barrau, J., Rosell, J., Ibanez, M., Frechette, L.G., Vilarrubi, M.: Design and test of shape memory alloy fins for self-adaptive liquid cooling device. Appl. Therm. Eng. **206**, 118010 (2022)
8. Liu, W., Bie, Y., Xu, T., Cichon, A., Krolczyk, G., Li, Z.: Heat transfer enhancement of latent heat thermal energy storage in solar heating system: A state-of-the-art review. J. Energy Storage **46**, 103727 (2022)
9. Paul, J., Pandey, A.K., Mishra, Y.N., Said, Z., Mishra, Y.K., Ma, Z., Jacob, J., Kadirgama, K., Samykano, M., Tyagi, V.V.: Nano-enhanced organic form stable PCMs for medium temperature solar thermal energy harvesting: Recent progresses, challenges, and opportunities. Renew. Sust. Energ. Rev. **161**, 112321 (2022)
10. Liu, J., Zhang, Y., Li, S., Valenzuela, C., Shi, S., Jiang, C., Wu, S., Ye, L., Wang, L., Zhou, Z.: Emerging materials and engineering strategies for performance advance of radiative sky cooling technology. Chem. Eng. J. **453**, 139739 (2023)
11. Liu, J., Tang, H., Jiang, C., Wu, S., Ye, L., Zhao, D., Zhou, Z.: Micro-nano porous structure for efficient daytime radiative sky cooling. Adv. Funct. Mater. **32**, 2206962 (2022)
12. Park, C., Joung, W.: Effect of heat load on pneumatic temperature control characteristics of a pressure-controlled loop heat pipe. Int. J. Heat Mass Transfer **186**, 122472 (2022)

13. Leng, Z., Yuan, Y., Cao, X., Zeng, C., Zhong, W., Gao, B.: Heat pipe/phase change material thermal management of Li-ion power battery packs: A numerical study on coupled heat transfer performance. Energy **240**, 122754 (2022)
14. Du, J., Nie, B., Zhang, Y., Du, Z., Wang, L., Ding, Y.: Cooling performance of a thermal energy storage-based portable box for cold chain applications. J. Energy Storage **28**, 101238 (2020)
15. Hao, M., Li, J., Park, S., Moura, S., Dames, C.: Efficient thermal management of Li-ion batteries with a passive interfacial thermal regulator based on a shape memory alloy. Nat. Energy **3**, 899–906 (2018)
16. Zhang, C., Yang, J., Li, Y., Song, J., Guo, J., Fang, Y., Yang, X., Yang, Q., Wang, D., Deng, X.: Vapor-liquid transition-based broadband light modulation for self-adaptive thermal management. Adv. Funct. Mater. **32**, 2208144 (2022)
17. Khalilmoghadam, P., Rajabi-Ghahnavieh, A., Shafii, M.B.: A novel energy storage system for latent heat recovery in solar still using phase change material and pulsating heat pipe. Renew. Energy **163**, 2115–2127 (2021)
18. Zhang, Z., Xu, L., Qu, T., Lei, M., Lin, Z.-K., Ouyang, X., Jiang, J.-H., Huang, J.: Diffusion metamaterials. Nat. Rev. Phys. **5**, 218–235 (2023)
19. Yang, F.B., Zhang, Z.R., Xu, L.J., Liu, Z.F., Jin, P., Zhuang, P.F., Lei, M., Liu, J.R., Jiang, J.-H., Ouyang, X.P., Marchesoni, F., Huang, J.P.: Controlling mass and energy diffusion with metamaterials. Rev. Mod. Phys. **96**, 015002 (2024). arXiv:2309.04711
20. Xu, L.-J., Huang, J.-P.: Transformation Thermotics and Extended Theories: Inside and Outside Metamaterials. Springer, Singapore (2023)
21. Yang, S., Wang, J., Dai, G., Yang, F., Huang, J.: Controlling macroscopic heat transfer with thermal metamaterials: Theory, experiment and application. Phys. Rep. **908**, 1–65 (2021)
22. Huang, J.-P.: Theoretical Thermotics: Transformation Thermotics and Extended Theories for Thermal Metamaterials. Springer, Singapore (2020)
23. Fan, C.Z., Gao, Y., Huang, J.P.: Shaped graded materials with an apparent negative thermal conductivity. Appl. Phys. Lett. **92**, 251907 (2008)
24. Wang, J., Dai, G., Huang, J.: Thermal metamaterial: Fundamental, application, and outlook. iScience **23**, 101637 (2020)
25. Huang, J.: Thermal metamaterials make it possible to control the flow of heat at will. ES Energy Environ. **7**, 1–3 (2020)
26. Huang, J.-P.: Thermal metamaterial: Geometric structure, working mechanism, and novel function. Prog. Phys. **38**, 220–238 (2018)
27. Ji, Q., Shen, X.-Y., Huang, J.-P.: Transformation thermotics: thermal metamaterials and their applications. Int. J. Mod. Phys. B **32**, 1840004 (2018)
28. Shen, X.-Y., Huang, J.-P.: Transformation thermotics: thermal metamaterials and their applications. Acta Phys. Sin. **65**, 178103 (2016)
29. Xu, L., Yang, S., Huang, J.: Thermal theory for heterogeneously architected structure: Fundamentals and application. Phys. Rev. E **98**, 052128 (2018)
30. Xu, L., Xu, G., Huang, J., Qiu, C.-W.: Diffusive fizeau drag in spatiotemporal thermal metamaterials. Phys. Rev. Lett. **128**, 145901 (2022)
31. Huang, J., Shen, X., Jiang, C., Wu, Z., Huang, J.: Thermal expander. Phys. B **518**, 56–60 (2017)
32. Zhuang, P., Xu, L., Tan, P., Ouyang, X., Huang, J.: Breaking efficiency limit of thermal concentrators by conductivity couplings. Sci. China Phys. Mech. Astron. **65**, 117007 (2022)
33. Li, Y., Shen, X., Huang, J., Ni, Y.: Temperature-dependent transformation thermotics for unsteady states: Switchable concentrator for transient heat flow. Phys. Lett. A **380**, 1641–1647 (2016)
34. Yang, F., Tian, B., Xu, L., Huang, J.: Experimental demonstration of thermal chameleonlike rotators with transformation-invariant metamaterials. Phys. Rev. Appl. **14**, 054024 (2020)
35. Jin, P., Yang, S., Xu, L., Dai, G., Huang, J., Ouyang, X.: Particle swarm optimization for realizing bilayer thermal sensors with bulk isotropic materials. Int. J. Heat Mass Transf. **172**, 121177 (2021)
36. Xu, L., Huang, J., Jiang, T., Zhang, L., Huang, J.: Thermally invisible sensors. EPL **132**, 14002 (2020)

37. Jin, P., Xu, L., Jiang, T., Zhang, L., Huang, J.: Making thermal sensors accurate and invisible with an anisotropic monolayer scheme. Int. J. Heat Mass Transf. **163**, 120437 (2020)
38. Xu, L., Yang, S., Huang, J.: Thermal transparency induced by periodic interparticle interaction. Phys. Rev. Appl. **11**, 034056 (2019)
39. Xu, L.-J., Huang, J.-P.: Active thermal wave cloak. Chin. Phys. Lett. **37**, 120501 (2020)
40. Shen, X., Jiang, C., Li, Y., Huang, J.: Thermal metamaterial for convergent transfer of conductive heat with high efficiency. Appl. Phys. Lett. **109**, 201906 (2016)
41. Yang, S., Xu, L.J., Wang, R.Z., Huang, J.P.: Full control of heat transfer in single-particle structural materials. Appl. Phys. Lett. **111**, 121908 (2017)
42. Xu, L., Huang, J.: Thermal convection-diffusion crystal for prohibition and modulation of wave-like temperature profiles. Appl. Phys. Lett. **117**, 011905 (2020)
43. Wang, J., Dai, G., Yang, F., Huang, J.: Designing bistability or multistability in macroscopic diffusive systems. Phys. Rev. E **101**, 022119 (2020)
44. Wang, B., Shih, T.-M., Huang, J.: Enhancing and attenuating heat transfer characteristics for circulating flows of nanofluids within rectangular enclosures. Int. Comm. Heat Mass Transf. **117**, 104800 (2020)
45. Xu, L., Dai, G., Huang, J.: Transformation multithermotics: Controlling radiation and conduction simultaneously. Phys. Rev. Appl. **13**, 024063 (2020)
46. Dai, G., Huang, J.: A transient regime for transforming thermal convection: Cloaking, concentrating, and rotating creeping flow and heat flux. J. Appl. Phys. **124**, 235103 (2018)
47. Xu, L., Wang, J., Dai, G., Yang, S., Yang, F., Wang, G., Huang, J.: Geometric phase, effective conductivity enhancement, and invisibility cloak in thermal convection-conduction. Int. J. Heat Mass Transf. **165**, 120659 (2021)
48. Xu, L., Yang, S., Dai, G., Huang, J.: Transformation omnithermotics: Simultaneous manipulation of three basic modes of heat transfer. ES Energy Environ. **7**, 65–70 (2020)
49. Wang, J., Yang, F., Xu, L., Huang, J.: Omnithermal restructurable metasurfaces for both infrared-light illusion and visible-light similarity. Phys. Rev. Appl. **14**, 014008 (2020)
50. Yang, S., Xu, L., Dai, G., Huang, J.: Omnithermal metamaterials switchable between transparency and cloaking. J. Appl. Phys. **128**, 095102 (2020)
51. Zhou, X.C., Lin, W.Y., Yang, F.B., Zhou, X.D., Shen, J., Huang, J.P.: Effective medium theory with hybrid impacts of phase symmetry and asymmetry for analyzing phase transition behavior. EPL **141**, 16001 (2023)
52. Lin, W., Zhang, H., Kalcheim, Y., Zhou, X., Yang, F., Shi, Y., Feng, Y., Wang, Y., Huang, J., Schuller, I., Zhou, X., Shen, J.: Direct visualization of percolating metal-insulator transition in V_2O_3 using scanning microwave impedance microscopy. Sci. China Phys. Mech. Astron. **65**, 297411 (2022)
53. Huang, T., Yang, F., Wang, T., Wang, J., Li, Y., Huang, J., Chen, M., Wu, L.: Ladder-structured boron nitride nanosheet skeleton in flexible polymer films for superior thermal conductivity. Appl. Mater. Today **26**, 101299 (2022)
54. Tian, B., Wang, J., Dai, G., Ouyang, X., Huang, J.: Thermal metadevices with geometrically anisotropic heterogeneous composites. Int. J. Heat Mass Transf. **174**, 121312 (2021)
55. Shen, X., Li, Y., Jiang, C., Huang, J.: Temperature trapping: Energy-free maintenance of constant temperatures as ambient temperature gradients change. Phys. Rev. Lett. **117**, 055501 (2016)
56. Huang, J.P.: Technologies for Controlling Thermal Energy: Design, Simulation and Experiment based on Thermal Metamaterial Theories including Transformation Thermotics. Higher Education Press, Beijing (2022)
57. Wang, J., Shang, J., Huang, J.P.: Negative energy consumption of thermostats at ambient temperature: electricity generation with zero energy maintenance. Phys. Rev. Appl. **11**, 024053 (2019)
58. Stedman, T., Woods, L.M.: Cloaking of thermoelectric transport. Sci. Rep. **7**, 6988 (2017)
59. Zhou, X., Xu, X., Huang, J.: Adaptive multi-temperature control for transport and storage containers enabled by phase-change materials. Nat. Commun. **14**, 5449 (2023)

60. Lin, N., Li, C., Zhang, D., Li, Y., Chen, J.: Emerging phase change cold storage materials derived from sodium sulfate decahydrate. Energy **245**, 123294 (2022)
61. Xu, X., Zhang, X.: Simulation and experimental investigation of a multi-temperature insulation box with phase change materials for cold storage. J. Food Eng. **292**, 110286 (2021)
62. Zhao, Y., Zhang, X., Xu, X., Zhang, S.: Development of composite phase change cold storage material and its application in vaccine cold storage equipment. J. Energy Storage **30**, 101455 (2020)
63. Ren, X.M., Nie, H., Zhang, M., Nikitchenko, Y.A., Tikhonovets, A.: Heat performance investigation of phase change materials for the cooling array system on vehicles. Appl. Therm. Eng. **171**, 115115 (2020)
64. Elefsiniotis, A., Becker, T., Schmid, U.: Thermoelectric energy harvesting using phase change materials (PCMs) in high temperature environments in aircraft. J. Electron. Mater. **43**, 1809–1814 (2014)
65. Zhang, Z., Xu, L., Huang, J.: Controlling chemical waves by transforming transient mass transfer. Adv. Theory Simul. **5**, 2100375 (2022)
66. Zhang, Z., Huang, J.: Transformation plasma physics. Chin. Phys. Lett. **39**, 075201 (2022)
67. Gao, Q., Ai, J., Tang, S., Li, M., Chen, Y., Huang, J., Tong, H., Xu, L., Xu, L., Tanaka, H., Tan, P.: Fast crystal growth at ultra-low temperatures. Nat. Mater. **20**, 1431–1439 (2021)
68. Ye, C., Huang, J.P.: Non-classical oscillator model for persistent fluctuations in stock markets. Phys. A **387**, 1255–1263 (2008)
69. Liu, L., Wei, J., Zhang, H., Xin, J., Huang, J.: A statistical physics view of pitch fluctuations in the classical music from Bach to Chopin: evidence for scaling. PLoS ONE **8**, e58710 (2013)
70. Gao, Y., Jian, Y.C., Zhang, L.F., Huang, J.P.: Magnetophoresis of nonmagnetic particles in ferrofluids. J. Phys. Chem. C **111**, 10785–10791 (2007)
71. Huang, J.P., Karttunen, M., Yu, K.W., Dong, L.: Dielectrophoresis of charged colloidal suspensions. Phys. Rev. E **67**, 021403 (2003)
72. Dong, L., Huang, J.P., Yu, K.W., Gu, G.Q.: Dielectric response of graded spherical particles of anisotropic materials. J. Appl. Phys. **95**, 621–624 (2004)

Part III
Metamaterials for Thermal Diffusion: Thermal Conduction and Radiation

Chapter 11
Radiative Metamaterials Based on Effective-Medium Theory

Haohan Tan and Liujun Xu

11.1 Opening Remarks

The research on diffusion metamaterials dates back to 2008 [1, 2]. Since then, the research in the field of diffusion metamaterials has made significant progress [3–12]. Researchers have designed numerous devices with novel functions, such as thermal cloaks [13–15], concentrators [16, 17], rotators [18], sensors [19–23], illusions [24], transparency [25, 26], and expanders [27, 28]. The development of metamaterials in the thermal field began with research on thermal conduction [29–32]. However, thermal radiation [33, 34], which is an important mode of thermal transport alongside conduction and convection [35–38], cannot be ignored in many cases. Finding ways to realize similar functions while considering this mechanism is an unavoidable problem. However, the nonlinearity of Stefan's law has posed significant obstacles to research in this field. Furthermore, it is unknown whether the dynamic equations for thermal conduction and radiation satisfy transformation invariance. Therefore, the design of thermal metamaterials considering conduction and radiation remains an unexplored topic, even many years after the proposition of thermal metamaterials. Xu et al. were the first to design diffusion metamaterials for manipulating thermal radiation. For convenience, they did not use Stefan's law but instead employed the Rosseland diffusion approximation. Based on this method, they designed devices with novel functions such as cloaks, transparency, and expanders.

H. Tan (✉)
Department of Physics, Key Laboratory of Micro and Nano Photonic Structures (MOE), and State Key Laboratory of Surface Physics, Fudan University, Shanghai 200438, China
e-mail: 22110190050@m.fudan.edu.cn

L. Xu
Graduate School of China Academy of Engineering Physics, Beijing 100193, China

F.-B. Yang and J.-P. Huang, *Diffusionics*,
https://doi.org/10.1007/978-981-97-0487-3_11

11.2 Effective-Medium Theory Under Rosseland Approximation

Xu et al. investigated a passive and steady process of heat transfer, focusing on the total heat flux $\boldsymbol{J}_{\text{total}}$, which comprises the conductive flux $\boldsymbol{J}_{\text{con}}$ and the radiative flux $\boldsymbol{J}_{\text{rad}}$. This heat flux satisfies the divergence-free condition:

$$\nabla \cdot \boldsymbol{J}_{\text{total}} = \nabla \cdot (\boldsymbol{J}_{\text{con}} + \boldsymbol{J}_{\text{rad}}) = 0. \tag{11.1}$$

The conductive flux $\boldsymbol{J}_{\text{con}}$ is given by:

$$\boldsymbol{J}_{\text{con}} = -\kappa \nabla T, \tag{11.2}$$

where κ represents the thermal conductivity. On the other hand, based on the Rosseland diffusion approximation, the radiative flux $\boldsymbol{J}_{\text{rad}}$ is expressed as:

$$\boldsymbol{J}_{\text{rad}} = -\gamma T^3 \nabla T, \tag{11.3}$$

Here, γ (given by $\gamma = 16\beta^{-1}n^2\sigma/3$) can be considered as the radiative coefficient. In this expression, β corresponds to the Rosseland mean extinction coefficient, n represents the relative refractive index, and σ is the Stefan-Boltzmann constant ($\sigma = 5.67 \times 10^{-8}\,\text{Wm}^{-2}\text{K}^{-4}$).

Xu et al. further consider a three-dimensional core-shell structure (Fig. 11.1a) which consists of a core with thermal conductivity κ_c, Rosseland mean extinction coefficient β_c, and relative refractive index n_c (radiative coefficient γ_c), coated by a shell with corresponding parameters κ_s, β_s, and n_s (radiative coefficient γ_s). The subscript c (or s) denotes the core (or shell). The semi-axis lengths of the core and shell are λ_{ci} and λ_{si}, respectively, where $i = 1,\ 2,\ 3$. Assuming that the ratio γ/κ of the core-shell structure is a constant α, specifically $\gamma_c/\kappa_c = \gamma_s/\kappa_s = \alpha$, Eq. (11.1) can be rewritten as

$$\nabla \cdot \left(-\kappa \nabla T - \alpha \kappa T^3 \nabla T\right) = \nabla \cdot \left(-\kappa \left(1 + \alpha T^3\right) \nabla T\right) = \nabla \cdot \left(-\kappa \nabla \left(T + \alpha T^4/4\right)\right) = 0. \tag{11.4}$$

By performing a variable substitution $\varphi = T + \alpha T^4/4$, we obtain

$$\nabla \cdot (-\kappa \nabla \varphi) = 0. \tag{11.5}$$

Therefore, the strongly nonlinear equation (Eq. (11.1)) can be transformed into a linear equation (Eq. (11.5)).

To proceed, Xu et al. introduced ellipsoidal coordinates (ρ, ξ, η), which are defined by the following equations:

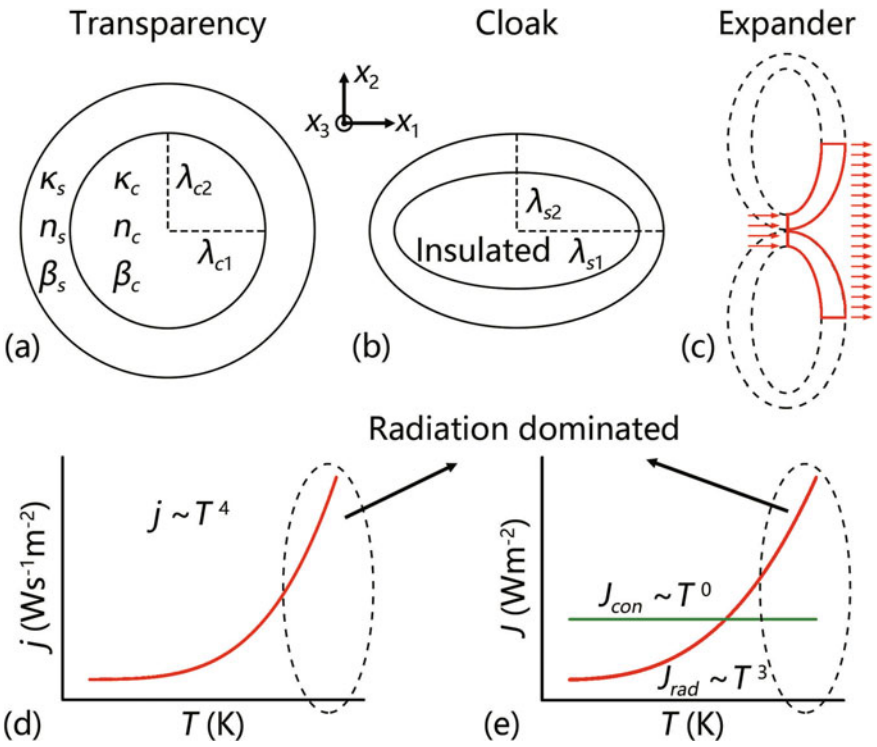

Fig. 11.1 Schematic diagrams of **a** thermal transparency, **b** thermal cloak, and **c** thermal expander. **d** and **e** qualitatively show the radiative emittance j, conductive flux J_{con}, and radiative flux J_{rad} as a function of temperature T. (from Ref. [39])

$$\begin{cases} \frac{x^2}{\rho+\lambda_1^2}+\frac{y^2}{\rho+\lambda_2^2}+\frac{z^2}{\rho+\lambda_3^2}=1 \text{ (confocal ellipsoids)} \\ \frac{x^2}{\xi+\lambda_1^2}+\frac{y^2}{\xi+\lambda_2^2}+\frac{z^2}{\xi+\lambda_3^2}=1 \text{ (hyperboloids of one sheet)} \\ \frac{x^2}{\eta+\lambda_1^2}+\frac{y^2}{\eta+\lambda_2^2}+\frac{z^2}{\eta+\lambda_3^2}=1 \text{ (hyperboloids of two sheets)} \end{cases} \tag{11.6}$$

In these equations, λ_1, λ_2, and λ_3 are three constants that satisfy $\rho > -\lambda_1^2 > \xi > -\lambda_2^2 > \eta > -\lambda_3^2$. Equation (11.5) can be expressed in ellipsoidal coordinates as:

$$\frac{\partial}{\partial\rho}\left(g(\rho)\frac{\partial\varphi}{\partial\rho}\right)+\frac{g(\rho)}{\rho+\lambda_i^2}\frac{\partial\varphi}{\partial\rho}=0, \tag{11.7}$$

where $g(\rho)=\sqrt{\left(\rho+\lambda_1^2\right)\left(\rho+\lambda_2^2\right)\left(\rho+\lambda_3^2\right)}$. Since Eq. (11.7) has the solution:

$$\varphi=\left(u+v\int_0^{\rho}\left(\rho+\lambda_i^2\right)^{-1}g(\rho)^{-1}d\rho\right)x_i, \tag{11.8}$$

where u and v are constants, and x_i ($i = 1,\ 2,\ 3$) denotes Cartesian coordinates. The temperatures of the core, shell, and background can be defined as φ_c, φ_s, and φ_b, respectively. These temperatures can be obtained as follows:

$$\begin{cases} \varphi_c = u_c x_i \\ \varphi_s = \left(u_s + v_s \int_{\rho_c}^{\rho} \left(\rho + \lambda_i^2 \right)^{-1} g\left(\rho\right)^{-1} d\rho \right) x_i \\ \varphi_b = u_b x_i \end{cases} \tag{11.9}$$

where u_c, u_s, and v_s are determined by the boundary conditions. The exterior surfaces of the core and shell are denoted by ρ_c and ρ_s, respectively. The boundary conditions require continuity of temperatures and normal heat fluxes, leading to the following equations:

$$\begin{cases} u_c = u_s \\ u_b = u_s + v_s \int_{\rho_c}^{\rho_s} \left(\rho + \lambda_i^2 \right)^{-1} g\left(\rho\right)^{-1} d\rho \\ u_c = 2 v_s \kappa_s \left(\kappa_c - \kappa_s \right)^{-1} g\left(\rho_c\right)^{-1} \\ u_b = 2 v_s \kappa_s \left(\kappa_{ei} - \kappa_s \right)^{-1} g\left(\rho_s\right)^{-1} \end{cases} \tag{11.10}$$

Here, κ_{ei} represents the effective thermal conductivity of the core-shell structure along the direction of x_i. To obtain the expression for κ_{ei}, one can solve Eq. (11.10). For this purpose, Xu et al. define the semi-axis lengths of the core, λ_{ci}, and the shell, λ_{si}, as follows:

$$\begin{cases} \lambda_{ci} = \sqrt{\lambda_i^2 + \rho_c} \\ \lambda_{si} = \sqrt{\lambda_i^2 + \rho_s} \end{cases} \tag{11.11}$$

Here, $i = 1,\ 2,\ 3$. Consequently, the volume fraction f can be expressed as:

$$f = \frac{\lambda_{c1}\lambda_{c2}\lambda_{c3}}{\lambda_{s1}\lambda_{s2}\lambda_{s3}} = \frac{g\left(\rho_c\right)}{g\left(\rho_s\right)} \tag{11.12}$$

Xu et al. also introduce the shape factor d_{wi} along the direction of x_i as follows:

$$d_{wi} = \frac{\lambda_{w1}\lambda_{w2}\lambda_{w3}}{2} \int_0^{\infty} \left(\tau + \lambda_{wi}^2 \right)^{-1} \left(\left(\tau + \lambda_{w1}^2 \right) \left(\tau + \lambda_{w2}^2 \right) \left(\tau + \lambda_{w3}^2 \right) \right)^{-1/2} d\tau, \tag{11.13}$$

Here, the subscript w can take the values c or s, representing the shape factor of the core or shell, respectively. Subsequently, they can obtain the following expression:

$$\int_{\rho_c}^{\rho_s}\left(\rho+\lambda_i^2\right)^{-1} g\left(\rho\right)^{-1} d\rho = \int_{\rho_c}^{\infty}\left(\rho+\lambda_i^2\right)^{-1} g\left(\rho\right)^{-1} d\rho - \int_{\rho_s}^{\infty}\left(\rho+\lambda_i^2\right)^{-1} g\left(\rho\right)^{-1} d\rho$$
$$= 2d_{ci}\, g\left(\rho_c\right)^{-1} - 2d_{si}\, g\left(\rho_s\right)^{-1}. \tag{11.14}$$

Finally, Xu et al. derive a concise expression for κ_{ei} as follows:

$$\kappa_{ei} = \kappa_s\left[\frac{f\left(\kappa_c-\kappa_s\right)}{\kappa_s+\left(d_{ci}-fd_{si}\right)\left(\kappa_c-\kappa_s\right)}+1\right]. \tag{11.15}$$

The method described above is the standard approach for calculating the Laplace equation. The shape factors satisfy the sum rule $d_{w1}+d_{w2}+d_{w3}=1$. In principle, the effective thermal conductivity of any core-shell structure can be obtained using Eq. (11.15) when the core-shell structure is confocal or concentric. In fact, Eq. (11.15) can be reduced to handle cylindrical (two-dimensional) cases by setting $\lambda_{w3}=\infty$, resulting in $d_{w1}=\lambda_{w2}/\left(\lambda_{w1}+\lambda_{w2}\right)$, $d_{w2}=\lambda_{w1}/\left(\lambda_{w1}+\lambda_{w2}\right)$, and $d_{w3}=0$ (the sum rule $d_{w1}+d_{w2}+d_{w3}=1$ is still satisfied).

Since γ/κ is a constant, the effective radiative coefficient can be expressed as:

$$\gamma_{ei} = \gamma_s\left[\frac{f\left(\gamma_c-\gamma_s\right)}{\gamma_s+\left(d_{ci}-fd_{si}\right)\left(\gamma_c-\gamma_s\right)}+1\right], \tag{11.16}$$

Here, γ_{ei} represents the effective radiative coefficient of the core-shell structure along the direction of x_i. By using Eqs. (11.15) and (11.16), one can predict the effective thermal conductivity and effective radiative coefficient. However, in order to achieve the same effect of conduction and radiation, it is necessary to maintain γ/κ as a constant.

Furthermore, to validate the theoretical analyses, Xu et al. conducted finite-element simulations. The radiative emittance j is shown in Fig. 11.1d to be proportional to T^4 according to the Stefan-Boltzmann law. The conductive flux J_{con} depends on the temperature gradient, while the radiative flux J_{rad} is proportional to T^3, as depicted in Fig. 11.1e. These qualitative analyses indicate the significant role of thermal radiation at high temperatures. Therefore, Xu et al. performed finite-element simulations at three temperature intervals: (I) 273–313 K, representing a small upper temperature limit where conduction (Con.) dominates; (II) 273–673 K, representing a medium upper temperature limit where conduction and radiation (Rad.) are approximately equal; and (III) 273–4273 K, representing a large upper temperature limit where radiation is the dominant mode of heat transfer.

Thermal transparency involves the design of a shell tailored to the object, ensuring an undistorted temperature profile outside the shell, as depicted in Fig. 11.2. By selecting appropriate parameters based on Eqs. (11.15) and (11.16), Xu et al. demonstrated that the temperature profile outside the shell remains undistorted, as shown in Fig. 11.2a–c or Fig. 11.2d–f. Consequently, the core-shell structure at the center becomes indistinguishable, as illustrated in Fig. 11.2g–i. Figure 11.2j–l present the corresponding theoretical results from the references using the same parameters

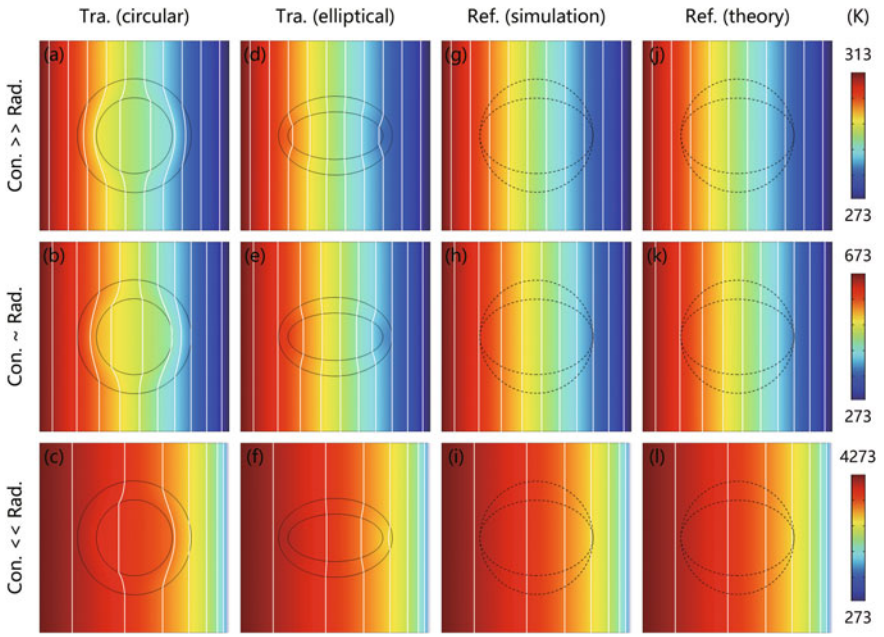

Fig. 11.2 Steady results of thermal transparency. **a–c** $\lambda_{c1} = \lambda_{c2} = 2$ cm, $\lambda_{s1} = \lambda_{s2} = 3$ cm, $\kappa_c = 2\,\mathrm{W\,m^{-1}K^{-1}}$, $\beta_c = 50\,\mathrm{m^{-1}}$, $\kappa_s = 0.62\,\mathrm{W\,m^{-1}K^{-1}}$, and $\beta_s = 161.1\,\mathrm{m^{-1}}$. **d–f** $\lambda_{c1} = 2.5$ cm, $\lambda_{c2} = 1.25$ cm, $\lambda_{s1} = 3$ cm, $\lambda_{s2} = 2.08$ cm, $\kappa_c = 0.5\,\mathrm{W\,m^{-1}K^{-1}}$, $\beta_c = 200\,\mathrm{m^{-1}}$, $\kappa_s = 1.61\,\mathrm{W\,m^{-1}K^{-1}}$, and $\beta_s = 62\,\mathrm{m^{-1}}$. **g–i** are the references with pure background parameters. **j–l** are the theoretical temperature distributions of the references. Circular (or elliptical) dashed lines are plotted for the comparison with circular (or elliptical) transparency. (from Ref. [39])

as Fig. 11.2g–i. The matching temperature profiles in both simulations and theory validate the theoretical analyses.

Furthermore, Xu et al. demonstrated that with a small upper temperature limit where conduction dominates, the temperature gradient outside the shell remains nearly uniform, as depicted in the first row of Fig. 11.2. As the upper temperature limit increases, the effect of radiation becomes prominent, resulting in nonuniform temperature gradients outside the shell, as shown in the last two rows of Fig. 11.2.

A thermal cloak is capable of shielding any object within it from detection. Generally, an insulated layer is employed to prevent heat flux from reaching the object. Consequently, the object along with the insulated layer can be treated as an insulated core, where $\kappa_c = \gamma = 0$. Moreover, Xu et al. designed a shell based on Eqs. (11.15) and (11.16) to eliminate the influence of the insulated core. The simulation results are presented in Fig. 11.3a–f. Evidently, the isotherms remain separated from the object, indicating that the heat flux is unable to enter the object. Additionally, the temperature profiles of the background remain undistorted. This successful outcome demonstrates the expected cloaking effect.

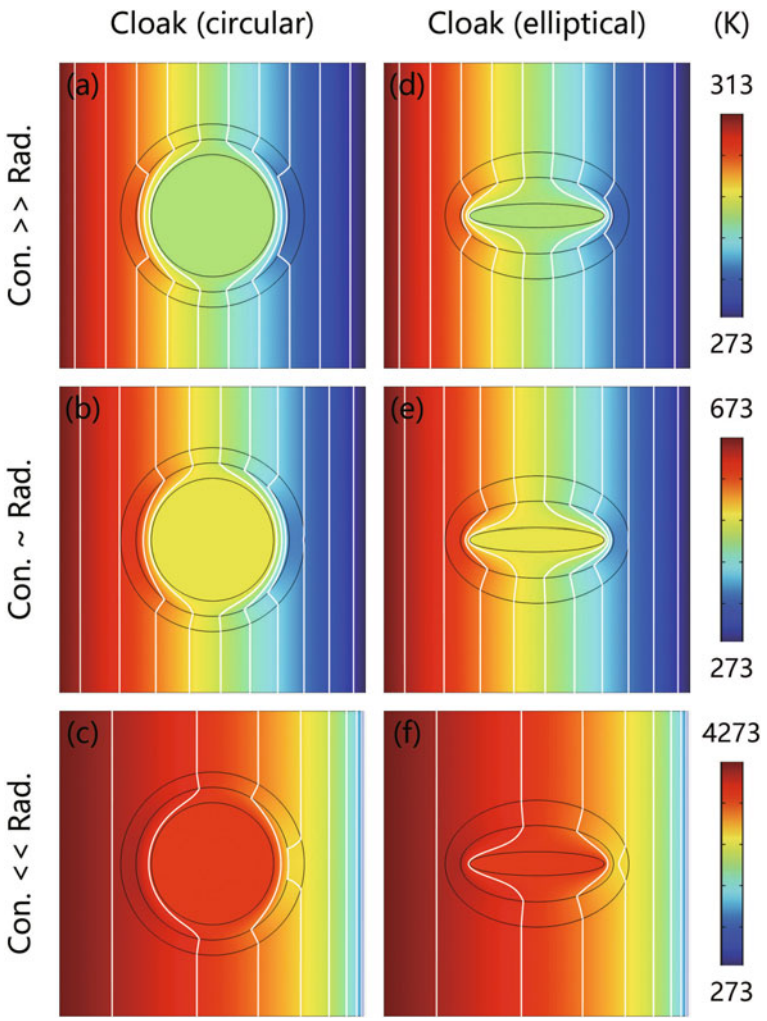

Fig. 11.3 Steady simulations of thermal cloak. An inner object is coated by an insulated layer with $\kappa = 10^{-5}$ W m^{-1}K^{-1} and $\beta = 10^5$ m^{-1}. Since the heat flux cannot enter into the insulated layer, the inner object plus the insulated layer can be equivalently regarded as an insulated core with $\kappa_c = 10^{-5}$ W m^{-1}K^{-1} and $\beta_c = 10^5$ m^{-1}. Other parameters are as follows. **a–c** $\lambda_{c1} = \lambda_{c2} = 2.5$ cm, $\lambda_{s1} = \lambda_{s2} = 3$ cm, $\kappa_s = 5.54$ Wm^{-1}K^{-1}, and $\beta_s = 18.1$ m^{-1}. d)-(f): $\lambda_{c1} = 2.5$ cm, $\lambda_{c2} = 1.25$ cm, $\lambda_{s1} = 3$ cm, $\lambda_{s2} = 2.08$ cm, $\kappa_s = 2.35$ W m^{-1}K^{-1}, and $\beta_s = 42.5$ m^{-1}. (from Ref. [39])

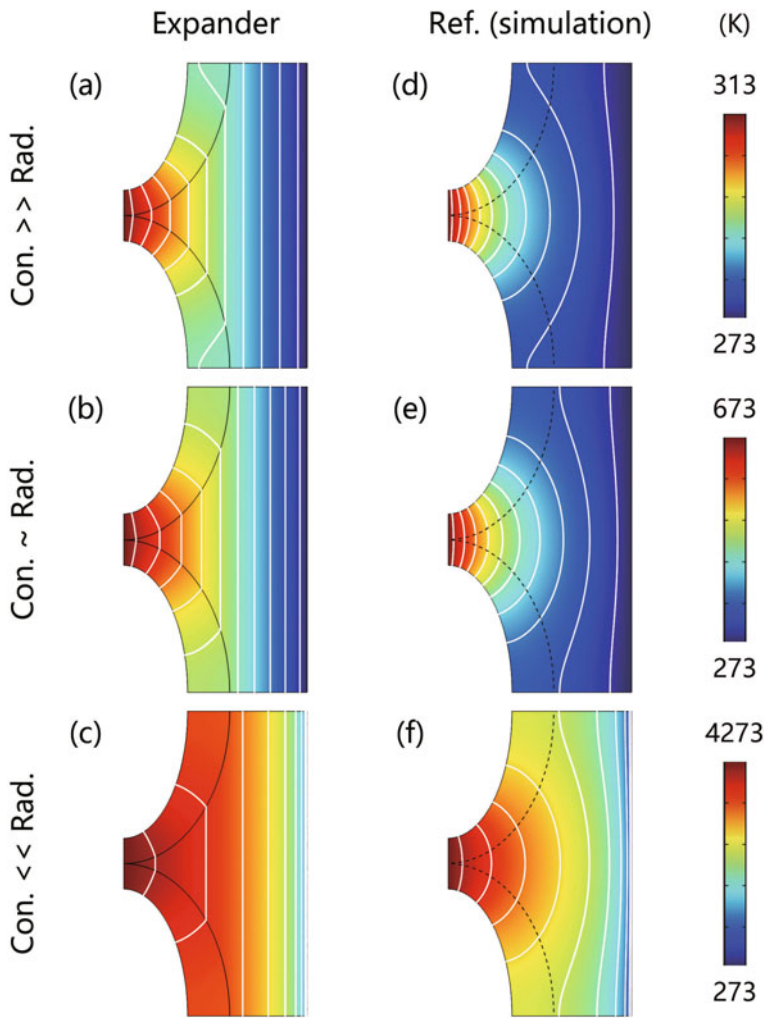

Fig. 11.4 Steady simulations of thermal expander. The sizes are $\lambda_{c1} = 2.08$ cm, $\lambda_{c2} = 4.17$ cm, $\lambda_{s1} = 3.46$ cm, $\lambda_{s2} = 5$ cm, and the width between hot and cold sources is 6 cm. Other parameters are as follows. **a–c** $\kappa_s = 4.91$ W m^{-1}K^{-1} and $\beta_s = 20.3$ m^{-1}. **d–f** pure background parameters. (from Ref. [39])

The thermal expander concept aims to magnify a small heat source into a larger one by utilizing the design of two elliptical cloaks. To demonstrate this effect, Xu et al. assembled two elliptical cloaks together and extracted a quarter of the entire structure as the expander, as depicted in Fig. 11.1c. According to the uniqueness theorem in thermotics, the temperature distribution of the background remains undistorted, thereby achieving the desired expander effect. Finite-element simulations were conducted and presented in Fig. 11.4a, c. Clearly, the isotherms of the background appear

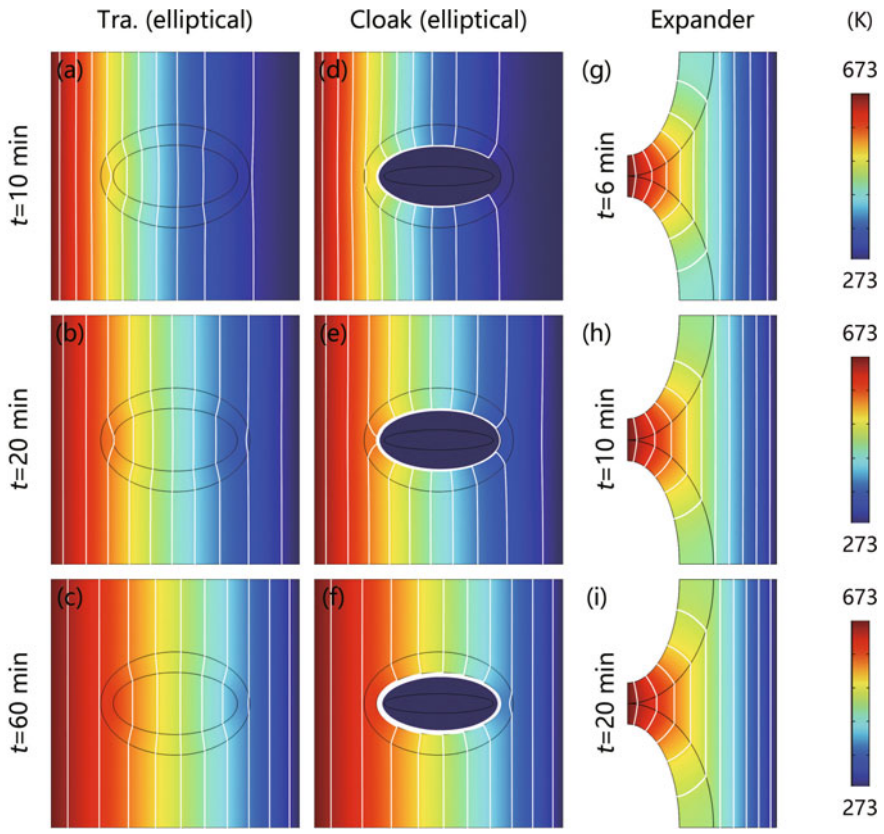

Fig. 11.5 Transient simulations of transparency, cloak, and expander. The sizes and material parameters of **a–c**, **d–f**, and **g–i** are the same as those for Fig. 11.2d–f, Fig. 11.3d–f, and Fig. 11.4a–c, respectively. The density and heat capacity of the background are $\rho C = 10^6$ J m^{-3}K^{-1}. Other parameters are as follows. **a–c** $(\rho C)_c = 5 \times 10^5$ J m^{-3}K^{-1} and $(\rho C)_s = 1.61 \times 10^6$ J m^{-3}K^{-1}. **d–f** $(\rho C)_s = 2.35 \times 10^6$ J m^{-3}K^{-1}. **g–i** $(\rho C)_s = 5 \times 10^5$ J m^{-3}K^{-1}. (from Ref. [39])

as straight lines, indicating the excellent performance of the proposed structure. For comparison, Xu et al. also provided simulation results for a pure background material. These results reveal that the isotherms of the background become distorted, as shown in Fig. 11.4d, f.

Xu et al. demonstrated that the theoretical analyses are applicable not only to steady states but also to transient cases. To illustrate this point, Xu et al. considered density and heat capacity. In order to design transient transparency and cloak, the value of heat diffusivity $\kappa/(\rho C)$ was set as a constant. Based on the simulation results, the performance of this approach remained satisfactory. The results at $t =$ 10, 20, 60 mins are depicted in Fig. 11.5a–c and 11.5d–f, respectively.

To showcase the effect of transient expansion and achieve the optimal transient effect, Xu et al. employed an optimization method and set the diffusivity of the shell to be larger than that of the background. The results at $t = 6,\ 10,\ 20$ mins are presented in Fig. 11.5g–i.

11.3 Potential Applications of Radiative Metamaterials: Thermal Camouflage and Radiative Cooler

The development of diffusion metamaterials for radiation control holds significant importance for our future lives, owing to its potential applications such as thermal camouflage [40, 41] and radiative cooling. Thermal camouflage refers to a device that not only prevents the detection of objects but also generates deceptive signals. Researchers have designed systems that can mislead the detection of cloaked objects. Additionally, encrypted thermal printing has been achieved, enabling object detection only when an appropriate heat source is applied. While the original structure for thermal camouflage is two-dimensional, there are also studies focusing on realizing the same functionality using three-dimensional structures.

Moreover, radiative cooling is another application field worth mentioning. Radiative cooling involves the automatic achievement of cooling effects without the need for an external source. The concept was first proposed in 1978, but at that time, it remained primarily theoretical. It was in 2014 that a practical radiative cooler was designed based on the photonic approach. The device operates by selectively reflecting electromagnetic waves in the mid-infrared range. Since then, researchers have developed more efficient methods to achieve the same functionality. Experimental results have also confirmed the effectiveness of these devices. We believe that in the future, radiative coolers could find widespread use in our daily lives, provided that the costs are reduced to a certain level.

11.4 Outlook: Radiative Metamaterials from Microscopic View

Over the past decades, research on diffusion metamaterials has undergone significant changes [42–46]. Initially, the focus was on single-function devices, but it has since shifted towards multi-functionality [47, 48]. Similarly, there has been a transition from linear to nonlinear response [49], from temperature-independent to temperature-dependent devices [50–52]. Furthermore, the research methodology has been applied to other fields as well, including plasma physics [53], mass diffusion [54, 55], and topology [56]. Novel concepts such as programmable metamaterials [57, 58], nonreciprocity metamaterials [59], intelligent metamaterials [60, 61], dipole-assisted thermotics [62], and negative thermal transport [63] have also been pro-

posed. In the future, the impact of diffusion metamaterials on the development of thermal diodes [64] is eagerly anticipated. Machine learning [65, 66] is also increasingly being incorporated into the research methodology. While significant progress has been made in the study of diffusion metamaterials for conduction and radiation, the research has primarily focused on macroscopic scales. Exploring the same effects at the microscopic scale is an intriguing topic [67]. To validate the Fourier law from a microscopic perspective, researchers have designed various models. The simplest among them is the harmonic lattice model [68, 69], which includes one-dimensional ordered cases [70], higher-dimensional ordered cases, one-dimensional disordered cases [71, 72], and two-dimensional disordered cases [73, 74]. Additionally, the harmonic lattices with self-consistent reservoirs have been studied [75]. More complex models involve interacting systems [76]. The research in this field can be divided into two parts: momentum-conserving models, such as the FPU model [77], and momentum-non-conserving models [78]. Some of these models provide essential insights into illustrating the Fourier law. Therefore, exploring the possibility of achieving novel functions such as cloaking and concentration in a similar manner is a worthwhile topic to explore. Furthermore, the experimental validation of microscopic theories poses a significant challenge. However, advancements in nanotechnology inspire us to move forward, and the combination of diffusion metamaterials with low-dimensional systems offers a new research field.

References

1. Xu, L.J., Huang, J.P.: Transformation Thermotics and Extended Theories: Inside and Outside Metamaterials. Springer, Singapore (2023)
2. Yang, S., Wang, J., Dai, G.L., Yang, F.B., Huang, J.P.: Controlling macroscopic heat transfer with thermal metamaterials: theory, experiment and application. Phys. Rep. **908**, 1–65 (2021)
3. Wang, J., Dai, G.L., Huang, J.P.: Thermal metamaterial: fundamental, application, and outlook. iScience. **23**, 101637 (2020)
4. Yang, F.B., Zhang, Z.R., Xu, L.J., Liu, Z.F., Jin, P., Zhuang, P.F., Lei, M., Liu, J.R., Jiang, J.-H., Ouyang, X.P., Marchesoni, F., Huang, J.P.: Controlling mass and energy diffusion with metamaterials. Rev. Mod. Phys. **96**, 015002 (2024)
5. Wang, C.M., Jin, P., Yang, F.B., Xu, L.J., Huang, J.P.: Click metamaterials: Fast acquisition of thermal conductivity and functionality diversities. Preprint at https://doi.org/10.48550/arXiv.2308.16057 (2023)
6. Jin, P., Liu, J.R., Yang, F.B., Marchesoni, F., Jiang, J.-H., Huang, J.P.: In-situ simulation of thermal reality. Research **6**, 0222 (2023)
7. Jin, P., Xu, L., Xu, G., Li, J., Qiu, C.-W., Huang, J.P.: Deep learning-assisted active metamaterials with heat-enhanced thermal transport. Adv. Mater. **36**, 2305791 (2024)
8. Dai, G.L., Yang, F.B., Xu, L.J., Huang, J.P.: Diffusive pseudo-conformal mapping: Anisotropy-free transformation thermal media with perfect interface matching. Chaos, Solitons & Fractals. **174**, 113849 (2023)
9. Xu, L.J., Liu, J,R., Xu, G.Q., Huang, J.P., Qiu, C.-W.: Giant, magnet-free, and room-temperature Hall-like heat transfer. Proc. Natl. Acad. Sci. U.S.A. **120**, e2305755120 (2023)
10. Zhang, Z.R., Xu, L.J., Qu, T., Lei, M., Lin, Z.K., Ouyang, X.P., Jiang, J.-H., Huang, J.P.: Diffusion metamaterials. Nat. Rev. Phys. **5**, 218–235 (2023)

11. Xu, L.J, Liu, J.R., Jin, P., Xu, G.Q., Li, J.X., Ouyang, X.P., Li, Y., Qiu, C.-W., Huang, J.P.: Black-hole-inspired thermal trapping with graded heat-conduction metadevices. Nat. Sci. Rev. **10**, nwac159 (2023)
12. Xu, L.J., Xu, G.Q., Huang, J.P., Qiu, C.-W.: Diffusive Fizeau Drag in Spatiotemporal Thermal Metamaterials. Phys. Rev. Lett. **128**, 145901 (2022)
13. Xu, L.J., Huang, J.P.: Active thermal wave cloak. Chin. Phys. Lett. **37**, 120501 (2020)
14. Yao, N.Z., Wang, H., Wang, B., Wang, X.S., Huang, J.P.: Convective thermal cloaks with homogeneous and isotropic parameters and drag-free characteristics for viscous potential flows. iScience. **25**, 105461 (2022)
15. Xu, L.J., Wang, J., Dai, G.L., Yang, S., Yang, F.B., Wang, G., Huang, J.P.: Geometric phase, effective conductivity enhancement, and invisibility cloak in thermal convection-conduction. Int. J. Heat Mass Transf. **165**, 120659 (2021)
16. Kapadia, R.S., Bandaru, P.R.: Heat flux concentration through polymeric thermal lenses. Appl. Phys. Lett. **105**, 233903 (2014)
17. Zhuang, P.F., Xu, L.J., Tan, P., Ouyang, X.P., Huang, J.P.: Breaking efficiency limit of thermal concentrators by conductivity couplings. Sci. China Phys. Mech. Astron. **65**, 117007 (2022)
18. Yang, F.B., Tian, B.Y., Xu, L.J., Huang, J.P.: Experimental demonstration of thermal chameleonlike rotators with transformation-invariant metamaterials. Phys. Rev. Appl. **14**, 054024 (2020)
19. Jin, P., Yang, S., Xu, L.J., Dai, G.L., Huang, J.P., Ouyang, X.P.: Particle swarm optimization for realizing bilayer thermal sensors with bulk isotropic materials. Int. J. Heat Mass Transf. **172**, 121177 (2021)
20. Wang, C.Q., Xu, L.J., Jiang, T., Zhang, L., Huang, J.P.: Multithermally invisible cloaks and sensors with complex shapes. Europhys. Lett. **133**, 20009 (2021)
21. Xu, L.J., Huang, J.P., Jiang, T., Zhang, L., Huang, J.P.: Thermally invisible sensors. Europhys. Lett. **132**, 14002 (2020)
22. Jin, P., Xu, L.J., Jiang, T., Zhang, L., Huang, J.P.: Making thermal sensors accurate and invisible with an anisotropic monolayer scheme. Int. J. Heat Mass Transf. **163**, 120437 (2020)
23. Yang, T.Z., Bai, X., Gao, D.L., Wu, L.Z., Li, B.W., Thong, J.T.L., Qiu, C.W.: Invisible sensors: Simultaneous sensing and camouflaging in multiphysical fields. Adv. Mater. **27**, 7752 (2015)
24. Wang, J., Yang, F.B., Xu, L.J., Huang, J.P.: Omnithermal restructurable metasurfaces for both infrared-light illusion and visible-light similarity. Phys. Rev. Appl. **14**, 014008 (2020)
25. Xu, L.J., Yang, S., Huang, J.P.: Thermal transparency induced by periodic interparticle interaction. Phys. Rev. Appl. **11**, 034056 (2019)
26. Liu, B., Xu, L.J., Huang, J.P.: Reinforcement learning approach to thermal transparency with particles in periodic lattices. J. Appl. Phys. **130**, 045103 (2021)
27. Huang, J.Y., Shen, X.Y., Jiang, C.R., Wu, Z.H., Huang, J.P.: Thermal expander. Phys. B **518**, 56–60 (2017)
28. Han, T.C., Yang, P., Li, Y., Lei, D.Y., Li, B.W., K. Hippalgaonkar, Qiu, C.W.: Full-parameter omnidirectional thermal metadevices of anisotropic geometry. Adv. Mater. **30**, 1804019 (2018)
29. Xu, L.J., Yang, S., Huang, J.P.: Thermal theory for heterogeneously architected structure: fundamentals and application. Phys. Rev. E **98**, 052128 (2018)
30. Xu, L.J., Yang, S., Dai, G.L., Huang, J.P.: Transformation omnithermotics: simultaneous manipulation of three basic modes of heat transfer. ES Energy & Environ. **7**, 65–70 (2020)
31. Yang, S., Xu, L.J., Wang, R.Z., Huang, J.P.: Full control of heat transfer in single-particle structural materials. Appl. Phys. Lett. **111**, 121908 (2017)
32. Vemuri, K.P., Bandaru, P.R.: Anomalous refraction of heat flux in thermal meta-materials. Appl. Phys. Lett. **104**, 083901 (2014)
33. Xu, L.J., Dai, G.L., Huang, J.P.: Transformation multithermotics: controlling radiation and conduction simultaneously. Phys. Rev. Appl. **13**, 024063 (2020)
34. Raman, A.P., Anoma, M.A., Zhu, L.X., Rephaeli, E., Fan, S.H.: Passive radiative cooling below ambient air temperature under direct sunlight. Nature **515**, 540 (2014)
35. Shen, X.Y., Jiang, C., Li, Y., Huang, J.P.: Thermal metamaterial for convergent transfer of conductive heat with high efficiency. Appl. Phys. Lett. **109**, 201906 (2016)

36. Dai, G.L., Huang, J.P.: A transient regime for transforming thermal convection: Cloaking, concentrating and rotating creeping flow and heat flux. J. Appl. Phys. **124**, 235103 (2018)
37. Li, Y., Peng, Y.G., Han, L., M.A. Miri, Li, W., Xiao, M., Zhu, X.F., Zhao, J.L., Alu, A., Fan, S.H., Qiu, C.W.: Antiparity-time symmetry in diffusive systems. Science **364**, 170 (2019)
38. Xu, L.J., Huang, J.P.: Robust one-way edge state in convection-diffusion systems. EPL **134**, 60001 (2021)
39. Xu, L.J., Huang, J.P.: Metamaterials for manipulating thermal radiation: transparency, cloak, and expander. Phys. Rev. Appl. **12**, 044048 (2019)
40. Han, T.C., Bai, X., Thong, J.T.L., Li, B.W., Qiu, C.W.: Full control and manipulation of heat signatures: cloaking, camouflage and thermal metamaterials. Adv. Mater. **26**, 1731 (2014)
41. Qu, Y.R., Li, Q., Cai, L., Pan, M.Y., P. Ghosh, K.K. Du, Qiu, M.: Thermal camouflage based on the phasechanging material GST. Light-Sci. Appl. **7**, 26 (2018)
42. Gao, Y., Jian, Y.C., Zhang, L.F., Huang, J.P.: Magnetophoresis of nonmagnetic particles in ferrofluids. J. Phys. Chem. C **111**, 10785–10791 (2007)
43. Dong, L., Huang, J.P., Yu, K.W., Gu, G.Q.: Dielectric response of graded spherical particles of anisotropic materials. J. Appl. Phys. **95**, 621–624 (2004)
44. Huang, J.P., M. Karttunen, Yu, K.W., Dong, L.: Dielectrophoresis of charged colloidal suspensions. Phys. Rev. E **67**, 021403 (2003)
45. Ye, C., Huang, J.P.: Non-classical oscillator model for persistent fluctuations in stock markets. Phys. A **387**, 1255–1263 (2008)
46. Liu, L., Wei, J., Zhang, H., Xin, J., Huang, J.P.: A statistical physics view of pitch fluctuations in the classical music from Bach to Chopin: evidence for scaling. PLoS ONE **8**, e58710 (2013)
47. Zhuang, P.F., Huang, J.P.: Multiple control of thermoelectric dual-function metamaterials. Int. J. Mech. Sys. Dyn. **3**, 127–135 (2023)
48. Shen, X.Y., Chen, Y.X., Huang, J.P.: Thermal magnifier and minifier. Commun. Theor. Phys. **65**, 375–380 (2016)
49. Zhuang, P.F., Wang, J., Yang, S., Huang, J.P.: Nonlinear thermal responses in geometrically anisotropic metamaterials. Phys. Rev. E **106**, 044203 (2022)
50. Li, Y., Shen, X.Y., Wu, Z.H., Huang, J.Y., Chen, Y.X., Ni, Y.S., Huang, J.P.: Temperature-dependent transformation thermotics: from switchable thermal cloaks to macroscopic thermal diodes. Phys. Rev. Lett. **115**, 195503 (2015)
51. Lei, M., Wang, J., Dai, G.L., Tan, P., Huang, J.P.: Temperature-dependent transformation multiphysics and ambient-adaptive multiphysical metamaterials. EPL **135**, 54003 (2021)
52. Li, Y., Shen, X.Y., Huang, J.P., Ni, Y.S.: Temperature-dependent transformation thermotics for unsteady states: switchable concentrator for transient heat flow. Phys. Lett. A **380**, 1641–1647 (2016)
53. Zhang, Z.R., Huang, J.P.: Transformation Plasma Physics. Chin. Phys. Lett. **39**, 075201 (2022)
54. Zhang, Z.R., Yang, F.B., Huang, J.P.: Intelligent chameleonlike metashells for mass diffusion. Phys. Rev. Appl. **19**, 024009 (2023)
55. Zhang, Z.R., Xu, L.J., Huang, J.P.: Controlling chemical waves by transforming transient mass transfer. Adv. Theory Simul. **5**, 2100375 (2022)
56. Jin, P., Liu, J.R., Xu, L.J., Wang, J., Ouyang, X.P., Jiang, J.-H., Huang, J.P.: Tunable liquid-solid hybrid thermal metamaterials with a topology transition. Proc. Natl. Acad. Sci. U.S.A. **120**, e2217068120 (2023)
57. Lei, M., Jiang, C.R., Yang, F.B., Wang, J., Huang, J.P.: Programmable all-thermal encoding with metamaterials. Int. J. Heat Mass Transf. **207**, 124033 (2023)
58. Zhou, Z.Y., Shen, X.Y., Fang, C.C., Huang, J.P.: Programmable thermal metamaterials based on optomechanical systems. ES Energy Environ. **6**, 85–91 (2019)
59. Xu, L.J., Huang, J.P., Ouyang, X.P.: Nonreciprocity and isolation induced by an angular momentum bias in convection-diffusion systems. Appl. Phys. Lett. **118**, 22190 (2021)
60. Xu, L.J., Huang, J.P.: Chameleonlike metashells in microfluidics: A passive approach to adaptive responses. Sci. China-Phys. Mech. Astron. **63**, 228711 (2020)
61. Yang, S., Xu, L.J., Huang, J.P.: Two exact schemes to realize thermal chameleonlike metashells. EPL **128**, 34002 (2019)

62. Xu, L.J., Yang, S., Huang, J.P.: Dipole-assisted thermotics: Experimental demonstration of dipole-driven thermal invisibility. Phys. Rev. E **100**, 062108 (2019)
63. Xu, L.J., Huang, J.P.: Negative thermal transport in conduction and advection. Chin. Phys. Lett. (Express Letter) **37**, 080502 (2020)
64. Li, B.W., Wang, L., G. Casati: Thermal Diode: Rectification of Heat Flux. Phys. Rev. Lett. **93**, 184301 (2004)
65. Zhang, C.X., Li, T.J., Jin, P., Yuan, Y., Ouyang, X.P., Marchesoni, F., Huang, J.P.: Extracting stellar emissivity via a machine learning analysis of MSX and LAMOST catalog data. Phys. Rev. D. **106**, 123035 (2022)
66. Liu, B., Xu, L.J., Huang, J.P.: Thermal transparency with periodic particle distribution: a machine learning approach. J. Appl. Phys. **129**, 065101 (2021)
67. Bao, H., Chen, J., Gu, X.K., Cao, B.Y.: A review of simulation methods in micro/nanoscale heat conduction. ES Energy Environ. **1**, 16 (2018)
68. Rieder, Z., Lebowitz, J.L., Lieb, E.: Properties of a harmonic crystal in a stationary nonequilibrium state. J. Math. Phys. **8**, 1073 (1967)
69. Nakazawa, H.: Prog. Theor. Phys. **39**, 236 (1968)
70. Roy, D., Dhar, A.: Heat transport in ordered harmonic lattices. J. Stat. Phys. **131**, 535 (2008)
71. Casher, A., Lebowitz, J.L.: Heat flow in regular and disordered harmonic chains. J. Math. Phys. **12**, 1701 (1971)
72. Payton, D.N., Rich, M., Visscher, W.M.: Lattice thermal conductivity in disordered harmonic and an harmonic crystal models. Phys. Rev. **160**, 706 (1967)
73. John, S., Sompolinsky, H., Stephen, M.J.: Localization in a disordered elastic medium near two dimensions. Phys. Rev. B **27**, 5592 (1983)
74. Yang, L.: Finite Heat Conduction in a 2D Disorder Lattice. Phys. Rev. Lett. **88**, 094301 (2002)
75. Bolsterli, M., Rich, M., Visscher, W.M.: Simulation of nonharmonic interactions in a crystal by self-consistent reservoirs. Phys. Rev. A **4**, 1086 (1970)
76. Giardina, C., Livi, R., Politi, A., Vassalli, M.: Finite thermal conductivity in 1D lattices. Phys. Rev. Lett. **84**, 2144 (2000)
77. E. Fermi, J. Pasta, S. Ulam: Studies of nonlinear problems, Los Alamos Document **LA**-1940 (1955)
78. Casati, G., Ford, J., Vivaldi, F., Visscher, W.M.: One-dimensional classical many-body system having a normal thermal conductivity. Phys. Rev. Lett. **52**, 1861 (1984)

Chapter 12
Diffusion Approximation and Metamaterial Design of Thermal Radiation

Yuguang Qiu, Liujun Xu, and Gaole Dai

12.1 Opening Remarks

As one of the three fundamental modes of heat transfer, radiative heat transfer maintains a pivotal position in the field of energy transport and consistently coexists with thermal conduction. Objects at temperatures above absolute zero inherently release thermal radiation, a principle expounded by the Stefan-Boltzmann law [1]. This phenomenon bears substantial importance within a multitude of disciplines.

However, the equations governing photon transport often exhibit significant nonlinearity and non-locality, imposing substantial computational demands even with the aid of abundant computing resources. In many cases, the diffusion approximation proves valuable in addressing computational challenges arising from various forms of thermal radiation [2]. While this approach reduces computational costs, it does entail some loss of precision. Among the diffusion approximations, the Rosseland approximation [1] is the most frequently employed, treating thermal radiation as photon diffusion and addressing the thermal coupling between radiation and conduction.

Concurrently, various radiation diffusion approximations, including Rosseland, are typically applicable only to situations involving far-field radiation [3]. In addition to far-field thermal radiation, extensive research has been conducted on near-field thermal radiation due to its enhanced near-field coupling effects [4], thus exhibiting different characteristics. These effects enable near-field radiation to overcome the

Y. Qiu (✉)
Department of Physics, Key Laboratory of Micro and Nano Photonic Structures (MOE), and State Key Laboratory of Surface Physics, Fudan University, Shanghai 200438, China
e-mail: 23110190059@m.fudan.edu.cn

L. Xu
Graduate School of China Academy of Engineering Physics, Beijing 100193, China

G. Dai
School of Sciences, Nantong University, Nantong 226019, China

F.-B. Yang and J.-P. Huang, *Diffusionics*,
https://doi.org/10.1007/978-981-97-0487-3_12

limitations imposed by the Stefan-Boltzmann law in the far-field regime, thereby influencing a multitude of thermal technologies.

On the other hand, as composite materials [5] with deliberately engineered structures, metamaterials [6, 7] have drawn significant attention due to their extraordinary physical properties that surpass those of natural materials [8–11]. A considerable amount of work has already been done in the fields of optics, electricity, fluid, acoustics, and other related areas. This has also propelled the development of numerous theories, with one of the key focal points being transformation theory [12]. This theory was initially proposed in the field of electromagnetics, connecting the physical space of material parameters with the virtual space of ideal modulation, enabling the flexible manipulation of physical field variations. Transformation theory, as a fundamental methodology, has expanded from electromagnetic and matter waves to water waves and even to diffusion systems encompassing thermal, plasma and electrical conduction as well as fluid dynamics [13], it may even extend to the social sciences [14, 15]. However, the conventional electromagnetic wave transformation theory is solely tailored for wave systems and cannot be directly applied to radiative heat transfer under the constraints of the Rosseland diffusion approximation. This necessitates researchers to innovate a novel transformation theory formulations to overcome this limitation.

In this chapter, we will commence by providing an overview of the integration of radiative heat transfer with thermal conduction under the framework of the Rosseland diffusion approximation, a method known as transformation multithermotics, making it amenable to transformation theory. Subsequently, we will briefly outline how this theory is harnessed for the design of thermal control devices related to radiative heat transfer, with a primary focus on thermal camouflage.Additionally, the design of metamaterials for thermal radiation beyond the scope of transformation theory is equally captivating. Considering the distinct natures of far-field and near-field radiative behaviors, we will separately elucidate recent research applications in radiative cooling and thermophotovoltaic devices within these two domains. Finally, we will conclude and offer insights into promising aspects of combining radiative heat transfer and thermal conduction.

12.2 Theory of Transformation Thermal Radiation under Rosseland Diffusion Approximation

12.2.1 Derivation of Rosseland Diffusion Approximation

To overcome the challenges of wave transformation theory's inapplicability to thermal radiation, Xu and colleagues integrated the Rosseland diffusion approximation of thermal radiation with the heat conduction equation, establishing a novel transformation theory known as transformation multithermotics [16].

The Rosseland approximation assumes that the mean free path of photons is significantly smaller than the material thickness, allowing the transport of radiative heat to be approximated as a diffusion process. Therefore, this approximation is applicable to optically thick media. In the following, we will outline the derivation of the Rosseland approximation [1].

First write the differential equation for the local light intensity I_ν:

$$\cos\theta \frac{dI_\nu}{dz} = \beta_\nu (S_\nu - I_\nu), \tag{12.1}$$

where S_ν is the source intensity, $\beta_\nu = (\rho\alpha_\nu)^{-1}$ is a coefficient measuring attenuation, ρ is mass density and α_ν is called Rosseland opacity. We assume that both S_ν and I_ν follow the Planck radiation formula:

$$I_\nu^{(0)} \approx S_\nu \approx B_\nu(T), \tag{12.2}$$

where $I_\nu^{(0)}$ is the zero-order solution of local intensity and it's easy to check that $B_\nu(\nu, T)$ satisfies

$$\int_0^\infty B_\nu(\nu, T)d\nu = \boldsymbol{n}^2 \frac{\sigma}{\pi} T^4. \tag{12.3}$$

Here σ is the Stefan-Boltzmann constant and $\boldsymbol{n}$ is the relative refraction index. Let $I_\nu \approx I_\nu^{(0)} + I_\nu^{(1)}$ and by combining Eqs. 12.1 and 12.2, we can obtain

$$\begin{aligned} I_\nu^{(1)} &= B_\nu(T) - \cos\theta \beta_\nu^{-1} \frac{\partial B_\nu(T)}{\partial z} \\ &= B_\nu(T) - \cos\theta \beta_\nu^{-1} \frac{\partial B_\nu(T)}{\partial T} \frac{\partial T}{\partial z}. \end{aligned} \tag{12.4}$$

Then we can calculate the radiative heat flux (density) $\boldsymbol{J}_{rad}$:

$$\begin{aligned} \boldsymbol{J}_{rad} &= \int_0^\infty d\nu \int_{\Omega_0} d\Omega I_\nu(T) \cos\theta \\ &= \int_0^\infty d\nu \int_{\Omega_0} d\Omega \cos\theta [2B_\nu(T) - \cos\theta \beta_\nu^{-1} \frac{\partial B_\nu(T)}{\partial T} \frac{\partial T}{\partial z}] d\Omega \\ &= \int_0^\infty d\nu \int_{\Omega_0} d\Omega \cos^2\theta [-\beta_\nu^{-1} \frac{\partial B_\nu(T)}{\partial T} \frac{\partial T}{\partial z}] \sin\theta d\theta d\psi \\ &= -2\pi \int_0^\infty d\nu \beta_\nu^{-1} \frac{\partial B_\nu(T)}{\partial T} \frac{\partial T}{\partial z} \int_{-1}^1 \mu^2 d\mu \\ &= -\frac{4\pi}{3} \frac{\partial T}{\partial z} \int_0^\infty \frac{\partial B_\nu(T)}{\partial T} \frac{1}{\beta_\nu} d\nu, \end{aligned} \tag{12.5}$$

where Ω_0 is the unit hemispherical surface. The $B_\nu(T)$ is isotropic and make a variable replacement $\mu = \cos\theta$. We use β to represent the average absorption coefficient:

$$\beta^{-1}\int_0^{\infty}\frac{\partial B_\nu(T)}{\partial T}d\nu=\int_0^{\infty}\frac{\partial B_\nu(T)}{\partial T}\frac{1}{\beta_\nu}d\nu, \tag{12.6}$$

then

$$\beta^{-1}=\frac{\pi\int_0^{\infty}\frac{\partial B_\nu(T)}{\partial T}\frac{1}{\beta_\nu}d\nu}{4\boldsymbol{n}^2\sigma T^3}. \tag{12.7}$$

Finally, the radiative flux $\boldsymbol{J}_{rad}$ according to the Rosseland diffusion approximation is

$$\begin{aligned}\boldsymbol{J}_{rad}&=-\frac{16}{3}\beta^{-1}\boldsymbol{n}^2\sigma T^3\cdot\nabla T\\&=\boldsymbol{\tau}T^3\cdot\nabla T,\end{aligned} \tag{12.8}$$

where denote $\boldsymbol{\tau}=-16/3\beta^{-1}\boldsymbol{n}^2\sigma$. Hence, the thermal radiation equation can be rephrased as a diffusion equation, wherein the thermal conductivity varies according to T^3. Consequently, we have the opportunity to utilize the principles of thermal conduction modulation for the purpose of regulating heat radiation. The subsequent discourse on the transformation theory provides an exemplary illustration of this concept.

12.2.2 Transformation Theory of Thermal Radiation

Next, we commence by showcasing the preservation of the fundamental equation in multithermotics as it transitions from a curvilinear space X to a physical space X'. This process will lead us to unveil the principles governing the transformation of multithermotics.

Assuming heat transfer is a passive process, the constitutive equation followed by multithermotics is as follows

$$\rho C\frac{\partial T}{\partial t}+\nabla\cdot(\boldsymbol{J}_{rad}+\boldsymbol{J}_{con})=0, \tag{12.9}$$

where ρ and C are the density and heat capacity of participating media, respectively. The conductive flux is determined by the Fourier law $\boldsymbol{J}_{con}=-\kappa\cdot\nabla T$, where κ is thermal conductivity.

Express the dominant equation in its component form. In curvilinear space with a contravariant basis $[\boldsymbol{g}^u,\boldsymbol{g}^v,\boldsymbol{g}^w]$, a covariant basis $[\boldsymbol{g}_u,\boldsymbol{g}_v,\boldsymbol{g}_w]$, and corresponding contravariant components $[\boldsymbol{x}^u,\boldsymbol{x}^v,\boldsymbol{x}^w]$, the radiative term can be rewritten as

$$\begin{aligned}\nabla \cdot [\boldsymbol{\tau} T^3 \cdot \nabla T)] &= \boldsymbol{g}^w \cdot \frac{\partial}{\partial x^w}[\tau^{uv} T^3 \boldsymbol{g}_u \otimes \boldsymbol{g}_v \cdot \boldsymbol{g}^l \frac{\partial T}{\partial x^l}] \\ &= \boldsymbol{g}^w \cdot \frac{\partial}{\partial x^w}[\tau^{uv} T^3 \boldsymbol{g}_u \boldsymbol{g}_u \frac{\partial T}{\partial x^v}] \\ &= \frac{\partial \tau^{vT^3}}{\partial x^u}\frac{\partial T}{\partial x^v} + \frac{\partial^2 T}{\partial x^u \partial x^v} T^3 + \boldsymbol{g}^w \cdot \frac{\partial \boldsymbol{g}_u}{\partial x^w}[\tau^{uv} T^3 \frac{\partial T}{\partial x^v}] \\ &= \partial_u[\tau^{uv} T^3 \partial_v T] + \Gamma^w_{wu} \tau^{uv} T^3 \partial_v T \\ &= \partial_u[\tau^{uv} T^3 \partial_v T] + \frac{1}{\sqrt{\boldsymbol{g}}}(\partial_u \sqrt{\boldsymbol{g}}) \tau^{uv} T^3 \partial_v T \\ &= \frac{1}{\sqrt{\boldsymbol{g}}} \partial_u [\sqrt{\boldsymbol{g}} \tau^{uv} T^3 \partial_v T],\end{aligned} \tag{12.10}$$

where $\boldsymbol{g} = \det^{-2}\mathrm{A}$ is the determinant of the matrix with components $\boldsymbol{g}_{ij} = \boldsymbol{g}_u \cdot \boldsymbol{g}_v$, A is the Jacobian transformation matrix and $\Gamma^w_{uv} = \partial \boldsymbol{g}_u / \partial x^v \cdot \boldsymbol{g}^w$ is the Christoffel symbol resulting in $\Gamma^w_{wu} = (\partial_u \sqrt{\boldsymbol{g}})/\sqrt{\boldsymbol{g}}$. Similarly, we can rewrite the conductive term as

$$\nabla \cdot [\boldsymbol{\kappa} \cdot \nabla T] = \frac{1}{\sqrt{\boldsymbol{g}}} \partial_u [\sqrt{\boldsymbol{g}} \kappa^{uv} \partial_v T] \tag{12.11}$$

Combining the two aforementioned expressions, the dominant equation can be reformulated as follows

$$\sqrt{\boldsymbol{g}} \rho C \partial_t T - \partial_u [\sqrt{\boldsymbol{g}} (\tau^{uv} T^3 + \kappa^{uv}) \partial_v T] = 0 \tag{12.12}$$

which is expressed in the curvilinear space. Then, rephrase it within the physical space to obtain the transformation rules for material properties,

$$\sqrt{\boldsymbol{g}} \rho C \partial_t T - \partial_{u'} \frac{\partial x^{u'}}{\partial x^u} [\sqrt{\boldsymbol{g}} (\tau^{uv} T^3 + \kappa^{uv}) \frac{\partial x^{v'}}{\partial x^v} \partial_v T] = 0, \tag{12.13}$$

where $\partial x^{u'/\partial x^u}$ and $\partial x^{v'/\partial x^v}$ are the components of the Jacobian transformation matrix A.

Finally, we substitute space transformation with material transformation,

$$\frac{\rho C}{\det \mathrm{A}} \partial_t T - \partial_{u'} [(\frac{A^{u'}_u \tau^{uv} A^{v'}_v}{\det \mathrm{A}} T^3 + \frac{A^{u'}_u \kappa^{uv} A^{v'}_v}{\det \mathrm{A}}) \partial_{v'} T] = 0. \tag{12.14}$$

We can notice that this equation maintains the initial structure of the diffusion equation, provided that the parameters adhere to the transformation rules outlined below:

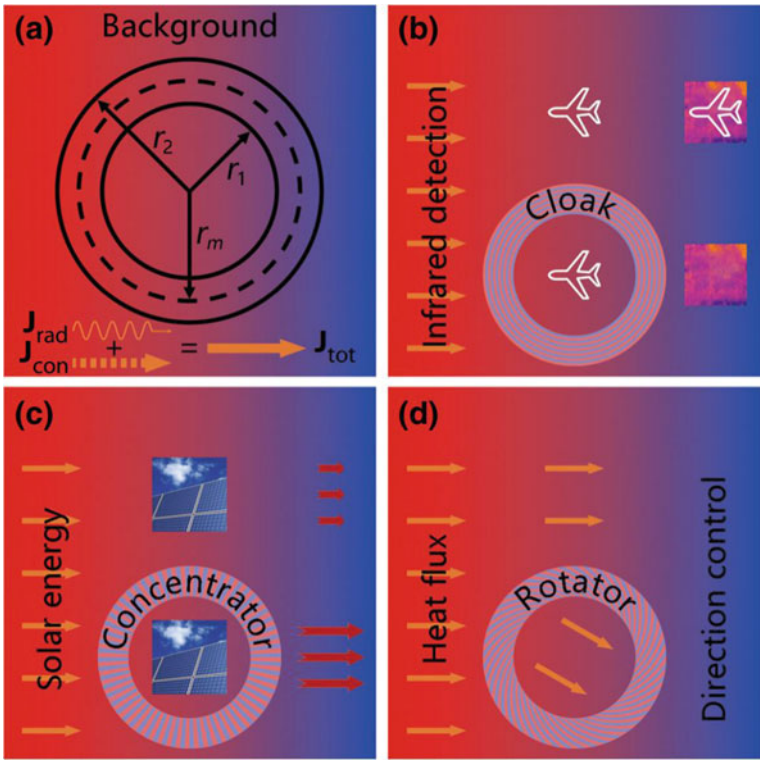

Fig. 12.1 Figure **a** illustrates different thermal flux representations through the use of unique arrow styles: the wavy, dashed, and solid arrows signify radiative flux, conductive flux, and total flux, respectively, in the domain of multithermotics. In Fig. **b**, the notion of cloaking is demonstrated, providing protection for internal objects, such as aircraft, against infrared detection. Figure **c** showcases a concentrator, highlighting its capacity to greatly improve energy utilization efficiency. Finally, Fig. **d** presents rotators, which enable controlled directional alterations in local heat flux. (from Ref. [16])

$$
\begin{aligned}
(\rho C)' &= \frac{\rho_0 C_0}{\det \mathrm{A}}, \\
\boldsymbol{\tau}' &= \frac{\mathrm{A}\boldsymbol{\tau}_0\mathrm{A}^{\mathrm{T}}}{\det \mathrm{A}}, \\
\boldsymbol{\kappa}' &= \frac{\mathrm{A}\boldsymbol{\kappa}_0\mathrm{A}^{\mathrm{T}}}{\det \mathrm{A}},
\end{aligned}
\tag{12.15}
$$

where ρ_0, C_0, τ_0, and κ_0 are the density, heat capacity, radiative coefficient, and thermal conductivity of the background respectively.

Now we have the capacity to engineer thermal metamaterials [17, 18] for use in radiative and conductive environments [19]. Figure 12.1 depicts the conceptual designs of the cloak, concentrator, and rotator, respectively. Since the concept of

transformation multithermotics is not limited by spatial dimensions, we opt for a two-dimensional system when creating these components.

Use the coordinate transformations for cloaks [20, 21]

$$\begin{cases} r' = (r_2 - r_1)r/r_2 + r_1 \\ \theta' = \theta \end{cases} \tag{12.16}$$

concentrators

$$\begin{cases} r' = r_1 r/r_m, r < r_m \\ r' = [(r_2 - r_1)r + (r_1 - r_m)r_2]/(r_2 - r_m), r_m < r < r_2 \\ \theta' = \theta \end{cases} \tag{12.17}$$

and rotators

$$\begin{cases} r' = r \\ \theta' = \theta + \theta_0, r < r_1 \\ \theta' = \theta + \theta_0(r - r_2)/(r_1 - r_2), r_1 < r < r_2 \end{cases} \tag{12.18}$$

The Jacobian transformation matrix can be calculated by

$$\mathrm{A} = \begin{pmatrix} \partial r'/\partial r & \partial r'/(r\partial\theta) \\ r'\partial\theta'/\partial r & r'\partial/(r\partial\theta) \end{pmatrix}. \tag{12.19}$$

In a broader context, thermal radiation, thermal conduction, and thermal convection may coexist simultaneously. By introducing terms representing convective flux into the equations, a method has been developed to manipulate all three fundamental heat transfer modes through the transformation of total heat [22]. It's worth noting that the parameters acquired through transformation multithermotics exhibit anisotropic characteristics, a feature rarely observed in natural materials. These material properties can be realized through the design of layered structures [23] and effective medium theories [24]. Additionally, achieving a similar effect is possible through the theories of scattering cancellation [24] and conformal mapping [25].

12.2.3 Thermal Camouflage with Transformation Theory

Thermal camouflage, often referred to as thermal illusion [26] serves the purpose of concealing the genuine thermal signal while projecting an altered signal to external detectors, resulting in deceptive effects. For instance, by modifying the thermal properties of an object, it can be camouflaged as an entirely different object during detection [27]. In another study, regionalization transformation techniques were employed to craft thermal illusions, successfully achieving encrypted thermal printing that reveals concealed information exclusively when exposed to the correct heat

source [28]. This concept was further extended into the realm of three dimensions to overcome limitations inherent in two-dimensional approaches [29].

The control over thermal radiation patterns can also be attained through the regulation of thermal conduction, enabling the concurrent management of both thermal radiation and conduction, as indicated by Dede et al. [30]. Li and his team introduced an inventive method to achieve conductive transformation thermotics specifically for radiative applications [31]. Their investigation delved into existing camouflage techniques, emphasizing the direct options of adjusting surface temperatures or emissivities for customizing typical infrared imaging. However, engineering emissivity methods rely on the background, which could limit their practicality. In this particular case, the camouflage surface was devised through a dual transformation approach, revealing a discreet concealed area on the device's surface, thus allowing objects to remain hidden from thermal radiation detection. By structuring layers of copper and polydimethylsiloxane in accordance with transformation theory, they successfully experimentally verified the anisotropic thermal conductivity. This advancement facilitated the integration of conductive transformations within radiative fields, expanding the scope of transformation applications. Notably, the concept of thermal camouflage surfaces was subsequently applied to three-dimensional scenarios [32]. In another strand of research, the application of regionalization transformation theory was explored for constructing thermal metamaterial structures that function as distinct infrared signatures [28]. By manipulating the thermal conductivity within distinct rectangular areas, one could harness heat from specific locations to create the thermal representation of a basic stroke. These individual strokes were then combined to construct the complete alphabet. This method allowed for the thermal encoding of information, exclusively visible in infrared imagery.

Expanding beyond individual physical domains, approaches for multifaceted physical camouflage have been investigated. An innovative multispectral camouflage apparatus, designed to cover the infrared, visible light, laser, and microwave spectra, has been put forth [33]. It is foreseeable that the convergence of diverse disciplines and the thinning of device profiles will likely emerge as predominant trends in the field of thermal camouflage.

12.3 Metamaterial Design of Far-Field and Near-Field Thermal Radiation Beyond Transformation Theory

The Rosseland diffusion approximation represents one variation of radiation diffusion approximations, primarily applicable to optically thick media. Frank Graziani presented an exposition on the fundamental principles of radiation transport, elucidating the genesis of the diffusion approximation and its accompanying transport corrections. He provided an overview of three radiation diffusion approximations and various numerical simulation techniques [2]. These diffusion approximation techniques are often linked with far-field phenomena. In addition to the aforementioned

concepts, progress in manipulating far-field thermal radiation has resulted in significant applications like daytime radiative cooling and thermophotovoltaic systems. On the other hand, as systems shrink to micro and nanoscale dimensions, the influence of evanescent waves becomes more pronounced. Near-field radiation can transcend the constraints of the Stefan-Boltzmann law in the far-field, thus significantly impacting various thermal technologies. In the forthcoming sections, we will present a concise overview of notable designs pertaining to radiative cooling and thermophotovoltaic devices, encompassing both far-field and near-field thermal radiation domains.

12.3.1 Far-Field Thermal Radiation

12.3.1.1 Radiative Cooling

Daytime radiative cooling, a passive process that demands no supplementary energy input, represents a promising frontier in renewable energy research. In the prevailing environmental temperatures of the universe, blackbody radiation extensively aligns with the Earth's atmospheric transparency window, wavelength range is 8–13 μm. This characteristic permits a substantial portion of objects on Earth to emit thermal energy into space, thereby achieving radiative cooling.

The utilization of titanium dioxide to create white paint for enhancing radiative cooling was first introduced as far back as 1978 [34]. However, this concept didn't receive significant attention at the time. It wasn't until 2014 that a photonic approach for developing radiative coolers was proposed, and it was subsequently experimentally realized [35]. This approach revolves around the design of a device that selectively reflects solar radiation while emitting thermal radiation in the mid-infrared spectrum. This unique property was achieved through a multilayer structure consisting of HfO_2 and SiO_2. Since then, substantial advancements have been made toward the widespread adoption of this technology [36]. Radiative cooling leverages the chill of the cosmos, carrying profound implications for the realm of energy technology and establishing a pioneering frontier in renewable energy research [37].

12.3.1.2 Thermophotovoltaic Systems

In the realm of solar energy harvesting, single-junction solar cells confront an efficiency limitation recognized as the Shockley-Queisser limit, which is capped at 41% [38]. The root cause of this reduced conversion efficiency lies in the broad spectrum of solar radiation, primarily spanning from 200 nm to 2500 nm. Photons with energy levels lower than the solar cell's bandgap cannot be absorbed, while photons with energy levels surpassing the bandgap lead to the descent of high-energy electrons to the band's edge, resulting in additional energy loss in the form of heat. Solar thermophotovoltaic (STPV) systems represent a pivotal approach for transcending the Shockley-Queisser limit. The concept of utilizing STPV technology to capture

thermal radiation energy was initially introduced in 1979 [39]. STPV operates as a solar-driven heat engine, extracting electrical energy from thermal radiation. The overarching objective is to absorb and convert the wide-ranging solar radiation spectrum into a narrower thermal emission spectrum, specifically tailored to match the spectral response of the photovoltaic (PV) cell [40].

Within the domain of STPV systems, an intermediate element absorbs incoming sunlight, undergoes heating, and subsequently emits thermal radiation, aligned with the bandgap of the solar cell, thus surpassing the theoretical limit. Although the theoretical efficiency ceiling can theoretically extend to as high as 85.4%, practical experimental results have encountered impediments owing to a range of optical and thermal losses. There is optimism for enhancing STPV efficiency through various approaches, including material selection, structural design, and elevating the operating temperatures of emitters and absorbers [42]. In STPV, the power source for PV cells encompasses not only thermal radiation but also various other forms of solar emissions. Furthermore, a notable advantage of STPV lies in its ability to function continuously, incorporating alternative heat sources or thermal storage [42].

Thermophotovoltaic (TPV) systems are closely related to STPV systems, harnessing thermal radiation from localized heat sources to generate electricity in photovoltaic cells [40]. In TPV systems, a key approach is to harness photovoltaic cells with minimal bandgap absorption and high-quality back reflectors for light recovery below the bandgap [40].

12.3.2 Near-Field Thermal Radiation

12.3.2.1 Radiative Cooling

Besides macroscopic radiative cooling, microscopic near-field scenarios, as discussed in [43], also enable the control of heat through radiative cooling.

Guha et al. showcased effective cooling through near-field radiative heat transfer in an innovative setup, as reported in [44]. This setup featured the direct integration of temperature sensors into thermally isolated hotspots. Bringing an oxidized probe in proximity to a SiO_2 membrane, measuring $100 \times 50\ \mu m^2$ and acting as a localized hotspot, resulted in a substantial near-field radiative heat flux that led to cooling by several tens of degrees. This cooling mechanism was accomplished without any physical contact, circumventing conductive heat transfer and introducing an innovative cooling capability. The observed trends in radiative cooling corresponded with theoretical predictions, primarily influenced by the geometry of the utilized probe and the minimum achievable separation within the experimental setup.

In another study by Zhou et al., the technique of nanoparticle doping was introduced into the near-field radiative negative luminescence cooling domain. By capitalizing on its light-modulating capability, cooling between the host material and the semiconductor was effectively realized [45].

Furthermore,Liu and colleagues introduced an intelligent radiative thermostatic system, driven by near-field radiative thermal diodes. This system integrates passive radiative cooling at the top layer and internal heat modulation. Remarkably, it has the capability to autonomously monitor its own temperature and regulate it to remain close to the desired set point, as discussed in [46].

12.3.2.2 Thermophotovoltaic Systems

Thermal objects emit electromagnetic radiation, and their far-field spectral features are delineated by Planck's thermal radiation theory. However, this emission is subject to limitations imposed by the blackbody effect, which arises because the gap between the emitter and the PV cell is significantly larger than the characteristic wavelength. When this radiation reaches a PV cell, it stimulates the generation of electron-hole pairs, which are separated by the built-in electric field of the PV cell, thus yielding an electric current, as described in [47].

The analysis of far-field thermophotovoltaic systems relies on classical thermal radiation theory for modeling the thermal properties of the emitter. The PV cell, on the other hand, is typically modeled using traditional PV cell device models. In contrast, near-field thermophotovoltaic systems integrate fluctuational electrodynamics (FED) with conventional PV cell device models. This approach involves coupling Maxwell's equations with stochastic current sources, in accordance with the fluctuation-dissipation theorem [48]. The radiative energy transfer is then computed by assessing the time-averaged Poynting flux. As depicted in Fig. 2 in [47], multiple electromagnetic modes are thermally excited within the thermal body, extending to the emitter-vacuum interface. Only modes with incident angles below the critical angle can propagate through the vacuum and reach the PV cell. These modes, sustained in the vacuum, are termed propagating waves and contribute to far-field radiative energy transfer. Modes with incident angles exceeding the critical angle experience total internal reflection (frustrated modes) and cannot traverse the vacuum gap. This phenomenon is responsible for the limiting constraint observed in blackbody radiative processes.

To significantly improve the power conversion efficiency of thermophotovoltaic devices, Whale and colleagues introduced the innovative concept of utilizing evanescent waves to enhance radiative power, as discussed in [49]. When the separation between objects is comparable to or much smaller than the dominant wavelength, employing surface plasmon resonances or surface phonon resonances can substantially boost the efficiency of near-field tunneling and expand the spatial spectrum range of evanescent wave thermal photons. This approach enables radiative energy transmission power that exceeds the Planck limit by a considerable margin. In the near-field regime, power densities up to ten times higher than those of standard devices can be achieved. In 2011, Francoeur and colleagues further investigated the influence of PV cell heating on the performance of near-field photovoltaic systems, as documented in [50]. Given the broadband nature of near-field enhancement, heat transfer to the PV cell is also intensified, potentially leading to challenges in thermal

management [47]. It is foreseeable that subsequent research endeavors have been dedicated to enhancing thermoelectric conversion possibilities in near-field thermophotovoltaic systems, with a focus on factors like emitter materials and spectral matching.

12.4 Conclusion and Outlook

Thermal radiation, a fundamental mode of heat transfer, coexists with thermal conduction in objects. The Stefan-Boltzmann law dictates that any object at a non-zero temperature emits thermal radiation, a phenomenon of paramount importance in various fields. This chapter commences by introducing the concept of transformation multithermotics theory, demonstrating how the Rosseland approximation is integrated within this framework to simultaneously account for both thermal conduction and radiation. Subsequently, we provide a concise overview of the design of thermal control devices related to thermal radiation using transformation theory, with a particular focus on the field of thermal camouflage. Additionally, we highlight the potential of utilizing thermal radiation in the designs of metamaterial devices that extend beyond the scope of transformation theory. Given the distinct behavior of radiation in far-field and near-field scenarios, we offer brief overviews of applications in both contexts, encompassing radiative cooling and thermophotovoltaics.

Beyond the applications mentioned above, thermal radiation plays a crucial role in various fields, including infrared thermal sensing [51], thermal diodes [52], thermal rectification [53], biosensors, and chemical sensors [54]. The interplay of thermal radiation and conduction [55] has led to innovative approaches in thermal control. Strategies like spatiotemporal modulation have significantly impacted the fields of thermal conduction and convection [56]. Emerging phenomena, including topological effects [57], thermal hall effects [58], and nonreciprocity [59], are also becoming pivotal in thermal control strategies, and the role of thermal radiation in these domains is poised for future exploration.

While thermal conduction follows diffusion equations, which are inherently distinct from electromagnetic wave radiation governed by wave equations, the study of non-Fourier heat conduction [60] highlights that thermal conduction also exhibits wave-like properties, particularly in micro- and nanoscale systems. On the other hand, considering that thermal radiation, under the diffusion approximation, is equivalent to diffusion heat transfer with nonlinear thermal conductivity, this equivalence provides a valuable tool for investigating nonlinear thermal phenomena [61]. Mathematically, the analogy between the electric field intensity in nonlinear optics and temperature gradient in nonlinear thermal physics is evident. However, in nonlinear thermal physics, thermal conductivity depends on temperature rather than temperature gradient. This analogy suggests the potential for uncovering surprising new physics.

References

1. Howell, J.R., Menguc, M.P., Siegel, R.: Thermal Radiation Heat Transfer, 5th edn. CRC Press, Boca Raton, London, New York (2010)
2. Graziani, F.: Radiation diffusion: An overview of physical and numerical concepts. In: Open Issues in Core Collapse Supernova Theory, pp. 29-66 (2005)
3. Li, J., Yu, B., Shen, S.: Scale law of far-field thermal radiation from plasmonic metasurfaces. Phys. Rev. Lett. **124**, 137401 (2020)
4. Basu, S., Zhang, Z.M., Fu, C.J.: Review of near-field thermal radiation and its application to energy conversion. Int. J. Energy Res. **33**, 1203–1232 (2009)
5. Clyne, T.W., Hull, D.:An Introduction to Composite Materials. Cambridge University Press (2019)
6. Wang, J., Dai, G.L., Huang, J.P.: Thermal metamaterial: Fundamental, application, and outlook. iScience **23**, 101637 (2020)
7. Xu, L.J., Yang, S., Huang, J.P.: Thermal theory for heterogeneously architected structure: Fundamentals and application. Phys. Rev. E **98**, 052128 (2018)
8. Yang, S., Xu, L.J., Wang, R.Z., Huang, J.P.: Full control of heat transfer in single-particle structural materials. Appl. Phys. Lett. **111**, 121908 (2017)
9. Gao, Y., Jian, Y.C., Zhang, L.F., Huang, J.P.: Magnetophoresis of nonmagnetic particles in ferrofluids. J. Phys. Chem. C **111**, 10785 (2007)
10. Dong, L., Huang, J.P., Yu, K.W., Gu, G.Q.: Dielectric response of graded spherical particles of anisotropic materials. J. Appl. Phys. **95**, 621–624 (2004)
11. Huang, J.P., Karttunen, M., Yu, K.W., Dong, L.: Dielectrophoresis of charged colloidal suspensions. Phys. Rev. E **67**, 021403 (2003)
12. Xu, L.J., Huang, J.P.: Transformation Thermotics and Extended Theories: Inside and Outside Metamaterials. Springer, Singapore (2023)
13. Dai, G.L., Huang, J.P.: A transient regime for transforming thermal convection: Cloaking, concentrating and rotating creeping flow and heat flux. J. Appl. Phys. **124**, 235103 (2018)
14. Ye, C., Huang, J.P.: Non-classical oscillator model for persistent fluctuations in stock markets. Phys. A **387**, 1255 (2008)
15. Liu, L., Wei, J.R., Zhang, H.S., Xin, J.H., Huang, J.P.: A statistical physics view of pitch fluctuations in the classical music from Bach to Chopin: Evidence for Scaling. PLoS ONE **8**, e58710 (2013)
16. Xu, L.J., Dai, G.L., Huang, J.P.: Transformation multithermotics: Controlling radiation and conduction simultaneously. Phys. Rev. Appl. **13**, 024063 (2020)
17. Shen, X.Y., Jiang, C.R., Li, Y., Huang, J.P.: Thermal metamaterial for convergent transfer of conductive heat with high efficiency. Appl. Phys. Lett. **109**, 201906 (2016)
18. Jin, P., Xu, L.J., Jiang, T., Zhang, L., Huang, J.P.: Making thermal sensors accurate and invisible with an anisotropic monolayer scheme. Int. J. Heat Mass Transf. **163**, 120437 (2020)
19. Xu, L.J., Yang, S., Huang, J.P.: Thermal transparency induced by periodic interparticle interaction. Phys. Rev. Appl. **11**, 034056 (2019)
20. Xu, L.J., Wang, J., Dai, G.L., Yang, S., Yang, F.B., Wang, G., Huang, J.P.: Geometric phase, effective conductivity enhancement, and invisibility cloak in thermal convection-conduction. Int. J. Heat Mass Transf. **165**, 120659 (2021)
21. Xu, L.J., Huang, J.P.: Active thermal wave cloak. Chin. Phys. Lett. **37**, 120501 (2020)
22. Xu, L.J., Yang, S., Dai, G.L., Huang, J.P.: Transformation omnithermotics: Simultaneous manipulation of three basic modes of heat transfer. ES Energy Environ. **7**, 65–70 (2020)
23. Liu, D.K., Li, C., Yao, J., Zhou, L.W., Huang, J.P.: Relation of lamellar structure and shear stress of dynamic PM-ER fluids. Int. J. Mod. Phys. B **25**, 971–977 (2011)
24. Xu, L.J., Huang, J.P.: Metamaterials for manipulating thermal radiation: Transparency, cloak, and expander. Phys. Rev. Appl. **12**, 044048 (2019)
25. Dai, G.L., Yang, F.B., Xu, L.J., Huang, J.P.: Diffusive pseudo-conformal mapping: Anisotropy-free transformation thermal media with perfect interface matching. Chaos, Solitons Fractals **174**, 113849 (2023)

26. Zhu, N.Q., Shen, X.Y., Huang, J.P.: Converting the patterns of local heat flux via thermal illusion device. AIP Adv. **5**, 053401 (2015)
27. Han, T., Bai, X., Thong, J.T., Li, B., Qiu, C.W.: Full control and manipulation of heat signatures: cloaking, camouflage and thermal metamaterials. Adv. Mater. **26**, 1731–1734 (2014)
28. Hu, R., et al.: Encrypted thermal printing with regionalization transformation. Adv. Mater. **31**, 1807849 (2019)
29. Hu, R., et al.: Illusion thermotics. Adv. Mater. **30**, 1707237 (2018)
30. Dede, E.M., Yu, Z., Schmalenberg, P., Iizuka, H.: Thermal metamaterials for radiative plus conductive heat flow control. Appl. Phy. Lett. **116**, 191902 (2020)
31. Li, Y., Bai, X., Yang, T., Luo, H., Qiu, C.W.: Structured thermal surface for radiative camouflage. Nat. Commun. **9**, 273 (2018)
32. Peng, Y.G., Li, Y., Cao, P.C., Zhu, X.F., Qiu, C.W.: 3D printed meta-helmet for wide-angle thermal camouflages. Adv. Funct. Mater. **30**, 2002061 (2020)
33. Zhu, H., et al.: Multispectral camouflage for infrared, visible, lasers and microwave with radiative cooling. Nat. Commun. **12**, 1805 (2021)
34. Harrison, A.W., Walto, M.R.: Radiative cooling in TiO_2 white paint. Sol. Energy **20**, 185–188 (1978)
35. Raman, A.P., Anoma, M.A., Zhu, L., Rephaeli, E., Fan, S.H.: Passive radiative cooling below ambient air temperature under direct sunlight. Nature **515**, 540–544 (2014)
36. Mandal, J., Fu, Y., Overvig, A.C., et al.: Hierarchically porous polymer coatings for highly efficient passive daytime radiative cooling. Science **362**(6412), 315–319 (2018)
37. Li, W., Fan, S.: Radiative cooling: harvesting the coldness of the universe. Opt. Photonics News **30**(11), 32–39 (2019)
38. Rephaeli, E., Fan, S.: Absorber and emitter for solar thermo-photovoltaic systems to achieve efficiency exceeding the Shockley-Queisser limit. Opt. Express **17**(17), 15145–15159 (2009)
39. Swanson, R.M.: A proposed thermophotovoltaic solar energy conversion system. Proc. IEEE **67**(3), 446–447 (1979)
40. Omair, Z., et al.: Ultraefficient thermophotovoltaic power conversion by band-edge spectral filtering. Proc. Natl. Acad. Sci. U.S.A. **116**, 15356–15361 (2019)
41. Li, Y., Li, W., Han, T., et al.: Transforming heat transfer with thermal metamaterials and devices. Nat. Rev. Mater. **6**(6), 488–507 (2021)
42. Wang, Y., Liu, H., Zhu, J.: Solar thermophotovoltaics: Progress, challenges, and opportunities. APL Mater. **7**(8) (2019)
43. DeSutter, J., Tang, L., Francoeur, M.: A near-field radiative heat transfer device. Nat. Nanotechnol. **14**(8), 751–755 (2019)
44. Guha, B., Otey, C., Poitras, C.B., Fan, S., Lipson, M.: Near-field radiative cooling of nanostructures. Nano Lett. **12**, 4546–4550 (2012)
45. Zhou, C., Zhang, Y., Qu, L., et al.: Near-field negative electroluminescent cooling via nanoparticle doping. J. Quant. Spectrosc. Radiat. Transfer **245**, 106889 (2020)
46. Liu, Y., Antezza, M., Zheng, Y.: Intelligent radiative thermostat induced by near-field radiative thermal diode. Mater. Today Phys. **27**, 100828 (2022)
47. Mittapally, R., Majumder, A., Reddy, P., et al.: Near-field thermophotovoltaic energy conversion: Progress and opportunities. Phys. Rev. Appl. **19**(3), 037002 (2023)
48. Rytov, S.M., Kravtsov, I.U.A., Tatarskii, V.I.: Principles of Statistical Radiophysics: Wave Propagation Through Random Media. Springer, Berlin (1989)
49. Whale, M.D., Cravalho, E.G.: Modeling and performance of microscale thermophotovoltaic energy conversion devices. IEEE Trans. Energy Convers. **17**, 130 (2002)
50. Francoeur, M., Vaillon, R., Menguc, M.P.: Thermal impacts on the performance of nanoscale-gap thermophotovoltaic power generators. IEEE Trans. Energy Convers. **26**, 686 (2011)
51. Shang, J., Tian, B.Y., Jiang, C.R., Huang, J.P.: Digital thermal metasurface with arbitrary infrared thermogram. Appl. Phys. Lett. **113**, 261902 (2018)
52. Li, Y., Shen, X.Y., Wu, Z.H., Huang, J.Y., Chen, Y.X., Ni, Y.S., Huang, J.P.: Temperature-dependent transformation thermotics: From switchable thermal cloaks to macroscopic thermal diodes. Phys. Rev. Lett. **115**, 195503 (2015)

53. Wang, L., Zhang, Z.: Thermal rectification enabled by near-field radiative heat transfer between intrinsic silicon and a dissimilar material. Nanoscale Microscale Thermophys. Eng. **17**, 337–348 (2013)
54. McDonagh, C., Burke, C.S., MacCraith, B.D.: Optical chemical sensors. Chem. Rev. **108**, 400–422 (2008)
55. Xu, L.J, Liu, J.R., Jin, P., Xu, G.Q., Li, J.X., Ouyang, X.P., Li, Y., Qiu, C-W., Huang, J.P.: Black-hole-inspired thermal trapping with graded heat-conduction metadevices. Nat. Sci. Rev. **10**, nwac159 (2023)
56. Xu, L.J., Xu, G.Q., Huang, J.P., Qiu, C.-W.: Diffusive Fizeau Drag in Spatiotemporal Thermal Metamaterials. Phys. Rev. Lett. **128**, 145901 (2022)
57. Jin, P., Liu, J.R., Xu, L.J., Wang, J., Ouyang, X.P., Jiang, J.-H., Huang, J.P.: Tunable liquid-solid hybrid thermal metamaterials with a topology transition. Proc. Natl. Acad. Sci. U.S.A. **120**, e2217068120 (2023)
58. Xu, L.J, Liu, J,R., Xu, G.Q., Huang, J.P., Qiu, C-W.: Giant, magnet-free, and room-temperature Hall-like heat transfer. Proc. Natl. Acad. Sci. U.S.A. **120**, e2305755120 (2023)
59. Xu, L.J., Huang, J.P., Ouyang, X.P.: Nonreciprocity and isolation induced by an angular momentum bias in convection-diffusion systems. Appl. Phys. Lett. **118**, 22190 (2021)
60. Zhmakin, A.I.: Non-Fourier Heat Conduction: From Phase-Lag Models to Relativistic and Quantum Transport. Springer Nature (2023)
61. Dai, G.L., Huang, J.P.: Nonlinear thermotics: Designing thermal metamaterials with temperature response (Invited review in Chinese). J. Nantong Univ. (Nat. Sci. Edn) **20**, 1–18 (2021)

Part IV
Metamaterials for Thermal Diffusion: Thermal Conduction, Convection, and Radiation

Chapter 13
Fundamental Methods and Design Paradigm for Omnithermotics

Chengmeng Wang, Liujun Xu, Jun Wang, and Shuai Yang

13.1 Opening Remarks

Thermal regulation has been an important issue since ancient times, and it is related to the survival and development of human beings. Therefore, thermal regulation has attracted countless researchers to continue to explore. Thermal metamaterials refer to artificially designed and prepared structural materials that can achieve novel thermal functions [1–5]. Since transformation thermotics was proposed by Fan et al. [6], thermal metamaterials have become a powerful tool to manipulate heat energy [1–3]. A lot of thermal metadevices based on transformation thermotics emerge endlessly, such as thermal cloaks [7–12], thermal transparency [13–16], thermal sensor [17–20], thermal concentrators [21, 22], thermal rotators [23] and thermal camouflages [23–27]. Although transformation theory has made breakthrough achievements, it requires that the parameters of thermal metamaterials are anisotropic and inhomogeneous, which makes the fabrication of devices quite troublesome. However, over the past ten years, the theory for designing thermal metamaterials has been continuously developed. In addition to the traditional transformation thermal theory, researchers have designed many thermal devices based on thermal effective medium theory [28–34] and numerical calculation methods. For thermal effective medium theory, the most representative one is scattering cancellation [35, 36], which uses double-layer isotropic materials to achieve a perfect thermal cloak. After that, the researchers also implemented a thermal concentrator using this bilayer structure [37]. Additionally,

C. Wang (✉) · S. Yang
Department of Physics, Key Laboratory of Micro and Nano Photonic Structures (MOE), and State Key Laboratory of Surface Physics, Fudan University, Shanghai 200438, China
e-mail: 22110190055@m.fudan.edu.cn

L. Xu
Graduate School of China Academy of Engineering Physics, Beijing 100193, China

J. Wang
School of Energy and Materials, Shanghai Polytechnic University, Shanghai 201209, China

F.-B. Yang and J.-P. Huang, *Diffusionics*,
https://doi.org/10.1007/978-981-97-0487-3_13

the thermal effective medium theory can not only design the functions predicted by the transformation theory, but also the functions predicted by the non-transformation theory, which greatly enriches the design ideas of thermal metamaterials. Since the core of the thermal effective medium theory is to calculate the equivalent thermal conductivity, it is a little weak to control the transient heat transfer process [8, 38, 39]. Therefore, some researchers also developed the transient heat transfer theory to regulate the wave-like temperature field [40–43], which also established a unified understanding of the diffusion system and the fluctuation system. Moreover, with the diversification of device functions, we have more precise and complex requirements for the spatial distribution of thermal conductivity. Therefore, numerical calculation methods have been developed to fabricate metamaterials with desired thermal conductivity. Printable freeform thermal metamaterials can directly create functional cells with certain thermal conductivity using transformation thermotics and topology optimization [44, 45]. These functional cells are local microstructures composed of die steel and polydimethylsiloxane. This approach solves challenges such as the limited shape adaptability of thermal metadevices and the need for prior knowledge of the background temperatures. Numerical methods have now become advanced and powerful for designing feasible thermal metamaterials with various applications. These days, inspired by the optical conformal mapping theory, thermal conformal mapping theory has been proposed to simplify the preparation of transformation thermotics and eliminate anisotropy [46]. All the theories mentioned above constitute the new research direction of theoretical thermodynamics [47, 48], which is regarded as an important part of the field of thermodynamics together with thermodynamic statistical physics and heat transfer [49, 50].

Based on these theories and methods, researchers design various functional thermal metamaterials to regulate thermal conduction at first [3]. Further, they also use thermal metamaterials to realize the coordinated regulation of heat convection and heat conduction [3, 51–55]. In 2020, Xu et al. unify thermal radiation into the framework of the theory of transformational thermotics [56], which can simultaneously deal with the three basic heat transfer modes of heat conduction, heat convection, and heat radiation. Based on this, they further design an omnithermal metamaterial to realize the functions of thermal cloaking, thermal concentration and thermal rotation. For the simultaneous regulation of three heat transfer modes using effective medium theory, Wang et al. fabricate omnithermal restructurable metasurfaces which show both illusion viewed in infrared light and in visible light by considering the three basic modes of heat transfer in theoretical designs [30]. Yang et al. propose an effective medium theory to handle conductive, radiative, and convective processes simultaneously, which is based on the Fourier law, the Rosseland diffusion approximation, and the Darcy law [29]. In addition to these unified paradigms, researchers have also utilized many artificially designed structures possessing three thermal transfer modes, such as radiative cooling and engineered cellular solids [57]. In this chapter, we will introduce the transformation omnithermotics in Sect. 13.2 and effective medium theory for omnithermotics in Sect. 13.3. At last, we will introduce radiative cooling and engineered cellular solids in Sect. 13.4.

13.2 Transformation Omnithermotics

Transformation Omnithermotics, as introduced by Xu et al. in their work [56], provides a comprehensive framework for understanding and manipulating the three basic modes of heat transfer: conduction, convection, and radiation simultaneously. They suppose that fluids are incompressible and laminar with a low speed and neglect the momentum conservation of fluids when handling thermal convection. Therefore, the transient process of heat transfer with conduction, convection, and radiation is dominated by

$$\begin{gathered}\rho_f C_f \partial T/\partial t + \nabla \cdot \left(-\boldsymbol{\kappa}_f \cdot \nabla T + \rho_f C_f \boldsymbol{v}_f T - \boldsymbol{\alpha}_f T^3 \cdot \nabla T\right) = 0, \\ \partial \rho_f/\partial t + \nabla \cdot \left(\rho_f \boldsymbol{v}_f\right) = 0,\end{gathered} \tag{13.1}$$

where ρ_f, C_f, κ_f, and $\boldsymbol{v}_f$ are the density, heat capacity, thermal conductivity, and velocity of fluids, respectively. $\boldsymbol{\alpha}_f = 16{\boldsymbol{\beta}_f}^{-1}{\boldsymbol{n}_f}^2\sigma/3$ can be treated as radiative coefficient where $\boldsymbol{\beta}_f$, $\boldsymbol{n}_f$, and $\sigma (= 5.67 \times 10^{-8}\,\mathrm{W/(m^2K^4)})$ are the Rosseland mean attenuation coefficient, relative refractive index, and the Stefan-Boltzmann constant, respectively.

Equation (13.1) can keep its form-invariance after a space transformation if the materials' parameters obey the following transformation rules:

$$\begin{aligned}\rho'_f &= \rho_f/\det\Lambda \\ C'_f &= C_f \\ \boldsymbol{\kappa}'_f &= \Lambda\boldsymbol{\kappa}_f\Lambda^{\tau}/\det\Lambda \\ \boldsymbol{v}'_f &= \Lambda\boldsymbol{v}_f \\ \boldsymbol{\alpha}'_f &= \Lambda\boldsymbol{\alpha}_f\Lambda^{\tau}/\det\Lambda\end{aligned} \tag{13.2}$$

where Λ is the Jacobian transformation matrix and Λ^{τ} is the transpose of Λ. As is shown in Eq. (13.2), for thermal convection, they have to transform flow velocity directly. It is extremely difficult in experiments. Therefore, they resort to porous media to control flow velocity and ensure feasibility. With the calculated Λ according to the expected function, they design three devices including omnithermal cloaking, concentrating, and rotating as model applications. Finite-element simulations are also provided to confirm these applications.

This work not only unifies the three basic modes of heat transfer within the theoretical framework of transformation omnithermotics, but also provides novel hints and potential applications to thermal management.

13.3 Effective Medium Theory for Omnithermotics

13.3.1 Omnithermal Restructurable Metasurfaces

In addition to manipulating the three basic modes of heat transfer with omnithermal metamaterials, Wang et al. design omnithermal restructurable metasurfaces which achieve both infrared-light illusion and visible-light similarity [30]. By considering the three basic modes of heat transfer (omnithermotics) in theoretical designs, the authors delve into the tuning of surface apparent temperature and emissivity, which can be executed synergistically. In the experimental demonstration, they use radiation-cavity effects to modulate the full-wavelength emissivity. They use a cylindrical cavity structure as it is easy to manufacture, demonstrated in Fig. 13.1. The whole metasurface consists of an array of those cylindrical cavity unit cells. The effective emissivity of an isolated cylindrical cavity ε_e depends on its area ratio of the mouth and the intra-cavity, which can be expressed as:

$$\varepsilon_e = \left[1 + \frac{S_0}{S_1}\left(\frac{1}{\varepsilon_b} - 1\right)\right]^{-1} \tag{13.3}$$

where S_0 and S_1 are the areas of the mouth and the inwall, respectively, and ε_{sur} is the intrinsic surface emissivity. Through adjusting the unit cells' emissivity, they can tailor the effective emissivity of the surface so as to form a specific apparent-temperature distribution in infrared imaging.

13.3.2 Omnithermal Metamaterials with Switchable Function

As illustrated in Sect. 13.2, Xu et al. manipulate the three basic modes of heat transfer with transformation omnithermotics. In contrast, Yang et al. propose an effective medium theory to handle conductive, radiative, and convective processes simultaneously, which is based on the Fourier law, the Rosseland diffusion approximation, and the Darcy law [29]. Moreover, They also discuss to what extent the three different heat transfer modes dominate the heat transfer process at different temperature intervals. In this circumstance, they design an omnithermal metamaterial switchable between transparency and cloaking, which results from the nonlinear properties of radiation and convection.

Theory—If we consider all methods of heat transfer in a porous medium, the conductive heat flux $\boldsymbol{J_1}$, radiative flux $\boldsymbol{J_2}$, and convective flux $\boldsymbol{J_3}$, are given by the Fourier law, the Rosseland diffusion approximation, and the Darcy law:

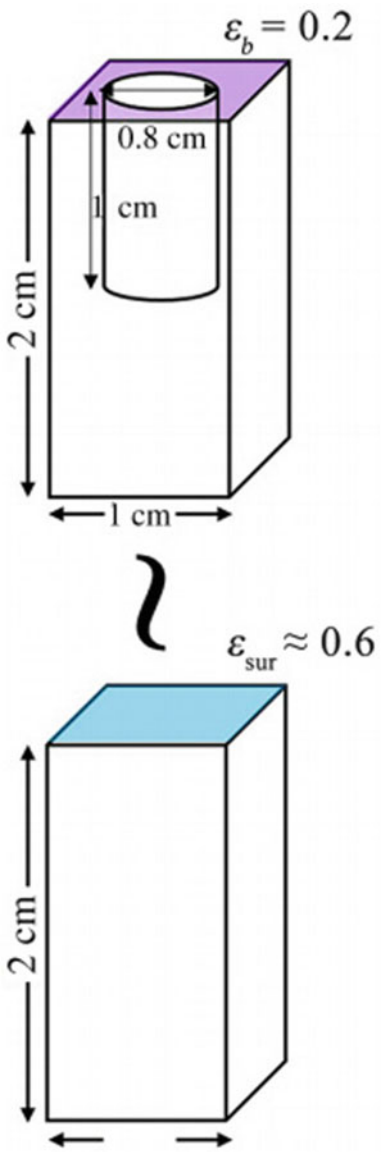

Fig. 13.1 Cavity structure (upper panel) and effective emissivity principle. The effective emissivity of a flat surface with a cavity (upper panel) is equivalent to $\varepsilon_s ur$ of another flat surface (lower panel), which is quantitatively expressed in Eq. (13.3). (from Ref. [30])

$$\begin{aligned} \boldsymbol{J_1} &= -\kappa \nabla T \\ \boldsymbol{J_2} &= -\gamma T^3 \nabla T \\ \boldsymbol{J_3} &= \rho_f c_f \boldsymbol{v} T \end{aligned} \tag{13.4}$$

where ρ_f and c_f are the density and heat capacity of the fluid. $\boldsymbol{v}$ represents the velocity of the fluid, which is given by the Darcy law $\boldsymbol{v} = -\varsigma/\eta_f \nabla P$, where ς is the permeability of the porous medium, η_f is the viscosity of the fluid, and P denotes pressure. κ is the thermal conductivity of the porous medium. $\gamma = 16\beta^{-1}n^2\sigma/3$ is the radiative coefficient, where β is the Rosseland mean extinction coefficient, n is the relative refractive index, which is set to 1 for brevity, and σ is the Stefan–Boltzmann constant. The total heat flux is $\boldsymbol{J} = \boldsymbol{J_1} + \boldsymbol{J_2} + \boldsymbol{J_3}$ which satisfy the Laplace equation:

$$\nabla \cdot \boldsymbol{J} = \nabla \cdot (\boldsymbol{J_1} + \boldsymbol{J_2} + \boldsymbol{J_3}) \tag{13.5}$$

Then, two boundary conditions are considered: (I) the temperature field and pressure field are parallel and (II) the temperature field and pressure field are perpendicular. Yang et al. confirm that the effective medium theory is applicable in both conditions.

Design—For omnithermal transparency (Fig. 13.2a), the radius of the core is r_c with the thermal conductivity κ_c, the Rosseland mean extinction coefficient β_c, and the permeability ς_c. The core is coated by a shell with the corresponding parameters r_s, κ_s, β_s, and ς_s. Based on the effective medium theory, three effective values can be obtained:

$$\begin{aligned} \kappa_e &= \kappa_s \frac{\kappa_c + \kappa_s + (\kappa_c - \kappa_s)\, p}{\kappa_c + \kappa_s - (\kappa_c - \kappa_s)\, p} \\ \beta_e^{-1} &= \beta_s^{-1} \frac{\beta_c^{-1} + \beta_s^{-1} + \left(\beta_c^{-1} - \beta_s^{-1}\right) p}{\beta_c^{-1} + \beta_s^{-1} - \left(\beta_c^{-1} - \beta_s^{-1}\right) p} \\ \varsigma_e &= \varsigma_s \frac{\varsigma_c + \varsigma_s + (\varsigma_c - \varsigma_s)\, p}{\varsigma_c + \varsigma_s - (\varsigma_c - \varsigma_s)\, p} \end{aligned} \tag{13.6}$$

where κ_e, β_{e-1}, and ς_e represent the effective thermal conductivity, the effective reciprocal of the Rosseland mean extinction coefficient and the effective permeability of the core-shell structure. $p = r_c/r_s$ is the area fraction.

For omnithermal cloaking (Fig. 13.2b), the radius of the core is r_c with thermal conductivity κ_c, reciprocal of the Rosseland mean extinction coefficient β_{c-1}, and permeability ς_c. The core is coated by an inner shell with parameters r_{s1}, κ_{s1}, β_{s1-1}, and ς_{s1} and an outer shell with parameters r_{s2}, κ_{s2}, β_{s2-1}, and ς_{s2}. Bilayer cloaking requires the inner shell to be insulated; i.e., $\kappa_{s1} \to 0$, $\beta_{s1-1} \to 0$, and $\varsigma_{s1} \to 0$. Then, the effective thermal conductivity, the effective reciprocal of the Rosseland mean extinction coefficient, and the effective permeability of the core-shell-shell structure can be derived:

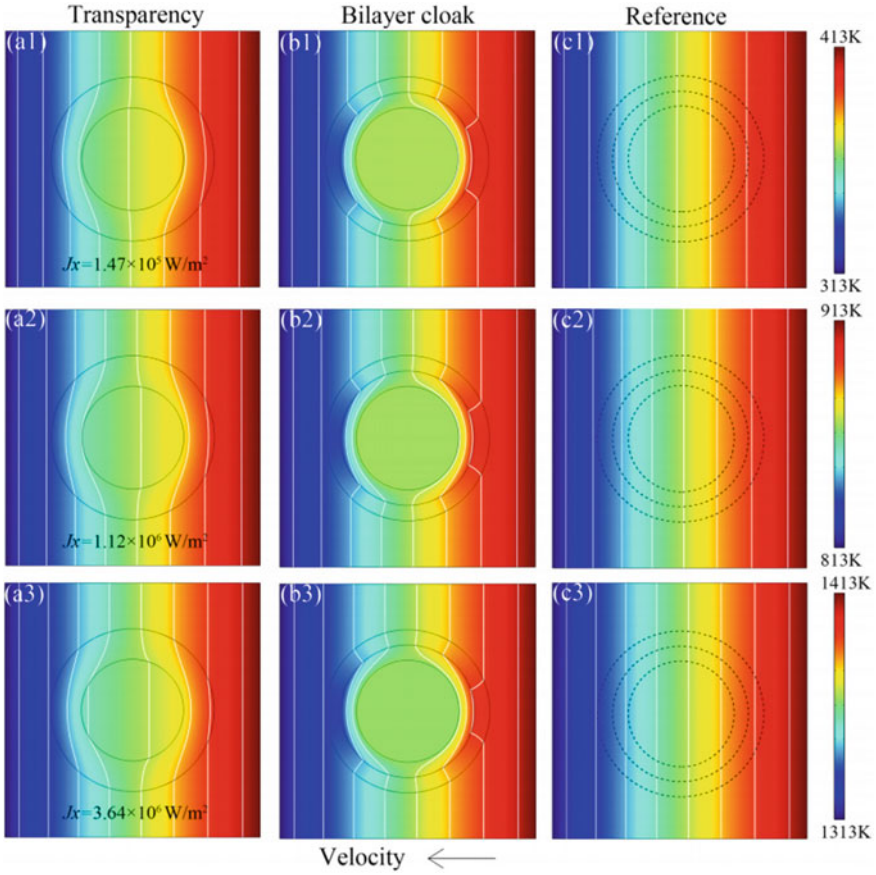

Fig. 13.2 Simulation results of (a1)–(a3) transparency, (b1)–(b3) cloaking, and (c1)–(c3) references with uniform fields. (from Ref. [29])

$$\begin{aligned} \kappa_e &= \kappa_{s2}\frac{1-p}{1+p} \\ \beta_e^{-1} &= \beta_{s2}^{-1}\frac{1-p}{1+p} \\ \varsigma_e &= \varsigma_{s2}\frac{1-p}{1+p} \end{aligned} \tag{13.7}$$

where $p = (r_{s1}/r_{s2})^2$ is the air fraction.

Ominthermal transparency and cloak—Fig. 13.2 shows the simulation results with boundary condition (I). The simulation results for omnithermal transparency, omnithermal cloaking, and references are presented in Fig. 13.2a1–a3, b1–b3, and c1–c3, respectively. The temperatures of the right and left boundaries are 413 and 313 K for Fig. 13.2a1–c1, 913 and 813 K for Fig. 13.2a2–c2, and 1413 and 1313 K

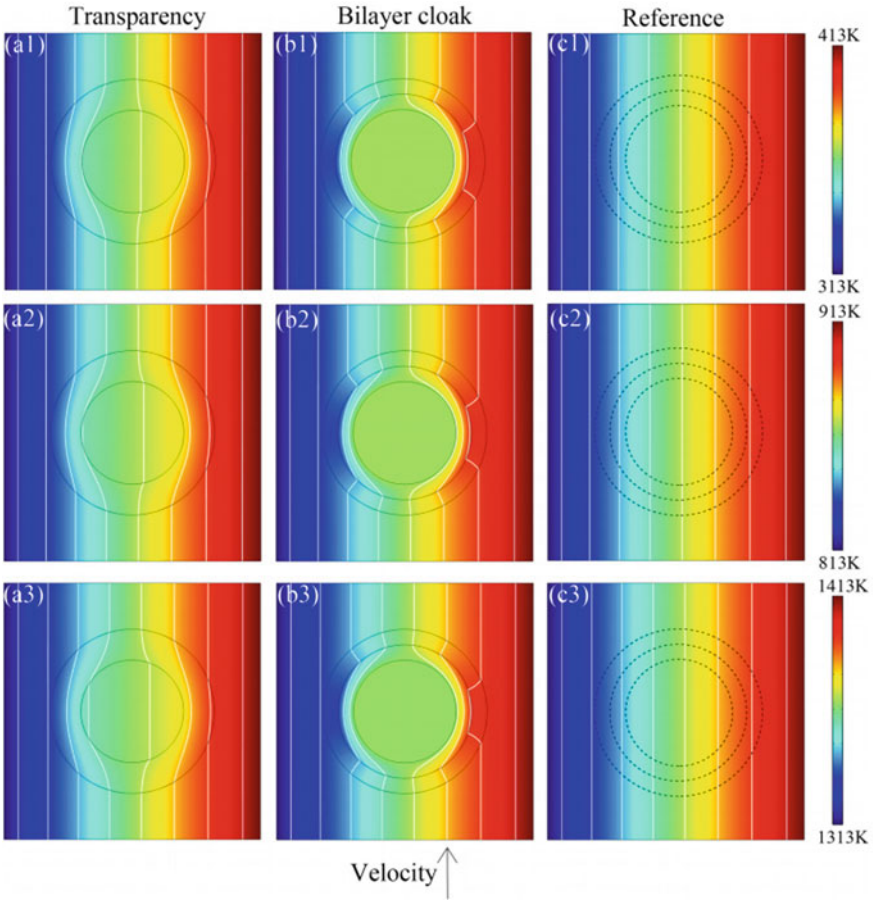

Fig. 13.3 Simulation results of (a1)–(a3) transparency, (b1)–(b3) cloaking, and (c1)–(c3) references with uniform fields. The pressures of the bottom and top boundaries are 1000 and 0 Pa, and the left and right boundaries are insulated. The other parameters are the same as those for Fig. 13.2. (from Ref. [29])

for Fig. 13.2a3–c3. The pressures of the right and left boundaries in Fig. 13.2a1–c3 are 1000 and 0 Pa, respectively. For omnithermal transparency, the temperature distribution in the background should be the same as the reference, as if there was no core-shell structure in the center. To ensure that omnithermal transparency works, setting $\kappa_b = \kappa_e$, $\beta_b = \beta_e$ and $\varsigma_b = \varsigma_e$ based on Eq. (13.6). For bilayer cloaking, the cloaking region should be at a constant temperature, and the temperature distribution in the background should not be disturbed. Thus κ_{s1}, ${\beta_{s1}}^{-1}$ and ς_{s1} should be set as very small values. Based on Eq. (13.7), the properties of the background should be equal to the effective properties of the bilayer cloak: $\kappa_b = \kappa_e$, $\beta_b = \beta_e$ and $\varsigma_b = \varsigma_e$. The results of omnithermal transparency and cloaking conditions confirm the theory.

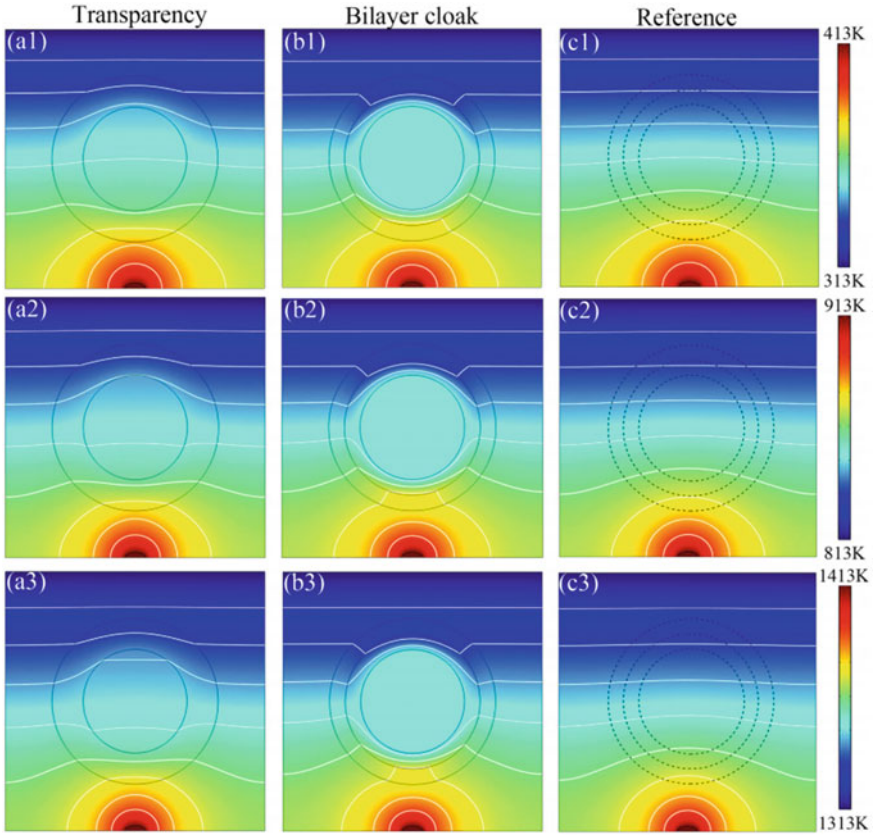

Fig. 13.4 Simulation results of (a1)–(a3) transparency, (b1)–(b3) cloaking, and (c1)–(c3) references with nonuniform fields. (from Ref. [29])

For boundary condition (II), the pressures of the bottom and top boundaries are at 1000 and 0 Pa, respectively. The other conditions are kept unchanged. Finite-element simulations are performed again with the new boundary conditions and the corresponding results are shown in Fig. 13.3. Obviously, this change does not influence the effects of omnithermal transparency and cloaking. Moreover, this scheme is robust when applying a nonuniform thermal field. The results are stable; see Fig. 13.4. In Fig. 13.4a1–c3, there is an elliptical source with high temperature and pressure at the bottom of the simulation box. Then fix the upper boundary at 0 Pa and the source boundary at 1000 Pa. The other boundaries are insulated. The temperature settings are 413–313 K for Fig. 13.4a1–c1, 913–813 K for Fig. 13.4a2–c2, and 1413–1313 K for Fig. 13.4a3–c3. The other parameters are same as those for Fig. 13.2.

Function switching between transparency and cloaking—The Rosseland diffusion approximation suggests that the radiative flux $\boldsymbol{J_2}$ is proportional to T_3. The convective flux $\boldsymbol{J_3}$ is proportional to T, and the conductive flux $\boldsymbol{J_1}$ is independent of

T. The total flux $\boldsymbol{J}$ are compared in Fig. 13.2a1–a3 and find that $\boldsymbol{J}$ increases with increasing concrete temperature (the temperature difference remains unchanged). In other words, the radiative and convective effects increase with increasing temperature. These nonlinear properties induce a switchable omnithermal metamaterial; see Fig. 13.5. When the device functions with a high-temperature interval (Fig. 13.5b), bilayer cloaking is presented. When the device functions with a normal temperature interval (Fig. 13.5c), it switches to transparency. Different from the previous work, Yang et al. introduce radiation and convection to achieve such an intelligent metamaterial that can adaptively switch its functions according to the external temperature. Actually, the switch between the different functions results from the competition between three mechanisms of heat transfer. Generally, thermal conduction is dominant at normal temperatures, and thermal convection and radiation are dominant at high temperatures. Therefore, Yang et al. design the parameters related to thermal conduction to meet the requirements of transparency and design the parameters related to thermal convection and radiation to meet the requirements of bilayer cloaking. Then, the device can exhibit the cloaking function at high temperatures and the transparency function at normal temperatures.

13.4 Other Artificially Designed Structures

13.4.1 Radiative Cooling

Theory—Radiative cooling is a prevalent phenomenon in our daily lives. For instance, the cool sensation we experience during nighttime arises because the sun's radiation is minimal, allowing the Earth to emit heat into outer space [58]. Figure 13.6 illustrates the principle of radiative cooling. Picture an object exposed to sunlight: it releases heat via radiation while simultaneously absorbing heat from the direct sun rays. Furthermore, natural convection and thermal conduction play roles in determining the object's temperature. To effectively cool the object, it's essential to encase it in a specially designed layer that amplifies its radiation and reflects sunlight. The net cooling power can be described as $P_{cool}(T) = P_{rad}(T) - P_{atm}(T) - P_{sun}(T) - P_{cond+conv}(T)$, where $P_{rad}(T)$ is the radiative power, $P_{atm}(T)$ is the absorbed power due to incident atmospheric thermal radiation, $P_{sun}(T)$ is the incident solar power absorbed by the object, and $P_{cond+conv}(T)$ is the power loss or gain due to convection and conduction. For the best cooling performance, the radiative cooler should emit powerfully and selectively within the atmospheric transparency window to amplify $P_{rad}(T)$. Simultaneously, it should reflect all other light, especially in the visible and near-infrared spectrum, to reduce $P_{atm+sun}(T)$. It's notable that in every application of radiative cooling, heat conduction and convection also significantly contribute. In other words, the combined impact of heat radiation, heat conduction, and heat convection produces the targeted cooling in specific areas.

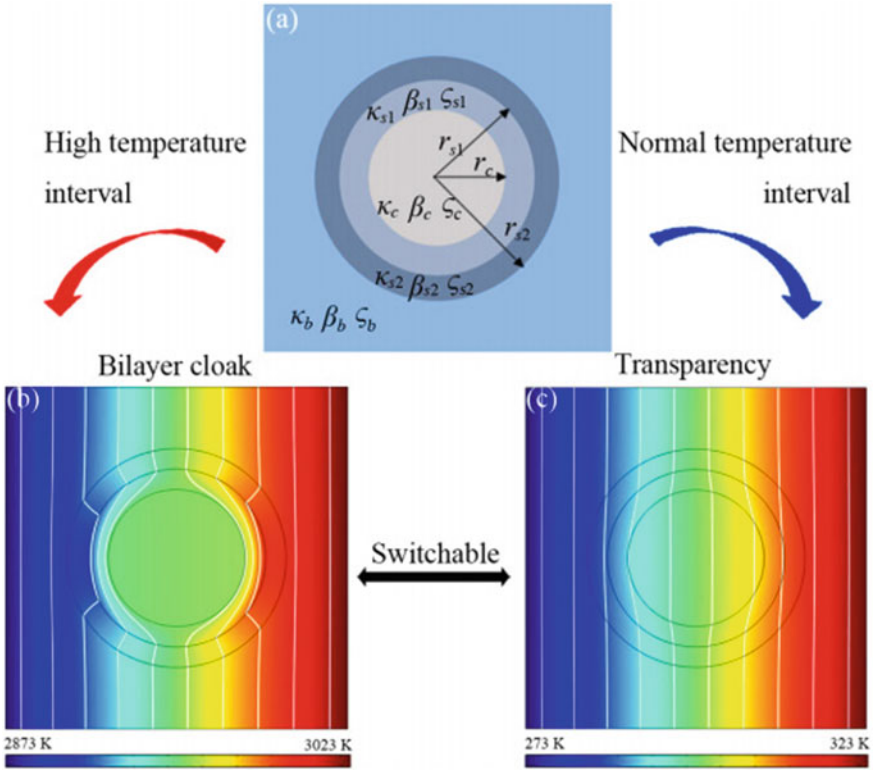

Fig. 13.5 Switchable omnithermal metamaterial. **a** Schematic diagram. **b** Bilayer cloak with a high-temperature interval. **c** Transparency with a normal temperature interval. The pressures of the right and left boundaries are 1000 and 0 Pa, and the other boundaries are insulated. (from Ref. [29])

Design—In 2013, Fan's team developed a metal-dielectric photonic structure that, through numerical simulations, minimized solar absorption and selectively emitted within the atmospheric transparency window [59]. This photonic crystal, boasting a multilayer micro-nano structure with periodic perforations, achieved a net cooling power surpassing 100 W/m^2. They later refined this multilayer design, crafting a photonic crystal from SiO_2, HfO_2, and Silver [60]. This new design managed to reach temperatures 5 degrees Celsius below ambient under direct sunlight. However, the complexity and expense of its fabrication posed challenges to its broad-scale adoption.

Addressing these challenges, other researchers introduced a novel randomized glass-polymer hybrid metamaterial crafted from polymethyl-pentene [61]. This design embedded tiny SiO_2 spheres, averaging eight microns in diameter, on one side of the material, while the opposite side was silver-coated. These 8-micron glass spheres emitted heat from beneath the material in the 8-14 μm infrared range, aligning with the atmospheric transparency window. Concurrently, the polymethyl-pentene

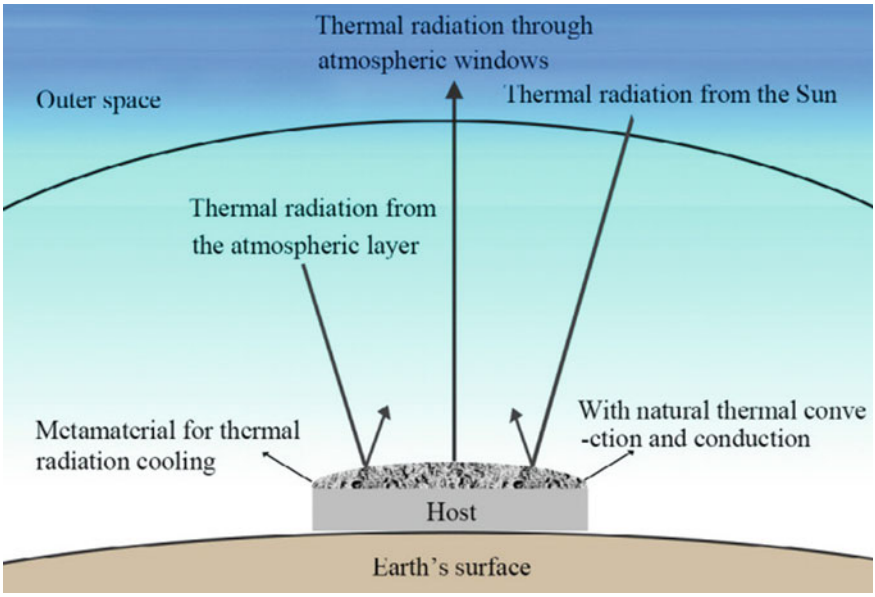

Fig. 13.6 Schematic diagram showing the full heat-transfer modes associated with radiative cooling. Adapted from Ref. [3]

and silver layers reflected a majority of incoming visible light. Demonstrating a radiative cooling power of 93 watts per square meter under direct sunlight, this metamaterial not only proved efficient but was also cost-effective and scalable for mass production. Consequently, such metamaterial films have been successfully mass-produced. In 2018, a group of researchers developed hierarchically porous poly coatings made from vinylidene fluoride-co-hexafluoropropene [62]. These coatings exhibited superior passive daytime radiative cooling properties. To create them, poly and water were combined in acetone and then air-dried. The evaporation process of both acetone and water led to the formation of micro-nano air cavities within the poly. Consequently, this coating boasted a high reflectance of 96% in the visible light spectrum and delivered a cooling power of 96 watts per square meter. This polymer method, being more user-friendly and simpler to produce than previous techniques, emerges as a promising contender in the field of passive radiative cooling materials.

The radiative cooling experiments described earlier are primarily effective in arid regions. Liu and his team delved into the impact of atmospheric water vapor on the efficiency of radiative cooling [63]. Both their theoretical analyses and experimental findings indicated that as the column of water vapor increases, the cooling power diminishes, albeit at a decreasing rate. This decline in cooling power is attributed to the enhanced absorption of atmospheric radiation by the radiative cooler due to the increase in water vapor. Their research offers valuable insights for the real-world implementation of radiative cooling across various climatic conditions.

13.4.2 Engineered Cellular Solids

Owing to the recent progress in 3D printing techniques and the capability to produce multifunctional materials with intricate nano/microstructures, rationally-designed lattices that form metamaterials and meta-structures have garnered significant interest [57]. Engineered cellular solids, mirroring the properties of their natural counterparts found in entities like wood, cork, bone, and coral, represent a notable category of these lightweight, high-performance materials. Beyond their mechanical attributes, the hydrodynamic and thermal characteristics of designed lattices, especially when evaluating various heat transfer modalities under diverse boundary scenarios, are crucial. Given the challenges in formulating a precise analytical model for integrated convective and radiative heat transfer, a computational approach leveraging the finite volume method (FVM) or finite element method (FEM) becomes imperative. Among the various lattice designs, the mechanical attributes of BCC lattices, representative of cubic cellular structures, have been extensively studied [57]. This is attributed to their straightforward production via additive manufacturing or molding and their applicability in fields such as energy engineering, infrastructure, transportation, and aerospace. In 2022, Shahrzadi et al. introduce the architecture of BCC lattices and a comprehensive study that includes contributions of all three modes of heat transfer for the BCC lattices has been conducted in this work. It's imperative to assess the thermal characteristics of lattices both with and without the influence of radiation, as this factor is often omitted to streamline the thermal performance analysis of designed lattices. Shahrzadi et al. ascertain situations where radiation heat transfer cannot be overlooked in the thermal analysis of BCC lattices, by comparing the results in the absence and the presence of radiation heat transfer. They also investigated the effect of different porosity and Reynolds numbers on the heat transfer in the BCC lattice.

Design—The design of the three-dimensional unit cell draws inspiration from BCC crystals within the cubic crystal system family. By adjusting the diameter of the cylindrical struts in the BCC unit cell, its porosity changes while the cell size remains constant; see Fig. 1(a) in Ref. [57]. Porosity is characterized as the proportion of the vacant space in the unit cell relative to its overall volume. The equivalent pore diameter refers to the size of the largest sphere that can be enclosed by the unit cell's struts. As shown in Fig. 1(b) in Ref. [57], the equivalent pore diameter can be calculated by:

$$\frac{d_p}{2} = \frac{L\sqrt{2}}{2}\sin\theta - \frac{d_s}{2} \tag{13.8}$$

Governing equations—The governing equations for the simulation of fluid flow and heat transfer in porous media are presented below, which are simplified based on steady-state, incompressible flow, and temperature-independent material property assumptions.

$$\begin{aligned}
\nabla \cdot (\rho \vec{v}) &= 0 \\
\rho(\vec{v} \cdot \nabla \vec{v}) &= -\nabla P + \mu \nabla^2 \vec{v} \\
\rho C_p(\vec{v} \cdot \nabla T) &= \nabla \cdot (k \nabla T) + \dot{q} \\
\nabla \cdot (I(\vec{r}, \vec{s})\vec{s}) + (a + \sigma_s) I(\vec{r}, \vec{s}) &= an^2 \frac{\sigma T^4}{\pi} + \frac{\sigma_s}{4\pi} \int_0^{4\pi} I\left(\vec{r}, \vec{s'}\right) \Phi\left(\vec{s} \cdot \vec{s'}\right) d\Omega'
\end{aligned} \tag{13.9}$$

which are corresponding continuity, momentum, and energy conservation equations along with the Discrete Ordinates equation for radiation heat transfer accordingly. $\vec{v}$ is velocity vector, ρ is density, P is pressure, μ is dynamic viscosity, C_p is specific heat, T is temperature, κ is thermal conductivity, q is the heat generation, I is radiation intensity, $\vec{r}$is position vector, $\vec{s}$is direction vector, $\vec{s'}$ is scattering direction vector, a is absorption coefficient, σ is scattering coefficient, n is reflective index, σ_s is the Stefan-Boltzmann constant, Φ is the phase function, and Ω' represents solid angle. All mentioned equations are used for the fluid phase, and the energy conservation equation is used for both fluid and solid phases. For the solid phase, the left side of the energy conservation equation is zero. The ANSYS meshing tool is used to generate computational unstructured meshes for the simulations.

Conductive thermal conductivity—By ignoring the thermal radiation effect, a certain temperature gradient is applied to the two opposite faces on the left and right of the BCC lattice unit cell. They calculate the conductive thermal conductivity (κ_{ec}); see Fig. 7 in Ref. [57]. The conductive thermal conductivity increases when porosity decreases. This is because the amount of the solid phase in the unit cell increases and the contribution of solid thermal conductivity is higher than that of fluid. Moreover, the parallel and series models specify the upper and lower bounds. The calculated conductive thermal conductivity agrees well with the experimental results for $\varphi > 0.9$.

Heat transfer with fluid flow—They also investigate the heat transfer and fluid flow in the BCC lattices with alternative porosities for various Reynolds numbers based on the pore diameter (Re_p). When the porosity decreases, the ability of convective heat transfer to cool down the unit cell also decreases. As the Reynolds number increases, the cooling capacity of the fluid increases, thereby reducing the temperature of the unit cell.

Radiation effects—The article also considers the radiation mechanism on the heat transfer in BCC lattices. A certain thermal gradient is applied to the opposing faces of the unit cell, then radiative thermal conductivity (κ_{er}) and effective thermal conductivity (κ_{eff}) are calculated by:

$$q = q_{\text{cond}} + q_{\text{rad}} = -(k_{ec} + k_{er}) \frac{\partial T}{\partial z} = -k_{eff} \frac{\partial T}{\partial z} \tag{13.10}$$

It is observed that the radiative thermal conductivity increases with increasing porosity. When the applied temperature is relatively high, the enhancement of porosity to radiative heat transfer is more obvious, as shown in Fig. 11a in Ref. [57]. At lower

porosities, thermal conduction plays an important role in effective thermal conductivity, while at higher porosities, radiative heat transfer plays an important role, as shown in Fig. 11c in Ref. [57].

13.5 Conclusion and Application

The domain of thermal metamaterials stands at the cusp of a transformative era, with the establishment of the theory of transformation omnithermotics serving as a linchpin. This theory not only unifies the three primary modes of heat transfer—conduction, convection, and radiation—but also paves the way for innovative applications. Model applications, as demonstrated in this chapter, include omnithermal cloaking, concentrating, and rotating devices, all of which have been validated through finite-element simulations. The incorporation of porous media to modulate flow velocity further underscores the comprehensive nature of this work.

Furthermore, the development of an effective medium theory in omnithermotics has enabled the simultaneous manipulation of conduction, radiation, and convection in porous media. This has led to the design of transparency, cloaking, and switchable omnithermal metamaterials. Such designs have vast potential in applications like thermal camouflage, thermal rectification, and other intelligent metamaterials. And the proposed restructurable metasurface, which exhibits both illusions in infrared light and similarity in visible light, holds promise for real-world applications, especially when structured meticulously.

Other artificially designed structures about the radiative cooling. It has been used in many practical applications, including those for making woods stronger and cooler. Some researchers also demonstrated the excellent effect of radiative cooling on daytime building cooling. Engineered cellular solids, inspired by their natural counterparts found in materials like wood and bone, have emerged as advanced lightweight materials with unparalleled properties. Their unique characteristics, such as low density and high permeability, make them indispensable in a plethora of applications. These include heat exchangers, thermal insulators, medical implants, solar energy systems, and aerospace sandwich panels [57].

References

1. Yang, F.B., Zhang, Z.R., Xu, L.J., Liu, Z.F., Jin, P., Zhuang, P.F., Lei, M., Liu, J.R., Jiang, J.-H., Ouyang, X.P., Marchesoni, F., Huang, J.P.: Controlling mass and energy diffusion with metamaterials. Rev. Mod. Phys. **96**, 015002 (2024)
2. Zhang, Z.R., Xu, L.J., Qu, T., Lei, M., Lin, Z.K., Ouyang, X.P., Jiang, J.H., Huang, J.P.: Diffusion metamaterials. Nat. Rev. Phys. **5**, 218–235 (2023)
3. Yang, S., Wang, J., Dai, G.L., Yang, F.B., Huang, J.P.: Controlling macroscopic heat transfer with thermal metamaterials: theory, experiment and application. Phys. Rep. **908**, 1–65 (2021)

4. Wang, J., Dai, G.L., Huang, J.P.: Thermal metamaterial: fundamental, application, and outlook. iScience **23**, 101637 (2020)
5. Jin, P., Liu, J.R., Yang, F.B., Marchesoni, F., Jiang, J.H., Huang, J.P.: In-situ simulation of thermal reality. Research **6**, 0222 (2023)
6. Fan, C.Z., Gao, Y., Huang, J.P.: Shaped graded materials with an apparent negative thermal conductivity. Appl. Phys. Lett. **92**, 251907 (2008)
7. Dai, G.L., Zhou, Y.H., Wang, J., Yang, F.B., Qu, T., Huang, J.P.: Convective cloak in Hele-Shaw cells with bilayer structures: hiding objects from heat and fluid motion simultaneously. Phys. Rev. Appl. **17**, 044006 (2022)
8. Xu, L.J., Huang, J.P.: Active thermal wave cloak. Chin. Phys. Lett. **37**, 120501 (2020)
9. Xu, L.J., Dai, G.L., Wang, G., Huang, J.P.: Geometric phase and bilayer cloak in macroscopic particle-diffusion systems. Phys. Rev. E **102**, 032140 (2020)
10. Xu, L.J., Wang, J., Dai, G.L., Yang, S., Yang, F.B., Wang, G., Huang, J.P.: Geometric phase, effective conductivity enhancement, and invisibility cloak in thermal convection-conduction. Int. J. Heat Mass Transf. **165**, 120659 (2021)
11. Xu, L.J., Yang, S., Huang, J.P.: Effectively infinite thermal conductivity and zero-index thermal cloak. EPL **131**, 24002 (2020)
12. Yang, S., Xu, L.J., Huang, J.P.: Thermal magnifier and external cloak in ternary component structure. J. Appl. Phys. **125**, 055103 (2019)
13. Xu, L.J., Huang, J.P.: Metamaterials for manipulating thermal radiation: transparency, cloak, and expander. Phys. Rev. Appl. **12**, 044048 (2019)
14. Xu, L.J., Yang, S., Huang, J.P.: Thermal transparency induced by periodic interparticle interaction. Phys. Rev. Appl. **11**, 034056 (2019)
15. Liu, B., Xu, L.J., Huang, J.P.: Reinforcement learning approach to thermal transparency with particles in periodic lattices. J. Appl. Phys. **130**, 045103 (2021)
16. Liu, B., Xu, L.J., Huang, J.P.: Thermal transparency with periodic particle distribution: a machine learning approach. J. Appl. Phys. **129**, 065101 (2021)
17. Jin, P., Yang, S., Xu, L.J., Dai, G.L., Huang, J.P., Ouyang, X.P.: Particle swarm optimization for realizing bilayer thermal sensors with bulk isotropic materials. Int. J. Heat Mass Transf. **172**, 121177 (2021)
18. Xu, L.J., Huang, J.P., Jiang, T., Zhang, L., Huang, J.P.: Thermally invisible sensors. Europhys. Lett. **132**, 14002 (2020)
19. Jin, P., Xu, L.J., Jiang, T., Zhang, L., Huang, J.P.: Making thermal sensors accurate and invisible with an anisotropic monolayer scheme. Int. J. Heat Mass Transf. **163**, 120437 (2020)
20. Wang, C.Q., Xu, L.J., Jiang, T., Zhang, L., Huang, J.P.: Multithermally invisible cloaks and sensors with complex shapes. Europhys. Lett. **133**, 20009 (2021)
21. Dai, G.L., Huang, J.P.: A transient regime for transforming thermal convection: cloaking, concentrating and rotating creeping flow and heat flux. J. Appl. Phys. **124**, 235103 (2018)
22. Shen, X.Y., Li, Y., Jiang, C.R., Ni, Y.S., Huang, J.P.: Thermal cloak-concentrator. Appl. Phys. Lett. **109**, 031907 (2016)
23. Yang, F.B., Tian, B.Y., Xu, L.J., Huang, J.P.: Experimental demonstration of thermal chameleonlike rotators with transformation-invariant metamaterials. Phys. Rev. Appl. **14**, 054024 (2020)
24. Xu, L.J., Huang, J.P.: Chameleonlike metashells in microfluidics: a passive approach to adaptive responses. Sci. China-Phys. Mech. Astron. **63**, 228711 (2020)
25. Yang, S., Xu, L.J., Huang, J.P.: Two exact schemes to realize thermal chameleonlike metashells. EPL **128**, 34002 (2019)
26. Xu, L.J., Yang, S., Huang, J.P.: Passive metashells with adaptive thermal conductivities: chameleonlike behavior and its origin. Phys. Rev. Appl. **11**, 054071 (2019)
27. Xu, L.J., Wang, R.Z., Huang, J.P.: Camouflage thermotics: a cavity without disturbing heat signatures outside. J. Appl. Phys. **123**, 245111 (2018)
28. Zhou, X.C., Lin, W.Y., Yang, F.B., Zhou, X.D., Shen, J., Huang, J.P.: Effective medium theory with hybrid impacts of phase symmetry and asymmetry for analyzing phase transition behavior. Eur. Phys. Lett. **141**, 16001 (2023)

29. Yang, S., Xu, L.J., Dai, G.L., Huang, J.P.: Omnithermal metamaterials switchable between transparency and cloaking. J. Appl. Phys. **128**, 095102 (2020)
30. Wang, J., Yang, F.B., Xu, L.J., Huang, J.P.: Omnithermal restructurable metasurfaces for both infrared-light illusion and visible-light similarity. Phys. Rev. Appl. **14**, 014008 (2020)
31. Xu, L.J., Yang, S., Huang, J.P.: Designing the effective thermal conductivity of materials of core-shell structure: Theory and simulation. Phys. Rev. E **99**, 022107 (2019)
32. Yang, S., Xu, L.J., Wang, R.Z., Huang, J.P.: Full control of heat transfer in single-particle structural materials. Appl. Phys. Lett. **111**, 121908 (2017)
33. Dong, L., Huang, J.P., Yu, K.W., Gu, G.Q.: Dielectric response of graded spherical particles of anisotropic materials. J. Appl. Phys. **95**, 621–624 (2004)
34. Xu, L.J., Yang, S., Huang, J.P.: Thermal theory for heterogeneously architected structure: fundamentals and application. Phys. Rev. E **98**, 052128 (2018)
35. Han, T., Bai, X., Gao, D., Thong, J.T.L., Li, B., Qiu. C.-W.: Experimental demonstration of a bilayer thermal cloak. Phys. Rev. Lett. **112**, 054302 (2014)
36. Xu, H., Shi, X., Gao, F., Sun, H., Zhang, B.: Ultrathin three-dimensional thermal cloak. Phys. Rev. Lett. **22**, 054301 (2014)
37. Qu, T., Wang, J., Huang, J.P.: Manipulating thermoelectric fields with bilayer schemes beyond Laplacian metamaterials. EPL **135**, 54004 (2021)
38. Zhang, Z.R., Xu, L.J., Huang, J.P.: Controlling chemical waves by transforming transient mass transfer. Adv. Theory Simul. **5**, 2100375 (2022)
39. Xu, L.J., Huang, J.P., Ouyang, X.P.: Tunable thermal wave nonreciprocity by spatiotemporal modulation. Phys. Rev. E **103**, 032128 (2021)
40. Li, X.W., Fan, C.R., Huang, J.P.: Magnetocontrollable high-pass behavior of waveguides with magnetorheological fluids. EPJ Appl. Phys. **63**, 21001 (2013)
41. Zhao, L., Liu, B., Gao, Y.H., Zhao, Y.J., Huang, J.P.: Enhanced scattering of acoustic waves at interfaces. Front. Phys. **7**, 319–323 (2012)
42. Huang, J.P., Yu, K.W.: Nondegenerate four-wave mixing in graded metallic films. J. Appl. Phys. **97**, 013102 (2005)
43. Huang, J.P., Karttunen, M., Yu, K.W., Dong, L.: Dielectrophoresis of charged colloidal suspensions. Phys. Rev. E **67**, 021403 (2003)
44. Sha, W., Xiao, M., Huang, M., Gao, L.: Topology-optimized freeform thermal metamaterials for omnidirectionally cloaking sensors. Mater. Today Phys. **28**, 100880 (2022)
45. Xu, L.J., Dai, G.L., Huang, J.P.: Transformation multithermotics: controlling radiation and conduction simultaneously. Phys. Rev. Appl. **13**, 024063 (2020)
46. Dai, G.L., Yang, F.B., Xu, L.J., Huang, J.P.: Diffusive pseudo-conformal mapping: Anisotropy-free transformation thermal media with perfect interface matching. Chaos Solitons Fractals **174**, 113849 (2023)
47. Xu, L.J., Huang, J.P.: Transformation Thermotics and Extended Theories: Inside and Outside Metamaterials. Springer, Singapore (2023)
48. Huang, J.P.: Theoretical Thermotics: Transformation Thermotics and Extended Theories for Thermal Metamaterials. Springer, Singapore (2020)
49. Ye, C., Huang, J.P.: Non-classical oscillator model for persistent fluctuations in stock markets. Phys. A **387**, 1255 (2008)
50. Liu, L., Wei, J.R., Zhang, H.S., Xin, J.H., Huang, J.P.: A statistical physics view of pitch fluctuations in the classical music from Bach to Chopin: evidence for Scaling. PLoS ONE **8**, e58710 (2013)
51. Xu, L.J, Liu, J,R., Xu, G.Q., Huang, J.P., Qiu, C-W.: Giant, magnet-free, and room-temperature Hall-like heat transfer. Proc. Natl. Acad. Sci. USA **120**, e2305755120 (2023)
52. Jin, P., Liu, J.R., Xu, L.J., Wang, J., Ouyang, X.P., Jiang, J.-H., Huang, J.P.: Tunable liquid-solid hybrid thermal metamaterials with a topology transition. Proc. Natl. Acad. Sci. USA **120**, e2217068120 (2023)
53. Shen, X.Y., Jiang, C.R., Li, Y., Huang, J.P.: Thermal metamaterial for convergent transfer of conductive heat with high efficiency. Appl. Phys. Lett. **109**, 201906 (2016)

54. Xu, L.J., Xu, G.Q., Huang, J.P., Qiu, C.W.: Diffusive Fizeau drag in spatiotemporal thermal metamaterials. Phys. Rev. Lett. **128**, 145901 (2022)
55. Gao, Y., Jian, Y.C., Zhang, L.F., Huang, J.P.: Magnetophoresis of nonmagnetic particles in ferrofluids. J. Phys. Chem. C **111**, 10785 (2007)
56. Xu, L.J., Yang, S., Dai, G.L., Huang, J.P.: Transformation omnithermotics: simultaneous manipulation of three basic modes of heat transfer. ES Energy Environ. **7**, 65–70 (2020)
57. Shahrzadi, M., Davazdah Emami, M., Akbarzadeh, A.H.: Heat transfer in BCC lattice materials: conduction, convection, and radiation. Compos. Struct. **284**, 115159 (2021)
58. Yang, L., Deng, P., Wen, C., Wang, W.Q., Shen, H., Xu, H.X.: Radiative heat transfer in nanophotonics: from thermal radiation enhancement theory to radiative cooling applications. Acta Physica Sinica **69**, 036501 (2020)
59. Rephaeli, E., Raman, A.P., Fan, S.H.: Ultrabroadband photonic structures to achieve high-performance daytime radiative cooling. Nano Lett. **13**, 1457 (2013)
60. Raman, A.P., Anoma, M.A., Zhu, L.X., Rephaeli, E., Fan, S.H.: Passive radiative cooling below ambient air temperature under direct sunlight. Nature **515**, 540 (2014)
61. Zhai, Y., Ma, Y.G., David, S.N., Zhao, D.L., Lou, R.N., Tan, G., Yang, R.G., Yin, X.B.: Scalable-manufactured randomized glass-polymer hybrid metamaterial for daytime radiative cooling. Science **355**, 1062–1066 (2017)
62. Mandal, J., Fu, Y., Overvig, A.C., Jia, M., Sun, K., Shi, N.N., Zhou, H., Xiao, X., Yu, N., Yang, Y.: Hierarchically porous polymer coatings for highly efficient passive daytime radiative cooling. Science **362**, 315–319 (2018)
63. Liu, C.Y., Wu, Y.Z., Wang, B.X., Zhao, C.Y., Bao, H.: Effect of atmospheric water vapor on radiative cooling performance of different surfaces. Sol. Energy **183**, 218–225 (2019)

Chapter 14
Omnithermal Metamaterials: Mastering Diverse Heat Transfer Modes

Yixi Wang, Liujun Xu, Shuai Yang, and Gaole Dai

14.1 Opening Remarks

Heat transfer operates through three fundamental modes: conduction, convection, and radiation. Each possesses unique attributes and mechanisms, yet they often function synergistically. Take, for instance, solar vapor generation as example. In this context, radiation is pivotal, associated with the capture of solar energy. Convection is manifest in the evaporation of seawater, while conduction is ubiquitously involved in nearly every phase. In the study of heat transfer within aerogels, it's imperative to consider all three modes. At its core, proficient thermal management hinges on the harmonious interaction of conduction, convection, and radiation.

The effective control or manipulation of heat flow is an evolving research field combining transformation thermodynamics and metamaterials. Transformation theory, as a general and powerful methodology, has already been extended from wave systems (e.g., electromagnetic propagation) to diffusion systems (e.g., heat conduction [1], Noise Shielding, thus yielding the rapid development of thermal metamaterials or metadevices, i.e. thermal cloaks, concentrators, rotators, camouflaging, invisible sensors [2] and thermal transparency, have been proposed [3, 4]. Moreover, some novel thermal metamaterials are also involved, such as digital thermal metasurfaces, thermal chameleon-like metashells, energy-free thermostat devices, thermal dipoles, thermal crystals, phonon transport, and printed circuit boards containing various thermal metamaterials for heat dissipation of electronic devices. In addition

Y. Wang (✉) · S. Yang
Department of Physics, Key Laboratory of Micro and Nano Photonic Structures (MOE), and State Key Laboratory of Surface Physics, Fudan University, Shanghai 200438, China
e-mail: yxwang22@m.fudan.edu.cn

L. Xu
Graduate School of China Academy of Engineering Physics, Beijing 100193, China

G. Dai
School of Sciences, Nantong University, Nantong 226019, China

F.-B. Yang and J.-P. Huang, *Diffusionics*,
https://doi.org/10.1007/978-981-97-0487-3_14

to the typical thermal convection metamaterials, we also summarize the phenomena of thermal wave [5], zero-index cloak, thermal anti-parity-time symmetry, thermal convection–conduction crystal, negative thermal transport, and so on.

Transformation-based thermal metadevices manipulate heat flows through tailored constitutive parameters. However, these thermal metamaterials take only conductive effects into consideration [6]. Recent studies have begun to incorporate convective effects into their exploration of thermal metamaterials, leading to the emergence of innovative applications. However, it's worth noting that these studies have often focused on only one or two of the fundamental conduction, convection [7, 8], and radiation modes. This selective consideration allows researchers to delve deeper into specific aspects while potentially paving the way for a more comprehensive understanding of thermal metamaterial behaviors and their practical uses. For example, Xu and Huang designed circular/elliptical core-shell structured metamaterials with functions like thermal transparency [9], cloaking (the shell or cloak can be single-layered or bilayered) and expanding within such a conduction-radiation system [10].

Within the prevailing research landscape, there's a conspicuous gap in a holistic transformation theory that encompasses conduction, convection, and radiation concurrently. Each mechanism, given its distinct attributes, presents challenges when pursued for amalgamation into a singular theoretical construct. Nevertheless, considering the routine simultaneous manifestations of these processes in numerous systems, both the academic and industrial spheres are voicing an escalating need for a transformation theory that can integrally address all three facets.

Classical thermodynamics often helps to passively describe macroscopic heat phenomena of natural systems, which means people almost cannot change the heat phenomena, but understand them according to the four thermodynamic laws. In contrast, thermal metamaterials, together with the governing theories, make it possible to actively manipulate macroscopic heat phenomena of artificial systems, which enables people to change the heat phenomena at will.

Within the vast domain of "Physics" as a foundational discipline, thermal metamaterials have emerged as an innovative thermal system [11, 12]. They shed light on distinctive thermodynamic behaviors and enrich our understanding of thermodynamics and statistical physics [13–18]. Turning to the primary discipline of "Power Engineering and Engineering Thermophysics", there lies a fresh approach to heat transfer regulation. Theoretical thermodynamics focuses on the proactive manipulation of macroscopic thermal phenomena in engineered systems. This approach is anchored in the theoretical architecture of transformation thermodynamics and its ancillary theories. In essence, transformation thermodynamics employs a technique encompassing coordinate shifts between two separate spaces, enabling a meticulous integration of spatial geometric parameters with thermal attributes such as thermal conductivity.

The theories previously highlighted stand as the pinnacle of recent progress in theoretical thermodynamics. In conjunction with statistical thermophysics and heat transfer, they constitute an essential pillar in the expansive domain of thermodynamics.

In addressing the previously discussed challenges, a comprehensive study by Xu et al. [19] delves into the formulation of the transformation omnithermotics theory. This theory incorporates all three fundamental heat transfer modes simultaneously. Drawing on this foundation, the team introduced three prototypical devices: omnithermal cloaking, concentrating, and rotating. Respectively, these devices serve to shield central objects from detection, enhance local heat flux, and control the direction of local heat flux. Finite-element simulations validate the efficacy of these devices, showing impressive results in both steady-state and transient scenarios. Moreover, the researchers employed porous media to modulate flow velocity, ensuring the practical viability of their approach. With the present theory, Yang et al. [20] further design an omnithermal metamaterial switchable between transparency and cloaking, which results from the nonlinear properties of radiation and convection. Moreover, Wang et al. [21] design an omnithermal restructurable thermal metasurface for infrared illusion. The following sections will delve deeper into the intricacies of this groundbreaking theory.

14.2 Omnithermal Metamaterials Based on Transformation Theory

14.2.1 Theory of Transformation Omnithermotics

Recently, several researchers introduced the notion of transformation omnithermotics, a holistic model designed to manipulate conduction, convection, and radiation concurrently. Initially, these scholars examined the heat transfer equation—a continuity equation representing total heat flux—and devised an array of devices, encompassing cloaking, concentrating, and rotating functionalities. Within this context, the radiative flux is characterized using the Rosseland diffusion approximation, transforming the heat transfer equation into a convection-diffusion equation. Here, the combined temperature-responsive conductivity integrates both conductive and convective elements. Notably, both conductive/radiative thermal conductivities and velocity undergo direct transformations in line with the transformation theory.

Subsequently, the focus shifted to a collection of equations that govern heat and mass transfer within porous media. This collection encompasses the Darcy law, the continuity equation for fluid motion, and the aforementioned heat transfer equation. Given the transformation convection theory highlighted earlier, the design of pertinent thermal devices involves altering both the permeability of porous media (or the dynamic viscosity of fluids in the case of convection) and the collective thermal conductivity for conduction-radiation. Intriguingly, porous media serve as a representative model that encapsulates all three primary heat transfer mechanisms, especially at elevated temperatures. Consequently, the researchers forecasted the emergence of omnithermal metamaterials capable of orchestrating heat conduction, convection, and radiation in unison. Detailed explorations are as followed.

Fluids and gases play a crucial role in convective heat transfer. Regardless of their varied forms, they obey the same heat transfer equation. Xu et al. studied the temporary heat transfer process in pure fluids or gases, considering conduction, convection, and radiation. This process can be described by

$$\begin{aligned} \rho_f C_f \frac{\partial T}{\partial t} + \nabla \cdot (-\kappa_f \cdot \nabla T + \rho_f C_f \boldsymbol{v}_f T - \boldsymbol{\alpha}_f T^3 \cdot \nabla T) = 0, \\ \frac{\partial \rho_f}{\partial t} + \nabla \cdot (\rho_f \boldsymbol{v}_f) = 0, \end{aligned} \tag{14.1}$$

where ρ_f, C_f, $\boldsymbol{\kappa}_f$, and $\boldsymbol{v}_f$ are the density, heat capacity, thermal conductivity, and velocity of fluid, respectively $\boldsymbol{\alpha}_f (= 16\beta_f^{-1}\boldsymbol{n}_f^2\sigma/3)$ can be regarded as radiative coefficient where β_f, $\boldsymbol{n}_f$, and $\sigma (= 5.67 \times 10^{-8} Wm^{-2}K^{-4}$ are the Rosseland mean attenuation coefficient, relative refractive index, and the Stefan–Boltzmann constant, respectively. T and t denote temperature and time, respectively. Physically speaking, the two equations in Eq. (1) describe the conservation of heat flux and mass flux, respectively. Conductive flux $\boldsymbol{J}_1$is determined by the Fourier law$\boldsymbol{J}_1 = -\kappa_f \cdot \nabla T$; convective flux $\boldsymbol{J}_2$ is given by $\boldsymbol{J}_2 = \rho_f C_f \boldsymbol{v}_f T$; radiative flux $\boldsymbol{J}_3$ is dealt with the Rosseland diffusion approximation $\boldsymbol{J}_3 = -\alpha_f T^3 \cdot \nabla T$; and total flux $\boldsymbol{J}_T$ is the summation of conductive, convective, and radiative fluxes $\boldsymbol{J}_T = \boldsymbol{J}_1 + \boldsymbol{J}_2 + \boldsymbol{J}_3$.

Equation (14.1) is form-invariant under the space transformation from a curvilinear space S to a physical space S', which is determined by the Jacobian transformation matrix ∇. To prove the form-invariance, Xu et al. wrote down the component form of Eq. (14.1). In the curvilinear space with a set of contravariant basis $(\boldsymbol{g}^i, \boldsymbol{g}^j, \boldsymbol{g}^k)$ and corresponding contravariant components (s^i, s^j, s^k), Eq. (14.1) can be rewritten as

$$\begin{aligned} \sqrt{g}\rho_f C_f \partial_t T + \partial_i (\sqrt{g}(-\kappa_f^{ij} \partial_j T + \rho_f C_f v_f^i T - \alpha_f^{ij} T^3 \partial_j T)) = 0, \\ \sqrt{g}\partial_t \rho_f + \partial_i (\sqrt{g}\rho_f v_f^i) = 0, \end{aligned} \tag{14.2}$$

where g is the determinant of the matrix $\boldsymbol{g}_i \cdot \boldsymbol{g}_j$, and $(\boldsymbol{g}_i, \boldsymbol{g}_j, \boldsymbol{g}_k)$ is a set of covariant basis. Equation (14.2) is written in the curvilinear space, which should be rewritten in the physical space with the Cartesian coordinates $(s^{i'}, s^{j'}, s^{k'})$,

$$\begin{aligned} \sqrt{g}\rho_f C_f \partial_t T + \partial_{i'} \frac{\partial s^{i'}}{\partial s^i} \left(\sqrt{g} \left(-\kappa_f^{ij} \frac{\partial s^{j'}}{\partial s^j} \partial_{j'} T + \rho_f C_f v_f^i T - \alpha_f^{ij} T^3 \frac{\partial s^{j'}}{\partial s^j} \partial_{j'} T \right) \right) = 0, \\ \sqrt{g}\partial_t \rho_f + \partial_{i'} \frac{\partial s^{i'}}{\partial s^i} (\sqrt{g}\rho_f v_f^i) = 0, \end{aligned} \tag{14.3}$$

where $\partial s^{i'}/\partial s^i$ and $\partial s^{j'}/\partial s^j$ are just the components of the Jacobian transformation matrix Λ, and $\sqrt{g} = 1/det\boldsymbol{\Lambda}$. The key to transformation theory is to turn space transformation into material transformation. For this purpose, Eq. (14.3) can be rewritten as

$$\frac{\rho_f}{det\mathbf{\Lambda}}C_f\partial_t T+\partial_{i'}\left(-\frac{\frac{\partial s^{i'}}{\partial s^i}\kappa_f^{ij}\frac{\partial s^{j'}}{\partial s^j}}{det\mathbf{\Lambda}}\partial_{j'}T+\frac{\rho_f}{det\mathbf{\Lambda}}C_f\frac{\partial s^{i'}}{\partial s^i}v_f^i T-\frac{\frac{\partial s^{i'}}{\partial s^i}\alpha_f^{ij}\frac{\partial s^{j'}}{\partial s^j}}{det\mathbf{\Lambda}}T^3\partial_{j'}T\right)=0,$$
$$\partial_t\frac{\rho_f}{det\mathbf{\Lambda}}+\partial_{i'}\left(\frac{\rho_f}{det\mathbf{\Lambda}}\frac{\partial s^{i'}}{\partial s^i}v_f^i\right)=0. \tag{14.4}$$

Thus, transformation rules can be derived as

$$\begin{cases}\rho_f'=\rho_f/det\mathbf{\Lambda},\\ C_f'=C_f,\\ \boldsymbol{\kappa}_f'=\mathbf{\Lambda}\boldsymbol{\kappa}_f\mathbf{\Lambda}^{\boldsymbol{\tau}}/det\Lambda,\\ \boldsymbol{v}_f'=\mathbf{\Lambda}\boldsymbol{v}_f,\\ \boldsymbol{\alpha}_f'=\mathbf{\Lambda}\boldsymbol{\alpha}_f\mathbf{\Lambda}^{\tau}/det\mathbf{\Lambda}.\end{cases} \tag{14.5}$$

where $\mathbf{\Lambda}^{\tau}$ is the transpose of $\mathbf{\Lambda}$.

The radiative coefficient is defined by two primary parameters: the Rosseland mean attenuation coefficient and the relative refractive index. Given that natural materials exhibit a limited range of relative refractive indices, there's no need to alter them, which means $\boldsymbol{n}_f'=\boldsymbol{n}_f$. Consequently, the transformation of the radiative coefficient $\boldsymbol{\alpha}_f$ is given by $\boldsymbol{\beta}_f'=\mathbf{\Lambda}^{-\tau}\boldsymbol{\beta}_f\mathbf{\Lambda}^{-1}det\mathbf{\Lambda}$. For simplicity, relative refractive indices were also left untransformed in the finite-element simulations.

14.2.2 Applications of Omnithermal Metamaterials Based on Transformation Theory

The space transformation of cloaking is

$$\begin{aligned}r'&=\frac{(R_2-R_1)r}{R_2}+R_1\\ \theta'&=\theta\end{aligned} \tag{14.6}$$

where R_1 and R_2 are the inner and outer radii. respectively.

The space transformation of concentrating is

$$\begin{aligned}r'&=\frac{R_1 r}{R_m},(r<R_m)\\ r'&=\frac{(R_1-R_m)R_2+(R_2-R_1)r}{R_2-R_m},(R_m<r<R_2)\end{aligned} \tag{14.7}$$

where R_m is a medium radius determining the concentrating ratio.

The space transformation of rotating is

$$\begin{aligned} r' &= r, \\ \theta' &= \theta + \theta_0, (r < R_1) \\ \theta' &= \theta + \frac{(r - R_2)\theta_0}{(R_1 - R_2)}, (R_1 < r < R_2) \end{aligned} \tag{14.8}$$

where θ_0 is a rotation degree. Then, the Jacobian transformation matrix of Eqs. (14.6)-(14.8) can be calculated by

$$\begin{pmatrix} \frac{\partial r'}{\partial r} & \frac{\partial r'}{r\partial \theta} \\ \frac{r'\partial \theta'}{\partial r} & \frac{r'\partial \theta'}{r\partial \theta} \end{pmatrix} = \Lambda \tag{14.9}$$

To explore the varying impacts of the three primary heat transfer methods, Xu et al. simulated three distinct scenarios. In the first scenario (I), the temperature range is between 300 and 360 K with the background velocity directed along the +x axis. Here, convection plays a predominant role. For the second scenario (II), the temperature spans from 300–1200 K and the background velocity remains on the +x axis. In this case, the effects of radiation become evident. In the third scenario (III), with the same temperature range as (II), the background velocity shifts to the -x axis. For this scenario, the overall flux diminishes due to the convective flux moving in the opposite direction compared to scenarios (I) and (II). When starting at an initial temperature of 300 K, it takes approximately 80, 30, and 50 min respectively for these scenarios to stabilize.

Figure 14.1 presents the transient simulation results of cloaking. The temperature evolutions with time under three different cases (say, I, II, and III) are demonstrated in Fig. 14.1a–d, e–h, and i-j, respectively. To avoid the problems of singular parameters, the boundary at r = R_1 is set with insulated and no-flow conditions. In this way, any object can be placed in the central white regions of Fig. 14.1. Moreover, the background isotherms are kept unchanged, thus confirming the cloaking effect. Xu et al. also plotted the conductive, convective, radiative, and total flux of the background in Fig. 14.1d, h, and l for quantitative analyses. The distributions of heat fluxes are presented in Fig. 14.2a–c.

The concentrating effect can be observed in Fig. 14.3. Central isotherms in each simulation are markedly denser than those in peripheral areas, signifying enhanced heat flux concentrations. This aligns with the expected concentration effect. In Fig. 14.4, the rotation effect is evident. The central isotherms take on a horizontal orientation, with higher temperatures prominent at the base. This denotes a vertically upward direction of heat flux, signifying a successful rotation of heat fluxes by an angle of $\pi/2$ rad.

In the aforementioned discussion, the flow velocity was directly transformed, given that the velocity field had been pre-established. While this approach is mathematically sound, it poses significant challenges in practical experimentation. To address this, Xu et al. modulated flow velocity using porous media, ensuring a more feasible execution.

To confirm the theoretical analyses, Xu et al. also performed finite-element simulations. The first row in Fig. 14.5 of Ref. [19] presents the results with transform-

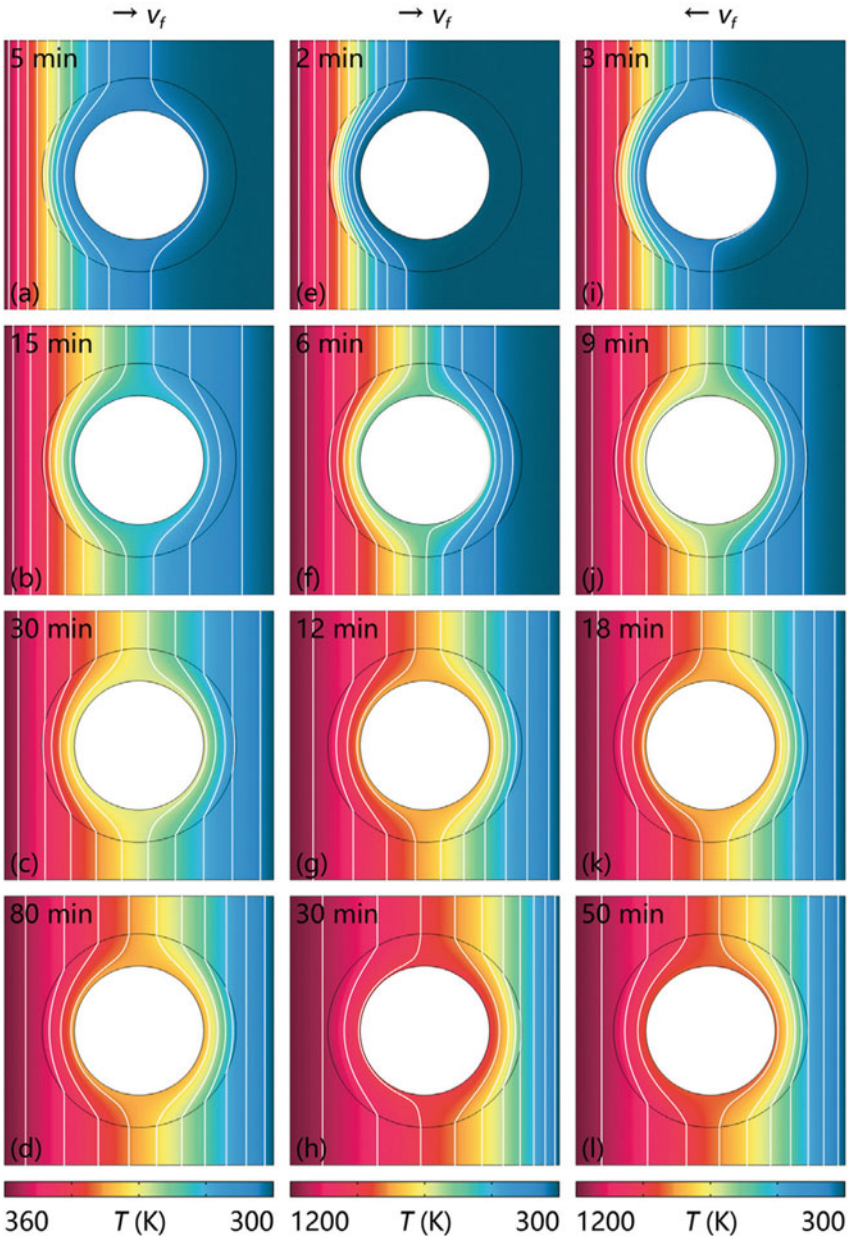

Fig. 14.1 Temporary cloaking simulations. The size of each simulation box is 0.1 m × 0.1 m, $R_1 = 0.024$ m, and $R_2 = 0.036$ m, where R_1 and R_2 are the inner and outer radii, respectively. The parameters of background fluid are as following: density of the fluid are as following: density of the fluid $\rho_f = 1000$ kg/m^3, heat capacity of the fluid $C_f = 1000$ J kg^{-1} K^{-1}, thermal conductivity of the fluid $\kappa_f = 1$ W m^{-1} K^{-1}, velocity of the fluids $\upsilon_f = 10^{-5}$ m/s, the Rosseland mean attenuation coefficient $\beta_f = 100$ m^{-1}, and relative refractive index $\boldsymbol{n}_f$=1. **a–d**, **e–h**, and **i–l** show the temperature evolutions over time with case I, II, and III, respectively. White lines represent isotherms, and color surfaces denote temperature distributions. (from Ref. [19])

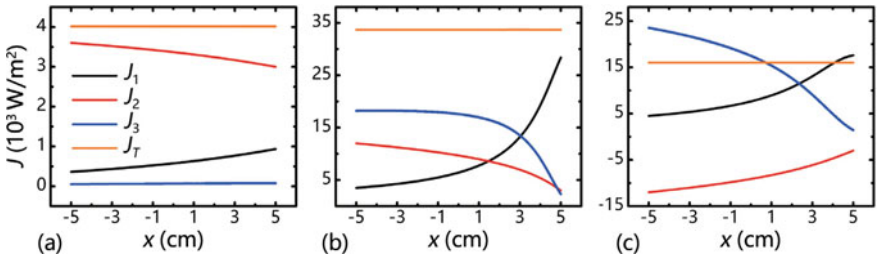

Fig. 14.2 Heat flux distributions in background along x axis. **a**, **b**, and **c** present the distributions of steady heat flux with the same boundary conditions applied in the first, second, and third columns in Fig. 14.1, respectively. (from Ref. [19])

ing the permeability of porous media as $\boldsymbol{\eta}_s' = \boldsymbol{\Lambda}\boldsymbol{\eta}_s\boldsymbol{\Lambda}^{\tau}/det\,\boldsymbol{\Lambda}$. The second row in Fig. 14.5 of Ref. [19] shows the results with directly transforming flow velocity as $\boldsymbol{v}_f' = \boldsymbol{\Lambda}\boldsymbol{v}_f/det\,\boldsymbol{\Lambda}$. As a result, they confirmed the feasibility of controlling flow velocity with designed permeability by comparing the velocity distributions of two different methods.

14.3 Omnithermal Metamaterials Based on Effective Medium Theory

In their work, Yang et al. [20] introduced an effective medium theory that simultaneously addresses conductive, radiative, and convective (termed as "omnithermal") processes. This theory is anchored on the Fourier law, the Rosseland diffusion approximation, and the Darcy law. By considering all heat transfer modalities within a porous medium, they deduced that the passive and stable heat transfer process is governed by the Laplace equation, expressed as follows:

$$\nabla \cdot (-\kappa \nabla T - \gamma T^3 \nabla T - \rho_f c_f \xi / \eta_f T \nabla P) = 0 \tag{14.10}$$

where ρ_f and c_f are the density and heat capacity of the fluid respectively. ξ is the permeability of the porous medium. κ is the thermal conductivity of the porous medium. γ is the radiative coefficient.

For the condition that the temperature field and the pressure field are perpendicular, Eq. (14.10) can be rewritten as

$$\begin{aligned} \nabla \cdot (-\kappa \nabla T - \gamma T^3 \nabla T) &= \rho_f c_f \nabla \cdot (\xi / \eta_f T \nabla P) \\ &= \rho_f c_f \nabla \cdot (-vT) = -\rho_f c_f v \cdot \nabla T \end{aligned} \tag{14.11}$$

Using the current theory, we have developed an omnithermal metamaterial that can switch between transparency and cloaking. This capability stems from the non-

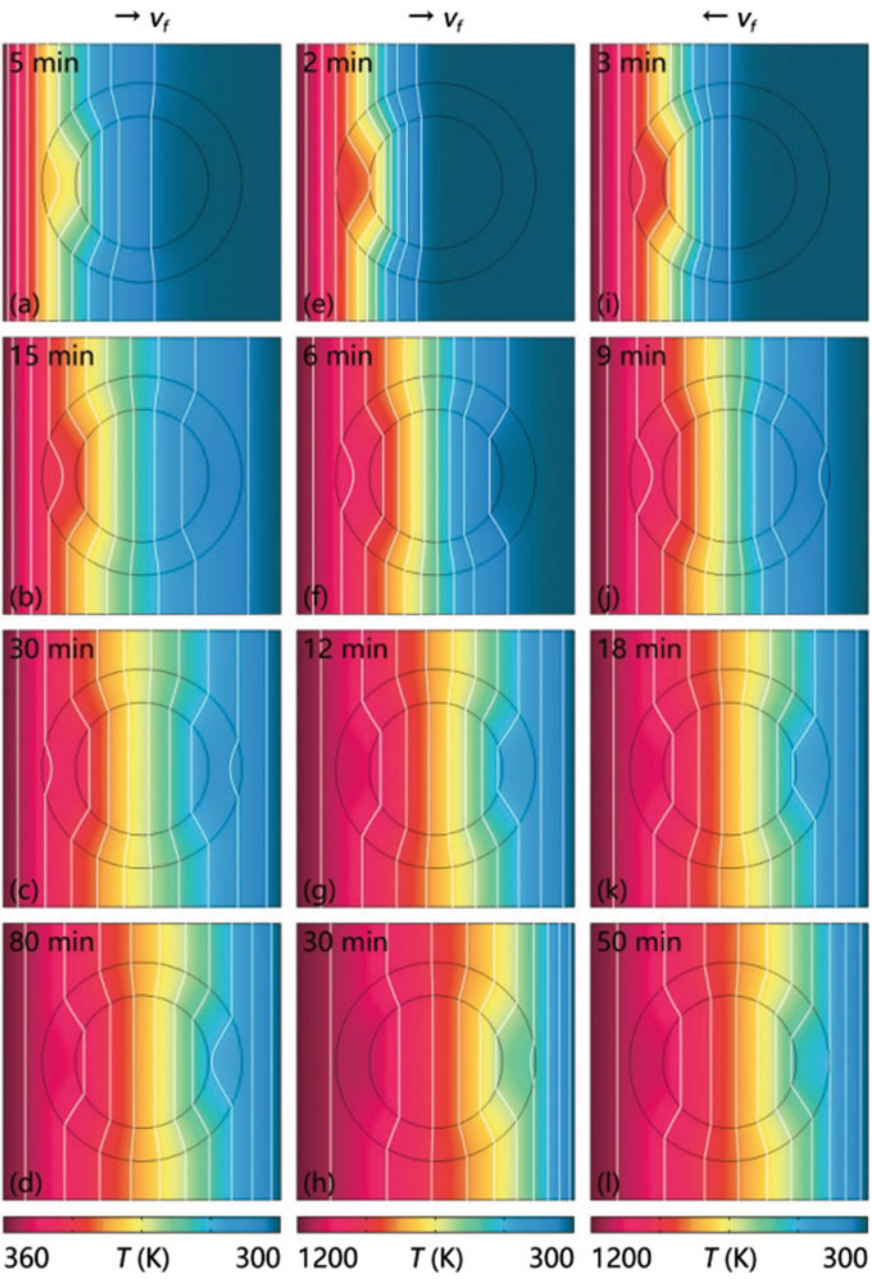

Fig. 14.3 Temporary concentrating simulations. The background parameters and boundary conditions are the same as those for Fig. 14.1. The transformation media and flow velocity are designed according to Eq. (14.7) where $R_m = 0.032$ m. (from Ref. [19])

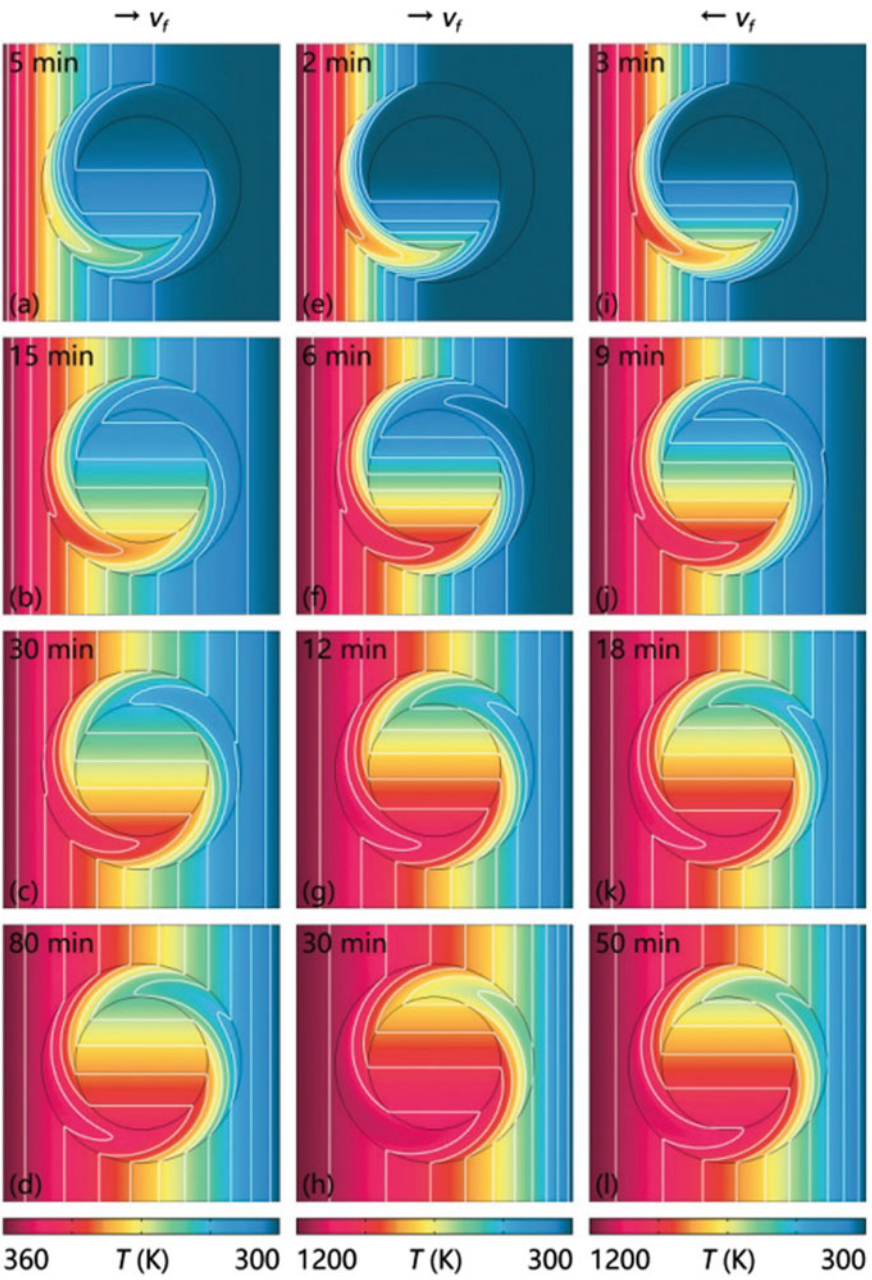

Fig. 14.4 Temporary rotating simulations. The background parameters and boundary conditions are the same as those for Fig. 14.1. The transformation media and flow velocity are designed according to Eq. (14.8) where $\theta = \pi/2$. (from Ref. [19])

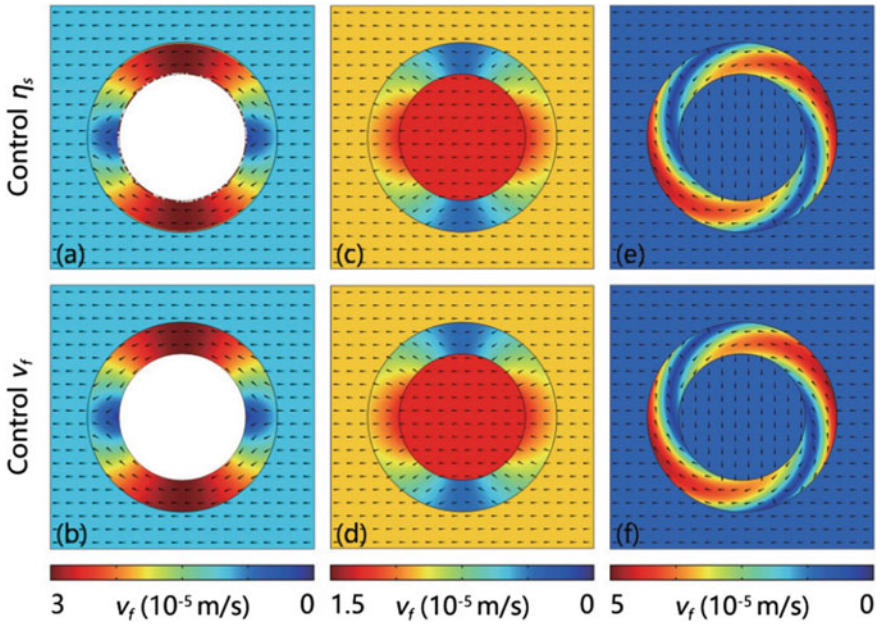

Fig. 14.5 Manipulating flow velocity with porous media. Color surfaces denote velocity distributions. **a**, **c**, and **e** are the velocity distributions obtained from transforming the permeability of porous media. **b**, **d**, and **f** are the velocity distributions obtained from directly transforming flow velocity. The boundary conditions of the first row are 1000 and 0 Pa for the left and right boundaries, and no-flow conditions for the upper and lower boundaries. The permeability of porous media in the background is $10^{-12}m^2$ (which is common in nature), and the dynamic viscosity of fluids is 0.001 Pa s. (from Ref. [19])

linear properties of radiation and convection. Finite-element simulations validate the robustness of our approach across varied boundary conditions.

Leveraging the nonlinear properties of radiation and convection, we introduce a switchable omnithermal metamaterial. This metamaterial can adaptively alternate between transparency, as shown in Fig. 14.6a, and cloaking, depicted in Fig. 14.6b, based on temperature variations. Finite-element simulations have been conducted to demonstrate the viability of our approach.

In their research, Wang et al. [21] incorporate the three fundamental modes of heat transfer, termed omnithermotics, into theoretical designs and utilize radiation-cavity effects in experimental fabrication. Our approach enables the synergistic tuning of surface temperature and emissivity. Notably, these metasurfaces operate effectively in environments with fluctuating temperatures and during transient states. This strategy offers not just a platform for designing adaptable thermal illusions, but also demonstrates resilience against multi-frequency detection.

They conceptualized an omnithermal, reconfigurable thermal metasurface for infrared illusion, as depicted in Fig. 14.7. By individually customizing each block

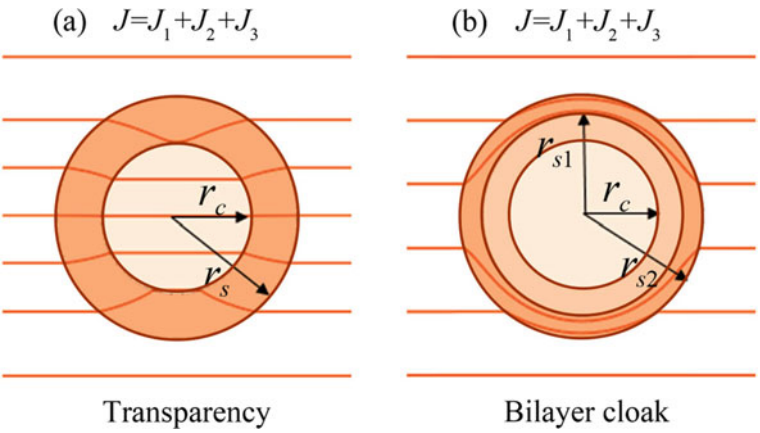

Fig. 14.6 Schematic diagrams of **a** transparency and **b** cloaking. Orange lines represent heat fluxes. $\boldsymbol{J}$ is the total heat flux and its components, i.e., conductive flux $\boldsymbol{J}_1$, radiative flux $\boldsymbol{J}_2$, and convective flux $\boldsymbol{J}_3$. (from Ref. [20])

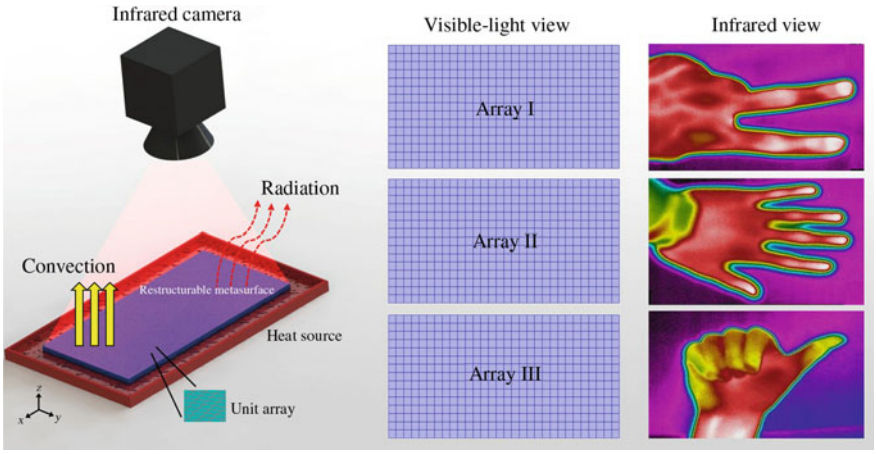

Fig. 14.7 The proposed thermal metasurface. The units are arranged in three arrays (array I, array II, and array III), which can form three different images (specific gestures) in an infrared camera (right column). Meanwhile, they are similar when viewed in visible light (middle column). (from Ref. [21])

unit and arranging them in a specific sequence, distinctive infrared patterns can be realized. Taking into account the three heat transfer modes—conduction, convection, and radiation (omnithermotics)—we observe their influence on surface temperatures. Through the radiation-cavity effect, for instance, the effective emissivity's reliance on the dimensions, forms, and ratios of surface cavities, it's possible to achieve a distinct emissivity for each unit over a broad temperature spectrum.

14.4 Challenges and Prospects of Transformation Omnithermotics

For many standard coordinate transformations, devising an anisotropic radiative conductivity or a radiative conductivity tensor is challenging. This mirrors the complexities in transformation multithermotics. A pragmatic approach involves the use of composites crafted from bulk homogeneous isotropic materials, each possessing distinct Rosseland mean opacities or radiative conductivities. Viewing this from a microscopic angle, the anisotropy within an anisotropic diffusive radiation model for porous media typically arises from the uniquely directional scattering and absorption processes. The radiative conductivity tensor is intricately related to the extinction and scattering coefficients. In many scenarios, the Beer–Lambert law may not hold true, necessitating adjustments or extensions to the Rosseland model. Nonetheless, if one requires a radiative transport equation characterized by anisotropic radiative thermal conductivity in transformed space, the radiation process doesn't strictly adhere to every assumption of the Rosseland diffusion approximation. Instead, a broader radiative Fourier law can encapsulate it.

For experimental demonstration, porous media can be harnessed, with tunable thermal conductivities, permeabilities, and extinction coefficients. Encouragingly, as alluded to above, experiments focusing on either conduction or convection have been executed. However, the pressing hurdle for current objectives is seamlessly integrating heat radiation into the established models.

Xu et al. [19] established the theory of transformation omnithermotics to control thermal conduction, convection and radiation simultaneously. In other words, within the theoretical framework of transformation omnithermotics, Xu et al. had achieved a unification among the three basic modes of heat transfer. They further designed three devices with functions of cloaking, concentrating, and rotating as model applications. Finite-element simulations are used to confirm the theory. To ensure the feasibility and completeness of this work, Xu et al. also applied porous media to control flow velocity. These results have potential applications, say, in solar vapor generation or aerogel insulation, where conduction, convection, and radiation must be taken into account simultaneously.

14.5 Conclusion

In conclusion, Xu et al. delved into the intricacies of conductive and radiation fluxes, employing the Fourier law and the Rosseland diffusion approximation respectively. While the Fourier law provides accurate predictions at the macroscopic scale, it falters at the nanoscale where phonons emerge as the primary heat transfer carriers. The Rosseland diffusion approximation holds relevance in optically dense media, denoting scenarios where the photon's mean free path is substantially shorter than the system's dimensions. Consequently, this approximation aligns with far-field effects.

While the current theory proficiently manages far-field thermal radiation, it is not inherently equipped to address near-field thermal radiation, which is steered by the classic fluctuating electrodynamics theory. Thus, delving deeper into near-field thermal radiation remains on the horizon. For convective flux, they employed the Darcy law, harnessing porous media to regulate flow velocity. The Navier-Stokes equation presents a viable alternative for managing drag-free thermal convection. These insights harbor significant implications, particularly in contexts necessitating the concurrent consideration of all three fundamental heat transfer modes.

Furthermore, the transformation theory doesn't confine designs to specific geometries, thus allowing for the adaptation of these omnithermal devices into intricate forms like ellipses. Importantly, this theory can also accommodate any blend of the three core heat transfer modes, as long as transformation protocols are upheld. For tangible demonstrations, one might consider the heat transfer properties exhibited by aerogels. Within aerogels, both fluids and gases can serve as the carriers of convective flux. Multilayered structures offer a platform to manifest anisotropy and non-uniformity. Additional porous materials, with adjustable porosity like ceramics, metals, and rocks, also emerge as promising candidates.

References

1. Fan, C.Z., Gao, Y., Huang, J.P.: Shaped graded materials with an apparent negative thermal conductivity. Appl. Phys. Lett. **92**, 251907 (2008)
2. Jin, P., Xu, L.J., Jiang, T., Zhang, L., Huang, J.P.: Making thermal sensors accurate and invisible with an anisotropic monolayer scheme. Int. J. Heat Mass Transf. **163**, 120437 (2020)
3. Huang, J.P.: Theoretical Thermotics: Transformation Thermotics and Extended Theories for Thermal Metamaterials. Springer, Singapore (2020)
4. Wang, J., Dai, G.L., Huang, J.P.: Thermal metamaterial: fundamental, application, and outlook. iScience **23**, 101637 (2020)
5. Xu, L.J., Huang, J.P.: Active thermal wave cloak. Chin. Phys. Lett. **37**, 120501 (2020)
6. Shen, X.Y., Jiang, C.R., Li, Y., Huang, J.P.: Thermal metamaterial for convergent transfer of conductive heat with high efficiency. Appl. Phys. Lett. **109**, 201906 (2016)
7. Dai, G.L., Huang, J.P.: A transient regime for transforming thermal convection: cloaking, concentrating and rotating creeping flow and heat flux. J. Appl. Phys. **124**, 235103 (2018)
8. Xu, L.J., Wang, J., Dai, G.L., Yang, S., Yang, F.B., Wang, G., Huang, J.P.: Geometric phase, effective conductivity enhancement, and invisibility cloak in thermal convection-conduction. Int. J. Heat Mass Transf. **165**, 120659 (2021)
9. Xu, L.J., Yang, S., Huang, J.P.: Thermal transparency induced by periodic interparticle interaction. Phys. Rev. Appl. **11**, 034056 (2019)
10. Xu, L.J., Dai, G.L., Huang, J.P.: Transformation multithermotics: controlling radiation and conduction simultaneously. Phys. Rev. Appl. **13**, 024063 (2020)
11. Xu, L.J., Yang, S., Huang, J.P.: Thermal theory for heterogeneously architected structure: fundamentals and application. Phys. Rev. E **98**, 052128 (2018)
12. Xu, L.J., Xu, G.Q., Huang, J.P., Qiu, C.-W.: Diffusive Fizeau drag in spatiotemporal thermal metamaterials. Phys. Rev. Lett. **128**, 145901 (2022)
13. Yang, S., Xu, L.J., Wang, R.Z., Huang, J.P.: Full control of heat transfer in single-particle structural materials. Appl. Phys. Lett. **111**, 121908 (2017)
14. Gao, Y., Jian, Y.C., Zhang, L.F., Huang, J.P.: Magnetophoresis of nonmagnetic particles in ferrofluids. J. Phys. Chem. C **111**, 10785 (2007)

15. Dong, L., Huang, J.P., Yu, K.W., Gu, G.Q.: Dielectric response of graded spherical particles of anisotropic materials. J. Appl. Phys. **95**, 621–624 (2004)
16. Huang, J.P., Karttunen, M., Yu, K.W., Dong, L.: Dielectrophoresis of charged colloidal suspensions. Phys. Rev. E **67**, 021403 (2003)
17. Ye, C., Huang, J.P.: Non-classical oscillator model for persistent fluctuations in stock markets. Phys. A **387**, 1255 (2008)
18. Liu, L., Wei, J.R., Zhang, H.S., Xin, J.H., Huang, J.P.: A statistical physics view of pitch fluctuations in the classical music from Bach to Chopin: evidence for scaling. PLoS ONE **8**, e58710 (2013)
19. Xu, L.J., Yang, S., Dai, G.L., Huang, J.P.: Transformation omnithermotics: simultaneous manipulation of three basic modes of heat transfer. ES Energy Environ. **7**, 65–70 (2020)
20. Yang, S., Xu, L.J., Dai, G.L., Huang, J.P.: Omnithermal metamaterials switchable between transparency and cloaking. J. Appl. Phys. **128**, 095102 (2020)
21. Wang, J., Yang, F.B., Xu, L.J., Huang, J.P.: Omnithermal restructurable metasurfaces for both infrared-light illusion and visible-light similarity. Phys. Rev. Appl. **14**, 014008 (2020)

Chapter 15
Omnithermal Metamaterials: Designing Universally Thermo-Adjustable Metasurfaces

Chuanxin Zhang, Jun Wang, Fubao Yang, and Liujun Xu

15.1 Opening Remarks

Thermal diffusion, the process of heat transfer from regions of higher temperature to lower temperature, is crucial in various natural and engineered systems [1–5]. The ability to control and manipulate thermal diffusion has significant practical implications in various fields, including thermal regulation, sensing, and imaging technologies [6–12]. Metamaterials have emerged as a powerful tool for achieving unprecedented control over physical phenomena, including heat, sound, and electromagnetic waves [13–19]. These artificial structures are designed to exhibit unique properties not found in naturally occurring materials, allowing researchers to manipulate wave propagation, bend light, create perfect lenses, and even realize cloaking devices [20–29]. In the context of thermal diffusion, metamaterials offer opportunities to tailor and enhance heat transfer processes.

Omnithermal restructurable metasurfaces, a specific class of metamaterials, have attracted considerable interest and research attention [30, 31]. These metasurfaces have the potential to control thermal diffusion not only in the infrared domain but

C. Zhang (✉)
Nanjing Institute of Astronomical Optics & Technology, Chinese Academy of Sciences, Nanjing 210042, China

CAS Key Laboratory of Astronomical Optics & Technology, Nanjing Institute of Astronomical Optics & Technology, Nanjing 210042, China
e-mail: cxzhang@niaot.ac.cn

J. Wang
School of Energy and Materials, Shanghai Polytechnic University, Shanghai 201209, China

F. Yang
Department of Physics, State Key Laboratory of Surface Physics, and Key Laboratory of Micro and Nano Photonic Structures (MOE), Fudan University, Shanghai 200438, China

L. Xu
Graduate School of China Academy of Engineering Physics, Beijing 100193, China

F.-B. Yang and J.-P. Huang, *Diffusionics*,
https://doi.org/10.1007/978-981-97-0487-3_15

also in the visible-light regime [32–35]. This capability opens up a wide range of applications, including invisible thermal camouflage, anticounterfeiting measures, novel imaging techniques, and precise temperature regulation.

This chapter aims to explore the realm of omnithermal restructurable metasurfaces, focusing on their design principles, experimental demonstrations, and potential applications. It will investigate how these metasurfaces can be tailored to achieve thermal infrared illusions, where objects appear to have different temperatures than their actual states, and visual similarities, where objects mimic the appearance of other materials. Through a comprehensive analysis of theoretical models and experimental findings, the chapter aims to provide a deep understanding of the underlying physics and engineering strategies behind these remarkable materials.

Recent advancements in infrared illusion have focused on two approaches: regulating surface temperatures and designing surface emissivities. For instance, Fig. 15.1 illustrates a human infrared thermogram captured using a digital thermal metasurface [2]. However, current research has limitations, as it often overlooks thermal convection and radiation in conductive systems, and surface structures remain distinguishable under visible light [36–38]. Tuning emissivities provides an alternative approach but requires phase-change materials and additional installations. The integration of both methods into a single platform presents challenges, as there is currently a lack of practical and synergistic solutions available.

To overcome these limitations, an omnithermal reconfigurable thermal metasurface is designed to simultaneously tune surface temperatures and emissivities on a single platform. By tailoring individual block units and assembling them into specific arrays, distinctive infrared patterns can be produced, as depicted in Fig. 15.2. The design incorporates all three modes of heat transfer: conduction, convection, and radiation, allowing for tailored surface temperatures and specific emissivities over a broad temperature range. This singular platform enables the symbiotic tailoring of both surface temperature and emissivity, achieving infrared illusions and visible-light similarities simultaneously. This chapter aims to uncover the potential of omnithermal restructurable metasurfaces in enhancing thermal diffusion, shedding light on their promising prospects for scientific advancement and technological innovation. Understanding the fundamental principles and capabilities of these metamaterials will pave the way for transformative progress in fields that rely on precise control of heat transfer processes.

The organization of this chapter is structured as follows: Firstly, it explores properties and design principles of omnithermal restructurable metasurfaces, emphasizing the consideration of all three heat transfer modes and the manipulation of surface temperature and emissivity. It then examines the experimental methods used to fabricate and characterize these metasurfaces, addressing the challenges in their practical realization. Finally, it discusses the potential applications of omnithermal restructurable metasurfaces, encompassing areas such as infrared illusion, visible-light similarity, anticounterfeiting measures, and temperature manipulation.

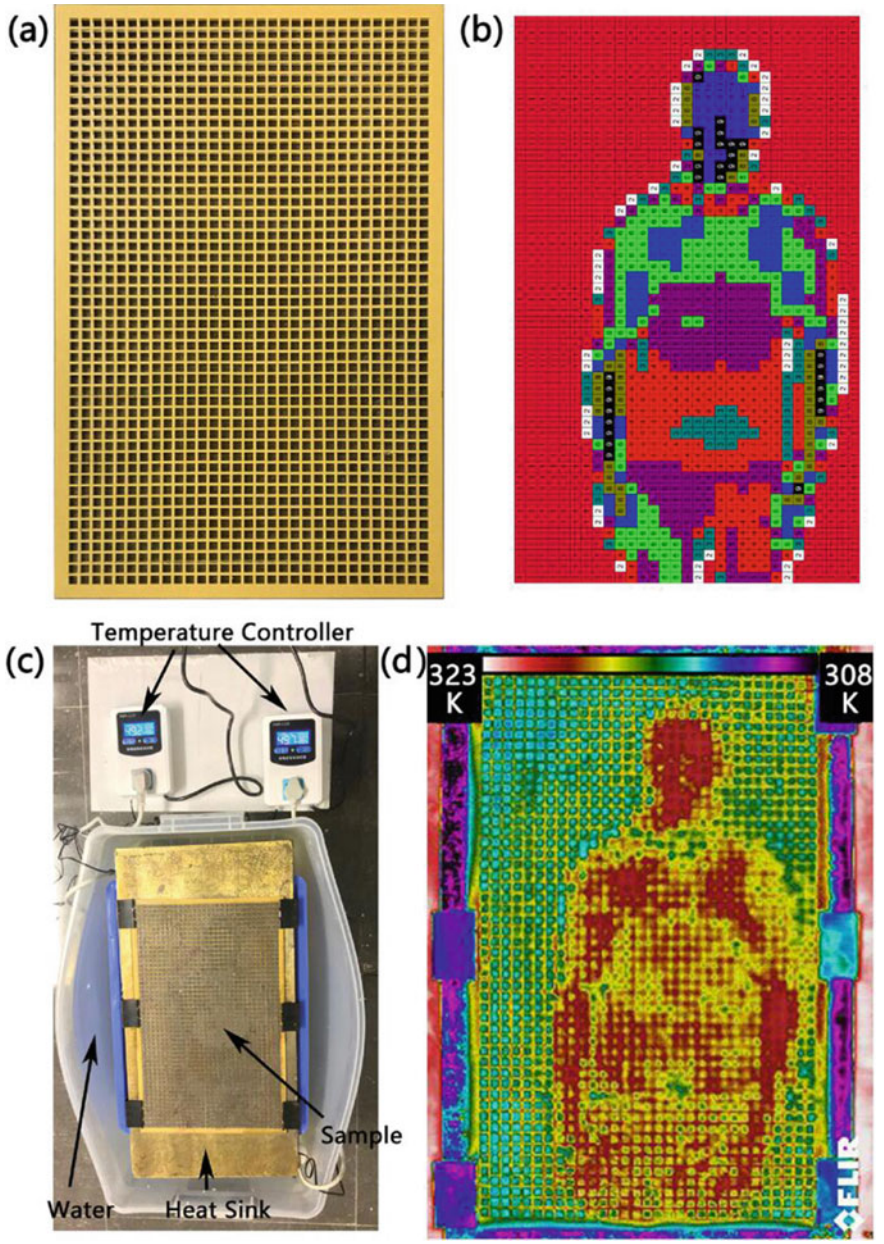

Fig. 15.1 Acrylic plate drilled with a square lattice of holes representing thermal pixels and corresponding thermal conductivities. (from Ref. [2])

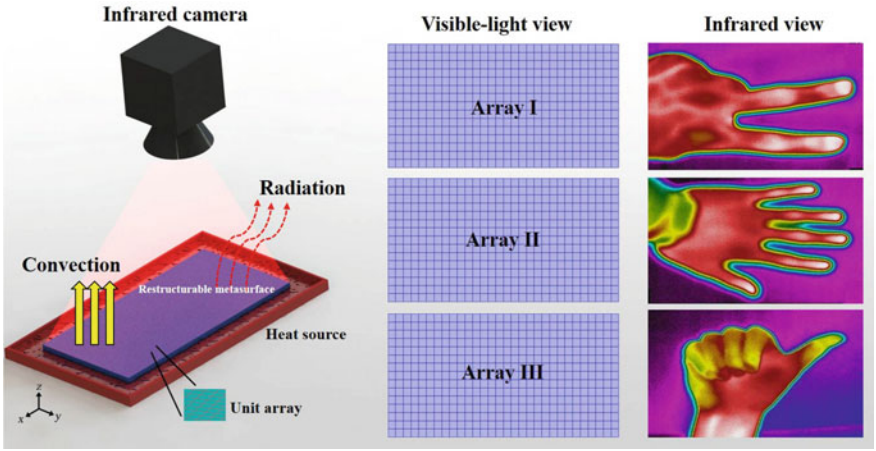

Fig. 15.2 Schematic illustration of the proposed thermal metasurface composed of three distinct arrays, generating unique images captured by an infrared camera and appearing similar in the visible light spectrum. (from Ref. [3])

15.2 Theoretical Framework of Universally Thermo-Adjustable Metasurfaces

The theoretical framework of universally thermo-adjustable metasurfaces is based on the Stefan−Boltzmann law [39]. According to this law, the total thermal radiative energy density of a black body is proportional to the fourth power of the surface temperature. In the context of infrared imaging, the actual spectral radiance received by an infrared camera deviates from the ideal case described by the Stefan-Boltzmann law. This deviation is captured by the spectral directional emissivity. The spectral directional emissivity represents the ratio of an object's actual spectral radiance to that of a black body with the same temperature and wavelength.

In most practical situations, a diffuse-emitter approximation is sufficient, and the surface emissivity can be simplified to depend only on the wavelength and surface temperature. However, if the surface temperature varies significantly across different parts of an object, the variation of emissivity with both wavelength and surface temperature needs to be taken into account.

To create controllable infrared illusions, the surface temperature and emissivity are independently tuned for each unit of the metasurface. The aim is to achieve the desired illusion by assembling these units in specific configurations. The tuning parameters include thermal conductivity, convective coefficient, radiative emissivity, and height of each unit, which correspond to the three modes of heat transfer. The temperature of the top surface T_{sur} for a steady state can be ascertained by applying the principles of heat flow conservation,

$$\boldsymbol{J}_{\mathrm{cond}} = \boldsymbol{J}_{\mathrm{conv}} + \boldsymbol{J}_{\mathrm{rad}}, \tag{15.1}$$

where $\boldsymbol{J}_{\text{cond}}$, $\boldsymbol{J}_{\text{conv}}$, and $\boldsymbol{J}_{\text{rad}}$ represent the densities of conductive, convective, and radiative heat flow, respectively. The height of the unit is denoted as H_b, while the thermal conductivity is represented by κ_b. The surface is characterized by the convective coefficient h_b and the radiative emissivity ε_b, respectively. Additionally, the temperatures of the heat source and the surrounding room are indicated by T_0 and T_{air}. $\boldsymbol{J}_{\text{cond}}$, $\boldsymbol{J}_{\text{conv}}$, and $\boldsymbol{J}_{\text{rad}}$ can be formulated as indicated below:

$$J_{\text{cond}} = \kappa_b \nabla T|_{\text{bulk}} = \kappa_b \frac{T_0 - T_{\text{sur}}}{H_b}, \tag{15.2a}$$

$$J_{\text{conv}} = h_b (T_{\text{sur}} - T_{\text{air}}), \tag{15.2b}$$

$$\begin{aligned} J_{\text{rad}} &= \varepsilon_b \sigma (T_{\text{sur}}^4 - T_{\text{air}}^4) \\ &= \varepsilon_b \sigma (T_{\text{sur}}^2 + T_{\text{air}}^2)(T_{\text{sur}} + T_{\text{air}})(T_{\text{sur}} - T_{\text{air}}) \\ &= R_b(T_{\text{sur}})(T_{\text{sur}} - T_{\text{air}}), \end{aligned} \tag{15.2c}$$

where $R_b(T) = \varepsilon_b \sigma (T_{\text{sur}}^2 + T_{\text{air}}^2)(T_{\text{sur}} + T_{\text{air}})$ represents the radiative characteristic of the surface. By incorporating Eqs. (15.1–15.2c), we can derive the temperature of the top surface T_{sur}

$$T_{\text{sur}} = \frac{\kappa_b T_0 / H_b + [h_b + R_b(T_{\text{sur}})]\, T_{\text{air}}}{\kappa_b / H_b + h_b + R_b(T_{\text{sur}})}. \tag{15.3}$$

The surface temperature can be predetermined to achieve a desired infrared illusion, and the remaining three parameters can be adjusted arbitrarily to attain the designed surface temperature. Tuning the surface emissivity becomes particularly important in cases where the surface temperature is nearly uniform within each unit, as it greatly influences the measured temperature.

Finally, these units are combined in a specific arrangement to generate the intended infrared illusion. Each unit serves as a pixel, and the contrast ratio of the imaging system relies on the highest and lowest reading temperatures. When the three modes of heat transfer are comparable, adjusting the surface temperature alone is enough to achieve the desired contrast ratio. However, if there is an imbalance in the heat transfer modes, adjusting the surface emissivity becomes necessary in order to create a discernible temperature distribution visible to the infrared camera.

The flexible arrangement of units enables reconfigurability without impacting the contrast ratio. Once the units are designed, the thermal metasurface consistently fulfills the resolution criteria of the infrared detector.

15.3 Finite-Element Simulation for Creating Infrared-Light Illusion and Visible-Light Similarity

To investigate the tuning of surface temperature, finite-element simulations were conducted using the commercial available software, COMSOL Multiphysics [40]. The computational simulations focused on adjusting thermal conductivity, convective coefficient, and radiative emissivity, while keeping the height fixed to maintain the geometric configuration of the metasurfaces. Initially, a metamaterial surface consisting of 15 × 30 units was created, where each unit was a 1 cm cube. These 450 units were divided into six groups, enabling the creation of six different patterns of , as shown in Fig. 15.3. The objective was to generate an illusion of the word "FUDAN". The groups were then constructed together, as depicted in Fig. 15.3a. For simplicity, a uniform heat source was applied to the entire lower surface, and the surrounding air temperature was maintained at 300 K. The lateral surfaces of the

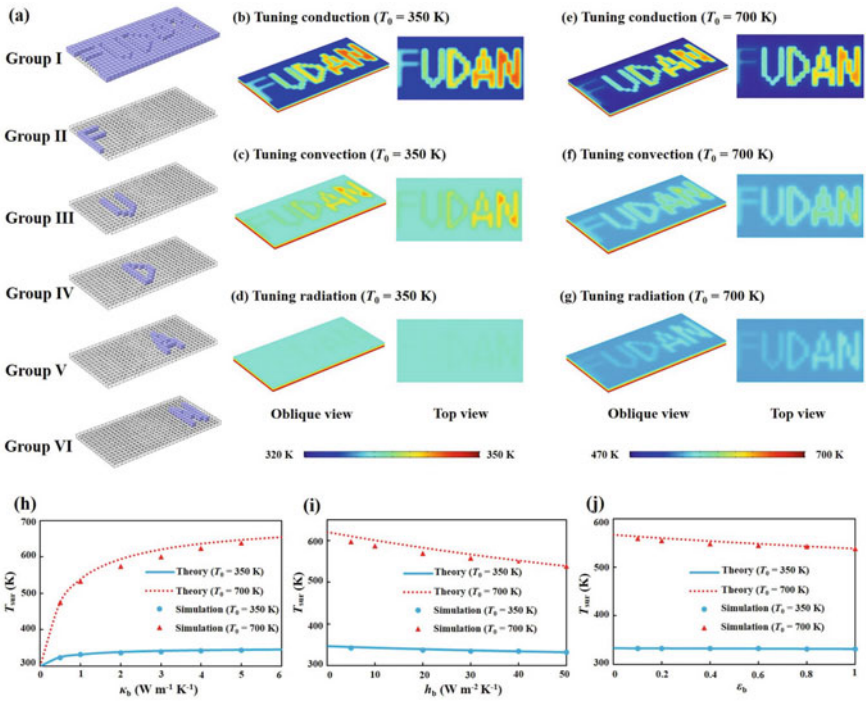

Fig. 15.3 Simulation results showing temperature distributions for different tuning methods of thermal conduction, thermal convection, and thermal radiation. Comparisons between theoretical and simulated surface temperature values are also illustrated. (from Ref. [3])

metasurface were thermally connected to neighboring units to simulate realistic conditions. It can be observed that convection and radiation have minimal effects under low-temperature conditions, with thermal radiation having nearly indistinguishable influence.

The results demonstrate that by individually adjusting the three modes of heat transfer, the desired patterns can be achieved. Convection prevails at low temperatures, while radiation dominates at high temperatures, thereby exerting a substantial impact on the contrast ratio of the pattern observed through the infrared camera. Figure 15.3h–j provide a comparison between theoretical data and simulation results for temperature under the three tuning modes. These figures exhibit excellent agreement at low temperatures but exhibit slight deviations at high temperatures due to thermal interactions between different units.

15.4 Experimental Verification Using Cavity Effects

The influence of engineered emissivities on the apparent temperature distribution in infrared imaging can be observed through the surface-cavity effect [41, 42]. The presence of cavity structures on the surface allows for modulation of the surface emissivity, resulting in a deviation between the captured apparent temperature and the actual temperature, thereby creating illusive patterns. To design the surface cavity structure, a simplified cylindrical shape is adopted, as shown in Fig. 15.4a. The heat transfer process occurs between the surface cavity and the surrounding free space, allowing us to neglect the angle factor associated with the cavity. As stated in Ref. [41], the effective emissivity of an isolated cylindrical cavity relies on the area ratio between its opening and inner wall. Given the blocks' regular shape and high thermal conductivities, we can assume a constant surface temperature. Since the plate surface only transfers energy into the environment, thermal interaction between cavities occurs exclusively. By manipulating the relative areas of the cavity and considering the inherent area ratio, one can tailor the effective emissivity of the surface. This customization allows for the creation of specific apparent temperature distributions in infrared imaging.

To experimentally investigate these effects, an FLIR E60 infrared camera with a resolution of 0.1 K is employed. For the experiments, a 10×15 array and two sets of customized units are utilized to design distinctive feature patterns. Copper cubes with a length of 2 cm are employed as block units, ensuring a homogeneous surface temperature due to copper's high thermal conductivity of approximately $397\,\mathrm{W\,m^{-1}\,K^{-1}}$. Group I comprises solid blocks with an inherent emissivity of 0.2, whereas Group II contains blocks with cylindrical holes. The holes have a diameter of 0.8 cm and a depth of 1 cm. The effective emissivity for Group II is approximately 0.6. Additionally, an acrylic plate with a 15×20 array of square holes is designed to encode the block units and allow for their insertion and fixation. By manually rearranging these units, feature patterns depicting a human figure, a machine gun, and the letters "FD' are created, as depicted in Fig. 15.4b–d. This process can

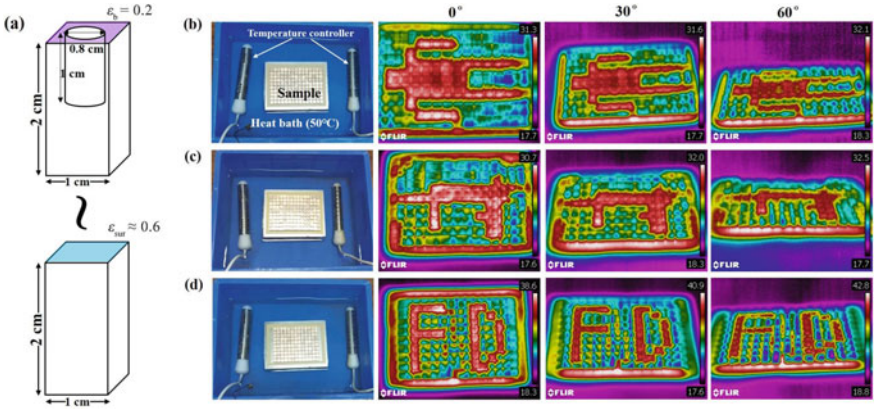

Fig. 15.4 Experimental measurements demonstrating the effective emissivity principle using cavity structures and various patterns observed at different angles. The experimental setup is positioned within a temperature-controlled bath. (from Ref. [3])

also be mechanically automated using additional active installations, resulting in an actively reconfigurable metasurface. The encoded surface is placed in a water bath maintained at a temperature of 50°C, while the room temperature remains around 20°C. Once the system reaches a steady state, the infrared camera captures the feature patterns. The metasurfaces arranged in different configurations are challenging to distinguish in visible-light view (similarity). Furthermore, the robustness of the patterns is observed from various angles, both in infrared and visible-light views, as depicted in Fig. 15.4b–d. It should be noted that when an anti-reflection film is applied to the surface, the feature pattern disappears, and the recorded temperatures are slightly higher than before. This confirms the effectiveness of the cavity engineering method in modifying the imaging process.

15.5 Discussion and Application of Universally Thermo-Adjustable Metasurfaces

The imaging patterns captured by infrared cameras are influenced by the emissivity and surface temperature of objects. Exploiting this understanding, two tuning methods have been demonstrated on the same platform, either through simulation or experimentation, to accomplish infrared illusion and visible-light similarity. In the previous study [2], a feasible approach for manipulating conduction processes was proposed to tune the temperature. However, additional research is required to effectively regulate convective and radiative fluxes to align with the theoretical predictions mentioned earlier. The emissivity plays a dual role in the customization process: it directs the radiative flow, impacting the surface temperature, and it masks the

actual temperature to deceive the infrared camera by presenting an apparent temperature. Therefore, the variable-controlling method is employed in the aforementioned simulations and experiments, demonstrating the flexibility and applicability of this platform for achieving infrared illusion.

Different tuning methods can be applied within various temperature ranges, and the encoding and assembling process of unit cells is non-destructive and replicable. The versatility in block assembly allows for the application of illusions in diverse situations. Furthermore, considering the limited dimensional resolution of infrared cameras, enhancing the quality of the illusion pattern is attainable when the dimensions of the units are on the same scale as the dimensional resolution. It should be noted that the proposed restructurability is fundamentally distinct from typical reconfigurability or adjustability [43]. This is because the former retains its properties but can be rearranged structurally, whereas the latter maintains its structure but allows for property adjustments. The suggested reconfigurable metasurface demonstrates both infrared-light illusion and visible-light similarity. In fact, the level of "similarity" can be enhanced to achieve "indistinguishability" with careful structuring of the surface, as shown in Fig. 15.4b–d. The feature holds significant potential for real-world applications.

One direct application of this scheme is for infrared anti-counterfeiting purposes. Anti-counterfeiting measures are widely employed across industries, military operations, and daily life. Conventional strategies rely on optical holograms [44–46], which can be detected either by the naked eye or specialized detectors. However, these technologies can be vulnerable as conventional patterns can be counterfeited. Recently, there has been a growing interest in the field of optical metasurfaces to address this challenge [47–50]. By designing two-dimensional microstructures, it becomes possible to tailor the amplitude, phase, and polarization of light arbitrarily, making the intrinsic signal characteristic and difficult to replicate. In such scenarios, the idea is to capture emissive electromagnetic-wave information exclusively for identification purposes. The intuitive approach is to tailor distinctive radiative signals to achieve anti-counterfeiting without requiring additional incident light. Encryption can be applied to the proposed metasurfaces, while decoding can be accomplished using infrared imaging. The key secret is challenging to forge due to its visual similarity in visible-light view. Furthermore, the reconfigurability of the metasurfaces enhances the level of difficulty for counterfeiting attempts. This anti-counterfeiting strategy finds extensive applicability in non-invasive and rapid-recognition scenarios.

15.6 Conclusion

In this chapter, we have presented a practical approach that enables the achievement of infrared-light illusion and visible-light similarity. By concurrently manipulating the surface temperature and emissivity, these parameters can be synergistically regulated. In comparison to existing thermal metamaterials, the proposed approach takes into account all three fundamental modes of heat transfer, thereby broadening the

scope of potential applications. Furthermore, the introduction of the cavity effect facilitates the customization of emissivity, simplifying the manufacturing process. We believe that this approach not only tackles the challenges associated with designing infrared illusions but also holds promise for immediate applications in various industries and commercial sectors. With its unique capabilities and versatility, it has the potential to revolutionize thermal diffusion and find widespread usage in fields such as energy management, electronics, aerospace, and more. Further research and development in this direction can unlock even more exciting possibilities in the realm of metamaterial-based thermal control.

References

1. Narayana, S., Sato, Y.: Heat flux manipulation with engineered thermal materials. Phys. Rev. Lett. **108**, 214303 (2012)
2. Shang, J., Tian, B.Y., Jiang, C.R., Huang, J.P.: Digital thermal metasurface with arbitrary infrared thermogram. Appl. Phys. Lett. **113**, 261902 (2018)
3. Wang, J., Yang, F.B., Xu, L.J., Huang, J.P.: Omnithermal restructurable metasurfaces for both infrared-light illusion and visible-light similarity. Phys. Rev. Appl. **14**, 014008 (2020)
4. Camacho, M., Edwards, B., Engheta, N.: Achieving asymmetry and trapping in diffusion with spatiotemporal metamaterials. Nat. Commun. **11**, 3733 (2020)
5. Peralta, I., Fachinotti, V.D., Álvarez Hostos, J.C.: A brief review on thermal metamaterials for cloaking and heat flux manipulation. Adv. Eng. Mater. **22**, 1901034 (2020)
6. Li, Y., Li, W., Han, T.C., Zheng, X., Li, J.X., Li, B.W., Fan, S.H., Qiu, C.W.: Transforming heat transfer with thermal metamaterials and devices. Nat. Rev. Mater. **6**, 488–507 (2021)
7. Hu, R., Xi, W., Liu, Y.D., Tang, K.C., Song, J.L., Luo, X.B., Wu, J.Q., Qiu, C.W.: Thermal camouflaging metamaterials. Mater. Today **45**, 120–141 (2021)
8. Li, J.X., Zhang, Z.X., Xu, G.Q., Sun, H.R., Dai, L.Z., Li, T.L., Qiu, C.W.: Tunable rectification of diffusion-wave fields by spatiotemporal metamaterials. Phys. Rev. Lett. **129**, 256601 (2022)
9. Martinez, F., Maldovan, M.: Metamaterials: Optical, acoustic, elastic, heat, mass, electric, magnetic, and hydrodynamic cloaking. Mater. Today Phys. **27**, 100819 (2022)
10. Zhang, X.W., He, X., Wu, L.Z.: Experimental investigation of thermal architected metamaterials for regulating transient heat transfer. Int. J. Heat Mass Transf. **193**, 122960 (2022)
11. Shirzadkhani, R., Eskandari, S., Akbarzadeh, A.: Non-Fourier thermal wave in 2D cellular metamaterials: From transient heat propagation to harmonic band gaps. Int. J. Heat Mass Transf. **205**, 123917 (2023)
12. Brighenti, R., Tatar, F.: Thermo-mechanical performance of two-dimensional porous metamaterial plates. Int. J. Mech. Sci. **238**, 107854 (2023)
13. Wang, J., Dai, G.L., Huang, J.P.: Thermal metamaterial: Fundamental, application, and outlook. iScience **23**, 101637 (2020)
14. Xu, L.J., Dai, G.L., Huang, J.P.: Transformation multithermotics: Controlling radiation and conduction simultaneously. Phys. Rev. Appl. **13**, 024063 (2020)
15. Xu, L.J., Yang, S., Huang, J.P.: Thermal transparency induced by periodic interparticle interaction. Phys. Rev. Appl. **11**, 034056 (2019)
16. Yang, S., Xu, L.J., Wang, R.Z., Huang, J.P.: Full control of heat transfer in single-particle structural materials. Appl. Phys. Lett. **111**, 121908 (2017)
17. Dai, G.L., Huang, J.P.: A transient regime for transforming thermal convection: Cloaking, concentrating and rotating creeping flow and heat flux. J. Appl. Phys. **124**, 235103 (2018)
18. Gao, Y., Jian, Y.C., Zhang, L.F., Huang, J.P.: Magnetophoresis of nonmagnetic particles in ferrofluids. J. Phys. Chem. C **111**, 10785–10791 (2007)

19. Dong, L., Huang, J.P., Yu, K.W., Gu, G.Q.: Dielectric response of graded spherical particles of anisotropic materials. J. Appl. Phys. **95**, 621–624 (2004)
20. Xu, L.J., Yang, S., Huang, J.P.: Thermal theory for heterogeneously architected structure: Fundamentals and application. Phys. Rev. E **98**, 052128 (2018)
21. Huang, J.P., Karttunen, M., Yu, K.W., Dong, L.: Dielectrophoresis of charged colloidal suspensions. Phys. Rev. E **67**, 021403 (2003)
22. Xu, L.J., Wang, J., Dai, G.L., Yang, S., Yang, F.B., Wang, G., Huang, J.P.: Geometric phase, effective conductivity enhancement, and invisibility cloak in thermal convection-conduction. Int. J. Heat Mass Transf. **165**, 120659 (2021)
23. Xu, L.J., Yang, S., Dai, G.L., Huang, J.P.: Transformation omnithermotics: Simultaneous manipulation of three basic modes of heat transfer. ES Energy Environ. **7**, 65–70 (2020)
24. Shen, X.Y., Jiang, C.R., Li, Y., Huang, J.P.: Thermal metamaterial for convergent transfer of conductive heat with high efficiency. Appl. Phys. Lett. **109**, 201906 (2016)
25. Xu, L.J., Xu, G.Q., Huang, J.P., Qiu, C.-W.: Diffusive fizeau drag in spatiotemporal thermal metamaterials. Phys. Rev. Lett. **128**, 145901 (2022)
26. Ye, C., Huang, J.P.: Non-classical oscillator model for persistent fluctuations in stock markets. Phys. A **387**, 1255–1263 (2008)
27. Liu, L., Wei, J.R., Zhang, H.S., Xin, J.H., Huang, J.P.: A statistical physics view of pitch fluctuations in the classical music from Bach to Chopin: Evidence for scaling. PLoS ONE **8**, e58710 (2013)
28. Xu, L.J., Huang, J.P.: Active thermal wave cloak. Chin. Phys. Lett. **37**, 120501 (2020)
29. Jin, P., Xu, L.J., Jiang, T., Zhang, L., Huang, J.P.: Making thermal sensors accurate and invisible with an anisotropic monolayer scheme. Int. J. Heat Mass Transf. **163**, 120437 (2020)
30. Zhang, Z.R., Xu, L.J., Qu, T., Lei, M., Lin, Z.K., Ouyang, X.P., Jiang, J.-H., Huang, J.P.: Diffusion metamaterials. Nat. Rev. Phys. **5**, 218–235 (2023)
31. Xu, L.J., Huang, J.P.: Transformation Thermotics and Extended Theories: Inside and Outside Metamaterials. Springer, Singapore (2023)
32. Qu, Y.R., Li, Q., Cai, L., Pan, M.Y., Ghosh, P., Du, K.K., Qiu, M.: Thermal camouflage based on the phase-changing material GST. Light Sci. Appl. **7**, 26 (2018)
33. Chen, T.Y., Weng, C.-N., Chen, J.-S.: Cloak for curvilinearly anisotropic media in conduction. Appl. Phys. Lett. **93**, 114103 (2008)
34. Narayana, S., Sato, Y.: Heat flux manipulation with engineered thermal materials. Phys. Rev. Lett. **108**, 214303 (2012)
35. Han, T.C., Bai, X., Gao, D.L., Thong, J.T.L., Li, B.W., Qiu, C.-W.: Experimental demonstration of a bilayer thermal cloak. Phys. Rev. Lett. **112**. 054302 (2014)
36. Hu, R., Huang, S.Y., Wang, M., Luo, X.B., Shiomi, J., Qiu, C.-W.: Encrypted thermal printing with regionalization transformation. Adv. Mater. **31**, 1807849 (2019)
37. Xu, C.Y., Stiubianu, G.T., Gorodetsky, A.A.: Adaptive infrared-reflecting systems inspired by cephalopods. Science **359**, 1495 (2019)
38. Lee, N., Kim, T., Lim, J.-S., Chang, I., Cho, H.H.: Metamaterial-selective emitter for maximizing infrared camouflage performance with energy dissipation. ACS Appl. Mater. Interfaces. **11**, 21250 (2019)
39. Cuevas, J.C., García-Vidal, F.J.: Radiative heat transfer. ACS Photon. **5**, 3896 (2018)
40. http://www.comsol.com/
41. Ohwada, Y.: Calculation of the effective emissivity of a cavity having non-Lambertian isothermal surfaces. J. Opt. Soc. Am. A **16**, 1059 (1999)
42. Mei, G., Zhang, J., Zhao, S., Xie, Z.: Simple method for calculating the local effective emissivity of the blackbody cavity as a temperature sensor. Infrared Phys. Technol. **85**, 372 (2017)
43. Bao, L., Cui, T.J.: Tunable, reconfigurable, and programmable metamaterials. Microw. Opt. Technol. Lett. **62**, 9 (2020)
44. Javidi, B., Horner, J.L.: Optical-pattern recognition for validation and security verification. Opt. Eng. **33**, 1752 (1994)
45. Zhang, X.S., Dalsgaard, E., Liu, S., Lai, H.K., Chen, J.Z.: Concealed holographic coding for security applications lay using a moire technique. Appl. Opt. **36**, 8096 (1997)

46. Aggarwal, A.K., Kaura, S.K., Chhachhia, D.P., Sharma, A.K.: Concealed moire pattern encoded security holograms readable by a key hologram. Opt. Laser Technol. **38**, 117 (2006)
47. Huang, L., Chen, X., Mühlenbernd, H., Zhang, H., Chen, S., Bai, B., Tan, Q., Jin, G., Cheah, K.-W., Qiu, C.-W., Li, J., Zentgraf, T., Zhang, S.: Three-dimensional optical holography using a plasmonic metasurface. Nat. Commun. **4**, 2808 (2013)
48. Wen, D., Yue, F., Li, G., Zheng, G., Chan, K., Chen, S., Chen, M., Li, K.F., Wong, P.W.H., Cheah, K.W., Pun, E.Y.B., Zhang, S., Chen, X.: Helicity multiplexed broadband metasurface holograms. Nat. Commun. **6**, 8241 (2015)
49. Zhang, C.M., Dong, F.L., Intaravanne, Y., Zang, X.F., Xu, L.H., Song, Z.W., Zheng, G.X., Wang, W., Chu, W.G., Chen, X.Z.: Multichannel metasurfaces for anticounterfeiting. Phys. Rev. Appl. **12**, 034028 (2019)
50. Sung, J., Lee, G.-V., Lee, B.: Progresses in the practical metasurface for holography and lens. Nanophotonics **8**, 1701 (2019)

Part V
Metamaterials for Particle Diffusion

Chapter 16
Geometric Phases in Particle Diffusion with Non-Hermitian Hamiltonian Structures

Jinrong Liu, Liujun Xu, Gaole Dai, and Gang Wang

16.1 Opening Remarks

Particle diffusion is a fundamental concept that describes the random motion of particles suspended in a fluid, resulting from their collision with the fast atoms or molecules in the gas or liquid. The traditional understanding of particle diffusion is based on the laws of Brownian motion and Fick's laws of diffusion [1–5]. However, real systems are often heterogeneous [6–9], and the traditional laws might not hold universally. The uniformity or non-uniformity of particle distribution can significantly alter the permeable [10, 11], mechanical [12, 13], thermal [14–19] and electrical [20–32] properties of composite materials. The interaction between particles and the fluid medium can lead to various emergent phenomena, such as altered electrical or optical properties [22–26, 33–37]. Moreover, Fick's law has been shown to be form-invariant under coordinate transformations, leading to the emergence of particle-diffusion metamaterials. This novel field offers potential for manipulating diffusion in new ways [38–45].

Beyond the conventional understanding of particle diffusion, there exists an intriguing aspect called the geometric phase [46] enlightened from thermal system [47–49]. This concept diverges from traditional diffusion models [50–53], introducing a phase factor with notable implications for particle behavior [54, 55]. Central

J. Liu (✉)
Department of Physics, Key Laboratory of Micro and Nano Photonic Structures (MOE), and State Key Laboratory of Surface Physics, Fudan University, Shanghai 200438, China
e-mail: 20110190007@fudan.edu.cn

L. Xu
Graduate School of China Academy of Engineering Physics, Beijing 100193, China

G. Dai
School of Sciences, Nantong University, Nantong 226019, China

G. Wang
School of Physical Science and Technology, Soochow University, Suzhou 215006, China

F.-B. Yang and J.-P. Huang, *Diffusionics*,
https://doi.org/10.1007/978-981-97-0487-3_16

to this concept is the non-Hermitian Hamiltonian H in the diffusion system. This Hamiltonian, which has been effectively characterized in two countermoving media [56], offers a fresh view on diffusion. It underscores the significance of geometric and topological factors in the diffusion process [57–61]. What's fascinating about its non-Hermitian nature is its potential to reveal diffusion behaviors not encompassed by traditional Hermitian quantum mechanics [56, 62–64].

In particle diffusion, the geometric phase introduces unexpected behaviors and effects not anticipated by traditional theories. One such effect is a deviation from standard diffusion patterns, manifesting as anomalous diffusion or new modes of diffusion [46]. These deviations can significantly impact fields from material science to biology, where precise control and comprehension of diffusion are vital.

16.2 Theory and Structures for Particle Diffusion with a Non-Hermitian Hamiltonian H

Diving deeper into the geometric phase's role in particle diffusion systems, we turn our focus to the intricate configurations that induce non-Hermiticity. A pivotal study in thermal domain has outlined a fundamental architecture comprising two dynamically moving rings and a stationary intermediary layer [56], which has been further developed in certain thermal systems [62, 63]. Figure 16.1a vividly illustrates the foundational components of this structure [46], where the particle interchange takes place. The rings move with equal velocities but opposite directions. The intermediary layer acts as a medium for particle interchange between these two dynamic rings. To formulate this particle-diffusion process mathematically, a non-Hermitian Hamiltonian H is employed:

$$H = \begin{pmatrix} -i(k^2 D + h) + ku & ih \\ ih & -i(k^2 D + h) - ku \end{pmatrix} \tag{16.1}$$

In this expression, k signifies the wave number, D denotes the diffusivity of the two dynamic rings, u represents the velocity, and $i = \sqrt{-1}$ is the imaginary unit. The term $h = \frac{D_m}{w \cdot d}$ encapsulates the rate of particle interchange between the two dynamic rings, where D_m is the diffusivity of the intermediary layer, and w and d are the thicknesses of the dynamic rings and the intermediary layer, respectively [46].

The evolution of eigenstates in a particle diffusion system with geometric phase is a subject of considerable interest. The eigenstates are not static but evolve over time, especially when the system involves non-Hermitian dynamics. The initial and final states of the system can be significantly different, depending on the parameters such as the velocity of the moving rings and the properties of the intermediate layer. The eigenvalues and eigenstates of this Hamiltonian in Eq. 16.1 are given by:

$$\omega = -i\left[(k^2 D + h) \pm \sqrt{h^2 - k^2 u^2}\right] \tag{16.2}$$

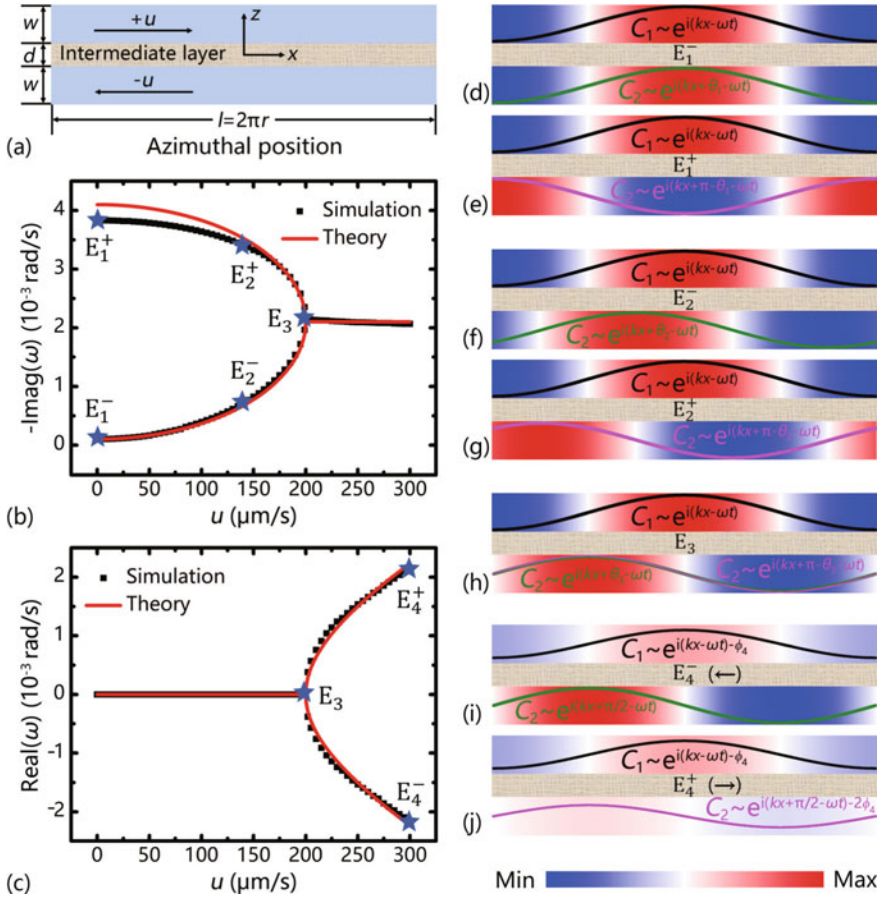

Fig. 16.1 This figure provides a comprehensive view of the eigenvalues and eigenstates in the system. Part **a** showcases a simplified two-dimensional model with specific parameters. Parts **b** and **c** plot the negative imaginary and real parts of the eigenvalue ω as a function of velocity u. Solid lines and block squares represent analytical and simulation results, respectively. Parts **d** to **j** display the eigenstates at various positions, which are indicated by stars in parts **b** and **c**. (from Ref. [46])

$$\psi_+ = \begin{cases} [1, e^{i(\pi-\theta)}]^T, & \text{if } u < u_{\text{EP}} \\ [e^{-\phi}, e^{i\pi/2-2\phi}]^T, & \text{if } u > u_{\text{EP}} \end{cases} \quad \psi_- = \begin{cases} [1, e^{i\theta}]^T, & \text{if } u < u_{\text{EP}} \\ [e^{-\phi}, e^{i\pi/2}]^T, & \text{if } u > u_{\text{EP}} \end{cases} \tag{16.3}$$

where $\varphi = \cosh^{-1}(ku/h), u_{\text{EP}} = h/k$. This unified expression provides a comprehensive view of how the eigenstates evolve depending on the velocity parameter u, and how they are influenced by the exceptional point u_{EP} in Fig. 16.1. The evolution of these eigenstates is influenced by the geometric phase, which can be expressed as:

$$\gamma_\pm = i \int \frac{\langle \psi_\pm(u), d\psi_\pm(u) \rangle}{\langle \psi_\pm(u), \psi_\pm(u) \rangle} \tag{16.4}$$

This geometric phase accumulates over time and plays a crucial role in the system's dynamics. For instance, when the system evolves around an exceptional point, the geometric phase takes on values of π or $-\pi$, depending on the direction of the closed loop. If the evolution route does not contain the exceptional point, the integral in a closed loop is naturally equal to zero.

In summary, the evolution of eigenstates and the accumulation of geometric phase are pivotal in understanding the complex dynamics of particle diffusion systems with geometric phase. These factors are not only theoretically intriguing but also have practical implications in designing systems for effective manipulation of particle diffusion.

16.3 Numerical Simulations of Eigenstate Evolution and Geometric Phase

Relying on the theoretical principles of eigenstate evolution and geometric phase, numerical analyses are executed utilizing COMSOL Multiphysics. A striking resemblance emerges between the dynamics within these particle diffusion systems and those in thermal convection-conduction systems. This similarity is grounded in the fact that both thermal convection and particle diffusion are manifestations of diffusion metamaterial systems, governed by a similar class of partial differential equations. Drawing from this observation, a recent thermal study [65], substituting the diffusivity D with the thermal coefficient $\kappa/\rho c$, the topological exceptional points (EPs) and the evolution pathways of states traverse the same topological branch. Despite the parallels, it's vital to discern the distinctive nuances that differentiate each system, thereby enriching our understanding of diffusion phenomena across various platforms.

Utilizing the finite element methods available in COMSOL Multiphysics, the simulations offer a granular perspective on the behavior of the geometric phase. Distinct velocity paths are selected for the simulations; some are designed to circumvent the exceptional point (EP), while others intentionally intersect with it. The simulations commence with an initial velocity of 100 μm/s and an initial state corresponding to the eigenvalue ω^-, characterized by a phase difference of $\pi/6$. In scenarios where the system's trajectory avoids the EP, the eigenvalue remains purely imaginary, thereby confirming the absence of any accrued phase difference. This specific trajectory ensures that the system reverts to its original concentration profile, as depicted in Fig. 16.2.

Conversely, when the system's trajectory encompasses the EP, a dramatic shift in the dynamics is observed. The EP serves as a critical nexus where the eigenvalues coalesce, resulting in a Hamiltonian that is non-diagonalizable. As the system traverses this point, real components of the eigenvalues emerge, signifying the introduction of an additional phase difference, thereby enriching our understanding of the geometric phase's influence on the system's behavior.

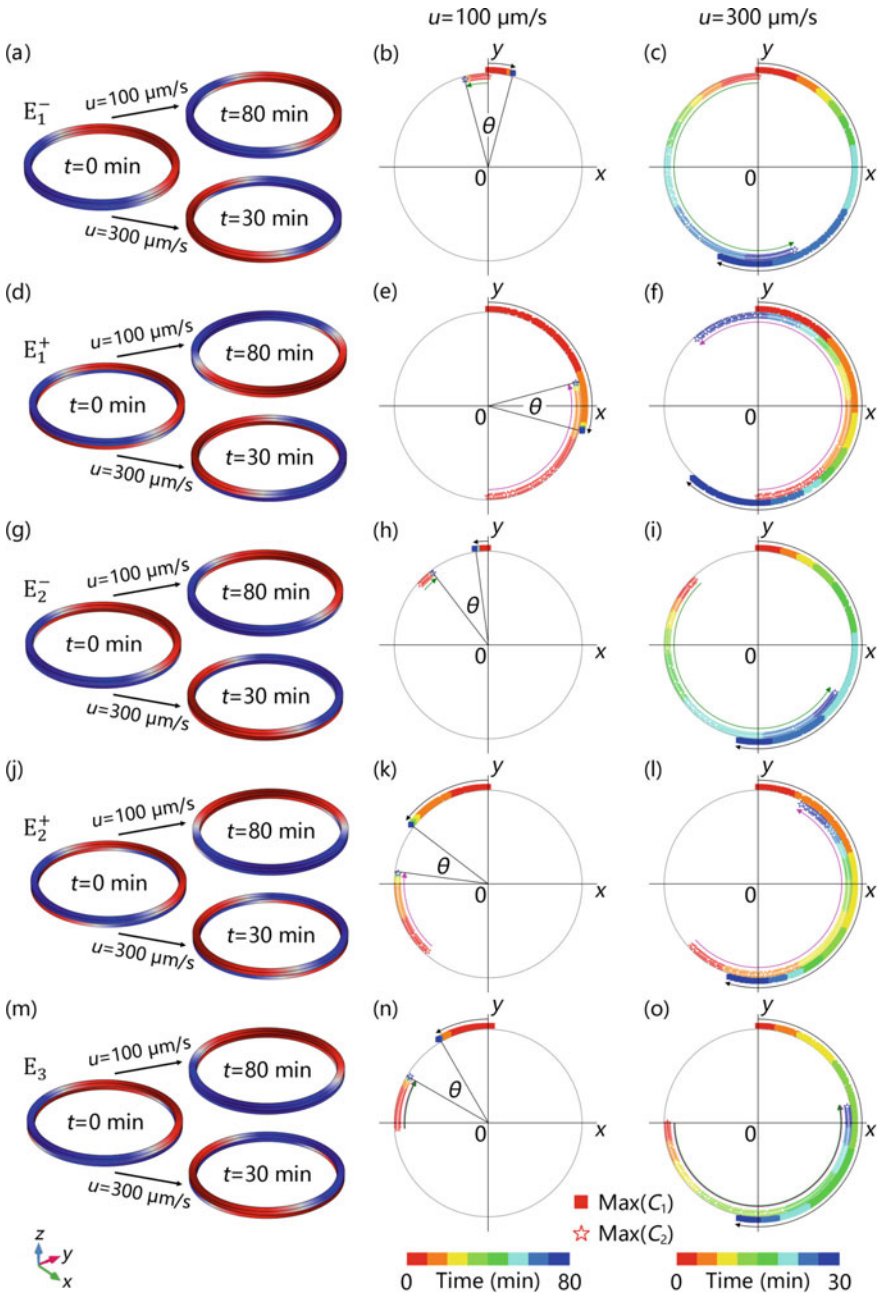

Fig. 16.2 This figure presents the initial and final states of the system at two different velocities. It also depicts the trajectories of the maximum concentrations Max($C1$) and Max($C2$) along the interior edges of the two moving rings. The parameters used for the simulations are $w = 0.5\,\text{cm}$, $d = 0.1\,\text{cm}$, $r = 10\,\text{cm}$, $r' = 11\,\text{cm}$, $D = 10^{-6}\,\text{m}^2/\text{s}$, and $D_m = 10^{-8}\,\text{m}^2/\text{s}$. (from Ref. [46])

To deepen the exploration of the geometric phase, the simulations also scrutinize the transition from non-eigenstates to eigenstates. Initial states are selected from a set of five distinct eigenstates, each defined in Cartesian coordinates. Velocities for these simulations are set at 100 μm/s and 300 μm/s, and the directions of velocity are clockwise for the upper ring and anticlockwise for the lower ring. The theoretical phase differences at $u = 100\,\mu$m/s are $\pi/6$ for ω^- and $5\pi/6$ for ω^+. Intriguingly, these initial states, which are not eigenstates at the outset, evolve to align with the eigenstates. Ultimately, all five initial states converge to a singular final state, corresponding to the eigenvalue ω^-. This convergence is ascribed to the non-orthogonality of the eigenstates across different branches, as illustrated in Fig. 16.3.

In summary, the numerical simulations executed in COMSOL Multiphysics not only substantiate the theoretical framework but also furnish a nuanced understanding of the role played by the geometric phase in particle diffusion systems. These insights are pivotal for guiding future experimental validations and practical applications.

16.4 Bilayer Particle-Diffusion Cloak: Design and Applications

Expanding beyond the theoretical realm of eigenstate evolution and geometric phase, the focus shifts to the cutting-edge application of the bilayer particle-diffusion cloak. This sophisticated design involves a dynamic interplay between two concentric moving rings and a static intermediate layer, leveraging the remarkable adaptability. By fine-tuning the individual rotational speeds of the rings, the system exhibits a robust cloak in different diffusivity D background, and even within rotational frames of reference.

The architectural blueprint of this cloak is delineated in Fig. 16.4. Initially, the presence of an object in the background perturbs the concentration profile. To mitigate this, a two-tiered strategy is employed. The first tier involves the deployment of a zero-diffusivity layer to encapsulate the object, thereby nullifying its diffusion influence on the surrounding environment. This results in the formation of a cloaked region, as illustrated in Fig. 16.4b. The second tier incorporates an additional layer consisting of two moving rings. These rings are meticulously engineered to counterbalance the diffusion effects of the isolated region. By judiciously modulating the velocities of these rings, which are antiparallel but equal in magnitude, a state of particle-diffusion invisibility can be realized.

To quantify the cloak's effectiveness, the enhanced diffusivity D' is given by the formula:

$$D' = D\left(1 + \frac{v^2\tau^2}{4}\right),$$

where D is the original diffusivity, v is the velocity of the moving rings, and τ is the relaxation time. Numerical simulations, represented in Fig. 16.5, corroborate the

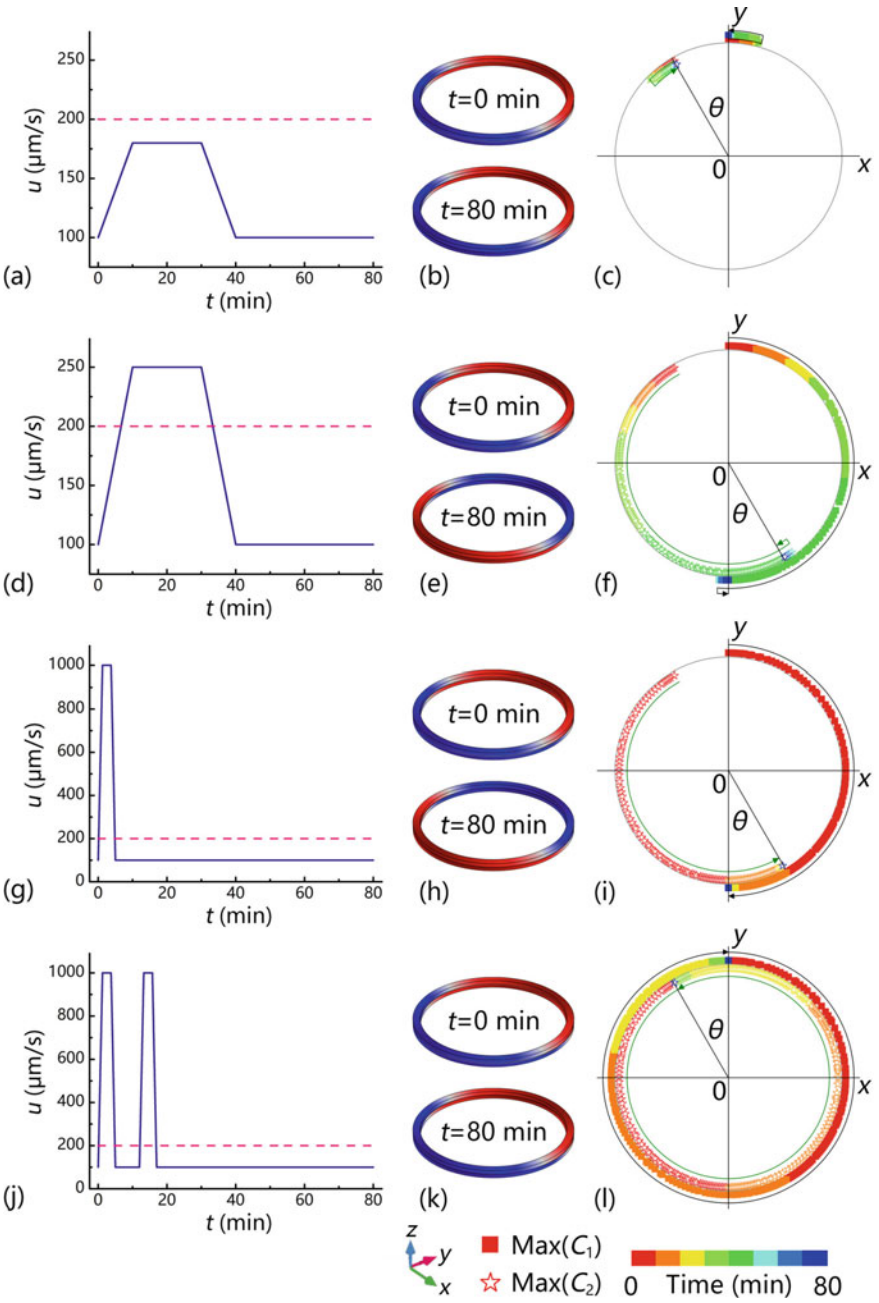

Fig. 16.3 The figure is divided into three columns. The left column outlines the time-varying paths of velocity. The middle column displays the initial and final states of the system, while the right column illustrates the trajectories of Max($C1$) and Max($C2$) along the interior edges of the channels. The parameters are consistent with those used in Fig. 16.2. (from Ref. [46])

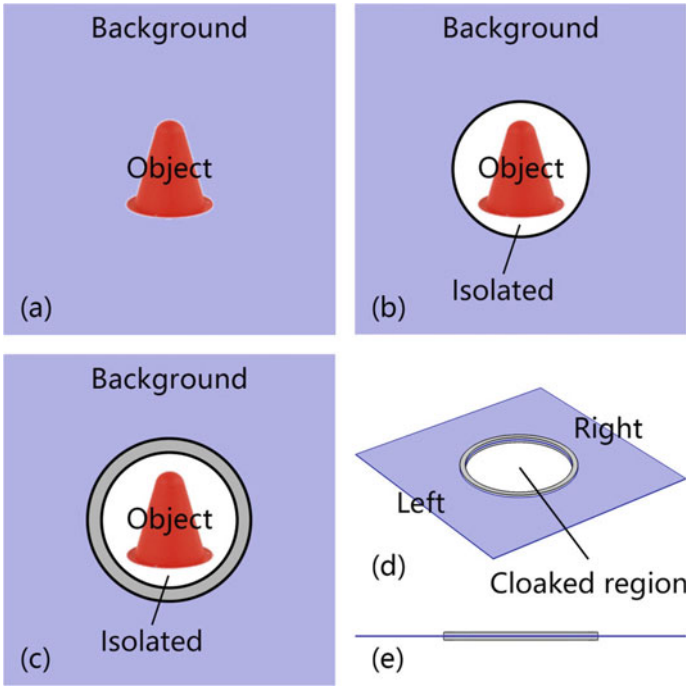

Fig. 16.4 The figure illustrates the design concept of a bilayer particle-diffusion cloak. Panel **a** shows an object in the background, disrupting the concentration profile. Panel **b** introduces an isolated layer with zero diffusivity to separate the object from the background. Panel **c** applies two moving rings to counteract the effects of the isolated layer. Panels **d** and **e** provide three-dimensional perspectives of the design. The bilayer cloak effectively renders the object undetectable, making it a promising application in chemical and biological systems. (from Ref. [46])

cloak's efficacy under both linear and nonlinear diffusion regimes. Specifically, the simulations indicate that a velocity setting of 37 μm/s for the moving rings yields an enhanced diffusivity that meets the criteria for effective cloaking. This results in an undistorted concentration profile in the background, thereby affirming the cloak's operational success.

A notable strength of this bilayer cloak lies in its adaptability and straightforward implementation. Standing in stark contrast to other cloaking techniques that require complex transformation optics or detailed multi-layered infrastructures, this innovative approach is grounded in consistent parameters and simple geometries. Such foundational simplicity underscores its practicality, enhancing its suitability for a plethora of real-world scenarios. A further testament to its user-friendly design is the cloak's operational versatility. The cloaking function can be effortlessly engaged or disengaged by altering the speed of the moving rings, demonstrating flexibility in various application settings.

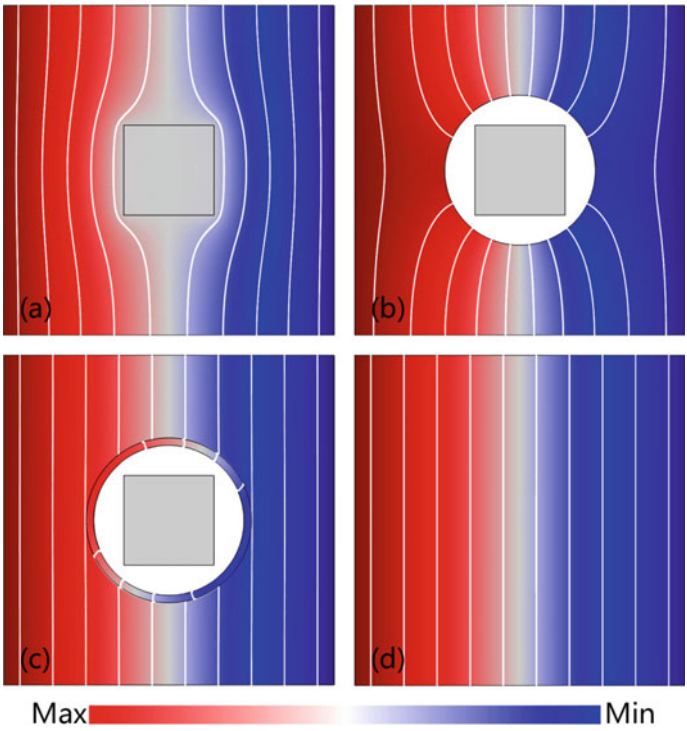

Fig. 16.5 This figure demonstrates the cloaking effect in a linear concentration field. The square plate measures $44 \times 44 \times 0.1$ cm^3 and has a diffusivity of 10^{-6} m^2/s. Two moving rings with widths of 0.5 cm and diffusivities of 10^{-8} m^2/s are used. Panel **a** shows a square object in the center with a width of 12 cm and diffusivity of 10^{-4} m^2/s. Panel **b** depicts an isolated hole in the center with a radius of 10 cm. Panel **c** features two rings with inner and outer radii of 10 cm and 11 cm, respectively, moving at equal-but-opposite velocities of 37 μm/s. Panel **d** shows a pure background for comparison. The cloaking effect is achieved by enhancing the diffusivity of the intermediate layer. (from Ref. [46])

Embarking on the quest to make particle diffusion invisible constitutes a significant breakthrough, heralding a spectrum of applications that permeate sectors as diverse as chemical engineering and biological systems. More than just a mechanism for concealment, this technology is strategically devised to navigate entities through a range of environments, introducing groundbreaking possibilities in areas like pollution abatement, precision-targeted healthcare delivery, and discreet environmental monitoring. This advanced level of control and finesse positions the bilayer particle-diffusion cloak as a pioneering development, reshaping traditional approaches to managing diffusion phenomena. Consequently, it ushers in a new benchmark for operational excellence across interdisciplinary scientific and industrial landscapes.

16.5 Conclusion

The field of geometric phases in particle diffusion is not merely an academic endeavor but a multidisciplinary area with far-reaching implications. The chapter began by laying the theoretical groundwork, elucidating the basic principles and significance of geometric phase in diffusion systems. It then delved into the intricacies of designing structures that can effectively manipulate particle diffusion, followed by a rigorous examination of eigenstate evolution and the role of geometric phase. The concept of a bilayer particle-diffusion cloak was introduced, offering a novel approach to controlling diffusion processes. Finally, the chapter culminated in discussing the real-world industrial applications, which are substantiated by methodological advancements and empirical research.

The interplay between theory, simulation, and practical application serves as a testament to the field's dynamism and its potential for groundbreaking innovations. While the chapter has provided a comprehensive overview, it is important to acknowledge that the field is continually evolving. New methodologies are being developed, novel applications are being discovered, and further research is being conducted to validate and refine existing theories.

In conclusion, the exploration of geometric phases in particle diffusion systems is a burgeoning field that promises to revolutionize both scientific understanding and industrial practices. The theoretical frameworks, simulation models, and industrial applications discussed in this chapter are but a snapshot of what the field has to offer. As research progresses, it is anticipated that the coming years will witness even more remarkable advancements, further solidifying the importance of this area in both academic and industrial landscapes.

References

1. Faucheux, L.P., Libchaber, A.J.: Confined brownian motion. Phys. Rev. E **49**(6), 5158 (1994)
2. Van Milligen, B.P., Bons, P.D., Carreras, B.A., Sanchez, R.: On the applicability of Fick's law to diffusion in inhomogeneous systems. Eur. J. Phys. **26**(5), 913 (2005)
3. Nguyen, T.D.T.: Fick law and sticky Brownian motions. J. Stat. Phys. **174**(2), 494–518 (2019)
4. Shankar, U., Naduvinamani, N.B., Basha, H.: A generalized perspective of Fourier and Fick's laws: Magnetized effects of Cattaneo-Christov models on transient nanofluid flow between two parallel plates with Brownian motion and thermophoresis. Nonlinear Eng. **9**(1), 201–222 (2020)
5. Kay, T., Giuggioli, L.: Extreme value statistics and Arcsine laws of Brownian motion in the presence of a permeable barrier. J. Phys. A: Math. Theor. **56**(34), 345002 (2023)
6. Xu, L.J., Dai, G.L., Huang, J.P.: Transformation multithermotics: Controlling radiation and conduction simultaneously. Phys. Rev. Appl. **13**, 024063 (2020)
7. Dai, G.L., Huang, J.P.: A transient regime for transforming thermal convection: Cloaking, concentrating and rotating creeping flow and heat flux. J. Appl. Phys. **124**, 235103 (2018)
8. Xu, L.J., Yang, S., Huang, J.P.: Thermal theory for heterogeneously architected structure: Fundamentals and application. Phys. Rev. E **98**, 052128 (2018)
9. Jin, P., Xu, L.J., Jiang, T., Zhang, L., Huang, J.P.: Making thermal sensors accurate and invisible with an anisotropic monolayer scheme. Int. J. Heat Mass Transf. **163**, 120437 (2020)

10. Malgaretti, P., Nizkaia, T., & Oshanin, G.: Splitting probabilities for dynamics in corrugated channels: Passive vs. active Brownian motion. Europhys. Lett. **142**(5), 57001 (2023)
11. Sposini, V., Krapf, D., Marinari, E., Sunyer, R., Ritort, F., Taheri, F., Oshanin, G.: Towards a robust criterion of anomalous diffusion. Commun. Phys. **5**(1), 305 (2022)
12. Fang, Z.N., Xue, H.T., Bao, W., Yang, Y., Zhou, L.W., Huang, J.P.: Electrorheological effects depending on the dispersity of lyophilic or lyophobic particles. Chem. Phys. Lett. **441**, 314–317 (2007)
13. Tian, W.J., Nakayama, T., Huang, J.P., Yu, K.W.: Scaling behaviors in settling process of fractal aggregates in water. EPL **78**, 46001 (2007)
14. Yang, W.Z., Huang, J.P.: Effective mass density of liquid composites: Experiment and theory. J. Appl. Phys. **101**, 064903 (2007)
15. Huang, J.P., Gao, L., Li, Z.Y.: Temperature effect on nonlinear optical response in metal/dielctric composite with interfacial layer. Solid State Commun. **115**, 347–352 (2000)
16. Xu, L.J., Yang, S., Huang, J.P.: Thermal transparency induced by periodic interparticle interaction. Phys. Rev. Appl. **11**, 034056 (2019)
17. Yang, S., Xu, L.J., Wang, R.Z., Huang, J.P.: Full control of heat transfer in single-particle structural materials. Appl. Phys. Lett. **111**, 121908 (2017)
18. Xu, L.J., Yang, S., Dai, G.L., Huang, J.P.: Transformation omnithermotics: Simultaneous manipulation of three basic modes of heat transfer. ES Energy Environ. **7**, 65–70 (2020)
19. Shen, X.Y., Jiang, C.R., Li, Y., Huang, J.P.: Thermal metamaterial for convergent transfer of conductive heat with high efficiency. Appl. Phys. Lett. **109**, 201906 (2016)
20. Huang, J.P., Karttunen, M., Yu, K.W., Dong, L.: Dielectrophoresis of charged colloidal suspensions. Phys. Rev. E **67**, 021403 (2003)
21. Dong, L., Huang, J.P., Yu, K.W., Gu, G.Q.: Dielectric response of graded spherical particles of anisotropic materials. J. Appl. Phys. **95**, 621–624 (2004)
22. Xiao, J.J., Huang, J.P., Yu, K.W.: Dynamic polarizability of rotating particles in electrorheological fluids. J. Phys. Chem. B **112**, 6767–6771 (2008)
23. Gao, Y., Tian, W.J., Wang, W., Huang, J.P.: Electroinduced simple harmonic oscillation of a microparticle. Appl. Phys. Lett. **92**, 122902 (2008)
24. Zhang, L.F., Huang, J.P., Yu, K.W.: Gradation-controlled electric field distribution in multilayered colloidal crystals. Appl. Phys. Lett. **92**, 091907 (2008)
25. Jian, Y.C., Gao, Y., Huang, J.P., Tao, R.: Structure of polydisperse inverese ferrofluids: Theory and computer simulation. J. Phys. Chem. B **112**, 715–721 (2008)
26. Xu, L., Tian, W.J., Wu, X.F., Cao, J.G., Zhou, L.W., Huang, J.P., Gu, G.Q.: Polar-molecules-driven enhanced colloidal electrostatic interactions and their applications in achieving high active electrorheological materials. J. Mater. Res. **23**, 409–417 (2008)
27. Fan, C.Z., Huang, J.P., Yu, K.W.: Dielectrophoresis of an inhomogeneous colloidal particle under an inhomogeneous field: A first-principles approach. J. Phys. Chem. B **110**, 25665 (2006)
28. Huang, J.P., Yu, K.W., Gu, G.Q., Karttunen, M., Dong, L.: Reply to Comment on the use of the method of images for calculating electromagnetic responses of interacting spheres. Phys. Rev. E **72**, 023402 (2005)
29. Huang, J.P., Yu, K.W.: Interparticle force in electrorheological solids: Many-body dipole-induced dipole model. Phys. Rev. E **70**, 061401 (2004)
30. Huang, J.P.: New mechanism for harmonic generation in magnetorheological fluids. J. Phys. Condes. Matter **16**, 7889–7894 (2004)
31. Huang, J.P., Yu, K.W.: Many-body dipole-induced dipole model for electrorheological fluids. Chin. Phys. **13**, 1065–1069 (2004)
32. Huang, J.P., Yu, K.W.: First-principles approach to electrorotation assay. J. Phys.: Condens. Matter **14**, 1213–1221 (2002)
33. Fan, C.Z., Wang, G., Huang, J.P.: Magneto-controllable photonic crystals based on colloidal ferrofluids. J. Appl. Phys. **103**, 094107 (2008)
34. Gao, Y., Jian, Y.C., Zhang, L.F., Huang, J.P.: Magnetophoresis of nonmagnetic particles in ferrofluids. J. Phys. Chem. C **111**, 10785 (2007)

35. Wang, G., Tian, W.J., Huang, J.P.: Response of ferrogels subjected to an AC magnetic field. J. Phys. Chem. B **110**, 10738 (2006)
36. Ye, C., Huang, J.P.: Non-classical oscillator model for persistent fluctuations in stock markets. Phys. A **387**, 1255 (2008)
37. Chen, Y.W., Zhang, L.F., Huang, J.P.: The Watts-Strogatz network model developed by including degree distribution: Theory and computer simulation. J. Phys. A: Math. Theor. **40**, 8237 (2007)
38. Ye, C., Huang, J.P.: Non-classical oscillator model for persistent fluctuations in stock markets. Phys. A **387**, 1255–1263 (2008)
39. Liu, L., Wei, J.R., Zhang, H.S., Xin, J.H., Huang, J.P.: A statistical physics view of pitch fluctuations in the classical music from Bach to Chopin: Evidence for scaling. PLoS ONE **8**, e58710 (2013)
40. Guenneau, S., Puvirajesinghe, T.M.: Fick's second law transformed: One path to cloaking in mass diffusion. J. R. Soc. Interface **10**, 20130106 (2013)
41. Guenneau, S., Petiteau, D., Zerrad, M., Amra, C., Puvirajesinghe, T.: Transformed Fourier and Fick equations for the control of heat and mass diffusion. AIP Adv. **5**, 053404 (2015)
42. Restrepo-Florez, J.M., Maldovan, M.: Mass separation by metamaterials. Sci. Rep. **6**, 21971 (2016)
43. Restrepo-Florez, J.M., Maldovan, M.: Rational design of mass diffusion metamaterial concentrators based on coordinate transformations. J. Appl. Phys. **120**, 084902 (2016)
44. Restrepo-Florez, J.M., Maldovan, M.: Mass diffusion cloaking and focusing with metamaterials. Appl. Phys. Lett. **111**, 071903 (2017)
45. Restrepo-Florez, J.M., Maldovan, M.: Metamaterial membranes. J. Phys. D Appl. Phys. **50**, 025104 (2017)
46. Xu, L.J., Dai, G.L., Wang, G., Huang, J.P.: Geometric phase and bilayer cloak in macroscopic particle-diffusion systems. Phys. Rev. E **102**, 032140 (2020)
47. Lei, M., Xu, L.J., Huang, J.P.: Spatiotemporal multiphysics metamaterials with continuously adjustable functions. Mat. Today. Phys. **34**, 101057 (2023)
48. Zhuang, P.F., Huang, J.P.: Multiple control of thermoelectric dual-function metamaterials. Int. J. Mech. Sys. Dyna **3**, 127–135 (2023)
49. Zhou, X.C., Lin, W.Y., Yang, F.B., Zhou, X.D., Shen, J., Huang, J.P.: Effective medium theory with hybrid impacts of phase symmetry and asymmetry for analyzing phase transition behavior. Eur. Phys. Lett. **141**, 16001 (2023)
50. Xu, L.J., Huang, J.P.: Active thermal wave cloak. Chin. Phys. Lett. **37**, 120501 (2020)
51. Yang, F.B., Tian, B.Y., Xu, L.J., Huang, J.P.: Experimental demonstration of thermal chameleonlike rotators with transformation-invariant metamaterials. Phys. Rev. Appl. **14**, 054024 (2020)
52. Wang, J., Dai, G.L., Huang, J.P.: Thermal metamaterial: Fundamental, application, and outlook. iScience **23**, 101637 (2020)
53. Xu, L.J., Huang, J.P., Jiang, T., Zhang, L., Huang, J.P.: Thermally invisible sensors. Europhys. Lett. **132**, 14002 (2020)
54. Xu, L.J., Huang, J.P.: Active thermal wave cloak. Chin. Phys. Lett. **37**, 120501 (2020)
55. Xu, L.J., Xu, G.Q., Huang, J.P., Qiu, C.-W.: Diffusive fizeau drag in spatiotemporal thermal metamaterials. Phys. Rev. Lett. **128**, 145901 (2022)
56. Li, Y., Peng, Y.G., Han, L., Miri, M.A., Li, W., Xiao, M., Zhu, X.F., Zhao, J., Alú, A., Fan, S., Qiu, C.-W.: Anti-parity-time symmetry in diffusive systems. Science **364**, 170 (2019)
57. Özdemir, ŞK., Rotter, S., Nori, F., Yang, L.: Parity-time symmetry and exceptional points in photonics. Nat. Mater. **18**, 783 (2019)
58. Wang, W., Wang, X., & Ma, G.: Non-Hermitian morphing of topological modes. Nature (London). **608**, 50 (2022)
59. Esaki, K., Sato, M., Hasebe, K., Kohmoto, M.: Edge states and topological phases in non-Hermitian systems. Phys. Rev. B **84**, 205128 (2011)
60. Yao, S., Wang, Z.: Edge States and Topological Invariants of Non-Hermitian Systems. Phys. Rev. Lett. **121**, 086803 (2018)

61. Takata, K., Notomi, M.: Photonic Topological Insulating Phase Induced Solely by Gain and Loss. Phys. Rev. Lett. **121**, 213902 (2018)
62. Xu, G., Li, Y., Li, W., Fan, S., Qiu, C.-W.: Configurable phase transitions in topological thermal material. Phys. Rev. Lett. **127**, 105901 (2021)
63. Xu, G., Yang, Y., Zhou, X., Chen, H., Alu, H., Qiu, C.-W.: Diffusive topological transport in spatiotemporal thermal lattices. Nat. Phys. **18**, 450 (2022)
64. Xu, G., Li, W., Zhou, X., Li, H., Li, Y., Fan, S., Zhang, S., Christodoulides, D.N., Qiu, C.-W.: Observation of Weyl exceptional rings in thermal diffusion. Proc. Natl. Acad. Sci. U.S.A. **119**, e2110018119 (2022)
65. Xu, L.J., Wang, J., Dai, G.L., Yang, S., Yang, F.B., Wang, G., Huang, J.P.: Geometric phase, effective conductivity enhancement, and invisibility cloak in thermal convection-conduction. Int. J. Heat Mass Transf. **165**, 120659 (2021)

Chapter 17
Particle Diffusion Process with Artificial Control: Diffusion Metamaterials

Pengfei Zhuang, Zeren Zhang, and Fubao Yang

17.1 Opening Remarks

Metamaterials [1, 2] are meticulously designed structures, built from functional building blocks densely packed into an effective medium [3, 4]. Although the concept of methodically engineering artificial materials has historical precedence, their exceptional design and fabrication flexibility are remarkable. This adaptability is primarily due to the principles of effective materials based on sub-characteristic length [5] structures, differentiating them from other synthetic materials like photonic and phononic crystals [6]. For example, wave metamaterials [7] consist of structures built from units smaller than their respective characteristic wavelengths. Similarly, diffusion metamaterials [8–11], another branch of the metamaterial family, are designed with characteristic lengths in mind, distinguishing them from other thermal synthetic materials.

In 2006, transformation optics, drawing inspiration from Einstein's general theory of relativity, linked virtual spatial distortions with the actual spatial inhomogeneities and general anisotropies of magneto-dielectric metamaterials [12] in Cartesian physical space. This approach offered a direct correlation between desired electromagnetic phenomena [13, 14] and the required material responses, providing a powerful tool for managing electromagnetic fields across various scales. Though metamaterials are often associated with negative refractive indices [1, 15, 16] and invisibility cloaking [17–19] in electromagnetism or optics [20, 21], the underlying concept of metamaterials reaches broader domains, including nonlinear optics [22, 23], acoustics [24], direct/alternating current [25, 26], and fluid dynamics [27, 28].

Heat transfer, a cornerstone of diffusion phenomena, governs energy transport and is generally propelled by spatial temperature disparities. The focal points of heat transfer research encompass temperature, heat flux management-ranging from

P. Zhuang (✉) · Z. Zhang · F. Yang
Department of Physics, Key Laboratory of Micro and Nano Photonic Structures (MOE), and State Key Laboratory of Surface Physics, Fudan University, Shanghai 200438, China
e-mail: 22110190096@m.fudan.edu.cn

F.-B. Yang and J.-P. Huang, *Diffusionics*,
https://doi.org/10.1007/978-981-97-0487-3_17

heating to cooling, and energy harvesting [29, 30], which pertains to the conversion of thermal energy from sources like the Sun into other forms of energy. Recent advancements have seen the crafting of various thermal metamaterials to achieve superior functionalities [31, 32] using passive frameworks, including transformation theory [8, 33], scattering cancellation [34, 35], and topology optimization [36, 37]. In addition, there are active methods [38, 39] utilizing external triggers to ensure exceptional thermal manipulation. Notably, the inherent dissipative nature of diffusion aligns closely with non-Hermitian physics [40].

Managing mass flow is crucial for a multitude of processes in chemical and biomolecular sciences [41]. Microscopically, particle diffusion usually appears as Brownian motion [42], a fundamental concept in statistical physics [43, 44]. Decoding the intricate mechanisms underlying particle diffusion is essential for creating efficient transport materials and innovative therapeutic techniques. On a macroscopic scale, diffusion adheres to Fick's law [45]. Given the similarities between particle diffusion and heat transport, the frameworks developed for thermal metamaterials are anticipated to be applicable to particle diffusion systems.

This chapter pivots on macroscopic particle diffusion, delving into theoretical designs, simulations, and experimental findings. In Sect. 17.2, traditional manipulation techniques within the convection-diffusion process are described. Subsequently, the spotlight shifts to chemical waves in Sect. 17.3, which are characterized by spatiotemporal [46] concentration variations. The chapter concludes with a discussion of the prevailing challenges and potential future directions in this field. It is hoped that this chapter elucidates the complexities of diffusion dynamics across diverse models and sheds light on outstanding challenges that merit future investigation.

17.2 Quasi-equilibrium Diffusion Model

17.2.1 General Transformation Theory

Metamaterials tailored for mass diffusion have garnered considerable interest since the debut of the particle cloak rooted in transformation theory. Their potential in fields like drug delivery underscores this interest. Numerous fundamental devices influencing mass diffusion have been documented, spanning from particle movement to light transmission. These devices encompass particle concentrators, electron cloaks, light-diffusive cloaks, and plasma rotators.

While the transformation theory doesn't precisely correlate with Fick's second equation, mass diffusion cloaking through the low-diffusivity approximation remains achievable. In 2013, Guenneau and colleagues [47] introduced a granular cloak grounded in transformation theory. Such a cloak holds potential, especially in safeguarding drugs during internal delivery. Their focus centered on the concentration of chemical species, potentially benefiting fields such as biophysics and bioengineering. They began by representing the convection-diffusion equation in a domain Ω as:

$$\frac{\partial c}{\partial t} = \sum_{i,j} \frac{\partial}{\partial x_i} \left(\kappa_{ij}(x) \frac{\partial c}{\partial x_j} \right) - \sum_i \frac{\partial}{\partial x_i} v_i c, \tag{17.1}$$

where c denotes the mass concentration in biochemistry, as a function of time $t > 0$, κ signifies the chemical diffusion (in units of $\mathrm{m}^3\ \mathrm{s}^{-1}$), and v is the velocity field. After a variable change $x \to y$ governed by a Jacobian matrix J where $J_{ij} = \partial y_i / \partial x_j$, the equation becomes:

$$\frac{1}{\det_{ij}} \frac{\partial c}{\partial t} = \sum_{i,j,k,l} \frac{\partial}{\partial y_i} \left(\frac{1}{\det J_{ij}} \mathrm{J}_{ik} \kappa_{kl} J_{jl}^T \frac{\partial c}{\partial y_j} \right) - \sum_{i,j} \frac{1}{\det J_{ij}} J_{ij}^T \frac{\partial}{\partial y_i} v_i c, \tag{17.2}$$

The transformed diffusivity and velocity are defined as:

$$\begin{cases} \kappa' = J \kappa J^T / \det J \\ v' = J^T v / \det J \end{cases} \tag{17.3}$$

With Eq. (17.3), a diffusion cloak was constructed that rendered enclosed objects undetectable against a background. Spheres coated with concentric layers of homogeneous isotropic diffusivity were employed to simulate the desired anisotropic heterogeneous diffusivity. The study introduced a novel perspective on cloaking in the context of mass diffusion, with potential implications for fields such as bioengineering and chemical engineering.

Following this, Zeng et al. [48] introduced an innovative technique to reduce steel corrosion in concrete. They designed a multilayered concrete cloak aimed at shielding against chloride ions. Simulation results indicated that the six-layer cloak effectively prevented the infiltration of chloride ions into the concrete. Experimental data corroborated that concentration gradients outside the cloak remained consistent, while gradients within the cloak were reduced.

The previous researches focused on geometrically isotropic structures, like circles, which might have limited their functional adaptability. Diversifying from this approach, Guenneau et al. [49] expanded the scope, moving from basic circular cylindrical designs to more complex geometries. They introduced a geometric transformation catering to cloaks of various shapes, denoted as:

$$\rho' = \frac{R_3(\theta) - R_1(\theta)}{R_3(\theta)} \rho + R_1(\theta), 0 < \rho < R_3(\theta), \tag{17.4}$$

where $R(\theta)$ denotes a continuous function with a periodicity of 2π and defines the cloak's cross-section. Equation (17.4) transitions the point $\rho = 0$ to the region $\rho' < R_1(\theta)$ and reshapes the space bounded by $0 < \rho < R_3(\theta)$ into the region $R_1(\theta) < \rho' < R_3(\theta)$. By integrating Eqs. (17.3) and (17.4), the parameters for the arbitrary cloak were determined. Using this methodology, concentrators and rotators of various forms were crafted. The potential to design invisibility carpets optimized for diffusion processes was also explored.

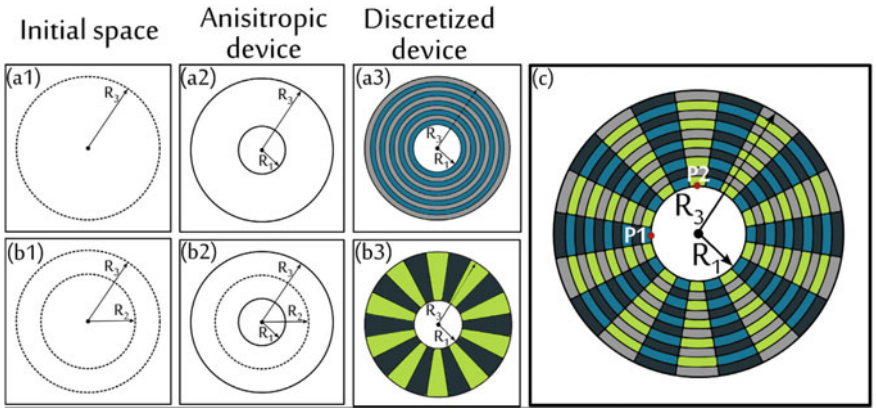

Fig. 17.1 Coordinate transformation applications in mass separation metamaterials: **a** Cloaking: Transformation of a point into a circle with radius R_1, accompanied by adjacent region compression. **b** Concentration: A circular region defined by $0 < r < R_2$ is compressed to $0 < r < R_1$, succeeded by expansion of the neighboring annulus from R_2 to R_1. **c** Bi-Functional Multilayer Design: The structure incorporates four distinct materials, represented in dark blue, grey, light blue, and light green. (from Ref. [50], licensed under CC-BY 4.0)

In 2016, Restrepo-Flórez et al. [50] delved into extensive investigations, as illustrated in Fig. 17.1. Utilizing linear transformations, they designed both cloaks and concentrators. The cloaking transformation morphed a circle of a predetermined radius into an annulus. In contrast, the design of concentrators entailed two operations: compressing one circular region into another and subsequently expanding an adjacent area. Through experimental implementations, they introduced multilayered designs, utilizing concentric rings for cloaking and lamellar structures for concentration. The research illuminated the simultaneous manipulation of different particles, presenting a viable approach for mixture separation. It showcased the cloaking of N_2 and the concentration of O_2 over designated time frames, culminating in a stable state. The team further explored molecule cloaking and concentrating, emphasizing the significance of mass concentration discontinuities due to varied solubilities. Understanding these discontinuities is essential for the meticulous design and assessment of mass diffusion metamaterial devices.

The transformation theory also presents opportunities in the domain of metamaterial membrane designs. In a separate 2016 study, Restrepo-Flórez et al. [51] leveraged coordinate transformations in tandem with metamaterial theory to enhance compound separation. By strategically designing spatial diffusivity for mass diffusion, they achieved localization of distinct compounds in specified regions, allowing for the separation of mixtures via a metamaterial membrane. Such an approach could hold relevance in various sectors necessitating separation processes.

17.2.2 Scattering Cancellation Theory

While prior discussions have underscored the potential of controlling mass diffusion through transformation theory, the inherent challenges of complex transformations, extreme parameters, and inhomogeneous functional regions pose considerable practical challenges. These issues may be more effectively circumvented by adopting the scattering cancellation theory for the design of metamaterial-based mass manipulations.

Li et al. [52, 53] considered a stable state without particle sources where the concentration distribution is governed by the equation:

$$\nabla \cdot (D\nabla c) = 0, \tag{17.5}$$

Here, ∇ is the operator in the Cartesian coordinate system and D denotes diffusivity. For a sphere of radius R_1 encapsulated by a bilayer spherical cloak having an inner radius R_2 and an outer radius R_3, the concentration distribution within this sphere is:

$$c_1 = -\sum_{l=1}^{\infty} \left[A_l r^l + B_l r^{-(l+1)}\right] P_l(\cos\theta) \quad (r \le R_1)\,, \tag{17.6}$$

where $P_l(\cos\theta)$ is a lth-order Legendre polynomial, and A_l and B_l are constants yet to be determined. They also presented the concentration distribution for the bilayer cloak as:

$$\begin{aligned} c_2 &= -\sum_{l=1}^{\infty} \left[C_l r^l + E_l r^{-(l+1)}\right] P_l(\cos\theta) \quad (R_1 < r \le R_2) \\ c_3 &= -\sum_{l=1}^{\infty} \left[F_l r^l + G_l r^{-(l+1)}\right] P_l(\cos\theta) \quad (R_2 < r \le R_3) \\ c_4 &= -\sum_{l=1}^{\infty} \left[H_l r^l + I_l r^{-(l+1)}\right] P_l(\cos\theta) \qquad (r > R_3) \end{aligned} \tag{17.7}$$

Given that $r \to \infty$, c_4 then equates to $-c_0 r\cos\theta$. Hence, it's only essential to consider $l = 1$. If $r \to 0$, then c_1 remains finite, making $B_1 = 0$. The continuity conditions at boundaries are expressed as:

$$\begin{aligned} c_i|_{r=R_1,R_2,R_3} &= c_{i+1}|_{r=R_1,R_2,R_3}\,, \\ D_i \frac{\partial c_i}{\partial r}\bigg|_{r=R_1,R_2,R_3} &= D_{i+1} \frac{\partial c_{i+1}}{\partial r}\bigg|_{r=R_1,R_2,R_3}\,, \end{aligned} \tag{17.8}$$

where D_i denotes the diffusivity of the central region, inner layer, outer layer of the bilayer cloak, and the background medium, with i incrementing from 1 to 4.

To maintain a uniform concentration within the sphere, they apply a inner layer with a zero diffusivity ($D_2 = 0$). Therefore, their focus shifts to the concentration distribution outside the cloak. Incorporating Eqs. (17.7) and (17.8) into Eq. (17.5), they derived:

$$H_1 = c_0 R_2^3 \frac{D_3\left(2R_2^3 - 2R_1^3\right) - D_4\left(2R_2^3 + R_1^3\right)}{D_3\left(2R_2^3 - 2R_1^3\right) + 2D_4\left(2R_2^3 + R_1^3\right)} \tag{17.9}$$

Ensuring H_1 equals 0 yields another parameter for the bilayer cloak:

$$D = \frac{2R_2^3 + R_1^3}{2\left(R_2^3 - R_1^3\right)} D_0. \tag{17.10}$$

In the case of 2D particle diffusion, this relationship can be rewritten as:

$$D = \frac{R_2^2 + R_1^2}{R_2^2 - R_1^2} D_0, \tag{17.11}$$

where D represents the diffusion coefficient of the bilayer cloak's outer layer, and D_0 is the diffusion coefficient of the surrounding medium.

The discussion reveals that a bilayer cloak requires an inner layer with a zero index and an external layer whose index corresponds to the background medium. A fan-shaped concentrator is also introduced, grounded in scattering cancellation theory. This concentrator can centralize particle concentrations. A notable "plug and switch" metamaterial concept was introduced, which allows modular functional units to be integrated into a primary board, offering switchable functionalities. This design offers adaptability and reconfigurability, fitting a wide range of applications without the need for a complete system redesign. Potential uses include sustained drug delivery, catalytic amplification, and the creation of bio-inspired cytomembranes.

However, using monolayer anisotropic materials presents practical fabrication difficulties. In 2021, Zhou et al. [54] introduced a bilayer meta-device designed to manipulate binary masses (O_2 and N_2). This model was developed from a direct interpretation of the static Fick's law, solely using homogeneous media. Numerical studies demonstrated the device's ability to mask O_2 concentrations and concentrate N_2 concentrations in both constant and transient states. The minimal interference in external concentration fields highlighted the robustness of the device's manipulation capabilities.

In environments such as vacuum and air, where light travels ballistically according to Maxwell's equations, designing a universally effective invisibility cloak is challenging. Schittny et al. [55] explored environments that cause multiple light scatterings, like clouds or frosted glass, where light conforms to Fick's diffusion equation. They constructed cylindrical and spherical invisibility cloaks, made from polydimethylsiloxane combined with melamine-resin microparticles. These cloaks, having hollow interiors, efficiently hid objects in a water-based diffusive setting across the entire visible spectrum. The discussions that followed emphasized the

transient scenario, presenting experimental evidence of the effectiveness of diffusive light cloaking in both constant and quasi-static states. This research on light diffusion cloaks indicates that, in a diffusive light scattering environment, passive, broadband invisibility cloaking for all light directions and polarizations might be feasible.

Traditional mass separation methods are based on the assumption of isotropic membrane material, which restricts directional mass-flow guidance. In 2018, Restrepo-Flórez et al. [56] presented a distinct separation device that uses an anisotropic polymeric membrane. These anisotropic membranes can be designed as multilayer structures, combining two isotropic materials with different diffusivities. The anisotropic technique achieved selectivities for O_2/N_2 separations, significantly outperforming the capabilities of leading isotropic polymers.

17.2.3 Transformation-Invariant Scheme

Traditional mass diffusion metamaterials have made remarkable strides, yet challenges persist when it comes to creating intelligent devices. Here, “intelligent" denotes a material’s ability to adaptively respond to environmental changes. A key limitation of conventional mass diffusion metamaterials is their rigidity; once their parameters undergo a transformation, they become static. This means that a device can function optimally in only one specific setting, restricting the broader applications of mass diffusion metamaterials. This underscores the critical need to explore mass diffusion metamaterials with adaptive capabilities. Transformation-invariant metamaterials present an intriguing avenue in this context.

Drawing inspiration from near-zero permittivity concepts, transformation-invariant metamaterials [57] first emerged within the realm of electromagnetics. These materials are predominantly recognized for their pronounced anisotropic properties. When applied to thermal diffusion, they manifest a pronounced anisotropic thermal conductivity. In the case of mass diffusion, the diffusion rate showcases this notable anisotropy: the rate is virtually zero in one direction while nearing infinity in another. Such distinctive characteristics ensure that transformation-invariant metamaterials maintain their robustness regardless of coordinate transformations. Consequently, they’ve attracted interest across electromagnetics, acoustics, and thermodynamics domains. Utilizing these materials to craft intelligent particle diffusion metamaterial shells holds promising potential.

17.2.3.1 Transformation-Invariant Approach in Mass Diffusion

In 2023, Zhang et al. [57] introduced designs for an irregular-shaped concentrator (Fig. 17.2a) and a circular rotator (Fig. 17.2b), specifically optimized to respond to environmental shifts. For the sake of clarity, the team assumed consistent solubilities for the chemical species and overlooked the effects of chemical potentials [58]. As a result, mass diffusion was predominantly directed by Eq. (17.5). Through the

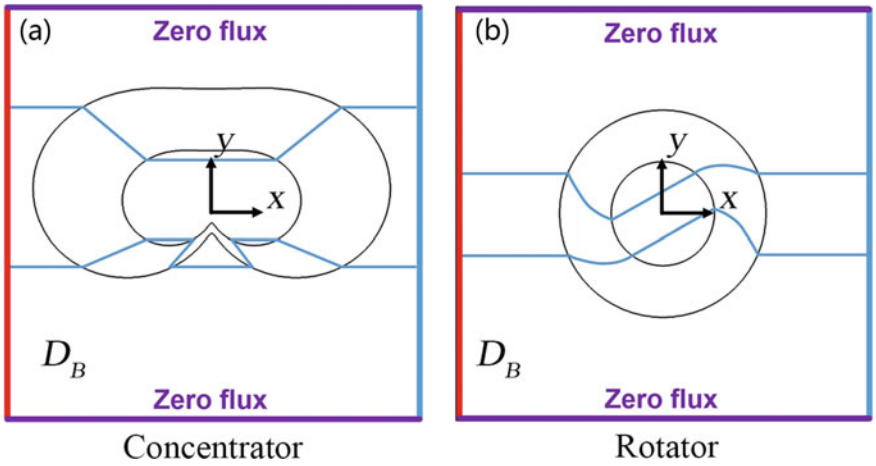

Fig. 17.2 Schematic diagram of chameleon-like **a** irregular concentrator and **b** circular rotator. The solid blue lines denote the mass flow. (from Ref. [57])

lens of transformation theory, the transparency characteristics of transformation-invariant metamaterials were detailed. Furthermore, it was demonstrated by them that the transparency maintained by these transformation-invariant metamaterials persists regardless of the specific finite coordinate transformation imposed. Given an arbitrary 2D coordinate transformation in cylindrical coordinates:

$$\begin{cases} r' = f(r,\theta), \\ \theta' = g(r,\theta), \end{cases} \tag{17.12}$$

where $f(r,\theta)$ and $g(r,\theta)$ are distinct functions of radius r and angle θ and the Jacobian matrix $\mathbf{J}$ can be expressed as:

$$\mathbf{J} = \begin{bmatrix} \partial_r f & \partial_\theta f/r \\ r'\partial_r g & r'\partial_\theta g/r \end{bmatrix}. \tag{17.13}$$

The transformed diffusivity, $\boldsymbol{D}'$, is derived from the transformation theory:

$$\boldsymbol{D}' = \frac{\mathbf{J}\boldsymbol{D}\mathbf{J}^{\tau}}{\det \mathbf{J}}, \tag{17.14}$$

where $\det \mathbf{J}$ denotes the determinant of $\mathbf{J}$ ($\mathbf{J}^{\tau}$ is its transpose). The components D_{rr} and $D_{\theta\theta}$ represent the radial and tangential diffusivities. The eigenvalues of $\boldsymbol{D}'$ are then:

$$\lambda_1 = \frac{D_{rr}}{\det \mathbf{J}} \left[(\partial_r f)^2 + (r' \partial_r g)^2 \right], \tag{17.15a}$$

$$\lambda_2 \approx \frac{D_{\theta\theta}}{\det \mathbf{J}}. \tag{17.15b}$$

Given that for transformation-invariant metamaterials $D_{rr} \approx \infty$ and $D_{\theta\theta} \approx 0$, Eq. (17.15) can be simplified to:

$$\lambda_1 \approx \infty, \tag{17.16a}$$

$$\lambda_2 \approx 0. \tag{17.16b}$$

Equation (17.16) indicates that the eigenvalues are consistent across various coordinate transformations, emphasizing the robustness of transformation-invariant metamaterials against coordinate changes.

The coordinate transformation corresponding to the standard concentrator of uniform shape is provided by

$$\begin{cases} r' = \dfrac{r_1}{r_m} r, & r' < r_1 F(\theta), \\ r' = Ar + BF(\theta), & r_1 F(\theta) < r' < r_2 F(\theta), \\ \theta' = \theta, \end{cases} \tag{17.17}$$

where r_m is a constant. The function $F(\theta)$ is defined as $F(\theta) = 1.2 + 0.5\sin(\theta) + 0.5\cos(2\theta)$, with constants A and B given by $A = (r_2 - r_1)/(r_2 - r_m)$ and $B = (r_1 - r_m)r_2/(r_2 - r_m)$, respectively. Regarding the chameleonlike rotator, its coordinate transformation is given by

$$\begin{cases} r' = r, \\ \theta' = \theta + \theta_0 (r - r_2)/(r_1 - r_2), & r_1 < r < r_2, \end{cases} \tag{17.18}$$

with θ_0 representing the rotation angle. This transformation can be interpreted as a rotation of a series of circles with varying angles determined by their corresponding radii. By integrating Eqs. (17.14) and (17.18), the transformed diffusivity was derived.

17.2.3.2 Finite-Element Simulation

To simulate the system, specific boundary conditions and parameters are established. The left boundary receives a high-concentration source, whereas the right boundary is exposed to a low-concentration source. Both the top and bottom boundaries are defined with no-flux conditions. The background diffusion rate is designated as $D_B = 10 D_0$. The subsequent transformed diffusivity can be ascertained using Eqs. (17.14), (17.17), and (17.18).

Figure 17.3a1 displays the concentration distribution along the x-direction for a translation-invariant concentrator. It becomes clear that the chameleon-like thermal concentrator functions efficiently in environments with high diffusivity. Conversely, as depicted in Fig. 17.3a2, the conventional concentrator is ineffective under such conditions. For a more granular assessment, data were extracted to facilitate a

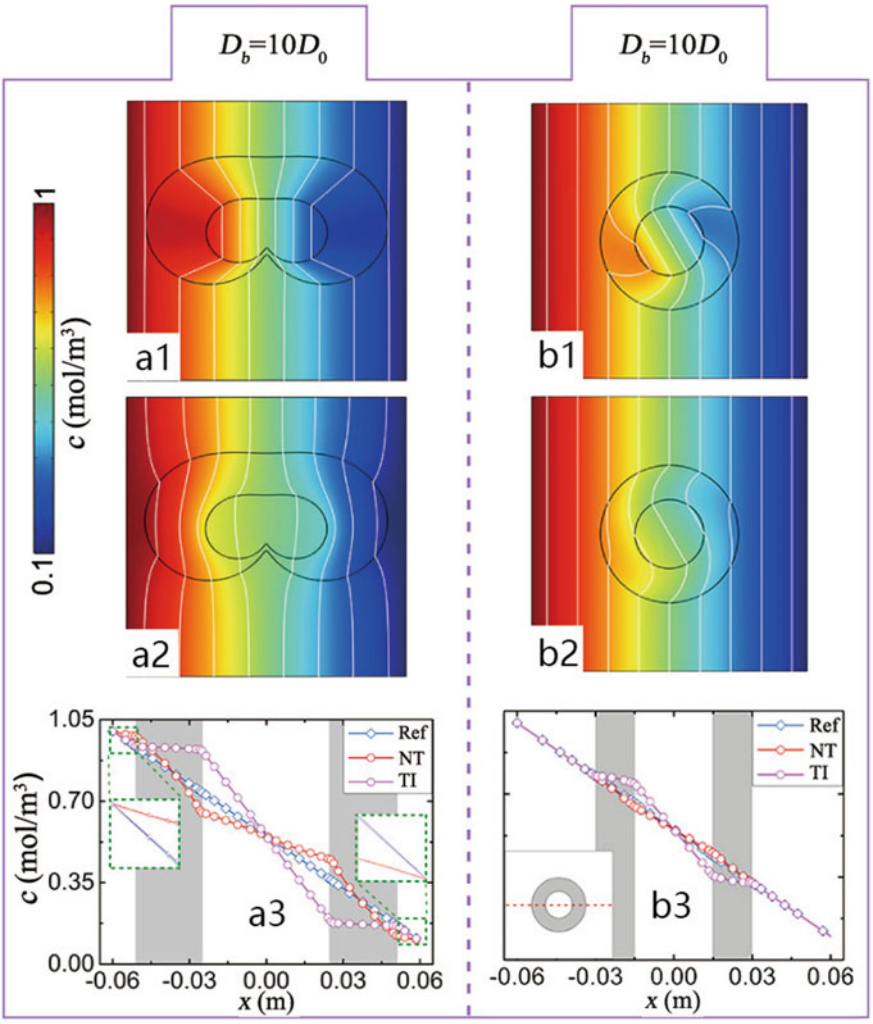

Fig. 17.3 Simulations of the transformation-invariant (a1) concentrator and (b1) rotator with background diffusivity $10D_0$. Simulations of the normal-transformation (a2) concentrator and (b2) rotator with background diffusivity $10D_0$. (a3) Comparison between reference, transformation-invariant concentrator, and normal-transforming concentrator. (b3) Comparison between reference, transformation-invariant rotator, and normal-transforming rotator. TI and NT denote devices based on transformation-invariant denotes normal-transforming schemes, respectively. The green dashed squares in (a3)(b3) are enlarged images. (from Ref. [57])

detailed quantitative analysis. The third row of Fig. 17.3a3 compares concentration data between the uniform background (serving as a reference line), the conventional concentrator, and the chameleon-like concentrator. Within this figure, the shell's location is demarcated by a gray area. The concentration curve for the conventional concentrator deviates noticeably from the reference curve in the device's surrounding background area. Importantly, within the device's core area, when D_B=10D_0, the concentration gradient of the conventional concentrator is even inferior to the gradient of the reference curve. This observation underscores that the conventional concentrator not only disrupts the background but also falls short in its aggregation function. In stark contrast, the translation-invariant concentrator closely aligns its concentration curve with the reference line in the surrounding background area. Additionally, its internal concentration gradient consistently surpasses the background gradient, reinforcing theoretical predictions. In Fig. 17.3a3, the purple curve's gradient surpasses that of the red curve, suggesting that even when the conventional concentrator operates as intended, its aggregation effect is still inferior to the chameleon-like concentrator. This phenomenon can be traced back to the inherent differences in aggregation degrees: while a conventional concentrator's degree is influenced by r_m/r_1, the chameleon-like concentrator's degree closely aligns with r_2/r_1. As a general observation, the aggregation degree of the conventional concentrator tends to be less pronounced compared to its chameleon-like counterpart.

Figure 17.3b1 showcases the chameleon-like rotator's performance across varied backgrounds. The chameleon-like rotator adeptly adjusts to environmental shifts, altering the transport direction in its core without perturbing the surrounding environment. In contrast, the conventional rotator, demonstrated in Fig. 17.3b2, operates optimally only within specific background parameters. Any deviation from these conditions incapacitates the conventional concentrator. Furthermore, Fig. 17.3b3 highlights a superior concentration gradient within the core of the chameleon-like rotator compared to the background gradient, implying the dual functionality of rotation and aggregation. However, the conventional rotator is devoid of this aggregation capability. This distinction arises from the intrinsic aggregation capabilities of the transformation-invariant metamaterial shell. The rotational transformation remains non-intrusive to the shell's native properties, echoing previous theoretical insights. Such findings accentuate the distinct attributes of the irregular chameleon-like concentrator and the annular chameleon-like rotator, both premised on the transformation-invariant metamaterial shell.

17.2.3.3 Experimental Suggestion

Although nature seldom offers extremely anisotropic materials, mimicking such effects remains achievable using two materials with pronouncedly different diffusion rates. An implementable experimental methodology is also delineated. Taking the chameleon-like concentrator depicted in Fig. 17.4a as a representative example, testing under varied background conditions necessitates media with differing diffusion rates. Conventionally, this calls for procuring a multitude of materials, adding

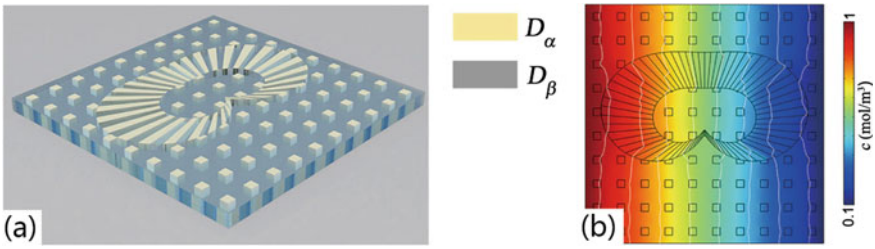

Fig. 17.4 **a** Diagrammatic figures and **b** simulation results of the experimental setup with chessboard structure. (from Ref. [57])

potential complexities to the experimental framework. As an alternative, leveraging a checkerboard design for the background medium is proposed, complemented by a layered approach for the concentrator's construction. This design strategy requires only two materials with distinctly varied diffusion rates, with water and resin emerging as potential candidates. Figure 17.4b illustrates the concentration distribution of the translation-invariant concentrator. Despite fluctuations in the background diffusion rate, the layered concentrator maintains its functionality without noticeably impacting the background, elevating the internal concentration gradient. Such results suggest that even with a two-material-based simulation, the experimental apparatus exhibits optimistic outcomes. Nonetheless, a point of contention remains: the simulation results reflect a subdued concentration effect within the concentrator's core, accompanied by slight background disturbances. These anomalies stem from inadequate background discretization and a rather dispersed distribution of inclusions, inducing pronounced localized discrepancies. A denser inclusion distribution is posited to refine the simulation results.

17.3 Non-equilibrium Diffusion Model

The precise regulation of mass transport plays a pivotal role in areas such as biochemical reactions, drug delivery, and particle separation. Certain drug components, for example, are designed to target specific cells exclusively. Yet, during the delivery phase, these components might be absorbed by non-target cells or even interact with chemical entities in the plasma, leading to diminished therapeutic efficacy. In industrial production and biochemistry, the tasks of particle separation, concentration, and detection are routine. This includes processes like the purification of hydrocarbon fuels from crude oil, the extraction of uranium from seawater, and monitoring harmful solutes in atmospheric or aquatic environments. From the standpoint of physics, the convection-diffusion equation typically underpins mass transport. Numerous methods, informed by this equation, have been suggested for its control, such as the scattering cancelation method and the transformation theory.

However, handling transient (or time-varying) mass transport presents challenges distinct from those of steady-state control. A paradigmatic example of this transient transport is the chemical wave [59], which are far from equilibrium [60], exhibiting concentration profiles characterized by spatiotemporal fluctuations. At its core, a chemical wave describes the dynamic variation in particle concentration across time and space. While the transformation theory fits well with steady-state mass transport, it falls short in transient situations. The primary reason is that the governing equation for transient mass transport doesn't retain its structure during coordinate transformations. While research on transient heat diffusion provides some direction, the methodologies are often bound to specific geometric configurations. As a result, devising a theoretical framework to control chemical waves remains a substantial challenge.

17.3.1 Theoretical Foundation

To address this challenge, researchers [61] developed an optimized transformation-mass-transfer theory. This methodology enables the meticulous control over chemical waves and sheds light on their propagation properties. In the investigation of chemical processes, specific chemical components were set aside, focusing instead on concentration gradients as the predominant factors. This led to the utilization of the advection-diffusion equation to represent chemical waves:

$$\partial c/\partial t = \nabla \cdot (\overleftrightarrow{D} \cdot \nabla c - vc) \tag{17.19}$$

In this equation, c, t, $\overleftrightarrow{D}$, and v are representative of concentration, time, tensorial diffusivity, and advection velocity, respectively. Without compromising generality, a one-dimensional scenario was considered, characterized by scalar diffusivity D and constant velocity v along the x-axis. This simplifies Eq. (17.19) to:

$$\frac{\partial c}{\partial t} = D\frac{\partial^2 c}{\partial x^2} - v\frac{\partial c}{\partial x} \tag{17.20}$$

For a chemical wave, considering the spatiotemporal variability in concentration, a plane-wave solution is appropriate:

$$c = c_a e^{i(\beta x - \omega t)} + c_r, \tag{17.21}$$

Here, c_a, β, ω, and c_r symbolize the concentration amplitude, wave number, circular frequency, and reference concentration of the chemical wave, respectively. It is observed that with a predetermined frequency of the concentration source, the concentration amplitude of the chemical wave diminishes upon propagation. This observation leads to the interpretation of the wave number β as a complex entity

given by $\beta = k + i\alpha$, where both k and α are real quantities. Therefore, Eq. (17.21) can be equivalently represented as $c = c_a e^{-\alpha x} e^{i(kx-\omega t)} + c_r$. Evidently, α designates the spatial dissipation of the chemical wave, while k stands for the real wave number. Incorporating this into Eq. (17.20) results in:

$$\begin{cases} \alpha = \dfrac{-2v + \xi}{4D} \\ k = \dfrac{\sqrt{v^4 + 16D^2\omega^2} - v^2}{16D^2\omega}\xi \end{cases} \tag{17.22}$$

with $\xi = \sqrt{2v^2 + 2\sqrt{v^4 + 16D^2\omega^2}}$. The consideration is limited exclusively to forward propagation, thus retaining only the positive solution. An evident increase in ω correlates with a rise in either α or k. Such a concentration profile might be conceptualized as a chemical wave. However, a comprehensive chemical wave model would be more sophisticated than the currently presented framework. Nevertheless, this basic model can shed light on the regulation of chemical waves, especially when utilizing the subsequent optimized-transformation theory crafted for transient mass transfer.

To elucidate the transformation rule, the component form of the advection-diffusion equation in curvilinear space was articulated using the corresponding coordinate x_i:

$$\sqrt{G}\partial_t c = \partial_i \left(\sqrt{G} D^{ij} \partial_j c - \sqrt{G} v_i c \right), \tag{17.23}$$

where G symbolizes the determinant of $G_i \cdot G_j$, with G_i and G_j being the covariant bases of the curvilinear space. This equation was then manifested in the physical space x_i':

$$\sqrt{G}\partial_t c = \partial_{i'} \frac{\partial x_i'}{\partial x_i} \left(\sqrt{G} D^{ij} \frac{\partial x_j'}{\partial x_j} \partial_{j'} c - \sqrt{G} v_i c \right), \tag{17.24}$$

In this context, $\partial x_i'/\partial x_i$ and $\partial x_j'/\partial x_j$ are components of the Jacobian-transformation matrix J. The determinant of J is represented as $1/\sqrt{G}$, which provides:

$$\frac{1}{\det J}\partial_t c = \nabla' \cdot \left(\frac{J \overleftrightarrow{D} J^\tau}{\det J} \nabla' c - \frac{Jvc}{\det J} \right), \tag{17.25}$$

where J^τ signifies the transpose of J. Intriguingly, when transformed parameters $J \overleftrightarrow{D} J^\tau/\det J$ and $Jv/\det J$ are denoted as $\overleftrightarrow{D}''$ and v'' respectively, a complete substitution from space transformation to material transformation remains elusive, attributed to the lack of a physical quantity preceding $\partial_t c$. Hence, the form-invariance for transient mass transfer under a coordinate transformation is confined to cases where $\det J = 1$.

To circumvent this constraint, an approximation was adopted, which excludes the $1/\det J$ term before $\partial_t c$, refining the equation to:

$$\partial_t c = \nabla' \cdot (J \overleftrightarrow{D} J^\tau \nabla' c - Jvc). \tag{17.26}$$

It should be highlighted that Eq. (17.26) serves predominantly as an approximation to Eq. (17.25), given the position-dependent attribute of $\det J$. Yet, subsequent simulations affirmed the feasibility of this approximation. As a result, the transformed parameters $\overleftrightarrow{D}'$ and v' can be deduced as:

$$\begin{cases} \overleftrightarrow{D}' = J \overleftrightarrow{D} J^\tau, \\ v' = Jv. \end{cases} \tag{17.27}$$

Therefore, it can be inferred that Eq. (17.26) maintains form invariance under coordinate transformation by approximation. The performance of Eq. (17.27) in simulations aligns with the optimized transformation-mass-transfer theory.

17.3.2 Model Application

Utilizing the optimized transformation mass transfer theory, four functional devices have been conceptualized as tangible illustrations for regulating chemical waves. These devices are tailored to achieve specific functions: cloaking, concentrating, rotating, and separating chemical waves. Figure 17.5 provides schematic representations of the four device models. Chemical waves are introduced from the left end

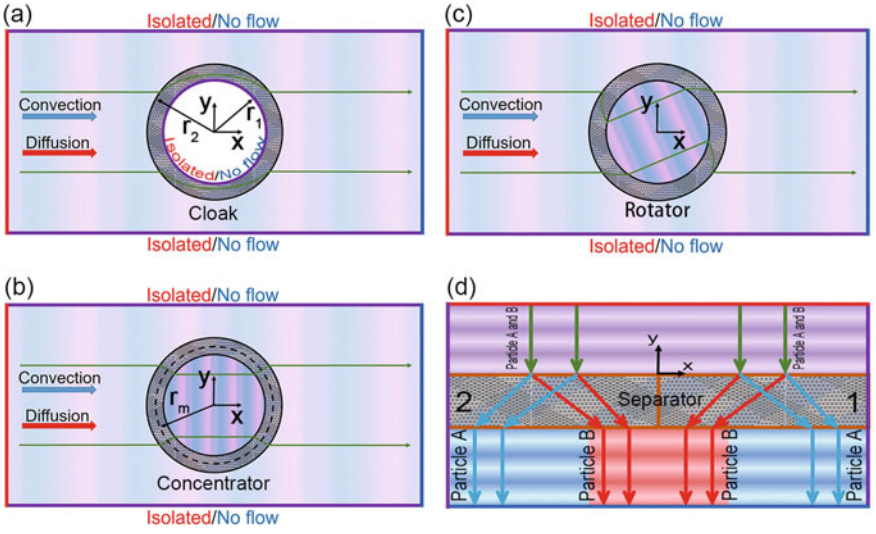

Fig. 17.5 **a–d** Schematic diagrams of cloaking, concentrating, rotating, and separating in two dimensions, respectively. (from Ref. [61])

of the rectangular medium, propagating along the x-direction, and flow through the functional devices without disturbing their waveforms. Maintaining the waveform of the chemical waves in the surrounding background medium is a critical feature of devices designed using transformation theory. Notably, the shielding device offers protection to entities within the core region from external material influences; the concentrator funnels chemical waves into the core, amplifying the concentration gradient; the rotator adjusts the chemical wave's propagation direction within the core, facilitating a seamless rotation angle adjustment; the separator has different guiding effects on different particles, realizing the separation effect.

For cloaking applications, a coordinate transformation maps the virtual space, described by (r, θ), to the physical space defined as $\left(r', \theta'\right)$. This transformation is governed by the relations $r' = ar + b$ and $\theta' = \theta$. The constants are given as $a = (r_2 - r_1)/r_2$ and $b = r_1$. In this context, r_1 and r_2 delineate the radii of the cloak's inner and outer boundaries, respectively, as depicted in Fig. 17.5a. The Jacobian transformation matrix, J, is derived as:

$$J_2 = \text{diag}\left[ar',\ a/\left(r' - b\right)\right] \tag{17.28}$$

For the concentrator, the coordinate transformation is characterized by $r' = hr$ for $r < r_m, r' = nr + m$ for $r_m < r < r_2$, and $\theta' = \theta$ for $0 < r < r_2$. The parameters are defined as: $h = r_1/r_m$, $n = (r_2 - r_1)/(r_2 - r_m)$, $m = (r_1 - r_m)\, r_2/(r_2 - r_m)$, with r_m being an intermediate radius between r_1 and r_2 as shown by the dashed line in Fig. 17.5b. Consequently, the Jacobian-transformation matrices for the concentrator in the domains $r' < r_1$ and $r_1 < r' < r_2$ are given by:

$$\begin{aligned} J_1 &= \text{diag}\left[h, h\right], \\ J_2 &= \text{diag}\left[n, r'n/\left(r' - m\right)\right]. \end{aligned} \tag{17.29}$$

It is essential to recognize that these coordinate transformations exclusively modify the radius, keeping the angle invariant. To induce a rotation in the chemical waves, a refined theory was applied. The corresponding coordinate transformations for this rotation are $r' = r$ for the domain $0 < r < r_2$, $\theta' = \theta + \theta_0$ for $r < r_1$, and $\theta' = \theta + g(r - r_2)$ for $r_1 < r < r_2$, as illustrated in Fig. 17.5c. Here, g is defined as $\theta_0/(r - r_2)$, with θ_0 denoting the rotation angle. The resultant Jacobian transformation matrices are:

$$\begin{aligned} J_1 &= \text{diag}\left[1, 1\right], (r' < r_1) \\ J_2 &= \begin{bmatrix} 1 & 0 \\ r'g & 1 \end{bmatrix}, (r_1 < r' < r_2). \end{aligned} \tag{17.30}$$

Then, they introduce an innovative chemical wave separator that transforms both the radius and the angle simultaneously. As depicted in Fig. 17.5d, a combined chemical wave comprising particles A and B enters from the top, moves past the separator (represented by grids), and eventually splits into separate channels, exiting from the bottom. During this progression, particles A and B are distinctly channeled into sep-

arate regions. The underlying principles of this separation mechanism are discussed in subsequent sections.

For an in-depth analysis, the separator is divided into two distinct regions. The rectangular section on the right is referred to as area-1, while the remaining portion is designated as area-2. The dimensions of area-1 are characterized by a length of x_0 and a width of y_0. To ensure clarity and visual coherence, a transformation in Cartesian coordinates is utilized. As such, the coordinate transformation for point A in area-1 is defined by $x' = (y/(2y_0) + 1) - x_0 y/(2y_0)$ and $y' = y$. Similarly, for point B, the transformation is expressed as $x' - x_0 = (y/(2y_0) + 1) + x_0 y/(2y_0)$ and $y' = y$. The corresponding Jacobian matrices are detailed as:

$$\begin{cases} J_{1A} = \begin{pmatrix} \left(y' + 2y_0\right)/(2y_0) & \left(x' - x_0\right)/\left(y' + 2y_0\right) \\ 0 & 1 \end{pmatrix}, \\ J_{1B} = \begin{bmatrix} \left(y' + 2y_0\right)/(2y_0) & x'/\left(y' + 2y_0\right) \\ 0 & 1 \end{bmatrix}, \end{cases} \tag{17.31}$$

In this context, J_{1A} represents the Jacobian-transformation matrix for point A in area-1, while J_{1B} denotes that for point B. With the Jacobian-transformation matrices for these four models established, the substitution of Eqs. (17.28), (17.29), (17.30), and (17.31) into Eq. (17.27) allows for the computation of the desired diffusivities and velocities.

17.3.3 Finite-Element Simulation

To validate the proposed theory, simulations were conducted using COMSOL Multiphysics through finite element analysis. The boundary conditions for cloaking, concentration, and rotation are depicted in Fig. 17.6a–f. A periodic concentration source is described as $c_b = c_a \cos(\omega_0 t) + c_r$ where $c_a = 0.5$ mol m^{-3}, $\omega_0 = \pi/10$ s^{-1}, and $c_r = 1$ mol m^{-3}. This source was introduced on the left boundary (highlighted in red). The decay rate, as determined by Eq. (17.22), is influenced by ω. Consequently, ω_0 was selected as $\pi/10$ s^{-1} to assure minimal dissipation. The right boundary was defined as an open boundary (marked in blue). Moreover, isolated and no-flow conditions were set for both the top and bottom boundaries. In Fig. 17.6a, the inner boundary received similar conditions. The diffusivity and advection velocity of the background were allocated values of D_0 and v_0 respectively. All parameters were deduced from Eqs. (17.27)–(17.30). The simulation results for cloaking, concentration, and rotation are featured in Fig. 17.6. Notably, in Fig. 17.6a, an obstacle is effectively cloaked, preserving concentration profiles in the background and upholding the chemical wave's integrity. The tangential diffusivity component significantly exceeds its radial counterpart when $r' \approx r_1$, directing chemical waves around the core region. This outcome aligns with the simulation findings. In Fig. 17.6b, the dashed line signifies concentration distribution in a pure background, while the solid line

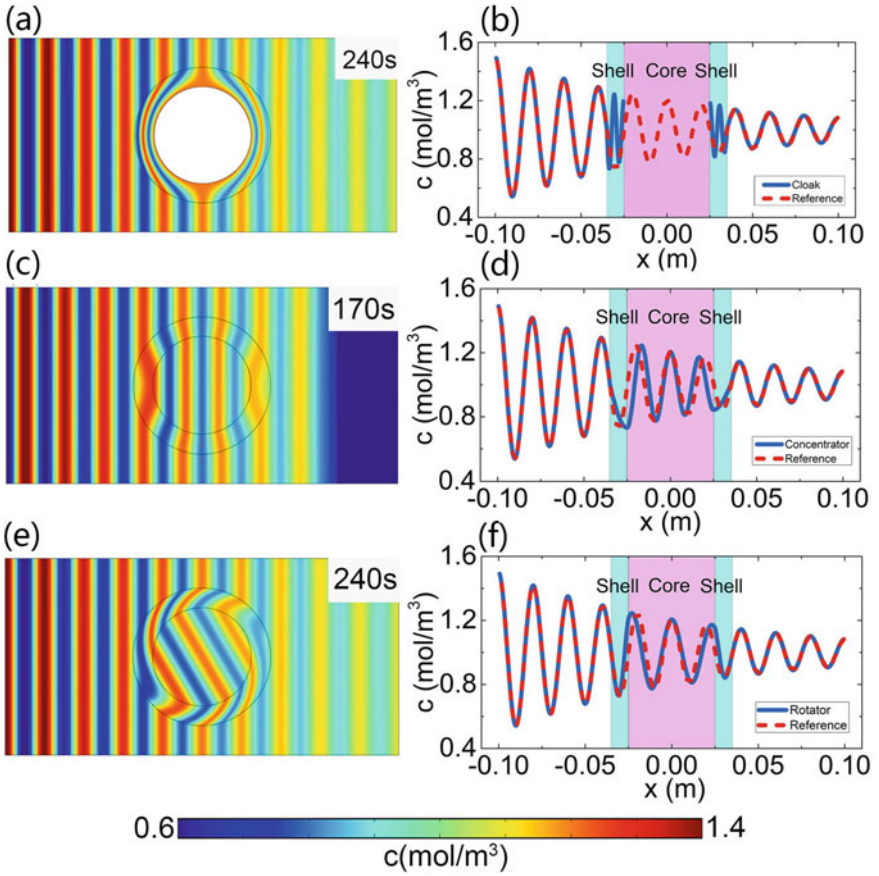

Fig. 17.6 Simulation results of **a, b** cloaking, **c, d** concentrating, and **e, f** rotating. (**a**), (**c**), (**e**) Concentration profiles at 240 s. Comparison between reference and (**b**) cloaking, (**d**) concentrating, and (**f**) rotating at 240 s. (from Ref. [61])

represents the same in the presence of a cloak. Detailed concentration outcomes are depicted in Fig. 17.6c–d. There is a pronounced concentration gradient, as shown in Fig. 17.6d where the solid line appears denser than its dashed counterpart in the core. Figure 17.6e showcases the rotation's impact on a chemical wave at 240 s, with the chemical wave in the core being deflected counter-clockwise by $\pi/6$, leaving the background concentration profile unaffected. For comparison, Fig. 17.6f illustrates the concentration distributions in both a pure background and one with a rotator.

The separator's model setup differs slightly from the preceding model. In the background medium, the diffusivity and convection velocities are denoted as D_{s0} and v_{s0} respectively. The geometric parameters incorporated include m_1 and m_2. A concentration $c_{sb} = c_{sa}\cos(\omega_{s0}t) + c_{sr}$, with parameters $c_{sa} = 0.5$ mol m^{-3}, $\omega_{s0} = \pi$ s^{-1}, and $c_{sr} = 1$ mol m^{-3}, was introduced at the top boundary. The bottom boundary

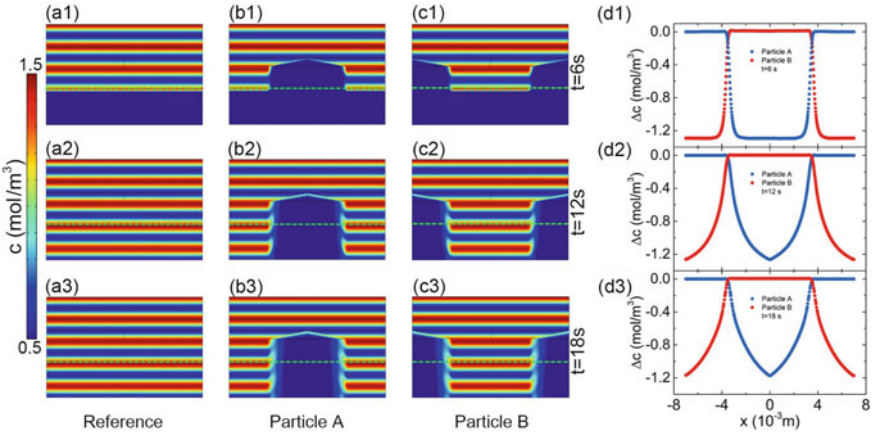

Fig. 17.7 Simulation Analysis of Separated Chemical Waves from Particles A and B: (a1)–(a3) Wave propagation in a pure medium at 6, 12, and 18 s, respectively. (b1)–(b3) Propagation of particle-A waves with a separator in the background medium at 6, 12, and 18 s, respectively. (c1)–(c3) Propagation of particle-B waves with a separator in the background medium at 6, 12, and 18 s, respectively. (d1) Concentration difference, $\triangle c$, of Particle A [or Particle B] between (b1) and (a1) [or between (c1) and (a1)] along the x-axis at 6 s, based on data from the x-directed green dashed lines in (b1) and (a1) [or in (c1) and (a1)]. Likewise, (d2) and (d3) display $\triangle c$ at 12 and 18 s, respectively. (from Ref. [61])

was marked as open, with isolated and no-flow conditions determined for the other sides. From Fig. 17.7a1–c3, it is evident that the same separator produces distinct guiding effects on different particles. Chemical waves of particle A converge on both sides, while those of particle B converge in the middle, achieving the separation of the two particles. Notably, the chemical waves of particles A and B retain their original phase information post-separation, marking a significant characteristic of this separator. Additionally, as time progresses, the separated chemical waves tend to diffuse towards each other, resulting in their recombination. For a more comprehensive understanding of the separation efficiency, quantitative data comparisons were made. As depicted in Fig. 17.7d1–d3, the concentration difference Δc between post-separation and pre-separation chemical waves of particles at 6, 12, and 18 s is displayed. Blue and red dot arrays represent the differences for particles A and B, respectively, with $\Delta c = c_A - c_{reference}$ and $\Delta c = c_B - c_{reference}$. Figure 17.7d1 reveals that the concentration of both particle types drops sharply at the interface of their respective aggregation regions, and is nearly zero in the opponent's aggregation region, attesting to the high purity of the freshly separated chemical waves and underscoring the superior performance of this separator. This validates the efficacy of the optimized transformation mass transfer theory when both radius and angle are varied simultaneously.

Regarding the experimental device, it was suggested to uniformly divide the separator into neatly arranged small segments. Each segment has a consistent diffusion rate parameter, which equals the value of the original separator's diffusion rate at the center point of that segment. In this manner, the originally spatially continuous

diffusion rate is replaced by a stepwise-changing diffusion rate. Clearly, this segmented approach serves as an approximation. Its accuracy depends on the granularity of the segmentation; the smaller the segments, the closer the outcome approaches the ideal scenario.

17.4 Conclusion and Outlook

This chapter provides a comprehensive examination of the evolution of metamaterials in particle dynamics, drawing inspiration from recent advancements in electromagnetism and thermotics. The foundational particle diffusion model, governed by the convection-diffusion equation, is elucidated. Owing to a restricted array of transformable parameters, the transformation theory does not fit perfectly with the transient governing equation. However, manifestations such as mass diffusion cloaking, concentrating, and rotating are feasible through the low-diffusivity approximation. Two significant challenges are evident. Firstly, the applicability of current mass-diffusion metamaterials is limited by their flexibility in dynamic environments. Addressing this, transformation invariant metamaterials have been utilized to craft adaptable chameleon-like metashells. These innovative metashells can autonomously adjust their effective parameters in response to environmental fluctuations without any energy consumption. The second challenge pertains to the typically anisotropic and singular parameters arising from the transformation, making experimental implementations intricate. In response, a myriad of research efforts have explored the scattering cancellation theory in particle diffusion systems, leading to the development of a range of mass diffusion meta-devices, encompassing cloaks, rotators, and separators. The article then delves into the chemical-wave model, characterized by its non-equilibrium state and concentration profiles that display spatiotemporal alterations. The propagation traits of this model can be manipulated via the transformation transient-mass transfer theory, leading to the proposition of four functional devices optimized for chemical wave management.

While there have been significant strides in the realm of particle diffusion metamaterials, several paramount challenges and queries remain unaddressed. Transformation thermotics and scattering cancellation are conventionally considered distinct methodologies for devising diffusion metamaterials. Yet, parameters derived from the former display anisotropy and inhomogeneity, whereas the latter grapples with transient particle diffusion and complex geometric designs. Of late, innovative solutions have surfaced to tackle these challenges. The introduction of the diffusive pseudo-conformal mapping [62] stands out, bridging the gap between diffusion and waves while ensuring optimal interface coherence. Noteworthy advancements in numerical techniques, including topology optimization algorithms [36, 37] and machine-learning strategies [63], provide sophisticated methodologies for crafting metamaterials apt for a diverse array of applications.

References

1. Veselago, V.G.: The electrodynamics of substances with simultaneously negative values of ϵ and μ. Sov. Phys. Usp. **10**, 509–514 (1968)
2. Kadic, M., Bückmann, T., Schittny, R., Wegener, M.: Metamaterials beyond electromagnetism. Rep. Prog. Phys. **76**, 126501 (2013)
3. Huang, J.P., Yu, K.W.: Effective nonlinear optical properties of graded metal-dielectric composite film of anisotropic particles. J. Opt. Soc. Am. B **22**, 1640–1647 (2005)
4. Yang, W.Z., Huang, J.P.: Effective mass density of liquid composites: Experiment and theory. J. Appl. Phys. **101**, 064903 (2007)
5. Cheben, P., Halir, R., Schmid, J.H., Atwater, H.A., Smith, D.R.: Subwavelength integrated photonics. Nature **560**, 565–572 (2018)
6. Huang, J.P., Yu, K.W.: Optical nonlinearity of colloidal crystals. Appl. Phys. Lett. **87**, 071103 (2005)
7. Zhang, J., Pendry, J.B., Luo, Y.: Transformation optics from macroscopic to nanoscale regimes: a chapter. Adv. Photonics **1**, 014001 (2019)
8. Fan, C.Z., Gao, Y., Huang, J.P.: Shaped graded materials with an apparent negative thermal conductivity. Appl. Phys. Lett. **92**, 251907 (2008)
9. Yang, S., Xu, L.J., Dai, G.L., Huang, J.P.: Omnithermal metamaterials switchable between transparency and cloaking. J. Appl. Phys. **128**, 095102 (2020)
10. Yang, S., Wang, J., Dai, G.L., Yang, F.B., Huang, J.P.: Controlling macroscopic heat transfer with thermal metamaterials: theory, experiment and application. Phys. Rep. **908**, 1–65 (2021)
11. Wang, J., Dai, G.L., Huang, J.P.: Thermal metamaterial: fundamental, application, and outlook. iScience **23**, 101637 (2020)
12. Zhao, X.X., Gao, Y., Huang, J.P.: A dielectrophoresis-based microchannel system. J. Appl. Phys. **105**, 064510 (2009)
13. Huang, J.P., Wang, Z.W., Holm, C.: Structure and magnetic properties of mono-and bi-dispersed ferrofluids as revealed by simulations. J. Magn. Magn. Mater. **289**, 234–237 (2005)
14. Huang, J.P., Yu, K.W.: First-principles approach to electrorotation assay. J. Phys.: Condens. Matter **14**, 1213–1221 (2002)
15. Pendry, J.B., Holden, A.J., Stewart, W.J., Youngs, I.: Extremely low frequency plasmons in metallic mesostructures. Phys. Rev. Lett. **76**, 4773–4776 (1996)
16. Pendry, J.B., Holden, A.J., Robbins, D.J., Stewart, W.J.: Magnetism from conductors and enhanced nonlinear phenomena. IEEE Trans. Microw. Theory Tech. **47**, 2075–2084 (1999)
17. Pendry, J.B., Schurig, D., Smith, D.R.: Controlling electromagnetic fields. Science **312**, 1780–1782 (2006)
18. Schurig, D., Mock, J.J., Justice, B.J., Cummer, S.A., Pendry, J.B., Starr, A.F., Smith, D.R.: Metamaterial electromagnetic cloak at microwave frequencies. Science **314**, 977–980 (2006)
19. Leonhardt, U.: Optical conformal mapping. Science **312**, 1777–1780 (2006)
20. Huang, J.P., Gao, L., Li, Z.Y.: Optical response of metal/dielectric composite containing interfacial layers. Commun. Theor. Phys. **36**, 251–256 (2001)
21. Pan, T., Huang, J.P., Li, Z.Y.: Optical bistability in metal-dielectric composite with interfacial layer. Phys. B **301**, 190–195 (2001)
22. Huang, J.P., Gao, L., Li, Z.Y.: Temperature effect on nonlinear optical response in metal/dielctric composite with interfacial layer. Solid State Commun. **115**, 347–352 (2000)
23. Huang, J.P., Li, Z.Y.: Effects of particle shape and microstructure on effective nonlinear response. Commun. Theor. Phys. **36**, 365–369 (2001)
24. Cummer, S.A., Popa, B.I., Schurig, D., Smith, D.R., Pendry, J.B., Rahm, M., Starr, A.: Scattering theory derivation of a 3D acoustic cloaking shell. Phys. Rev. Lett. **100**, 024301 (2008)
25. Xu, B., Huang, J.P., Yu, K.W.: Theory of nonlinear ac responses of inhomogeneous two-component composite films. Phys. Lett. A **357**, 475–478 (2006)
26. Tian, W.J., Huang, J.P., Yu, K.W.: Theory of nonlinear ac susceptibilities of dynamic electrorheological fluids under a dc electric field. Chem. Phys. Lett. **427**, 101–106 (2006)

27. Fan, C.Z., Huang, J.P., Yu, K.W.: Dielectrophoresis of an inhomogeneous colloidal particle under an inhomogeneous field: A first-principles approach. J. Phys. Chem. B **110**, 25665–25670 (2006)
28. Tian, W.J., Nakayama, T., Huang, J.P., Yu, K.W.: Scaling behaviors in settling process of fractal aggregates in water. Europhys. Lett. **78**, 46001 (2007)
29. Chen, Y.X., Shen, X.Y., Huang, J.P.: Engineering the accurate distortion of an object's temperature-distribution signature. Eur. Phys. J. Appl. Phys. **70**, 20901 (2015)
30. Shen, X.Y., Jiang, C.R., Li, Y., Huang, J.P.: Thermal metamaterial for convergent transfer of conductive heat with high efficiency. Appl. Phys. Lett. **109**, 201906 (2016)
31. Li, Y., Shen, X.Y., Wu, Z.H., Huang, J.Y., Chen, Y.X., Ni, Y.S., Huang, J.P.: Temperature-dependent transformation thermotics: From switchable thermal cloaks to macroscopic thermal diodes. Phys. Rev. Lett. **115**, 195503 (2015)
32. Li, Y., Shen, X.Y., Huang, J.P., Ni, Y.S.: Temperature-dependent transformation thermotics for unsteady states: Switchable concentrator for transient heat flow. Phys. Lett. A **380**, 1641–1647 (2016)
33. Gao, Y., Huang, J.P., Yu, K.W.: Multifrequency cloak with multishell by using transformation medium. J. Appl. Phys. **105**, 124505 (2009)
34. Huang, J.Y., Shen, X.Y., Jiang, C.R., Wu, Z.H., Huang, J.P.: Thermal expander. Phys. B **518**, 56–60 (2017)
35. Yang, S., Xu, L.J., Wang, R.Z., Huang, J.P.: Full control of heat transfer in single-particle structural materials. Appl. Phys. Lett. **111**, 121908 (2017)
36. Jin, P., Yang, S., Xu, L.J., Dai, G.L., Huang, J.P., Ouyang, X.P.: Particle swarm optimization for realizing bilayer thermal sensors with bulk isotropic materials. Int. J. Heat Mass Transf. **172**, 121177 (2021)
37. Sha, W., Xiao, M., Zhang, J., Ren, X., Zhu, Z., Zhang, Y., Xu, G. Q., Li, H, G., Liu, X. L., Chen, X., Gao, L., Qiu, C. W., Hu, R.: Robustly printable freeform thermal metamaterials. Nat. Commun. **12**, 7228 (2021)
38. Jin, P., Liu, J.R., Xu, L.J., Wang, J., Ouyang, X.P., Jiang, J.H., Huang, J.P.: Tunable liquid-solid hybrid thermal metamaterials with a topology transition. Proc. Natl. Acad. Sci. USA **120**, e2217068120 (2023)
39. Xu, L.J., Liu, J,R., Xu, G.Q., Huang, J.P., Qiu, C.W.: Giant, magnet-free, and room-temperature Hall-like heat transfer. Proc. Natl. Acad. Sci. USA **120**, e2305755120 (2023)
40. Xu, L.J., Huang, J.P.: Robust one-way edge state in convection-diffusion systems. Europhys. Lett. **134**, 60001 (2021)
41. Tan, P., Tian, W.J., Wu, X.F., Huang, J.Y., Zhou, L.W., Huang, J.P.: Saturated orientational polarization of polar molecules in giant electrorheological fluids. J. Phys. Chem. B **113**, 9092–9097 (2009)
42. Li, X.H., Yang, G., An, K.N., Huang, J.P.: Human behavioral regularity, fractional Brownian motion, and exotic phase transition. Phys. Lett. A **380**, 2912–2919 (2016)
43. Huang, J.P.: Statistical-mechanical theory of the overall magnetic properties of mesocrystals. Phys. Rev. E **70**, 041403 (2004)
44. Zhou, W.C., Xu, H.C., Cai, Z.Y., Wei, J.R., Zhu, X.Y., Wang, W., Zhao, L., Huang, J.P.: Peculiar statistical properties of Chinese stock indices in bull and bear market phases. Phys. A **388**, 891–899 (2009)
45. Fick, A.: On liquid diffusion. J. Membr. Sci. **100**, 33–38 (1995)
46. Xu, L.J., Xu, G.Q., Huang, J.P., Qiu, C.W.: Diffusive Fizeau Drag in Spatiotemporal Thermal Metamaterials. Phys. Rev. Lett. **128**, 145901 (2022)
47. Guenneau, S., Puvirajesinghe, T.M.: Fick's second law transformed: One path to cloaking in mass diffusion. J. R. Soc. Interface **10**, 20130106 (2013)
48. Zeng, L., Song, R.: Controlling chloride ions diffusion in concrete. Sci. Rep. **3**, 3359 (2013)
49. Guenneau, S., Petiteau, D., Zerrad, M., Amra, C., Puvirajesinghe, T.: Transformed Fourier and Fick equations for the control of heat and mass diffusion. AIP Adv. **5**, 053404 (2015)
50. Restrepo-Flórez, J.M., Maldovan, M.: Mass separation by metamaterials. Sci. Rep. **6**, 21971 (2016)

51. Restrepo-Flórez, J.M., Maldovan, M.: Metamaterial membranes. J. Phys. D-Appl. Phys. **50**, 025104 (2016)
52. Li, Y., Liu, C., Li, P., Lu, T., Chen, C., Guo, Z., Su, Y., Qiao, L., Zhou, J., Bai, Y.: Scattering cancellation by a monolayer cloak in oxide dispersion-strengthened alloys. Adv. Funct. Mater. **30**, 2003270 (2020)
53. Li, Y., Yu, C.Y., Liu, C.B., Xu, Z.J., Su, Y.J., Qiao, L.J., Zhou, J., Bai, Y.: Mass Diffusion Metamaterials with "Plug and Switch" modules for ion cloaking, concentrating, and selection: design and experiments. Adv. Sci. **9**, 2201032 (2022)
54. Zhou, X., Xu, G., Zhang, H.: Binary masses manipulation with composite bilayer metamaterial. Compos. Struct. **267**, 113866 (2021)
55. Schittny, R., Kadic, M., Bückman, T., Wegener, M.: Invisibility cloaking in a diffusive light scattering medium. Science **345**, 427–429 (2014)
56. Breaking separation limits in membrane technology: Restrepo-Flórez, J.M., Maldovan, M. J. Membr. Sci. **566**, 301–306 (2018)
57. Zhang, Z.R., Yang, F.B., Huang, J.P.: Intelligent chameleonlike metashells for mass diffusion. Phys. Rev. Appl. **19**, 024009 (2023)
58. Avanzini, F., Falasco, G., Esposito, M.: Chemical cloaking. Phys. Rev. E **101**, 060102 (2020)
59. Steinbock, O., Kettunen, P., Showalter, K.: Chemical wave logic gates. J. Phys. Chem. **100**, 18970–18975 (1996)
60. Xin, C., Yang, G., Huang, J.P.: Ising game: Nonequilibrium steady states of resource-allocation systems. Phys. A **471**, 666–673 (2017)
61. Zhang, Z.R., Xu, L.J., Huang, J.P.: Controlling Chemical Waves by Transforming Transient Mass Transfer. Adv. Theory Simul. **5**, 2100375 (2022)
62. Dai, G.L., Yang, F.B., Xu, L.J., Huang, J.P.: Diffusive pseudo-conformal mapping: anisotropy-free transformation thermal media with perfect interface matching. Chaos Solitons Fractals. **174**, 113849 (2023)
63. Liu, B., Xu, L.J., Huang, J.P.: Thermal transparency with periodic particle distribution: a machine learning approach. J. Appl. Phys. **129**, 065101 (2021)

Part VI
Metamaterials for Plasma Diffusion

Chapter 18
Diffusion Metamaterials for Plasma Transport

Fubao Yang and Zeren Zhang

18.1 Opening Remarks

Since ancient times, energy has always been one of the core needs for human development. Over the past few centuries, people have developed and used various sources of energy, such as fossil fuels, hydropower, and nuclear energy. However, with the growth of the world's population and economy, the demand for energy has also been continuously increasing, posing significant challenges to global energy resources. Now, we face a deepening energy crisis, including the depletion of fossil resources and the severe environmental impacts of carbon emissions. Against this backdrop, the sustainability of energy and how to efficiently use existing energy resources have become hot topics of global concern, urgently requiring solutions. Therefore, energy management and regulation have become crucial. We need to explore various measures to achieve active control of energy, thereby using it more efficiently. In this process, the development of metamaterials has become a prominent field and is one of the key means to achieve active energy control.

Metamaterials refer to novel materials that achieve extraordinary properties through artificial structures. Their origin can be traced back to the phenomenon of negative refraction proposed by Professor Veselago in 1968 [1]. However, due to the limited material and technological levels at that time, this phenomenon went unverified experimentally for a long time. It wasn't until the end of the 20th century that Professor Pendry's team demonstrated the feasibility of negative refraction experimentally through metal wire arrays and split-ring resonator structures [2, 3]. Since then, the research on electromagnetic metamaterials has attracted widespread attention. Particularly, the establishment of transformation optics theory in 2006 provided a powerful tool for designing electromagnetic metamaterial devices with novel functionalities, enabling the free manipulation of electromagnetic wave propagation

F. Yang (✉) · Z. Zhang
Department of Physics, Key Laboratory of Micro and Nano Photonic Structures (MOE), and State Key Laboratory of Surface Physics, Fudan University, Shanghai 200438, China
e-mail: 18110190009@fudan.edu.cn

F.-B. Yang and J.-P. Huang, *Diffusionics*,
https://doi.org/10.1007/978-981-97-0487-3_18

as desired [4, 5]. This marks a new height in mankind's active control over physical fields, greatly propelling the development of the electromagnetic metamaterials field [6–9].

The successful application of metamaterials in wave systems laid a solid foundation for their expansion into diffusion systems. In 2008, Professor Huang Jiping's team from Fudan University established the transformation thermotics in the heat conduction system and predicted the functionality of a thermal cloak [10], inaugurating the field of diffusion metamaterials [11–13]. Over the next decade, transformation theory continually developed in diffusion systems [14–17], with an increasing number of extended theories proposed, including effective medium theory [18–22], scattering cancellation theory, and optimization algorithms, among others [23, 24]. Accordingly, various diffusion metamaterial devices were designed or fabricated. Diffusion metamaterials have provided a novel approach for controlling the diffusion of energy and matter and have become a current hotspot in research. The in-depth study of diffusion metamaterials may also bring inspiration and vitality to classical thermodynamic and statistical physics [25–27] or soft condensed matter physics [28, 29].

Plasma diffusion, as a specific form of mass diffusion, has seen limited progress in the research of metamaterials designed for its regulation. Plasma, often referred to as the fourth phase of matter, consists of a gaseous blend of free ions, electrons, and various reactive species, granting it strong electrical conductivity. While it's not typically found on Earth's crust, plasma can be synthetically produced by electrifying gases using direct/alternating currents or sources of radio/microwave frequencies. See Fig. 18.1. Given its distinct nature, plasma-based technologies hold significant importance across sectors including micro/nanoelectronics, chemical research, bio-

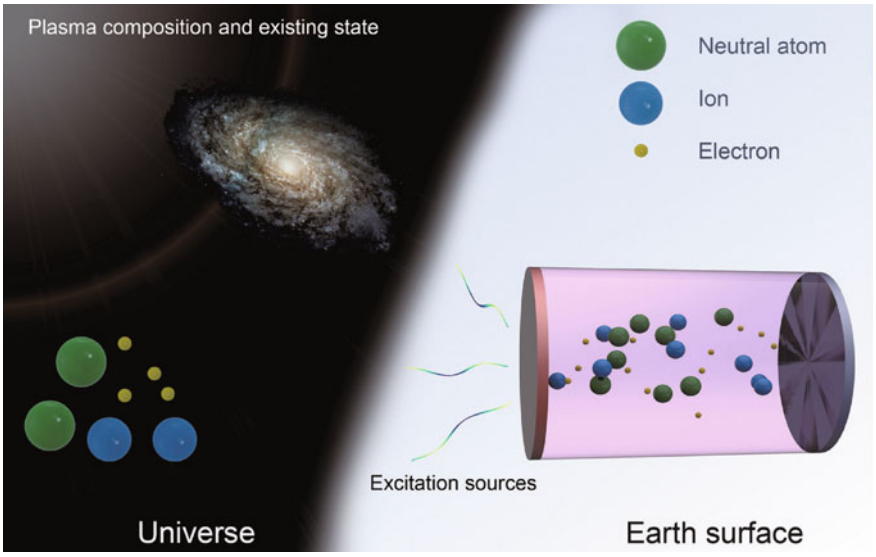

Fig. 18.1 Schematic diagrams of plasma components and distribution

medicine, aerospace, and materials science [30–33]. While there has been a plethora of theoretical and empirical research, mastering the control over plasma transportation remains a formidable task. Traditional methods of directing charged particles primarily rely on external magnetic fields, a straightforward approach that may curtail precise control. Over recent years, the transformation theory, which substitutes spatial transformation with material alteration, has gained prominence in wave and diffusion systems as an effective strategy to steer matter or energy trajectories [34–36]. Yet, its application in the domain of plasma transportation, which can be viewed as a distinct diffusion mechanism, remains unexplored. The intricate motion dynamics within plasmas might explain this gap. Only recently, reports have suggested the potential application of transformation theory to plasma transport [37]. Although this work merely used a toy model to describe the plasma diffusion process, it has paved the way for new possible approaches to control plasma.

18.2 Transformation Theory for Plasma Transport

18.2.1 For Steady-State Plasma Transport

Compared to traditional diffusion systems, the transport in actual plasmas is more complex. This is because collisions between charged particles, and between charged and neutral particles, often result in reactions. Furthermore, the intrinsic electric field within the plasma can affect the movement of charged particles. Here, we do not consider collisions that result in nuclear reactions. Hence, the governing equation for the transport of charged particles in plasma can be written as:

$$\partial_t n + \nabla \cdot \Gamma = 0, \tag{18.1a}$$

$$\nabla \cdot \Gamma = -\nabla \cdot (D \cdot \nabla n) \pm \nabla \cdot (\mu \boldsymbol{E} n) + \nabla \cdot (\boldsymbol{v} n), \tag{18.1b}$$

where n, D, μ, $\boldsymbol{E}$, and $\boldsymbol{v}$ represent the plasma density, diffusion coefficient, mobility, electric field, and advective velocity, respectively. The first term on the right-hand side of Eq. (18.1b) represents the diffusion term. The second term represents the mobility term, with the positive sign indicating the mobility of cations and the negative sign indicating the mobility of anions or electrons. The third term denotes the effect of convection. The transport equation for plasma also needs to be coupled with the Poisson's equation:

$$\nabla \cdot \boldsymbol{E} = \frac{e}{\epsilon_0} (n_i - n_e), \tag{18.2}$$

where e, ϵ_0, n_i, and n_e represent the elementary charge, permittivity of free space, cation density, and electron density, respectively. Assuming the plasma is electrically neutral internally, the right-hand side of the above equation is zero. For simplicity, we will not consider the advective process for now [38]. Therefore, Eq. (18.1) can be written as:

$$\partial_t n - \nabla \cdot (D \cdot \nabla n) \pm \nabla \cdot (\mu \boldsymbol{E} n) = 0. \tag{18.3}$$

Note that in plasmas, the relationship between the diffusion coefficient and mobility is given by the Einstein relation:

$$\mu = \frac{De}{Tk_B} = \frac{D}{T_i}, \tag{18.4}$$

where T is the particle temperature, k_B is the Boltzmann constant, and $T_i = Tk_B/e$ is the reduced temperature in volts (V). Assuming the temperature is constant, the reduced temperature is also constant. Using the Einstein relation, we can simplify parameters and further reduce the plasma transport equation to:

$$\partial_t n - \nabla \cdot (D \cdot \nabla n) \pm \nabla \cdot \left[\left(\frac{D \cdot \boldsymbol{E}}{T_i} \right) n \right] = 0. \tag{18.5}$$

Next, we will study the transformation theory in plasmas based on the above equation. First, we discuss the transport under steady-state conditions.

In the steady state, where the plasma density does not vary with time, Eq. (18.5) becomes:

$$-\nabla \cdot (D \cdot \nabla n) \pm \nabla \cdot \left[\left(\frac{D \cdot \boldsymbol{E}}{T_i} \right) n \right] = 0. \tag{18.6}$$

To visualize the transformation results more intuitively, the equation above is converted into its component form in curved space [39]:

$$-\partial_i \left(\sqrt{A} D^{ij} \partial_j n \right) \pm \partial_i \left[\left(\frac{\sqrt{A} D^{ij} E_j}{T_i} \right) n \right] = 0. \tag{18.7}$$

The curved space corresponds to coordinates x_i, with its covariant base vectors denoted as $\boldsymbol{a}_i$ and $\boldsymbol{a}_j$. In Eq. (18.7), A is the determinant of $\boldsymbol{a}_i \cdot \boldsymbol{a}_j$. The transformed Eq. (18.7) in physical space is expressed as:

$$-\partial_{i'} \left[\frac{\partial x_i'}{\partial x_i} \sqrt{A} D^{ij} \frac{\partial x_j'}{\partial x_j} \partial_{j'} n \mp \frac{\partial x_i'}{\partial x_i} \left(\frac{\sqrt{A} D^{ij} E_j}{T_i} \right) n \right] = 0, \tag{18.8}$$

Here, the physical space coordinates are denoted as x_i'. Thus, $\partial x_i'/\partial x_i$ and $\partial x_j'/\partial x_j$ are components of the Jacobian matrix $\mathbf{J}$, and the determinant of this Jacobian matrix satisfies $\det \mathbf{J} = 1/\sqrt{A}$. This equation can then be rewritten as:

$$-\nabla' \cdot \left(\frac{\mathbf{J} D \mathbf{J}^{\tau}}{\det \mathbf{J}} \cdot \nabla' n \right) \pm \nabla' \cdot \left(\frac{\mathbf{J} D \cdot \boldsymbol{E}}{\det \mathbf{J} T_i} n \right) = 0, \tag{18.9}$$

We can simplify Eq. (18.9) by incorporating the extra metric through physical parameters, resulting in:

$$-\nabla' \cdot \left(D' \cdot \nabla' n\right) \pm \nabla' \cdot \left(\frac{D' \cdot \boldsymbol{E}'}{T_i} n\right) = 0, \tag{18.10a}$$

$$D' = \frac{\mathbf{J} D \mathbf{J}^{\tau}}{\det \mathbf{J}}, \tag{18.10b}$$

$$\boldsymbol{E}' = \mathbf{J}^{-\tau} \boldsymbol{E}. \tag{18.10c}$$

Here, ∇' indicates the differential in the new coordinate system; $\mathbf{J}^{\tau}$ is the transpose of $\mathbf{J}$; $\mathbf{J}^{-\tau}$ represents the inverse of $\mathbf{J}^{\tau}$. Comparing Eqs. (18.6) and (18.10a) shows they have the same form, implying that the migration diffusion equation in the steady state strictly maintains its transformation form. Hence, we can design parameter control for steady-state plasma transport using Eqs. (18.10b) and (18.10c).

18.2.2 For Transient-State Plasma Transport

Although the transformation theory fits well with steady-state plasma transport, the situation under transient conditions is quite different. Re-examining Eq. (18.5) and processing it in a manner similar to the steady-state, we obtain:

$$\frac{1}{\det \mathbf{J}} \partial_t n - \nabla' \cdot \left(\frac{\mathbf{J} D \mathbf{J}^{\tau}}{\det \mathbf{J}} \cdot \nabla' n\right) \pm \nabla' \cdot \left(\frac{\mathbf{J} D \cdot \boldsymbol{E}}{\det \mathbf{J} T_i} n\right) = 0, \tag{18.11}$$

Substituting Eqs. (18.10b) and (18.10c) into Eq. (18.11), we obtain:

$$\frac{1}{\det \mathbf{J}} \partial_t n - \nabla' \cdot \left(D' \cdot \nabla' n\right) \pm \nabla' \cdot \left(\frac{D' \cdot \boldsymbol{E}'}{T_i} n\right) = 0, \tag{18.12}$$

Comparing Eqs. (18.5) and (18.12), we notice an irreducible parameter in front of the time-dependent term. The transformed equation has changed its form, indicating that the transformation theory fails for transient plasma transport. Approximating Eq. (18.12), we get:

$$\partial_t n - \nabla' \cdot \left(D'' \cdot \nabla' n\right) \pm \nabla' \cdot \left(\frac{D'' \cdot \boldsymbol{E}''}{T_i} n\right) = 0, \tag{18.13a}$$

$$D'' = \mathbf{J} D \mathbf{J}^{\tau}, \tag{18.13b}$$

$$\boldsymbol{E}'' = \mathbf{J}^{-\tau} \boldsymbol{E}. \tag{18.13c}$$

Where Eqs. (18.13b) and (18.13c) are parameter transformation rules. In this manner, the equation retains its transformation-invariant characteristics. Similar to the convection-diffusion equation, Eq. (18.13a) is an approximate form of Eq. (18.5). Only when $\det \mathbf{J} = 1$, does Eq. (18.13a) strictly transform to Eq. (18.5).

Revisiting Eq. (18.11) and multiplying both sides by $\det \mathbf{J}$, we get:

$$\partial_t n - \det \mathbf{J}\left[\nabla' \cdot \left(\frac{\mathbf{J}D\mathbf{J}^\tau}{\det \mathbf{J}} \cdot \nabla' n \mp \frac{\mathbf{J}D \cdot \boldsymbol{E}}{\det \mathbf{J} T_i} n\right)\right] = 0, \tag{18.14}$$

Then, decomposing the differential terms and isolating $1/\det \mathbf{J}$, we get:

$$\begin{aligned} &\det \mathbf{J}\left[\nabla'\left(\frac{1}{\det \mathbf{J}}\right) \cdot \left(\mathbf{J}D\mathbf{J}^\tau \cdot \nabla' n\right) + \frac{1}{\det \mathbf{J}} \nabla' \cdot \left(\mathbf{J}D\mathbf{J}^\tau \cdot \nabla' n\right)\right] \\ &\mp \det \mathbf{J}\left[\nabla'\left(\frac{1}{\det \mathbf{J}}\right) \cdot \left(\frac{\mathbf{J}D \cdot \boldsymbol{E}}{T_i} n\right) + \frac{1}{\det \mathbf{J}} \nabla' \cdot \left(\frac{\mathbf{J}D \cdot \boldsymbol{E}}{T_i} n\right)\right] = \partial_t n \end{aligned} \tag{18.15}$$

Combining the terms that include $\nabla'(1/\det \mathbf{J})$, we get:

$$\partial_t n = \nabla' \cdot \left(\mathbf{J}D\mathbf{J}^\tau \cdot \nabla' n \mp \frac{\mathbf{J}D \cdot \boldsymbol{E}}{T_i} n\right) + \Delta, \tag{18.16a}$$

$$\Delta = \det \mathbf{J} \nabla'\left(\frac{1}{\det \mathbf{J}}\right) \cdot \left(\mathbf{J}D\mathbf{J}^\tau \cdot \nabla' n \mp \frac{\mathbf{J}D \cdot \boldsymbol{E}}{T_i} n\right). \tag{18.16b}$$

We observe that if Δ is sufficiently small to be ignored, then Eq. (18.16a) reverts to Eq. (18.13a). Now, analyzing the specific expression of the error in Eq. (18.16b), which involves the Jacobian determinant, plasma diffusion coefficient, plasma density, temperature, and electric field. The spatial transformation determines the form of the Jacobian. Hence, Δ is related to the physical parameters of the system and the specific form of spatial transformation. To minimize the error, both diffusion coefficients and electric field need to be sufficiently small. Moreover, there exist special spatial transformations for which $\det \mathbf{J} = 1$, making the error $\Delta = 0$. In this case, Eq. (18.13a) is strictly the same as Eq. (18.5).

18.3 Potential Applications for Transformation-Based Plasma Metamaterials

To validate our theory, we introduce three conceptual plasma devices: the plasma cloak, concentrator, and rotator. See Fig. 18.2. A unique feature they share is that while achieving their respective functionalities, they do not affect the plasma distribution in the background medium, which is quite distinctive in the plasma field. Specifically, the cloak can protect the core region, meaning that the background does not affect the core, and vice versa; the concentrator can concentrate plasma flow, enhancing the density gradient in the core region; the rotator can alter the propagation direction of the plasma in the core region. Next, we will detail the coordinate transformation relations for implementing the functionalities of these three devices, starting with the cloak.

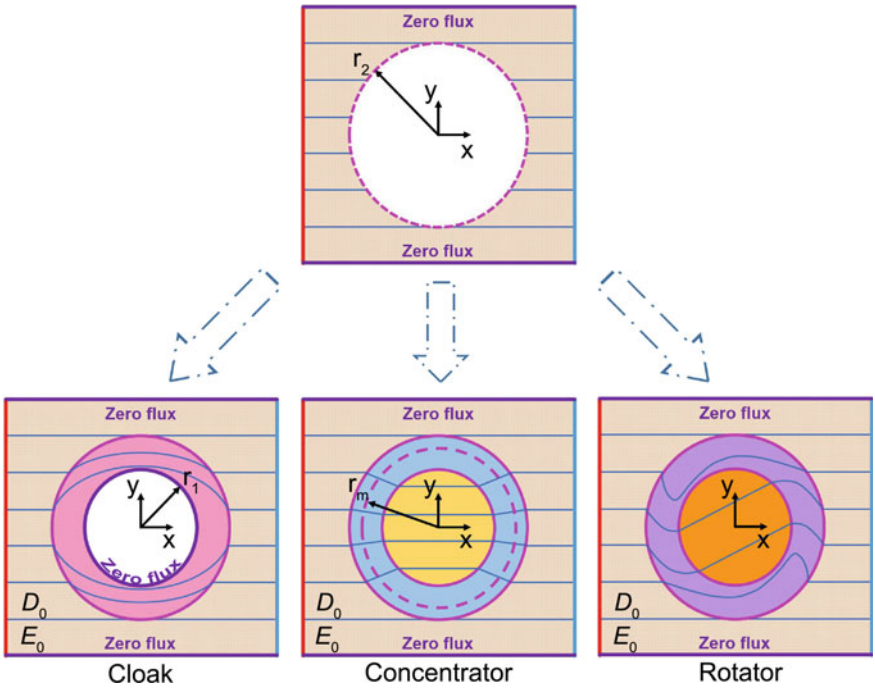

Fig. 18.2 Schematic diagrams of the three plasma devices. From left to right: cloak, concentrator, and rotator. The blue solid lines represent the direction of the plasma flow. The side length of the square background in the model is set to $l = 0.12$ m. The diffusivity of the background is set as $D_0 = 9.2 \times 10^{-7}$ m s^{-1}, and the field strength is $E_{x0} = 1.04 \times 10^4$ V m^{-1}. Other parameter values: $r_1 = 0.020$ m, $r_2 = 0.030$ m, $r_m = 0.025$ m, $\theta_0 = \pi/3$, and the reduced temperature is set to $T_0 = 2.0$ V. (from Ref. [37])

18.3.1 Cloak

To realize the plasma cloak, we can express the coordinate transformation relationship from the virtual space r_i to the physical space r_i' as

$$\begin{aligned} r' &= \frac{r_2 - r_1}{r_2} r + r_1, \\ \theta' &= \theta, \end{aligned} \tag{18.17}$$

where r_1 and r_2 represent the inner and outer diameters of the cloak, respectively. Identical to the transformation relationship of the chemical wave cloak in the previous work, the spatial transformation here also expands the point at the center in the virtual space into an inner circle, thereby compressing the outer circle into a ring with an inner diameter equivalent to the radius of the small circle. We can then compute the Jacobian matrix based on Eq. (18.17), expressed as

$$\mathbf{J} = \begin{bmatrix} \frac{r_2 - r_1}{r_2} & 0 \\ 0 & \frac{(r_2 - r_1)r'}{r_2(r' - r_1)} \end{bmatrix}. \tag{18.18}$$

Next, based on Eqs. (18.13b) and (18.13c), the transformation parameters required for the cloak can be calculated as

$$D'' = \begin{bmatrix} D_0 \left(\frac{r_2 - r_1}{r_2}\right)^2 & 0 \\ 0 & D_0 \left[\frac{(r_2 - r_1)r'}{r_2(r' - r_1)}\right]^2 \end{bmatrix}, \tag{18.19a}$$

$$\boldsymbol{E}'' = \begin{bmatrix} \frac{r_2}{r_2 - r_1} E_r \\ \frac{r_2(r' - r_1)}{(r_2 - r_1)r'} E_t \end{bmatrix}, \tag{18.19b}$$

where D_0 is the diffusion rate of the background, and E_r and E_t are the radial and tangential components of the background electric field $\boldsymbol{E}_0$, respectively. In this model, the background electric field is set in the x direction, so $\boldsymbol{E}_0 = [E_{x0},\ 0]^\tau$ V m^{-1}. Thus, based on the conversion relationship between Cartesian coordinates and cylindrical coordinates, the specific forms of E_r and E_t are

$$\boldsymbol{E}_0 = \begin{bmatrix} E_r \\ E_t \end{bmatrix} = \begin{bmatrix} E_{x0} \cos\theta \\ -E_{x0} \sin\theta \end{bmatrix}. \tag{18.20}$$

Since the transient mass transfer theory is an approximation, the electric field is not continuous at the boundary between the cloak and the background medium. One potential solution is to artificially control the potential at this boundary. Then, with Eq. (18.19), we can achieve transient plasma cloaking.

18.3.2 Concentrator

For the concentrator, the spatial transformation corresponding to the coordinate transformation can be designed as,

$$\begin{aligned} r' &= \frac{r_1}{r_m} r, \qquad r < r_m \\ r' &= \frac{r_1 - r_m}{r_2 - r_m} r_2 + \frac{r_2 - r_1}{r_2 - r_m} r, \quad r_m < r < r_2 \\ \theta' &= \theta. \end{aligned} \tag{18.21}$$

r_m is a constant between r_1 and r_2 (represented by a dashed line in Fig. 18.2). Similarly, this spatial transformation can be understood in virtual space, where a circle with radius r_2 is divided into two parts by a circle with radius r_m. One part is the inner circle with a radius of r_m and the remaining part is an annulus with an inner diameter of r_m and an outer diameter of r_2. The radius of the inner circle is then compressed to r_1 and the inner diameter of the annulus is stretched to r_1.

For convenience, let $p = \frac{r_2 - r_1}{r_2 - r_m}$, $q = \frac{r_1 - r_m}{r_2 - r_m} r_2$, and $f = \frac{r_1}{r_m}$. Based on Eq. (18.21), the Jacobian matrix of the concentrator is obtained as,

$$\mathbf{J}_1 = \begin{bmatrix} f & 0 \\ 0 & f \end{bmatrix}, \quad r' < r_1 \tag{18.22a}$$

$$\mathbf{J}_2 = \begin{bmatrix} p & 0 \\ 0 & \frac{r'p}{r'-q} \end{bmatrix}, \quad r_1 < r' < r_2 \tag{18.22b}$$

According to Eqs. (18.13b) and (18.13c), the transformation parameters of the concentrator at $r' < r_1$ (D_1'' and $\boldsymbol{E}_1''$) and $r_1 < r' < r_2$ (D_2'' and $\boldsymbol{E}_2''$) are obtained as,

$$D_1'' = \begin{bmatrix} D_0 f^2 & 0 \\ 0 & D_0 f^2 \end{bmatrix}, \tag{18.23a}$$

$$\boldsymbol{E}_1'' = \begin{bmatrix} E_r / f \\ E_t / f \end{bmatrix}, \tag{18.23b}$$

$$D_2'' = \begin{bmatrix} D_0 p^2 & 0 \\ 0 & D_0 \left(r' p / \left(r' - q\right)\right)^2 \end{bmatrix}, \tag{18.23c}$$

$$\boldsymbol{E}_2'' = \begin{bmatrix} E_r / p \\ E_t \left(r' - q\right) / r' p \end{bmatrix}. \tag{18.23d}$$

The efficiency of the concentrator is related to the value of r_m / r_1. The larger the r_m, the higher the concentration efficiency, corresponding to a larger density gradient. This can be understood from the physical image of the space transformation. When r_m is larger, the compressed area of the inner circle is larger, which corresponds to a higher degree of concentration. With Eq. (18.23), we can achieve the transient plasma concentration.

18.3.3 Rotator

For the rotator, the spatial transformation corresponding to the coordinate transformation is given by,

$$\begin{aligned} r' &= r, \\ \theta' &= \theta + \theta_0, \quad r < r_1 \\ \theta' &= \theta + \theta_0 \frac{r - r_2}{r_1 - r_2}, \quad r_1 < r < r_2 \end{aligned} \tag{18.24}$$

where θ_0 is a constant rotation angle. This spatial transformation can be understood as a series of circles with radius $r \in [r_1, r_2]$ rotating around their center, with their rotation angles linearly varying with their sizes.

For convenience, let $g = \theta_0/(r_1 - r_2)$. The Jacobian matrix of the rotator can then be obtained as,

$$\mathbf{J}_1 = \begin{bmatrix} 1 & 0 \\ 0 & 1 \end{bmatrix}, \qquad r' < r_1 \tag{18.25a}$$

$$\mathbf{J}_2 = \begin{bmatrix} 1 & 0 \\ r'g & 1 \end{bmatrix}. \quad r_1 < r' < r_2 \tag{18.25b}$$

Noting that $\det \mathbf{J}_1 = \det \mathbf{J}_2 = 1$, the Eq. (18.13) becomes an exact solution. Similarly, using Eqs. (18.13b) and (18.13c), the transformation parameters for the rotator in the regions $r' < r_1$ (D_1'' and $\boldsymbol{E}_1''$) and $r_1 < r' < r_2$ (D_2'' and $\boldsymbol{E}_2''$) can be computed as,

$$D_1'' = \begin{bmatrix} D_0 & 0 \\ 0 & D_0 \end{bmatrix}, \tag{18.26a}$$

$$\boldsymbol{E}_1'' = \begin{bmatrix} E_r \\ E_t \end{bmatrix}, \tag{18.26b}$$

$$D_2'' = \begin{bmatrix} D_0 & D_0 r'g \\ D_0 r'g & D_0\left[(r'g)^2 + 1\right] \end{bmatrix}, \tag{18.26c}$$

$$\boldsymbol{E}_2'' = \begin{bmatrix} E_r - r'gE_t \\ E_t \end{bmatrix}. \tag{18.26d}$$

In practical simulations, the $\boldsymbol{E}''$ must be rotated. Since the parameters after transformation are taken from the new coordinate system, and the new coordinates are rotated by a certain angle relative to the old coordinates, the Eq. (18.26) cannot be used directly if the system's coordinate system is not adjusted. The core parameters in the old cylindrical coordinate system should be,

$$D_1'' = \begin{bmatrix} D_0 & 0 \\ 0 & D_0 \end{bmatrix}, \quad \boldsymbol{E}_1'' = \begin{bmatrix} E_r(\theta - \theta_0) \\ E_t(\theta - \theta_0) \end{bmatrix}, \tag{18.27}$$

and the shell parameters are,

$$D_2'' = \begin{bmatrix} D_0 & D_0 rg \\ D_0 rg & D_0\left[(rg)^2 + 1\right] \end{bmatrix}, \quad \boldsymbol{E}_2'' = \begin{bmatrix} E_r(\theta - \theta_r) - rgE_t(\theta - \theta_r) \\ E_t(\theta - \theta_r) \end{bmatrix}, \tag{18.28}$$

where $E_r(\theta - \theta_0)$ and $E_t(\theta - \theta_0)$ represent the values of E_r and E_t at $\theta = \theta - \theta_0$; $E_r(\theta - \theta_r)$ and $E_t(\theta - \theta_r)$ represent the values of E_r and E_t at $\theta = \theta - \theta_r$; and $\theta_r = g(r - r_2)$. E_r and E_θ are determined by Eq. (18.20). The transformation form of the diffusion rate is not affected by the rotation of the coordinate system, because rotation of the scalar D has no meaning. Up to this point, we have derived the parameter transformation rules for regulating the plasma, namely the cloak, the concentrator, and the rotator, which are (18.19), (18.23), (18.27) and (18.28). Finite-element simulation is used to verify the model.

18.3.4 Simulation Verification

The models for the three devices have been presented in Fig. 18.2. In order to visually depict the transient distribution of the plasma, a periodically fluctuating plasma source n_b is chosen to impose on the left boundary of the square background. The specific expression for this is given by:

$$n_b = n_1 \cos(\omega_0 t) + n_0, \tag{18.29}$$

where $n_1 = 5.0 \times 10^{15}\ \mathrm{m}^{-3}$, $\omega_0 = \frac{2\pi}{10}\ \mathrm{s}^{-1}$, and $n_0 = 1.0 \times 10^{17}\ \mathrm{m}^{-3}$. The right side of the background is set as the outflow boundary, while the top and bottom boundaries are set as no flux. For the shield, its internal boundary should also be specifically set as no flux. In this context, the diffusion coefficient in the background is set as a constant D_0, and the electric field is set as a uniform electric field along the x-direction, represented by $\boldsymbol{E}_0$. Then all the parameters can be designed according to the above transformation rules, and the simulation results of cloaking, concentrating, and rotating are shown in Figs. 18.3, 18.4 and 18.5, respectively.

Figure 18.3 illustrates the transient simulation of plasma transport under three conditions, namely, transporting in a pure background medium (set as the reference), in a background medium with a bare obstacle, and in a background medium with an obstacle covered by the cloak. The columns from left to right are screenshots of distributions of the plasma density at 10 s, 22 s, and 40 s, respectively. Due to the boundary condition of harmonically oscillating density, the plasma streams forward in a wave-like form. Moreover, the amplitude attenuation of the plasma flow reflected from the figures is caused by the diffusion, whose decay rate is codetermined by the oscillation frequency, diffusivity, and electric field. As a result, suitable values are carefully chosen to make the results more intuitive. The cloak designed with the transformation theory helps to cancel the scattering induced by the obstacle. Therefore, the density profiles of the background plasma keep nearly undisturbed, which shows the validity of the theory.

The transient simulation results for the concentrator and rotator are shown in Fig. 18.4. The first row of snapshots shows the converging effect of the gradient of plasma density. In addition, as a determinant of the converging effect, a bigger ratio (r_m/r_1) would bring a higher converging effect. And the maximum ratio is r_2/r_1. For the rotator, the rotation of plasma flow appears in Fig. 18.3b1–b3. Linearly deflecting concentric circles in the virtual space can account for the gradual deflection of the density profiles. The target rotation angle in the core region is determined by θ_0 in Eqs. (18.24). Particularly, $\det \mathbf{J} = 1$ for rotators helps to completely eliminate the disturbance to background plasma density.

To further explore the performance of the devices, the density values along a horizontal line (denoted by the yellow dashed lines in Fig. 18.5) from the results at 40 s are extracted and the density distribution of functional devices is compared with that of reference. See Fig. 18.5b1–b3. Two regions should be remarked. One is the core region of the device, the other is the background. All the red dashed lines in

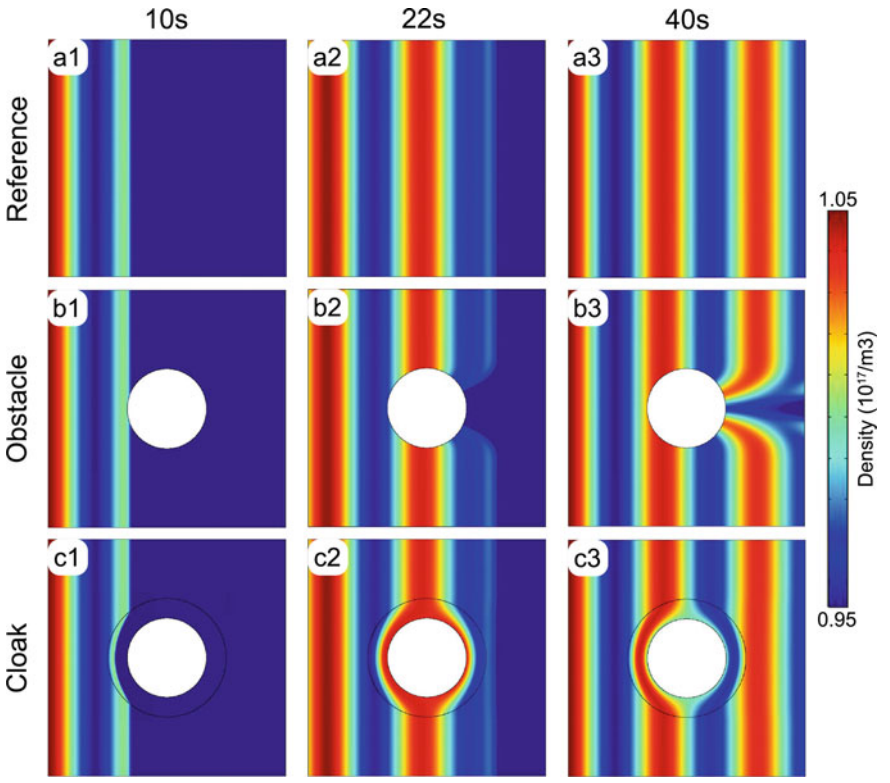

Fig. 18.3 Simulation results of the cloak at transient states. (a1)–(a3) Density profiles for pure background at 10 s, 22 s, and 40 s, respectively. (b1)–(b3) Density profiles for background with an obstacle at 10 s, 22 s, and 40 s, respectively. (c1)–(c3) Density profiles for background with the cloak at 10 s, 22 s, and 40 s, respectively. (from Ref. [37])

Fig. 18.5b1–b3 denote the data of the reference, while the blue dotted lines represent the data of the cloak, concentrator, and rotator, respectively. In Fig. 18.5b1, it is clear that the data are well overlapped in the background, and the plasma is excluded well from the core region. Moreover, the relative difference in the plasma density in the background region was less than 0.15%. In Fig. 18.5b2, the dotted line is indeed denser than the dashed line in the core region without being seriously dislocated in the background. And the relative difference was less than 0.13%. In Fig. 18.5b3, the relative difference was less than 0.01% which is far smaller than the value of the cloak or concentrator. As mentioned above, the accurate transformation form of Eq. (18.13a) may account for this nearly zero difference. Overall, the simulation can confirm the feasibility and reliability of the theory.

The progression in plasma physics has paved the way for novel technologies and methods, finding cutting-edge applications in biomedicine, the crystal industry, and materials science [31]. See Fig. 18.6. We envisage several potential applications for

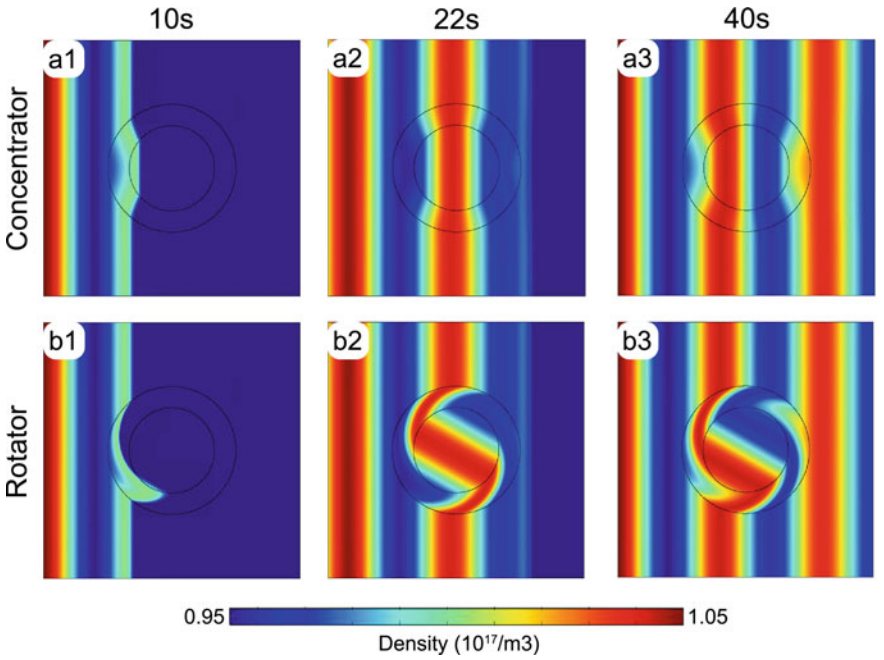

Fig. 18.4 Simulation results of concentrator and rotator at transient states. (a1)–(a3) Density profiles for the concentrator at 10 s, 22 s, and 40 s, respectively. (b1)–(b3) Density profiles for the rotator at 10 s, 22 s, and 40 s, respectively. (from Ref. [37])

devices crafted based on transformation theory. Consider the cloak, which has an isolated core region, as a prime candidate for safeguarding healthy tissue during plasma treatments of infected wounds. In catalyst development, a plasma flow convergence, characterized by a higher density of active particle clusters, augments the interaction between the plasma and the catalyst. This makes the concentrator an ideal tool to enhance catalytic performance. Furthermore, in aerospace, the concentrator might hold promise in elevating the efficiency of plasma-assisted engines. Beyond the uses already mentioned, the principles of coordinate transformation could be harnessed to achieve plasma separation or guidance, proving valuable for plasma etching or depositing. Additionally, transformation theory could contribute to the development of plasma metamaterials intended for electromagnetic wave manipulation [40, 41].

Indeed, the proposed approach rooted in transformation theory holds merit. Even with the inherent challenges in manifesting the transformed diffusivities and electric fields, alternative techniques can be employed to achieve similar outcomes. Plenty of research has delved into customizing particle diffusivities. For instance, the scattering cancellation method allows for the creation of a bilayer diffusive cloak using two homogeneous materials [42]. The complex diffusivity might be attainable through the effective medium theory [43] or even machine learning techniques [44]. When

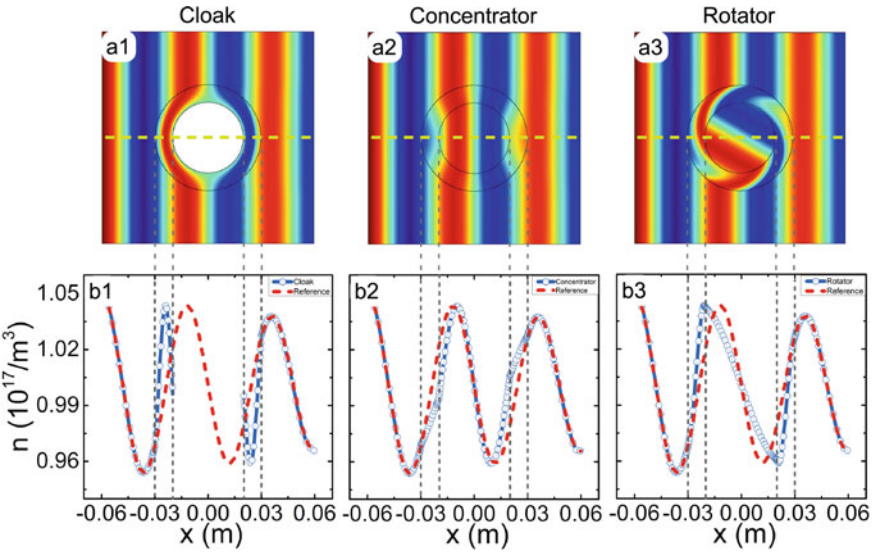

Fig. 18.5 (a1)–(a3) Color mapping of density profiles at 40 s with a cloak, concentrator, and rotator, respectively. (b1)–(b3) Comparisons between density profiles in the pure background (reference) and those with a cloak, concentrator, and rotator, respectively. The grey dashed lines denote the position of the devices. The data are extracted along the yellow dashed line (y = 0) in (a1)–(a3). (from Ref. [37])

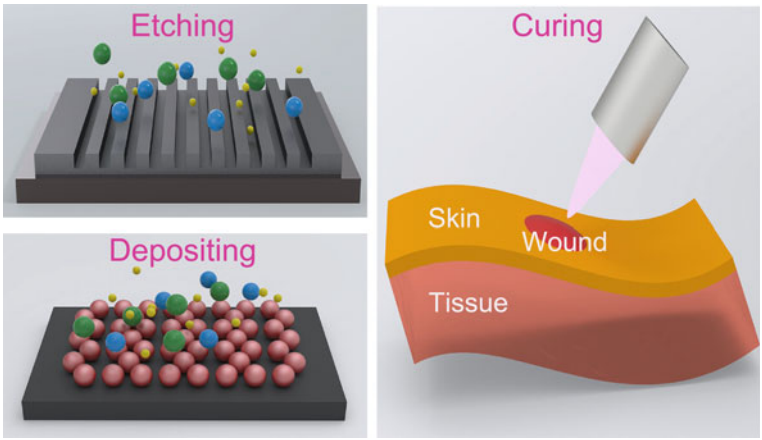

Fig. 18.6 Applications of plasmas. Adapted from Ref. [12]

it comes to electric field manipulation, insights from studies on electrostatic and magnetic cloaks could be illuminating [45, 46].

While the future is ripe with possibilities, it also presents its fair share of challenges. Under broader circumstances, we must factor in the effects of magnetic fields

and gas-phase reactions within the plasma. Truly exerting control over diffusivities and electric fields is a daunting task due to the intricate interplay between charged particles and electromagnetic fields. As such, it becomes paramount to incorporate alternative theoretical models or methodologies, such as the particle-in-cell/Monte Carlo collision model [47] or the nonequilibrium Green's function approach [48]. Additionally, plasma temperatures tend to fluctuate over time or space, especially in transient states, leading to a shift in transformation principles. In some scenarios, advection may play a role in plasma transport. Accounting for this term could diversify plasma regulation techniques. Furthermore, the emerging focus on spatiotemporal modulation in heat diffusion could provide new insights into plasma physics [49]. In conclusion, refining the transformation theory for plasmas requires heightened focus, research, and dedication.

18.4 Potential Impacts for Novel Physics

The realm of plasma transport transformation, being in its nascent stage, harbors a vast expanse of uncharted physics awaiting exploration. Among the intriguing avenues is the challenge of nonreciprocal plasma transport. Given the consistent display of space-inversion symmetry in diffusion equations, pinpointing nonreciprocal mechanisms within plasma transport proves daunting. An effective approach might involve the application of spatiotemporal modulations or nonlinear parameters, as found in the dynamics of heat and particle diffusion [50–54]. Another captivating area is topological plasma transport [55]. With lessons drawn from well-established mechanisms in topological particle and heat diffusion [56–64], researchers could embark on a variety of experimental strategies. For instance, formulating a plasma analog of the Su-Schrieffer-Heeger model might shed light on the intricate interplay between bulk-boundary and the emergence of edge states [65]. Additionally, the exploration into the presence of exceptional points and geometric phases promises rich insights. In a linear context, the use of Chern numbers can act as descriptors for the unconventional topologies found in plasma. Furthermore, the introduction of elements such as flow shear or a density gradient could lead to non-Hermiticity in systems, thereby highlighting plasma as a key medium for delving into the complexities of non-Hermitian physics. Given these vast possibilities, we anticipate a slew of groundbreaking discoveries in this domain in the near future.

18.5 Conclusion

In this chapter, a toy model, specifically the diffusion-migration model, has been utilized to elucidate plasma transport. This investigation has highlighted the practicality of the transformation theory. It was revealed that the transformed diffusion-migration equation maintains form-invariance at steady states but deviates at transient states.

However, it was also illustrated that by setting minimal diffusivities, the transformed transient equation can attain an approximate form-invariance. Based on this, three conceptual model devices were conceptualized, serving as plasma cloaks, concentrators, or rotators for transient plasma transport. Such findings can potentially expand methods for manipulating plasma flow and offer applications across multiple sectors, including medicine and aerospace. In conclusion, controlling plasma may serve as a nexus between diffusion and wave metamaterials. Although there are evident differences between diffusion and wave metamaterials, simultaneous control over diffusion and wave propagation signifies a notable progression. Plasma transport predominantly follows a diffusion process, but plasmas are frequently harnessed to regulate electromagnetic waves due to their distinctive permittivity. As such, the convergence of diffusion and wave propagation within a singular system can be a precursor to the emergence of new physics.

References

1. Veselago, V.G.: The electrodynamics of substances with simultaneously negative values of ϵ and μ. Sov. Phys. Usp. **10**, 509–514 (1968)
2. Pendry, J.B., Holden, A.J., Stewart, W.J., Youngs, I.: Extremely low frequency plasmons in metallic mesostructures. Phys. Rev. Lett. **76**, 4773–4776 (1996)
3. Pendry, J.B., Holden, A.J., Robbins, D.J., Stewart, W.J.: Magnetism from conductors and enhanced nonlinear phenomena. IEEE Trans. Microw. Theory Tech. **47**, 2075–2084 (1999)
4. Leonhardt, U.: Optical conformal mapping. Science **312**, 1777–1780 (2006)
5. Pendry, J.B., Schurig, D., Smith, D.R.: Controlling electromagnetic fields. Science **312**, 1780–1782 (2006)
6. Chen, H., Chan, C.T., Sheng, P.: Transformation optics and metamaterials. Nat. Mater. **9**, 387–396 (2010)
7. Zheludev, N.I., Kivshar, Y.S.: From metamaterials to metadevices. Nat. Mater. **11**, 917–924 (2012)
8. Kadic, M., Bückmann, T., Schittny, R., Wegener, M.: Metamaterials beyond electromagnetism. Rep. Prog. Phys. **76**, 126501 (2013)
9. Fu, X., Cui, T.J.: Recent progress on metamaterials: From effective medium model to real-time information processing system. Prog. Quantum Electron. **67**, 100223 (2019)
10. Fan, C.Z., Gao, Y., Huang, J.P.: Shaped graded materials with an apparent negative thermal conductivity. Appl. Phys. Lett. **92**, 251907 (2008)
11. Wang, J., Dai, G.L., Huang, J.P.: Thermal metamaterial: fundamental, application, and outlook. iScience **23**, 101637 (2020)
12. Zhang, Z.R., Xu, L.J., Qu, T., Lei, M., Lin, Z.K., Ouyang, X.P., Jiang, J.-H., Huang, J.P.: Diffusion metamaterials. Nat. Rev. Phys. **5**, 218–235 (2023)
13. Yang, F.B., Zhang, Z.R., Xu, L.J., Liu, Z.F., Jin, P., Zhuang, P.F., Lei, M., Liu, J.R., Jiang, J.-H., Ouyang, X.P., Marchesoni, F., Huang, J.P.: Controlling mass and energy diffusion with metamaterials. Rev. Mod. Phys. **96**, 015002 (2024)
14. Dai, G.L., Huang, J.P.: A transient regime for transforming thermal convection: cloaking, concentrating and rotating creeping flow and heat flux. J. Appl. Phys. **124**, 235103 (2018)
15. Xu, L.J., Dai, G.L., Huang, J.P.: Transformation multithermotics: controlling radiation and conduction simultaneously. Phys. Rev. Appl. **13**, 024063 (2020)
16. Xu, L.J., Yang, S., Dai, G.L., Huang, J.P.: Transformation omnithermotics: simultaneous manipulation of three basic modes of heat transfer. ES Energy Environ. **7**, 65–70 (2020)

17. Xu, L.J., Huang, J.P.: Active thermal wave cloak. Chin. Phys. Lett. **37**, 120501 (2020)
18. Shen, X.Y., Jiang, C.R., Li, Y., Huang, J.P.: Thermal metamaterial for convergent transfer of conductive heat with high efficiency. Appl. Phys. Lett. **109**, 201906 (2016)
19. Yang, S., Xu, L.J., Wang, R.Z., Huang, J.P.: Full control of heat transfer in single-particle structural materials. Appl. Phys. Lett. **111**, 121908 (2017)
20. Xu, L.J., Yang, S., Huang, J.P.: Thermal theory for heterogeneously architected structure: fundamentals and application. Phys. Rev. E **98**, 052128 (2018)
21. Xu, L.J., Yang, S., Huang, J.P.: Thermal transparency induced by periodic interparticle interaction. Phys. Rev. Appl. **11**, 034056 (2019)
22. Jin, P., Xu, L.J., Jiang, T., Zhang, L., Huang, J.P.: Making thermal sensors accurate and invisible with an anisotropic monolayer scheme. Int. J. Heat Mass Transf. **163**, 120437 (2020)
23. Xu, L.J., Wang, J., Dai, G.L., Yang, S., Yang, F.B., Wang, G., Huang, J.P.: Geometric phase, effective conductivity enhancement, and invisibility cloak in thermal convection-conduction. Int. J. Heat Mass Transf. **165**, 120659 (2021)
24. Xu, L.J., Xu, G.Q., Huang, J.P., Qiu, C.-W.: Diffusive Fizeau drag in spatiotemporal thermal metamaterials. Phys. Rev. Lett. **128**, 145901 (2022)
25. Dong, L., Huang, J.P., Yu, K.W., Gu, G.Q.: Dielectric response of graded spherical particles of anisotropic materials. J. Appl. Phys. **95**, 621–624 (2004)
26. Ye, C., Huang, J.P.: Non-classical oscillator model for persistent fluctuations in stock markets. Phys. A **387**, 1255–1263 (2008)
27. Liu, L., Wei, J., Zhang, H., Xin, J., Huang, J.: A statistical physics view of pitch fluctuations in the classical music from Bach to Chopin: evidence for scaling. PLoS ONE **8**, e58710 (2013)
28. Huang, J.P., Karttunen, M., Yu, K.W., Dong, L.: Dielectrophoresis of charged colloidal suspensions. Phys. Rev. E **67**, 021403 (2003)
29. Gao, Y., Jian, Y.C., Zhang, L.F., Huang, J.P.: Magnetophoresis of nonmagnetic particles in ferrofluids. J. Phys. Chem. C **111**, 10785–10791 (2007)
30. Samal, S.: Thermal plasma technology: the prospective future in material processing. J. Clean. Prod. **142**, 3131–3150 (2017)
31. Liang, H., Ming, F., Alshareef, H.N.: Applications of plasma in energy conversion and storage materials. Adv. Energy Mater. **8**, 1801804 (2018)
32. Tamura, H., Tetsuka, T., Kuwahara, D., Shinohara, S.: Study on uniform plasma generation mechanism of electron cyclotron resonance etching reactor. IEEE T. Plasma Sci. **48**, 3606–3615 (2020)
33. Li, M., Wang, Z., Xu, R., Zhang, X., Chen, Z., Wang, Q.: Advances in plasma-assisted ignition and combustion for combustors of aerospace engines. Aerosp. Sci. Technol. **117**, 106952 (2021)
34. Hu, R., Zhou, S., Li, Y., Lei, D.Y., Luo, X., Qiu, C.W.: Illusion thermotics. Adv. Mater. **30**, 1707237 (2018)
35. Hu, R., Huang, S., Wang, M., Luo, X., Shiomi, J., Qiu, C.W.: Encrypted thermal printing with regionalization transformation. Adv. Mater. **31**, 1807849 (2019)
36. Zhang, J., Huang, S., Hu, R.: Adaptive radiative thermal camouflage via synchronous heat conduction. Chin. Phys. Lett. **38**, 010502 (2021)
37. Zhang, Z.R., Huang, J.P.: Transformation plasma physics. Chin. Phys. Lett. **39**, 075201 (2022)
38. Cui, S., Wu, Z., Lin, H., Xiao, S., Zheng, B., Liu, L., An, X., Fu, R.K.Y., Tian, X., Tan, W., Chu, P.K.: Hollow cathode effect modified time-dependent global model and high-power impulse magnetron sputtering discharge and transport in cylindrical cathode. J. Appl. Phys. **125**, 063302 (2019)
39. Dai, G.L.: Designing nonlinear thermal devices and metamaterials under the Fourier law: a route to nonlinear thermotics. Front. Phys. **16**, 53301 (2021)
40. Rodríguez, J.A., Abdalla, A.I., Wang, B., Lou, B., Fan, S., Cappelli, M.A.: Inverse design of plasma metamaterial devices for optical computing. Phys. Rev. Appl. **16**, 014023 (2021)
41. Inami, C., Kabe, Y., Noyori, Y., Iwai, A., Bambina, A., Miyagi, S., Sakai, O.: Experimental observation of multi-functional plasma-metamaterial composite for manipulation of electromagnetic-wave propagation. J. Appl. Phys. **130**, 043301 (2021)

42. Zhou, X., Xu, G., Zhang, H.: Binary masses manipulation with composite bilayer metamaterial. Compos. Struct. **267**, 113866 (2021)
43. Restrepo-Flórez, J.M., Maldovan, M.: Mass separation by metamaterials. Sci. Rep. **6**, 21971 (2016)
44. Hu, R., Iwamoto, S., Feng, L., Ju, S., Hu, S., Ohnishi, M., Nagai, N., Hirakawa, K., Shiomi, J.: Machine-learning-optimized aperiodic superlattice minimizes coherent phonon heat conduction. Phys. Rev. X **267**, 021050 (2020)
45. Narayana, S., Sato, Y.: DC magnetic cloak. Adv. Mater. **24**, 71–74 (2012)
46. Lan, C., Yang, Y., Geng, Z., Li, B., Zhou, J.: Electrostatic field invisibility cloak. Sci. Rep. **5**, 16416 (2015)
47. Huang, C.W., Chen, Y.C., Nishimura, Y.: Particle-in-cell simulation of plasma sheath dynamics with kinetic ions. IEEE T. Plasma Sci. **43**, 675–682 (2015)
48. Yu, Z.Z., Xiong, G.H., Zhang, L.F.: A brief review of thermal transport in mesoscopic systems from nonequilibrium Green's function approach. Front. Phys. **16**, 43201 (2015)
49. Xing, G., Zhao, W., Hu, R., Luo, X.: Spatiotemporal modulation of thermal emission from thermal-hysteresis vanadium dioxide for multiplexing thermotronics functionalities. Chin. Phys. Lett. **38**, 124401 (2021)
50. Torrent, D., Poncelet, O., Batsale, J.-C.: Nonreciprocal thermal material by spatiotemporal modulation. Phys. Rev. Lett. **120**, 125501 (2018)
51. Zang, J.W., Correas-Serrano, D., Do, J.T.S., Liu, X., Alvarez-Melcon, A., Gomez-Diaz, J.S.: Nonreciprocal wavefront engineering with time-modulated gradient metasurfaces. Phys. Rev. Appl. **11**, 054054 (2019)
52. Guo, X.X., Ding, Y.M., Duan, Y., Ni, X.J.: Nonreciprocal metasurface with space-time phase modulation. Light-Sci. Appl. **8**, 123 (2019)
53. Camacho, M., Edwards, B., Engheta, N.: Achieving asymmetry and trapping in diffusion with spatiotemporal metamaterials. Nat. Commun. **11**, 3733 (2020)
54. Li, J., Li, Y., Cao, P.-C., Qi, M., Zheng, X., Peng, Y.-G., Li, B., Zhu, X.-F., Alù, A., Chen, H., Qiu, C.-W.: Thermal reciprocity in metamaterials. Nat. Commun. **13**, 167 (2022)
55. Liu, Z.F., Huang, J.P.: Topological plasma transport from a diffusion view. Chin. Phys. Lett. **40**, 110305 (2023)
56. Gong, Z.P., Ashida, Y., Kawabata, K., Takasan, K., Higashikawa, S., Ueda, M.: Topological phases of non-Hermitian systems. Phys. Rev. X **8**, 031079 (2018)
57. Kawabata, K., Shiozaki, K., Ueda, M., Sato, M.: Symmetry and topology in non-Hermitian physics. Phys. Rev. X **9**, 041015 (2019)
58. Hasan, M.Z., Kane, C.L.: Colloquium: Topological insulators. Rev. Mod. Phys. **82**, 3045 (2010)
59. Qi, X.-L., Zhang, S.-C.: Topological insulators and superconductors. Rev. Mod. Phys. **83**, 1057 (2011)
60. Lu, L., Joannopoulos, J.D., Soljačić, M.: Topological photonics. Nat. Photonics **8**, 821 (2014)
61. Ozawa, T., Price, H.M., Amo, A., Goldman, N., Hafezi, M., Lu, L., Rechtsman, M.C., Schuster, D., Simon, J., Zilberberg, O., Carusotto, I.: Topological photonics. Rev. Mod. Phys. **91**, 015006 (2019)
62. Yang, Z.J., Gao, F., Shi, X.H., Lin, X., Gao, Z., Chong, Y.D., Zhang, B.L.: Topological acoustics. Phys. Rev. Lett. **114**, 114301 (2015)
63. Xue, H.R., Yang, Y.H., Zhang, B.L.: Topological acoustics. Nat. Rev. Mater. **7**, 974 (2022)
64. Huber, S.D.: Topological mechanics. Nat. Phys. **12**, 621 (2016)
65. Parker, J.B.: Topological phase in plasma physics. J. Plasma Phys. **87**, 835870202 (2021)

Chapter 19
Summary and Prospect

Fubao Yang and Jiping Huang

19.1 Summary

This book encompasses eighteen chapters dedicated to elucidating the concept of "diffusionics." The content is systematically organized into three distinct segments. The initial segment, comprising the parts I-IV, delves into the realm of metamaterials in the context of thermal diffusion processes. This section provides a detailed exploration of transformation thermotics and thermal metamaterials. The subsequent segments, encompassing parts V and VI, extend the discourse to metamaterials pertinent to particle diffusion and plasma diffusion, respectively. This comprehensive treatise offers an in-depth overview of the latest advancements in diffusion metamaterials, emphasizing aspects of heat diffusion, particle dynamics, and plasma transport. By integrating foundational theories, computational simulations, and laboratory experiments related to diffusion metamaterials, this book endeavors to serve as an impetus for pioneering innovations at the intersection of physics, thermodynamics, and materials science, and a primer for readers interested in this fast growing field.

19.2 Prospect

Since 2008, notable advancements have been made in the field of diffusionics, yet significant challenges persist. Transformation theory often yields anisotropic and singular transformed parameters, complicating practical realization due to the current

F. Yang (✉) · J. Huang (✉)
Department of Physics, Key Laboratory of Micro and Nano Photonic Structures (MOE), and State Key Laboratory of Surface Physics, Fudan University, Shanghai 200438, China
e-mail: 18110190009@fudan.edu.cn

J. Huang
e-mail: jphuang@fudan.edu.cn

F.-B. Yang and J.-P. Huang, *Diffusionics*,
https://doi.org/10.1007/978-981-97-0487-3_19

limitations of material science. The inaccessibility of extremely high parameters hampers the performance of designed diffusion metamaterials. Additionally, current research on multifunctional and intelligent diffusion metadevices involving multiple physical fields is inadequate. Such devices promise enhanced performance and new capabilities, but the lack of comprehensive studies hinders progress. Addressing these complexities and knowledge gaps is essential for the evolution of diffusionics into a more robust and application-ready field.

Furthermore, the focus of most diffusion metamaterial research has traditionally emphasized macroscopic physical properties, while studies at the micro- and nano-scales have been notably less frequent [1, 2]. Delving into the phonon diffusion at these smaller scales could significantly advance the field, as phonons play a pivotal role in thermal transport in materials [3–6]. At these dimensions, the interfacial thermal resistance becomes a dominant factor in heat transfer. This resistance is mainly a consequence of disparities in air gaps and the lattice structures of adjoining materials [7–10]. Although this effect can be negligible in bulk materials [11, 12], it cannot be ignored at the micro- and nano-scales. In such scenarios, even minor lattice mismatches can have a pronounced impact on the thermal conductivity of materials. Research into understanding and controlling interfacial thermal resistance could thus lead to the development of more effective thermal management systems and inform the design of next-generation metamaterials with tailored thermal properties [10].

Diffusionics can intuitively realize phenomena more challenging in wave systems, such as anti-parity-time symmetry implementation due to natural dissipation [13]. Besides, implementing various topological states is a burgeoning trend, with topological wave metamaterials inspiring topological thermal metamaterials [14, 15]. Floquet thermal metamaterials, created by spatiotemporal modulation of material parameters [16], and higher-dimensional non-Hermitian topology in diffusion systems [17, 18], are also emerging interests. In addition, recent advances in diffusive pseudo-conformal mapping have bridged transformation thermotics and scattering cancellation [19], once thought to be disparate mechanisms for crafting diffusion metamaterials. This approach uses an angle-preserving mapping to align transformation thermotics with scattering cancellation parameters, particularly in the design of bilayer cloaks. As a result, the anisotropic parameters typically required by transformation thermotics can be bypassed, eliminating the need to directly solve diffusion equations. This streamlined method represents a significant step forward, simplifying the design of diffusion metamaterials and potentially transforming wave manipulation technology.

Although diffusionics encompasses fundamental theories, more practical applications are needed. For example, with nanotechnology's rapid advancement, one of the future goals for thermal metamaterials are device versatility and miniaturization. Regarding mass diffusion, the challenge lies in the imperfect applicability of transformation theory to transient cases, and fortunately the optimized transformation theory shows promise [20]. This paves the way for devices analogous to those in thermal systems. Many functional devices in thermal systems can be adapted for mass diffusion systems, enhancing mass diffusion metamaterials for applications like drug transport [21], particle separation [20, 22], protein diffusion inside bacte-

ria [23], and metastatic diffusion of cancer [24, 25]. For plasma physics, it has been pivotal in spawning novel technologies and methodologies, notably in the realms of energy transduction and the advancement of materials for storage applications [26]. Theoretical advances in transformation optics have been applied to plasma science, providing fresh insights into the control and regulation of plasma behavior [27]. This interdisciplinary approach has paved the way for the creation of highly functional plasma-based metamaterials and metadevices by integrating principles from diffusionics, such as targeted plasma cloaks for medical applications and concentrators to boost catalytic reactions. Although practical realization remains challenging, techniques like scattering cancellation present viable alternatives for achieving the desired effects in plasma manipulation. Beyond the realms of energy and mass diffusion, the spread of information emerges as a distinct phenomenon. Though not strictly a physical process, the propagation of information can still be effectively described using the mathematical language of physics [28–30]. Envisioning information as akin to a molecular gas moving across a gradient allows us to explore the possibilities of directing its flow using physical paradigms, drawing on the fundamentals of transformation theory.

Moreover, as the structural design of metamaterial devices becomes increasingly complex and functional demands escalate, the physical models of metamaterial devices have become too intricate to be solved by rigorous mathematical models alone, necessitating the use of optimization algorithms. Artificial intelligence algorithms can assist in designing and optimizing the structure of metamaterials to achieve enhanced performance and higher efficiency. For instance, deep learning algorithms can be employed to identify the microstructures and material compositions of metamaterials and to predict their physical and mechanical properties. Furthermore, intelligent diffusion metamaterials possess multifunctionality, strong adaptability, high energy efficiency, and sustainability. The integration of artificial intelligence algorithms in the design of intelligent diffusion metamaterials represents a cutting-edge and future-focused area of research [31].

This book focuses on three types of diffusion systems: thermal diffusion, particle diffusion, and plasma diffusion. Currently, research on the thermal diffusion system still dominates the field of diffusionics. Further in-depth research will be conducted on the existing particle diffusion system and plasma diffusion system, and the research work will be extended to more types of diffusion systems in the future. Considering the fruitful achievements already made in the thermal diffusion system, the upcoming research is clearly highly anticipated. After all, the methodology presented in this book can be equally applied to handle more diffusion systems that can be described by (generalized) diffusion equations.

In conclusion, diffusionics has made remarkable strides in recent times [32], yet it remains a considerable journey away from realizing large-scale engineering applications and demands further progression. The exploration into the diffusion metamaterials is in its early stages. Unquestionably, the horizon for diffusionics is luminous, harboring promise in the realms of fundamental research, practical applications, and in its potential to make a profound impact across diverse domains.

References

1. Ye, Z.-Q., Cao, B.-Y.: Nanoscale thermal cloaking in graphene via chemical functionalization. Phys. Chem. Chem. Phys. **18**, 32952 (2016)
2. Choe, H.S., Prabhakar, R., Wehmeyer, G., Allen, F.I., Lee, W., Jin, L., Li, Y., Yang, P.D., Qiu, C.-W., Dames, C., Scott, M., Minor, A., Bahk, J.-H., Wu, J.Q.: Ion write microthermotics: Programing thermal metamaterials at the microscale. Nano Lett. **19**, 3830–3837 (2019)
3. Gu, X.K., Wei, Y.J., Yin, X.B., Li, B.W., Yang, R.G.: Thermal management and non-reciprocal control of phonon flow via optomechanics. Nat. Commun. **9**, 1207 (2018)
4. Seif, A., DeGottardi, W., Esfarjani, K., Hafezi, M.: Thermal management and non-reciprocal control of phonon flow via optomechanics. Nat. Commun. **9**, 1207 (2018)
5. Hu, R., Luo, X.: Two-dimensional phonon engineering triggers microscale thermal functionalities. Natl. Sci. Rev. **6**, 1071–1073 (2019)
6. Gandolfi, M., Giannetti, C., Banfi, F.: Temperonic crystal: A superlattice for temperature waves in graphene. Phys. Rev. Lett. **125**, 265901 (2020)
7. Li, J., Gao, Y., Huang, J.: A bifunctional cloak using transformation media. J. Appl. Phys. **108**, 074504 (2010)
8. Canbazoglu, F.M., Vemuri, K.P., Bandaru, P.R.: Estimating interfacial thermal conductivity in metamaterials through heat flux mapping. Appl. Phys. Lett. **106**, 143904 (2015)
9. Zheng, X., Li, B.W.: Effect of interfacial thermal resistance in a thermal cloak. Phys. Rev. Appl. **13**, 024071 (2020)
10. Chen, J., Xu, X.F., Zhou, J., Li, B.W.: Interfacial thermal resistance: Past, present, and future. Rev. Mod. Phys. **94**, 025002 (2022)
11. Narayana, S., Sato, Y.: Heat flux manipulation with engineered thermal materials. Phys. Rev. Lett. **108**, 214303 (2012)
12. Schittny, R., Kadic, M., Guenneau, S., Wegener, M.: Experiments on transformation thermodynamics: Molding the flow of heat. Phys. Rev. Lett. **110**, 195901 (2013)
13. Anti-parity-time symmetry in diffusive systems: Li, Y., Peng, Y.-G., Han, L., Miri, M.-A., Li, W., Xiao, M., Zhu, X.-F., Zhao, J.l. Alú, A., Fan, S.H., Qiu, C.-W. Science **364**, 170–173 (2019)
14. Lu, L., Joannopoulos, J.D., Soljačić, M.: Topological photonics. Nat. Photon. **8**, 821–829 (2014)
15. Feng, L., El-Ganainy, R., Ge, L.: Non-Hermitian photonics based on parity-time symmetry. Nat. Photon. **11**, 752–762 (2017)
16. Yin, S.X., Galiffi, E., Alú, A.: Floquet metamaterials. eLight **2**, 8 (2022)
17. Zhang, X., Tian, Y., Jiang, J.-H., Lu, M.-H., Chen, Y.-F.: Observation of higher-order non-Hermitian skin effect. Nat. Commun. **12**, 5377 (2021)
18. Zhang, K., Yang, Z.S., Fang, C.: Universal non-Hermitian skin effect in two and higher dimensions. Nat. Commun. **13**, 2496 (2022)
19. Dai, G.L., Yang, F.B., Wang, J., Xu, L.J., Huang, J.P.: Diffusive pseudo-conformal mapping: Anisotropy-free transformation thermal media with perfect interface matching. Chaos, Solitons Fractals **174**, 113849 (2023)
20. Zhang, Z.R., Xu, L.J., Huang, J.P.: Controlling chemical waves by transforming transient mass transfer. Adv. Theory Simul. **5**, 2100375 (2022)
21. Guenneau, S., Puvirajesinghe, T.M.: Fick's second law transformed: One path to cloaking in mass diffusion. J. R. Soc. Interface **10**, 20130106 (2013)
22. Restrepo-Flórez, J.M., Maldovan, M.: Mass separation by metamaterials. Sci. Rep. **6**, 21971 (2016)
23. Sadoon, A.A., Oliver, W.F., Wang, Y.: Revisiting the temperature dependence of protein diffusion inside bacteria: Validity of the stokes-einstein equation. Phys. Rev. Lett. **129**, 018101 (2022)
24. Stacker, S.A., Caesar, C., Baldwin, M.E., Thornton, G.E., Williams, R.A., Prevo, R., Jackson, D.G., Nishikawa, S.-I., Kubo, H., Achen, M.G.: VEGF-D promotes the metastatic spread of tumor cells via the lymphatics. Nat. Med. **7**, 186–191 (2001)

25. Kennecke, H., Yerushalmi, R., Woods, R., Cheang, M.C.U., Voduc, D., Speers, C.H., Nielsen, T.O., Gelmon, K.: Metastatic behavior of breast cancer subtypes. J. Clin. Oncol. **28**, 3271–3277 (2010)
26. Liang, H.F., Ming, F.W., Alshareef, H.N.: Applications of plasma in energy conversion and storage materials. Adv. Energy Mater. **8**, 1801804 (2018)
27. Zhang, Z.R., Huang, J.P.: Transformation plasma physics. Chin. Phys. Lett. **39**, 075201 (2022)
28. Iribarren, J.L., Moro, E.: Impact of human activity patterns on the dynamics of information diffusion. Phys. Rev. Lett. **103**, 038702 (2009)
29. Zhang, Z.K., Liu, C., Zhan, X.-X., Lu, X., Zhang, C.-X., Zhang, Y.-C.: Dynamics of information diffusion and its applications on complex networks. Phys. Rep. **651**, 1–34 (2016)
30. Yurevich, P.A., Olegovich, M.A., Mikhailovich, S.V., Vasilievich, P.Y.: Modeling conflict in a social system using diffusion equations. SIMULATION **94**, 1053–1061 (2018)
31. Chen, J., Hu, S., Zhu, S., Li, T.: Metamaterials: From fundamental physics to intelligent design. Interdiscip. Mater. **2**, 5–29 (2023)
32. Yang, F.B., Zhang, Z.R., Xu, L.J., Liu, Z.F., Jin, P., Zhuang, P.F., Lei, M., Liu, J.R., Jiang, J.-H., Ouyang, X.P., Marchesoni, F., Huang, J.P.: Controlling mass and energy diffusion with metamaterials. Rev. Mod. Phys **96**, 015002 (2024)